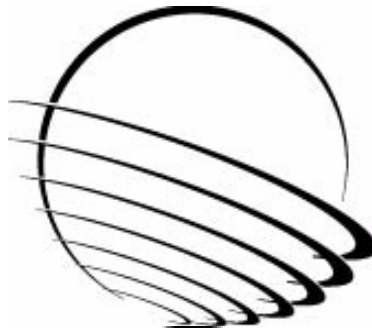


NASA/CP-2004-212073



37th Aerospace Mechanisms Symposium

Compiled by: Edward A. Boesiger



Proceedings of a symposium held at
Moody Gardens Hotel, Galveston, TX
Hosted by the Johnson Space Center and
Lockheed Martin Space Systems Company
Organized by the Mechanisms Education Association

May 19-21, 2004

The NASA STI Program Office . . . in Profile

Since its founding, NASA has been dedicated to the advancement of aeronautics and space science. The NASA Scientific and Technical Information (STI) Program Office plays a key part in helping NASA maintain this important role.

The NASA STI Program Office is operated by Langley Research Center, the lead center for NASA's scientific and technical information. The NASA STI Program Office provides access to the NASA STI Database, the largest collection of aeronautical and space science STI in the world. The Program Office is also NASA's institutional mechanism for disseminating the results of its research and development activities. These results are published by NASA in the NASA STI Report Series, which includes the following report types:

- **TECHNICAL PUBLICATION.** Reports of completed research or a major significant phase of research that present the results of NASA programs and include extensive data or theoretical analysis. Includes compilations of significant scientific and technical data and information deemed to be of continuing reference value. NASA's counterpart of peer-reviewed formal professional papers but has less stringent limitations on manuscript length and extent of graphic presentations.
- **TECHNICAL MEMORANDUM.** Scientific and technical findings that are preliminary or of specialized interest, e.g., quick release reports, working papers, and bibliographies that contain minimal annotation. Does not contain extensive analysis.
- **CONTRACTOR REPORT.** Scientific and technical findings by NASA-sponsored contractors and grantees.

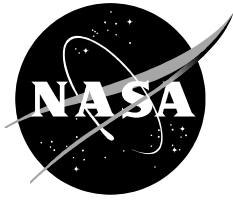
- **CONFERENCE PUBLICATION.** Collected papers from scientific and technical conferences, symposia, seminars, or other meetings sponsored or cosponsored by NASA.
- **SPECIAL PUBLICATION.** Scientific, technical, or historical information from NASA programs, projects, and mission, often concerned with subjects having substantial public interest.
- **TECHNICAL TRANSLATION.** English-language translations of foreign scientific and technical material pertinent to NASA's mission.

Specialized services that complement the STI Program Office's diverse offerings include creating custom thesauri, building customized databases, organizing and publishing research results . . . even providing videos.

For more information about the NASA STI Program Office, see the following:

- Access the NASA STI Program Home Page at <http://www.sti.nasa.gov>
- E-mail your question via the Internet to help@sti.nasa.gov
- Fax your question to the NASA Access Help Desk at (301) 621-0134
- Telephone the NASA Access Help Desk at (301) 621-0390
- Write to:
NASA Access Help Desk
NASA Center for AeroSpace Information
7121 Standard
Hanover, MD 21076-1320

NASA/CP-2004-212073



37th Aerospace Mechanisms Symposium

Compiled by: Edward A. Boesiger

Proceedings of a symposium held at
Moody Gardens Hotel, Galveston, TX
Hosted by the Johnson Space Center and
Lockheed Martin Space Systems Company
Organized by the Mechanisms Education Association

May 19-21, 2004

Available from:

NASA Center for AeroSpace Information
7121 Standard
Hanover, MD 21076-1320

National Technical Information Service
5285 Port Royal Road
Springfield, VA 22161

This report is also available in electronic form at <http://techreports.larc.nasa.gov/cgi-bin/NTRS>

PREFACE

The Aerospace Mechanisms Symposium (AMS) provides a unique forum for those active in the design, production and use of aerospace mechanisms. A major focus is the reporting of problems and solutions associated with the development and flight certification of new mechanisms. Organized by the Mechanisms Education Association, the National Aeronautics and Space Administration and Lockheed Martin Space Systems Company (LMSSC) share the responsibility for hosting the AMS. Now in its 37th symposium, the AMS continues to be well attended, attracting participants from both the U.S. and abroad.

The 37th AMS, hosted by the Johnson Space Center (JSC) in Galveston, Texas, was held May 19, 20 and 21, 2004. During these three days, 34 papers were presented. Topics included deployment mechanisms, tribology, actuators, pointing and optical mechanisms, Space Station and Mars Rover mechanisms, release mechanisms, and test equipment. Hardware displays during the supplier exhibit gave attendees an opportunity to meet with developers of current and future mechanism components.

The high quality of this symposium is a result of the work of many people, and their efforts are gratefully acknowledged. This extends to the voluntary members of the symposium organizing committee representing the eight NASA field centers, LMSSC, and the European Space Agency. Appreciation is also extended to the session chairs, the authors, and particularly the personnel at JSC responsible for the symposium arrangements and the publication of these proceedings. A sincere thank you also goes to the symposium executive committee who is responsible for the year-to-year management of the AMS, including paper processing and preparation of the program.

The use of trade names of manufacturers in this publication does not constitute an official endorsement of such products or manufacturers, either expressed or implied, by the National Aeronautics and Space Administration.

CONTENTS

Symposium Schedule	vii
Symposium Organizing and Advisory Committees.....	xi
A Description of Mechanisms used in the Low Resolution Airglow & Aurora Spectrograph.....	1
Philip Kalmanson, Russell Starks, Stefan Thonnard & Kenneth Dymond	
STEREO/SECCHI Coronagraph Hollow-Core Motor Development and Testing	15
Augustus Moore, Alexander Price, David Akin & Ralph Horber	
Design and Development of the Primary and Secondary Mirror Deployment Systems for the Cryogenic JWST	29
Paul Reynolds, Charlie Atkinson & Larry Gliman	
A Boresight Adjustment Mechanism for use on Laser Altimeters.....	45
Claef Hakun, Jason Budinoff, Gary Brown, Fil Parong & Armando Morell	
Deployment Mechanism for the Space Technology 5 Micro Satellite	59
Peter Rossoni, Caner Cooperrider & Gerard Durback	
Development of a Strain Energy Deployable Boom for the Space Technology 5 Mission.....	73
Stew Meyers & James Sturm	
Latch-up Anomaly Study for Reflector Deployment of INSAT-2E Satellite.....	87
G. Nagesh, S. Ravindran & N. Bhat	
A Strain Free Lock and Release Mechanism for an Elastically Suspended Two-Axis Gimbal	97
Armond Asadurian, Richard Pugh & Jim Hammond	
Force and Torque Margins for Complex Mechanical Systems.....	107
Robert Postma	
Establishing Adequate Performance Margin for Space Flight Stepper Motor Mechanisms.....	119
David Marks	
HST Solar Array 3 Latches	131
Mike Garrah	
Lessons Learned on Cryogenic Rocket Engine's Gimbal Bearing Lubrication Selection	137
Christian Neugebauer & Manfred Falkner	
The Integration of a Load Limiter to an Orbiter Over-Center Mechanism	143
Adam Gilmore & Tim Rupp	
Minimizing Torque Disturbance of Stepper Motors	147
Jim Sprunck	
SARA21 - A New Rotary Actuator for Space Applications	153
Olivier Secheresse, Laurent Cadiergues & Julien Rabin	
Rolamite Joints for Spacecraft Subsystem Vibration Isolation	163
Gregory Compton & Matthew Botke	
Free Space Optical Communications System Pointer.....	171
Mark Rosheim & Gerald Sauter	

Space Applications of MEMS: Initial Vacuum Test Results from the SwRI Vacuum Microprobe Facility.....	179
Philip Valek, D. McComas, G. Miller, J. Mitchell & S. Pope	
The Challenges of Designing the Rocker-Bogie Suspension for the Mars Exploration Rover	185
Brian Harrington & Chris Voorhees	
Deployment Process, Mechanization, and Testing for the Mars Exploration Rovers	197
Ted Iskenderian	
Development of Mars Exploration Rover Lander Petal Actuators	211
Boz Sharif & Ed Joscelyn	
Brake Failure from Residual Magnetism in the Mars Exploration Rover Lander Petal Actuator.....	221
Louise Jandura	
High Gain Antenna Gimbal for the 2003-2004 Mars Exploration Rover Program.....	237
Jeff Sokol, Satish Krishnan & Laoucet Ayari	
A Low Mass Translation Mechanism for Planetary FTIR Spectrometry using an Ultrasonic Piezo Linear Motor	251
Matthew Heverly, Sean Dougherty, Geoffrey Toon, Alejandro Soto & Jean-Francois Blavier	
Pancam Mast Assembly on Mars Rover.....	263
Robert Warden, Mike Cross & Doug Harvison	
Rock Abrasion Tool.....	277
Thomas Myrick, Kiel Davis & Jack Wilson	
Review of International Space Station Mechanical System Anomalies	291
David McCann	
Space Station Berthing Mechanisms.....	301
Robert Foster, John Cook, Paul Smudde & Mark Henry	
Mechanism Analysis and Verification Approach for ISS Truss Assembly.....	315
Wesley Bruner, Carlos Enriquez & Sreekumar Thampi	
Life of Scanner Bearings with Four Space Liquid Lubricants.....	333
Dean Bazinet, Mark Espinosa, Stuart Loewenthal, Lois Gschwender, William Jones, Jr. & Roamer Predmore	
Hubble Space Telescope Fine Guidance Sensor Post-Flight Bearing Inspection	343
Joe Pellicciotti; Stuart Loewenthal, William Jones, Jr. & M. Jumper	
Effect of Test Atmosphere on Moving Mechanical Assembly Test Performance.....	357
David Carre & P. Bertrand	
The X-38 V-201 Fin Fold Actuation Mechanism	363
Christian Lupo, Brandan Robertson & George Gafka	
The X-38 V-201 Flap Actuator Mechanism.....	377
Jeff Hagen, Landon Moore, Jay Estes & Chris Layer	

SYMPOSIUM SCHEDULE

WEDNESDAY, 19 MAY 2004

- 8:00 Wednesday Presenters' Breakfast – Vine I Room
- 8:00 **CHECK-IN AND REFRESHMENTS** – Group Registration Desk and South Ballroom Foyer
- 9:00 **INTRODUCTORY REMARKS** - Moody II Room
Christopher Hansen, Host Chairman
NASA Johnson Space Center, Houston, TX
Edward A. Boesiger, Operations Chairman
Lockheed Martin Space Systems Company, Sunnyvale, CA
- CENTER WELCOME
General Jefferson D. Howell Jr., Center Director
NASA Johnson Space Center, Houston, TX
- 9:30 **SESSION I – Instrument Mechanisms**
Robert Renken, Session Chair
Ball Aerospace & Technologies, Boulder, CO
- A Description of Mechanisms used in the Low Resolution Airglow & Aurora Spectrograph
Philip Kalmanson, Praxis, Inc., Alexandria, VA; Russell Starks, EVI Technology, Columbia, MD;
Stefan Thonnard & Kenneth Dymond, Naval Research Laboratory, Washington, D.C.
 - STEREO/SECCHI Coronagraph Hollow-Core Motor Development and Testing
Augustus Moore, Alexander Price & David Akin, Lockheed Martin Space Systems, Palo Alto, CA;
Ralph Horber, H. Magnetics Inc., Marshfield, MA
 - Design and Development of the Primary and Secondary Mirror Deployment Systems for the Cryogenic JWST
Paul Reynolds, Charlie Atkinson & Larry Gliman, Northrop Grumman Space Technology, Redondo Beach, CA
 - A Boresight Adjustment Mechanism for use on Laser Altimeters
Claef Hakun, Jason Budinoff, Gary Brown, Fil Parong & Armando Morell, NASA Goddard Space Flight Center, Greenbelt, MD
- 11:30 LUNCH BREAK – Box lunch is provided
- 12:45 **SESSION II – Release, Deploy and Margins**
Patrice Kerhousse, Session Chair
ESA/ESTec, Noordwijk, The Netherlands
- Deployment Mechanism for the Space Technology 5 Micro Satellite
Peter Rossoni, Caner Cooperrider & Gerard Durback, NASA Goddard Space Center, Greenbelt, MD
 - Development of a Strain Energy Deployable Boom for the Space Technology 5 Mission
Stew Meyers & James Sturm, NASA Goddard Space Center, Greenbelt, MD
 - Latch-up Anomaly Study for Reflector Deployment of INSAT-2E Satellite
G. Nagesh, S. Ravindran & N. Bhat, Indian Space Research Organization, Bangalore, India
 - A Strain Free Lock and Release Mechanism for an Elastically Suspended Two-Axis Gimbal
Armond Asadurian, Richard Pugh & Jim Hammond, Moog, Inc., Chatsworth, CA
 - Force and Torque Margins for Complex Mechanical Systems
Robert Postma, The Aerospace Corporation, El Segundo, CA
 - Establishing Adequate Performance Margin for Space Flight Stepper Motor Mechanisms
David Marks, Moog, Inc., Durham, NC
- 3:45 BREAK

4:00 **Announcement – Moving Mechanical Assemblies Standard for Space and Launch Vehicles**
Brian Gore
The Aerospace Corporation, El Segundo, CA

4:15 **SESSION III – Poster Preview**

Kornel Nagy, Session Chair

Johnson Space Center, Houston, TX

- HST Solar Array 3 Latches

Mike Garrah, Swales Aerospace, Beltsville, MD

- Lessons Learned on Cryogenic Rocket Engine's Gimbal Bearing Lubrication Selection

Christian Neugebauer & Manfred Falkner, Austrian Aerospace GmbH, Vienna, Austria

- The Integration of a Load Limiter to an Orbiter Over-Center Mechanism

Adam Gilmore & Tim Rupp, NASA Johnson Space Center, Houston, TX

- Minimizing Torque Disturbance of Stepper Motors

Jim Sprunck, Starsys Research Corporation, Boulder, CO

- SARA21 - A New Rotary Actuator for Space Applications

Olivier Secheresse, SNECMA Moteurs, Cramayel, France; Laurent Cadiergues, CNES,

Toulouse, France; Julien Rabin, ACSIENCE, Paris, France

- Rolamite Joints for Spacecraft Subsystem Vibration Isolation

Gregory Compton & Matthew Botke, ABLE Engineering, Goleta, CA

- Free Space Optical Communications System Pointer

Mark Rosheim & Gerald Sauter, Ross-Hime Designs, Inc., Minneapolis, MN

- Space Applications of MEMS: Initial Vacuum Test Results from the SwRI Vacuum Microprobe Facility

Philip Valek, D. McComas, G. Miller, J. Mitchell & S. Pope, Southwest Research Institute, San Antonio, TX

6:30-9:30 **RECEPTION & DISPLAYS AT THE MOODY GARDENS AQUARIUM**

Invited component and software suppliers display current products and provide tutorials.

THURSDAY, 20 MAY 2004

7:15 Thursday Presenters' Breakfast - Vine I Room

7:45 Light Refreshments - South Ballroom Foyer

8:15 **SESSION IV - Mars I - Moody II Room**

Randall Lindemann, Session Chair

Jet Propulsion Laboratory, Pasadena, CA

- The Challenges of Designing the Rocker-Bogie Suspension for the Mars Exploration Rover

Brian Harrington & Chris Voorhees, Jet Propulsion Laboratory, Pasadena, CA

- Deployment Process, Mechanization, and Testing for the Mars Exploration Rovers

Ted Iskenderian, Jet Propulsion Laboratory, Pasadena, CA

- Development of Mars Exploration Rover Lander Petal Actuators

Boz Sharif & Ed Joscelyn, Aeroflex Motion Control Products, Hauppauge, NY

- Brake Failure from Residual Magnetism in the Mars Exploration Rover Lander Petal Actuator

Louise Jandura, Jet Propulsion Laboratory, Pasadena, CA

10:15 BREAK

- 10:30 **SESSION V – Mars II**
 William Skullney, Session Chair
 Johns Hopkins University Applied Physics Laboratory, Laurel, MD
 • High Gain Antenna Gimbal for the 2003-2004 Mars Exploration Rover Program
 Jeff Sokol & Laoucet Ayari, Ball Aerospace & Technologies Corp., Boulder, CO; Satish Krishnan,
 Jet Propulsion Laboratory, Pasadena, CA
 • A Low Mass Translation Mechanism for Planetary FTIR Spectrometry using an Ultrasonic Piezo
 Linear Motor
 Matthew Heverly & Sean Dougherty, Alliance Spacesystems Inc., Pasadena, CA; Geoffrey Toon,
 Alejandro Soto & Jean-Francois Blavier, Jet Propulsion Laboratory, Pasadena, CA
 • Pancam Mast Assembly on Mars Rover
 Robert Warden, Mike Cross & Doug Harvison, Ball Aerospace & Technologies Corp., Boulder,
 CO
 • Rock Abrasion Tool
 Thomas Myrick, Kiel Davis & Jack Wilson, Honeybee Robotics, New York, NY
- 12:30 LUNCH BREAK – Box lunch is provided
- 1:30 **SESSION VI – ISS**
 Scott West, Session Chair
 The Boeing Company, Houston, TX
 • Review of International Space Station Mechanical System Anomalies
 David McCann, The Boeing Company, Houston, TX
 • Space Station Berthing Mechanisms
 Robert Foster & John Cook, The Boeing Company, Houston, TX; Paul Smudde, The Boeing
 Company, Huntington Beach, CA; Mark Henry, The Boeing Company, Huntsville, AL
 • Mechanism Analysis and Verification Approach for ISS Truss Assembly
 Wesley Bruner, Carlos Enriquez & Sreekumar Thampi, The Boeing Company, Houston, TX
 • International Space Station Solar Array Wing Deployment Anomaly Resolution
 David McCann, The Boeing Company, Houston, TX
- 3:30 BREAK
- 3:45 **SPECIAL PRESENTATION – NASA Astronaut**
 Joe Tanner will give his insights into using and handling mechanisms in space. A veteran of three
 space flights, Tanner has logged over 742 hours in space, including over 33 EVA hours in 5
 space walks including those for HST servicing and installing the Space Station solar arrays.
- 5:30-10:30 **SYMPOSIUM BANQUET AT LONE STAR FLIGHT MUSEUM**
- 5:30 Walk to Moody Gardens 3-D IMAX Theater
- 7:00 Tram to Lone Star Flight Museum – Bar-B-Que Dinner, Band & Displays
 Entertainment provided by Ezra Charles and the Works
- 10:00 Return to the hotel via tram

FRIDAY, 21 MAY 2004

7:30 Friday Presenters' Breakfast – Vine I Room

8:00 Light Refreshments - South Ballroom Foyer

8:30 **SESSION VII – TRIBOLOGY/DEPLOYMENT** - Moody II Room

Lois Gschwender, Session Chair

Air Force Research Laboratory, Dayton, OH

• Life of Scanner Bearings with Four Space Liquid Lubricants

Dean Bazinet, Mark Espinosa & Stuart Loewenthal, Lockheed Martin Space Systems, Sunnyvale, CA; Lois Gschwender, Air Force Research Laboratory, Dayton, OH; William Jones, Jr., SEST Inc., Middleburg Heights, OH; Roamer Predmore, Swales Aerospace, Beltsville, MD

• Hubble Space Telescope Fine Guidance Sensor Post-Flight Bearing Inspection

Joe Pellicciotti, NASA Goddard Space Center, Greenbelt, MD; Stuart Loewenthal, Lockheed Martin Space Systems, Sunnyvale, CA; William Jones, Jr., SEST Inc., Middleburg Heights, OH; M. Jumper, BEI Precision Systems & Space Division, Maumelle, AR

• Effect of Test Atmosphere on Moving Mechanical Assembly Test Performance

David Carre & P. Bertrand, The Aerospace Corporation, El Segundo, CA

• The X-38 V-201 Fin Fold Actuation Mechanism

Christian Lupo, Brandan Robertson & George Gafka, NASA Johnson Space Center, Houston, TX

• The X-38 V-201 Flap Actuator Mechanism

Jeff Hagen, Lockheed Martin Space Operations, Houston, TX; Landon Moore & Jay Estes, NASA Johnson Space Center, Houston, TX; Chris Layer, Moog, Inc., East Aurora, NY

11:00 **PRESENTATION: An Overview of JSC**

11:45 **TECHNICAL SESSIONS CONCLUSION**

• PRESENTATION OF THE HERZL AWARD

• CLOSING REMARKS

Stuart H. Loewenthal, General Chairman

Lockheed Martin Space Systems Company, Sunnyvale, CA

1:30 **BUSES DEPART HOTEL FOR JSC TOUR**

2:00-4:00 **JOHNSON SPACE CENTER FACILITY TOUR**

SYMPOSIUM ORGANIZING COMMITTEE

Christopher P. Hansen, Host Chairman, NASA JSC

Stuart H. Loewenthal, General Chairman, Lockheed Martin
Edward A. Boesiger, Operations Chairman, Lockheed Martin

Obie H. Bradley, Jr., NASA LRC
Carlton L. Foster, NASA MSFC
Claf F. Hakun, NASA GSFC
Patrice Kerhousse, ESA/ESTeC
Alan C. Littlefield, NASA KSC
Edward C. Litty, JPL
Fred G. Martwick, NASA ARC
Martha E. Milton, NASA MSFC
Wilfredo Morales, NASA GRC
Robert P. Mueller, NASA KSC
Fred B. Oswald, NASA GRC
Minh Phan, NASA GSFC
Donald R. Sevilla, JPL
Mark F. Turner, NASA ARC
James E. Wells, NASA LRC

SYMPOSIUM ADVISORY COMMITTEE

David F. Engelbert, NASA ARC (ret)
Robert L. Fusaro, NASA GRC (ret)
Ronald E. Mancini, NASA ARC (ret)
Stewart C. Meyers, NASA GSFC
John W. Redmon, Sr., NASA MSFC (ret)
William C. Schneider, NASA JSC (ret)
Bowden W. Ward, Jr., NASA GSFC (ret)

A Description of Mechanisms used in the Low Resolution Airglow & Aurora Spectrograph

Phillip Kalmanson^{*}, Russell Starks⁺, Stefan Thonnard^{**} and Kenneth Dymond^{**}

Abstract

The Low Resolution Airglow & Aurora Spectrograph (LORAAS) was an aeronomy Instrument designed by the Naval Research Laboratory (NRL). LORAAS was launched into polar orbit on February 23, 1999 aboard the ARGOS spacecraft and operated successfully until the shutdown of the spacecraft in April of 2002. Data gained from the on-orbit performance of the LORAAS mechanisms will be presented along with the performance data taken during ground testing.

There were three mechanisms used in LORASS design and are as follows; a guillotine style dust cover door assembly (DCDA), a one-axis scan mirror assembly (SMA), and a detector door mechanism (DDM). These mechanisms are unique in that they must all adhere to the stringent requirements of contamination control due to the sensitivity of the optics used. In addition to supporting instrument operation while in space, some of these mechanisms, such as the DDM and DCDA, were essential for instrument operation while on the ground to aid in instrument construction, calibration and storage. This paper will present a description of the aforementioned mechanisms including an overview of the requirements driving their design, analysis performed on the mechanisms and their components, and final costs.

Introduction

LORAAS was built and designed by the NRL to observe the diffuse airglow emitted by the thermosphere and ionosphere region of the atmosphere at altitudes between 70 and 700 km. The LORAAS passband operated in the Far Ultraviolet (FUV) and Extreme Ultraviolet (EUV) range between 80 – 170 nm. The data obtained by LORAAS was used for studies of upper atmospheric structure, composition, and sun-earth interaction.



Figure 1. LORAAS Instrument

^{*} Praxis Inc., Alexandria, Virginia

^{**} Naval Research Laboratory, Washington D.C.

⁺ Formerly with Praxis Inc. – Now With EVI Technology, Columbia, Maryland

Instrument Overview

The LORAAS instrument was comprised of four main components; the Ultraviolet Spectrograph Assembly (USA), the control electronics, the high voltage power supply (HVPS), and the harness assembly. The USA contains the optical bench and the mechanisms used on the instrument that support the optics. Mounted separately from the USA, the control electronics contain the circuits used to provide power and control to the mechanisms. The high voltage power supply is used to provide the high voltage necessary to operate the wedge and strip style FUV/EUV detector located in the USA. The wire harness provides the necessary power and signal connections between the control electronics, mechanisms, detector, and HVPS. Although each of the main components can be further broken down into subcomponents, only the USA will be discussed in detail.

Ultraviolet Spectrograph Assembly

The optical design of the USA is a 0.25-m focal length f/3 spectrograph in a near-Wadsworth configuration¹. The optical components as shown in Figure 2 are: a one-axis scan mirror assembly (SMA), a mechanical grid collimator, a diffraction grating, and an imaging detector. The mechanisms supporting the optics are the Dust Cover Door Assembly (DCDA), the Detector Door mechanism (DDM). Also mounted to the USA but not shown are the sunshade, sun sensors, and the detector electronics. The Spectrograph had a Field Of View (FOV) defined by the collimator of 0.15-degree Full Width at Half Maximum (FWHM) in the vertical direction and 2.4 degrees FWHM in the horizontal direction. This FOV translated in to an image resolution of 5 km by 120 km on the earth's limb as viewed by the LORAAS instrument while on orbit.

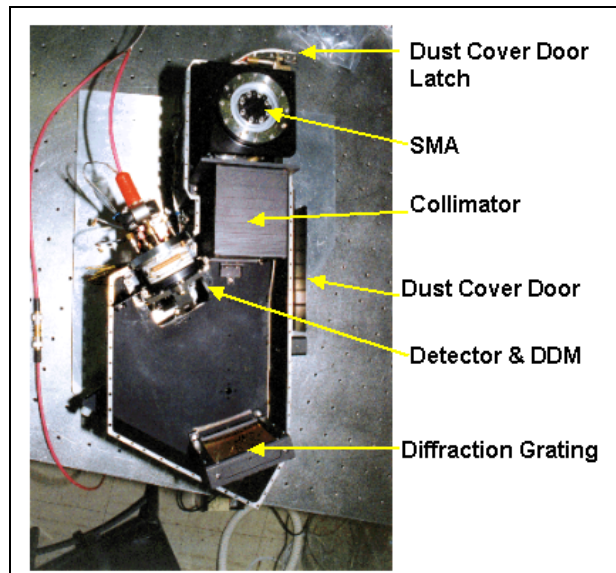


Figure 2. Inside of USA with Cover and Sun Shade Removed

Scan Mirror Assembly

Design

The SMA defined the instrument Field Of Regard by rotating a counterweighted silicon carbide mirror measuring 128 mm X 90 mm with a mass of approximately 0.41 kg. The SMA components are shown in Figure 3. In addition to being able to survive the operational and lifetime requirements the following drove the design of the SMA, the SMA must:

- Rotate a scan mirror from -5 to -13.5 degrees in 90 seconds and return the mirror back to its starting position in under 5 seconds. (This motion was part of the normal operating mode)
- Be able to rotate the scan mirror to -20 degrees (This motion was required only rarely)
- Provide an accuracy of mirror pointing knowledge to ± 0.017 degree.

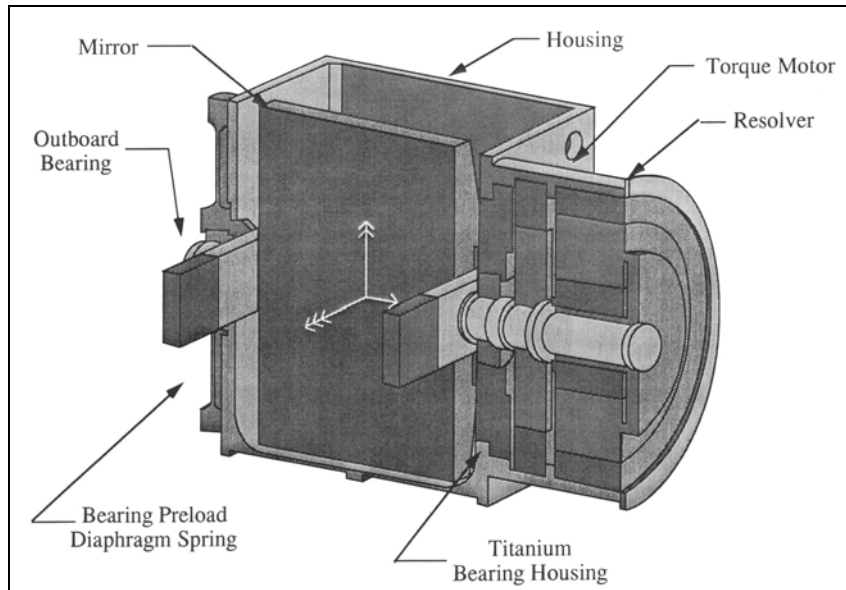


Figure 3. Scan Mirror Assembly Component Layout

The unique quality of the SMA was its ability to provide stable and continuous scans for the duration of the mission. The stability of the SMA was in simplicity of construction. All the moving parts, i.e. the mirror, motor rotor, and resolver rotor, share a common shaft supported by two ball bearings forming one of the two main subassemblies. By using a common shaft configuration the SMA was also able to eliminate any errors in position due to backlash as well as reduce single point failure areas. The scan mirror is attached to the shaft through the use of flexure mounts joined to the mirror's structural ribs. Early in the design stepper motors were considered but were ruled out due to concerns in lifetime.

Mirror Actuation is provided by a limited rotation, brushless, samarium cobalt permanent magnet torque motor with redundant windings. A limited rotation motor was used to achieve zero ripple torque. Torque for the motor ranged from 0.085 N-m/Amp at the null position to 0 at ± 50 degrees. Positional feedback is provided by a 16-speed brushless resolver with redundant windings with an accuracy of ± 20 arcseconds over 22.5 degrees.

The other subassembly was the housing, which supported the ball bearings and contained the stators of the motor and resolver. Two separable race ball bearings supported the rotor on either side of the scan mirror, inboard closest to the motor and outboard farthest from the motor. The bearing housing for the SMA was made from titanium to match the thermal expansion of the bearings. Bearing preload was achieved through the use of a diaphragm spring on the outboard side and adjusted with shims. To reduce the amount of frictional torque the axial preload was kept low.

During operation, images were acquired while the mirror scanned and while the SMA held the mirror at fixed position. Normal operation involved scan speeds ranging from 0.14 to 0.28 degree/second followed by a return to starting position at 6 degrees/second¹. The control system diagram is shown in Figure 4. As can be seen the SMA operated with a closed loop system using software component models and filters to modulate the control signal for maximum stability.

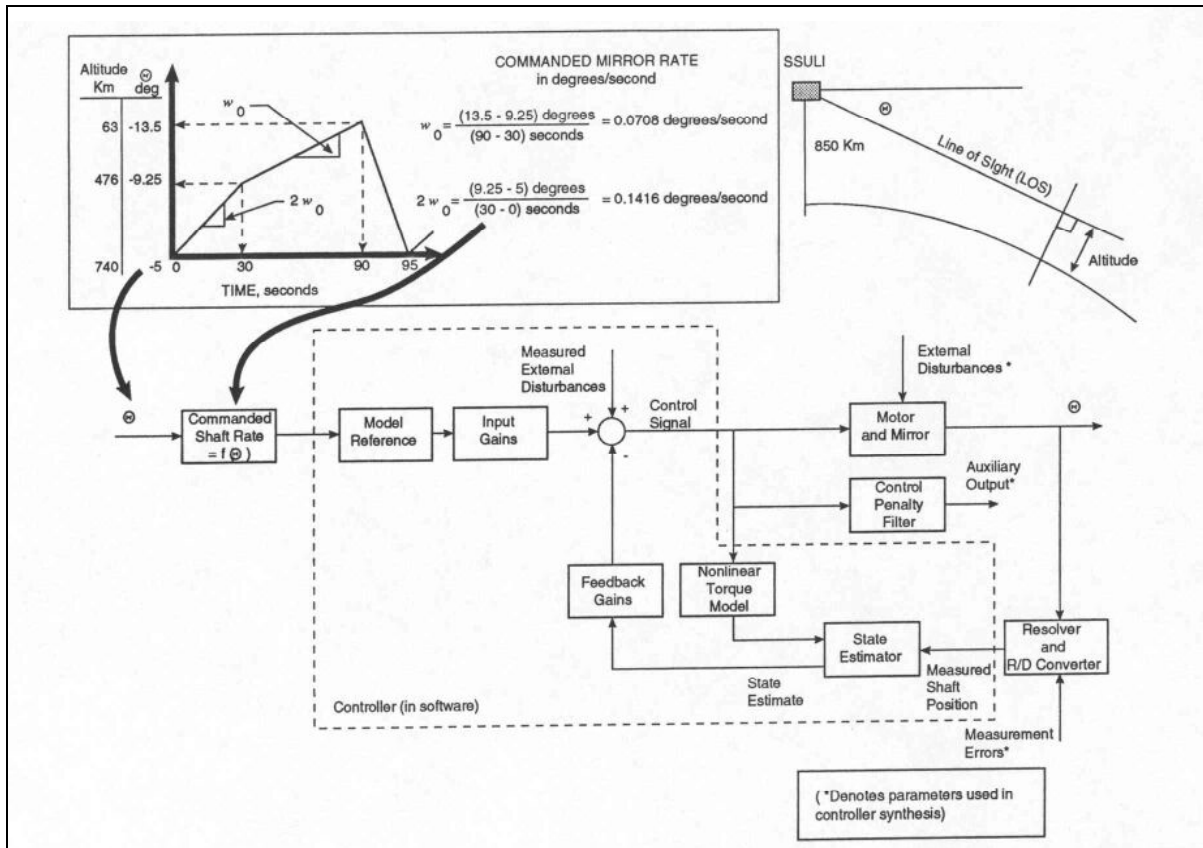


Figure 4. SMA Control System Diagram

Testing

In order to decrease the time needed for lifetime tests to fit within the program schedule, two parallel tests were run on two mechanisms. It was determined that a single accelerated test would not be accurate enough to determine the SMA's behavior while in operation. One test was an accelerated test and the other was a test duplicating on-orbit scanning. These tests were performed in vacuum and primarily measured two signatures; average motor current to determine any change in mechanical characteristics, and frequency content to determine if any bearing degradation occurred.

Another test conducted on the SMA was tensile testing of the joints between the mirror and its flexure mounts. During this testing several catastrophic failures occurred resulting in the loss of several mirrors. These failures were due to incorrectly estimated values of the mirror tensile strength. First numbers used for tensile strength of Sintered Silicon Carbide 227.5E3 kPa did not take into account the wide variability of the material from 90E3 kPa to 345E3 kPa. After an in-house analysis, which incorporated margins, 62E3 kPa was chosen to represent the tensile strength of the mirror. This new number then resulted in a design change of how the mirror mounts were attached to spread the load over a greater area.

SMA On-Orbit Performance

The performance of the SMA on orbit was most often determined primarily by measuring the known position of a star with the expected position of the SMA. Unfortunately, this method would be accurate to within a few tenths of a degree due to the nature of the optics. In addition, for the LORAAS mission, any errors that were less than 0.1 degree would be unnoticeable anyway due to larger errors from the attitude determination of the ARGOS spacecraft. ARGOS horizon sensors provide spacecraft's attitude with fluctuation up to 0.2 degree with one sigma error. As for mechanism state of health the down-linked telemetry included resolver errors as well as torque motor current. During the entirety of the mission errors occurred that would have compromised the instrument data beyond that due the spacecraft attitude control system.

In addition to the scanning mirror mechanism, the nature of the optics and detectors used for the EUV and FUV necessitate having two other mechanisms used by LORAAS, the DCDA and the DDM.

Dust Cover Door Assembly

As with all optics, contamination from dirt and hydrocarbons is an issue that deserves special attention. The sensitivity of VUV optics to contamination is greater than for optics in other wavelengths especially when the contamination arises from thin layers of oils or other hydrocarbons. A mirror with a hydrocarbon layer measuring on the order a few tens of angstroms thick can have its throughput reduced by as much as half in the reflected VUV. This sensitivity to contamination drives the need for the LORAAS one time activation dust cover door assembly, shown in Figure 5. Unlike most instrument doors the LORAAS DCDA is unique in that it uses a guillotine type of operation rather than a swing-away or clamshell type of operation. The driver for the guillotine operation was to preserve envelope constraints imposed by the rest of the spacecraft. The DCDA is also unique in that it uses no lubrication even though it is a sliding mechanism. The lack of lubricants was due to the sensitivity of the scan mirror to contamination. For this particular optic, a stray droplet of lubricant would cause more damage than a dust particle. Also unlike other door mechanisms, the DCDA is not mounted over the front aperture of the instrument instead it is mounted after the sunshade and therefore had additional constraints imposed on it by the sunshade mounting scheme and structure. The use of the guillotine-type door required an extensive amount of analysis to be conducted to ensure satisfactory performance of the DCDA while on earth and in orbit. The result of this analysis was to determine operational temperatures, lifetimes, resistances due to friction, and operating margins for the actuation springs and door latch.

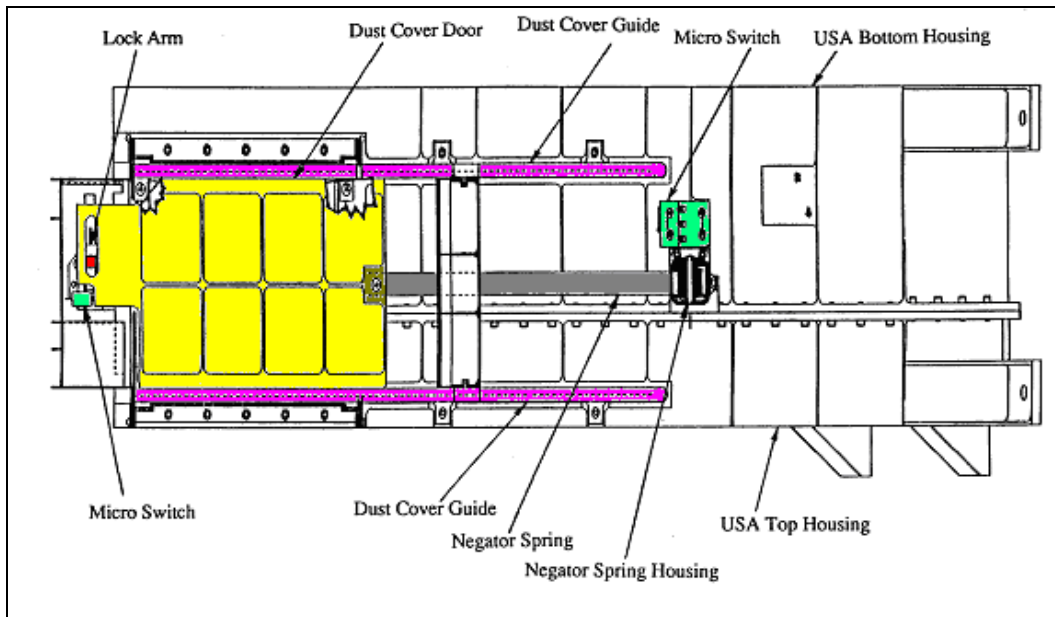


Figure 5. DCDA Component Layout

The DCDA consists of an Aluminum 6061-T6 plate that slides downward from the area between the USA and the sunshade. Two of the outer edges of the door are confined within aluminum tracks that constrain its motion downward along the USA. A wound metal strip called the negator spring as is shown in Figure 6 drives the motion of the door. During launch and storage the door is held in place by a lock arm as shown in Figure 6. The lock arm is rotated out the door-latching hole by a Starsys Research Corporation paraffin actuator with redundant heaters. DCDA status is monitored by three sets of hermetically sealed microswitches. One microswitch is located in the latching system for lock arm rotation status. The second and third set of microswitches, a primary and backup unit is located at the door limits of travel and confirms that the door is either fully closed or fully open.

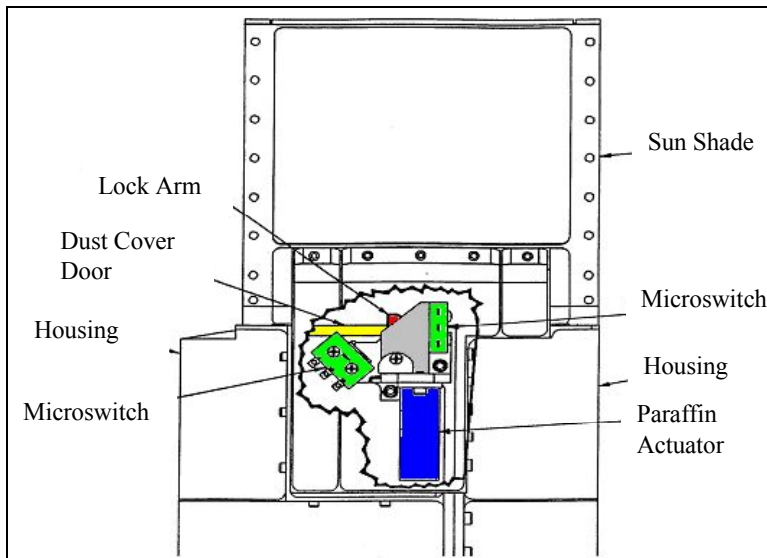


Figure 7. DCDA Latching System Components

In designing the DCDA analysis was done to aid in sizing the negator spring and latching system. The analysis shown in Figure 7 was used to determine the negator spring size. Shown along the curved lines are spring margins at different values of coefficients of friction between aluminum on aluminum. Three curved lines are plotted for springs that exerted different values of force on the door at its closed position. The design margin of 250% is plotted as the thick horizontal line in the lower portion of the graph. The high margin helps to ensure successful opening of the DCDA by providing enough force to overcome any higher than normal frictional forces. The higher frictional forces may occur from sticking or mild galling from using similar metals in sliding contact. To help minimize the shock from opening, the spring margin was not raised higher than what is listed. Any spring which exerts more than 2.2 N of force upon the door at closed position operates a 250% margin or above. This analysis helped to reduce the size of the negator spring by 10% from what was detailed in earlier designs.

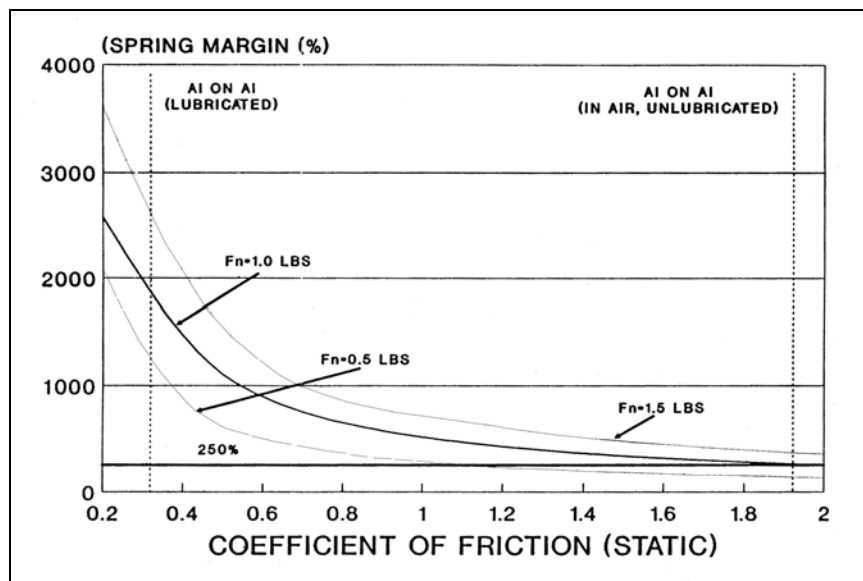


Figure 7. DCDA Door Slide Spring Margins

Another analysis was done to determine how the negator spring margin would be affected by temperature change. This analysis is shown in Figure 8. The margin was determined to be sufficient to operate the

DCDA up to the 67°C testing limit. However as the temperature increases the margin decreases as shown and is reduced to 120% at the testing limit.

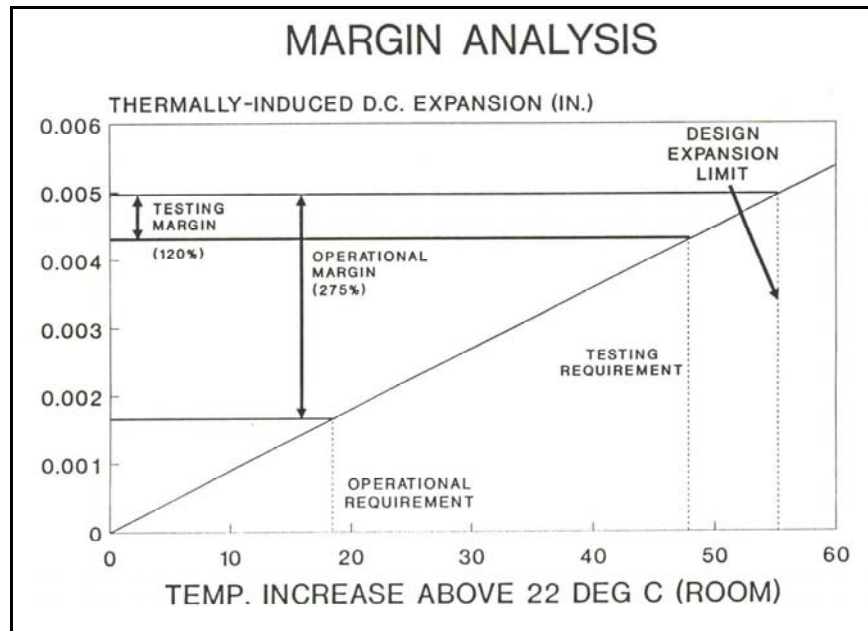


Figure 8. DCDA Operational Temperature Margins

The DCDA Latching system is designed so that there exists sufficient frictional force between the lock-arm and the door (exerted by the negator spring) to prevent the door from opening prematurely during launch vibrations. The negator spring and the latching system were also analyzed. This analysis was to determine if there would be sufficient force exerted on the lock arm by the paraffin actuator to release the door. One analysis determined the amount of force exerted on the lock arm by the paraffin actuator at different rotation angles. Another analysis as shown in Figure 9, determined the amount of operating margin from the actuator above that required to release the door. The margins are above 1000% of that needed to open the door. This data could have been used to reduce the size of the latching system for weight reduction. However, the paraffin actuator used at the time was the already the smallest available. Fortunately for this particular mechanism, high margins are desirable in that a failure of this mechanism would result in a complete mission failure.

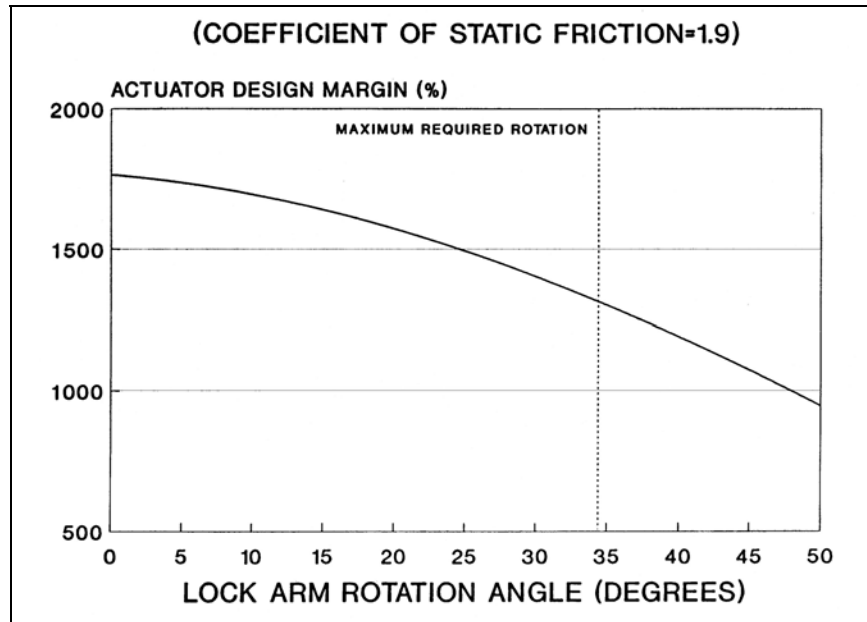


Figure 9. DCDA Door Latching System Margins

In hindsight the high margins benefited the LORAAS program unexpectedly as a result from a slight flaw in the wiring of the paraffin actuator. Normal operation of a paraffin actuator requires a continuous flow of current in the primary heater with the redundant heater available but not energized. In an identical application for another NRL instrument both the primary and redundant heaters were wired in parallel. It was decided that rewiring the instrument to prevent the power applied from going over the specified values would be too costly and inconvenient. A software solution was found which involved modulating the duty cycle of power applied. This resulted in the pulsing of power with a 50% duty cycle on the order of one second per cycle so that on average the power remains within specified limits. If one of the heaters were to burn out, a new command could be uploaded to power the remaining heater continuously. Ground testing was done to confirm this method would work. Because of the high margins for the latching system, the loss of heat that may occur during pulsed operation should not cause failure in that the actuator would still be working well below its specified limits.

Detector Door Mechanism

The vast majority of VUV detectors have photocathode films deposited onto their active surfaces to increase sensitivity in a given passband. The LORAAS detectors used cesium iodide, CsI. Unfortunately, CsI is hygroscopic and breaks down on the order of hours when exposed to moisture. Long-term storage of CsI, on the order of years, is best performed by sealing it under high vacuum as compared to a rough vacuum or a dry atmosphere³. The DDM, shown in Figure 10, was used to maintain the high vacuum on the detector. Ordinarily a transparent window would be used to seal off the high vacuum interior of the detector from the ambient atmosphere. However, the lack of a material that is transparent at the wavelengths of interest prevents the use of a window. A detector door mechanism was designed and built to provide the necessary high-vacuum hermetic seal during instrument construction, between calibrations as well as during ground storage, transport, and launch.



Figure 10. Two Detector Door Mechanisms with Mounted Detectors

DDM Features

The majority of detector doors designs operate only once from closed to open and then have to be manually reset. The LORASS DDM is unique in that it can open and close without needing to be reset. The DDM's have a design lifetime of over 100 open and close cycles without severe degradation in performance. This lifetime requirement follows from the number of open/close cycles predicted for calibration purposes of the detector and the instrument while on the ground rather than for flight use. Designing the DDM to the aforementioned lifetime requirements was complicated by the added requirements that the DDM be able to withstand a high temperature bakeout of 200°C. It is standard practice in FUV and EUV instrumentation to bakeout components used in the optical system due to the extreme sensitivity to contamination.

Another unique quality of the DDM is its extremely low mass. The DDM can provide the necessary sealing forces and lifetime in a package that weighs slightly less than 1 kg. Presently all DDM's used at NRL have provided the unpowered high vacuum seal for many months at a time with no loss of performance after tens of cycles. Unlike other detector door mechanisms, which are custom designed for a particular detector, the LORAAS DDM is adaptable for use with other detectors. This adaptability is due to the detector housing being an independent structure from the DDM support frame. The detector is mounted to the DDM by clamping a flange, which is part of the detector housing, to the DDM flange. As long as the detector housing possesses a flanged face it should be compatible with the DDM barring any kind of mechanical interference from another portion of the detector. Figure 10 shows two DDMs with two different models of detector mounted. The clamp-mounting scheme employed by the LORAAS DDM also allows the detector to be rotated at any orientation with respect to the DDM. Sometimes this is necessary as it is with the LORAAS instruments when the detector/DDM assembly might go through several iterations during calibration to determine the best orientation.

DDM Design and Kinematics

The DDM is built around a 4-Bar toggle linkage system to achieve the necessary torque multiplication. Weight was minimized by properly matching the linkage to use the smallest input torque possible while still providing the necessary force to seal the detector. Sealing the detector requires a force of 136 kilograms to compress, by 30%, a 75-durometer Viton-A o-ring with a 1.8-mm (0.07") cross section. In addition, the torque on the door arm exerted by the seal is not enough to back-drive the motor against its detent torque. Proper matching the linkage components helps give the DDM its ability to provide the vacuum seal while unpowered.

The DDM linkage consists of the following components: the DDM Door, the door arm, the toggle bar, and the crankshaft. A spur gear with a 3:1 reduction is connected to the crankshaft and is driven by a Rapsyn stepper motor providing 0.073 N-m of torque at 22 VDC. The output of the motor is transferred to a Globe 4-Spage planetary gearbox with a 319:1 estimated minimum Torque ratio and 760.6:1 Speed ratio. The drive system rotates the crankshaft which is connected to the toggle bar. The toggle bar rotates the door arm and closes the door. The components of the linkage and drive system are shown in Figure 11.

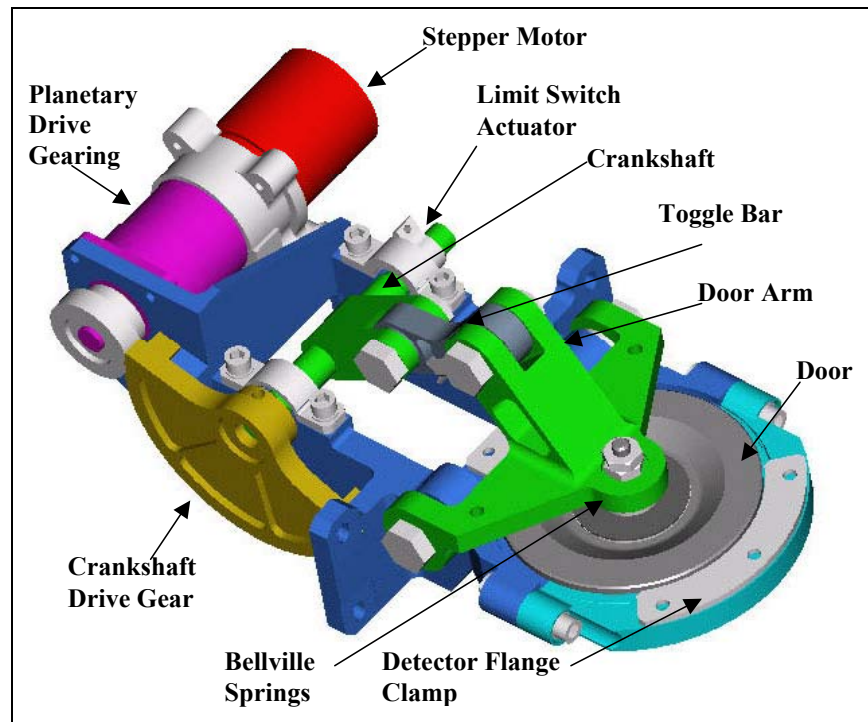


Figure 11. DDM Component Layout

The DDM Linkage was designed so that the force imparted by the door increases as the door moves closer to the clamping surface. As the door closes, the linkage moves to its toggle position where the angle between the crankshaft and the toggle approaches zero, as shown in Figure 12. This toggle position occurs just before the door is closed and this is where the maximum clamping force is achieved with the minimum amount of input torque. The closing force produced by the linkage is adjusted and regulated through the use of two custom Bellville washers located between the door and door arm. The Bellville washers have a small range of deflection (about 0.5 mm) in which the force exerted by them remains relatively constant. This constant force helps to ensure the proper amount of preload is exerted despite any linkage relaxation or thermal distortions, and provides margin for any tolerances in the DDM system. If desired, the preload can be adjusted by changing the Bellville stack characteristics. However, any change in preload must be done so that back-driving does not occur. Regulation of the DDM is also accomplished through the use of two mechanical stops. One stop limits the door travel to 95 degrees and the other stop prevents the toggle from going over center. Stopping the toggle from moving over the center prevents any resistance during door opening from the Bellville washers and o-ring. Minimizing the resistance during opening was another requirement driving the DDM design.

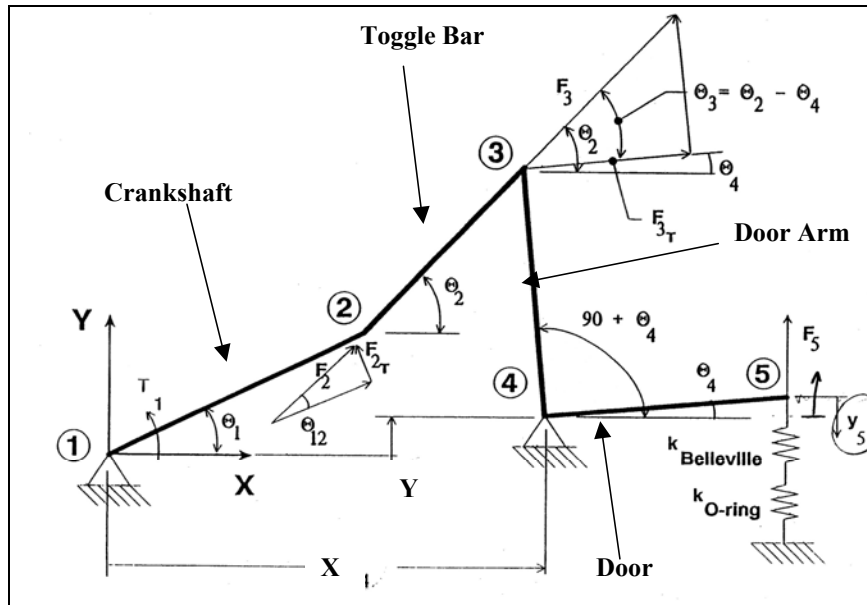


Figure 12. DDM Kinematic Diagram

To minimize resistance from friction in the linkage, extra-precision needle bearings from Torrington were used in all linkage joints. These needle bearings were modified by removing the cup which allowed for cleaning and lubricant insertion. The lubricant used for the bearings as well as for the drive system was Demnum 200-L-280 Perfluoropolyether. The crankshaft gear used impregnated Teflon for lubrication. Out-gassing and the requirement to survive the bakeout procedure drove lubricant selection. Surviving the bakeout procedure influenced the design of the DDM structure as far as how the components were attached.

Bake-outs mostly occur during the detector integration period. These bake-outs can be low level where the detector is brought to 100°C for a minimum of one hour and they can be at high level where temperatures can reach up to 200°C. Rather than increase the cost of the DDM by using components that can withstand these temperatures it was decided that the DDM should be made easy to disassemble. During a high level bakeout the door arm is fastened to the frame and maintains the seal while it is disconnected from the linkage. The entire linkage and drive system can then be disconnected from the one-piece frame. For low-level bakeout the detector and DDM system remain as a unit with a temperature control channel placed on the drive system to ensure that it does not go above 100°C.

DDM Analysis

Extensive analysis was conducted on the DDM design to ensure satisfactory performance during operation, achieve a saving in weight and meet its lifetime requirements. The analysis performed on the DDM determined the bearing radial loads at each joint, crankshaft stresses during operation, toggle torque, and structural stiffness of the frame and linkage components. When possible these analyses were verified with data from direct measurement as is shown in Figure 14. The bottom line shows the door force as it relates to position. As was described earlier, the applied force increases as the door closes until the Belleville washer deflection point is reached. At this point force remains constant until the door is closed. The door force margin is determined when the measurements of the actual door force is combined with the calculations for the available door arm force which is the top line. The margin is the difference between the top and bottom lines and is represented by the middle line. The force exerted by the door was measured by using a load cell located in the place that the detector would occupy. A strain gauge mounted on the toggle is used to measure DDM performance when a detector is in place, such as in instrument level environmental test. This mapping of the strain experienced by the toggle as the door closes was the result of the analysis during design verified by direct measurement on a finished unit.

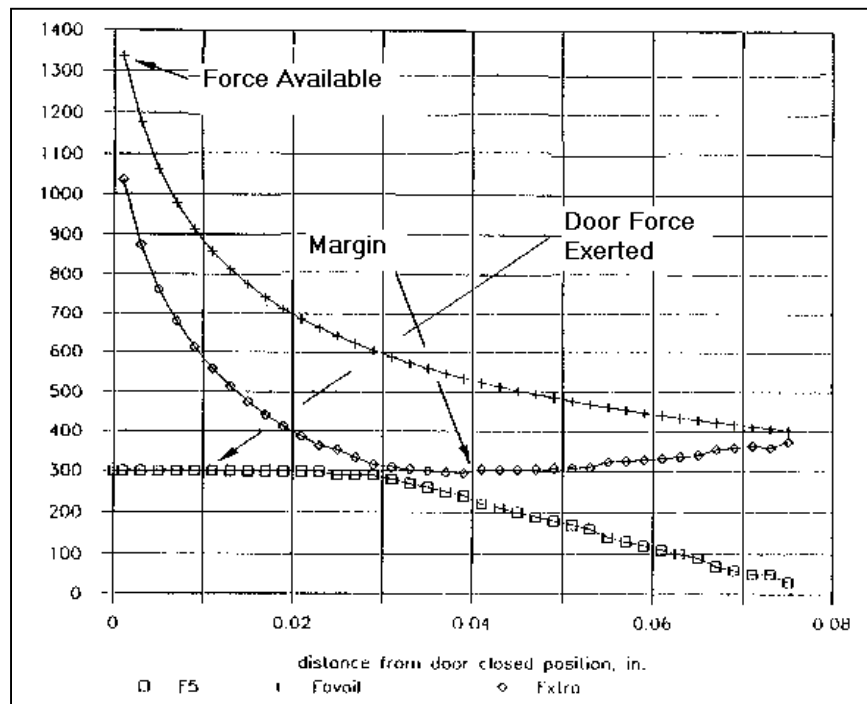


Figure 14. DDM Force Margin

The analysis that was conducted during design allowed several changes to take place to produce a final model with a lower weight and less components than earlier estimated. The original 38-mm diameter gearbox was replaced with one 31.75 mm in diameter. The motor was also replaced from the original Globe brushless motor to a Rapidsyn stepper motor. Simplification was achieved by changing both the crankshaft and door arm from 3 piece assemblies to single parts.

DDM Cost

Due to the long design history of the DDM any detailed costs have been lost as personnel have come and gone from the project. The best estimates for the total nonrecurring costs are between \$350,000 and \$500,000. Most of these costs are due to the extensive amount of analysis conducted in addition to that incurred by DDM design. The recurring costs for each unit is somewhere around \$55,000 per unit. All testing was done at NRL, which greatly reduces the cost. The cost for testing was between \$3,000-\$5,000 per DDM. All costs are approximate and in 1993 dollars. Ten flight units were made so a total cost would be just under a million dollars. Since the design has been so successful it has been used on two other missions and will most likely be used on many future missions. This will help offset the initial nonrecurring costs and make the design even more valuable.

In addition to the LORAAS missions, a modified form of the engineering design unit was successfully flown on NRL's Joint Astrophysical Plasmadynamic Experiment sounding rocket mission. The modifications for this DDM was the reduction of the opening time from 30 minutes to about 30 seconds by changing the motor/drive system to a motor with higher torque and less reduction in the gears. These modifications were needed to accommodate the already short amount of time available to take data. The cost of this modification was on the order of \$30,000 for the new parts and analysis to verify the DDM would still provide the necessary seal. Also an identical form of the DDM as that flown on LORAAS was used successfully in the NRL High Resolution Ionospheric Thermospheric Spectrograph instrument.

Conclusion

The mechanisms presented in this paper were designed to conform to the idiosyncrasies of optics in the far and extreme ultraviolet. How these mechanisms were to be used on the ground was just as important in their design as how they were to be used in space. Analysis and test was used extensively to determine if the mechanisms would meet their requirements. In certain cases these analyses proved beneficial for improving an already satisfactory design or finding flaws before they could affect the mission. NRL is continuing to benefit from the effort put forth into these mechanisms as their designs are incorporated into future instruments.

Acknowledgements

The Air Force Space Test Program funded the ARGOS spacecraft. The LORAAS mechanisms described in this paper were contracted out to the following institutions: Swales Aerospace, Inc. for the analysis and construction of the DDM, and Research Systems Inc. for the design and construction of the USA.

References

1. McCoy, Robert P. et al; "Special Sensor Ultraviolet Limb Imager: An Ionospheric and Neutral Density Profiler for the Defense Meteorological Satellite Program Satellites." *Optical Engineering*, Vol. 33 No. 2 (February 1994) 423-429.
2. Samson, James A., Ederer, David L. Vacuum Ultraviolet Spectroscopy. Academic Press (2000)
3. Whitely, M.J., Pearson, J.F., Fraser, G.W., and Barstow, M.A., "The Stability of CsI-Coated Microchannel Plate X-Ray Detectors" *Nuclear Instruments and Methods in Physics Research*, Vol 224 (1984) 287-297

STEREO / SECCHI Coronagraph Hollow-Core Motor Development and Testing

Augustus S. Moore*, Alexander D. Price**, David J. Akin*, Ralph Horber†

Abstract

A hollow-core motor was developed by the Lockheed Martin Solar and Astrophysics Laboratory for use in two coronagraph telescopes in the Sun Earth Connection Coronal and Heliospheric Investigation (SECCHI) instrument suite on the two spacecraft of Solar Terrestrial Relations Observatory (STEREO). The HCM has a 48-mm aperture and rotates a polarizer on the optical axis of the telescopes. Here we describe the development of the mechanism and testing methods as well as the results of testing and life simulation. The HCM was proven to be robust and capable of performing in excess of its prime mission life. In addition, we present the limitations to the design and the lessons learned for future mechanisms.

Introduction

A hollow-core motor (HCM) was developed to be incorporated into the two coronagraph telescopes in the Sun Earth Connection Coronal and Heliospheric Investigation (SECCHI) suite of instruments on each of the two spacecraft of the STEREO mission that will be launched in early 2006. Two coronagraph

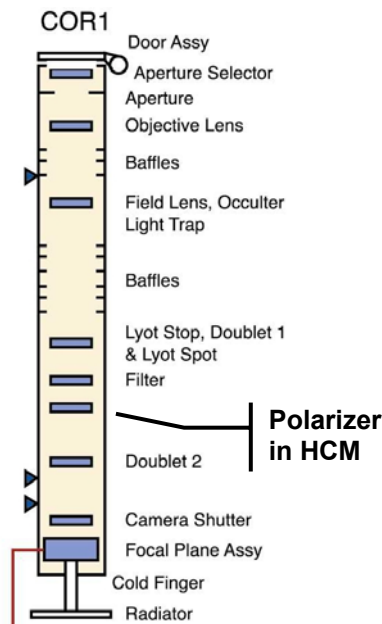


Figure 1. Location of the SECCHI HCM in the COR1 Telescope

telescopes are being developed: COR1, which will have a field of view of $1.3 - 4 R_{\text{sun}}$ that is being developed by the Goddard Space Flight Center, and COR2, which will have a field of view of $2 - 15 R_{\text{sun}}$ and is being developed by the Naval Research Laboratory. Each of the two STEREO spacecraft will carry a COR1 and COR2 telescope. The Naval Research Laboratory principal investigator responsible for the overall SECCHI program is Dr. Russell Howard [5]. The Lockheed Martin Space System Company Solar and Astrophysics Laboratory (LMSAL) is developing two other telescopes for the SECCHI program (the Extreme Ultraviolet Imager and the Guide Telescope) and is responsible for the coronagraph shutter motors and HCMs [8].

Solar coronagraphs like COR1 and COR2 are designed to observe the faint corona that is normally only visible to the naked eye during a solar eclipse [2]. Coronagraphs accomplish this by blocking the view of the visible solar disk in order to observe the faint extended corona whose intensity is several orders of magnitude less bright than the solar disk. The light from the corona originates in the photosphere and is Thompson scattered into the field of view of the coronagraph telescopes. As a result, the detected light is significantly polarized. By taking advantage of this polarization, the true coronal emission can be isolated from background and instrumental sources. The HCM is placed on the optical axis of the coronagraph (Fig. 1) and contains a linear polarizer. During observations, the HCM will rotate the polarizer so images may be acquired in multiple polarization states.

* Lockheed Martin Space System Company, Solar and Astrophysics Laboratory, Palo Alto, California

** Lockheed Martin Space System Company, Solar and Astrophysics Laboratory, Palo Alto, California and Dartmouth College, Hanover, New Hampshire

† H. Magnetics Inc., Marshfield, Massachusetts

The STEREO mission has a prime observing period of two years. During this time, each coronagraph telescope will require 600,000 motions of the HCM. The typical demands of spaceflight instrumentation required the HCM design to be lightweight, low power, and relatively low cost. Because of its function within the optical path of the telescope, it is required to have rigorous mechanical tolerances, highly repeatable motion, and to be extremely clean, as particulates can be a significant source of stray light scatter in a coronagraph.

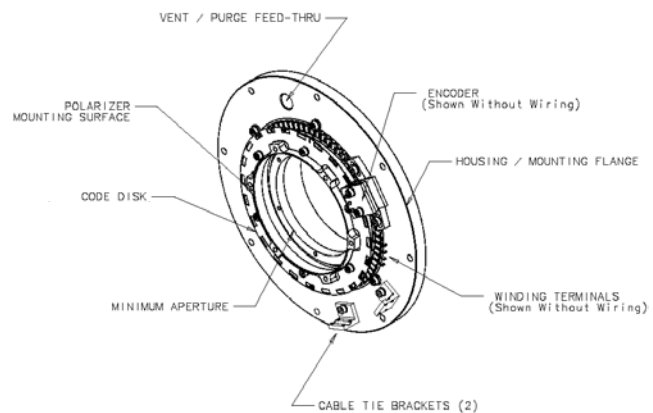
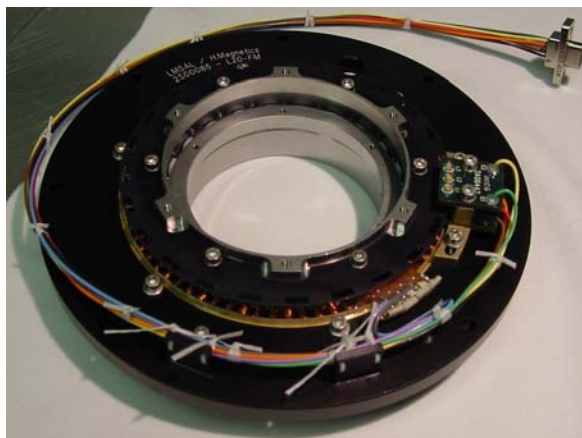
The HCM was designed, built and tested by collaboration of LMSAL with H. Magnetics [1]. Here we describe the development and testing of proto-qualification mechanism that was built to flight specifications and subjected to full lifetime simulation that included vibration, thermal cycling, operation under vacuum, and a full battery of pre- and post-life functional testing. Specifically, we discuss a method developed to characterize the repeatability of the HCM. This test verified that the mechanism performs within specifications over its projected life but also revealed the limitation our particular design.

Finally, we present the results of testing of the four flight mechanisms that have been delivered to the coronagraph teams and the impact of our development effort on designs for similar motors on the upcoming Helioseismic Magnetic Imager (HMI) on the Solar Dynamics Observatory (SDO).

Hollow-Core Motor Requirements and Design

The SECCHI HCM is shown in Figure 2. It is derived from a similar thin-section motor, the Michelson Tuning Motor (MTM), that is presently being used in the Michaelson Doppler Imager (MDI) on the Solar and Heliospheric Observatory [1]. Three of these mechanisms have performed more than 70 million operations during a continuing mission of more than eight years. Modified versions of the MDI MTMs are also being successfully used in the guide telescope on the Transition Region and Coronal Explorer which has been in orbit for more than 5 years.

The HCM has an overall fairly simple design. A 48-mm-diameter aperture is surrounded by a thin-section bearing and a brushless DC motor. The motor consists of a three-phase, wye winding on a 72-pole iron stator paired with a 48-magnet rotor. This design results in 144 discrete detents with a static detent torque of approximately 64 mN•m. A space industry standard Timken thin-section bearing with Teflon toroid separators was selected for this design. The bearing was deemed a low-risk choice because of its long heritage in space-based applications and successful use in previous LMSAL mechanisms. In addition, the mechanism's modest life requirement could easily be accommodated with this type of bearing. Two bearings were used in a back-to-back hard pre-loaded condition to approximately 100 N.



Figures 2a & 2b. SECCHI Hollow-Core Motor

The mechanism has a three-channel, 144 counts-per-revolution optical encoder that is nominally aligned to the detents of the motor. The encoder is robust in design and provides a simple signal to a Field Programmable Gate Array (FPGA) based control system that commutates the motor and increments the position count on the edges of the signal waveform. The encoder is designed such that all three signals are driven by the same track on the mechanism code disk, that produce a unique signal every six counts. This arrangement provides constant feedback to the control FPGA about the rotor's position with respect to the motor's six electrical cycles to facilitate correct commutation of the motor without a need to find the mechanism home, or zero, position. A small slot in the code disk provides a once-around unique signal for this zero position.

Table 1. HCM Design & Performance Requirements

Minimum Aperture	48 mm
Operating Temperatures	0 – 40°C
Survival Temperatures	-20 – 55°C
Total Torque Margin	100%
Position Repeatability	30 arcseconds 1-σ
Time for 180° Move	< 1 second
Required Life	600,000

Table 2. Hollow-Core Motor Design

Phases	Three-Phase Wye Winding
Stator Teeth	72
Total Detents	144
Step Size	2.5°
Coil Resistance	~ 128 ohm
Nominal Drive Voltage	15 V
Motor Constant	110 mN•m / sqrt(W)
Static Detent Torque	~ 64 mN•m

In normal operation (shown schematically in Figure 3), where the HCM rotates the polarizing optic to a specific position from many steps away, the motor is commutated on the edges of the encoder signal with no speed control. Rotor braking is passive and is accomplished by shorting together the three phases of the motor winding. The resulting dynamic braking plus bearing friction and detent torque allow the rotor to coast to a stop, typically in a detent. Because the encoder has a resolution only sufficient to commutate the motor, there is neither closed-loop control on stopping position nor reporting of position to greater than 2.5° of accuracy. Thus, the finite stopping distance must be taken into account when driving the mechanism.

The solution developed for mechanisms at LMSAL, and used in the HCM, is to continue commutating the motor for a short time after the target encoder transition is reached. This extra commutation time, or “delay” pushes the mechanism reliably into the detent past the defined

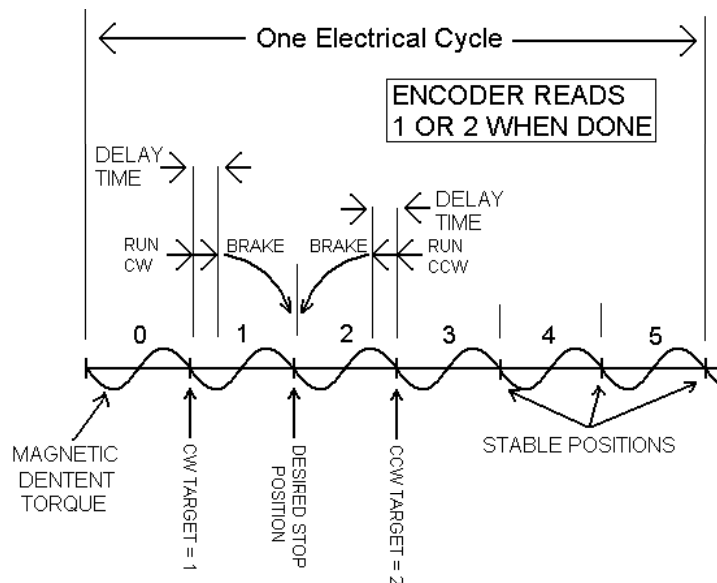


Figure 3. HCM Operational Concept

encoder transition and allows the HCM to be tuned so that it occurs reliably for the unique detent positions. The delay setting is an 8-bit, on-orbit settable parameter with 64μs units. The total range of settings from 0 to 255 provides a time range of 16.32 ms. At the HCM nominal spin speed of about 5.5 rad/s (315 deg/s), this range allows for adjustability over about 5 degrees, or two detents. In a normal move, the undriven portion of a movement is a fraction of a step, typically between 1° and 2°. The design not only provides a level of robustness for on-orbit operations, but also provides a flexible option for testing the mechanism. Figure 3 illustrates the operational concept of the HCM when moving to the “1” target detent.

HCM Functional Testing

Functional testing of the HCM emphasized the characteristics and performance of the mechanism as a whole, rather than the properties of individual components such as the bearing or encoder electronic parts. All testing was completed with the mechanism fully assembled and yielded bulk measurements of the mechanism properties and direct information about how the mechanism would operate on-orbit.

Specific tests were used to verify the HCM's two key requirements of 100% torque margin and repeatability-to-position of less than 30 arcseconds standard deviation. The total torque margin requirement specified that the motor be capable of operating normally given a 100% increase in total friction. The repeatability requirement specified that the distribution of the stopping position of the rotor must have a standard deviation of less than 30 arcseconds.

A special metric was devised to test the total HCM torque margin. The motor drive voltage was increased incrementally from a small value – typically 4V – as the motor was commanded to move from each of its 144 positions. The minimum voltage, and thus the minimum current for the stalled motor, at which the motor was able to commutate normally from all positions was recorded as the mechanism minimum start-up voltage. Minimum start-up voltages less than 7.5V indicated a torque margin of greater than 100%.

This test reflected the typical operational mode of the mechanism and provided an aggregate measure of bearing performance. It was extremely effective in mapping the effect of bearing life on torque margin during both the functional testing and the vacuum operation portion of the qualification series. Changes in the measurement over the lifetime of the mechanism could then be attributed to changing bearing break-away torque and low-speed friction. Testing the motor with decreased drive voltages not only verified that the mechanism could operate with decreased spacecraft bus voltage, but was also used as an analog for increased bearing friction.

Early in the functional testing of the HCM, it was obvious that the repeatability requirement of 30 arcseconds standard deviation (also denoted as $1-\sigma$) could not be efficiently verified with our current measurement methods. In the case of MDI's Michelson Tuning Motors, a theodolite was employed to spot check the motor's stopping position for a few motor detents. This method was extremely time consuming and was not easily adapted to statistical analysis of the repeatability of all the HCM motor positions. In addition, it was also necessary to test the mechanism at a large number of potential delay settings to select the one that would result in its most robust and repeatable operation. A total of more than 50,000 measurements were required to verify the mechanism repeatability and effectively tune its performance.

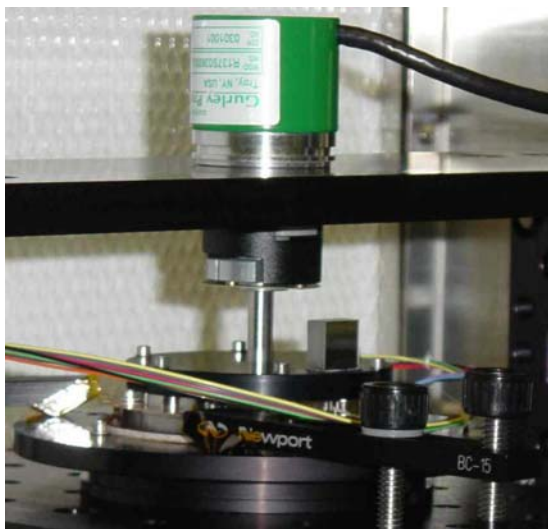


Figure 4. External Encoder Configuration

The solution was to attach a small but highly accurate external encoder (Figure 4) to the HCM and perform an automated test sequence that rotated the mechanism to all of the motor targets many times at a range of delay settings. An optical incremental encoder manufactured by Gurley Precision Instruments was chosen because its inertia and friction were small and it was accurate enough to obtain data with arcsecond resolution. The external encoder was attached to a shaft mounted in an aluminum puck designed to simulate the mass and inertia of the polarizing optic. The motor was commanded to make moves to each position a statistically relevant number of times (typically 40). This was done for 8 to 10 delay settings.

Manual spot checks of the accuracy of the external encoder system with a theodolite showed good agreement between the two measurements and

confirmed the accuracy and reliability of automated testing method.

It was immediately observed that the total angular distance of the move greatly impacted the repeatability-to-position of the mechanism. Short moves of less than 30° (12 steps) showed poor repeatability with standard deviations above 10 arcminutes. As the move distance increased, the repeatability was improved. Move distances of 60° showed standard deviations of less than 60 arcseconds and move distances of greater than 90° were repeatable to less than 20 arcseconds. It was also observed that the repeatability of each of the mechanism's 144 target detents was different for a given delay setting. As a corollary, the best repeatability of each target detent occurred at different delay setting.

As a result, the repeatability requirement on the HCM was refined to reflect the nominal operational modes of the HCM. The nominal move distance and direction of 120° clockwise (CW) that will be used on orbit was defined as a baseline movement for all repeatability testing.

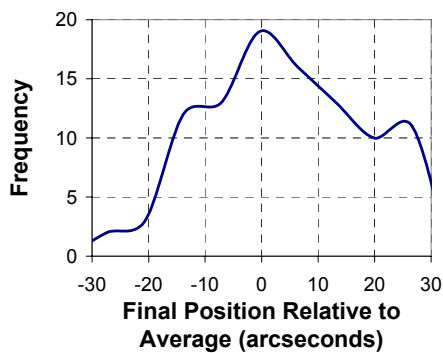


Figure 5. Histogram of HCM Rotor Stopping Positions of 120° Rotations

Figure 5 is a histogram of the stopping position of the HCM rotor when driven 120° to target position no. 10, 200 times at a delay setting of 80. The distribution has a single standard deviation ($1-\sigma$) of 20 arcseconds where the average stopping position has been normalized to zero. This measurement was made early in the life of the mechanism. Similar measurements showed that each of the 144 target positions had unique distributions and that they would change over time and with modifications to the delay setting.

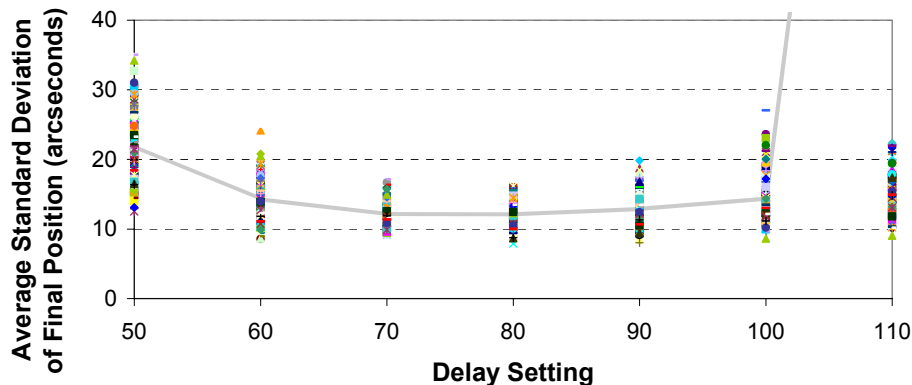


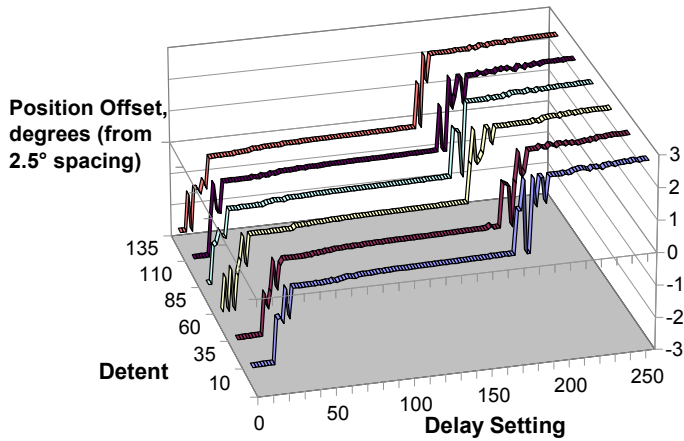
Figure 6. Results of an Automated External Encoder Run Used for Delay Setting Selection and Repeatability Specification Verification

Figure 6 shows the results of an automated test sequence. Each of the points recorded on the plot represent the standard deviation of the stopping position for each of the 144 motor detents after a 120° rotation. The aggregate delay for each delay setting has been superimposed on the plot and is represented by the gray solid line. The minimum point of this aggregate measure shows that a delay setting of 80 and a repeatability of 13 arcseconds are the nominal mechanism delay and the mechanism repeatability at this delay.

The encoder system proved instrumental in developing a better understanding of the dynamics of the motor, especially in its stopping behavior and

how the delay setting controls the final position. With a delay setting of zero, the inertia of the rotor is not enough to carry the motor over to the next detent, so it returns to the detent before the target position. With the maximum delay setting of 255, the delay time provides sufficient commutation time to drive the motor through the target detent and into the next detent. There are unstable delay settings that can result in the motor sliding forwards to the next detent, backwards to the previous detent, or even coming to rest at the top of the detent potential between steps. The extremes of the automated run results shown in Figure 6, where the aggregate repeatability is poor enough not to be shown on the scale, are the result of

this instability. As can be seen, some of the detent positions are very repeatable, but the aggregate repeatability is dominated by those target detents that are not.



The position of this unstable transition region varies slightly between positions, as shown in Figure 8, but there is a wide range of stable delay values common to all motor positions. The most repeatable movements occur approximately at the middle of the stable delay range. The high delay settings that cause consistent overshooting of the target position are also stable, but are much less repeatable. In this case, of course, the mechanism also stops approximately 2.5° from its intended position.

Figure 7. Stopping Positions for 120° Rotations to Six HCM Target Detents While Varying Delay Setting

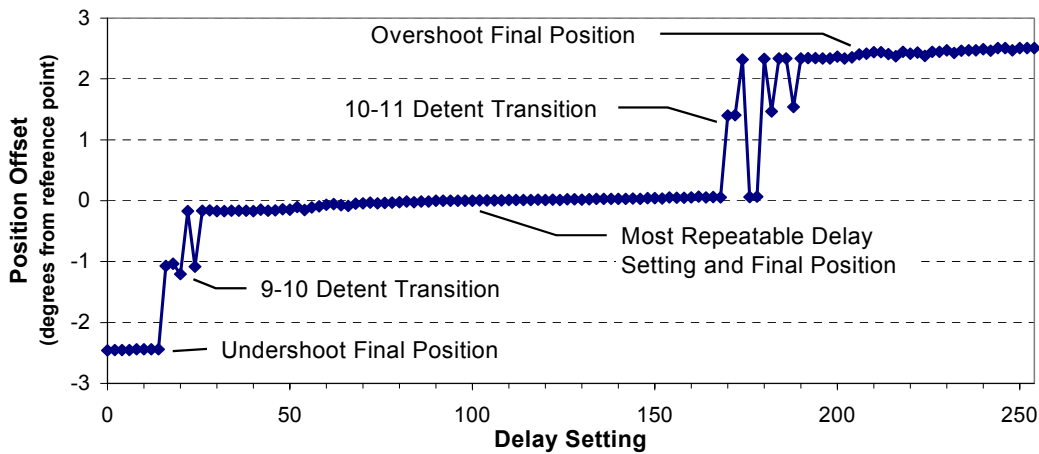


Figure 8. Annotated Plot of Stopping Positions for 120° Rotations to Target Detent 10. Delay Setting Varied by 2 from 0 to 254.

Mechanism Qualification Testing

The SECCHI HCM was qualified and its performance characterized through lifetime simulation testing a single mechanism. This life-test consisted of construction and testing of the mechanism to flight specifications, vibration testing, thermal functional testing at ambient pressure to the mechanism's operating temperature extremes, operation in vacuum to four times the estimated mission life, post-test functional testing, and disassembly and inspection. Figure 9 shows the sequence and requirements for a single sequence.

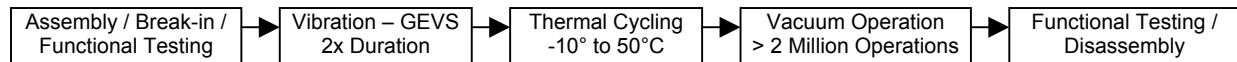


Figure 9. HCM Qualification Basic Sequence

Two life-test sequences, both discussed here, were required to qualify the mechanism. During the first sequence, contamination in the motor bearing resulted in a stall in the vacuum operation portion of the test. In the second sequence, the mechanism performed well throughout the test.

HCM Thermal Functional Testing

After a standard vibration test sequence, a thermal functional test was completed to characterize the performance of the mechanism over the extremes of its operating temperatures. Although the nominal predicted temperature range for the HCM is 20 to 30°C, the mechanism was operated over five temperature cycles from -10 to 50°C while performing movements similar to those expected on-orbit. Periodic automated functional tests that measured the motor friction and steady state spin-speed provided information on the changes in the mechanism at different temperatures.

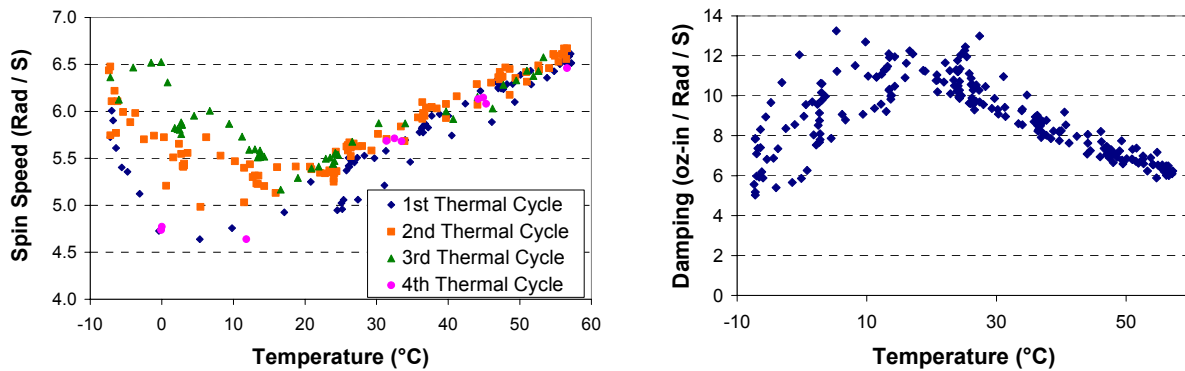


Figure 10. Mechanism Speed Dependent Friction and Nominal Voltage Spin Speed with Temperature

Figure 10 shows the change in mechanism aggregate friction over the temperature range. In the figure, the components of friction have not been separated and consist of changes in motor hysteresis as well as changes in the friction properties of the bearing. The results from the thermal functional test confirmed the expected correlation between motor friction and temperature. The HCM performance with variations in temperature is typical of the performance of Braycote grease lubricated bearings [4]. The decreased friction at lower temperatures – with the attendant increase in running speed – is typical to grease lubricants and indicates that there is a thinner layer of lubricant bearing since the bearing has forced away the higher viscosity Teflon binder. Understanding this effect is critical to designing a tuning scheme if lower than anticipated temperatures are encountered during on orbit operations.

The external encoder system was used during the thermal functional test to characterize temperature induced change in the repeatability of the mechanism and to provide guideline information for tuning the

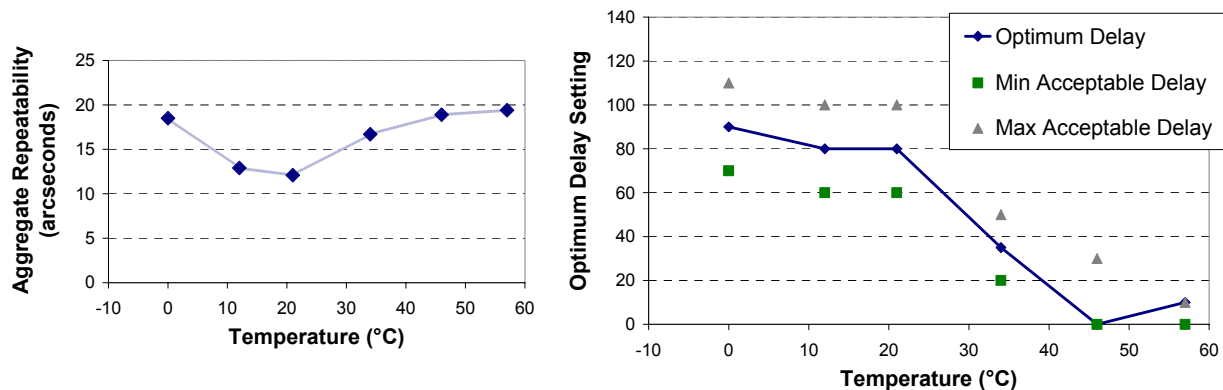


Figure 11a & 11b. HCM Repeatability Delay Setting with Temperature

mechanism delay setting for best operation given the actual on-orbit operating temperature of the mechanism. This testing was limited to temperatures above 0°C because of limitations on the operation of the external encoder.

As assumed in the design of the mechanism, changes in bearing friction – and the corresponding loss of repeatability – could be mitigated by modifying the mechanism delay setting. At higher temperatures where total friction is less, the delay setting can be decreased to maintain acceptable repeatability. Increasing the delay setting compensates for higher than nominal friction. Figures 11a and 11b illustrates the correspondence between the delay setting at best repeatability and temperature for the HCM. Modifying the delay setting –1.75 units (112 μsec) per degree Celsius for temperatures changes from the nominal mechanism test temperature of 20°C provided roughly the best mechanism repeatability performance. The minimum and maximum acceptable delay settings bracket the range of delay settings where the aggregate repeatability of the mechanism meets the 30 arcsecond requirement.

HCM Lifetime Vacuum Operation

The key component of the HCM qualification effort was a four-times life operation sequence while under vacuum and at elevated temperature. As in the thermal functional test portion of the effort, the mechanism performed a series of operations similar to those expected on-orbit with periodic automated functional tests to assess the health of the mechanism and trend changes in mechanism performance. The mechanism lifetime simulation was performed at the upper limit of the mechanism operating temperature of 40°C in order to provide the greatest stress to the bearing grease lubricant. The external encoder system was not employed during this section of the qualification effort due to the complexity of adapting the system for use in vacuum.

In the first life-test effort, the proto-qualification HCM was placed in the vacuum chamber after approximately 850,000 break-in and other testing operations had been completed. The mechanism performed as expected while under vacuum and the friction-with-time profile was as expected for a Braycote 600 lubricated bearing with Teflon toroids. However, after 1.8 million operations under vacuum (or about 2.6 million total operations), the mechanism stalled during a standard move sequence. To that point, the mechanism had shown no adverse signs of wear or incipient failure.

An anomaly investigation was initiated to isolate the cause of the stall prior to breaking vacuum. The life-test support equipment was tested and checked. An attempt was made to command the motor to move in the same direction the motor had been moving during the test. The motor did not move and drew full stall current. Next, the motor was commanded to run in the opposite direction. The motor stuttered at first, and then began to operate normally. Figure 12 is the mechanism drive current trace during the stall recovery. Evidence such as this indicated possible particle contamination.

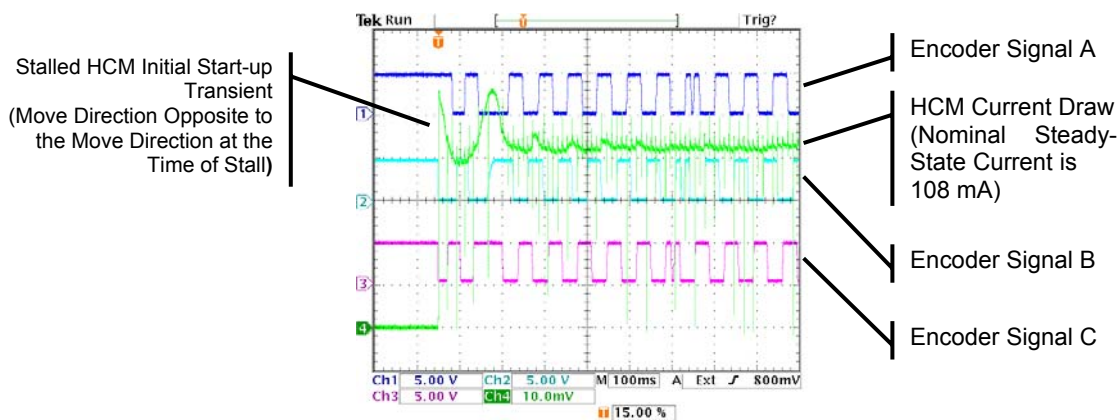


Figure 12. Current and Encoder Trace of Failure Recovery

The motor subsequently passed its standard functional test, in both clockwise and counterclockwise directions, with no anomalies in its operation. Although this stall failure was recovered through software operations that could be accomplished on orbit, the test sequence was discontinued and the motor removed from the life-test chamber for disassembly and inspection.

Inspection of the bearings showed that the lubricant was in good condition. However, several small metallic particles (as in Figure 13) were found in one of the two bearings in the assembly. Chemical analysis revealed that the particles were 6061 series aluminum with traces of chromate from irridite. Chemical analysis also revealed that the bearing lubricant was not otherwise contaminated by the stainless steel used in both the balls and races of the bearing. This suggested that there had been little significant wear to the bearing races or balls.

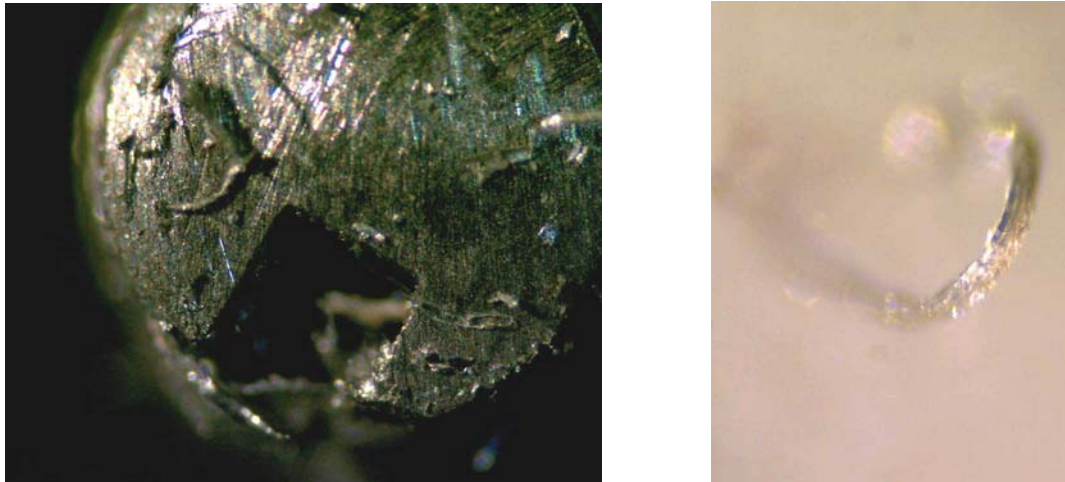


Figure 13a & 13b. Proto-Qualification HCM Contamination: Locking Feature on Mechanism Screw (left) and an Aluminum and Chromate Particle Removed from the Bearing (right)

The housing design of the life-test motor was examined to determine the source of the particles that were found in the bearing and lubricant. It was concluded that the probable source was the irridited, threaded holes in the motor's aluminum housing, close to the contaminated bearing. Inspection of these fasteners (in place in Figure 13A) revealed that the screws' locking features damaged the threads in the housing and pushed the resulting debris into the motor's rotor cavity. The previous vibration testing and other handling brought the particles into contact with the bearing where they could be captured by the lubricant. With time, the particles caused the stall when one or more particles became lodged between the balls and the races. When the motor was commanded to move in the opposite direction, the particles were moved out of the way or crushed (explaining the observed "stuttering" behavior), and the motor began to operate as before.

Table 3. HCM Life-Test Second Sequence

Operation	Sequence 2 Ops
Break-in CW Spin	56,200
Pre-Lifetest Functional Testing	138,180
Vibration Test	138,180
Thermal Functional Testing	704,340
Software Verification	727,570
Vacuum Operation	3,573,250
Post-Lifetest Functional Testing	3,691,832
Additional Repeatability Testing	4,276,882

The key corrective action for this anomaly was to add an intermediate cleaning step to the HCM assembly procedure that removes the free particles that were generated during assembly.

The HCM was re-built to flight specifications with an identical bearing and second life-test series was initiated immediately. The motor was broken-in and received the full battery of functional testing. A vibration test and thermal functional test, identical to the first sequence, were performed and the

mechanism was placed into vacuum cycling. Table 3 shows number of operations at steps during the second lifetime simulation sequence.

While under vacuum, the mechanism performed as expected for 2.8 million operations – slightly more than five times the expected life. As shown in Figure 14, the free-run speed profile of the HCM in the second series was similar to that of the first series and the minimum start-up voltage for the mechanism remained under the goal of 7.5 V for the duration of the vacuum run. The 1 Volt, or 21%, increase in the minimum start-up voltage indicated a decrease in torque margin from 160% to about 115%.

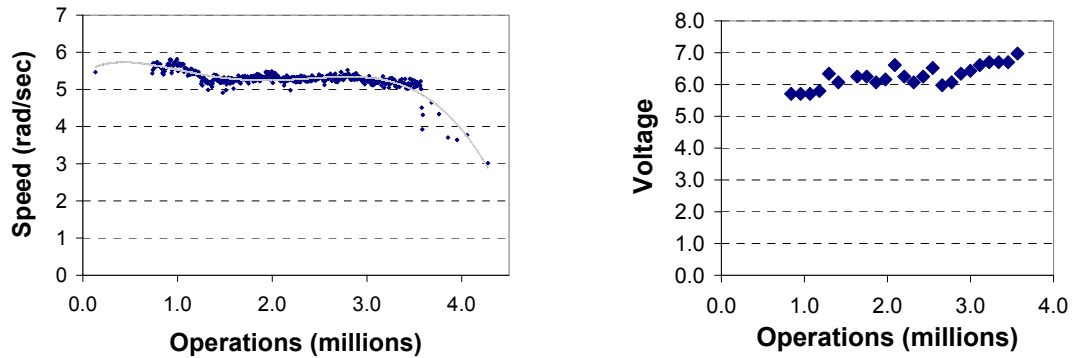


Figure 14a & 14b. HCM Qualification Testing Results – Steady State Spin Speed and Minimum Start-up Voltage

Upon completion of the vacuum portion of the second qualification series, the HCM was subjected to functional testing for comparison to the baseline parameters. Both pre- and post-life-test functional testing was performed at 19 to 21°C.

In most parameters, as shown in Table 4, the post-life measurements compared well with the early life measurements. However, the aggregate repeatability of the mechanism decreased by more than 200%. The final value of 38 arcseconds fell slightly outside of the requirement that the mechanism repeatability-to-position be less than 30 arcseconds. The free run speed also decreased over the lifetime from a value of 5.47 rad/sec to 4.65 rad/sec for a total change of 15%.

Subsequent repeatability testing with the external encoder system eliminated measurement error as a possible source of the discrepancy but also showed a drastic decline in the repeatability of the mechanism from test-to-test over the next 600,000 operations.

Table 4. HCM Life Test Results

Parameter (Bench Test ~20°C)	Pre-LT	Post-LT	Change
Detent Torque + Start-up Friction (mN•m)	67.1	77.7	15.8%
Speed Dependent Friction (mN•m / rad/sec)	10.0	17.2	71.8%
Drag (mN•m)	35.5	35.2	1.0%
Nominal Average Spin Current (mA)	106.2	106.6	0.4%
Minimum Spin Voltage (V)	45.9	53.0	15.4%
Minimum Full Motor Start-up Voltage (V)	52.3	55.8	6.8%
Nominal Delay Setting	80	100	25.0%
Repeatability at Nominal Delay Setting (arcseconds, 1- σ)	12	38	216.7%

A decrease in free-run speed was also noted during this period, accompanied by an increase in the variability of the spin-speed over multiple revolutions.

The HCM was disassembled and inspected. No damage to the motor or the bearing balls and races was observed, nor was extensive wear to the Teflon toroid ball separators.

The Braycote grease lubricant showed slight wear characterized by small patches of viscous and slightly darkened material pushed away from the bearing races. No particle contamination like that seen in the previous HCM failure was found in the lubricant.

Table 5. Post-Life-Test Additional Repeatability Testing

Ops	Spin Speed (Rad / sec)	Spin σ	Repeatability (arcsec 1- σ)	Delay Setting
134,360	5.47	0.05	12	80
3,683,930	4.65	0.12	38	100
3,760,952	4.34	0.13	62	120
3,854,396	3.71	0.14	80	150
3,951,228	3.64	0.14	140	150
4,057,168	3.77	0.16	160	160
4,276,882	3.02	0.17	250	160

The mechanism was reassembled with a new set of bearings and subjected to break-in sequences and functional testing identical to the previous two qualification series. The mechanism performed as expected in all measured parameters and showed an aggregate repeatability of 13 arcseconds single standard deviation and was tuned for best performance at a delay setting of 100.

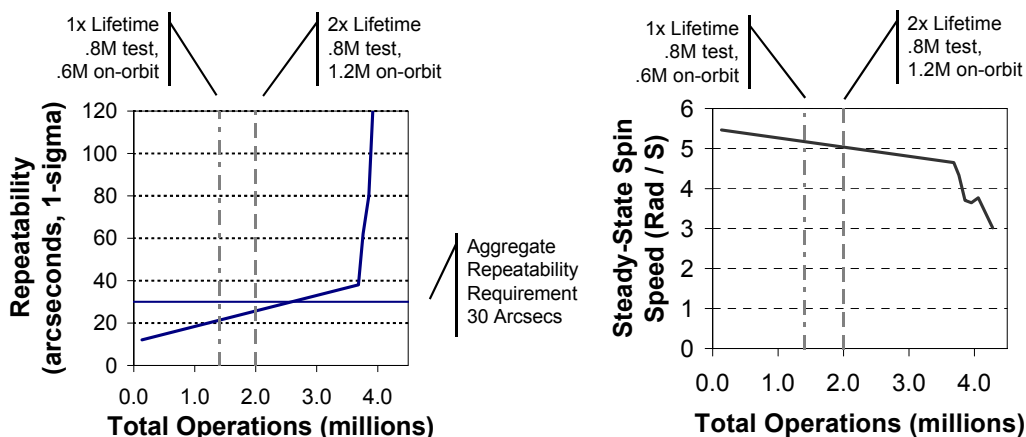


Figure 15a & 15b. Lifetime Repeatability Measurements (with Requirements) and Mechanism Speed

Flight Mechanism Acceptance Testing

Four HCMs were constructed and tested for flight at LMSAL. The testing of these mechanisms provided more information about the characteristics of the design and the relationship between each of the properties. The key early-life testing results for these mechanisms are presented in Table 5. As expected, the results for the flight mechanisms were quite similar to those for the HCM development testing. The HCMs with higher friction had lower steady-state spin speeds and higher minimum start-up voltages and required greater delay settings for optimum repeatability. All of the mechanisms exceeded the repeatability and torque margin requirements for the mechanism.

Table 5. Flight Mechanism Pre-Shipment Testing Results

Parameter	L20-FM	L30-FM	L40-FM	L50-FM
Minimum Spin Voltage	5.9	6.3	5.5	5.5
Minimum Full-Motor Start-up Voltage (V)	7.2	7.5	7.4	7.3
Damping (mN•m / rad/sec)	10.5	18.9	14.3	14.1
Drag (mN•m)	20.1	23.2	2.8	18.5
Spin Current (mA)	97	103	92	92
Nominal Free-Run Speed (rad / sec)	6.8	4.0	6.0	5.6
Nominal Delay Setting (20°C)	30	130	50	90
Aggregate Repeatability at Nominal Delay Setting	19	14	17	15
Total Ops Prior to Shipment	254,000	281,000	284,000	324,000

Discussion

The HCM qualification testing verified that the mechanism is robust in design and construction and has sufficient torque margin, on-orbit adjustability, and lifetime margin to complete its two-year nominal mission. However, the degradation of the repeatability performance over the mechanism's lifetime was shown to be a limitation of our design. A full explanation of the HCM performance and limitations to performance would require analysis and testing that are beyond the scope of this development program. However, several general observed phenomena may explain the performance of the HCM throughout its development and testing.

The decrease in the repeatability of the HCM over its life can be traced to selection of Braycote 600 EF grease as a lubricant. While this decision was conservative, based its heritage and compatibility with the designs of the COR1 and COR2 telescopes, typical small changes in its properties over life greatly affected the performance of the HCM design. It was expected that increases or decreases in bearing friction could be counteracted by increasing or decreasing the HCM delay setting. However, it was not the total change in bearing friction, but variation of bearing friction at low speeds and small angular distances that decreased the mechanism repeatability over the course of its life. It has been demonstrated that bearing torque noise increases as the grease lubricant begins to deteriorate. This effect is especially strong at low speeds where slight torque variations affect the rotation speed relatively more [3].

The effect of increasing torque noise is strongly linked to the repeatability of the mechanism. After cessation of commutation, the rotor coasts, with moderate braking, to a stop in a detent. Changes in the friction torque over the 2° braking phase prior to stop that cause 1% change in average rotor speed could affect the final stopping position of the rotor by as much as 70 arcseconds. Since it appears that the noise is random, and based in certain locations in the bearing, the torque noise is different for each movement to a particular location and causes the rotor to stop in an ever-widening range of positions.

Slight wear in greases do not typically affect the average running torque of the bearing at high speeds. However, variation in the average steady-state spin speed of the HCM, typically about 5 rad/s (280 °/s), showed some effects of torque noise. Sampling the revolution time of the mechanism over several thousand revolutions at the mechanism end-of-life showed that the speed varied as much as 10% between consecutive rotations and typically varied about 5%. This compares to beginning-of-life spin speeds that were typically 1% different from rotation to rotation.

The total speed dependent bearing friction increased a total of 71% during the approximately 3.4 million testing and lifetime simulation operations, manifesting itself in an approximately 20% decrease in spin speed. Because this data was derived from measures of the spin speed over a revolution, the increase is likely due to increasing torque noise.

It is unknown what effect temperature will have on repeatability at the end of the HCM life. A decrease in repeatability was seen with increasing temperature during the thermal functional test performed early in the life of the mechanism. It is likely that this trend will be exacerbated with mechanism life due to the greater stress to the grease lubricant.

The drastic decline seen over the last 600,000 operations of the HCM test sequence (shown in Figure 15a) is not easily explained. Catastrophic degradation of performance of mechanisms with Teflon toroid separated bearings lubricated with Braycote greases was seen previously in several LMSAL mechanisms constructed for NASA's Solar B Focal Plane Package. These mechanisms, however, operated at constant velocity in a single direction, instead of intermittently as in the SECCHI HCM. Their failure was characterized by a sharp increase in bearing friction at approximately 20 million revolutions and was caused by significant wear to the Teflon separators. While this failure mode is quite different than seen in the HCM, there is evidence that torque noise also increased in Solar B motors prior to their failure.

Conclusions and Next Steps

The design of the HCM was validated through our qualification testing. The effort also provided valuable information about optimizing the flight mechanisms while on-orbit and how to improve future designs for similar motors.

Several operations rules are recommended based on the results of the testing sequence. First, because it was shown that the HCM is most repeatable when the move angle was 90° or greater, key moves of the HCM during observations will be at least this large with a nominal observing rotation of 120°. Rotations that are smaller than 30° will be preceded by a full revolution. Second, while it is intended that little or no adjustment in the HCM delay settings be required during the SECCHI prime mission. Increases in the flight mechanism delay settings may be required in extreme cases to offset increasing friction in order to maintain high repeatability. Evidence in the coronagraph images will be exploited to indicate changing repeatability in the mechanism. Finally, adjustments to the delay setting may also be required should the instrument temperature be lower or higher than the nominal projected temperature. While the mechanism itself cannot provide sufficient feedback to make these adjustments, the temperature feedback available while on orbit will be used to re-tune the mechanism during the mission.

The lessons learned in this study provided valuable design information for the development of a similar hollow-core motor for the Helioseismic Magnetic Imager (HMI) on the Solar Dynamics Observatory (SDO) (Scherrer 2002). The HMI HCM is to have a minimum aperture of 35.6 mm and will be expected to perform more than 80 million operations during a five-year nominal mission with the same repeatability as the SECCHI HCM. The design relies on the use of a smaller bearing with a one-piece, phenolic retainer, instead of the Teflon toroid separated bearing used in the SECCHI HCM. Nye 2001B oil will be used as a lubricant. With the additional design difference of much lower cogging torque than the SECCHI HCM, this arrangement is anticipated to produce much less variability in the bearing friction – and less torque noise – during the lifetime of the mechanism. This will allow for high lifetime repeatability performance. A control system identical to that used for SECCHI will be used for HMI. The smaller cogging torque will allow for much simpler correlation between delay setting and motor stopping position and less variability in the bearing friction will ensure that the stopping position is as repeatable as possible.

The challenges in this design will be characterizing the motor friction through a comprehensive lifetime testing and careful correlation of friction data to delay settings for on-orbit tuning. The variation in the bearing friction will be measured during low speed operation and an attempt will be made to measure the mechanism repeatability continuously during the course of the vacuum lifetime operation.

References

1. Akin, David, et al. "Three High Duty Cycle, Space-Qualified Mechanisms." *Proceedings of the 27th Aerospace Mechanisms Symposium* (1993)
2. Brueckner, G.E., et al. "The Large Angle Spectroscopic Coronagraph (LASCO)." *Solar Physics*, Volume 162, pp 357-402 (1995)
3. Conley, Peter L. Ed. *Space Vehicle Mechanisms: Elements of a Successful Design*. John Wiley & Sons, Inc. pp. 315 (1998)
4. Harris, Tedric A. "Rolling Bearing Analysis." *John Wiley & Sons, Inc.* pp. 452 (2001)
5. Howard, R.A., Moses, J.D. and Socker, D.G. "The Large Angle Spectroscopic Coronagraph (LASCO)." *Proceedings of the SPIE*, Volume 4139, pp 259-283 (2000)
6. Scherrer, P. H. "The Helioseismic and Magnetic Imager for the Solar Dynamics Observatory." *American Geophysical Union, Fall Meeting* (2002)
7. Thompson, William T., et al. "The COR1 Inner Coronagraph for STEREO-SECCHI." *Proceedings of the SPIE*, Volume 4853 (2003).
8. Wülser, J.-P., et al. "EUVI: The STEREO-SECCHI Extreme Ultraviolet Imager." *Proceedings of the SPIE*, Volume 5171 (2003).

Design and Development of the Primary and Secondary Mirror Deployment Systems for the Cryogenic JWST

Paul Reynolds*, Charlie Atkinson* and Larry Gliman*

Abstract

With a 7-meter primary mirror (PM) aperture, the James Webb Space Telescope (Figure 1) will require structures that remain stable to levels on the order of 10 nanometers out of plane under dynamic and thermal loading while operating at cryogenic temperatures. Moreover, the JWST will be the first telescope in space to deploy primary and secondary mirrors. The resulting primary mirror (PM) aperture will not only be segmented, but will have hinge-lines and associated latches. The secondary mirror will be deployed with folding booms that latch to support it approximately 7 m away from the PM. This paper describes the design of the JWST Optical Telescope Element (OTE) structures and mechanisms, focusing primarily on the primary and secondary mirror deployment systems. It discusses the driving design requirements, how the resulting designs satisfy those requirements, and how the risk associated with these very large, stable, deployed structures was reduced through development and testing of the Development Optical Telescope Assembly (DOTA).

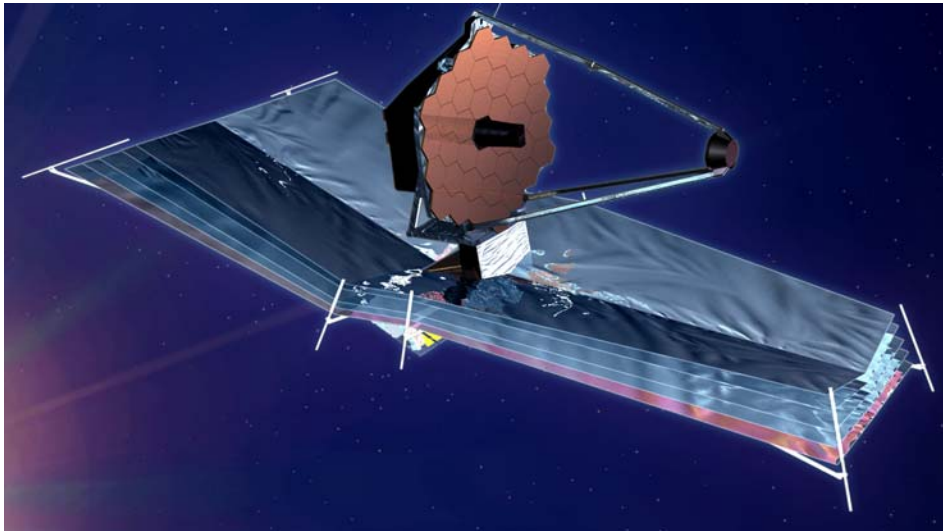


Figure 1. James Webb Space Telescope

Introduction

The James Webb Space Telescope (JWST) is a 7-m cryogenic telescope with near and mid-infrared instruments for imaging and spectroscopy. It will be used to help understand the shape and chemical composition of the universe, and the evolution of galaxies, stars and planets. The program held its Systems SRR in December of 2003, with PDR scheduled for 3/06, CDR in 3/07 and launch in 2011. NASA's Goddard Space Flight Center runs the JWST project out of Greenbelt, Maryland and is also responsible for delivering the Integrated Science Instrument Module (ISIM) to the observatory. Northrop Grumman Space Technologies (NGST) is the prime contractor and is teamed with: Ball Aerospace, who will provide the telescopes optics and wavefront sensing and control system, Kodak, who will integrate the optics onto the telescope structure assembly, and Alliant Techsystems, who will design and build the OTE's precision backplane structure and Secondary Mirror Support Structure (SMSS) struts. As the prime contractor, NGST has overall program responsibility and is responsible for the design and fabrication of

* Northrop Grumman Space Technology, Redondo Beach, CA

the OTE, spacecraft, and sunshield and the overall integration of the observatory. As part of NGST's responsibilities we are designing and building the deployment systems for the OTE. The OTE has 4 principal deployments: a tower deployment that thermally isolates the cryogenic telescope from the warm spacecraft and sunshield, two primary mirror wing deployments, and a secondary mirror deployment.

This paper will focus on the development of the deployment systems for the primary mirror wings and the secondary mirror. The discussion will center on some of the unique design challenges including deployment and operation at cryogenic temperatures, and the need for nanometer level stability over extended observations and after slewing from one target to the next. It will also discuss in detail the development and testing of the DOTA structures and mechanisms, how the DOTA designs relate to the JWST designs, and how the DOTA test results relate to the JWST requirements.

Requirements and Design Drivers

The JWST observatory will orbit the second Lagrangian point, L2, which is located 1.5 million kilometers from earth, in line with the earth and sun (Figure 2). The reason for this choice of orbit is the desire to passively cool the telescope to cryogenic temperatures with a deployable sunshield that blocks light from the Sun, Earth and Moon. The telescope needs to be at cryogenic temperatures to prevent it from emitting more radiation than the infrared light from faint and very distant objects.

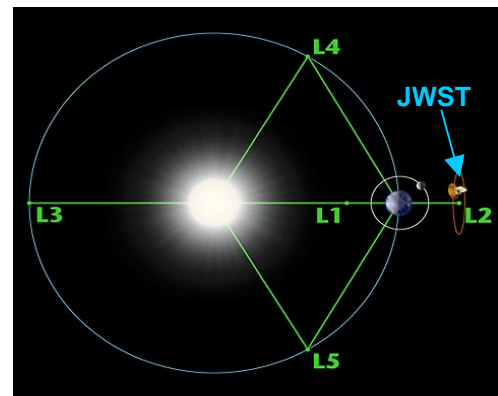


Figure 2. JWST Orbit Around L2

One of the primary drivers to shape the JWST architecture was the need to configure a large primary mirror that would stow along with its associated secondary mirror, instrument suite, sunshield, and spacecraft, within the volume provided by a medium Evolved Expendable Launch Vehicle (EELV). Essential to this objective was the need to keep deployments as low risk as possible and create optics support structures stable to nanometer levels.

Figure 3 shows the deployed observatory with some of its critical dimensions. The primary mirror is 7 m in diameter and the secondary mirror is 7.2 m forward of the primary mirror vertex. The sunshield, which passively cools the telescope, is approximately 25 m long by 10 m wide. A telescoping deployment tower extends 1.5m to separate the OTE from the spacecraft, resulting in a total observatory height of over 10m.

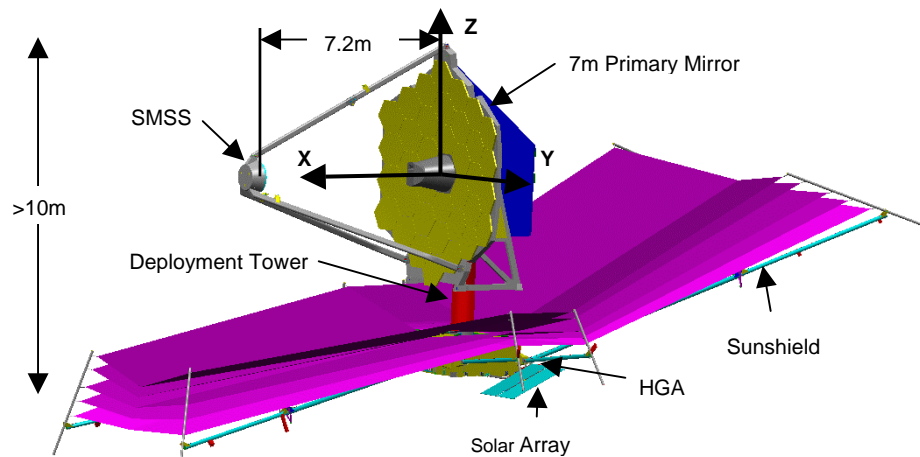


Figure 3. Deployed JWST

Since the EELV static envelope is 4.2 m in diameter, the primary mirror, secondary mirror, sunshield, solar arrays, radiator shades and High Gain Antenna (HGA) needed to be folded or compressed to fit within the allowable volume. The OTE to Spacecraft Deployment Tower raises the OTE off of its launch

lock attachment to the spacecraft and also provides thermal separation. Figure 4 shows the stowed observatory with the two wings and SMSS folded to provide clearance to the Atlas V static envelope.

The launch stiffness requirements for the observatory are specified in the EELV users guide. Based on the requirements and maturity of the design, the observatory is being designed to have a stowed natural frequency of 11 Hz. It must also be designed to survive the EELV launch loads listed in Table 1.

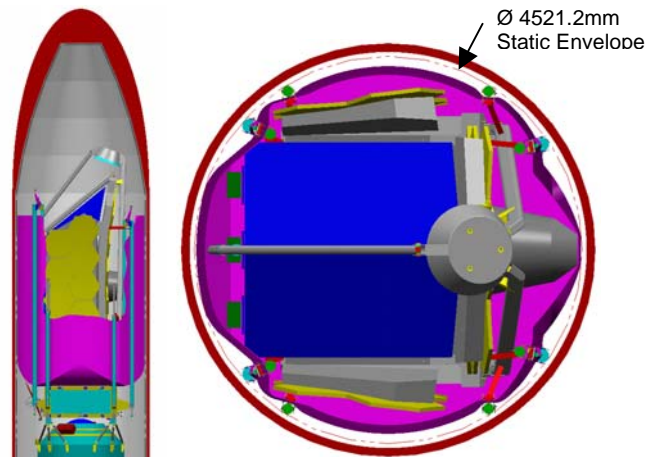


Figure 4. Stowed Observatory in Atlas V

Table 1. EELV Inertial Launch Loads

Case	Axial	Lateral		
Maximum Axial	2.0 ±5.5	2.0 at OTE/SV Interface	2.6 at OTE Top	Linear variation between
Maximum Lateral	2.0 ±2.60	3.5 at OTE/SV Interface	4.5 at OTE Top	Linear variation between

Once the observatory has separated from the launch vehicle, the solar arrays and radiator shades are deployed so the observatory can begin generating power. This is followed by the deployment of the HGA. The sunshield is deployed next and must deploy prior to the OTE since it cocoons the OTE when it is stowed. Next, the tower deploys the telescope away from the spacecraft and sunshield for thermal isolation. The planned deployment sequence has the SMSS deploying next, followed by the +Y and -Y primary mirror wings, though this order is not required.

Nominally, the tower, SMSS and wings deploy directly after the sunshield, while the telescope is still well above its cryogenic operating temperature. However, the OTE must be designed for any contingency including delays that could result in structure and mechanism temperatures as low as 30K prior to deployment. A combination of cryogenic deployment motors, heaters and careful selection of the mechanism materials will be used to make deployment at these very low temperatures possible.

Both the Primary Mirror Segment Assemblies (PMSA's) and the Secondary Mirror Assembly (SMA) have active control to correct for deployment errors or distortions that occur during cool down. However, the amount of allowable deployment error is limited by the wavefront sensing and control systems ability to capture an initial image so it can make its corrections. The deployment repeatability requirements are shown below in Table 2.

Table 2. Deployment Repeatability Requirements

JWST Requirement	X Despace (mm)	Y Decenter (mm)	Z Decenter (mm)	Theta Z (arcmin)
Primary Mirror Wings	1	0.1	0.1	1
Secondary Mirror	3	3	3	5

Once the OTE is deployed, the primary and secondary mirror support structures and mechanisms must remain stable to prevent degradation of telescope image quality and to eliminate the need for time-consuming adjustment of the adaptive optics. The thermal stability requirements of the primary mirror wing latches and SMSS (shown in Table 3) are provided in the form of allowable distortions during the worst case operational temperature swings. The sources of these distortions include non-zero CTE materials, variations in CTE within a material, manufacturing tolerances and thermal gradients across the structures and mechanisms.

Table 3. Thermal Stability Requirements

PM Latch Distortion Parameter	req't	units	SM Motion Parameter	req't	units
Z translation (parallel to hinge line (HL))	0.05	μm dec	Focus	1.34	□m
Y translation (perpendicular to HL)	0.1	μm dec	Translation	5	□m
Piston of Mirror Segment	0.005	μm piston	Tip/Tilt	0.5	arcsec
Rotation about HL (Z)	0.01	μrad			
Rotation perpendicular to HL (about Y)	0.0025	μrad			
Gamma rotation (about X)	1	μrad			

In addition to errors caused by changes in the thermal environment, there are allocations for errors due to nano-lurching caused by stresses internal to the structures and mechanisms and/or on-orbit loading. The JWST image quality requirements allow for 20 nm of wavefront error (WFE) for these micro-dynamic events. Because of these requirements, the systems must be designed with micro-dynamics in mind and will be tested under operational load conditions to demonstrate stability within their allocation.

Disturbances from the spacecraft (e.g. reaction wheels) are attenuated by a 1-Hz isolator located at the base of the OTE deployment tower. Deployed natural frequency requirements have also been set for the OTE to further prevent the spacecraft disturbances from causing unacceptable motions of the primary mirror. These are referred to as line of sight (LOS) and WFE jitter requirements. The required natural frequencies for jitter are determined through integrated modeling using NASTRAN finite element math models in conjunction with Code V optical analysis models. Based on these models, the PM wings and SMSS must have deployed natural frequencies of 15 Hz and 7 Hz respectively.

The Design

Design Practices for Deployable Optics

When we began our mechanisms design, NASA Langley Research Center, with the help of JPL and the University of Colorado had recently published a study identifying guidelines for good design practices for micro dynamically stable deployable optics. Much of the design practices, however, had not been proven out in working designs. The approach NGST took for the PM and SMSS latch designs was to apply the published good design practices [1] that fit with our design approach, along with standard practices typically applied to mechanism design at NGST. Then an in-house system was developed to test the performance of the resulting hinge and latch designs.

Among the good design practices applied was to have kinematic (or quasi-kinematic) interfaces between optical components. One of the primary benefits we saw with a kinematic interface was the ability to preclude the development of unwanted interface loads (i.e., loads due to manufacturing and assembly tolerances and thermal loading due to cool-down), hence reducing the likelihood of friction-induced slippage. In addition, we believed using this type of interface in a deployment latch would result in good deployment repeatability. This is clearly demonstrated in the PM wing latch design.

Non-conforming contact geometries (i.e., point or line contacts) were used at the latching interfaces on the PM wing latches and for the mid-hinge of the SMSS. It is believed that this type of interface helps insure that the interface stress distribution is accurately known and prevents sensitivity to localized imperfections over large mating surfaces. However, in our applications we found that trying to use non-conforming contact geometries in a truly kinematic configuration resulted in unacceptably low stiffness.

Therefore, it was necessary to sacrifice determinacy in the load path by adding redundant non-conforming contacts for some degrees of restraint (DOR) to meet our minimum stiffness requirements.

Having a hinge as part of the deployed load path of a precision deployment mechanism adds complexity and uncertainty. Using a loose hinge pin that controls deployment but takes the hinge out of the latched load path can alleviate the uncertainty while minimizing complexity. We found this to be the case for the PM wing latches. However, we found the benefits of this approach to be application specific and felt that the SMSS mid-hinge design was better with the hinge designed as part of the deployed load path.

In other instances it was difficult to have semi-kinematic or non-conforming interfaces and the loads needed to be taken by friction joints. This was the case for the SMSS end-hinges. To compensate, the load capacity (i.e., stick-slip load) of the interface was designed per the recommendation of [1], to be much greater (e.g., a factor of 10 greater) than the maximum expected operating load of the mechanism.

In all applications the deployment mechanisms were located in-line with the primary load carrying members of the structure and the footprint of the latches was maximized to minimize the sensitivity to instabilities at the latch interfaces. In addition, the stiffness of the latches was maximized by minimizing their effective length and maximizing the elastic stiffness with high-modulus materials (e.g., titanium). This also proved to be beneficial for thermal stability since it minimized the length of the higher CTE materials.

Distributed preload systems were used in most applications since it was not practical from a mass and cost standpoint to have an independent preload device for each latch interface. However, the preload mechanisms were designed to be much more compliant than the interface fittings which transfer the operational loads. Providing this compliance keeps the preload device out of the primary stiffness path and maintains a relatively constant preload across the interfaces.

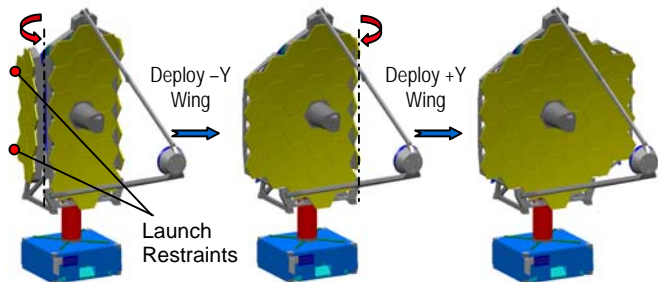


Figure 5. Primary Mirror Wing Deployment

Primary Mirror

The primary mirror deployment and latch mechanisms consist of a pair of hinges and four latches for each wing. The deployment hinges and wing latches act as independent systems.

Wing Deployment Hinges

The hinges have a dual function. First, the hinges, along with two launch restraint mechanisms, carry the wing launch loads. Second, they rotate the wings 103 degrees into the capture range of the deployed wing latches. The wing deployment sequence is shown in Figure 5. Each hinge has a pair of lug and clevis fittings joined by a loose hinge pin providing redundant rotating surfaces. The hinge pin has sufficient clearance to the lug and clevis fittings to preclude it from being in the load path after the latches have been secured. This guarantees the hinges will not affect deployment repeatability or generate loads during operation that could cause micro-dynamic instabilities at the critical latch interface.

A stepper gear-motor mounted to the lug of one of

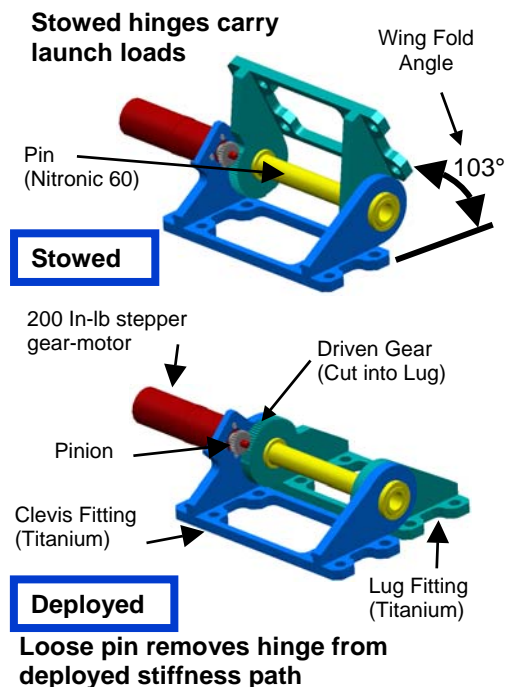


Figure 6. Deployment Hinge Design Details

the two deployment hinges is used to rotate the wing from the stowed to the deployed position. The gear-motor drives the clevis fitting through spur gears that provide a 4/1 gear ratio over the motors 22.5 Nm (200 in-lb) output torque capability for roughly 90 Nm (800 in-lb) of available deployment torque. The hinge fittings are machined out of titanium and the hinge pins are Nitronic 60 to prevent galling. The bolt hole pattern on the titanium fittings has a single pinned hole along with oversized and slotted holes to allow the fittings to shrink with respect to the near zero CTE composite backplane structure. MoS₂ dry film lubricant is used on the hinge gears, hinge pins, and the spacers between the lug and clevis ears. The details of the hinge design are shown in Figure 6.

Wing Latches

The latches have a singular role and are not in the load path during launch. Their function is to align and secure the deployed backplane wings to the backplane center section, thus creating the stable backplane structure that supports the 36 primary mirror segments. The driving requirements for the wing latch design were deployment repeatability, deployed stiffness (to meet LOS and WFE jitter requirements), thermal stability and micro dynamic stability.

We believed the best way to achieve good wing deployment repeatability was to use a kinematic interface with fittings specific to the six degrees of restraint (DOR). The six DOR are implemented at three locations across the interface between each wing and the backplane center section. At the first location a 3-DOR latch set provides a sphere-in-cup interface that locates the wing in the two in-plane directions and provides one of the three points that defines the interface plane. The second location holds a 2-DOR latch set that provides a sphere in groove interface that fixes the rotation about the first fitting set and establishes the second point of the interface plane. The third location holds a 1-DOR latch set that is a sphere on a flat and is the final point needed to define the latch interface plane. The latches are shown in Figure 7. They are lubricated with MoS₂ for low friction between the mating pairs and to prevent cold welding, and a 2669-N (60-lb) preload is used to drive the fittings into the same determinate position each time.



Figure 7. Latch Sets

Because the wing to center section is long and slender, it wasn't possible to provide the deployed wing natural frequency required for LOS and WFE jitter with just three fitting sets. Therefore, five adjustable non-conforming 1-DOR (A1 Fittings) sets were added and configured in pairs as shown in Figure 8 with a cryogenic preload device centered between each pair. The pairs of fittings were located as far apart as possible using the entire depth of the backplane to provide the largest footprint and most efficient stiffness path.

The latch sets, shown in Figure 7, are Ti 6Al-4V ELI. More exotic, lower coefficient of thermal expansion (CTE) materials such as silicon carbide were considered for the latch materials. However, these materials would have been very costly. By keeping the cross sections of the latches thin, this common, robust metallic could be used while maintaining overall thermal distortions to well within the allocation. The final latch design was 12.7-mm (0.5") thick (shown in Figure 9).

To eliminate loads at the latch interface due to thermal cool-down, cryogenic preload devices are engaged and only lightly loaded during the initial deployment. Then, after the OTE has cooled to its final operating temperature, the devices are backed off to remove any stresses in the system. Finally, the latch sets are preloaded again to their flight operational levels.

To keep the Hertzian stresses low on the titanium latch sets with a 2669-N (600-lbf) preload, a 100-mm (~4") radius was required on the spherical half of the set. This was easy to accomplish with the 1-DOR latch set that consisted of a spherical fitting interfacing with a flat. It was slightly more difficult for the 2-DOR and 3-DOR latch sets since it was desirable for the spherical surfaces to interface with flats at a 45° angle to provide similar stabilizing forces in the axial and transverse directions. The limits of 12.7 mm

(0.5") thickness, 100-mm (4") spherical radius and 45° interface flats drove the resulting geometry. Since the resulting fittings had a diameter of 83 mm (3.25"), the fittings had to be installed with a single fastener centered on the fitting so that positioning was maintained, and the CTE mismatch between the fittings and the near-zero CTE backplane structure would not result in unacceptably high loads.

- The Quasi-Kinematic I/F reduces stresses due to initial adjustment mis-alignments and thermal deformations from cool-down

- Cryo motors allow for final latching after cool-down

- The wing deployment repeatability is within .075 mm- V1 & .1 mm V2 & V3 (At the Latch Interface)

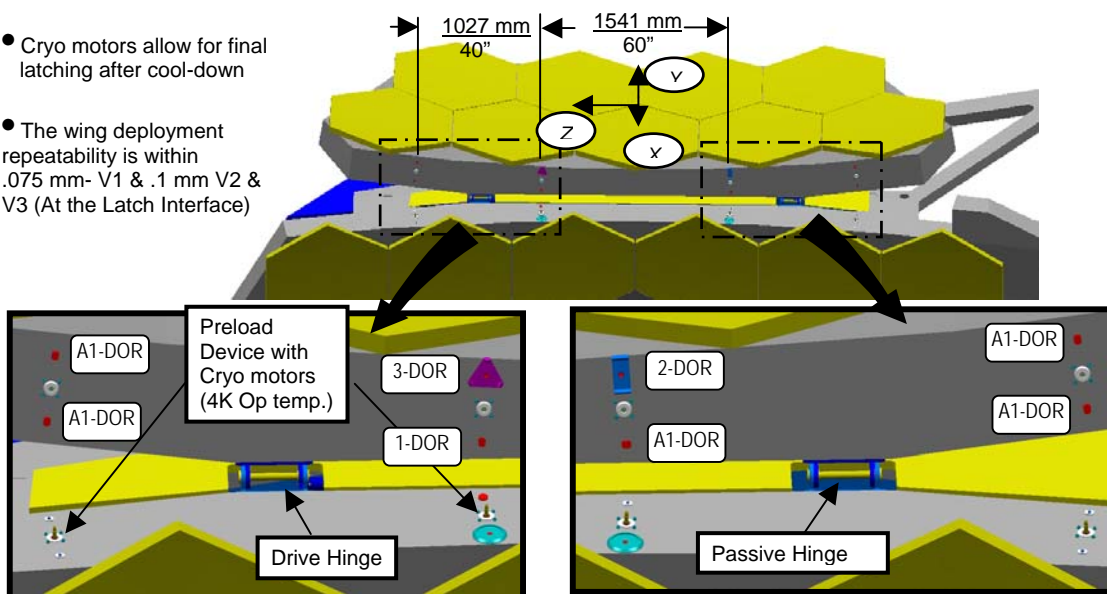


Figure 8. Primary Mirror Hinge and Latch Sets

The preload device for the latches uses a 3/8-24 UNJF-3A screw driven by a stepper gear-motor that engages and screws into a floating nut in the mating latch (Figure 10). The two halves of the device are pulled toward each other but never bottom out so the preload device never provides a stiff load path. It is critical to have the nut properly aligned to the drive screw before it starts turning to prevent cross threading. The floating nut is spring loaded in a loose housing that prevents nut rotation during tightening but allows a small amount of angular motion for nut to drive screw alignment during engagement. A feature was also added to the tip of the drive screw to guide the nut onto the screw and prevents the nut from rotating the mating threads out of alignment. The screw material is A286 CRES chosen for its high strength, and Nitronic 60 was chosen for the mating nut for its anti-galling characteristics. To minimize the torque resistance to the gear-motor, the drive screw has MoS₂ lubrication and a thrust bearing was used between the base of the drive screw and its housing. The thrust bearing also provides a desired compliant element to the preload device.

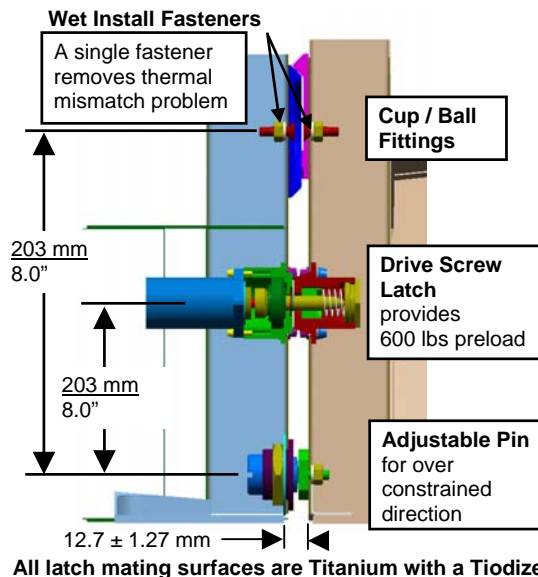


Figure 9. Latch Design Details

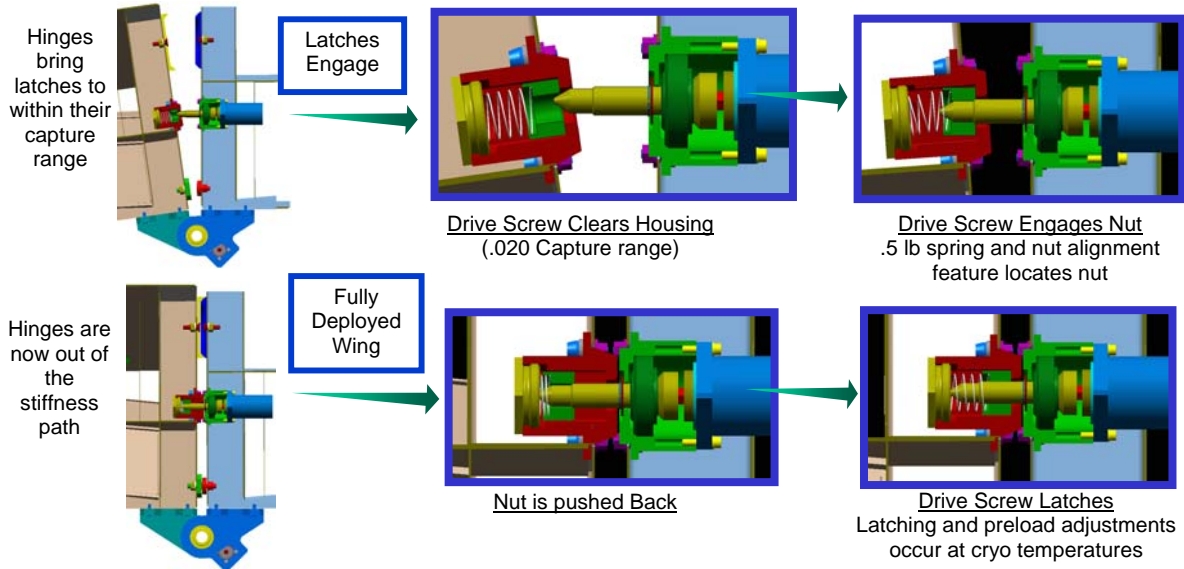


Figure 10. Wing Latch Engagement and Preload

Secondary Mirror Support Structure

The SMSS design is a deployed tripod as shown in Figure 11. A tripod design was selected because of its superior dynamic stability and mass efficiency. The deployment system is a four-bar linkage driven by a stepper gear-motor. Since wavefront error (WFE) is very strongly affected by axial despace (defocus) of the secondary mirror assembly (SMA), the design uses a very low CTE composite material system in the SMSS tubes. This produces a very small despace contribution to wave front error over the worst-case hot-to-cold conditions.

SMSS Deployment Drive

The SMSS is driven by a single stepper gear-motor located at the inboard single strut hinge as shown in Figure 12. This hinge was selected as the drive location since it provides the best mechanical advantage for the system. The gear-motor pinion drives a spur gear mounted on the inboard single strut providing an additional 4/1 gear ratio over the 22.5 Nm (200 in-lb) torque capability of the gear-motor. This provides roughly 90 Nm (800 in-lb) of drive torque capability.

The SMSS, like the PM wings, is configured to minimize stresses in the system while latching. Although all five SMSS hinges are latched, the mid-hinge is the only one to be preloaded into hard stops. Because

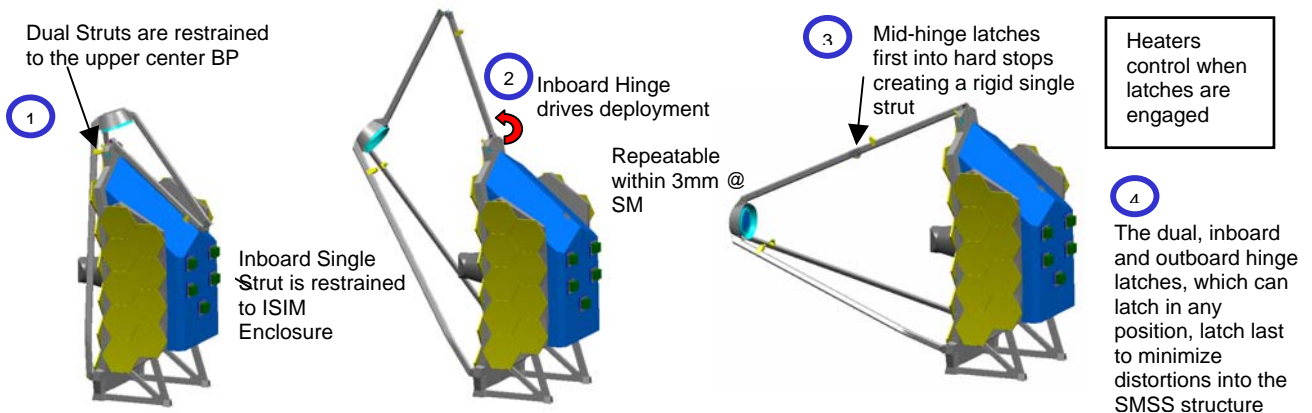


Figure 11. Secondary Mirror Support Structure

the four remaining latches take advantage of the thermal shrinkage of their aluminum components to clamp them in place during cooldown to operating temperature, they can latch at any angle of rotation.

SMSS Mid-hinge

The mid-hinge is deployed through a 168-degree rotation and bottoms out on hard stops at the end of its travel. There are two leaf spring latches (one on each side of the hinge) that engage at this point capturing catch fittings on the mating hinge half. The catch and latch base fittings are machined titanium and the leaf-spring latch is 7075 Aluminum. The latches are centered on the hinge (Figure 13), so that as the temperature drops from RT down to ~30K, the aluminum latches shrink and preload the M55J composite hinge at its two adjustable hard stops and two hinge pin to bushing interfaces. The stops provide non-conforming sphere-on-flat interfaces and the pin bushings are notched to provide non-conforming line contact interfaces.

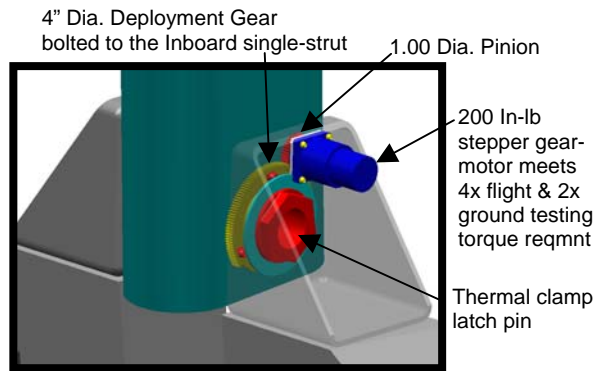
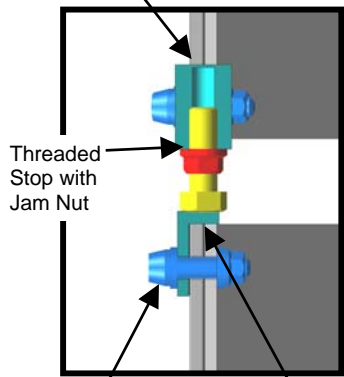


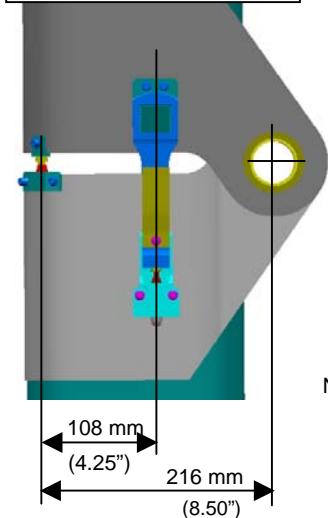
Figure 12: SMSS Deployment Drive

Adjustable Stop Design

Stops give high deployment repeatability and balanced thermal stability
Stops Bear on Hinge Fittings and Strut Tubes

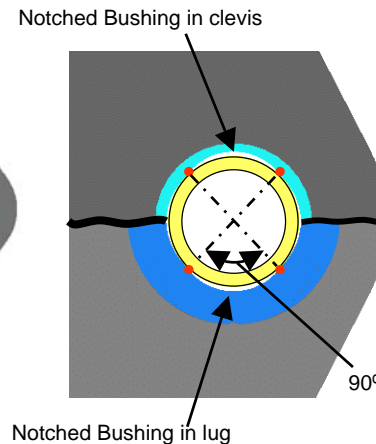


The Thermal Spring latches provide 2224N (500 lb) min. to preload both the pin and adjustable stops



Pin Design

Notches provide an anti-jitter feature



The Bushings are notched to give "Line Contact" at 4 locations for reduced jitter and improved repeatability

Figure 13. Mid-hinge Latches and Hard Stops

A spring feature was added to the latch to help compensate for any creep that could occur over the life of the mission and help provide a well-defined stiffness path. The stack of Bellville washers, shown in Figure 14, is roughly half the stiffness of the aluminum latch and has a 1-mm (0.040") stroke. Two stops were required to meet the natural frequency requirement of the hinge, and the process for adjusting them to get an equal load distribution has been demonstrated on the DOTA hardware.

SMSS End-hinge

The end hinge design is common to the dual strut hinges and the inboard and outboard single strut hinges. It has a rotation pin that provides precision deployment location plus a clamping pin that preloads the lug and clevis bushings together once the hinges are in their final deployed locations. The latches will

latch in any position without forcing the hinge to a preset location and provides a 10x load carrying capability over operational loading. The end hinge design details are shown in Figure 15.

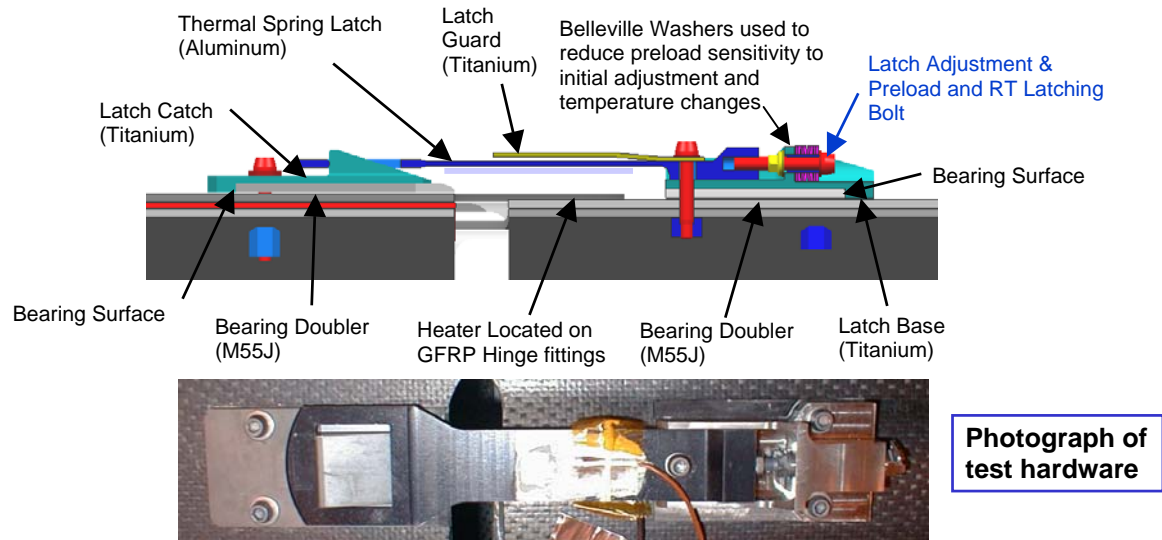


Figure 14. Mid-hinge Preload Mechanism

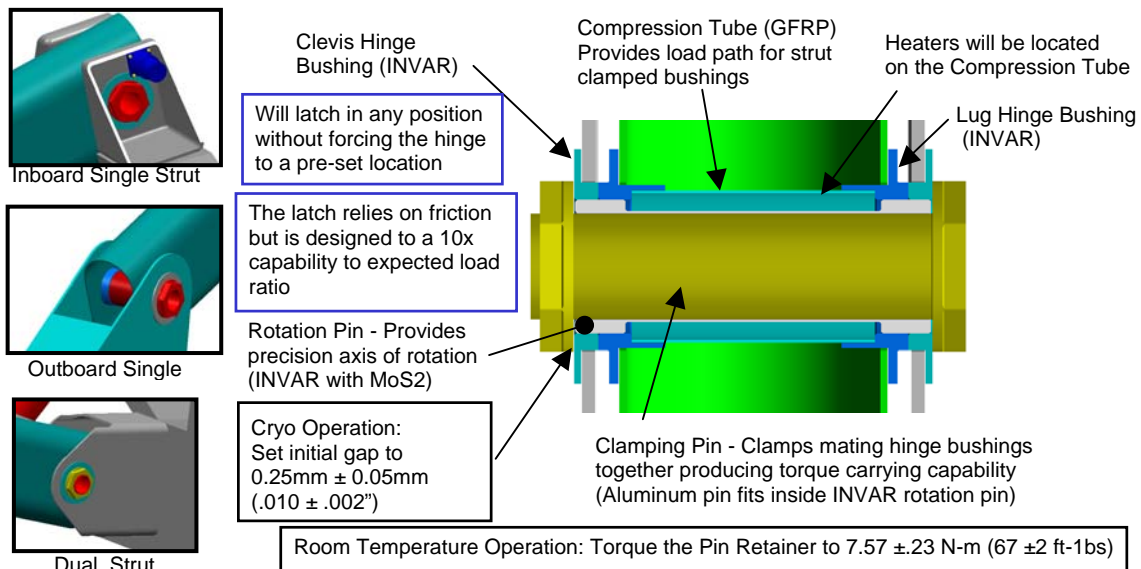


Figure 15. End Hinge Latch Design

Deployment Repeatability

The deployment repeatability of the SMSS must be such that once the latches are engaged and preloaded, the secondary mirror is within the wavefront capture range of the wavefront sensing and control system (WFS&C). The tripod design is a geometrically robust design for locating the SMA within the allowable capture range and is driven primarily by the size of the gap between the end hinge pins and bushings. The repeatability requirement and analysis result are shown in Table 5.

Table 5. SMSS Deployment Repeatability

	X Despace (mm)	Y Decenter (mm)	Z Decenter (mm)	Theta Z (arcmin)
Requirement	3	3	3	1
Analysis Result	< 1	< .5	< .5	< .5

Development Testing

This section covers the DOTA testing and associated results including; deployment capability and measurements of the repeatability of the PM wing mechanisms, characterization of the micro-dynamic stability of the wing latching system, functional latching of the SMSS hinge latches, and measurement of the load carrying capability of the SMSS end hinge. Details of the test metrology and procedures and additional thermal stability results can be found in [2].

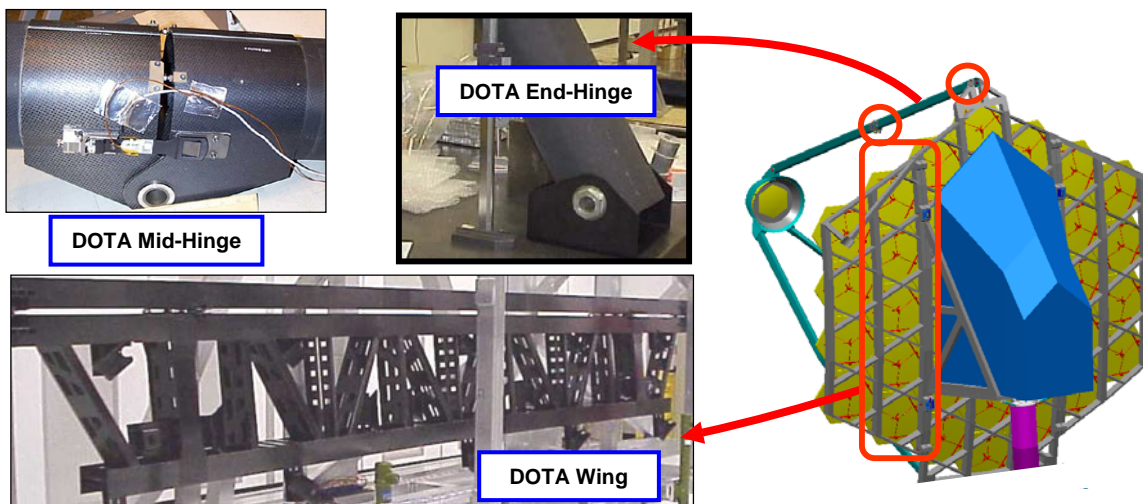


Figure 16. Cryogenic Development Optical Telescope Assembly (DOTA)

In order to understand the behavior and reduce the risk associated with very large, deployed optics support structures, NGST developed and tested the DOTA PM wing and SMSS hinges. The DOTA wing replicates a full-scale portion of the JWST PM support structure and includes a hinge-line with a full set of latches so the overall stability of the system can be characterized. The DOTA SMSS hinges and latches replicate full-scale end and mid-hinges. The DOTA hardware is shown in Figure 16.

The DOTA wing hinge/latch testing was broken into two parts. The first part had the hinges and latches integrated into an aluminum test fixture that simulated the flight structure. They were then tested as a unit at room temperature (RT) for deployment repeatability and micro-dynamic stability. Once this testing was complete, the mechanisms were removed from the test fixture and integrated onto the DOTA wing structure. Then, as an integrated structure, the DOTA wing was tested at cryogenic temperatures for thermal and micro-dynamic stability.

Hinge/latch repeatability

The fixture that the wing hinges and latches were tested on is shown in Figure 17. The hinge-line was scaled down in the Z direction to facilitate testing. The deployment repeatability requirements are derived from the JWST need to have the Primary Mirror within the capture range of the WFS&C system. Deployment repeatability was measured in X, Y, Z and Theta Z directions. For each test, the hinge was driven 103 degrees from the stowed to the deployed position using a flight-like stepper gear-motor. The latches were then engaged using a torque wrench to accurately assess the torque being applied. The test was repeated 10 times for both a 1.13 Nm (10 in-lb) latching torque and the 11.25 Nm (100 in-lb) latching

torque. Repeatability measurement results are given in Table 6. The latch repeatability tests demonstrate that the DOTA wing latches easily meet the repeatability requirements for wavefront capture. The repeatability tended to degrade with higher preload and we believe this was due to the lack of stiffness in the aluminum test fixture. Although the test data met all the requirements with margin, even smaller repeatability errors are expected with the stiffer flight backplane.

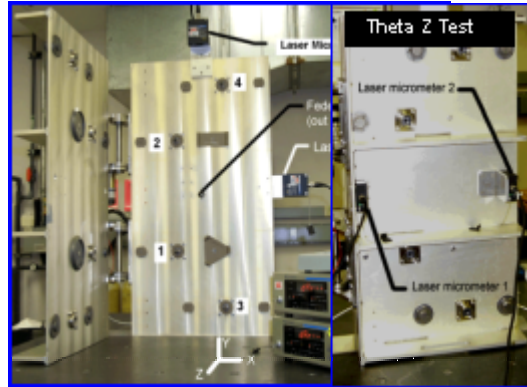


Figure 17. Test Configurations for Repeatability Measurements.

Table 6. Deployment and latching repeatability results, one-sigma

	X Despace (mm)	Y Decenter (mm)	Z Decenter (mm)	Theta Z (arcmin)
1.13 Nm error	0.020	0.030	0.043	0.15
11.25 Nm error	0.033	0.043	0.030	0.74
Requirement	1	0.1	0.1	1.0

Latch Micro-dynamic Testing

Over 100 load cycles were applied during the RT micro-dynamic testing of the DOTA latches with shear and moment loads significantly higher than those expected operationally. The first set of tests applied cyclical quasi-static loading at 0.1 Hz in each shear direction. Since it's believed that the micro-dynamics in a deployable structure is related to hysteretic response, the displacements were measured in all three directions and the hysteresis was determined by removing the linear response. Sample hysteresis results are shown in Figure 19.

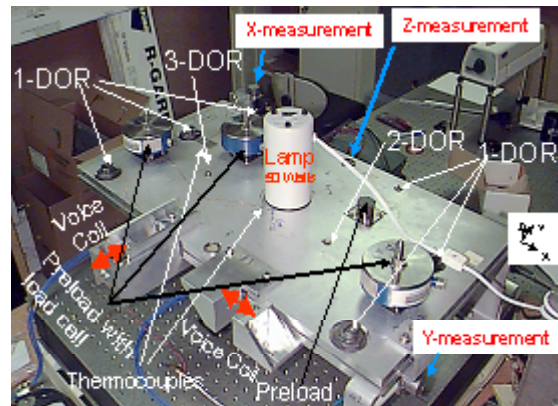


Figure 18: μ-dynamics Testing

The next set of testing also applied cyclical loading to the latch interface, while looking for evidence of “nanolurches”. Sample results for this testing are shown in Figure 20. The 9-nm lurch shown occurred with the latches at half of the operational preload and with an applied load 100 times operation loading. The final set of tests run with this latch micro-dynamic test setup applied a thermo-elastic load across the latched interface 10,000x greater than the operational thermo-elastic load. The series of tests revealed no evidence of “nanolurches” when the preload applied to the latch was consistent with its operational design of 2669 N (600 lb). Moreover, only 3 nanolurches were detected during all of the testing, with these occurring when latch preloads of 1334.5 N (300 lb) or less were applied.

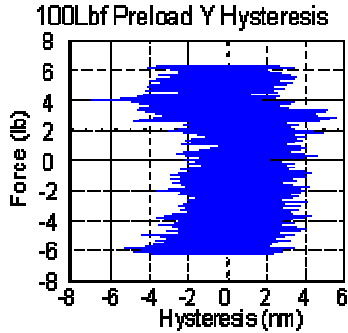


Figure 19. Sample Hysteresis Test

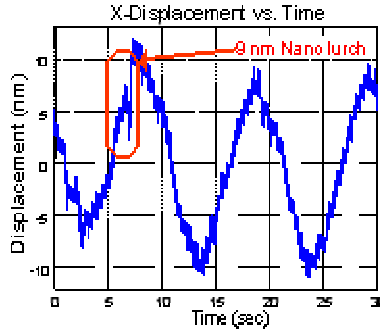


Figure 20. Sample Nano-lurch detection

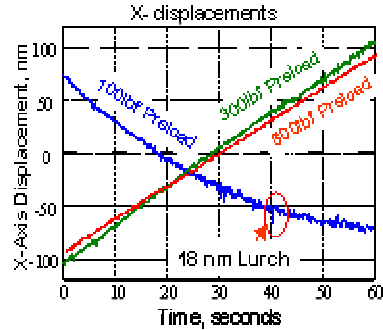


Figure 21. Sample μ dynamic Thermal Test

Thermal Stability Testing

After the latch testing was completed, the latches were integrated onto the DOTA wing structure. The DOTA wing was then transported to the Marshall Space Flight Center in Huntsville, Alabama for thermal stability testing down to cryogenic temperatures in the X-Ray Calibration Facility. Figure 22 illustrates how distance-measuring interferometers were configured to monitor the latch interface at several locations along the hinge-line. Similar to the micro-dynamics testing discussed previously, the interferometers were used to look for discontinuities in the latch behavior.

The interferometers detected frequent slips as the DOTA first achieved temperature, as depicted in Figure 23. Three of the four latches were powered for the DOTA testing and these latches were released and re-tightened (Figure 24) as planned after cool-down. As expected, this significantly reduced the amplitude and frequency of the slips. Bulk temperature testing and gradient testing was then performed on the DOTA. The bulk temperature testing consisted of a 20K thermal excursion. This was 100 times larger than the expected on-orbit thermal excursion of 0.2K creating 100x the thermal loading in the latch interface. Moreover, the gradient testing far exceeded this multiplier compared to on-orbit expectations.

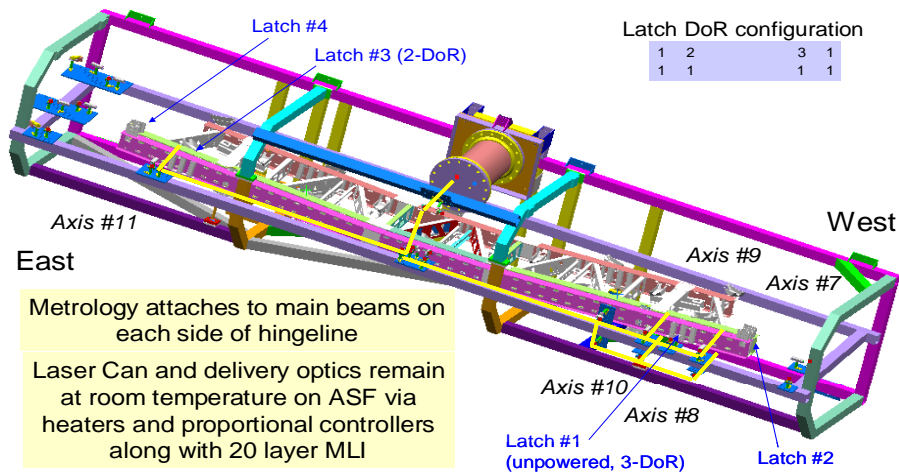


Figure 22. DOTA Hinge-line Metrology Beam Paths

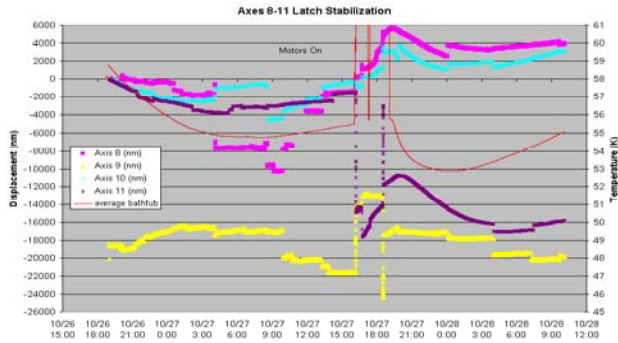


Figure 23. Hinge-line Displacements at the End of the Cool-down

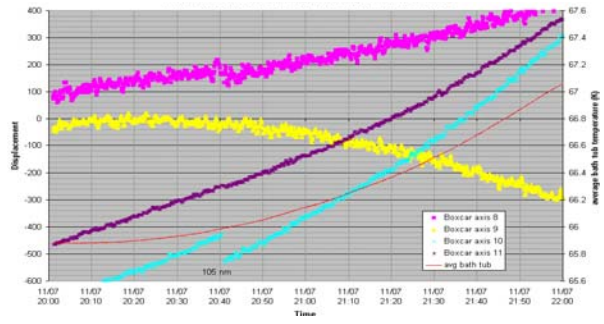


Figure 24. Latch Interferometer Data During Bulk Temperature Test

Under these high loads, interferometer axis 10 exhibited stick-slip behavior in two instances, with no other measurable discontinuities in the data. Without the ability to re-torque this latch, it suffered the loss in pre-load that results from cooling from room temperature to 50K. The observed slippage at the latch with the lower preload that is absent at the latches with operational preloads correlates with the room temperature micro-dynamic performance measurements.

DOTA SMSS Hinge / Latch Testing

To verify the key components of the SMSS, a prototype of each type of hinge (i.e., a mid-hinge and an end hinge) was built and tested. The purpose of the testing was to verify functional latching at cryogenic temperatures. In addition, the end hinge was tested to show that it has a minimum 10x margin against operational loads. Micro-dynamic stability testing on the hinges is also planned for early 2005.

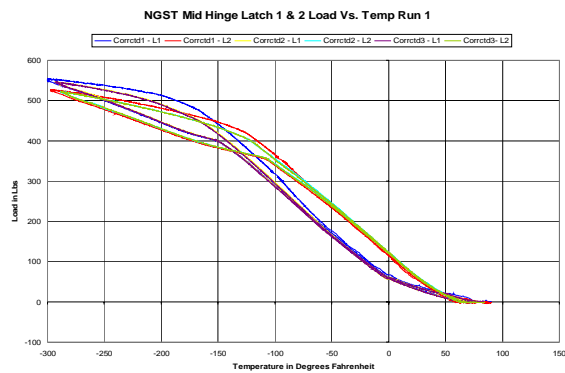


Figure 26. SMSS Mid-hinge Load vs. Temp

The cold box shown in Figure 25 was used to take the hinges down to ~88K using LN₂. Flight temperatures of ~20K could have been reached using liquid helium; however, the added expense couldn't be justified given that flight preloads were achieved at the higher LN₂ temperatures by simply adjusting the initial latch gaps accordingly.



Figure 25. SMSS Hinge Testing

Mid-hinge Testing

To test the Mid-hinge thermal latches, the preload in the spring latches needed to be monitored as the hinge assembly was taken to cryogenic temperatures. The two aluminum spring latches were instrumented with thermistors and strain gages that were calibrated down to 80K. The latch gap between the spring latch and the catch was set for a desired preload of 2335 N \pm 111 N (525 lb \pm 25 lb). The latches were then cycled down to \sim 88K (-300°F) and back to room temperature 3 times to characterize any creep due to loading and unloading the assembly. The results of the testing in the form of preload verses temperature curves are shown in Figure 26.

Several things were apparent from the test results that will help in the design of the flight latches. First, the latches proved to be very repeatable with the cool-down curves for the three cycles lying nearly on top of each other. Also, the stiffness of the latch preload paths for latch 1 & 2 were very well matched, but only after the initial cool-down from room temperature to \sim 255K (0°F). The Bellville washer stacks demonstrated good repeatability and well matched stiffness during cool-down, but the non-linear behavior and large amounts of hysteresis that is often associated with Bellville washers was evident as the latches warmed back up to room temperature.

In addition to setting the initial gap of the latches, the preload in the Bellville washer stacks is set to just below the desired operational preload. This was accomplished for the DOTA testing by measuring the desired compression of the washer stack by counting turns on the preload nut. Since this method lacked precision, the resulting initial preloads of latch 1 & 2 were off by roughly 445 N and 663 N (100 lb and 140 lb) respectively. This, however, was balanced by the added compliance in latch 1 and both latches achieved the desired flight preload.

The Bellville washers served their purpose for the DOTA test and demonstrated the advantage of having a compliant member in the latch stiffness path. However, we are currently looking into replacing the Bellville washers with a machined spring in order to increase the compliance, further reducing the sensitivity to thermal changes, and to reduce the non-linearity of the latch.

End Hinge Testing

The end hinge DOTA testing was very similar to the mid-hinge test. The clamping pin was instrumented with thermistors and a strain gage and taken down to 88K. The hinge was cycled 5 times and demonstrated very good repeatability as shown in Figure 27.

In addition, a cable with a spring and a load cell was attached to the end of the end hinge strut and tensioned with a motor until the latch broke loose. An LVDT was used to measure displacements of the strut near the latch and clearly indicated when the torque generated by the motor exceeded the torque carrying capability of the latch. The test was repeated 3 times at six temperatures (preloads), and as expected, proved to be very repeatable. The results are plotted in Figure 28 as applied slip force verses latch preload. The flight preload of 13,345 N (3000 lbf) provided an 8.47 N-m (75 in-lb) torque carrying capability, which is 10x greater than the expected on-orbit loads.

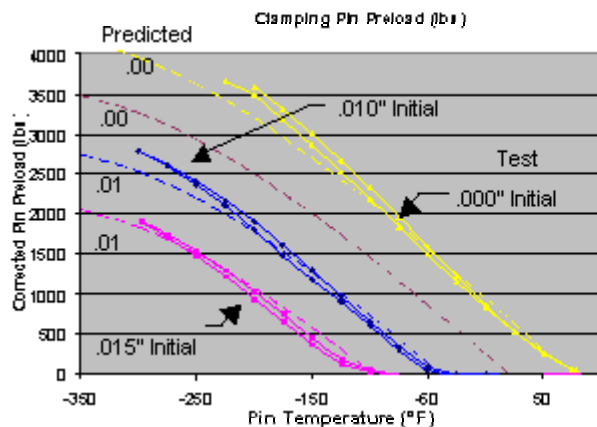


Figure 27. End-hinge Preload vs. Temperature

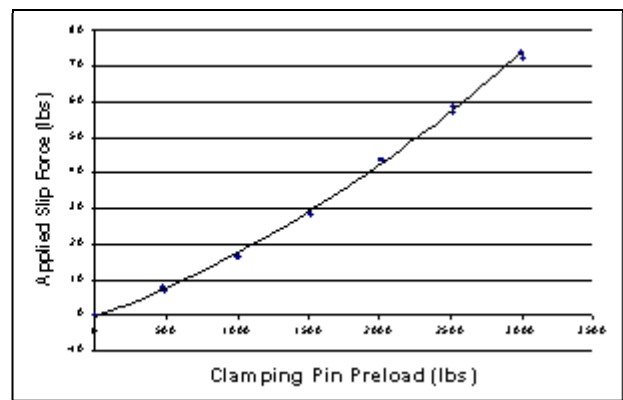


Figure 28. SMSS End-hinge Force vs. Preload Plot

Concluding Remarks

The observatory architecture and design details described in this paper are a “point in time” design that was submitted as part of the Phase 2 JWST proposal in October 2001. The program had a replan exercise in an effort to reduce program cost. This replan effort resulted in several significant changes to the architecture including a reduction in the PM diameter from 7 m to 6.5 m and a change to the number of segments in the primary mirror from 36 to 18. These architecture changes have resulted in some small impacts to the designs described in this paper, but essentially, the designs have stayed the same. As a result of the DOTA early development testing, the OTE’s primary deployment system designs have been shown to satisfy their driving requirements. Consequently, this testing has proven to be very effective in reducing the program risk associated with these optically stable deployable structures.

References

1. Lake, Mark S. and Hachkowski, M. Roman. “Design of Mechanisms for Deployable, Optical Instruments: Guidelines for Reducing Hysteresis.” NASA/TM-2000-210089, (March 2000)
2. Atkinson, Charlie, Gilman, Larry and Reynolds, Paul. “Technology Development for Deployable Telescope Structures and Mechanisms.” SPIE Conference Paper 4850-45 (June 2002)

A Boresight Adjustment Mechanism For Use on Laser Altimeters

Claef Hakun*, Jason Budinoff*, Gary Brown*, Fil Parong* and Armando Morell*

Abstract

This paper describes the development of the Boresight Adjustment Mechanism (BAM) for the Geoscience Laser Altimeter System (GLAS) Instrument. The BAM was developed late in the integration and test phase of the GLAS instrument flight program. Thermal vacuum tests of the GLAS instrument indicated that the instrument-boresight alignment stability over temperature may be marginal. To reduce the risk that GLAS may not be able to meet the boresight alignment requirements, an intensive effort was started to develop a BAM. Observatory-level testing and further evaluation of the boresight alignment data indicated that sufficient margin could be obtained utilizing existing instrument resources and therefore the BAM was never integrated onto the GLAS Instrument. However, the BAM was designed fabricated and fully qualified over a 4 month timeframe to be capable of precisely steering (< 1 arcsec over ± 300 arcsec) the output of three independent lasers to ensure the alignment between the transmit and receive paths of the GLAS instrument. The short timeline for the development of the mechanism resulted in several interesting design solutions. This paper discusses the requirement definition, design, and testing processes of the BAM development effort, how the design was affected by the extremely tight development schedule, and the lessons learned throughout the process.

Introduction

The GLAS instrument was successfully launched aboard the Ice, Cloud, and Land Elevation Satellite (ICESat) into a near polar orbit on January 12, 2003. NASA's ICESat will accurately measure the height of the earth's polar ice masses, land and ocean surfaces using the advanced precision 1064-nm laser altimetry technology of the GLAS instrument¹. The instrument also uses 532-nm LIDAR to measure clouds and aerosols in the atmosphere². ICESat was designed to operate for 3 to 5 years.

The GLAS receive path (Figure 1) consists of a 1-meter-diameter beryllium telescope, and an aft-optics assembly which splits the incoming reflected laser signal into 2 beams by wavelength, 532 nm and 1064 nm. The 532-nm LIDAR beam is directed onto a fast steering mirror, through an etalon filter, and into an array of 8 single-photon counting modules. The 1064-nm altimetry channel is directed into the primary altimeter detector assembly or shunted via a flip mirror mechanism, (the Altimeter Detector Select Mechanism or ADSM³) into the redundant altimeter assembly.

A view of the laser transmit path is shown in Figure 1. The laser transmit path uses one of three Nd:YAG 4-watt lasers, each producing a 25-mm x 25-mm square beam. The lasers are used one at a time, and all fire along a common beam path². The first laser, Laser 1, fires until it fails. The on-orbit laser lifetime is projected to be approximately 18 months. Laser 1 reflects off a fixed fold mirror and is directed to a second fixed fold mirror. The laser beam then passes through a pick-off mirror and exits the instrument along the transmit path boresight. The pick-off mirror re-directs a small portion of the laser energy into the Laser Reference System, which monitors laser output and provides precision beam pointing knowledge. Lasers 2 and 3 can be selected via precision flip mirrors, which are deployed into the optical path by the Laser Select Mechanisms (LSM's)³. In the case of a laser being powered on out of sequence, beam dumps provided safety for the instrument detectors, personnel, and the lasers themselves. The individual optical alignment and stability requirements placed on these transmit path components were extremely tight, with < 5 arcsec stability over a 30 °C temperature range.

* NASA Goddard Space Flight Center, Greenbelt, MD

The boresight alignment between the transmit path and the receive path is critical to the performance of the GLAS instrument. The alignment requirement between the transmit and receive paths was <30 arc seconds for full science, and <42 arcseconds for 50% (FWHM) response. The 50% response is considered the minimum acceptable range for science. These alignment requirements had to be met pre-launch to post launch, and within a thermal range of 15°C to 23° C⁵

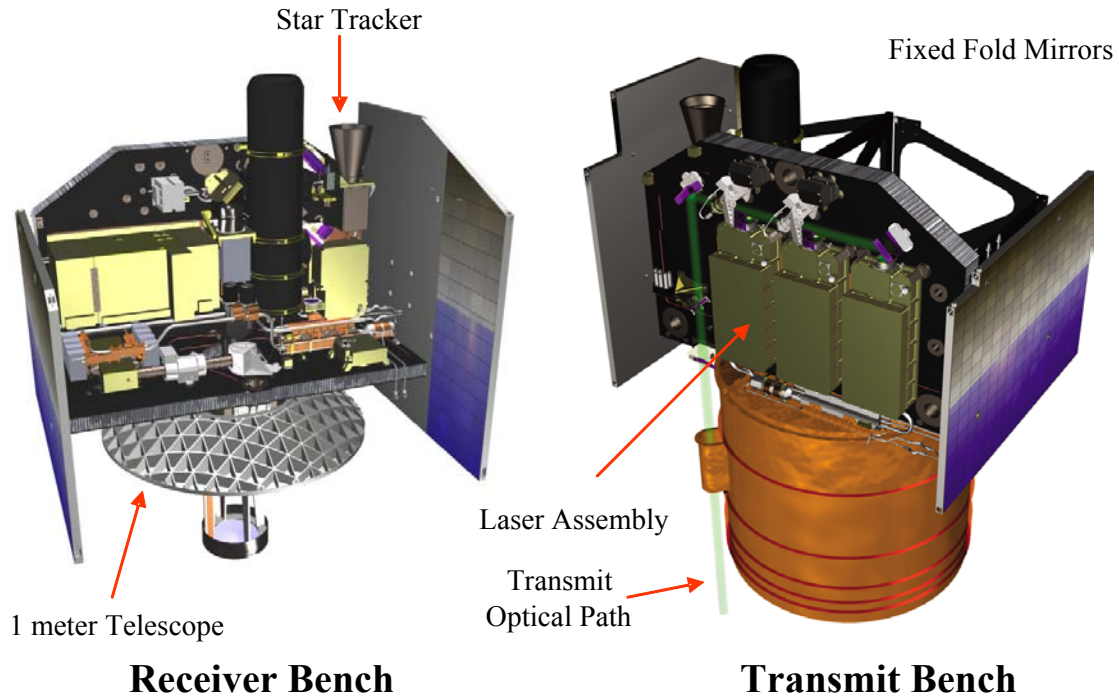


Figure 1. GLAS Receiver and Transmit Bench

Since testing indicated that the boresight alignment over temperature may be marginal, it was decided to pursue rapid development of a Boresight Adjustment Mechanism. This effort, in parallel with continued environmental testing of GLAS, was intended to mitigate potential marginal alignment performance should further tests and data reduction indicate that the GLAS instrument was failing to meet its alignment budgets. Final testing and data reduction later indicated that the boresight alignment and stability budgets could be maintained using existing instrument resources. At that time, it was determined that the integration of the BAM onto the GLAS instrument was not required. The BAM would have been mounted as shown in Figure 2 had it been integrated into the GLAS instrument.

The operating principle, requirements, design, and testing of the BAM are described. The BAM was developed over a 4-month period. During that time a proto-flight mechanism, flight electronics, spare electronics, and ground support equipment were designed, fabricated, and fully flight qualified. Photographs of the BAM and the BAM Electronics (BAME) are shown in Figure 3. The BAM utilizes two motorized counter-rotating prisms to precisely steer the incoming laser radiation. This configuration is commonly referred to as a risley pair. This simple, yet precise, beam steering technique was the baseline for the BAM.

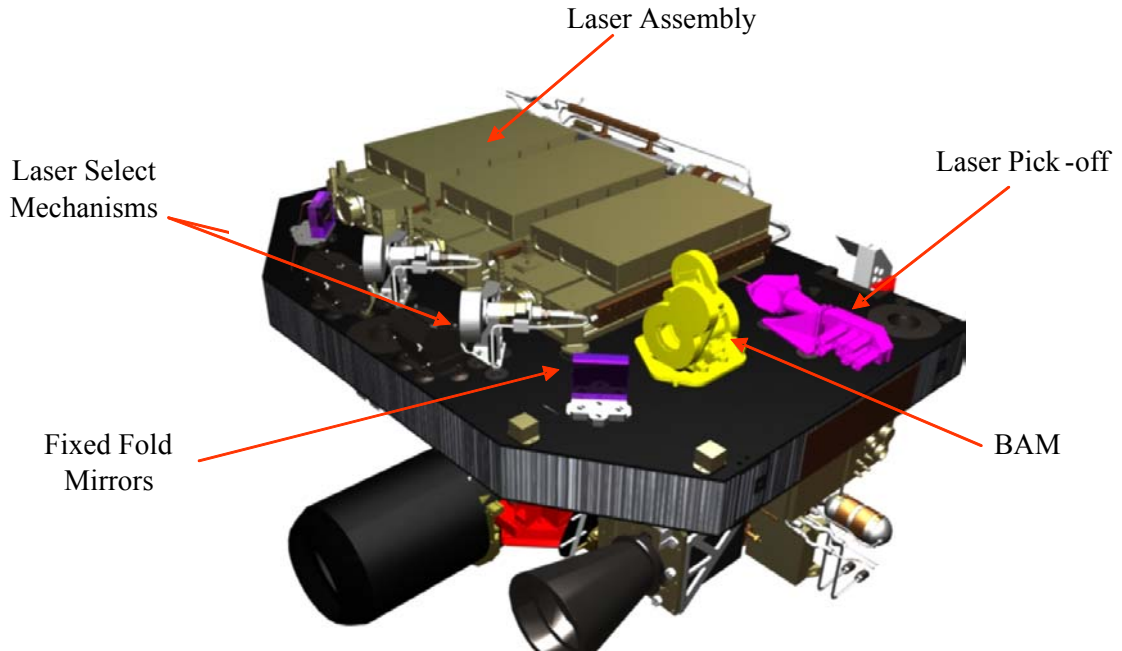


Figure 2. Proposed BAM Location on GLAS Laser Transmit Bench

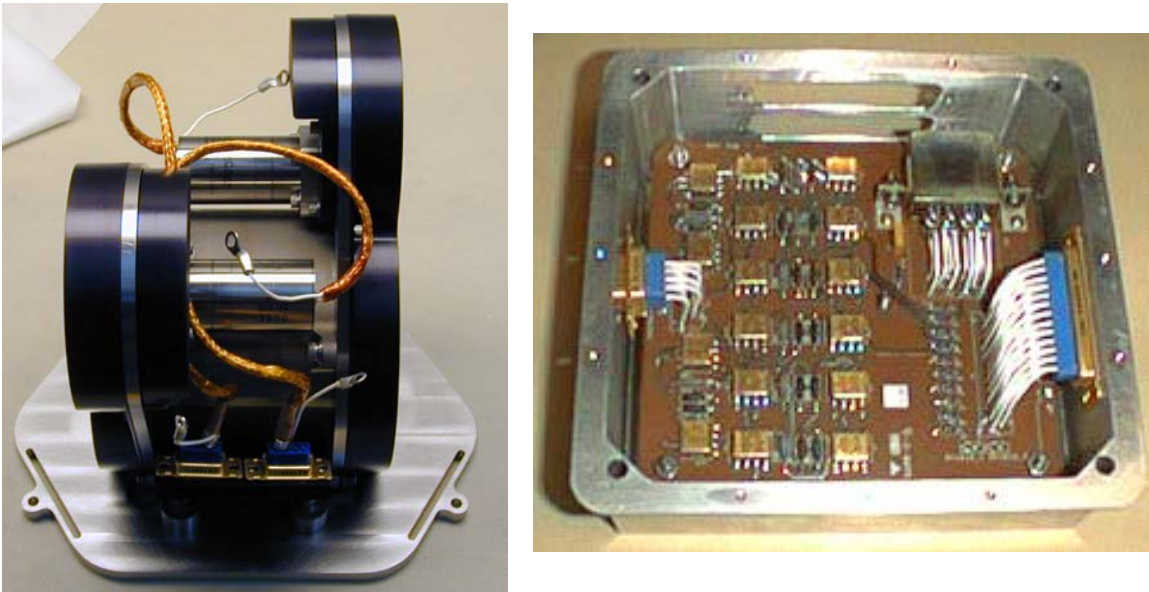


Figure 3. Photos of the BAM and the BAME

Operating Principle (Risley Pair Equations)

The angular deviation δ of a beam passing through a single prism is given by:

$$\delta = \alpha(n - 1)$$

Where α = prism angle and n = refractive index of prism

If the prism is rotated about the incoming beam axis, the beam is rotated, forming a conical scan pattern of half angle δ . If the beam is then passed through a second identical prism, the subsequent deviation provides a second degree of freedom. This allows for a variety of scan patterns, including linear scans. The net angular deviation of a beam passing through a pair of identical prisms is the sum of the two individual prism angular deviations. We define angular beam deviation about two orthogonal axes as δ_x and δ_y . Thus the deviation of a beam passing through a pair of identical prisms at arbitrary rotational positions can be defined as:

$$\delta_x = \delta \cos(A_1) + \delta \cos(A_2) \quad \delta_y = \delta \sin(A_1) + \delta \sin(A_2)$$

Where A_1 = rotational position of first prism and A_2 = rotational position of second prism

If $A_1 = -A_2$, a linear scan along the X axis is realized, $\delta_y = 0$

If $A_1 = 90^\circ - A_2$, a linear scan of slope 1 is realized, $\delta_x = \delta_y$

If $A_1 = 180^\circ - A_2$, a linear scan along the Y axis is realized, $\delta_x = 0$

For continuous maximum deviation of 2δ : $A_1 = A_2$

For continuous minimum or nulled (zero) deviation: $A_1 = A_2 + 180^\circ$

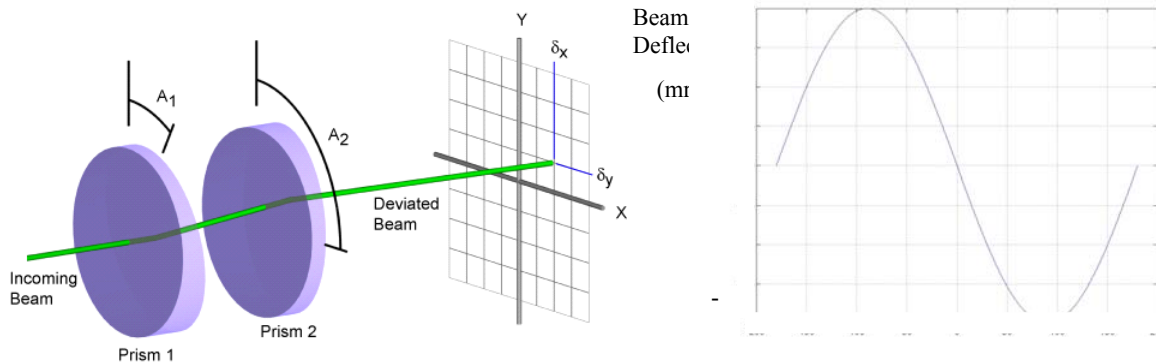


Figure 4. Risley Prism Principle and Theoretical Beam Deviation

The maximum angular deviation of the prism pair is 2δ . Therefore, only the prism angle, α , and index of refraction, n , determine the stroke of a risley prism pair scanner. Errors in deviation occur if the prism angles or index of refraction are not perfectly matched. Differences in α or n of the prisms result in small linear variations of δ . Angular resolution within the stroke is limited only by rotational positioning resolution of the individual prisms.

Operation

Whenever the wedges are aligned such that the wedge angles are 180° out of phase, then incoming radiation is not deviated. This is called a nulled position of the prisms. When the prisms are counter rotated from this position the incoming laser radiation is then deviated depending on the amount of counter rotation and the wedge angle present on the prisms. The beam deviation is along a line that is parallel to the null position of the wedges. Therefore, in order to sweep out a cone it is required to first define the nulled position angle and then counter rotate the prisms to move along this angle to deviate the incoming radiation. The risley prism principle of operation and the theoretical optical beam deviations given the parameters of the prisms used in the BAM are shown in Figure 4.

The critical factor defining pointing resolution is matching the geometric and optical properties of each prism. Risley pairs have several desirable attributes as applied to precision pointing of lasers or other refractive systems:

(1) Precise angular steering (2 arcsec or better) is possible without precision location or alignment of the supporting mechanism structure.

- (2) The individual alignment requirements of the rotating prisms relative to each other are loose.
- (3) Large opto-mechanical advantage can be obtained depending on the wedge angle and index of refraction of the individual prisms.

The BAM utilized risley pairs that were already fabricated for the Laser assemblies. The laser risley pairs were used to complete a static alignment of the laser assemblies to the transmit path and were adjusted manually. Due to the long lead times required for precision matched risley prism pairs, the rapid BAM development (< 4 months) could probably not have been achieved if spare matched risley pairs were not available.

Requirements

In order to not affect the GLAS schedule, the development of the BAM could have no impact on the testing of the GLAS instrument. All resources required and requirements developed for the BAM must be consistent with this non-interference requirement. The BAM had to be developed utilizing only "spare" resources of the spacecraft and instrument. Based on the amount of possible boresight misalignment and resources available, the GLAS science team, with inputs from the engineering team, developed the following requirements for the BAM:

Environmental and Resource Requirements

- Volume: < 22.9 cm (9") high, 17.8 cm (7") wide, 20.3 cm (8") long
- Mass: < 5 kg
- Power: < 13.5 watts peak, < 5 watts average
- Vibration: Sine Burst: X 9.75 g, Y & Z; 5 g
Random: ~ 7 GRMS X, Y, & Z axes
- Vibration: Minimum Resonant Frequency >100 Hz
- Thermal: -25°C to +40°C Survival, 0°C to 30°C Operation
- Thermal: < 30° C rise (30 minute operation, 60 minutes to cool)
- Duty Cycle: 12 alignment sequences (<50K motor revs.)
- Contamination Levels: 100 A
- Magnetic Leakage: < 10 milligauss @ 30 cm
- EMI/EMC Tested to Spacecraft Specification

Optical Requirements

- Beam Adjustment Range: 0.75 milliradians
- Beam steering precision: 30-50 microradians
- Wedge Physical Diameter: 5.4 cm (2.126") Existing Wedge Spares
- Risy Rate (Linear): 35 microradians/degree
- Clear Aperture: < 5.1 cm (2") existing optics
- Launch Stability: < 10 microradians
- Wedge Angle: 0.127 ± .005 degree Existing Wedge Spares
- Thickness: 0.55 cm (~0.217") Existing Wedge Spares
- Optical Axis to Bench: 6 cm (2.360") As built
- Rotational Rate: 180°/minute desired, but not critical
(achieved 50°/minute, deemed acceptable)
- Stability over observation: < 20 microradians (4 arcsec.)
- Stability Observation to Observation: < 20 microradians (4 arcsec.)
- Knowledge of Rotation: 0.6 ± 0.05 degree (by counting motor steps)
- Relative Rotational Accuracy: 0.6 ± 0.05 degree (by counting motor steps)
- Prism to Prism Gap Tolerance: Limited by Clear Aperture
- Allowable element Tilt: <10 degrees
- Allowable Assembly Tilt: Rx and Ry = 5 degrees, Rz is Controlled
- Allowable element shear: Limited by Clear Aperture

Electrical

BAM Electronics (BAME) Requirements

- Drive the 2-Phase stepper motors on the BAM
- No resources available from the GLAS instrument
- Commanding limited to using spare High Level Discrete Command (HLDC) lines from spacecraft
 - Each HLDC is a commandable solid state relay output
 - Only one HLDC can be high at a time
 - Logic high = +24 to +31V Logic low = high impedance
 - Fixed 50 ms \pm 5 ms pulse width with rise and fall time $>1 \mu\text{sec}$ and $<10 \mu\text{sec}$
 - Maximum of 10 Hz command rate
 - Maximum current per command line 280mA
- Additional power available from spare laser heater supply circuit: +30V, 28 watts peak
- No telemetry available
- Must provide 100% electrical isolation from motor when not operating
- Electronics Box Mass: $<2 \text{ kg}$
- Harness length: $>3 \text{ m}$ and $<10 \text{ m}$
- Design using available spare flight approved parts from other GSFC programs

Mechanism Description

The BAM assembly is composed of the following components: the mounting plate, the main structure and two identical prism drive assemblies. The drive assemblies are mounted back to back on either side of the main structure. Each drive assembly supports one of the risley pair prisms on the inner diameter of the rotating shaft. The laser radiation travels through the center of the BAM as defined by the rotational axes of the shafts. Figure 5 shows a photograph and a cross-section of the BAM. Each drive assembly independently rotates the respective prism via a spur gear that meshes with the output pinion of the stepper motor actuators. The main structure was bolted to the mounting plate through a shimmed 3-point mount to provide centerline to mounting plane height adjustment capability.

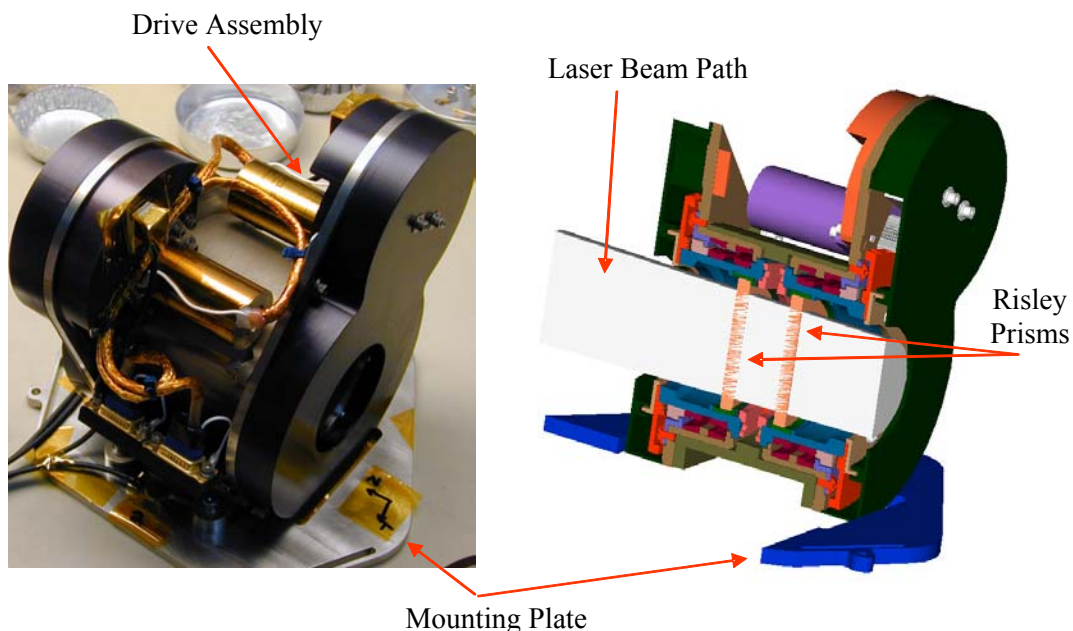


Figure 5. BAM Photograph and Cross-Section

The main structural components of the BAM, the mounting plate, main housing, and bearing housings were made of Titanium Ti6Al4V. This material provided a good CTE match to the bearings and compliance flexures cut into the mounting plate provided ample margin for the CTE mismatch between the BAM plate and composite optical bench. Since the BAM would have been attached after the fact,

Click-bonds (#10-32 studs) were to be adhesively attached to the optical bench. The compliance in the mounting plate was sized to maintain the minimum resonant frequency requirement and also to ensure that thermally induced stresses would remain well below the allowable stress calculated for the Click-bond to composite structural adhesive bond. The titanium did present a thermal problem since maximum thermal gradient requirements had been established for the BAM due to the close proximity of the mechanism to the laser assemblies. The actuators were mounted to Aluminum 6061-T6 motor housings that were thermally coupled directly to the aluminum cover. The housings and the cover act as radiators to the interior of the GLAS instrument and represent the primary transfer path to shed heat from the actuators. The motor housings also incorporated additional mass to increase the thermal time constant and minimize the maximum temperature experienced under operating conditions.

Drive Assembly Description

A cross-section and photograph of the BAM prism drive assembly are shown in Figure 6. It consists of the following components: stepper motor actuator and mount, GSE step verification sensor, bearing housing, angular contact ball bearings and preload spring, spur gear, shaft, risley prism assembly and preload spring, and gear cover. The risley prism is preloaded within the rotating shaft, which is driven by the actuator thru a spur gear attached to the outboard end of the shaft. The shaft is supported by angular contact ball bearings which are outboard of the risley prism outer diameter and are preloaded in a back to back configuration into the drive assembly housing via a custom designed wave spring. Labyrinth seals were utilized on either side of the bearing pair and between the spur gear and gear cover to minimize potential contamination. Photographs of selected components of the BAM during the assembly of the mechanism are shown in Figure-7

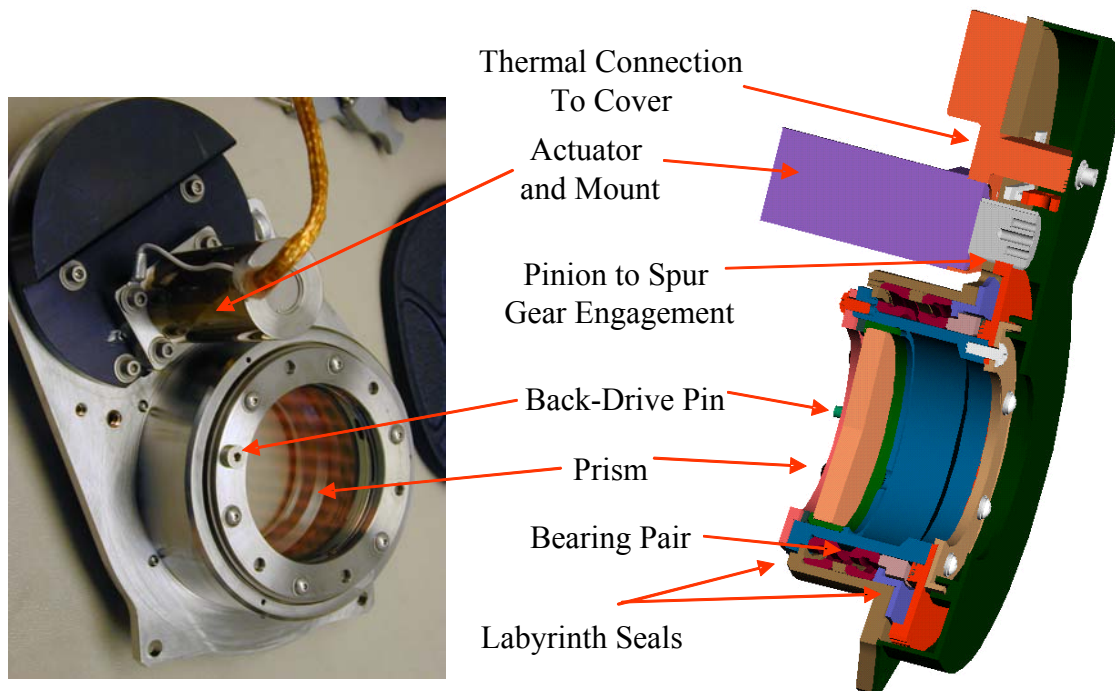


Figure 6. Drive Assembly Cross-section and Photographs

Drive Train

The drive train consisted of a stepper motor actuator and spur gear. The actuators were obtained from CDA Intercorp. They were 30° stepper motors with a two stage, 50:1 planetary gear reduction. They incorporated a custom mounting flange and an integral output pinion. The spur gears were obtained from PIC and were modified to allow alignment and attachment to the drive assembly shaft. The gear also acted to compress the bearing preload spring when bolted to the shaft. The 303 SS gear provided the additional 264:38 gear reduction. Combining the risley rate of 35 microradians/degree of counter-rotation,

the 30° steps of the stepper motor, and the planetary/spur gear reductions, each motor step resulted in ~0.6 arcsec of beam deviation.

Torque margin was measured by determining the minimum voltage at which the mechanism would still step consistently during the thermal vacuum testing of the mechanism at both temperature extremes. It was determined that the BAM/BAME could be operated with voltages as low as 6V under worst-case beginning of life conditions. Given the nominal operating voltage of +30V, this margin was deemed sufficient for this relatively low duty cycle application. During the test program over 80,000 steps were logged on the actuators without incident.

Although there was no redundancy requirement placed on the BAM, a failsafe feature was incorporated into the design that would allow for continued operation of the BAM given the failure of one of the drive assemblies. Backdrive pins protrude from the inner surfaces of the rotating shafts of each drive assembly. They overlapped in the axial direction such that if one drive assembly continued to rotate it would engage the pin of the second drive assembly thus backing driving the second drive assembly. It would therefore be possible to rotate both wedges to any desired position. In addition, if for any reason the orientation of the two prisms relative to each other was in doubt, the back driving pins could be used to re-establish a known relationship between the prisms.

Prism Mounts and Preloading

The prism assemblies were taken as a “qualified” assembly. The fused silica prisms are bonded into an invar ring. These assemblies were preloaded and locked in rotation by a custom designed titanium wave spring. The spring provided axial preload of the prism cell to the shaft while also engaging angular slots in both the cell and the capture ring to ensure that the prism could not rotate relative to the shaft.

Bearings and Lubrication

The ball bearings (MPB # 4050) were 440C stainless angular contact ball bearings mounted in a back to back configuration with a spacer between the outer-races and were preloaded with a custom designed titanium wave spring applying 133 N (~30 lb) to the inner race. They were cleaned post delivery and lubricated at GSFC using Braycote 815z oil and 601 grease. The output pinion and spur gear were also lubricated with a light coating of the same lubricant. This lubricant was selected primarily for its low outgassing characteristics and availability. The actuator was also lubricated with the same lubricant by the vendor. An anti-wetting coating was applied to critical surfaces to inhibit creep of the lubricant to unwanted surfaces. Great care was taken to ensure that no lubricant came in contact with the prism assemblies or any surfaces they interface with. There was concern that the high-energy laser radiation may breakdown the lubricant and either reduce optical throughput or cause failure of the coatings applied to the prisms which could prove to be a catastrophic failure of the laser transmit path. The transparency of Braycote to the wavelengths of light in question was investigated but it was determined that the effects of the high energy radiation on the lubricant were unknown. The same lubricant was also utilized in the laser assemblies, which had even more stringent contamination requirements.

GSE Sensors

Two sensors were incorporated into the BAM for ground testing purposes. The BAME had no available telemetry, so the sensors were operated and monitored using Ground Support Electronics (GSE). A magneto-resistive sensor was placed in proximity to the output pinion of each of the actuators. The pinions were made of a soft magnetic material. As the teeth of the pinion passed by the sensor, the variations in the gap were sensed and recorded. The resolution of the sensors provided an easily visible response for each and every step taken by the motors. This valuable data was used to verify that the motor never missed steps during characterization, thermal vacuum, and EMI/EMC testing as well as provided a means of determining torque margin. Although there is no reason that this sensor could not have flown, the plan was to remove it prior to flight.



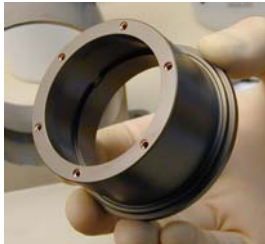
Mounting Plate
Compliant



BAM Structure and
Assembly



Bearing
(OD of Bearings)



Drive Assembly



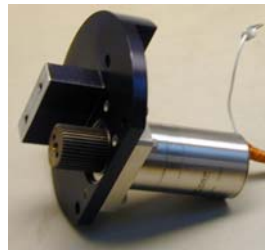
Shaft Inserted into
Bore w/ Preload Wave



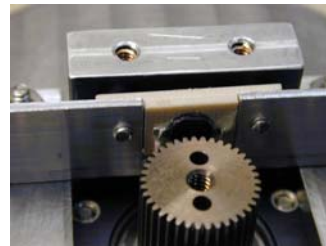
Modified Spur



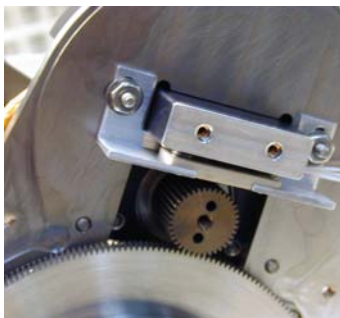
Bearing Preload
Assembly



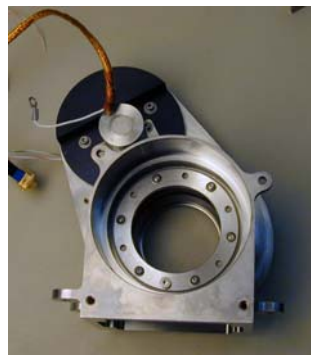
Actuator in
Motor



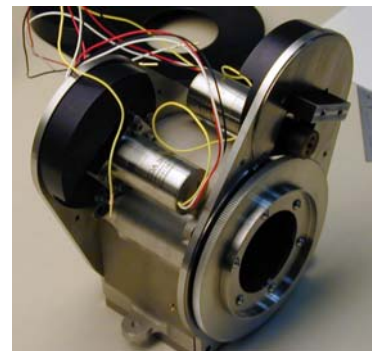
GSE Step
Sensor



Pinion to Spur
Engagement



Housing w/ One
Assembly



Preliminary BAM Assembly
(No Cover or Mounting)

Figure 7. BAM Assembly

BAME Design and Operation

Given the limitations in time, parts, and command capability, the BAME design had to be as simple and reliable as possible. A latching, mechanical relay (part# JL-D2A-108) was included to completely isolate the BAM from the spacecraft bus when not being operated. Using one HLDC to close and one HLDC to open the latching relay, the BAME was connected or isolated from the spare laser heater power line providing a peak power capability of 28 watts. Other HLDCs were used to drive optically coupled solid state relays (part# HSSR-7111) in an H-bridge configuration to drive current in each phase of each motor (Figure 8). Each separate HLDC was a unique commutation state for one of the two BAM motors. By sequencing the HLDCs, each motor could be commanded one step at a time clockwise or counter-clockwise with a 50-msec pulse at a maximum rate of 10-Hz. Since only one HLDC could be activated at a time, the H-bridge could not inadvertently be shorted by commanding a node high and low simultaneously. The inputs diodes of the relays only required between 5 mA and 20 mA each, so the HLDC limit of 280 mA provided ample margin to drive two at a time. Each motor coil was about 60 ohms, so using the +30-V supply, a maximum current of 0.5 A was drawn at any time. The solid state relays and spacecraft heater power lines were rated to supply 1 A, so the BAME had 50% derating for those components. All of the BAME parts, including associated resistors and capacitors, were spare flight parts primarily left over from the TRIANA project. Even the enclosure was a flight qualified leftover from the Shuttle small payloads program. The biggest limitations were no telemetry was available and no memory resided on the BAME. The boresight alignment information had to be determined by the GLAS pick-off and each motor's commutation state had to be tracked by the spacecraft ground ops. However, the proposed operation of the BAM could easily accommodate these issues and provide an excellent means of fine tuning the GLAS boresight alignment at any point during the mission.

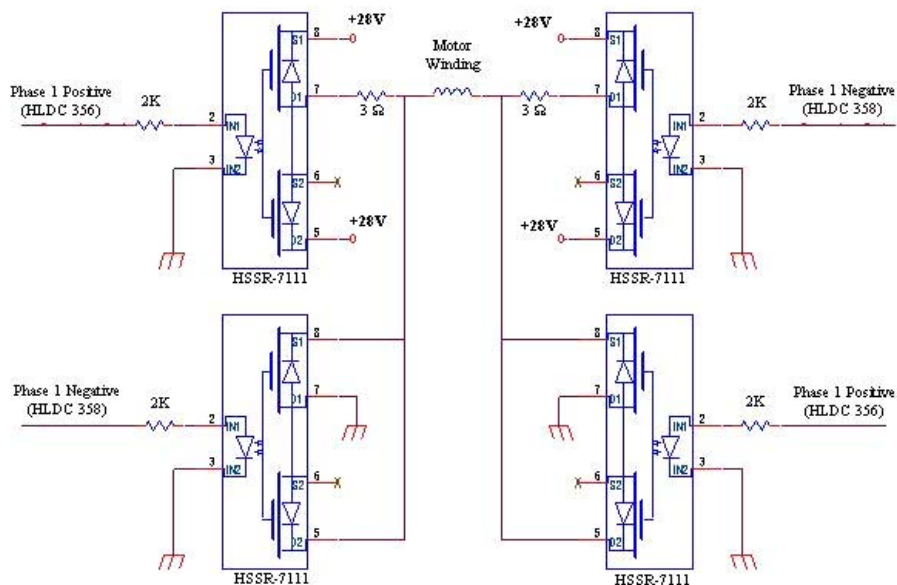


Figure 8. Simplified Schematic of H-Bridge Driver – One Motor Phase

Verification and Test

Although the development schedule for the BAM was extremely tight, all phases of the review/verification process were completed. The design of the BAM was subjected to preliminary and critical design reviews and a post environmental testing delivery review. Analysis of all critical components was performed to evaluate margins for performance and strength. The BAM was subjected to baseline performance testing (beam deviation and torque margin), protoflight vibration testing, thermal vacuum cycling and performance testing, EMI/EMC, magnetic leakage, and post environmental performance testing. The BAM successfully passed all verification tests. During the testing program the BAM executed >80,000 motor steps which is approximately 1.6 times the expected on orbit lifetime.

Vibration Testing

The Bam and the BAME were both subjected to protoflight random and sine burst vibration levels at the GSFC. Both components passed the tests. Post-test inspection of the BAM did raise some concerns. A chip on the edge of one of the risley prisms was “discovered”. It was determined that the chip was probably present prior to vibration. Further discussion of this event is given in the lessons learned section.

Thermal Vacuum Testing

The BAM and BAME were tested simultaneously in the same chamber using two separate cold/heater plates. The performance of the system was verified over the operating and survival temperature ranges. Figure 9 shows a schematic of the thermal vacuum test set-up. The units were subjected to a minimum of ten hot-to-cold operating cycles and two hot-to-cold survival cycles. This test lasted approximately 2 weeks. Torque margins were measured for the worst-case conditions utilizing the GSE step counter sensor. Behavior of the system with the BAME hot and the BAM cold and vice versa was characterized. The BAM and BAME were instrumented with thermal couples on critical components to characterize the thermal behavior of the units. A typical thermal profile during continuous operation of the BAM is shown in Figure 10 along with a photo of the BAM in the thermal vacuum chamber. In addition, outgassing data was collected by witness samples and a cold finger to verify the cleanliness of the units.

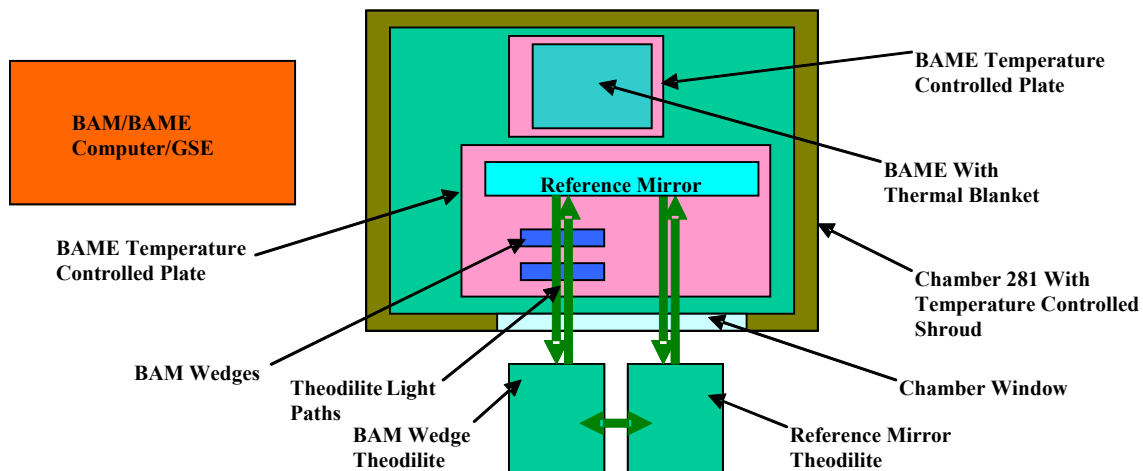


Figure 9. Thermal Vacuum Testing Setup

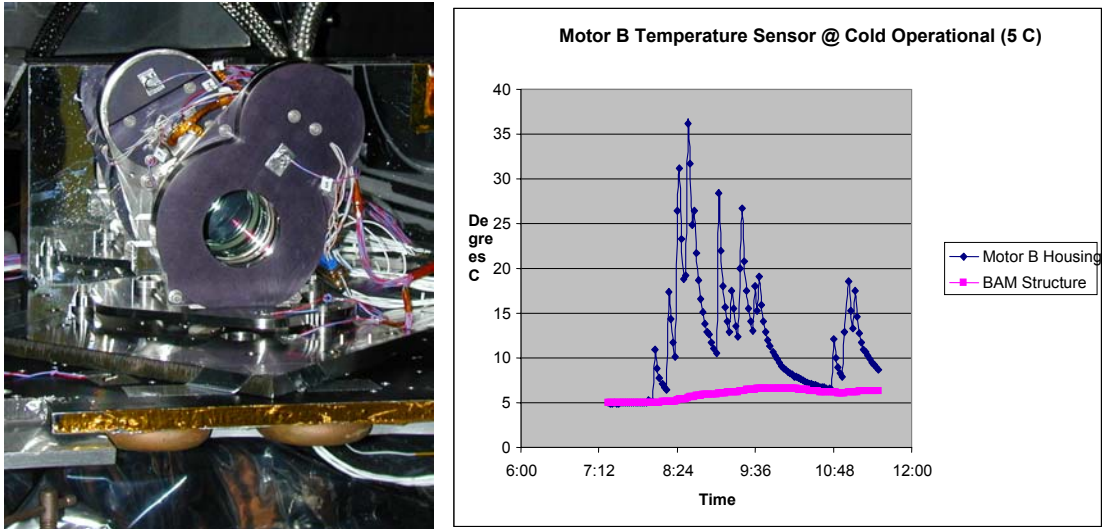


Figure 10. Characterization of Thermal Behavior During BAM/BAME Thermal Vacuum Testing

Performance

The performance test to characterize the beam steering capability of the BAM was accomplished using an auto-collimator in a double pass configuration. A large flat mirror was placed behind the BAM. The autocollimator was aligned to the reference mirror. As the risley prisms rotate the beam deviation was observed by the autocollimator. Since the BAM is only required to correct for possible boresight alignment errors on a seasonal basis no dynamic measurements were required. The same technique was also utilized during the thermal vacuum testing however an additional autocollimator was used to monitor the reference mirror through the thermal vacuum chamber window. Performance tests were conducted after assembly (to obtain a baseline) during the environmental testing, and post environmental testing. No degradation in performance was observed. Figure 11 shows a photograph of the basic test set-up and the actual beam steering capability as compared to the theoretical curve. It demonstrates that the performance of the BAM was within the measurement capabilities of the set-up.

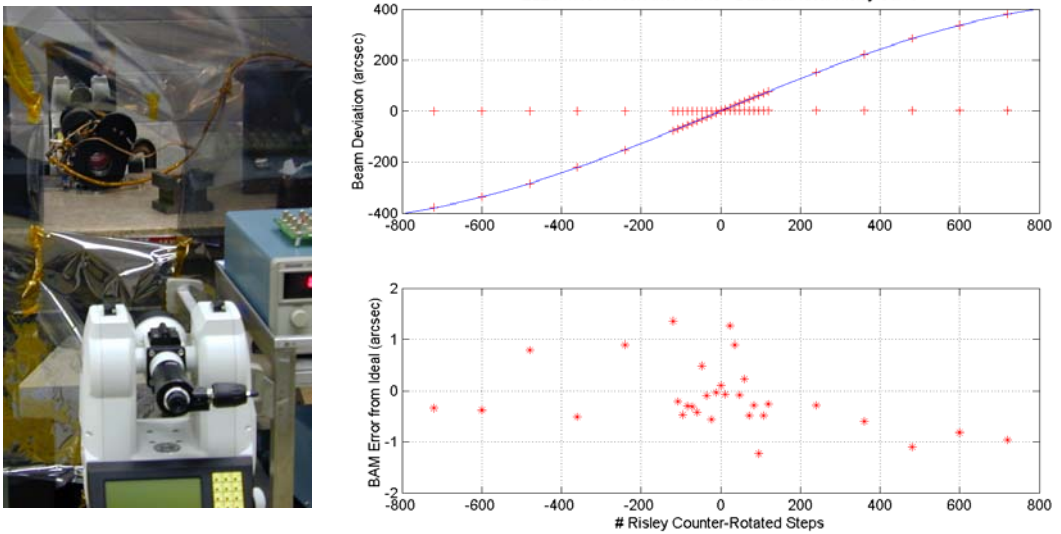


Figure 11. Performance Verification Setup and Elevation Axis Results (similar results for azimuth)

Lessons Learned

Tailor requirements and design concepts for success

The utilization of the risley prism concept made it possible to develop a flight qualified precision boresight adjustment mechanism in <4 months. The alignment capability of the mechanism allowed loose installation alignment requirements and made the BAM a viable risk reduction option that could be implemented late in the I&T phase of the GLAS instrument. By thorough engineering and trade negotiations, we were able to tailor most of the BAM design requirements to readily available resources. We made our job as easy as possible while still meeting the goals of providing a precision mechanism to reduce the risk of marginal boresight alignment stability performance of the GLAS instrument. This lesson can and should be applied to every project at every phase of instrument mechanism development. Always look to ways that can reduce sensitivity and increase the robustness of a design.

Photographs May Prove to Be Invaluable

The BAM utilized spare risley prisms from the laser assemblies. The paper work documenting the characterization of the prism assemblies was examined and the two closest matching prisms were selected for the BAM. Great care was taken not to contaminate the prisms as molecular or particulate contamination could be fatal to the transmission of the relatively high power laser radiation refracting through the prisms. After final assembly and baseline performance testing the protoflight unit was vibrated. The BAM assembly was inspected post vibration for any signs of potential failures. A chip was "discovered" in one of the prisms. The records of all of the spare risley prisms were investigated to determine whether the chip was pre-existing or a result of the vibration test. The documentation of the spare risleys was lacking. They were relegated to spare status because of less than perfect coatings or matches to other risleys. It was impossible to determine whether or not the chip had existed prior to vibration. After microscopic inspection of the area in question, and review of numerous photographs taken during the assembly and testing of the BAM, it was determined that there was evidence that the chip existed prior to vibration. Unfortunately, it had not been noted during the cursory visual inspections that were limited by the desire to minimize potential contamination of the prisms. A lesson learned here is to fully inspect "already qualified" or "spares" items and to take numerous pictures during the development process.

Utilize Off-the-Shelf/Spare parts for other Projects and Industry Contacts

When time is of the essence the design engineer must utilize the parts that are available and design around them. In order to develop a viable flight worthy mechanism design in an extremely short period of time, it is essential that the proposed design reflect hardware that is available within the development schedule required. Contacts made through association with the Aerospace Mechanism Symposium undoubtedly were crucial to the timely development of the BAM. It was believed that the longest lead item would be the procurement of the actuators and flight qualified electronics. The vendor of the actuators acted extremely quickly and delivered 4 flight units in ~6 weeks. As it turned out, the delivery fit perfectly into the development schedule and did not cause any impact to the development program. The BAM and BAME designs were founded on what was immediately available or easily fabricated with minimal modification of otherwise off the shelf parts.

Keep it Simple

The old axiom axiom "Keep It Simple" does pay off and was demonstrated in the designs of both the BAM and the BAME. The BAM utilized a basic spur-gear train to provide the required angular resolution to meet the beam steering requirements levied on the BAM. Given the limited command line resources and spare parts available, the extremely simple BAME design proved to be a reliable and robust solution for driving the BAM. The BAM is a good example of a simple yet clever design implementation, executed under a severe time and resource constraint.

Conclusions

The BAM and BAME components were successfully developed from drawing board concept to flight qualified units in approximately 4 months. Test results indicate that all objectives were met and all requirements verified. The components could have been utilized had they been required. The BAM is a precise, robust mechanism with high torque margins. The beam steering capability of the BAM is excellent. It demonstrated a null stability of ± 2 arcsec, a repeatable beam steering rate of 0.62 arcsec/step, and a linear range of ± 300 arcsec. Any future mission with similar requirements to GLAS should seriously consider incorporating a device such as this into the design up front. The risley pair concept provides precise steering capability while not imposing precise alignment requirements of the mechanism to the rest of the system. The risk of adding an additional mechanism must be weighed against the complexity and cost of maintaining extremely tight alignment and stability requirements between the transmit and receive paths of a laser altimeter instrument.

Acknowledgements

Science Support:	Jim Abshire
Optical:	Luis Ramos-Izquierdo
Designers:	Bryan Grammer, David Pfenning
Fabrication/Assembly:	Sid Johnson, Paul Haney, Cindy Rosmarynowski
Bearing/Contamination:	Mark McClendon
Analysis:	Jeff Bolognese, Anthony Melak

References

1. *IceSAT's Laser Measurements of Polar Ice, Atmosphere, Ocean, and Land*, H.J. Zwally, B. Schutz, W. Abdalati, J. Abshire, C. Bentley, A. Brunner, J. Bufton, J. Dezio, D. Hancock, D. Harding, T. Herring, B. Minster, K. Quinn, S. Palm, J. Spinhirne, and R. Thomas, *Journal of Geodynamics* 34, 3-4, 2002
2. *Precision Optical Structures & Mechanisms for the Geoscience Laser Altimetry System & the Solar Ozone Limb Sounding Experiment II*, J. Budinoff, SPIE 5176-24, Society of Photo-Optical Instrumentation Engineers (SPIE) August 2003
3. *IceSAT – Ice, Cloud and land Elevation Satellite*, FS-2002-9-D47-GSFC
4. *Introduction to Infrared System Design*, W. Wolfe, SPIE Optical Engineering Press, Volume TT24 ©1996 pages 85-86
5. *GLAS 1064 nm Boresight Alignment Analysis*, J. Abshire, E. Ketchum, H. Riris, X. Sun, B. Minster, NASA GSFC Laser Remote Sensing Branch, 10/04/2002

Deployment Mechanism for the Space Technology 5 Micro Satellite

Peter Rossoni*, Caner Cooperrider* and Gerard Durback*

Abstract

Space Technology 5 (ST5) is a technology mission that will send three spin-stabilized, 25-kg satellites into a highly elliptical Earth orbit. Each of these satellites must be deployed separately from the same launch vehicle with a spin rate of 3.4 rad/s (32.4 rpm). Because of the satellite's small size and the requirement to achieve its mission spin rate on deploy, typical spin table, pyrotechnic deployment devices or spin up thrusters could not be used. Instead, this new mechanism design employs a "Frisbee" spin up strategy with a shape memory alloy actuated Pinpuller to deploy each satellite. The mechanism has undergone several design and test iterations and has been successfully qualified for flight.

Introduction

The ST5 mission has several important purposes. The first is to integrate new scaled down technologies into a miniature spacecraft constellation operating in an environment typical of future magnetospheric mapping missions. The second is to serve as a pathfinder for development, integration, and deployment of larger constellations of miniaturized spacecraft. The final purpose is to take highly accurate science measurements. The ST5 three-small-satellite configuration was originally slated to launch as a secondary payload on an Atlas V, Delta IV, or Ariane 5 expendable launch vehicle (LV). Currently, ST5 is a likely candidate for launch on a Pegasus in late 2005. As a result of this LV uncertainty, the ST5 spacecraft bus, deployer, and mechanisms faced the added challenge of being designed to survive the worst-case launch levels and envelopes for all of these possible LVs.

Initial Deployer Design

The ST5 deployer was initially designed to satisfy a number of requirements. These are:

- Deployer must deploy the spacecraft with a spin rate of 3.4 rad/s (32.4 rpm) +/- 10% with tip-off Nutation <10°. The mission spin rate of 2.6 rad/s (25 rpm) is achieved by de-spin upon boom deploy.
- Deployer and spacecraft must survive worst-case LV loads applied uniaxially in all three directions. These include 17.5 G acceleration, 12.0 Grms random vibration, and 3.75 G sine sweep testing.
- Deployer and spacecraft must fit inside the worst case LV envelope of a 60-cm cube.
- Deployer and spacecraft must have a natural frequency of at least 35 Hz.
- Deployer and spacecraft must minimize the use of magnetic materials.
- Deployer and spacecraft must survive ST5's ascent and early orbit temperatures of -55 °C to 60 °C.
- Deployer and spacecraft must function in its operating temperature range of -20 °C to 50 °C.

The ST5 Deployer designed to satisfy these requirements is shown in Figure 1. The deployer base is 7.62-cm (3 in) thick aluminum honeycomb sandwiched by 1.52-mm (.06 in) thick aluminum face sheets. Co-cured inserts accept the twelve NAS6705U54 bolts that interface to the LV and also provide rigid attach points for the three machined aluminum stanchions in the corners and for the four machined aluminum braces that laterally support these stanchions. The spacecraft bus is supported in the deployer at the three mechanisms at the tops of these stanchions. The spacecraft interface is semi-kinematic.

The spacecraft is fixed in its Y and Z directions by the YZ mechanism shown in Figure 2. The 455-stainless-steel pin of the shape-memory-alloy-actuated Pinpuller on the deployer fits into the aluminum clevis of the spacecraft's YZ hardpoint. This YZ hardpoint clevis accommodates a TufLite® bushing with a clearance around this pin of 0.051 mm (0.002 in) to 0.102 mm (0.004 in).

* NASA Goddard Space Flight Center, Greenbelt, MD

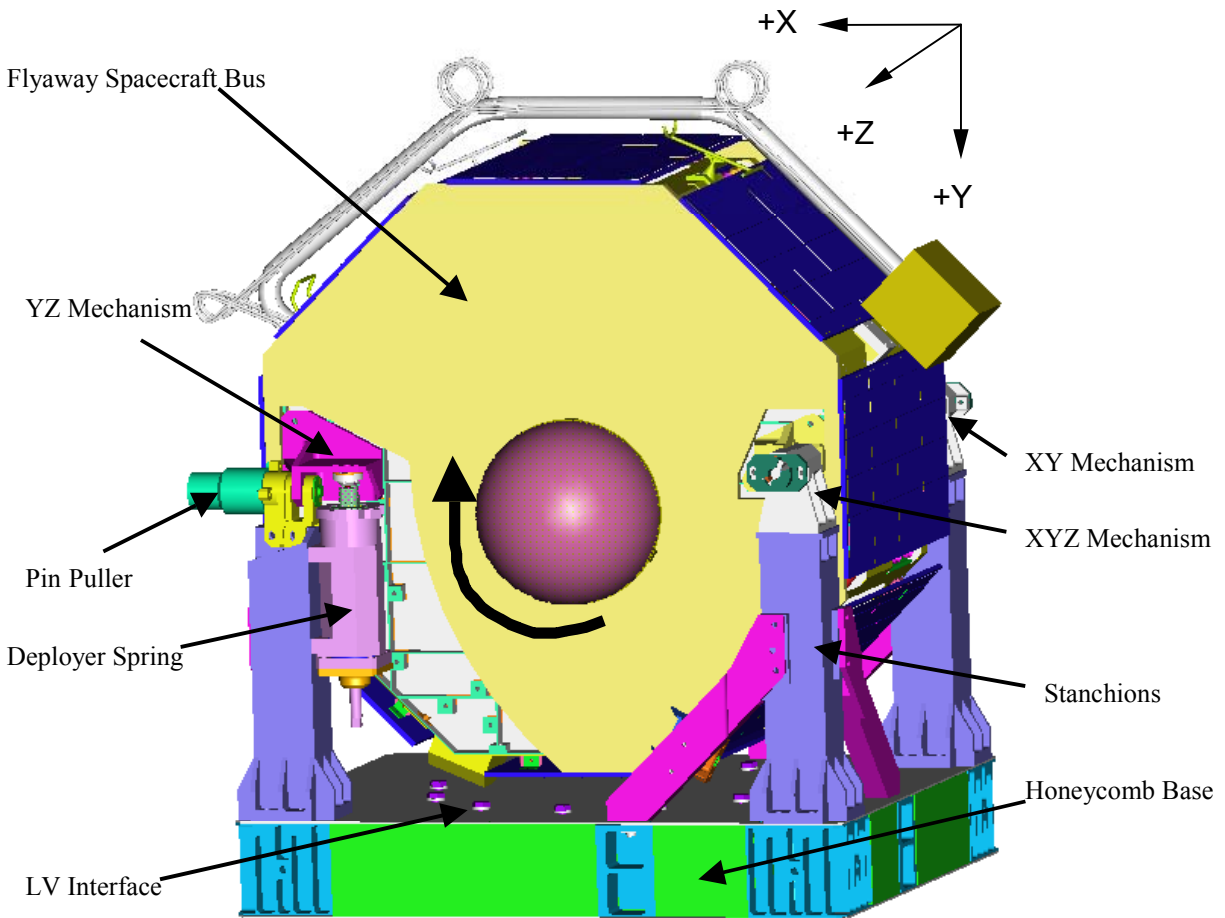


Figure 1. Initial Design of the ST5 Deployer Structure showing Spin Direction and Semi-Kinematic Restraint

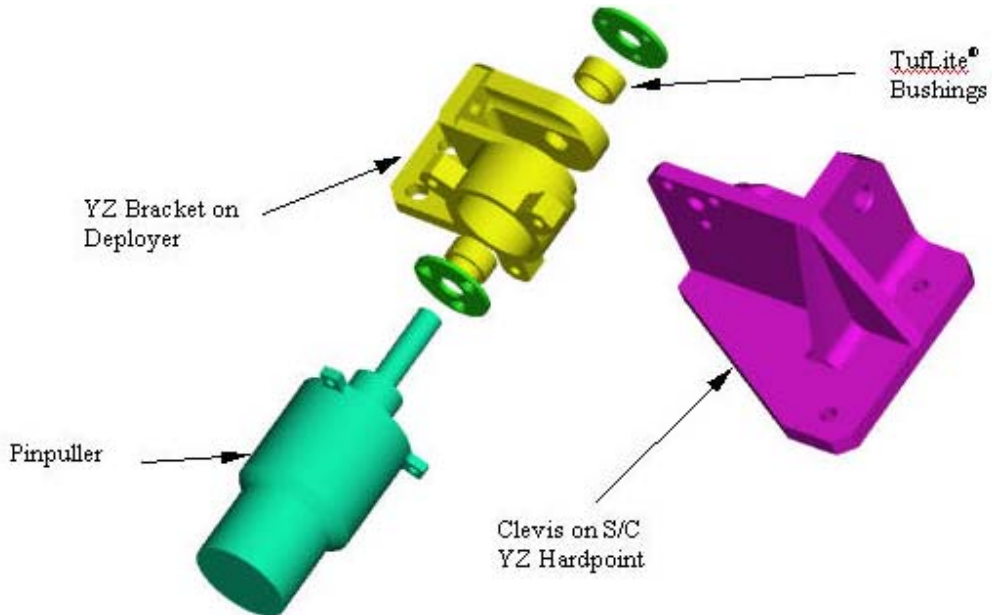


Figure 2. Initial Design of ST5 YZ Mechanism

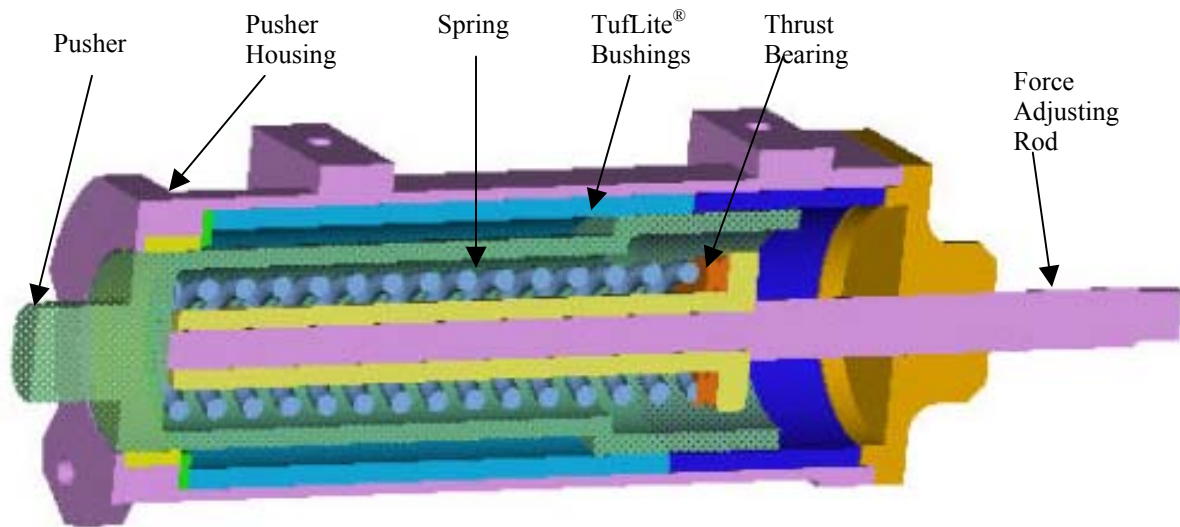


Figure 3. Cutaway View of Initial Design of ST5 Pusher Assembly

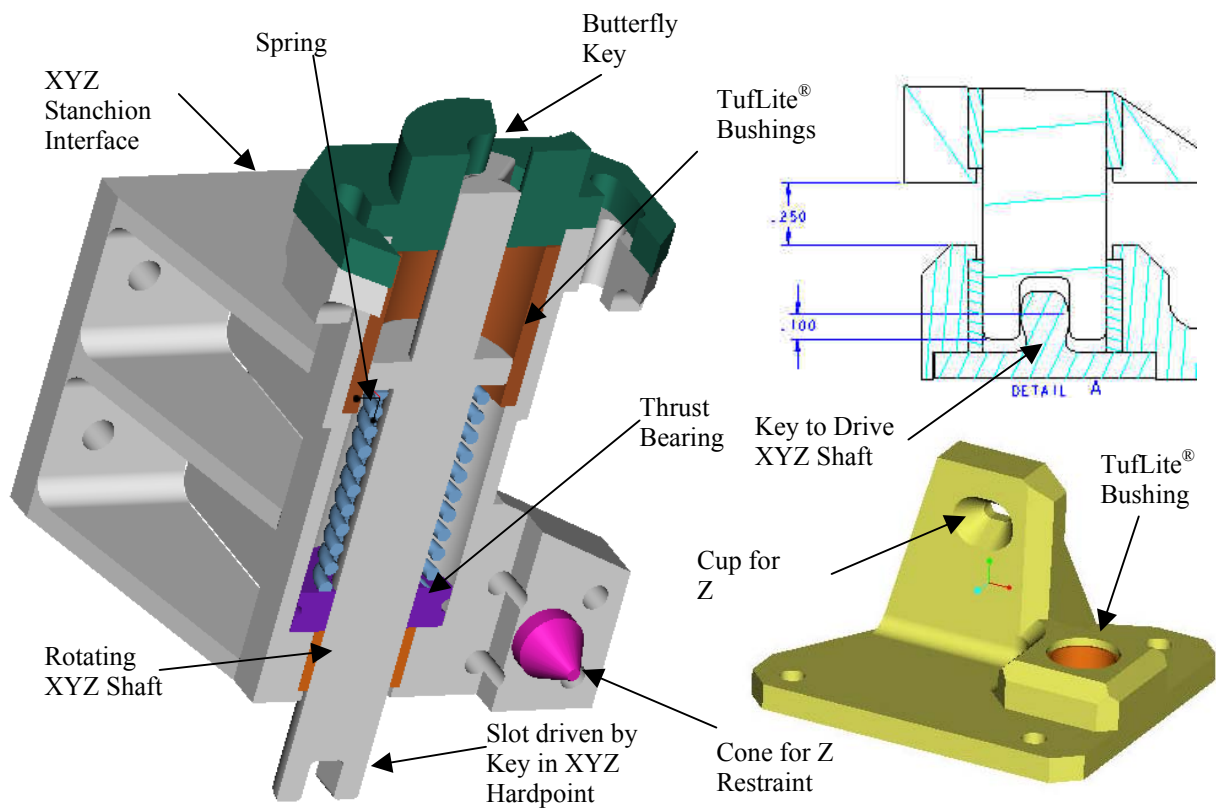


Figure 4. Initial Design of XYZ Hardpoint (right) and Cutaway View of XYZ Mechanism (left)

The ST5 aluminum pusher shown in Figure 3 contains a spring of type LHL-1000A-13 that imparts the 400-N spin up force. The spring's compression is adjusted by a threaded rod. The tip of the pusher pushes against a stainless-steel-440C roller ball on the YZ Hardpoint on the spacecraft. Additional TufLite® bushings are located between the pusher and the aluminum pusher housing mounted on the YZ Mechanism stanchion.

The spacecraft is fixed in the X, Y, and Z directions by the XYZ mechanism shown in Figure 4. A stainless steel shaft on the deployer fits into and is driven by a key in the aluminum XYZ hardpoint on the spacecraft. These two surfaces in metal to metal contact are impregnated with Polytetrafluoroethylene (PTFE) to reduce friction. TufLite® bushings in the XYZ hardpoint encircle the XYZ shaft. On the other end of this XYZ shaft there is a butterfly key. There is a spring of type LC-080-8 compressed inside the XYZ housing. When the XYZ shaft turns 20 deg, the butterfly key fits into the keyed slot and the XYZ shaft retracts out of the spacecraft. To provide restraint in the Z direction, a 410-stainless-steel cone reacts against an aluminum-7075 cup on the XYZ hardpoint. A similar XY-only mechanism, on the opposite side of the spacecraft acts coaxially and completes the hinge line. There is no Z-direction restraint needed.

There are several stages required for the deployer design to spin up the spacecraft and deploy it from the LV. First, a LV separation pulse causes the Pinpuller to pull the pin from the clevis in the YZ mechanism, which releases the YZ hardpoint clevis. The spacecraft is then driven by the pusher to rotate about the XY and XYZ hardpoints. The key in each of these two hardpoints forces the two shafts to spin with the spacecraft. At about 7-deg, the pusher completes its throw and the spacecraft has reached its final rotational velocity. The spacecraft, now no longer in contact with the pusher, continues to rotate about the coaxial XY and XYZ shafts until it reaches a 20-deg angle. Finally, the two driven XY and XYZ shafts retract out of the slots in the XY and XYZ mechanisms. The spacecraft is then unrestrained and spins with a rate of 3.35 rad/s (32.4 rpm) about the Z-axis. Its translational speed is ~.72 m/s (28 in/s) at an angle of 20 deg from the interface plane normal.

Low Shock Pinpuller

The TiNi Aerospace Model P50-1310-4RS Pinpuller was selected for its flight-demonstrated reliability, compatibility with existing LV separation pulses, and low shock imparted to the surrounding structure. Its ball-lock detent mechanism is initiated by a Nitinol shape-memory-alloy wire trigger [2]. It fires with a margin of 1.5 under the 400-N (90-lbf) shear load imparted by the ST5 pusher. The Pinpuller pin is coated with Braycote lubricant to minimize friction as it retracts. Extensive subassembly-level testing at operational temperatures and worst-case electrical parameters verified this margin.

The Pinpuller originally came with a 222-N (50-lbf) nominal retraction force. Assuming a friction coefficient of 0.4 and a 445-N (100-lbf) shear load led to a low analytical margin of 0.2 for release of the spacecraft. This was unacceptable for a mission critical element. The spring was upgraded to music wire, which gave a retraction force of 310 N (70 lbf). The mission spin rate requirement was also relaxed to lower the required pusher force to 400 N (90 lbf).

Pinpuller Testing

Subassembly testing was conducted on the YZ mechanism to verify that the Pinpuller could operate with a margin of 1.5 above the flight pusher shear load of 400 N (90 lbf). To do this, an Instron® Universal Test Machine was used to apply the normal shear load on the pin in a temperature-controlled test cell. The Pinpuller was tested under the goal 1000 N (225 lbf) load at five temperatures: cold survival at -35 °C, cold qualification at -20 °C, ambient +20 °C, hot qualification at +50 °C, and hot survival at +60 °C.

Discussions with LV providers introduced the possibility that the current to the Pinpuller might be limited to 5 A, as opposed to the initially planned 7.5-A limit. Because of this possibility, the Pinpuller was also tested at the 5-A current levels at all five temperatures. In total, there were 44 test conducted with the Pinpuller under a 1000-N (225-lbf) shear load: six trials for each current case at ambient temperature and four trials for each current case at the four temperatures.

Prior to every test, low-vapor-pressure lubricant Braycote 601 was applied to the pin. Prior to each hot or cold test, the test fixture was held for one hour at a soak temperature of 70 °C or -70 °C, respectively, to simulate the possibility that the spacecraft would be at a more extreme environment before moderating to one of the allowable temperatures for deployment. During each test, the Pinpuller was fired with a custom circuit that limited pulse voltage, current, and duration to prevent damage to the shape-memory-alloy wire inside the Pinpuller. After each test, the chamber had to be brought back to ambient temperature in order to reset the Pinpuller.

A typical actuation time versus temperature profile for the Pinpuller at the two current levels appears in Figure 5. In all 44 tests at the various temperature and current levels, the Pinpuller fully retracted under goal shear loading of 1000 N (225 lbf). This demonstrated a Pinpuller release margin of 1.5.

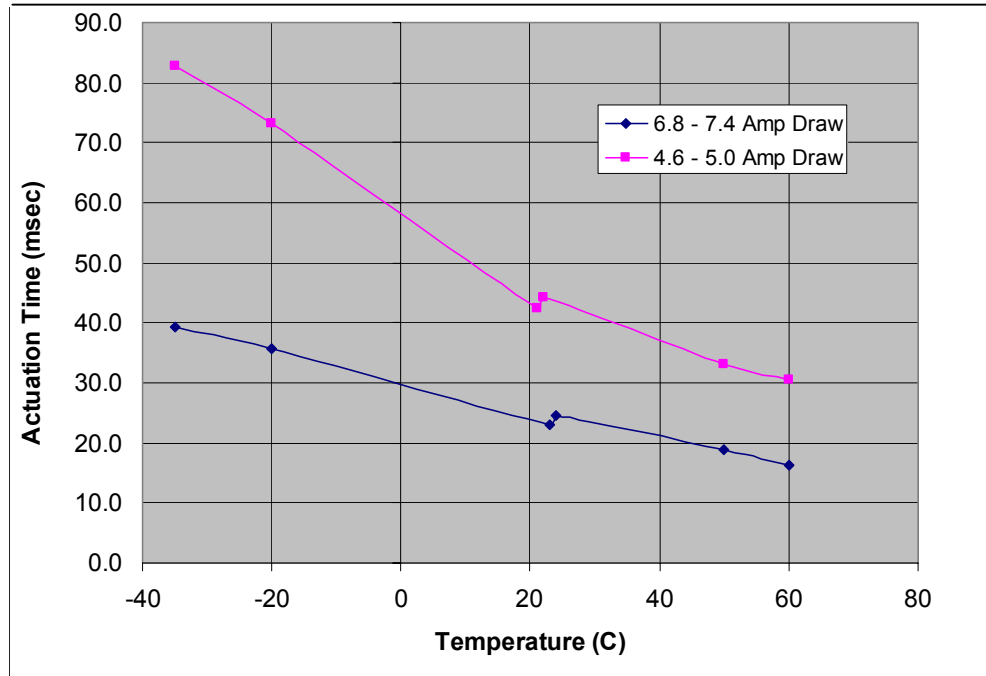


Figure 5. Actuation Time Versus Temperature for Two Pinpuller Testing Current Cases

Structural Analysis

The ST5 deployer was structurally analyzed using a NASTRAN finite element analysis (FEA) model to predict its natural frequencies and structural response to the worst case LV loads [3]. The minimum predicted natural frequency for the final deployer design was 51.1 Hz, which exceeds the minimum natural frequency requirement of 35 Hz. A thorough stress analysis of the deployer structure was also conducted using classical analytical techniques. The results appear in Table 1. The minimum fastener margin of safety was +0.52 including 50% preload and occurred in the XYZ mechanism. The minimum component margin of safety was +0.55 and occurred in the bushings in the XYZ and XY mechanism. Based on this analysis, the deployer structure was deemed in compliance with the requirements set out in the ST5 Mechanical System Specification document [4].

Table 1. ST5 Deployer Structure Margin of Safety Table

COMPONENT/ DWG NUMBER	FAILURE MODE/ DESCRIPTION	MARGINS OF SAEFTY (ULTIMATE FS = 1.40, YIELD FS = 1.25)						MIN MS
		LOAD CASE 1		LOAD CASE 2		LOAD CASE 3		
		YLD	ULT	YLD	ULT	YLD	ULT	
Deployer Base	Facesheet Strength	7.6	8.2	> 10	> 10	6.8	7.4	6.8
	Fastener Interaction	NA	0.99	NA	0.86	NA	0.93	0.86
Honeycomb Inserts	Pull-out Shear Failure	NA	2.3	NA	6.5	NA	3.8	2.3
Stanchions	Strength Failure	2.8	3.1	> 10	> 10	3.1	3.4	2.8
Braces	Fastener Interaction	NA	0.63	NA	0.97	NA	0.62	0.62
XYZ Mechanism/XY Mechanism	Shaft Strength Failure	2.3	2.4	2.1	2.2	> 10	> 10	2.1
	End-Pad Bending	> 10	> 10	3.0	4.2	3.4	4.6	3.0
	Z-tongue Strength	> 10	> 10	> 10	> 10	11.0	11.3	> 10
	Bushing Strength	> 10	> 10	> 10	> 10	NA	0.55	0.55
	Fastener Interaction	NA	0.59	NA	0.72	NA	0.56	0.52
YZ Mechanism	YZ Pin Strength	> 10	> 10	5.3	5.0	5.4	5.1	5.0
	Lug Analysis	NA	> 10	NA	2.0	NA	4.6	2.0

Deployment Analysis

Deployment analysis was conducted using several different methods to determine how much the deployer spring should be compressed to deploy the spacecraft at the desired spin rate. The first analysis method used was the energy balance method. To compare with testing, analysis was conducted assuming that the spacecraft was deployed in a gravity field. The energy balance equation for the

$$\frac{1}{2} \cdot k_{pusher} \cdot (x_1)^2 + m_{sc} \cdot g \cdot h_{cg} = \frac{1}{2} \cdot m_{sc} \cdot v_{release}^2 + \frac{1}{2} \cdot I_{g,sc} \cdot \omega_{release}^2 \tag{1}$$

deployment is:

- where k_{pusher} = the spring constant of the pusher spring
- x_1 = the amount the spring is compressed
- m_{sc} = the mass of the spacecraft
- $I_{g,sc}$ = the mass moment of inertia of the spacecraft in the direction of spin
- $v_{release}$ = the speed of the spacecraft at the instant of release
- $\omega_{release}$ = the spin rate of the spacecraft at the instant of release
- h_{cg} = the initial height of the spacecraft center of gravity (CG) above its height at release
- g = the acceleration of gravity

From dynamics, it can be shown that:

$$v_{release} = L_{hinge.cg} \cdot \omega_{release} \tag{2}$$

where $L_{hinge.cg}$ is the distance from the hinge line to the spacecraft CG. Substituting (2) into (1) gives:

$$\omega_{release} := \sqrt{\frac{\frac{1}{2} \cdot k_{pusher} \cdot (x_1)^2 + m_{sc} \cdot g \cdot h_{cg}}{\frac{1}{2} \cdot [m_{sc} \cdot (L_{hinge.cg})^2 + I_{g,sc}]}} \tag{3}$$

By solving (3), the theoretical spin rate for the spacecraft can be determined. This equation can also easily be solved for x_1 to determine how far the spring should be compressed to produce a certain spin rate. In addition to energy methods, a Newton force balance approach was used to determine a differential equation for the angular acceleration. Numerically solving this equation and then integrating to find angular velocity gave a release spin rate that was within 0.5% of the energy balance result.



Figure 6. ETU Deployer with ETU Spacecraft During Initial Qualification Vibration Testing

Two 3-D simulation software packages were also used to visualize the deployment and further confirm the computational results. ADAMS, the industry-standard 3-D simulation software, was used to develop a spacecraft and mechanisms model. The resulting deployed spin rate again agreed with both the energy and differential equation methods to within 0.5%. Working Model Software was also used and again results were consistent with previous analytical methods to within 0.5%.

Initial Qualification Vibration Testing

A flight-like engineering test unit (ETU) spacecraft and ETU deployer were subjected to qualification vibration testing in March 2003 as shown in Figure 6. In all three axes it received 17.1-Grms random vibration, 20-G sine burst, 250-G shock, 1-G sine sweep, and low level sine signature testing. The requirements for the structure to be successfully qualified were that in each axis:

- The pre- and post-vibration sine signatures must be substantially identical
- The FEA model must be correlated
- The natural frequency must be above the 35 Hz requirement
- The Pinpuller must fire and deploy the spacecraft successfully
- The structure must be pass visual inspection and show no significant wear

During this initial qualification vibration test the first four requirements were satisfied. The testing produced substantial wear at three of the mechanism interfaces, requiring redesign in those areas.

Discussion of Wear and Mechanism Redesign

After vibration, significant wear, shown in Figure 7, was seen in the PTFE-wrapped journal bushings in both the XY and XYZ hardpoints. This wear was likely caused by Z-axis motion of the two stanchions, which caused the XY and XYZ shafts to slide in and out of the XY and XYZ hardpoints. Because the key-driven slot was a through feature with fairly sharp edges in the end of each shaft, this motion ultimately chewed up the bushings.

The shafts were redesigned to incorporate a pocket by closing off the ends, which allowed full material contact between shaft and bushing, especially in the Y-axis. The tang was shortened to fit in the shaft pocket with 0.013-cm (0.005-in) clearance on all sides to prevent load transfer through it. In addition, the Tuf-Lite bushing was replaced by custom-machined Vespel. A brace was added to the XY stanchion to reduce the Z translation of the shafts.

Significant wear also occurred at end of the aluminum pusher. There was major dimpling of the pusher, shown in Figure 8, where it met the stainless steel roller ball on the deployer. The pusher was redesigned by cutting it back 0.508 cm (0.2 in) and installing a 17-7-stainless-steel tip to contact the roller ball.

Finally, there was significant wear on the cup and cone interface of the XYZ mechanism. Brinelling occurred where the stainless-steel-410 cone rubbed on the aluminum-7075 cup and was likely due to the previously discussed Z translation of the spacecraft. This interface was redesigned as an aluminum-7075 tongue in a Vespel bushing as shown in Figure 9. The Vespel slot aligns itself in the housing and contains a diagonal cut-back that assures that the tongue is clear of the Vespel slot when the spacecraft has deployed 6 deg, before the pusher stroke ends at 7.25 deg.

The deployer was analyzed structurally again. All of these design changes had positive margins despite using conservative assumptions. It was also shown by test (see next section) that none of these changes would affect the deployment of the spacecraft.

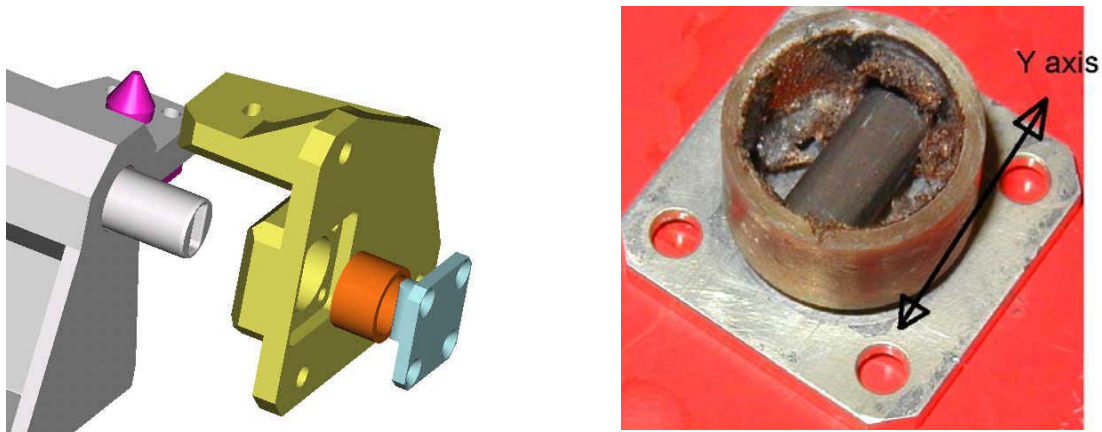


Figure 7. Wear of XY and XYZ Journal Bushings (right) and Tang in Pocket Redesign (left)

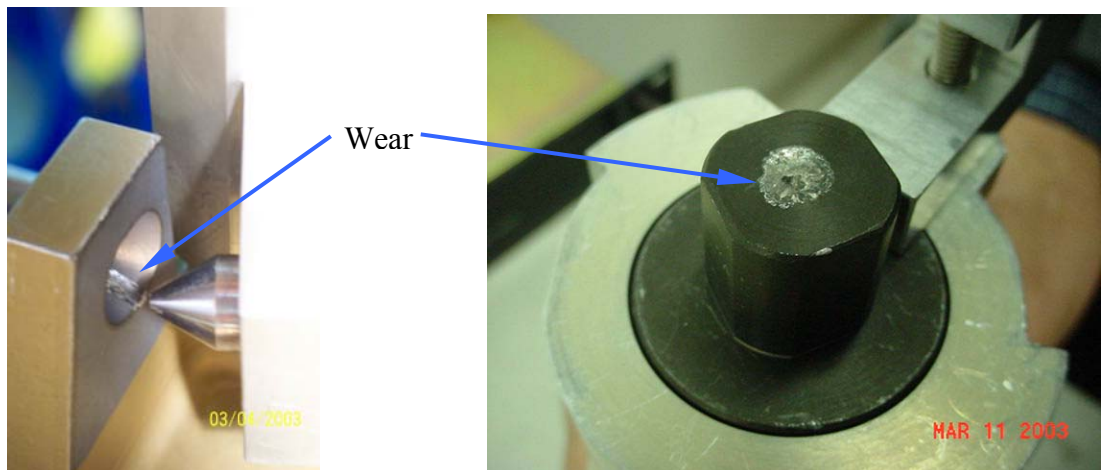


Figure 8. Brinelling of the Cup on the XYZ Hardpoint (left) and Dimpling of Pusher (right)

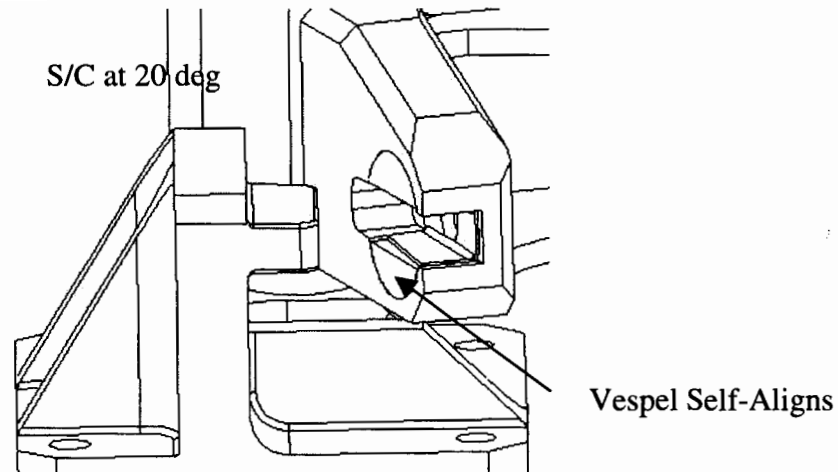


Figure 9. Redesign for the Z constraint on the XYZ Mechanism

Thermal Vacuum Qualification Deployment Testing

Testing Procedure

The goals of thermal vacuum qualification deployment testing were to show that the ETU deployer could deploy the ETU spacecraft at a spin rate within 10% of the desired value and with a tip-off angle of $< 10^\circ$ as the spacecraft leaves the stanchions. These two goals had to be met at ambient conditions as well as in a vacuum at hot and cold qualification temperatures of -55°C to 60°C respectively.

The ETU deployer, with ETU spacecraft stowed, was clamped onto a test stand in a 3.6-m (12-foot) diameter vacuum chamber at GSFC as shown in Figure 10. A high-speed video camera was set up outside so that it looked through a glass portal into the chamber facing perpendicular to the plane of fall of the spacecraft. Photo targets were taped to the front deck of the spacecraft to help in determining spin rate, as well as to tabs extending from the front and rear decks to help in determining the tip-off angle. Lights were set up throughout the chamber to illuminate the spacecraft and a mirror was hung so that precise time of release of the rear hinge could be seen and compared with the time of release of the front hinge. The spacecraft was caught after each fall by cables connected to four pistons, which crushed aluminum honeycomb to dissipate the spacecraft's energy.

The qualification deployment testing involved two different deployment configurations, shown in Figure 11. The purpose of using both configurations was to envelop the effect gravity has on the friction in the mechanisms. This assures that in one configuration the friction will be at least as large as it will be in the flight deployment. Since gravity affects the spin rate, in each configuration two ambient deploys were conducted: one with the deployer spring and gravity effective and one with only gravity effective. Then two thermal vacuum tests, at -55°C and 60°C , were conducted in each configuration. The two ambient, gravity-only deploys were eventually used with the six spring-and-gravity deploys to determine what the spacecraft's spin rate would have been in zero-g. A high-speed video camera recorded each of the eight deploys at a rate of 250 frames per second.

Data Reduction Methods

RedLake® Imaging Software was used analyze the images. The origin of each video file was defined as its top left corner with the X-axis pointed right and the Y-axis pointed down. The image was then calibrated by picking on two photo targets that were a known distance apart and specifying that distance. The frame in which the spacecraft first began to move was time zero and each frame afterward had a time 4 ms later than the last. Picking the pixel in the center of a photo target in any frame yielded the X and Y positions of that target and the time when that position occurred.

To study the true position of these points, the effect of camera parallax had to be considered. Since all measurements were desired in the plane of fall of the ETU spacecraft, only the position in the exact

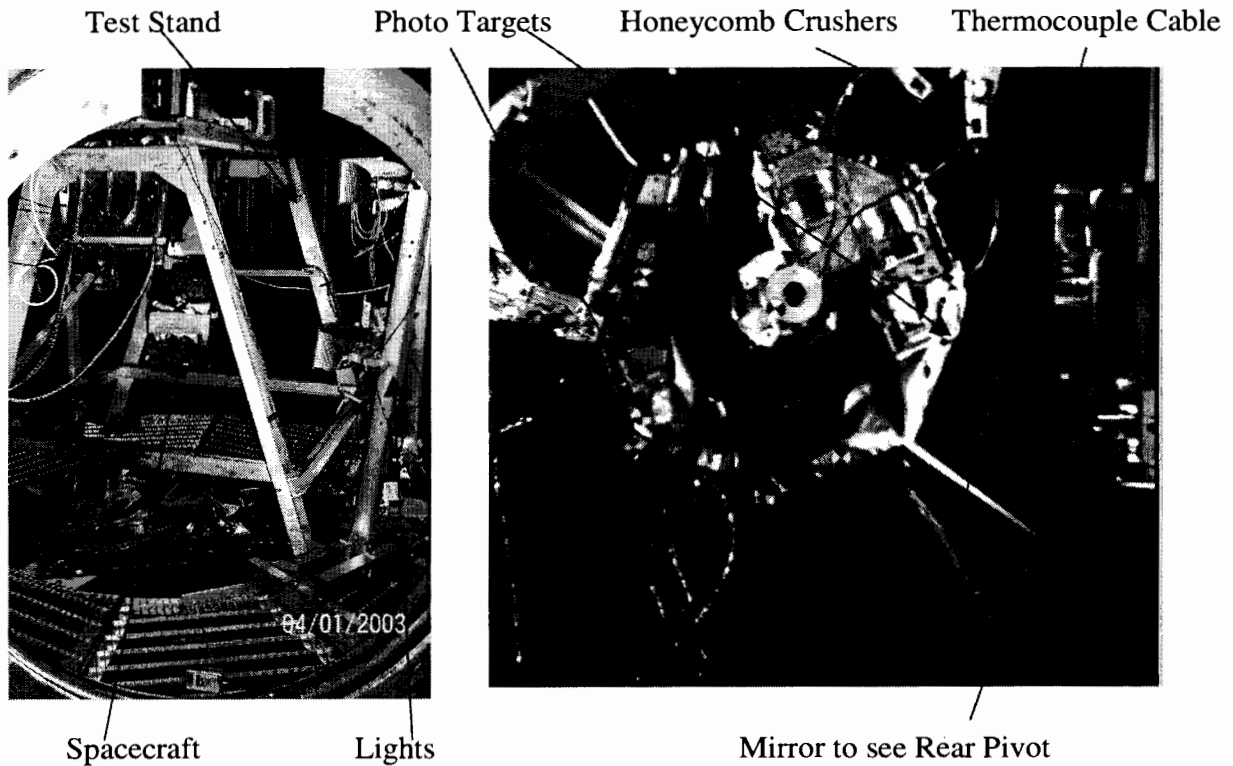


Figure 10. Deployment Testing Inside Chamber (left) and High-Speed Video Image (right)

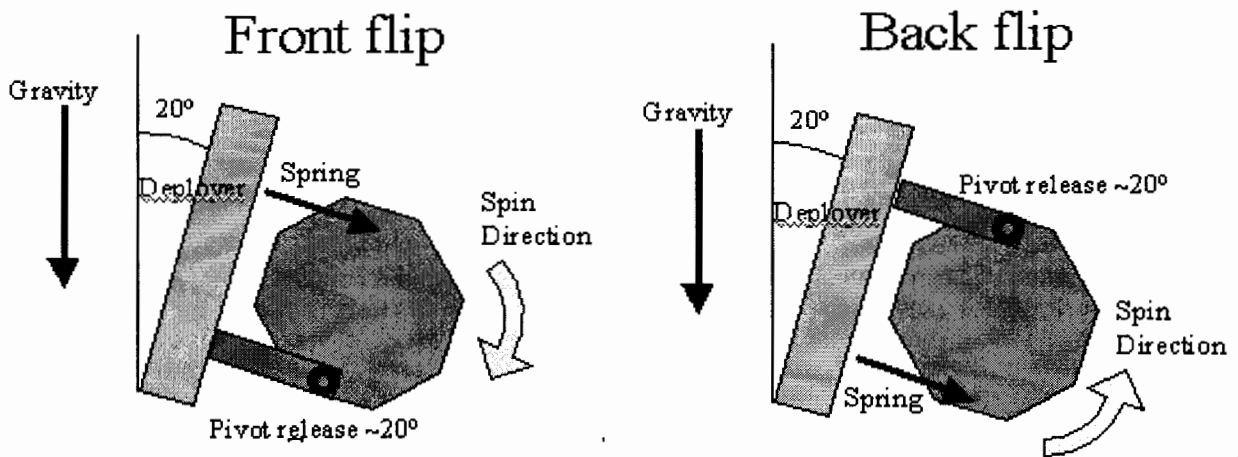


Figure 11. Front flip (left) and Back flip (right) Configurations for Qualification Deployment Testing

center of the image was precise. All other positions in the plane of fall were actually further from the camera than they looked. To account for this, all X and Y positions were adjusted using these equations:

$$x_{actual} = x_{apparent} \frac{81}{\sqrt{(81^2 - y_{apparent}^2 - x_{apparent}^2)}} \quad (4)$$

$$y_{actual} = y_{apparent} \frac{81}{\sqrt{(81^2 - y_{apparent}^2 - x_{apparent}^2)}} \quad (5)$$

where x_{apparent} and y_{apparent} are the apparent positions in inches, x_{actual} and y_{actual} are the actual positions in the spacecraft's plane of the fall, and 81 is the distance in inches from camera to the plane of fall.

To determine the spin rate for each deploy, two photo targets were chosen on the spacecraft such that each was visible during the entire fall of the spacecraft. The positions of these two targets were found at 8 ms intervals beginning just after the XY and XYZ mechanisms released the spacecraft until just before it was caught by the cables roughly 200 ms later. The two target positions gave an angle of the spacecraft at every time. Then the spin rate could be found by taking the change in this angle divided by the elapsed time between the frames where the spacecraft angles occurred. 26 angles for each deploy determined the average spin rate of the spacecraft.

To determine the zero-g spin rate for each deploy, the average spin rates from the six spring-and-gravity deploys were compared to the average spin rates from the two gravity-only trials. From equation (3), it can be shown that the gravity-only spin rate squared equals the spring-and-gravity spin rate squared minus the gravity-only spin rate squared.

Spin Rate Results

The primary goal for the qualification deployment testing was to show that the measured spin rate in zero-g was within 10% of the desired value. While the spin rate values were fairly consistent for all temperatures and flip types, the data showed that the six zero-gravity spin rates were an average of 13% less than the 3.4 rad/s (32.4 rpm) spin rate predicted by the analytical models.

To explain this discrepancy, the possible error sources were lumped into five categories:

- 1) Deployment stand flexibility (Stand recoiled on deploy)
- 2) Modeling error (Imperfect values for x_1 , m_{sc} , $I_{\text{g,sc}}$, $L_{\text{hing,cg}}$ and h_{cg})
- 3) Friction and losses due to non-flight interfaces (Catching cables)
- 4) Measurement error (Imperfect pixel picking)
- 5) Friction and losses due to flight interfaces (Pusher and XY and XYZ mechanisms)

These possible error sources were then examined and quantified to determine how much each contributed to the 13% difference between the measurement and the model, keeping in mind that the first four were caused by imperfect techniques and that the first and fifth would likely be present on flight.

The first error source, energy loss due to stand recoil, was a major contributor to the discrepancy. From the video files, it was determined that the stand deflected roughly 3.0 mm (0.12 in) as the spacecraft deployed. A separate test revealed that a 356 N (80 lbf) tug on the stand caused a 2.0 mm (0.08 in) deflection, which meant that the stand had a lateral stiffness of roughly 175 N/mm (1000 lbf/in). The

$$\%EnergyLost = \frac{PE_{lost}}{PE_{total}} \cdot 100 = \frac{.5k_{stand}\delta_{stand}^2}{.5k_{spring}\delta_{spring}^2} \cdot 100 \quad (6)$$

following equation gave the percentage of the spring's potential energy that was lost due to this recoil:

where k_{stand} and δ_{stand} were the measured stiffness and deflection of the stand and k_{spring} and δ_{spring} were the known properties of the spring. Completing this calculation showed that stand recoil caused a loss of about 7% of the spring's energy and resulted in a 3.7% loss of spin rate.

The second error source, modeling error, was also significant. A large bundle of thermocouple cables hung from the spacecraft to the chamber wall, adding roughly 0.45 kg (1 lbm) to its mass and about 0.118 kg-m² (400 lbm-in²) to its inertia. Incorporating these additions into the model reduced the predicted spin rate prediction by another 3.4%.

The third error source, non-flight interface friction, had a very small contribution to the discrepancy. About 0.25% of the spin rate was lost due to the catching cables wrapped around spools on the spacecraft. The final testing-induced error source, measurement error, was principally due to imperfect pixel picking and did not contribute to the discrepancy. Measurement error did cause a 3 σ uncertainty bound of about 0.6%

around each spin rate measurement, meaning that there was a 99.9% chance that the true spin rate was within 0.6% of the value calculated.

By summing the effects of these testing error sources, the model spin rate was reduced by 7.35%. This reduced the average measurement versus model discrepancy to 6.0%.

Table 2. Spin Rate Measurements in Zero-Gravity versus Each Model for All Deployment Trials

Trial	Test Configuration		Zero-G Spin Rates (RPM)			Zero-G Spin Rates (RPM)		
			Using Original Model			Using Corrected Model		
Number	Flip	Temp	Deploy	Model	% Diff	Deploy	Model	% Diff
1	Back	Ambient	29.07	32.37	-10.18	29.05	29.99	-3.13
2	Back	Hot	27.77	32.37	-14.20	27.77	29.99	-7.40
3	Back	Cold	27.83	32.37	-14.03	27.83	29.99	-7.21
4	Front	Ambient	28.17	32.37	-12.97	28.17	29.99	-6.07
5	Front	Hot	27.43	32.37	-15.25	27.43	29.99	-8.53
6	Front	Cold	28.95	32.37	-10.55	28.95	29.99	-3.45

The zero-g spin rates for each deploy are compared to the original model and the corrected model in Table 2. After this model correction, all deploys had spin rates within 10% of expected values. Thus, the primary goal of the qualification deployment testing was satisfied.

For completeness, friction in the flight mechanisms was analyzed to try to explain the remaining 6% discrepancy. Testing on the pusher showed that dimpling sustained during vibration testing (even on the harder SS pusher tip) made it more difficult for the roller ball to turn and thus caused increased friction in the pusher housing. This resulted in about a 2.5% loss of spin rate. Testing on the bushings in the XY and XYZ mechanisms showed that friction there resulted in about a 0.5% loss of spin rate. Neither of these friction sources was significantly affected by the presence of gravity and this 3% loss is likely to occur during flight. The remaining 3% discrepancy could not be explained by friction and is most likely due to additional modeling errors resulting from imperfect test conditions.

Tip Off Angle Methods and Results.

The second goal of this qualification deployment testing was to show the spacecraft had a tip-off angle of less than 10 deg when it moved beyond the deployer stanchions for all flip cases and temperature conditions. Tip-off angles were calculated by comparing the relative movement of photo targets on tabs extending from the front and rear decks of the ETU.

The camera parallax correction was extremely important for this calculation because targets were located at different distances from the camera. To account for this, equations (4) and (5) had to be modified by changing the 81 on top of the fraction to 92, which was the distance in inches from the camera to the rear deck. This correction was much less dramatic for the spin rate calculations, where correcting for parallax changed the results by only 0.5%.

The measured tip-off angles for each deployment are shown in Table 3. The average tip-off angle was 5.9 deg and the largest value was 7.7 deg. All of the measured tip-off angles were less than 10 deg and therefore the second goal of deployment testing was met.

Table 3. Tip-Off Angle Measurements for all Trials

Trial	Test Configuration		Tip-Off Angle (Deg)
	Flip	Conditions	
1	Back	Ambient	3.6
2	Back	Hot	4.4
3	Back	Cold	7.7

4	Front	Ambient	6.6
5	Front	Hot	6.9
6	Front	Cold	6.2

Table 4. Natural Frequency Response Results Obtained During Requalification Vibration Testing

Axis	Pre-Sweep (Hz)	Low Random (Hz)	High Random (Hz)	Post-Sweep (Hz)	Analysis (Hz)
X	49	44	50	49	55
Y	125	100	124	114	68
Z	41	42	50	41	52

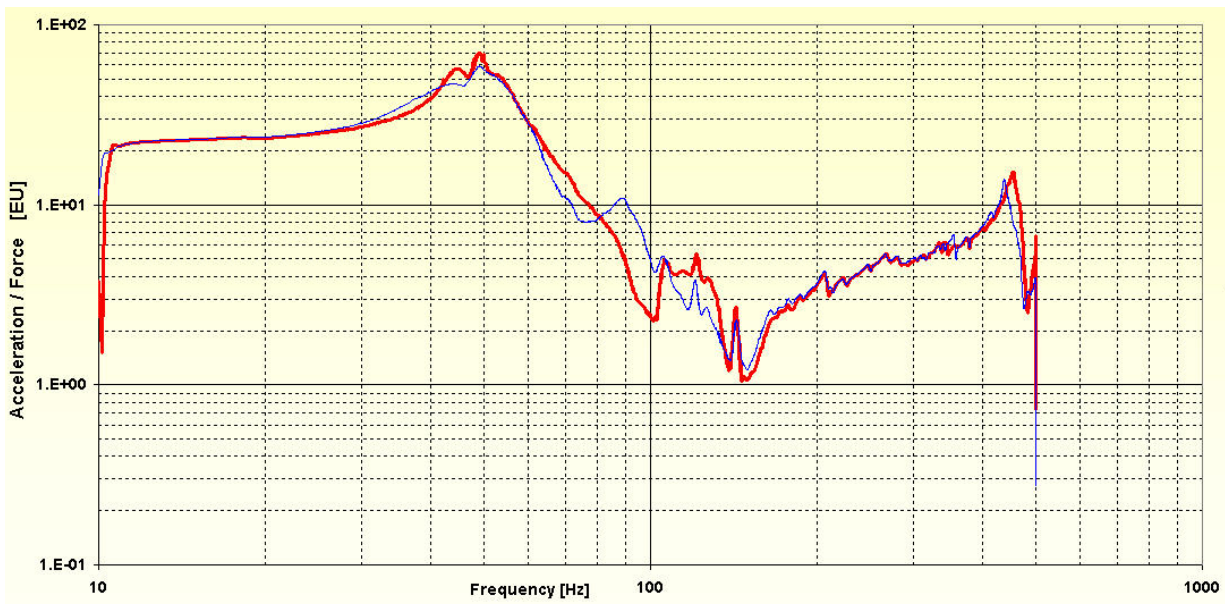


Figure 12. Comparison of X Force Sum in X-Axis Vibration Pre (red) and Post (blue) Signatures During the Requalification Vibration Test

Requalification Vibration Testing

The final step that remained to qualify the deployer was to show that the redesigned mechanisms would not wear during qualification vibration levels. Just as in the initial qualification vibration test, the ETU deployer and ETU spacecraft were subjected to 17.1-Grms random vibration, 20-G sine burst, 250-G shock, 1-G sine sweep, and low level sine signature testing in all three axes. After each axis of testing, the Pinpuller fired and the S/C was successfully deployed.

In each axis, initial sine signature sweeps and those run post testing remained very similar to each other. These frequencies are shown in Table 4 and a representative frequency plot comparing pre- and post-signatures in the X-axis is shown in Figure 12. The ETU successfully withstood structural loads and demonstrated substantially identical pre- and post- sine signatures and its fundamental frequencies of 49 Hz in the X-axis, 114 Hz in the Y-axis, and 41 Hz in the Z-axis all exceeded the minimum frequency requirement of 35 Hz. After each axis of testing, the Pinpuller fired and the S/C was successfully deployed.

It should be noted that due to clearances in the mechanisms, the response of the ETU spacecraft and deployer is very nonlinear. In all the three axes, the fundamental frequencies differed significantly between the high (full) level random and the low (-18 dB) level random runs. The requirement to correlate

the FEA Model was satisfied by adjusting the spring constants for each mechanism in each direction until the model matched the test results.

The only vibration requirement left to satisfy was the post-vibration visual inspection. The aluminum tongue in Vespel slot interface of the XYZ mechanism was of particular concern. The Vespel slot was initially 0.645-mm (0.254-in) wide and remained 0.645-mm (0.254-in) wide after X-axis and Y-axis testing. After Z-axis testing the slot opened up only slightly to 0.650-mm (0.256-in) wide, which was within specification. Virtually no debris was collected in the tent placed around mechanism and no traces of Vespel were found by contamination inspection. The redesigns made to the other mechanisms also proved successfully and, aside from minor pusher tip dimpling, there was no significant wear detected in any of the interfaces.

Thus, the ETU deployer and ETU spacecraft passed the post-vibration visual inspection requirement and successfully completed all of the requirements imposed on it for qualification for space flight use.

Lessons Learned

- Transducer-based rate sensors are not the only choice for velocity data. High-speed video gave direct spin rate information, though data had some pixel-picking error and parallax had to be accounted for. The photo technician and equipment rental cost about \$10,000 for 2 weeks.
- All parts of a test setup that may lead to discrepancies from a theoretical model should be considered before testing. Correcting a model afterwards to match a test is not as convincing.
- Determining the on-orbit spin rate from ground data compounded errors. This would have been the case even with on board transducers. The most straightforward measurement would have required a Zero-Gravity research lab, with its own set of constraints and significantly higher cost.
- When a mechanism is going to face vibration, sharp edges should always be avoided to reduce the chances of gouging or chewing up hardware.
- Hard plastics, such as Vespel, could be used instead of metals if a mechanism shows wear.
- In our drive for miniaturized components, we started with innocently low assumptions for margin requirements and had to pay for it with extra testing. Instead of margins in the 1-2 range, 4 is recommended for initial design. When this extra margin is not achievable due to resource limitations on micro-satellites, component testing must make up the difference in confidence level.

Conclusions

The Frisbee spin up is a viable technique for imparting a mission-critical spin rate to a micro sat. Deck space is preserved, the design is simple, and rate precision has been demonstrated to better than $\pm 10\%$ with low tip-off. The spin rate was measured by high-speed video frame capture of the target locations on the deploying spacecraft. The design was demonstrated with development hardware and a flight-like engineering test unit qualified the design.

Low design margin and heritage was compensated by more component-level testing in a “skunkworks” environment. In the move towards miniaturized spacecraft for constellation science missions, new ways of dealing with risk must be adopted. This single-string spacecraft mission afforded the opportunity to research strategies for mechanism development under a less risk-averse atmosphere. Reliable suppliers, adequate facilities, and experienced personnel made up the balance of the success formula.

References

- [1] “ST-5 Critical Design Review” Presentation¹, Peter Rossoni June 2002
- [2] Michael Bokaie and Kevin Barajas: “Non-Explosive Pinpuller and Rotary Actuators” 32nd Aerospace Mechanisms Symposium, NASA Kennedy Space Center, May13-15 1998
- [3] SAI-ANYS-396 William McGill¹, Swales Aerospace, 2003

¹ ST-5 internal project document, subject to export control restrictions

Development of a Strain Energy Deployable Boom for the Space Technology 5 Mission

Stew Meyers* and James Sturm*

The ST-5 Mission

The Space Technology 5 (ST5) mission is one of a series of technology demonstration missions for the New Millennium Program. This mission will fly three fully functional 25-kilogram micro-class spacecraft in formation through the Earth's magnetosphere; the primary science instrument is a very sensitive magnetometer. The constraints of a 25-kg "Micosat" resulted in a spin stabilized, octagonal spacecraft that is 30 cm tall by 50 cm diameter and has state-of-the-art solar cells on all eight sides. A non-magnetic boom was needed to place the magnetometer as far from the spacecraft and its residual magnetic fields as possible. The ST-5 spacecraft is designed to be spun up and released from its deployer with the boom and magnetometer stowed for later release. The deployer is the topic of another paper. This paper describes the development efforts and resulting self-deploying magnetometer boom.

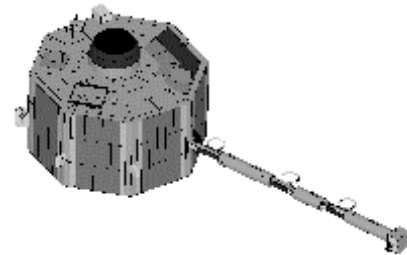


**Figure 1. ST-5 Spacecraft
Boom Deployed**

Deployed requirements

- The spacecraft shall include structure and mechanisms that deploy the magnetometer sensor away from the vehicle central body.
- The magnetometer sensor shall be at least 1.5 spacecraft diameters away from the central body.
- The magnetometer alignment to the spacecraft coordinate system after deployment shall be repeatable to within 0.25 degree of nominal orientation and within 1.0 cm of nominal distance.
- The natural frequency of the deployed structure for the magnetometer shall be between 5 and 11Hz.
- Any initial disturbance on the deployed structure shall be reduced by 95%, as measured as the peak-to-peak displacement at the magnetometer sensor head, within 20 seconds of the impulse.
- The spacecraft shall be designed so that generated electric and/or magnetic fields do not interfere with magnetometer measurements.
- Spacecraft-induced magnetic fields as measured at the magnetometer sensor location shall be less than 10.0 nano Tesla (D.C.), and less than 0.5 nano Tesla (A.C., at 200Hz).

Stowed requirements

- Coupled Rigid Natural Frequency shall be greater than 50 Hz.
- Fixed-base Natural Frequency shall be greater than 100 Hz.
- Deploying Torque Margin shall be at least 2:1 (GEVS)
- Design Loads shall be 16G in each axis independently
- Mass budget for the magnetometer boom, without magnetometer sensor head elements shall be less than 750 g
- Survival temperature limits shall be from -80°C to +70°C
- Operating temperature limits shall be from -55°C to +50°C

(These temperature limits are under review because of the shift from a secondary payload on a Delta/Atlas class launch vehicle to a primary payload on a Pegasus launch vehicle.)

* NASA Goddard Space Flight Center, Greenbelt, MD

Obviously, meeting these requirements was a challenge. Further complicating the task was the fact that no launch vehicle had been selected, thus requiring the worst case load conditions enveloping Ariane, Delta, and Atlas be used.

The Initial Concept

From the start, it made sense to use a composite boom for the magnetometer to minimize the magnetic contamination. The boom needs to be folded around the periphery to get the length required and minimize volume and deployer interference. This boom wrap-around design requires three hinges, anthropomorphically referred to as the shoulder, elbow and wrist joints. Integral folding “carpenter tape” hinges with no sliding or rotating parts were chosen as the simplest way to ensure positive deployment torque-ratios at the least mass while avoiding the issues of designing for friction and damping. This boom design relies on the strain energy in the buckled hinge to straighten the hinge and deploy the boom.

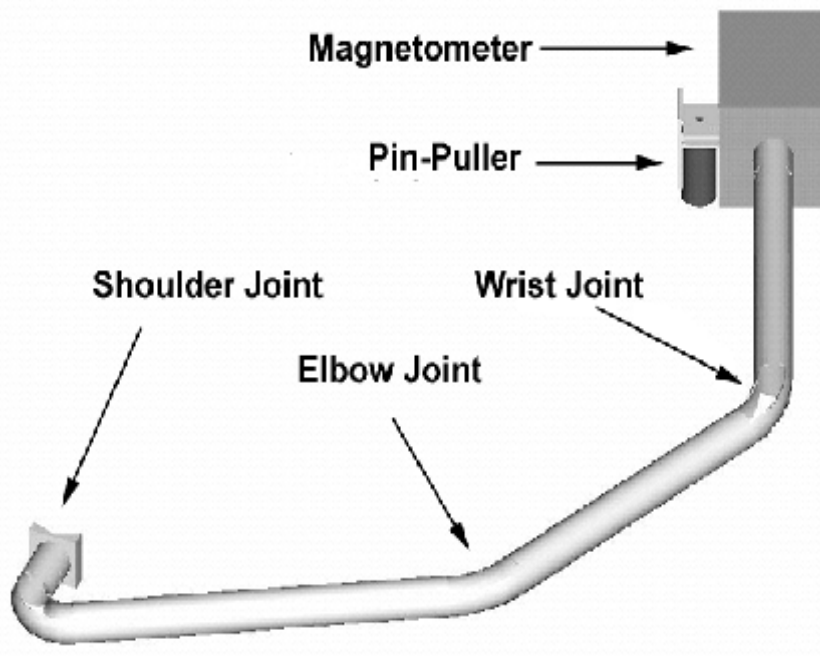


Figure 2. Boom Layout

Mounting

The sides of the spacecraft are covered with solar panels and hard points are available only at two vertices of the octagon. These coincide with the cast aluminum card cage that provides the primary load path of the satellite. The shoulder joint of the boom is attached at one of these reinforced vertices and the pin puller that holds the magnetometer uses the other. Thus the ends holding the boom are connected to the card cage rather than the sheet metal sides that support the solar arrays. The intermediate elbow and wrist joints are supported at the intermediate vertices by snubbers mounted to the sheet metal.

Boom Release

The method of boom release was driven by the low-power low-mass characteristics of the ST-5 micro-satellite. Low-power actuators from both Starsys and TiNi Aerospace were considered. Pyro actuators had been ruled out early on because of concern for shock in a very compact structure and the current requirements on a 5-volt spacecraft bus. In the end TiNi produced a modified version of their P5-404-6SC pin-puller that was selected. The magnetometer is held to the spacecraft through a tang and clevis design

that utilizes the pin-puller pin in double shear. This holds the boom to the spacecraft in the stowed configuration. The magnetometer mount is a semi-kinematic design consisting of a cup-cone and spring arrangement. The relatively low minimum lateral load capability of the pin puller, only 67 N (15 lb) shear in the worst case condition over the entire operating range, further drives the stowage scheme. To establish this number rather extensive testing was done with a test rig using parts that were as flight like as possible. To maintain a release force margin of two to one, 33 N (7.5 lb) was used as the maximum allowable shear load on the pin puller. This value limits the maximum tension that can be applied to the boom stowed.

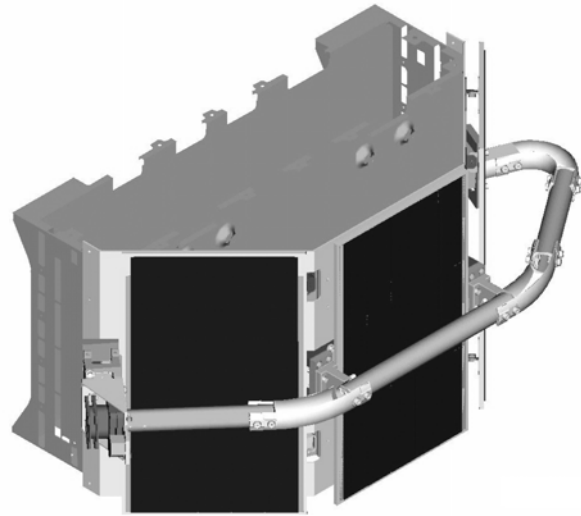


Figure 3. Boom mounted on Spacecraft

Design Trades

Initially it was hoped that an all-composite “monolithic” design could be made with sections of the boom cut away to create the hinges. While graphite fiber is not normally considered a flexible material, when used in this design, it allows the boom to bend over 90° and has many features that make it optimal for its intended use. The graphite provides an electrically conductive path to bleed off static charge – a great benefit on the highly charged mission orbit. It resists creep and remains stable under large temperature fluctuations, allowing for precise science measurements even under direct solar radiation. The thermal conductance is optimum for controlling heat loss from the spacecraft. Furthermore, the composite material exhibits nearly none of the thermal magnetic effects that currently plague the metal hinge units.

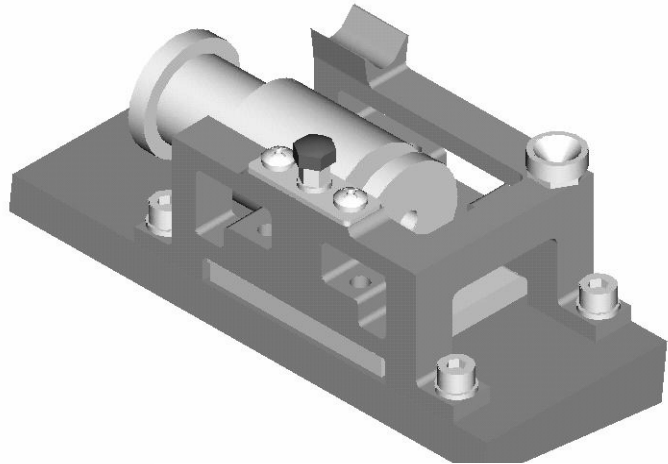
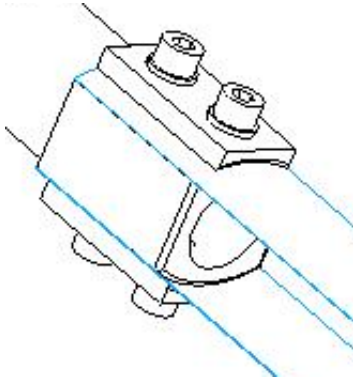


Figure 4. Boom Release

Considerable effort was expended developing this concept. Various shapes were tried for the cut outs and different materials were tried, including Kevlar®, E-Glass, S-Glass, and various weaves and types of carbon fiber. Different lay-ups of the materials were also tried. One notable result from this study was the fact that the desired radius of a tubular boom section was not usually the optimal radius of curvature of the leaf or blade element of the hinge. An oval section boom with cutouts for the hinge section was considered, but rejected in favor of a saddle piece to adapt the different radii. Once it was realized that the hinge design requirement was necessarily different than that of the basic tube, the concept of cutting windows in a tube to create a monolithic boom was abandoned. It was also found that adding a fourth facet in attempt to move the magnetometer further from the spacecraft resulted in the boom hitting the solar array on deployment.



Saddle Adapter to Provide Larger Radius for Hinge



Monolithic Boom With Integral Hinge Cut Out



Oval Attempt to Have Larger Radius for Hinge Area

Figure 5. Hinge

Design Development

Titanium adapter shoes were bonded to the boom with the hinge blades bolted to them. A variety of composite and metallic blades were tried. The problem was to make a hinge that was stiff enough when deployed, but that would buckle at a low enough strain energy not to destroy itself. The boom joints are made up of two different length carpenter tape hinges (longer at the shoulder joint and shorter at the wrist and elbow). The length of the hinges is driven by the angle through which the hinge has to bend (120 degrees, shoulder and 45 degrees, wrist and elbow). Each hinge is made up of four "carpenter-tape" blades stacked two thick on each side. Analysis and development testing showed that the bending strain in a single blade that was as thick as the two stacked blades was too high. Every time the thick hinges were bent they permanently deformed. Splitting the hinge into two separate tapes cut the bending strain in half for each individual blade. This allows the boom to buckle and deploy as designed and still have almost all the stiffness of the earlier single hinge design. While these experiments and trades continued, another approach using either Elgiloy or Beryllium-Copper hinges was pursued as a back up.

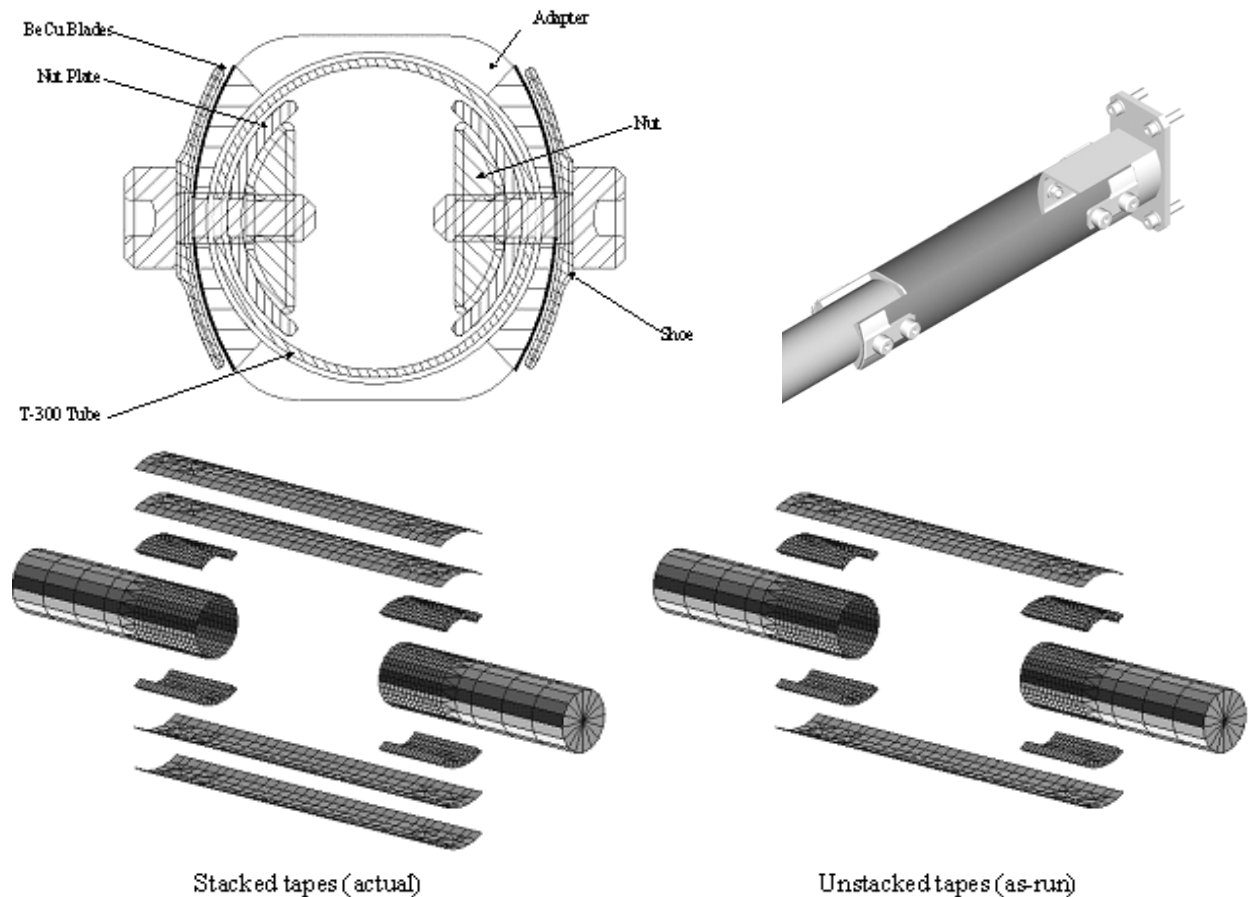


Figure 6. Hinge Tape Stacks

The Analysis Program

Hinge development involved both analysis and testing. This boom design relies on the strain energy in the buckled hinge to straighten the hinge and deploy the boom. The deployed boom results in the hinges being in a state that requires considerably more force to buckle again. Deployment tests of the complete boom system have shown that the stored strain energy is sufficient to cause the shoulder hinge to snap over. This snap over is the buckling of a hinge in the direction of deployment (opposite its originally stowed state). However, after several cycles the system damps out with the boom deployed. The buckled state required a non-linear approach for analysis. There was significant effort in developing and correlating stowed hinge behavior models. Through strain-gauged mechanical bending tests and photo-stress methods a high degree of correlation between the analysis models and the physical models was achieved. This correlation between analysis and test has given confidence to the modeling technique employed. Through this analytical tool material, lay-ups, hinge length and subtended angle were traded off against strain and peak snap-over moment. Thus a few highly likely candidates were selected for further testing. The stress/strain results indicated that a successful composite blade would have to be very thin. Subsequent testing showed that the very thinnest composite hinges did work, but the resulting booms had very low deployed natural frequency and long snap-over damping times.

The stiffest 1.9-cm (3/4") diameter boom with composite hinges tested had a frequency of about 2.7 Hz. The diameter of the boom was increased above the nominal 3/4" in an effort to get the deployed frequency above the required 5 Hz. It was determined that even significant increases in tube diameter resulted in only small increases in the deployed boom's natural frequency. In addition, the project

objected to the increased shadowing of the solar arrays. In the summer of 2002 the design effort was concentrated on the metallic BeCu hinge.



Figure 7. Analytical snap-thru and stow sequence for joint with 0.15-mm (0.006-in) thick tape and 8.26-cm (3.25-in) window

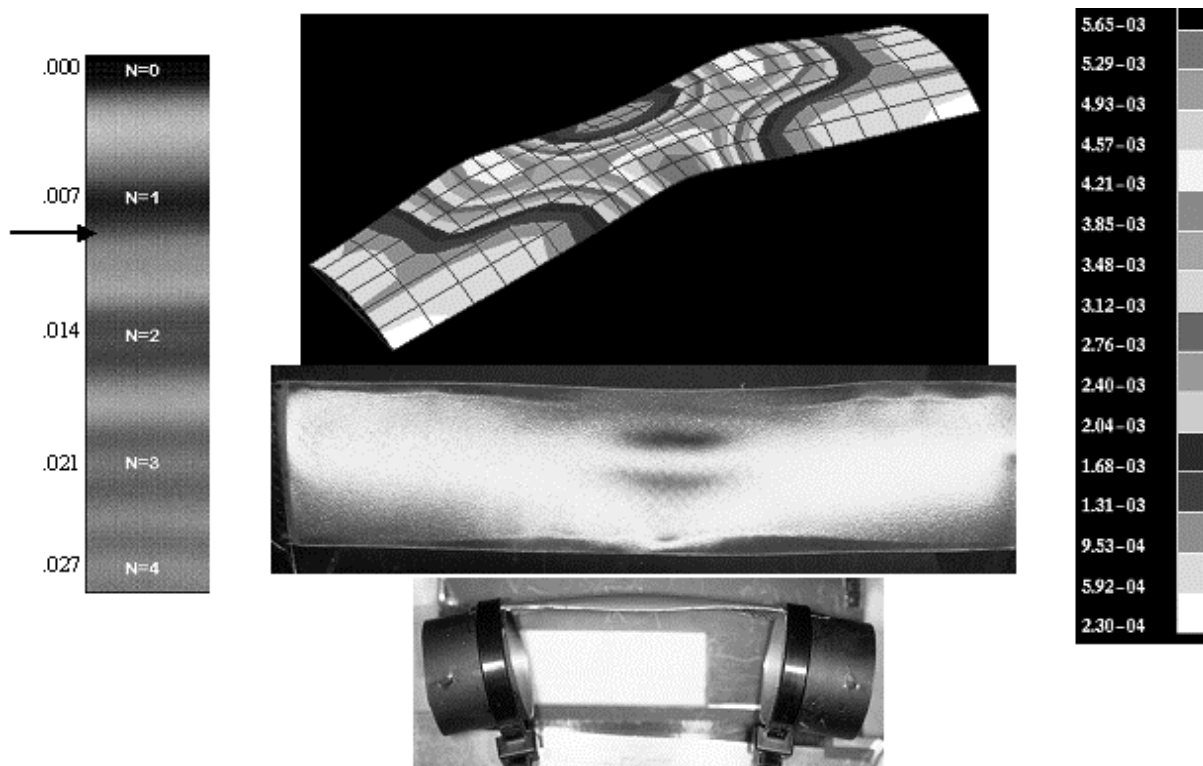


Figure 8. Correlation of Analysis to Experiment for the 72-degree case

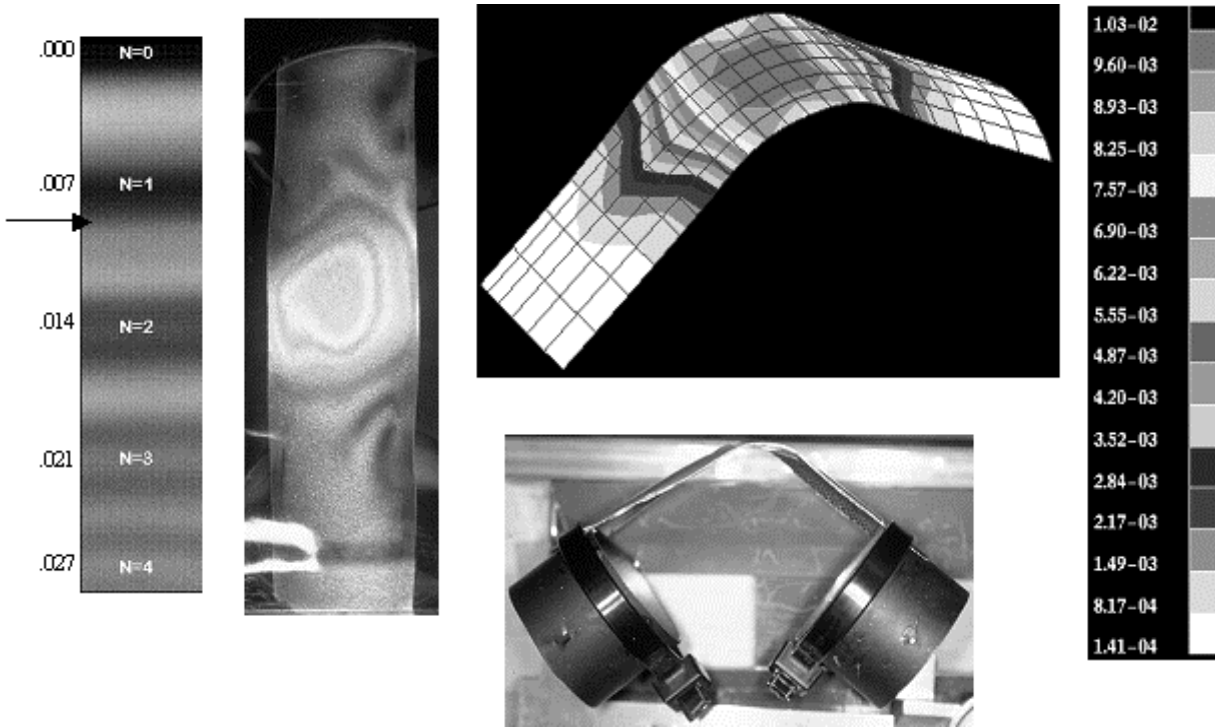


Figure 9. Correlation of Analysis to Experiment for the 22-degree correlation

Moment /Life test fixture

Hinge testing falls into two categories: characterization and qualification. Sometimes, of course, these distinctions are artificial. In order to determine the deployed frequency, the deployed stiffness in the folding plane and normal to it need to be measured. Since the deployment force is the buckled restoring force, this force needs to be measured as a function of angle of buckle. The cycle life, how many buckling operations can the hinge survive, also needed to be known. A Moment /Life test fixture was built to make these measurements. The torque resistance of the harness was also measured with this rig. The fixture was designed to operate in thermal chambers so that measurements could be taken over a range of environments.

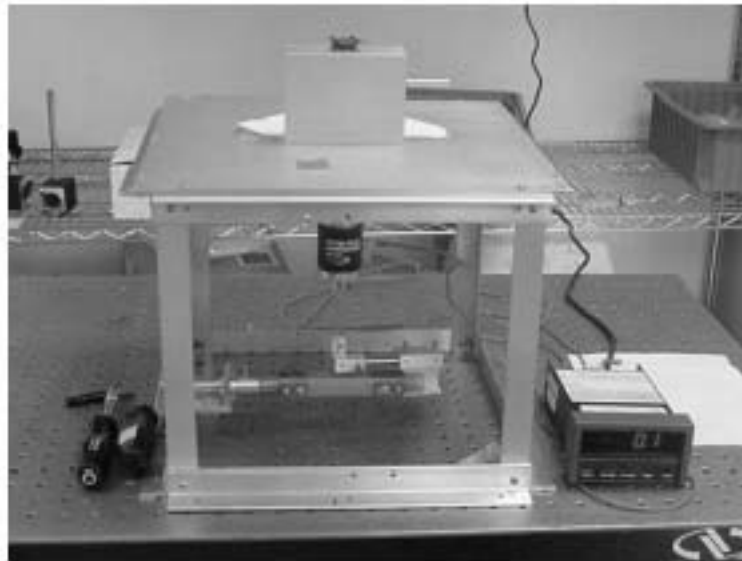


Figure 10. Test Fixture

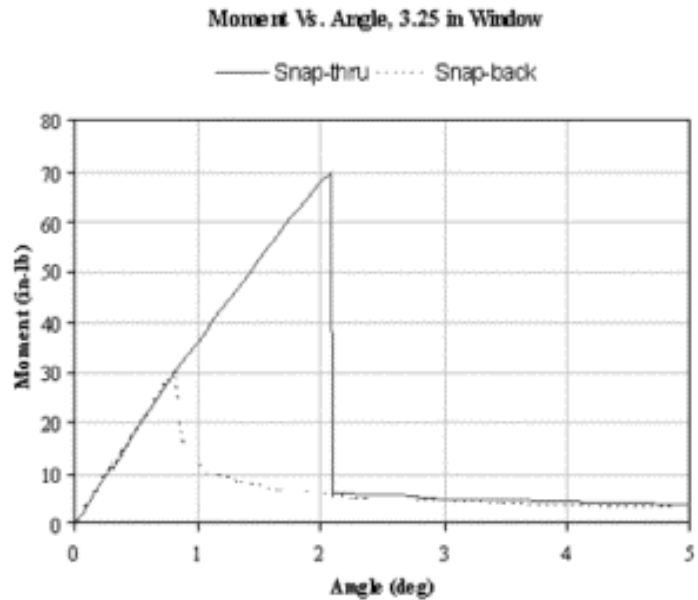
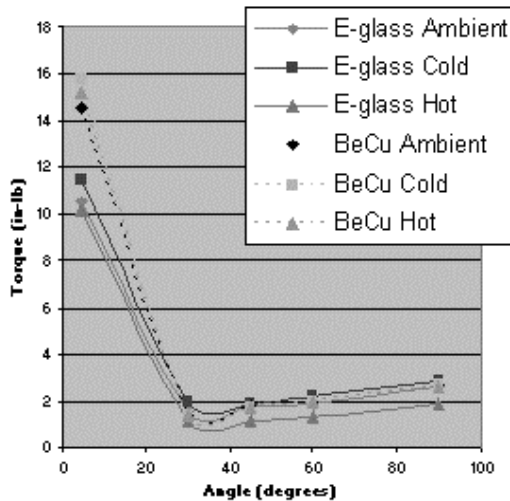


Figure 11. Torque vs. Angle

The ratio of peak snap-back moment is less than half of peak snap-thru moment. This is the damping action that makes the deployment stable.

Deployment Testing of a Complete Boom.

Once it is deployed, the boom is able to support itself under gravity; however it needs a "g" negation system while it deploys. During deployment, the collapsed hinges do not have enough lateral rigidity to support the boom. A low-friction trolley was developed to support the boom payload mass during deployment. The trolley consists simply of a spring-loaded support for the magnetometer on a trolley base. This trolley moves along a flat plate of aluminum. A simulated spacecraft structure holding the boom is also mounted to this plate. Because of the boom's deployment characteristics, the plate is 1.5 m x 1.8 m (5 ft x 6 ft). This trolley has been designed to be compatible with the requirements of the thermal-vacuum test chambers. The boom deploys from the outboard segments inward (e.g. the wrist joint locks in first, followed by the elbow and then the shoulder joint). Extensive testing of the full boom has shown that the shoulder joint snaps over (the hinge collapses in the opposite direction) on all deployments. The number of times that the hinge snaps over is a function of the deploying energy. During ambient, horizontal testing the boom snaps over an average of just one time. The angle that the plate is mounted with respect to the horizontal allows gravity to simulate the rotational "g" field. During life testing, when the centripetal acceleration of the spinning spacecraft is taken into account the boom snaps over an average of seven times at the lowest energy level and nine times at the highest energy level.

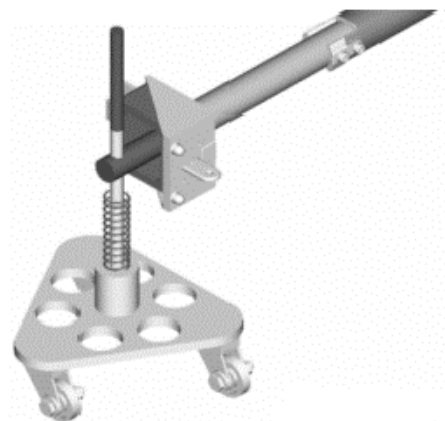


Figure 12. Special Test Equipment



Figure 13. Trolley on Tilt table

Vibration Tests

Another dummy spacecraft was built as a vibration fixture adapter to allow the stowed configuration to be tested. The vibration survival of the stowed boom turns out to be a real concern. The magnetometer mount is held securely by the pin puller, but not much tension force is available to retain the boom sections in the snubbers. Consequently during vibration the flexible collapsed hinges allow considerable motion of the boom segments. It is a rattling fit in the snubbers. This in turn results in the boom system behaving non-linearly under vibration. A finite element model exists for the boom in its stowed configuration, but because of the non-linear nature of the stowed boom extensive testing was needed. The stowed boom "natural frequency" is very dependent on the vibration environment. Extensive sine sweep testing has determined that at low levels, less than 1G, the boom resonates around 50 Hz. As input levels increase towards 8G's, the boom "natural frequency" drops to around 20 Hz. Naturally this means qualifying the stowed configuration by test. Such extensive testing, obviously, is going to result in a few failures.

In Figures 14 and 15, note the Y response of the center segment of the boom moving transversely has the most non-linear characteristics, followed by the X response moving out of the snubbers, as the collapsed hinges are softest in these directions.

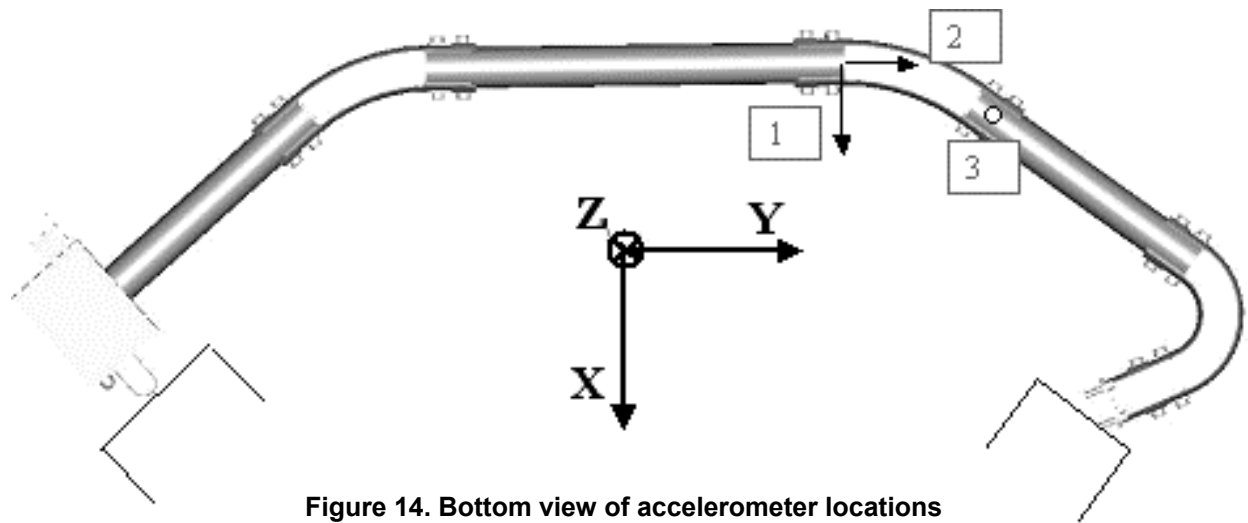
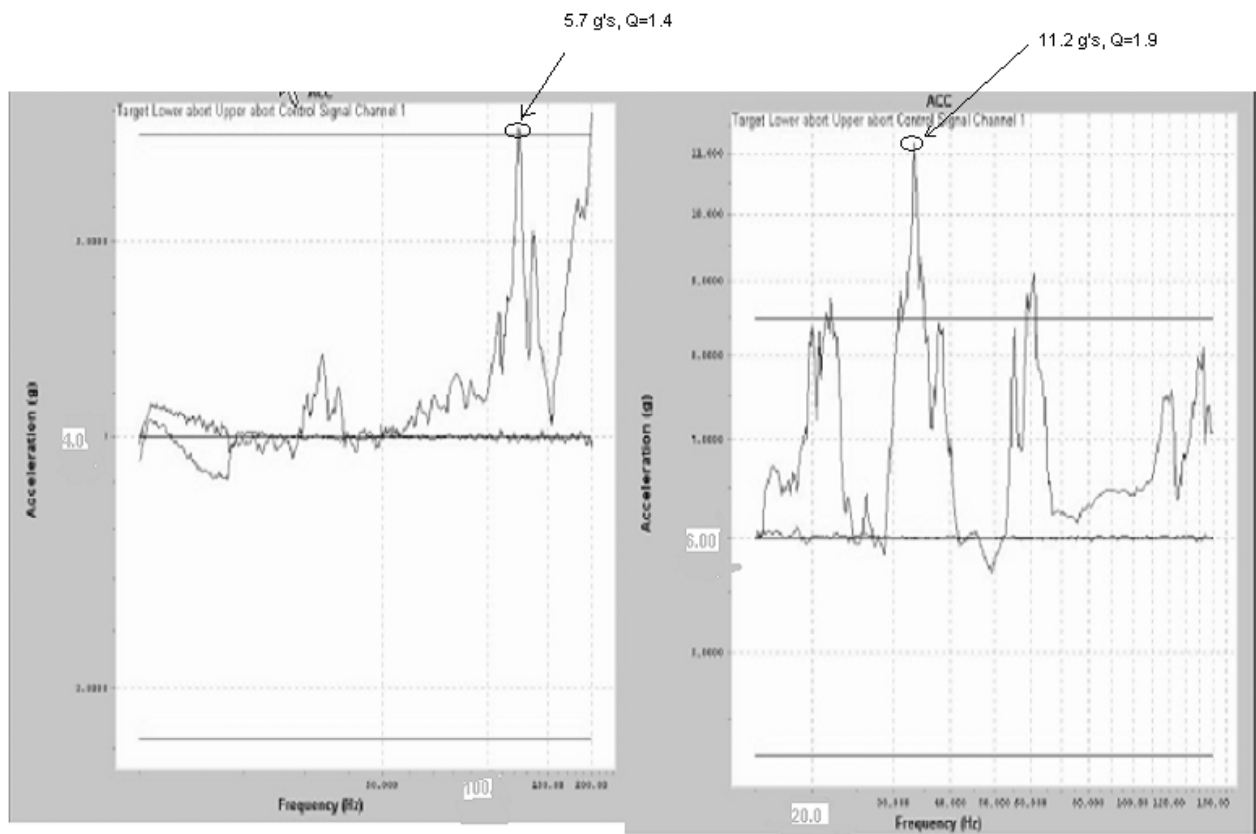
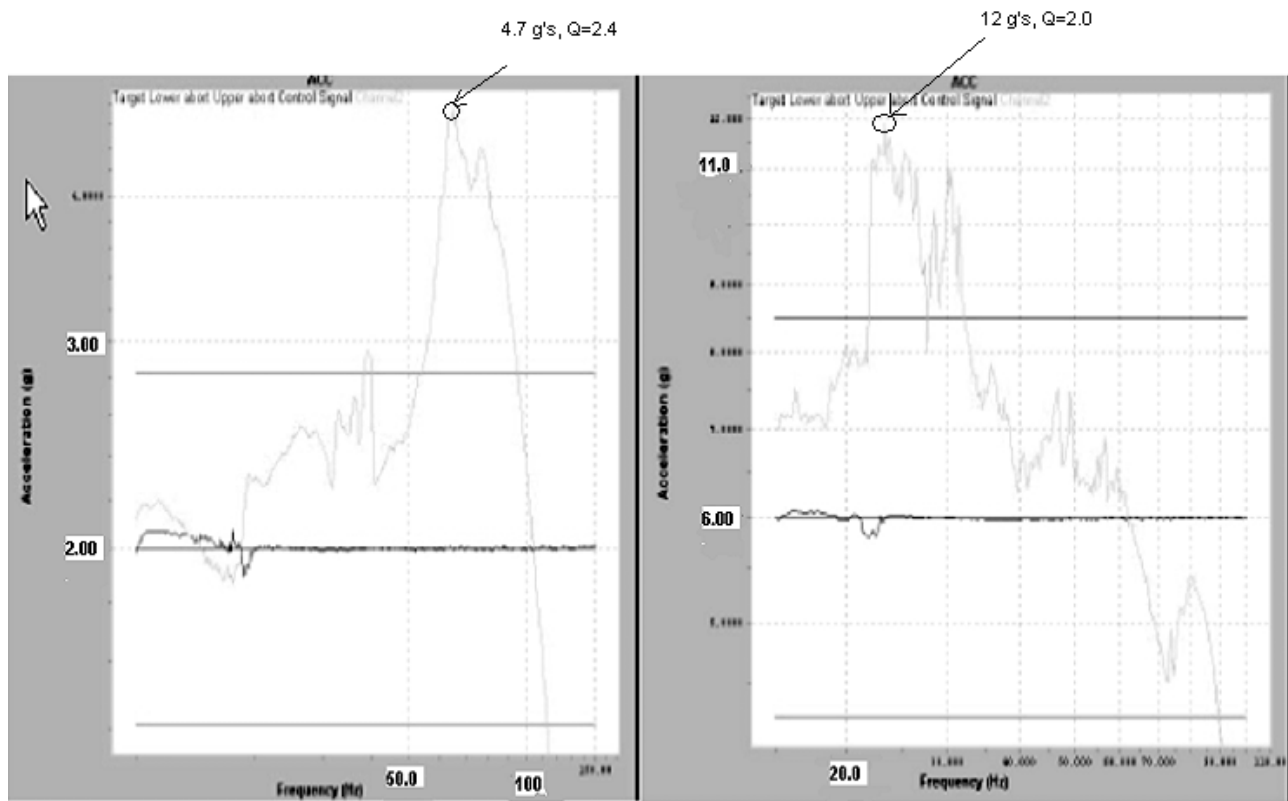


Figure 14. Bottom view of accelerometer locations



X Axis Response vs. Input. Left is 4-g input and right is 6-g Input



Y-Axis Response vs. Input. Left is 2-g Input and Right is 6-g Input

Figure 15. Accelerometer Responses (X-axis and Y-axis)

Failures

During an ETU spacecraft qualification test, the stowed boom was included to gather information about its capabilities. In general, the boom behaved as expected. However, the Ultem tang that holds the magnetometer mount to the spacecraft broke during a 17 GRMS random vibration run. The tang, it turned out, had been manufactured thinner than the drawing called for. Materials investigation of the part showed there were two failures. There was an initial fatigue failure at the junction between the top hat and the tang and this led to a subsequent fatigue failure of the tang itself. The tang was remade to the correct dimensions and the testing proceeded. It was later decided to replace the Ultem tang with a titanium piece, which was non-magnetic and stronger.

During a subsequent 8.5G, 15-Hz sine burst test in the last axis (during the same time frame) the outer elbow tape failed. A materials investigation of this hinge showed that it had failed due to low cycle fatigue. Further study of this problem revealed that the hinge shoes that hold the hinges to the boom were causing a sharp bend in the hinge just before it attached to the boom. The fatigue failure of the hinge had occurred right where the sharp bend was identified. The shoes have been modified to cure this.

The outer elbow tape again failed during a 17G, 14-Hz sine burst test. This failure was due to an oversight by the mechanical team. Following the ETU sine burst failure it was realized that the natural frequency of the stowed boom was so close to the sine burst frequency that a burst test on the stowed boom was out of the question. During planning for this testing, this detail was overlooked. Materials

investigation of the failed hinge showed that it had failed as a result of a single event overload. No changes to the design were needed to fix the problem.

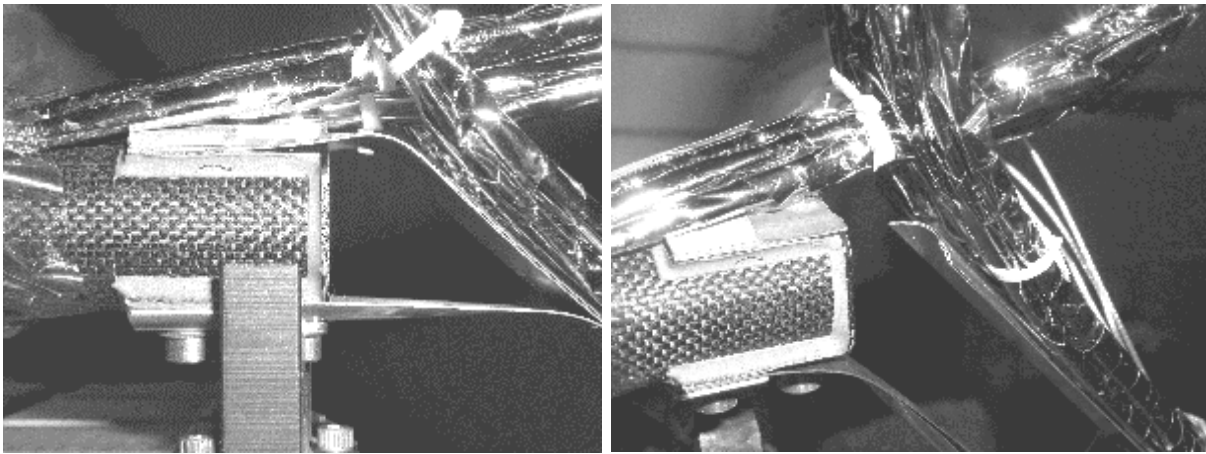


Figure 16. Before and After Sine Burst

Production Problems

The ETU 1.9-cm (3/4") T300 boom sections were fabricated by a local contractor, and the initial test pieces worked fine. The flight units, however, were made by an "improved" technique with the mandrel continuously wrapped with the lay-up rather than by using cut layers. The resulting booms had resin-starved sections. Another delay to order new materials and do it right. Since hinge blades were not going to be made from the material, it was changed to M55J, higher modulus but less tough.

Thermal Magnetic Considerations

Now some thermal results began coming in and the scientist became concerned with thermal gradients producing Peltier voltages which in turn would produce eddy currents and a resulting magnetic field higher than the extremely low fields he was setting out to measure. All metallic pieces became suspect. In particular the titanium tang with its low heat conductivity gave rise to big gradient. The tang was changed to polished aluminum and the surface was coated with SiO. The hinge leaves were also gold plated to cut down on the thermal gradients across them. The composite boom had already been blanketed, as had the cabling. The desire on the part of science to apply thermal blankets to the working hinges was resisted in the favor of their working. The stainless screws were replaced by custom-built titanium shoulder screws.

A new Launch Vehicle

At this point the idea of getting a ride as a secondary payload on a large Expendable Launch Vehicle faded as the primaries raised objections. The option of a ride to orbit as the primary on a Pegasus became a real possibility. A new support structure was required because the honeycomb base of the baseline deployer system was designed as an adapter to an ELV Payload Attach Fitting. Most of the loads are well under those enveloping Ariane, Delta, and Atlas. Because the ST5 mission consists of three spacecraft, the dimensional limitations of the Pegasus fairing drove the support structure to a new cantilevered design. This has led to concerns about the coupling between the Pegasus environments and the primary modes of the support structure, the ST5 spacecraft bus and the stowed boom. The driving technical question is the response of the boom to the Pegasus drop transient and captive carry random vibration. Again the non-linear aspect of the boom precludes a direct analytical approach. Orbital Science Corporation has been given a finite element model of the payload with the boom represented by a sprung

mass. The results of a coupled loads analysis will be applied to an ETU boom on the test fixture to make sure it can survive the drop transient and captive carry response. After a technical interchange meeting with OSC the support structure was redesigned to raise the frequency from 22 to 37 Hz.

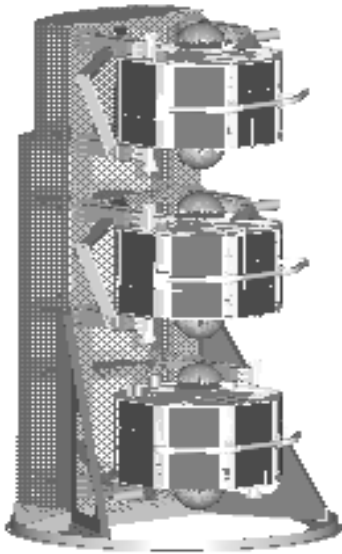


Figure 17.
On Launch Adapter

Test Results

A capability test of the spacecraft and boom was performed with preliminary support structure response data to determine problem areas. The boom survived the drop transient excitation, which was modeled as a 10 G peak 10 Hz input and a random vibration environment that had a peak of 0.2 g^2/Hz below 60 Hz. A similar environment with a peak input of 0.4 g^2/Hz below 60 Hz, however, caused the elbow hinge to fail with what looks like a single event overload. The application of this load based on the softer support structure was a gamble that did not pay off. The random response that is expected with the new stiffer support structure is expected to have a peak value closer to 0.2 g^2/Hz below 60 Hz. No action is being taken until the new levels are in and the boom is tested to them.

Current Flight Boom Status

The boom comprises three 1.9-cm (3/4") diameter M55J graphite composite tube segments with Titanium adapters at each end to mount "carpenter tape" spring hinge blades. Each hinge is made up of four "carpenter-tape" blades stacked two thick on each side. These blades are formed from a Beryllium-Copper alloy strip (0.15-mm (0.006") thick) that has been tempered to meet design needs. When stowed, the boom folds around three sides of the spacecraft. It is supported with stand-offs at either end of the middle segment to keep it off the solar panels. A low-shock, SMA pin puller from TiNi Aerospace, Inc. is used in conjunction with a kinematic retention cage to restrain the sensor head during the launch phase of the mission. The thermal treatment consists of gold plating the hinges and blanketing everything else except the magnetometer mount tang which is coated with SiO. Titanium screws are used throughout the boom system. This boom system is about to undergo flight qualification testing.

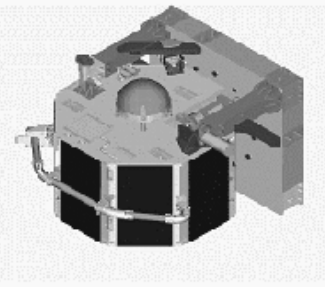


Figure 18. ST-5 on ELV
Deployer Mount

The Future?

In order to fully satisfy the science requirements for a magnetically clean boom system, at least the wrist joint nearest the magnetometer should be completely non-metallic to reduce thermal magnetic contamination. This is probably achievable with more development work. The center boom section between the wrist and elbow should be positively restrained. This will take another actuator but is readily doable and will greatly improve the boom's ability to resist random vibration. A custom cable made from printed circuits on Kapton would further enhance the system being lighter and able to be run inside the tube. The large external cable loops currently over hanging the joints contribute to the non-linear response of the system.

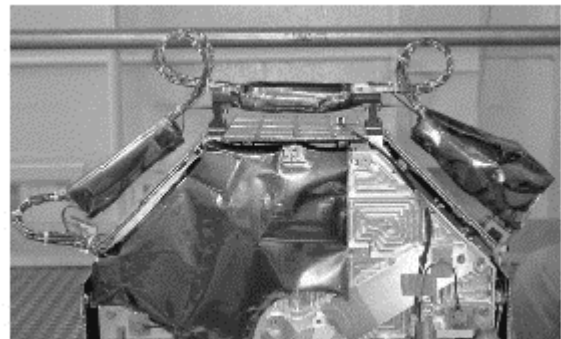


Figure 19. Flight hardware

Latch-up Anomaly Study for Reflector Deployment of INSAT-2E Satellite

G. Nagesh*, S. Ravindran* and N. C. Bhat*

Abstract

INSAT-2E Spacecraft (S/C) has two deployable antenna reflectors of which one of the reflectors showed a non-nominal latching behavior during the ground deployment test with a couple of bounce backs before a final positive latch-up. Similar phenomenon was not observed during the test on the other reflector. Detailed analysis revealed the inherent limitation in the design for the former reflector. This limitation was confirmed by subsequent tests. This paper describes in detail the analysis carried out, the various tests conducted and the optional design modification worked out to correct the same. However, in view of the capability of the present design to latch positively, it was decided to fly this mechanism without any changes in INSAT-2E. The observed on-orbit performance is also reported here.

Introduction

INSAT-2E is a multipurpose spacecraft intended for communication and meteorological purposes. It has two antenna reflectors one on the west side and the other on the east side henceforth called as West reflector and East reflector respectively as shown in Figure 1. These reflectors are in the stowed configuration during launch and are deployed in orbit. As the configuration of the two reflectors are different and due to the constraints on the spacecraft structure with respect to the reflector interfaces the reflector deployment mechanisms are different for both the reflectors. During the ground deployment tests on the reflectors, it was observed that the deployment of the East reflector was nominal, whereas the West reflector after the first latch-up was found to rebound and the forward - reverse oscillatory motion repeated a couple of times before the final latch up of the reflector.

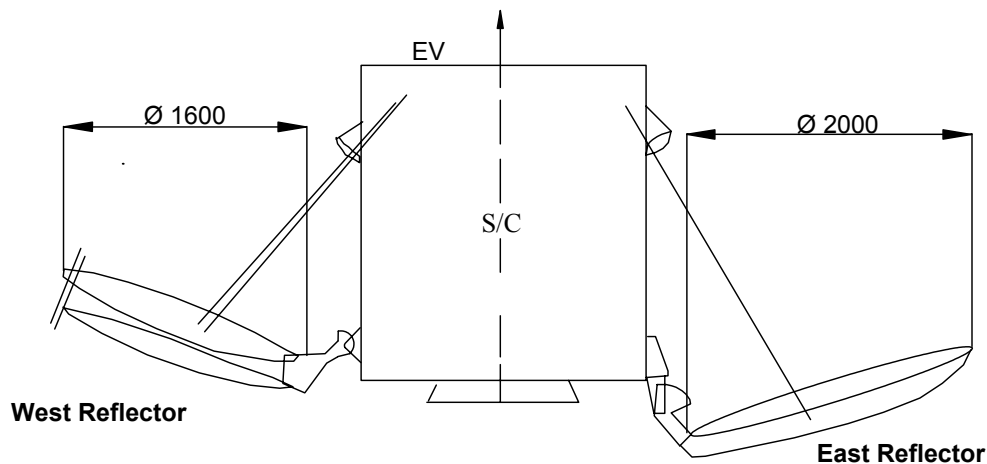


Figure 1. INSAT -2E S/C with Both Reflectors Deployed

* Spacecraft Mechanisms Group, ISAC, Bangalore, India

Anomaly description

The two reflectors were received at an advanced stage of the INSAT-2E program. Both the reflectors and the deployment mechanism were taken up directly for assembly and tests at S/C level.

The East reflector after integration was successfully deployed and the performance of all mechanism elements were nominal. However, the West reflector was found to rebound a couple of times before the final latch-up. A thorough analytical study of the two hinge assemblies was carried out in order to understand the above behavior. This was followed up by tests on hinge assembly of both the reflectors. The latching characteristics of both reflectors were studied by a latching test under simulated zero 'g'. As this problem occurred late in the program, there was a need to verify the required functioning even with this anomaly by subjecting the reflector to the expected on – orbit disturbances. A design modification of West reflector to correct the above anomaly was also worked out as a backup / or for use in future S/C.

Description of Reflector deployment mechanism

The East and West reflectors in the deployed configuration are interfaced to the spacecraft through a pair of hinges each. A typical hinge assembly of the East reflector and West reflector is as shown in Figure 2a and 2b. Each hinge assembly consists of two brackets - an Inboard bracket connected to S/C and an Outboard bracket connected to the reflector. These two brackets are pivoted by a mono ball spherical bearing mounted on a shaft supported by the inboard bracket. The dry lubricated spherical bearing takes care of misalignments caused due to assembly or thermal environments. A locking linkage is provided with one end hinged to the inboard bracket. The out-board bracket has a circular cam sector over which a roller mounted on the other end of the locking linkage rolls during the deployment and latches into the slot provided in the sector at the end of deployment. Two torsion springs mounted on the shaft provide the necessary energy for deployment. The torsion springs on the locking linkage shaft ensures positive latching at the end of deployment. The locking linkage also provides for minor adjustment of the opening angle of the reflector. A micro-switch mounted on the inboard bracket confirms the hinge lockup at the end of deployment.

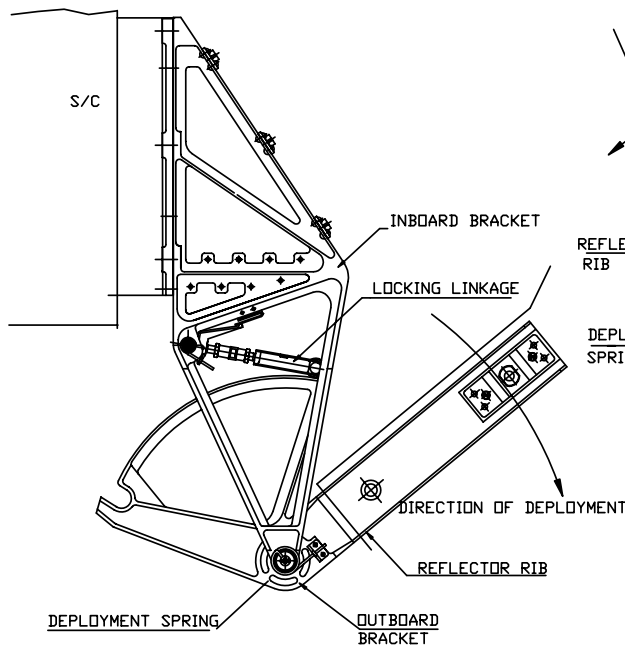


Figure 2a. Hinge assembly of East reflector
– INSAT-2E

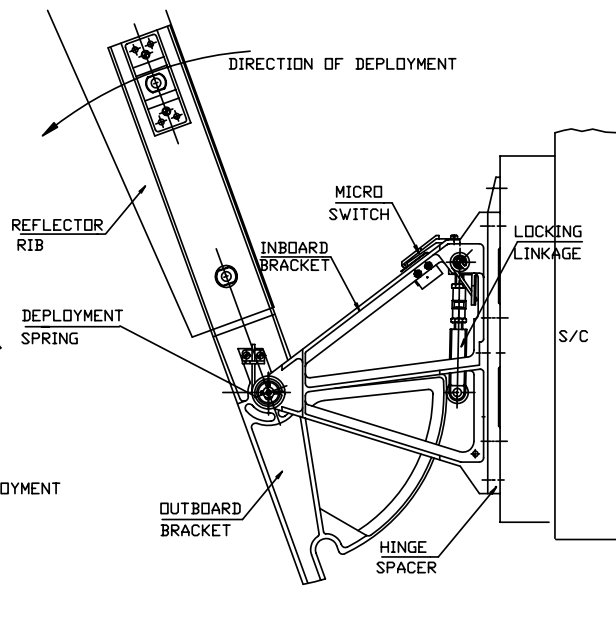


Figure 2b. Hinge assembly of West reflector
– INSAT-2E

Investigation of anomaly - Analytical study

The reflectors deploy due to the spring torques at the hinge assemblies of the deployment mechanism. On latch-up, the kinetic energy of the deploying appendage results in a forward shock followed by a reverse shock at the locking linkage – outboard bracket pair. While the latch-up performance was nominal for East reflector, the West reflector showed 3 rebounds before final latching. Once the roller of the locking linkage enters the slot at the end of deployment, the configuration should resist the forward and reverse shocks without instability. In the case of West reflector the reverse shock was dislodging the roller from the slot and the roller was riding over the outboard bracket sector till the motion comes to rest and subsequently due to the spring torque the motion was initiated in the forward direction. This action repeated a couple of times before the final locking.

In order to analyze the rebounding behavior of the hinge mechanism for the reverse shock loads, studies were carried out by applying static moments in the reverse (stowing) direction for both the reflector hinge configurations. The analytical studies were carried out with the following assumptions:

- Friction torques at the interfaces has been neglected. As the presence of friction opposes the motion the results obtained by neglecting the same will be on the conservative side.
- The structural stiffness of the brackets are assumed to be high and all the movements analyzed are due to the kinematics of the mechanism only and the structural deflections are not considered.
- A combined radial clearance of 0.05 mm is assumed to be present between the roller- pin - slot.

The schematic configuration of the outboard bracket and locking linkage assembly for the East and West reflectors are as shown in Figure 3a and Figure 3b. Under equilibrium conditions due to the action of the spring torques on the outboard bracket and the locking linkage the point of contact of the roller in the slot is at point ' A '. When an external torque (T) is applied in the reverse (stowing) direction the roller moves in the slot and the position of equilibrium changes depending on the magnitude of the applied torque. The relation between the applied torque and the angular movement of the outboard bracket (θ) can be computed based on the equations of equilibrium for the locking linkage and the out-board bracket. The derived equations for West reflector are as follows for a hinge line spring torque (T_s) of 0.863Nm and locking linkage spring torque (T_L) of 1.324Nm:

$$T = 0.863 - \left(\frac{1.324 \times 0.122}{0.093 \sin(\alpha) - 0.02 \cos(\alpha)} \right) \times \cos(\alpha) \quad \& \quad \theta = \sin^{-1} \left(\frac{0.05 \cos(\alpha)}{\sqrt{122^2 + 0.05^2 - 2 \times 122 \times 0.05 \cos(90 - \alpha)}} \right)$$

Nomenclature:

P = Reaction on the roller under equilibrium condition.

α = Angle subtended by reaction P with horizontal.

C = Extreme point on semicircular slot in forward direction.

B = Extreme point on semicircular slot in reverse direction.

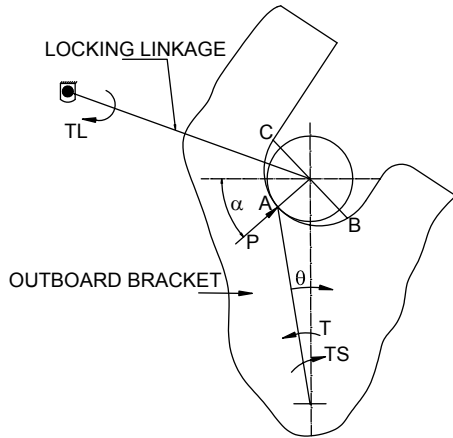


Figure 3a. Schematic configuration of bracket & Locking linkage- East reflector

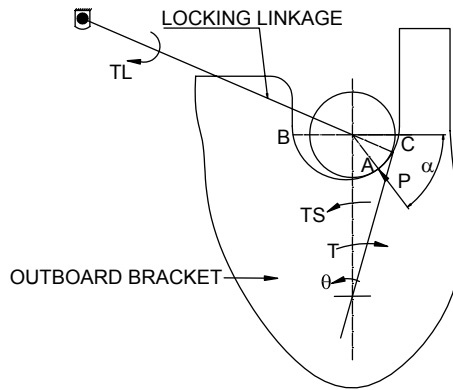


Figure 3b. Schematic configuration of bracket & Locking linkage- West reflector

Results of the analysis for both the reflectors

In the case of the East reflector as the applied torque in the reverse direction increases the point of contact at 'A' shifts towards 'B'. The plot of torque vs. angular movement of the out-board bracket is given in Figure 4. It is seen that as the point of contact shifts towards 'B' the assembly tends to become self-locking and the locking linkage does not get lifted up for any magnitude of the external torque. In the case of the West reflector the point of contact at 'A' shifts towards 'B' with increase in applied torque. Once the point of contact is at 'B' the mechanism becomes unstable and the locking linkage has a tendency to get lifted even for lower values of applied torque as shown in Figure 4. If the application of the torque is continued, the locking linkage gets lifted and rides over the sector allowing for rotation of the reflector in the stowing direction.

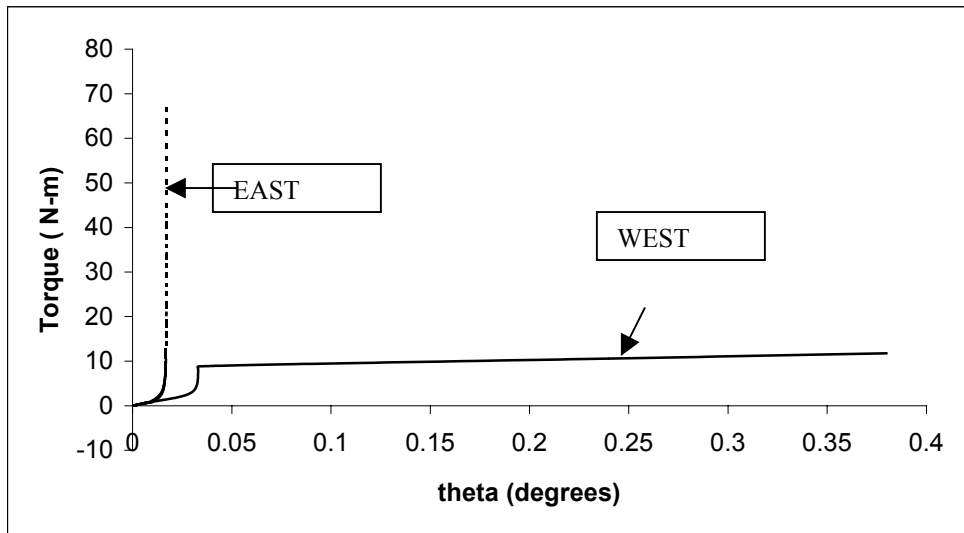


Figure 4. Estimated torque vs. Angular movement of Outboard bracket for reverse moment

Similar plots for a disturbing torque in the forward direction for both the reflectors is as shown in Figure 5. As the torque increases the mechanism becomes self-locking and does not allow for further rotation of the reflector.

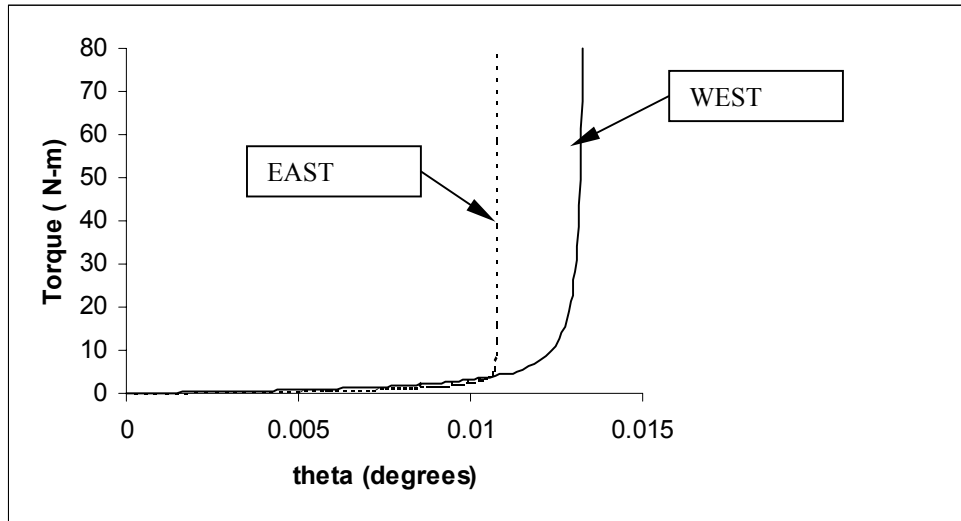


Figure 5. Estimated torque vs. Angular movement of Out-board bracket for forward moment

From the above analysis it is seen that:

- For the East reflector, the locking linkage and out-board bracket geometry is such that the assembly once locked becomes self-locking for torques in both the forward and reverse direction.
- For the West reflector, the locking linkage and out-board bracket geometry is such that the assembly once locked becomes self-locking for torque in the forward direction, whereas for a reverse torque exceeding 10 Nm the locking link gets lifted up and allows the outboard bracket to rotate in the reverse direction.

Tests conducted on East and West reflector mechanism

Tests were conducted in different phases for the following:

- Single hinge characterization to verify the analysis.
 - System level tests on spacecraft to characterize the latching phenomenon and capability to ensure the specified pointing accuracy under external disturbances.

Single hinge characteristics

The above analysis was verified experimentally at subassembly level by applying a reverse torque on a hinge assembly. A single hinge assembly of East and West reflector was characterized for Torque vs. angular movement of Outboard bracket. The test setup is as shown in the Figure 6a. A gradually increasing load (P) was applied at one end of the out-board bracket and the corresponding rotational movement of the bracket was computed from the dial indicator readings as shown in the test setup. The rotational movement of the Outboard bracket vs. applied torque in the reverse direction is shown in Figure 6b.

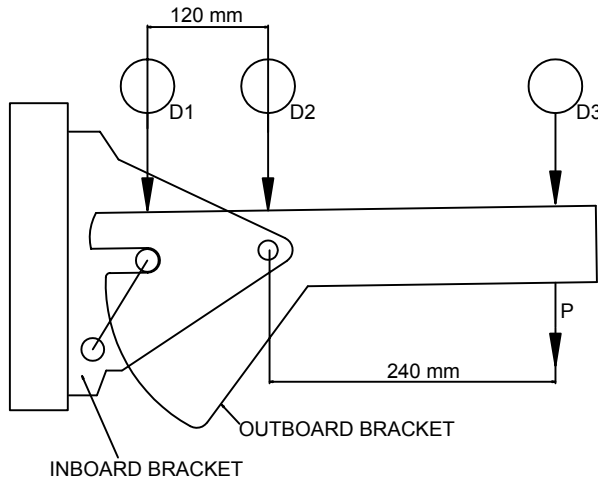


Figure 6a. Test set-up for hinge assembly.

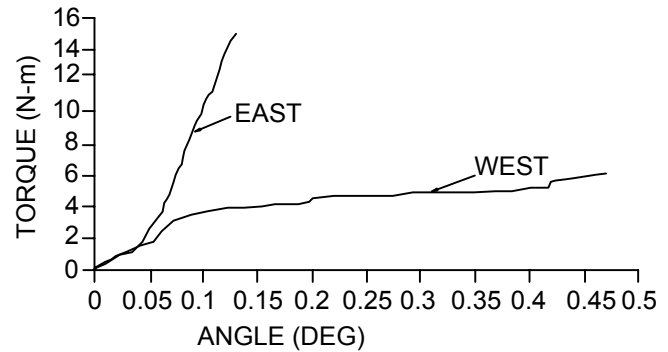


Figure 6b. Characteristics for reverse torque

It is seen from the above measured characteristics for a single hinge assembly that the locking linkage starts riding over the out-board bracket for an applied reverse torque of 6 Nm which works out to 12 Nm for the reflector assembly. The computed number of 10 Nm (Ref Figure. 4) with the inclusion of measured friction torque of 2 Nm also works out to 12 Nm thus validating the analysis. The difference in the measured and computed angles can be attributed to the presence of clearances at the spherical bearing joint and due to measurement limitations as the corresponding numbers involved are very small.

Tests on East and West reflectors

Tests on the reflector assembly under Zero 'g' were conducted in order to study the latching characteristics for both the reflectors. The Reflector assembly was supported on a surface plate through an air-bearing pad as shown in Figure 7a. Accelerometers mounted on the reflectors provided the response of the system. The reflector was stowed back by 3 degree (approx.) with respect to the latched position and allowed to latch. The response plots for the East and west reflectors are shown in Figure 7b and 7c. The plots show that the West reflector has rebounded three times before the final latch (as can be seen from the rigid body modes), whereas the East reflector shows pure vibratory mode, which indicates proper latching, and no disturbance to the locking linkage assembly due to the reverse shock. This test also demonstrates the presence of positive torque margins at angles very close to the final position. This is all the more important for the West reflector as a positive latch-up demonstrates the presence of potential energy in the spring system to initiate motion as the momentum in the system reduces to zero each time the motion initiates in the forward direction.

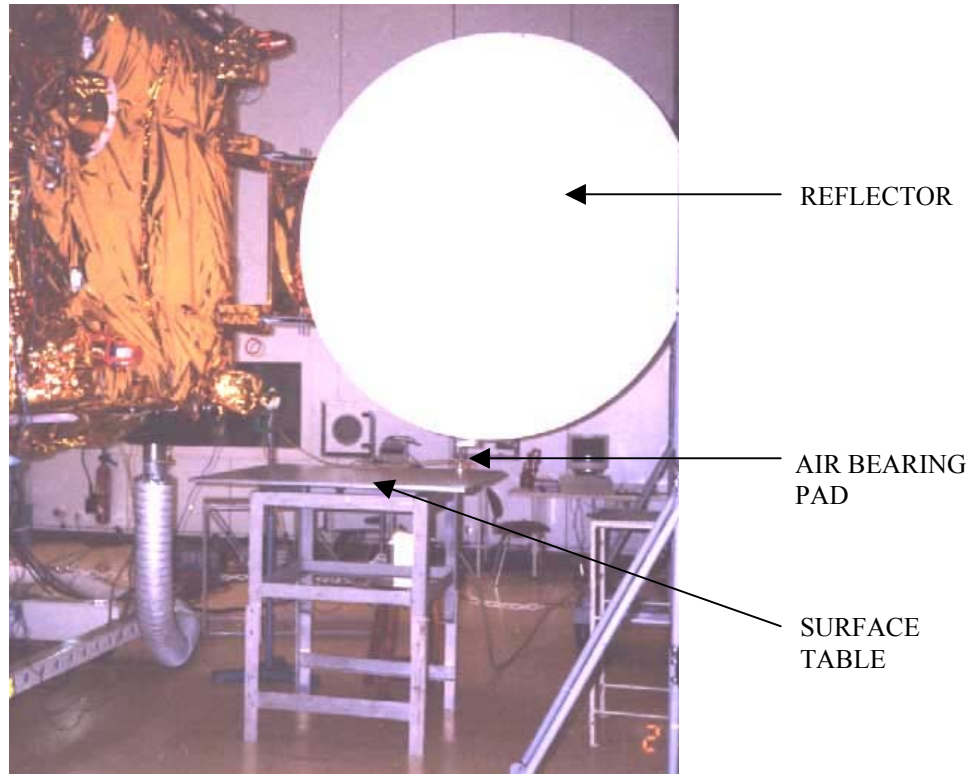


Figure 7a. Test set-up for reflector deployment under zero'g'

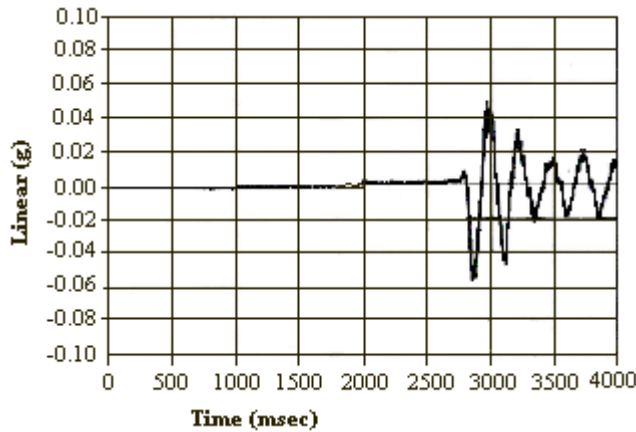


Figure 7b. Response plot for East reflector

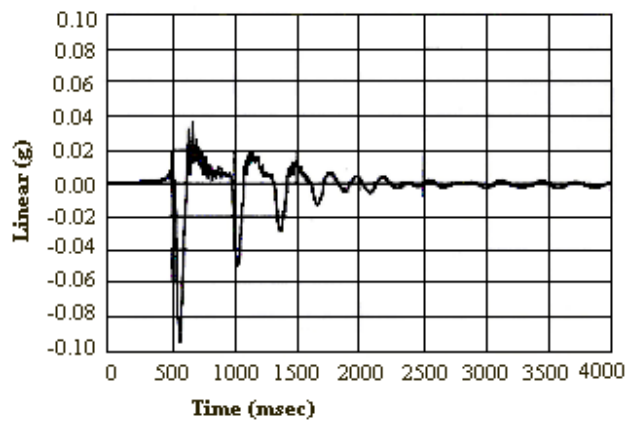


Figure 7c. Response plot for West reflector

Another test conducted was to measure the response of the reflector in the latched position for disturbing torques that is experienced by the reflector during the thruster firing operations for the purpose of station keeping of the S/C. This test on the West reflector was required in order to verify at system level the torque required for unlatching of the reflector. The root moment at the hinge axis due to thruster firing was computed to be 0.35 Nm. An actual moment of 4 Nm was applied and released suddenly on the West reflector in the deployed condition under zero'g'. The response of the West reflector is as shown Figure 8.

It is seen that the mechanism assembly is stable without any rigid body motions thus demonstrating a margin of > 10 with respect to the adequacy of locking mechanism for 4 Nm disturbing torque.

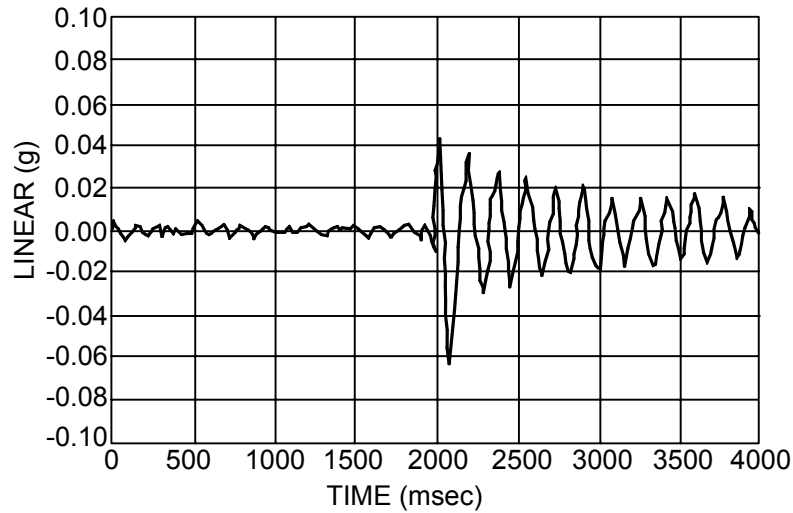


Figure 8. Response plot for West reflector.

Design modification in West reflector bracket to correct the anomaly.

A modification in the geometry of the slot as shown in Figure 9a with all other details remaining identical was analyzed for the behavior of the locking linkage for reverse and forward torque. The mechanism characteristic is identical to the earlier configuration for a forward torque while for a reverse torque the mechanism becomes self-locking as in the case of East reflector. The plot of torque vs. angular movement of the out-board bracket for both forward and reverse torque is given in the Figure 9b.

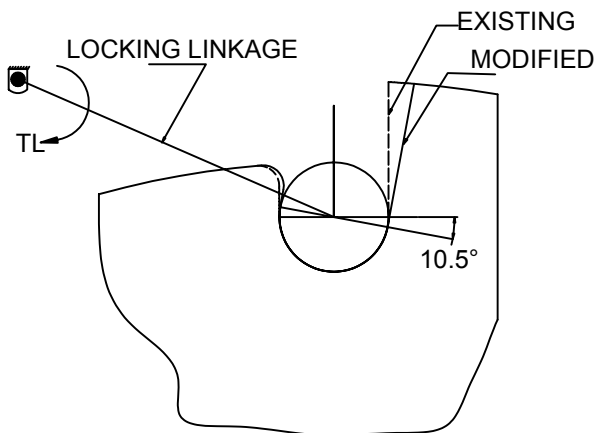


Figure 9a. Modified configuration of bracket & Locking linkage- West reflector

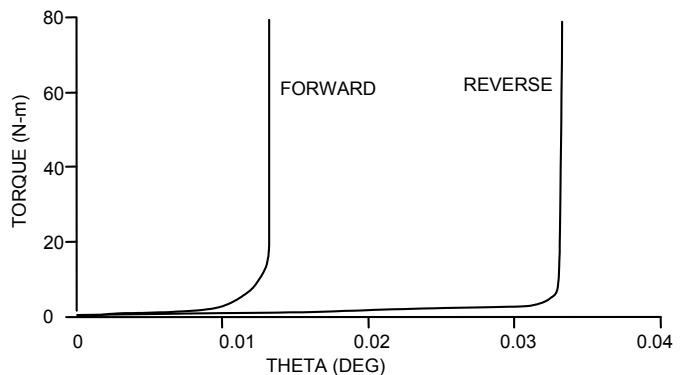


Figure 9b. Plot of torque vs. angular movement of the Out-board bracket

From the above analysis it is clear that a minor modification in the slot geometry of the outboard bracket with all other elements remaining identical as before will eliminate the rebound anomaly seen in the West reflector mechanism.

Design requirements for satisfactory performance

All the analysis and tests concluded that the West reflector mechanism design limitations have resulted in the rebound a couple of times on deployment. However, once the final latch up occurs the mechanism was stable for all on-orbit loads. A modified design for the West reflector was worked out in which the above limitations were overcome. However, before implementation of the same minimum requirements for the satisfactory performance of the deployment mechanism for the West reflector were critically looked into and worked out as follows:

- Positive latch-up in spite of rebounds to be ensured. i.e. as the reflector moves backwards and forward after each latch, it is to be ensured that sufficient torque margin exists even just before the final latch. This is extremely important as only the potential energy initiates the motion since the kinetic energy at the start of motion is absent.
- The configuration of the latched reflector has to be stable even under the on-orbit disturbances caused during the S/C maneuvers. The maximum torque that the reflector experiences during thruster firings are to be analyzed and adequate margin demonstrated to ensure that the deployed reflector is stable.

The extensive analysis and tests have conclusively demonstrated that:

- Positive latch-up has been ensured by design, as a torque margin of >2 exists which has been demonstrated by tests also.
- ♦ Positive margin >10 exists with respect to 0.35 Nm (max) torque that will be experienced by the antenna during thruster firings and the same was demonstrated by tests.

As all the above requirements were met, the design was cleared in the present form, i.e., without any modifications with a full understanding of the rebound phenomenon, which would happen on-orbit during latching.

On-orbit performance

INSAT-2E was launched on April 2, 1999 and both the reflectors were deployed successfully. As predicted for West reflector, subsequent to the first locking, rebounds as seen on ground were observed on-orbit also. The dwelled plots of the pitch rate of the S/C in Figure 10 indicate three rebounds before the final latch-up. The micro-switch status indication as seen in Figure 10 also has toggled from 'locked' to 'unlocked' showing three rebounds as expected. The station keeping maneuvers which have been carried out till date does not indicate any disturbances to the deployed reflector, which validates the analysis and tests.

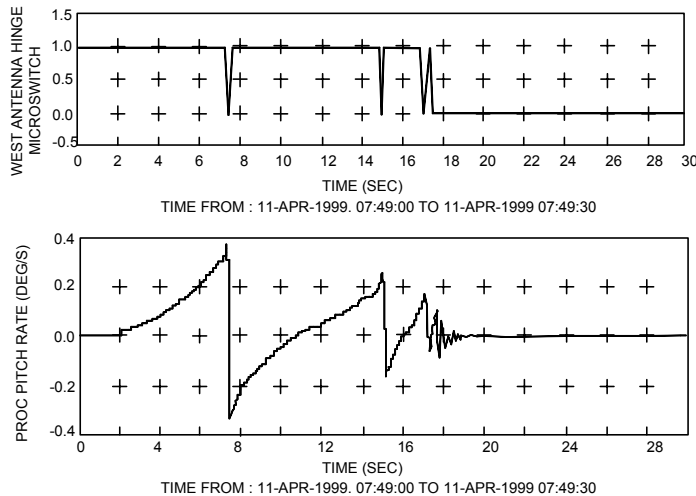


Figure 10. Micro-switch status and Pitch rate of S/C during West reflector deployment.

Lessons learned

A couple of lessons learned from the above experience can be summarized as follows:

1. Design changes, which may look minor, should not be ignored and must be thoroughly looked into before implementing. The designs were verified for the dynamic loads assuming the assembly to be equivalent to a structure after latch-up. As the degrees of freedom were constrained during the above study the anomaly was missed during the analysis. Henceforth, the designs are to be verified for adequacy of withstanding the dynamic load as a mechanism also. The geometry of the mechanism after locking is to be such that in either direction the mechanism must become self-locking.
2. Any new design, even with minor geometrical changes should be tested for integrated mode encompassing all possible loads. This provides sufficient lead-time for understanding and correcting non-nominal behaviors if any. Otherwise surprises if any will be revealed only at later stage wherein even minor modifications may be difficult to be implemented.

Conclusion

Analytical studies and instrumented tests were carried out in view of the anomaly noticed in the West reflector. The analytical results match well with the tests carried out and clearly explain the phenomenon noticed during the deployment tests. The East reflector was also analyzed and results explain the observed behavior. A modification in the geometry of the outboard bracket of West reflector has been worked out to overcome the above anomaly. However, as it was evident that the existing design was adequate to meet the on-orbit requirements in spite of the non-nominal behavior the same was flown without any corrections. The on-orbit observations match well with the ground tests and predictions.

Acknowledgements

Thanks are due to Sri. A.Shankara, Sri H.N.Suresha kumar and Sri S.Narendra for their participation during the course of the above work. Authors also thank Sri.V.Sridharamurthy DPD (Mechanisms)-INSAT-2E for his guidance. Authors wish to thank Sri. M.Nageswara Rao, Group Director-Spacecraft Mechanisms Group for his critical evaluation and constant guidance during the course of the above work. The authors also thank Sri.A.Bhaskaranarayana, Project Director, INSAT-2E, Shri.V.R.Katti, Geosat Programme Director, Sri. H. Narayana murthy, Deputy Director, Mechanical Systems Area and Dr.P.S.Goel , Director, ISAC for their continuous review during the above work and support.

References

1. Spacecraft Mechanism Group, ISAC, "INSAT-2E Mechanism Detailed Design Review Document" September 1997.
2. Spacecraft Mechanism Group, ISAC, "A note on analysis and tests carried out for latch-up anomaly of West reflector deployment- INSAT-2E", November 1998.
3. Spacecraft Mechanism Group, ISAC, "INSAT- 2E On orbit performance of deployment mechanisms", July 1999.

A Strain-Free Lock and Release Mechanism for an Elastically Suspended Two-Axis Gimbal

Armond Asadurian*, Richard Pugh*, Jim Hammond*

Abstract

A single-point-actuated, multi degree-of-freedom restraining launch latch mechanism was developed for a two-degree-of-freedom tilt table antenna gimbal. The design of the launch latch protects the gimbal pivots and actuators through launch vibration, and precludes any high forces on sensitive gimbal components as a result of operation of the latch mechanism itself. At the same time, stringent requirements on stiffness for the latched gimbal and payload are met.

The launch latch design was carried through to qualification largely as initially conceived; however, detail design changes and improvements were made during development as a result of prototyping and development testing.

Introduction

Both the structure and the actuation paths of efficiently designed spaceflight mechanisms are typically not sized to carry the inertial loads generated by launch vibration acting on the mechanism payload. When this is the case, additional structural load paths are required during the launch phase. Subsequently, the structure so introduced must be removable on command to allow normal on-orbit operation of the mechanism.

Mechanism payloads typically are articulated in one or two degrees of freedom (although there can be more), and constrained otherwise by the mechanism joints. If the mechanism power sources are capable of position holding in the launch phase, usually power off, then the phase of the mechanism is nominally fixed. The launch lock device then must support that mechanism configuration with parallel load paths, which are adequately sized for launch loads; so that no damage or degradation of the structure, links, or bearings occurs during launch.

Addition of redundant parallel load paths to a completed mechanism creates concern that local overloading of mechanism elements by the simple act of engaging the locking device could occur. This is a primary design driver for the locking device itself. Stiffness parameters of the locking device elements must be tailored in such a way as to avoid high loads in cross-axis directions when the lock is engaged.

Functionally, launch latches vary from a simple single degree of freedom constraint (e.g., pin joint), to more complex multiple degree of freedom restraints, depending on payload size and mass and other requirements. The subject of this paper is a clamping-type launch latch, which fully restrains the payload.

Launch Latch Requirements

The gimbal actuators control the output platform angular orientation actively in the power-on condition and maintain it passively in the power-off condition. However, in the launch phase of the mission, both stiffness and load carrying capability must be enhanced in all six degrees of freedom. For this application, a launch latch has been designed integral to the main gimbal pivot.

* Moog, Chatsworth Operations, Chatsworth, CA

The specific design requirements for the launch latch are as follows.

Stiffness: ~50% increase in gimbal natural frequency over unlocked configuration.

Interface Parallelism: $\pm 0.046^\circ$ between mounting I/F plate and payload I/F plate

Life: 1 on-orbit unlatch + 50 latch/unlatch cycles during pre-flight testing

Reliability: Single fault tolerant electrical operation

Status Indication: Position sensing must provide feedback for latched/un-latched mechanism status.

Environment: 1200g shock, 30g sine vibration, 26grms random vibration

Operations: Mechanism must be re-settable with a quantifiably controlled preload

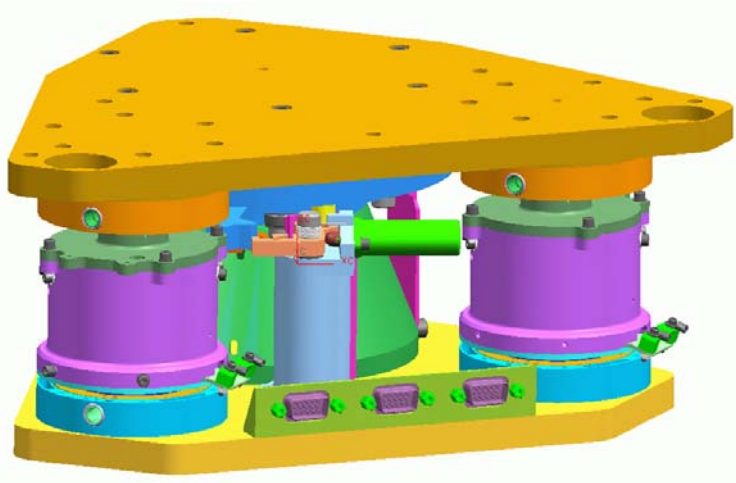


Figure 1. Gimbal Showing Launch Latch Assembly

Launch Latch Design

The Antenna Pointing Mechanism (APM) two-axis gimbal is a tilt-table gimbal operable in two degrees of freedom. It consists of an output platform mounted on a center pivot, tilted in two axes by orthogonal linear actuators articulated between the output platform and a similarly shaped base plate that mounts the assembly to the spacecraft. The center pivot is a two degree-of-freedom assembly of elastic flex pivots configured as a Cardan joint. Angular range of the elastic flex pivots is sufficient to support the gimbal motion. The gimbal is designed to minimize required envelope, which results in a derived requirement for compact design of the latch mechanism to fit in the available space between the center pivot assembly and the two linear actuators. The requirement for pre-launch access to reset the mechanism results in challenging ergonomic and for packaging the constraints.

The launch latch mechanism is designed to rigidize and strengthen the center pivot of the tilt table gimbal. Its function is to tie the gimbal output platform directly to fixed structure through four spring beam members arrayed in a circular pattern surrounding the center pivot. The stiffness of the launch latch members protects the center pivot, and the combination of the center pivot suspension and the launch latch is sufficiently stiff to prevent damaging loads from being transferred to the linear actuators.

The operational range of the gimbal is from 3 to 5 deg of tilt on each axis. Therefore, displacement of the gimbal output plate is relatively small near the pivot. The launch latch mechanism is located near the pivot, so that the motion of the restraining members upon release can be small, while accommodating the operational envelope of the gimbal output plate.

The potential for overstressing of the elastic suspension members of the center pivot exists. Avoiding this potential problem is a key issue addressed in the design of the launch latch. Four pins on the underside of the gimbal top platform are engaged by spring beam members when the launch latch is engaged. The

spring beam members move radially outward to engage the pins, generating a symmetrical set of radial forces that have no net resultant force on the center pivot assembly. Rotation of the ring produces two orthogonal sets of equal opposing forces, and no net lateral reaction on the center pivot.

Engagement of the rotating ring member with the pins and beams is a manual function. Rotation of the ring moves its rollers into contact with the ramp faces of the spring beams, moving the beams outward by cam action. The outer faces of the spring beams contact the locking pins, and the spring beams are captured and compressed between the rollers and the locking pins. When all parts are fully engaged, the ring is secured by a latch mechanism, which holds it in position. The gimbal then stays in the latched configuration until the ring is released by an Unlatch command. The Unlatch command extends the plunger of a hot wax actuator, releasing the ring latch and freeing the gimbal.

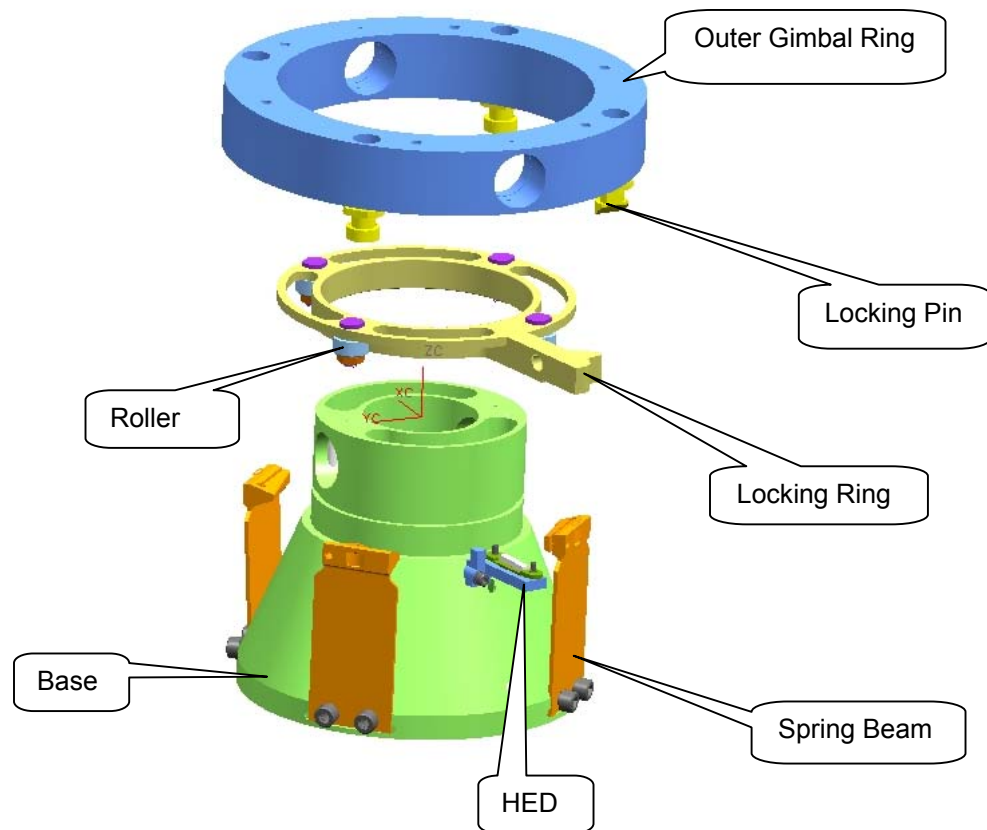


Figure 2. Exploded View of Gimbal and Launch Latch

Latched Position

The ring, the member designed for manual rotation to the latched position, is equipped with four roller assemblies. Each roller assembly is positioned to engage an adjacent spring member and locking pin. As the ring is manually rotated, the roller assemblies simultaneously contact the spring beams and deflect them outward toward the locking pins. Once contact is made between the spring beam and the locking pin, an integral spring establishes the desired preload in the joint. The ring continues to rotate until its arm engages a locking pawl, which latches it in the launch latched position.

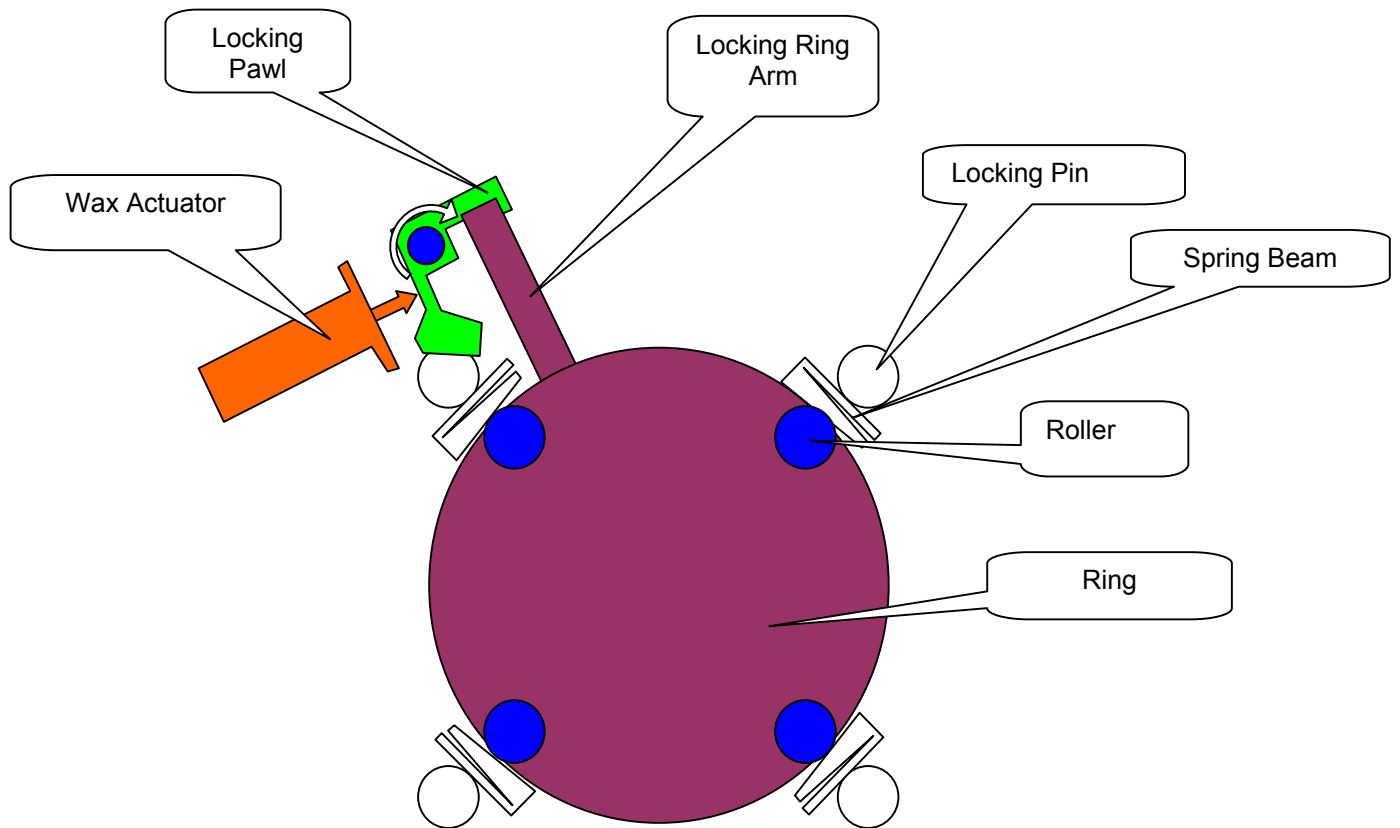


Figure 3

Preload Latching Point

The deflection of the preload spring feature is limited to prevent oscillation of the spring under vibration. The preload spring bottoms on a stop, with its further deflection due to higher loads (higher than the preload) prevented. The stop is formed by an adjustable set screw in one arm of the spring member.

The latched position and the preloads on the locking pins are established when the arm on the rotating ring engages the locking pawl. The locking pawl rotates on a fixed pivot. Its engagement with the arm on the locking ring is so configured that the line of action of the contact force passes through the pawl pivot, and no component of that force tends to unlatch the pawl. The mechanism is self-locking until released by the Unlatch command.

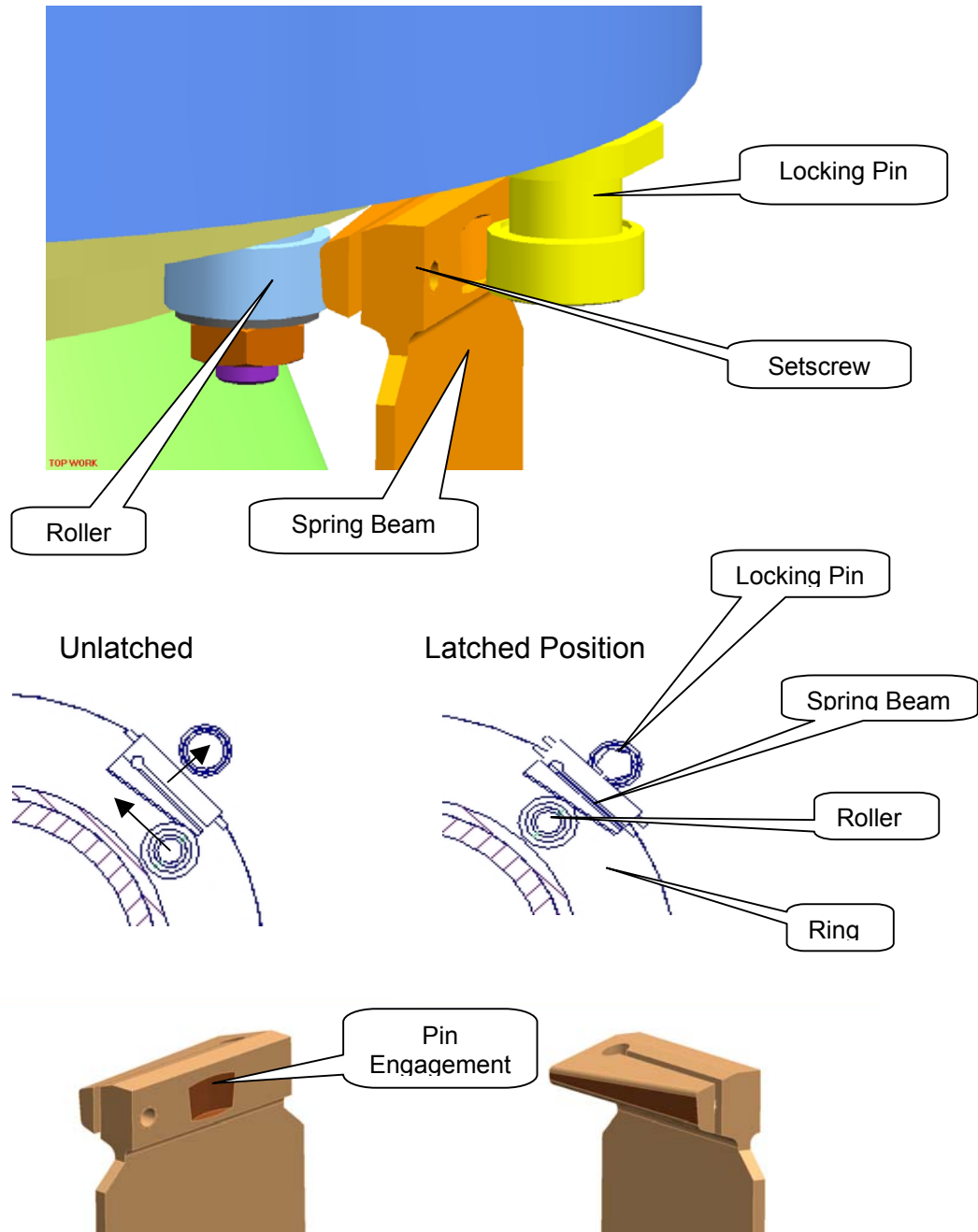


Figure 4

Unlatched Position

Unlatching occurs when the hot wax motor output is extended on command. The force exerted on the pawl by the actuator rotates the pawl out of the latched position. The torque exerted is adequate to overcome the contact friction between the pawl and the locking ring arm and releases the pawl from the ring. The torque component of the roller-to-spring beam preload forces causes the ring to rotate out of the latched position, and the ring then rotates back to its original unlatched position.

The launch latch assembly is accessible from one side of the gimbal (Fig.1). The arm on the locking ring is oriented for access from the side, and is configured with a threaded receptacle. Resetting is accomplished by installing a resetting tool in the receptacle and rotating the ring to the latched position.

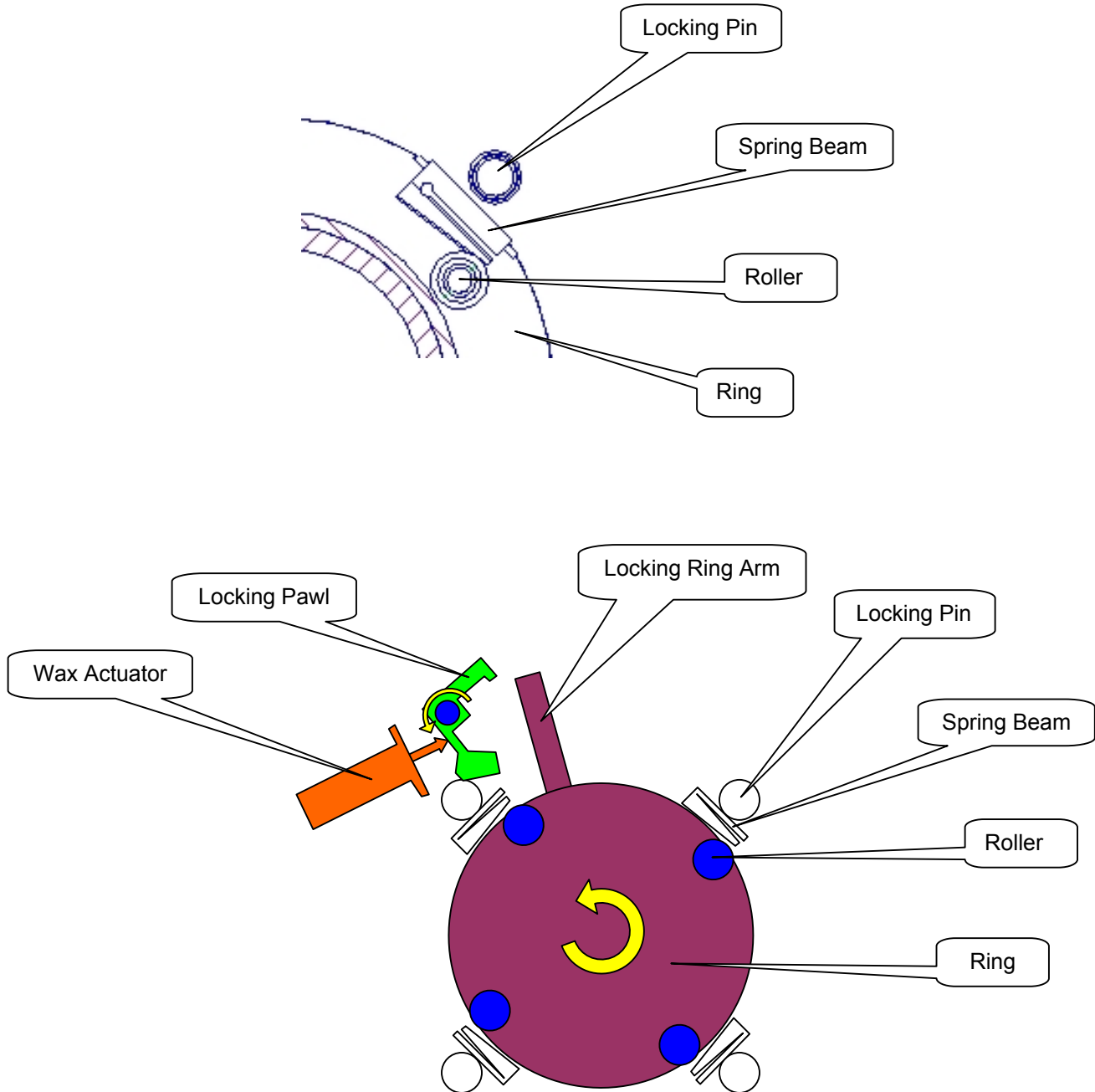


Figure 5

Trigger Mechanism

The trigger mechanism consists of the wax actuator, the locking pawl, and the latch arm (integral with the rotating ring). A manual input force is exerted on the latch to rotate the ring, allowing the locking pawl to engage the latch and prevent rotation of the ring. The locking arm pawl engagement is maintained by the preload applied at the contact point between the locking pawl and the ring. This preload is due to the lateral components of the forces at the spring beam-to-roller contacts, and the resulting torque on the ring. A torsional spring is used to return the pawl to its latched position, regardless of the orientation of the ring. Release of the latch is initiated by applying power to the wax actuator. The actuator output rod extends, contacting the locking pawl as shown in the figure below, and inducing a torque on the locking pawl to release it from the latch arm. With the locking pawl rotated away from the latch arm, the ring is free to rotate and relieve the preload on the locking pins.

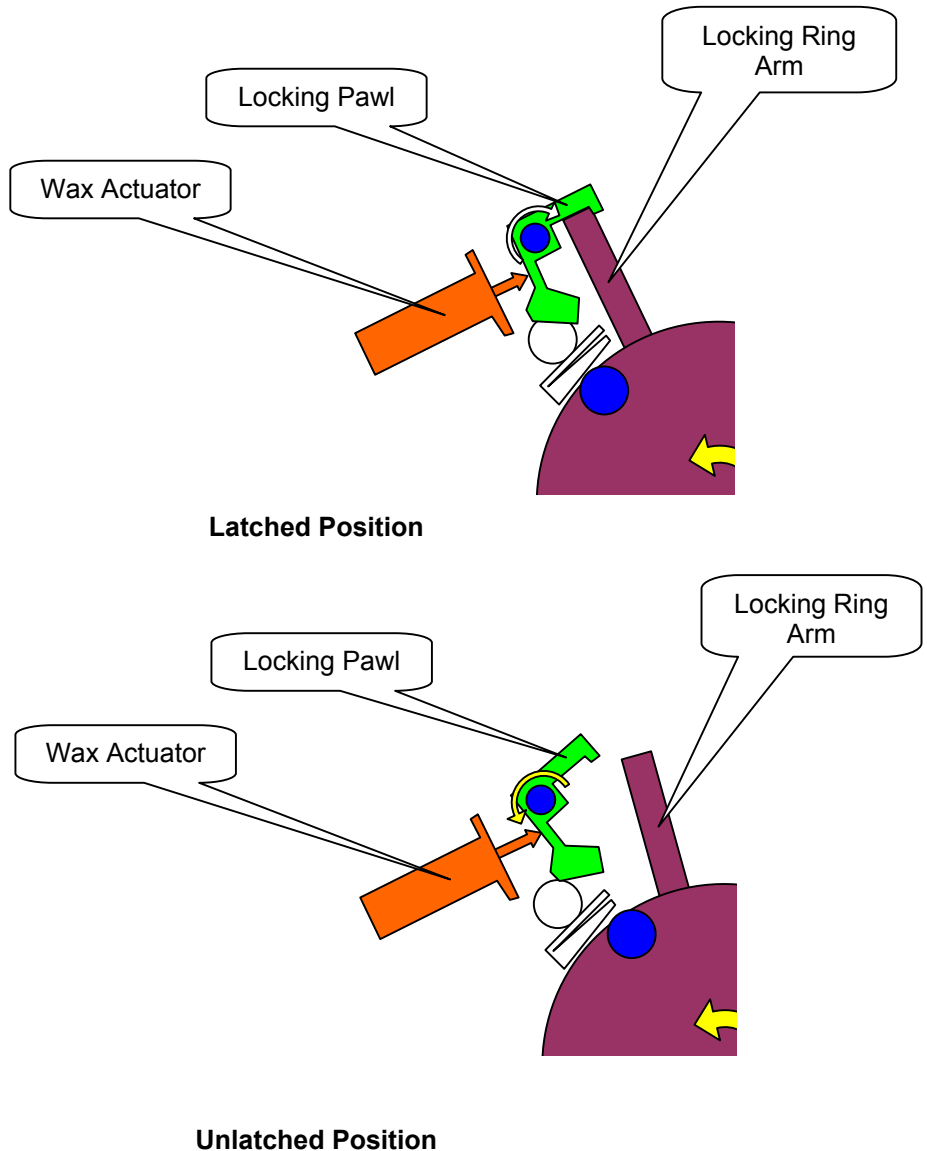


Figure 6

Development and Testing

Development test hardware was constructed to prove out the launch latch design. The test hardware was designed to simulate the main gimbal pivot and the launch latch mechanism. On one gimbal axis, a previously built linear actuator was used to simulate the mass and CG location of the flight actuator, for accurate system dynamic simulation and also for the capability of tilting the platform on that axis in subsequent testing. An articulated dummy link, again simulating the mass and CG location of the flight actuator, was used in the orthogonal location of the second actuator. The launch lock mechanism moving parts were free of any wet lubricant, to prevent contamination of the payload, and sliding surfaces were coated with Tiolube 1175 dry lubricant. Dicronite dry lubricant was used in the rollers for the launch latch to reduce sliding friction in the mechanism during engagement. The payload mass and center of gravity location were simulated by tooling as shown in the figure to provide a valid configuration for dynamic testing (i.e., shock, random vibration, and sine vibration).

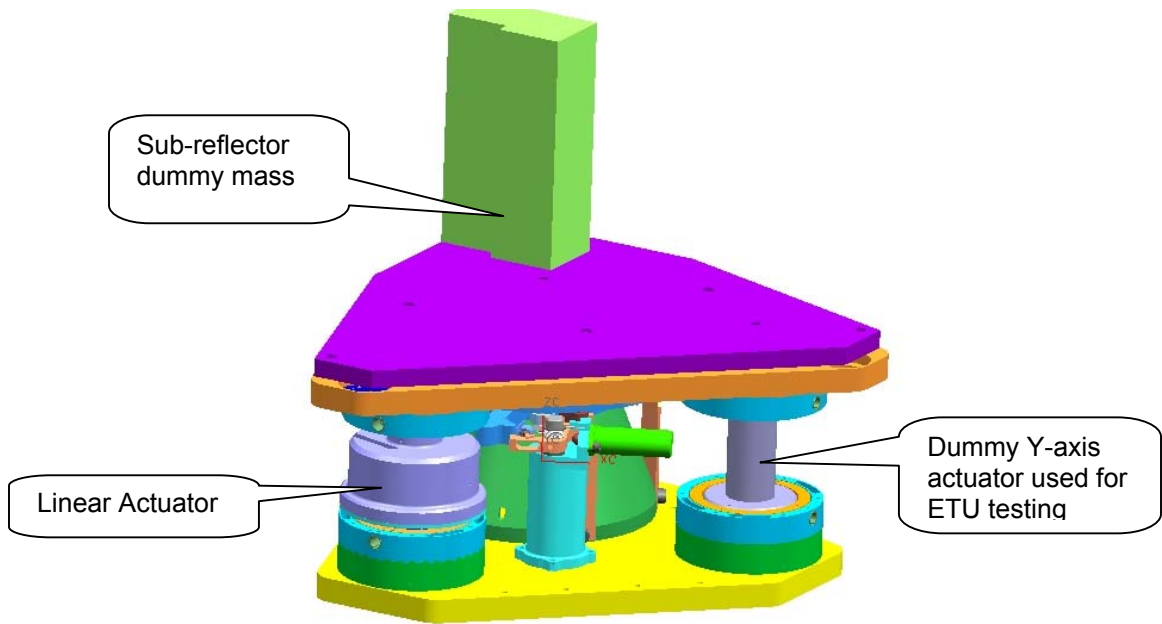


Figure 7

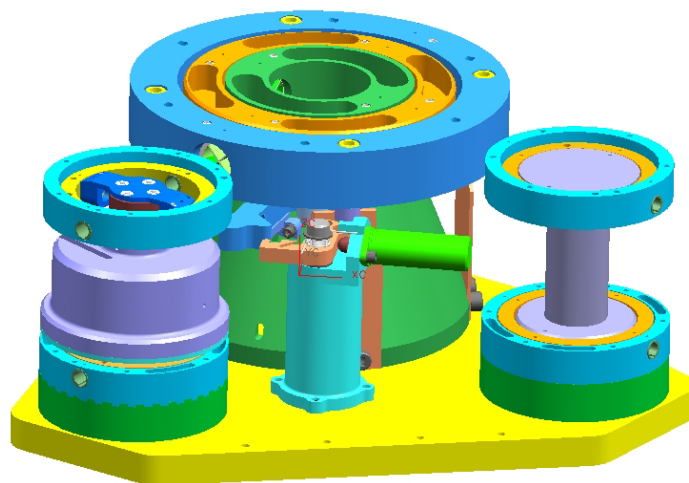


Figure 8. Developmental Test Unit (Subreflector plate is removed for clarity)

Lessons Learned

Lessons learned in the development of the launch latch mechanism involved issues of materials compatibility, linkage design, optimization, ergonomics, and structured optimization. The resulting design changes were incorporated in the development test unit.

Material and Surface Compatibility

The launch latch design is not friction-based, and sliding contact of heavily loaded members is generally avoided. However, some sliding contact does occur. Titanium is used as the basic material in the latch mechanism, chosen for its low weight and high stiffness. The surface properties of titanium are not ideal for highly stressed or sliding contacts, and therefore surface modification through anodic coatings and lubricant films was pursued. Ti-dioxide surface conversion treatment and Tiolube lubricant films were used. The highest contact forces occur between the spring beam and the locking pin and between the roller and the spring beam. With the original untreated parts, some galling was observed at these interfaces. After the surface treatment of the titanium spring beam and roller, and hard chromium plating of the steel locking pin, no further galling occurred.

Latch Design

A perceived problem with the locking ring arose during development testing. Although the locking ring is loosely suspended on the center pivot base, and the bearing surfaces are dry film-lubricated, the simple large size of the bearing led to the concern that the locking ring might be prevented by friction from reaching its full unlatched position. This possibility was addressed both by the application of dry film lubrication to the locking ring bearings surfaces, and to the addition of a secondary cam surface to the pivoting latch pawl. After triggering of the unlatching function- and after the high force demand on the hot wax actuator- continued travel of the pivoting pawl engages the cam surface with a mating follower ramp on the arm of the locking ring, insuring its full travel.

Latch/Reset Force

During development testing, the force required to reset the latch mechanism was found to be undesirably high from the standpoint of operator ergonomics. Operator effort was reduced, and adequate latched stiffness preserved, by modifying the width and thickness of the spring beam members.

Upper Plate Deformation

Bending of the upper plate, or output member, of the gimbal was observed in testing, as a result of the high forces applied to the locking pins by the latch mechanism. Design changes to the plate were made to increase stiffness at the locking pin mounting points, and this change eliminated plate bending as a problem.

Latch Point Engagement

Because of manufacturing tolerances and the curved motion of the spring beams, some dimensional allowance must be made at the beam-to-latch pin contact point. In the initial design, the allowance was generous, and the holding ability of the latch in the Z direction was augmented by frictional forces. In fact, mating surfaces were textured by grit blasting in order to enhance friction. It was found in testing that texturing actually aggravated galling of the mating surfaces, and that design feature was deleted. Smooth surfaces were used instead, with surface treatment for hardening. Tolerances were tightened, and it was then possible to reduce the dimension of the pocket in the spring beam in which the locking pin seats. The upper and lower shoulders of the pocket offer positive restraint of the locking pin which is not dependent on friction.

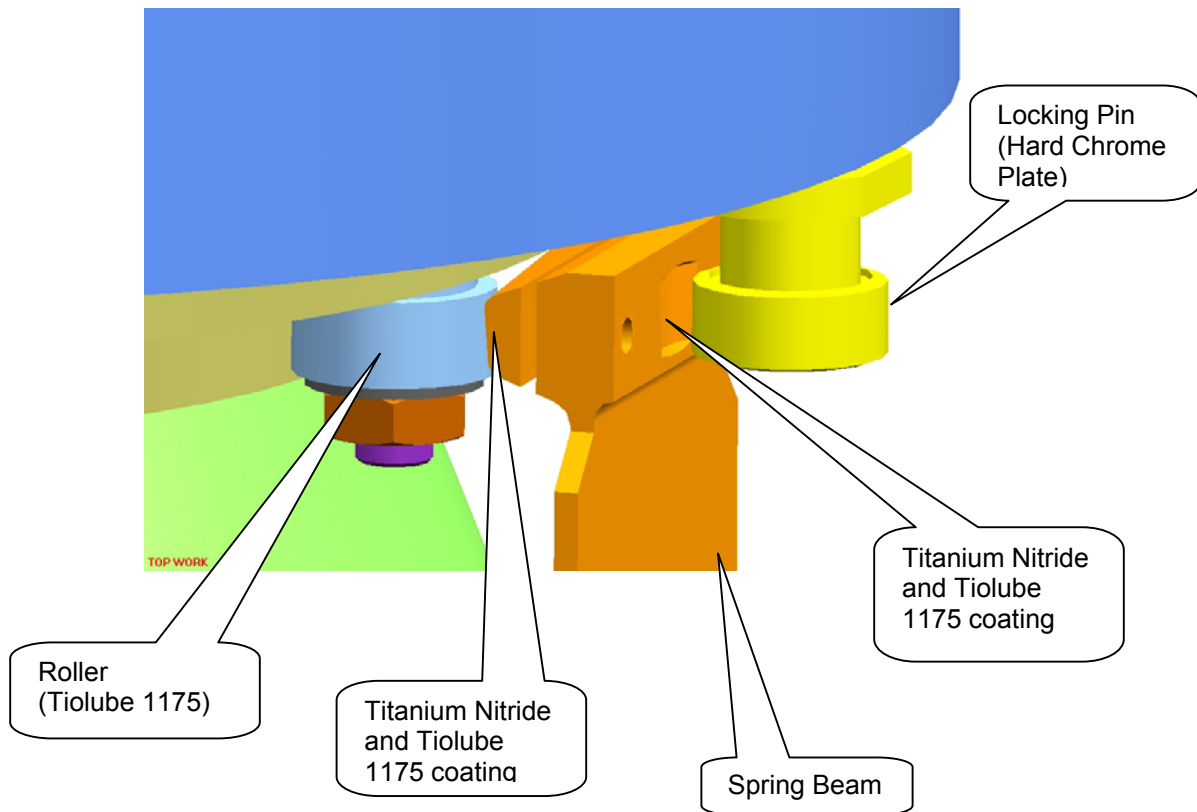


Figure 9

Conclusion

It was found possible to design an effective gimbal launch latch for a very restricted space. Rather than maximizing the radius of action or the length of the lever arms from the gimbal articulation point to the points of fixity, the arm were kept tot a minimum. The restraints, rather than being simple point restraints, are multi-axis lengths clamp points with a higher degree of restraint. The possibility of generating high loads and overstressing the protected structure is avoided by design of the clamping mechanism to accommodate the strength and stiffness properties of the gimbal. A single release point for the multi-point latch mechanism maximizes simplicity and reliability, and also meets operational access and ergonomics criteria. The concept has growth potential to cover larger diameters and heavier payloads.

Acknowledgements

Special thanks to Mr. Akira Fukatsu of NEC Toshiba Limited, Yokohama, Japan for his continued support and guidance.

Force and Torque Margins for Complex Mechanical Systems

Robert W. Postma*

Abstract

Force and torque margins are commonly used within the aerospace community to determine if the actuator for a mechanism has sufficient force or torque to ensure successful operation. Typical mechanism functions include deploying an antenna, releasing a launch restraint, rotating a solar array, controlling an antenna pointing mechanism, operating a valve, or releasing an interface connector. The definition of force margin relates to the ratio between the driving forces and the resisting loads. For example, if the driving force is twice the resisting load, the force margin is 100 percent. The calculation of force and torque margins is relatively straightforward for a simple mechanism such as a spring-loaded hinge. However, for complex mechanisms employing gear trains, linkages, and jackscrews, the basic arithmetical process becomes more complex.

The method described herein references drive forces, and resisting forces and moments, as equivalent forces and moments at a selected point in the mechanism. This is done by multiplying each force or moment by the ratio of its displacement to the displacement at that selected coordinate point. These equivalent forces from the various points of the mechanism are then summed at the selected common point, keeping driving forces separate from resisting forces, for use in the basic force and torque margin formulas. It is shown that force and torque margins can be calculated as energy margins, power margins, or virtual work margins, and that these margins have a simple relationship to mechanical efficiency.

Introduction

Force and torque margins are the functional counterparts of structural safety factors and stress margins. Functional margins as such are relatively new, having been instituted three decades ago because of failures of launch vehicle and spacecraft mechanisms to operate as intended. The definition of force margin relates to the ratio between the driving forces and the resisting loads. If the driving force is greater than the resisting load, the mechanism will start to move with an initial acceleration that is a function of the magnitude of the margin. For example, if the driving force is twice the resisting load, the force margin is 100 percent.

Typical spacecraft and launch vehicle mechanism functions include deploying an antenna, releasing a launch restraint, rotating a solar array, controlling an antenna pointing mechanism, operating a valve, or releasing an interface connector. The drive force or torque is typically provided by a spring-driven actuator, a pneumatic or hydraulic piston, an electromechanical device such as a motor or solenoid, or thermal expansion from an expanding wax actuator or shape memory alloy.

The resisting forces or torques typically include friction from sliding surfaces, bearings, and gears. The internal friction and the stiffness of wire harnesses routed across moving joints or interfaces are a major source of mechanical resistance in a deployable device. The type of friction of greatest concern is static friction (Coulomb friction), which is usually somewhat greater than the sliding friction that follows the onset of motion. Resisting loads can also be due to gravity or acceleration during the launch phase. Valves may have loads due to fluid pressure, and solenoid actuated devices may have loads due to residual magnetism or a return spring.

*The Aerospace Corporation, El Segundo, CA

Although referred to as a static margin, the calculation involves aspects of mechanical dynamics as well as statics. Of particular interest is the imminent or initial motion of a machine, and in some cases the following continuous motion. One example is a deployable such as a solar array being released from a launch lock and then moving to its final position; another is a scanning mechanism coming to a stop and then reversing direction.

For static margins, the resisting loads do not include velocity-dependent loads from rate controllers. Coulomb friction from bearings, a hysteresis damper, or between a paddle and housing in a viscous damper, would be included, however. The object is to determine if there is sufficient driving force to ensure that the mechanism will start and then not stall at any point in its operational path or cycle.

The calculation of force and torque margins is relatively straightforward for a simple mechanism such as a spring-loaded hinge. However, for complex mechanisms employing gear trains, linkages, or jackscrews, the basic arithmetic process needs special adaptation. For example, the drive actuator can be separated from the driven members by multiple gear meshes having sources of friction drag at various points. The problem becomes more complex if the gear train includes a crank or jackscrew to convert rotary motion to linear motion, which leads to the question as to whether to calculate a force margin or a torque margin.

The method described herein references drive forces and resisting forces, and moments, as equivalent forces and moments at a single selected point in the mechanism. This is done by multiplying each force or moment by the ratio of its displacement to the displacement at that selected coordinate point. The displacement ratios times their respective forces or moments, from the various points of the mechanism, are then summed to collect them as equivalent forces and moments at the selected common point. As an example of the calculation of margins for a complex mechanism, the method will be applied to a motor driving a worm gear, in turn driving a crank and piston through a spur gear. Then the formula will be stated in general terms.

The procedure will be developed using small displacements and mechanical work. The discussion will include the relationship of this approach to the method of virtual displacements and virtual work. It will also be shown that force and torque margins can be calculated as energy margins, power margins, or virtual work margins, and that these margins have a simple relationship to mechanical efficiency.

DEFINITION OF FORCE AND TORQUE MARGIN

Force and Torque Margins were first defined in a USAF "Specification for Moving Mechanical Assemblies for Space Vehicles..." (MMA Specification, Ref. 1, 1975), and twice revised (Ref. 2, 1978 and Ref. 3, 1988). The basic definition is used by NASA in a similar form (GEVS, Ref. 4), and in recent years has been generally adopted by the aerospace industry and incorporated into company design specifications. Static force margins required for mechanisms range from 100 percent (Refs. 1 to 3) to 200 percent (Ref. 4). These are equivalent to safety factors of 2 to 1 and 3 to 1 respectively. In some cases, weight or power restrictions or a manufacturer's past practice has led to the use of margins less than 100 percent.

From Reference 1, static force margin and static torque margin expressed as a percentage, are defined as follows:

$$\text{Static Force Margin} = \left[\frac{\text{Drive Force}}{\text{Resisting Force}} - 1 \right] \cdot 100 \quad (1)$$

$$\text{Static Torque Margin} = \left[\frac{\text{Drive Torque}}{\text{Resisting Torque}} - 1 \right] \cdot 100 \quad (2)$$

In Reference 3 (1988), a change was made to the formula, in that the force required for acceleration is subtracted from the drive force. This will be discussed later. To minimize repetition, in the following discussions the use of the term force margin will include its counterpart, torque margin, and vice versa.

Extension of Force Margins to Complex Systems

The static force or torque margin as stated in Equations 1 and 2 applies explicitly to the case of a single drive force or torque and a single resisting force or torque at the same translating or rotating point of the mechanism. The equation can also be directly applied when there are multiple driving and resisting forces and torques applied at different points of the same element. The calculation then requires direct summation of all the forces and torques on the common element, the driving forces going in the numerator and the resisting loads in the denominator. This often occurs when driving forces and resisting loads are collinear on the same sliding element, and all of the drive and load points move in the same direction at the same rate.

$$\text{Static Force Margin} = \left[\frac{\sum \text{Drive Forces}}{\sum \text{Resisting Forces}} - 1 \right] \cdot 100 \quad (3)$$

The related situation for rotation occurs when all of the applied forces and resisting loads are on a common shaft. Any linear forces are multiplied by their individual radii relative to the axis of rotation, and thus are easily reduced to torques about the shaft. In this case, the formula for static torque margin would have the same form as Equation 3 above.

If, on the other hand, the mechanism involves multiple gear meshes, or combined rotation and translation from a linkage or jackscrew, the interpretation of the standard force margin formula is not as simple. For a complex mechanism the multiple drive forces and resisting loads at different points of the mechanism need to be related to a single point by the use of multipliers, sometimes called influence coefficients. These coefficients are the displacement ratios or velocity ratios between the elements. To be consistent with the concept of a static force margin, where the displacements and velocities are initially zero, it may be more theoretically correct to speak of virtual displacements, as discussed later. However, the mechanism is in a state of imminent motion if the margin is positive, and the concept of small displacements can be used. If the mechanism comprises only elements that have constant displacement ratios, such as gears and belts, this distinction is less significant. If linkages are included, these ratios will change continuously with the changing geometry of the linkage, and the concept of sufficiently small displacements is important. In the following example, displacements are meant to mean very small displacements.

This discussion of more complex mechanisms assumes a single degree of freedom, and that the motions or imminent motions do not involve flexibility of connecting members. This assumption is implicit in the basic definitions of static torque and force margins. The rotation or translation of these members is referred to using the term "coordinates" to define displacement or velocity vectors. Associated with a single degree of freedom, the displacements and velocities are said to be constrained. For example, two spur gears in mesh would have a rotational coordinate for each gear shaft, and these coordinates are constrained to rotate at rates relative to each other by the ratio of the numbers of teeth (gear ratio). In this case the angular displacement or angular velocity ratio between the elements is the reciprocal of the gear ratio. A 10:1 reduction ratio would result from having ten times as many teeth in the driven gear as in the drive pinion, giving a displacement or velocity ratio of 1:10, relative to the pinion. The torque multiplication ratio, excluding friction drag, is equal to the reciprocal of the displacement ratio, i.e. 10:1. This ratio is sometimes called the mechanical advantage.

Taking a jackscrew as another example, one coordinate would be at the rotation of the drive nut, and the other coordinate the translation of the screw. These two coordinates are constrained to have a displacement ratio that is a function of the lead angle and the pitch diameter of the screw threads. Again, the torque-to-force ratio, excluding friction drag, is equal to the reciprocal of the displacement ratio (i.e. radians/in = lb/in-lb).

Example Procedure

In the procedure to be described, a crank and piston will illustrate change of motion from rotation to translation. A crank linkage will be used, rather than a jackscrew, to illustrate variable mechanical advantage depending on the position of the crank. In Figure 1, a worm gear set, driven by an electric motor, drives a spur gear set and crank linkage. The crank drives a piston having fluid pressure as the resisting load.

Figure 1 also shows the coordinates defining rotation and translation. The driving point coordinate for the rotation of the motor shaft and the attached worm pinion is θ_1 . The second coordinate is the driven worm gear and intermediate shaft rotation, θ_2 . The third coordinate is the rotation of the crankshaft, θ_3 . The rotational coordinates for the linkage bearings are Φ_4 and θ_5 . The piston translation is Δ_6 . These displacements are referenced to ground, except for Φ_4 , which is the rotation of the lower (crankshaft) link relative to the upper (piston) link.

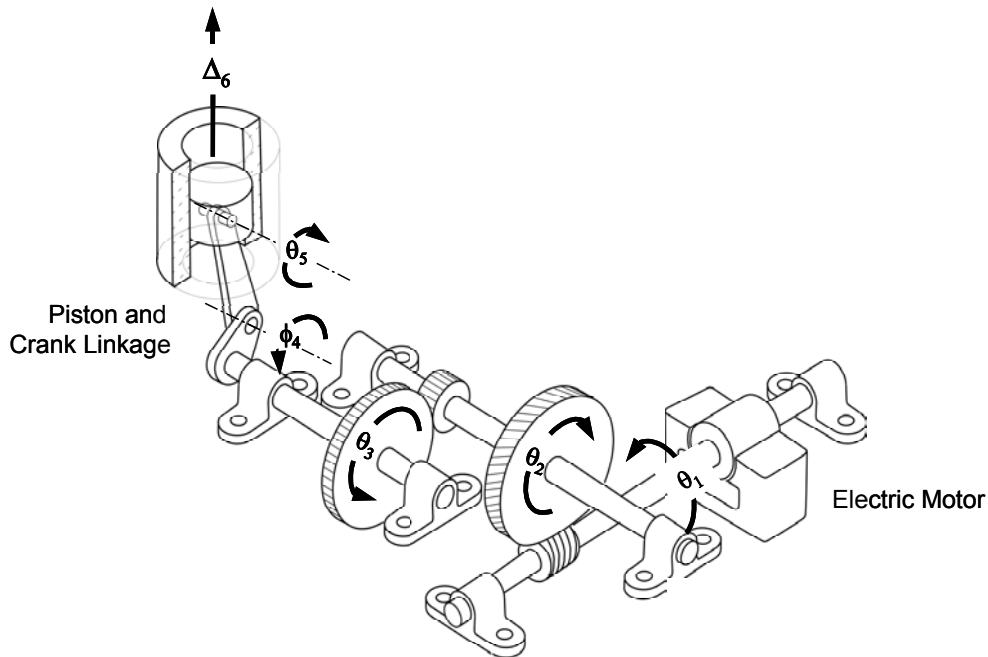


Figure 1
Displacement Coordinates

The driving torque and resisting torques and forces are shown in Figures 2 through 4 as external forces on the shafts, gears, linkage, and piston. The exception is the resisting torque, T_{4B} , at the crank bearing, Coordinate 4, which represents a relative displacement, Φ_4 . This resisting torque, T_{4B} , is an interface torque between the upper and lower crank links.

These figures represent portions of Figure 1, and are not free body diagrams showing reaction forces in opposition between the diagrams. It is that type of more complex representation and analysis procedure that this method being presented endeavors to avoid.

Reference Point, Coordinate 1, Motor Drive Shaft Loads (Fig.2)

The reference point for the calculation of equivalent loads will be chosen arbitrarily as the motor pinion drive shaft, θ_1 . The driving torque applied to this coordinate (point) is provided by the electromagnetic torque, T_{1M} , on the motor armature.

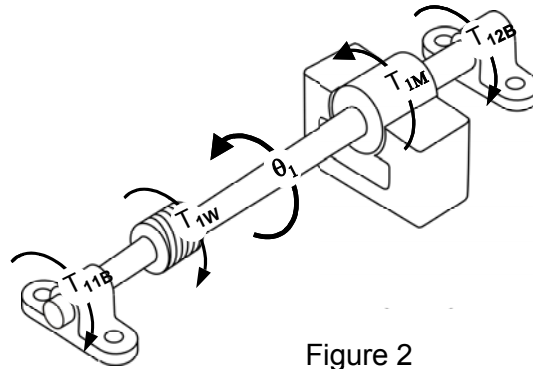


Figure 2
Drive Torques and Resisting
Torques on Drive Shaft

The resisting friction torques, T_{11B} and T_{12B} , from each of the two drive shaft bearings, act in the direction opposite to the drive torque. The drag forces from friction at the worm and gear tooth contact point will be represented as a resisting torque, T_{1W} , acting on the driveshaft. Thus far, we have the friction torque load on the driveshaft as the sum of three components.

$$T_{1R} = T_{11B} + T_{12B} + T_{1W} \quad (4)$$

(Bearing drag torque is partially a function of the reaction force at the bearing, which is in turn, a function of the drive torque. Thus, the values of bearing drag torque would need to be consistent with the motor drive torque, and would be calculated as the solution to simultaneous equations. This also applies to the worm gear friction torque, which likewise depends on the drive torque and can be represented by the efficiency of the gear set times the torque on the worm pinion. This friction torque is in effect applied to the worm but not to the gear).

Coordinate 2, Intermediate Shaft Loads (Fig. 3)

Coordinate 2 is represented by θ_2 at the intermediate gear shaft. As shown in Figure 3, this coordinate is also common to the spur gear pinion.

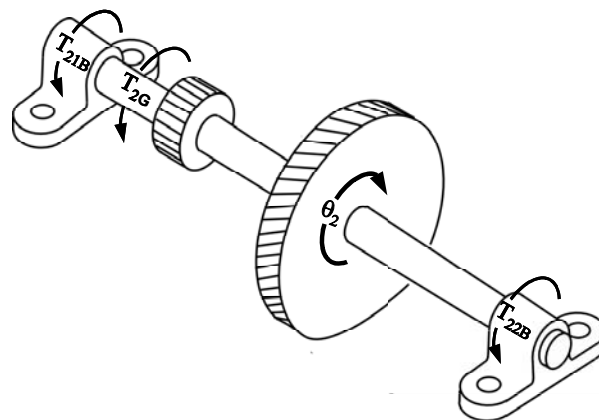


Figure 3
Resisting Torques on Intermediate Shaft

According to this methodology, the torques on this second shaft will be referenced to the selected drive point coordinate by the displacement ratio, θ_2/θ_1 . There are two friction torques from the shaft bearings, T_{21B} and T_{22B} . The drag torque from sliding friction at the spur gear teeth will be included with the drag

torque on this shaft as T_{2G} . (The friction torque on a spur gear varies with the relative positions of the contacting gear teeth, and is zero when contact is at the pitch line. However, since this friction is small compared to bearing friction, it can be represented as a constant efficiency times the torque on the pinion. The friction torques at the two bearings are likewise a function of the torque on the intermediate shaft). The three friction torques on this shaft are summed to give the resisting torque at Coordinate θ_2 .

$$T_{2R} = T_{21B} + T_{22B} + T_{2G} \quad (5)$$

To reference this net drag torque summation at Coordinate 2 to the drive point at Coordinate 1, it is multiplied by the displacement ratio θ_2/θ_1 .

$$T_{2/1R} = T_{2R} (\theta_2/\theta_1) \quad (6)$$

The quantity $T_{2/1R}$ constitutes an equivalent or virtual load at the drive point. The term "virtual" here is based on the dictionary definition, "being in effect, but not in fact". (This general definition of "virtual" has a more restricted meaning later when we apply it to virtual work and virtual displacements). In other words, the effect on the acceleration of the mechanism is the same as if the original drag loads at the intermediate shaft were replaced by their equivalent load $T_{2/1R}$ at the drive shaft. The key to the definition of the equivalent loads is that they must do the same amount of positive or negative mechanical work as the original loads. By this process, the loads from the intermediate shaft are referenced to the drive shaft, so that the definition of torque margin for a single rotating coordinate can be used.

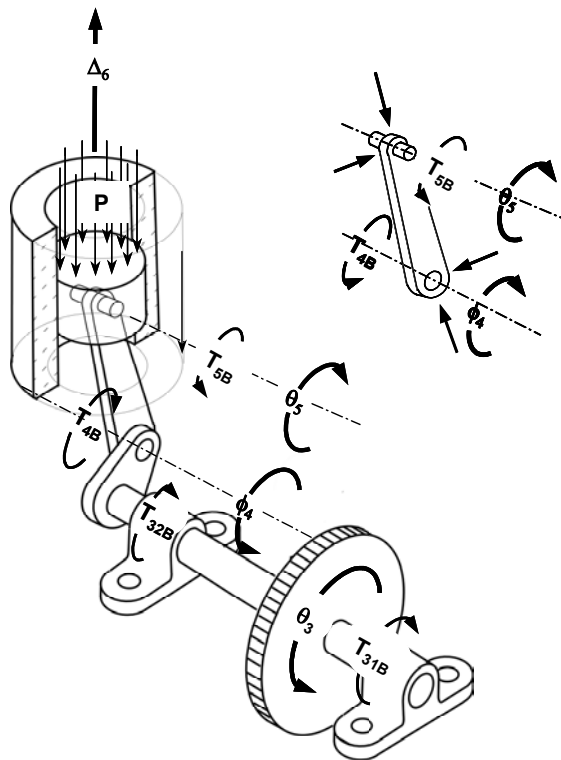


Figure 4
Resisting Forces and Torques
on Crank Shaft and Piston

Coordinate 3, Crankshaft Loads (Fig. 4)

The intermediate shaft drives a crankshaft with angular Coordinate θ_3 , having two bearing drag torques T_{31B} and T_{32B} . These two drag torques could be referenced directly to the drive shaft, skipping the intermediate shaft (θ_2), by their displacement ratio to the drive shaft (θ_3/θ_1). However, this task is more systematically organized by first collecting the loads from the crank and piston, and then referencing their sum from the crankshaft (θ_3) to the driveshaft (θ_1).

Coordinates 4, 5, and 6, Linkage Bearing Loads and Piston Loads (Fig. 4)

Although the friction torque from the intermediate crank bearing T_{4B} also acts directly on the crankshaft, this bearing's displacement, Φ_4 , is relative to its two mating crank linkages. This relative displacement, Φ_4 , is greater than the displacement θ_3 of the lower link relative to the crankshaft, in the crank position shown.

$$\Phi_4 = \theta_3 + \theta_5 \quad (7)$$

The friction torque of this crank bearing acts on both the upper crank and the lower crank. Thus, the combined effect of this friction torque on the crankshaft is greater than the reaction torque of only this bearing on the shaft. The reason can be seen from the free body diagram of the upper link in Figure 4. The reaction of this bearing friction torque on the upper crank link results in a moment on this upper link with an associated couple and a reaction force against the lower link. Thus the energy dissipated by this friction torque is increased by the relative rotation of the upper crank linkage. This is one example of the simplification inherent in this energy method. It avoids the need for separating the crank linkage, crankshaft and piston bearing into three separate free body diagrams.

The effect of the friction torque, T_{4B} , of this bearing on the crankshaft is determined by multiplying it by the angular displacement ratio (Φ_4/θ_3).

$$T_{4B/3} = T_{4B} (\Phi_4/\theta_3) \quad (8)$$

The drag torque T_{5B} on the piston bearing is referenced to the crankshaft in the same way, using the angular displacement ratio of the upper crank linkage to the crank, θ_5/θ_3 .

$$T_{5B/3} = T_{5B} (\theta_5/\theta_3) \quad (9)$$

Since the direction and magnitude of Φ_4 and θ_5 are variable with position, their displacement ratios are also variable. Note that for some positions of the crank, Φ_4 is less in magnitude than θ_3 .

The fluid pressure force on the piston is equal to the pressure, P , times the piston area, A . The equivalent load could be directly referenced to the motor driveshaft, Coordinate 1, by the ratio of the linear displacement of the piston, Δ_6 , divided by the angular displacement of the motor shaft, θ_1 . However, to be consistent with the previous treatment of the two crank bearings, this force will first be referenced to the crankshaft by the ratio between Δ_6 and θ_3 , and then referenced to the θ_1 coordinate by the ratio between θ_3 and θ_1 . Likewise, the drag load from the friction, F_{6P} , between the piston and its cylinder is referenced to Coordinate θ_3 by this same displacement ratio. The equation for the forces and torques referenced to the crankshaft is as follows.

$$T_{3R} = (T_{31B} + T_{32B}) + T_{4B} (\theta_3 + \theta_5)/\theta_3 + T_{5B} (\theta_5/\theta_3) + (P \cdot A + F_{6P})(\Delta_6/\theta_3) \quad (10)$$

If these were referenced directly to the motor drive shaft, the result would be:

$$T_{3/1R} = (T_{31B} + T_{32B})(\theta_3/\theta_1) + T_{4B} (\theta_3 + \theta_5)/\theta_1 + T_{5B} (\theta_5/\theta_1) + (P \cdot A + F_{6P})(\Delta_6/\theta_1) \quad (11)$$

The ratio Δ_6/θ_3 constantly varies throughout the cyclical motion of the piston, as does the fluid pressure P . Note that the algebraic sign of the friction force, F_P , between the piston and cylinder would also change as the piston changes direction at the top and bottom of its stroke. Likewise, the contribution of these torques and forces to the final torque margin also varies throughout the cycle of motion.

Because of the varying displacement ratios, it is important that the displacements be taken over sufficiently small increments such that any errors introduced are negligible. If exact formulas for the kinematic relationship between the piston motion and the crankshaft are used, the derivatives of the individual displacements to the reference displacement θ_1 can be used as the displacement ratios.

Final Static Torque Margin

The static torque margin equation for this example now comprises the drive torque at the drive pinion divided by the resisting torques on the motor shaft, plus the other resisting loads from the intermediate shaft and crankshaft referenced to Coordinate 1 as equivalent loads.

$$\text{Static Force Margin} = \left[\frac{T_{1M}}{T_{1R} + T_{2/1R} + T_{3/1R}} - 1 \right] \cdot 100 \quad (12)$$

General Force and Torque Margin Formulas

The static margin derived for this example can be stated in general as the sums of drive forces divided by the sums of resisting loads. Each drive force or torque and resisting load is multiplied by its displacement ratio, and each is referenced to one arbitrarily chosen coordinate, shown in the following equation as Coordinate j. The displacement ratios can be called influence coefficients, k_{ij} . Using F to represent either driving force or torque and L to represent either resisting force or torque, the static margin is defined as:

$$\text{Static Force or Torque Margin} = \left[\frac{k_{1j}F_1 + k_{2j}F_2 + \dots + k_{mj}F_m}{k_{1j}L_1 + k_{2j}L_2 + \dots + k_{nj}L_n} - 1 \right] \cdot 100 \quad (13)$$

where m equals the number of driving points,
n equals the number of resisting points,

The F_i and L_i terms represent the sums of driving forces and torques or resisting loads at the respective coordinates, or already referenced to those coordinates from other coordinates by related influence coefficients. The influence coefficients, k_{1j} , k_{2j} , k_{3j} , etc., are the displacement ratios referenced to element Coordinate j. Using the letter u to represent small displacements, either rotational or translational,

$$k_{ij} = u_i/u_j \quad (14)$$

where i is the coordinate of interest, and j is the reference coordinate.

One of the coordinates ($i = 1,2,3,\dots$ etc) will be at the reference point j. Thus, that particular influence coefficient will be equal to unity.

$$k_{ij} = 1 \text{ for } i = j \quad (15)$$

As a general note, the reference coordinate j can be a totally fictitious or virtual coordinate (i.e., $j=0$, having an arbitrarily chosen influence coefficient k_{10} relative to Coordinate 1), as long as the other influence coefficients are consistently referenced to this coordinate ($j=0$).

Expressing the summation of Equation 10 in a more general form gives:

$$\text{Static Force or Torque Margin} = \left[\frac{\sum_{i=1,m} k_{ij}F_i}{\sum_{i=1,n} k_{ij}L_i} - 1 \right] \cdot 100 \quad (16)$$

Force and Torque Required for Acceleration

In the Reference 3 revision of the MMA specification, (1988), the drive torque and force required for acceleration were added to the formulas for static torque and force margins. The requirement for the margin to be 100 percent or greater remained the same as before.

$$\text{Static Torque Margin} = \left[\frac{\text{Drive Torque} - \text{Torque Required for Acceleration}}{\text{Resisting Torque}} - 1 \right] \cdot 100 \quad (17)$$

Formulas for Kinetic Force and Torque Margin were also included. The requirement specified was 25 percent.

$$\text{Kinetic Torque Margin} = \left[\frac{\text{Drive Torque} - \text{Resisting Torque}}{\text{Torque Required for Acceleration}} - 1 \right] \cdot 100 \quad (18)$$

In these formulas, the drive force and torque required for acceleration are part of the requirement rather than being inherent in the mechanism. Accordingly, the methodology for translating the drive and resisting forces and torques to a common point would not necessarily be needed for these specified acceleration torques. One example of drive torque required for acceleration is the torque required for a stepper motor to overcome detent torque and accelerate the rotor past each individual step. This torque can be calculated by a dynamic analysis or determined from test data. Since this additional resisting torque is considered to be a specification, it can be inserted into the formulas already developed (Eqns.12 through 16). Generally, this detent torque would be relatively small.

Force and Torque Margins as Energy and Power Margins

The general force and torque margin equation can be restated as an energy margin. Taking Equation 13 and restating it terms of the displacement ratios, we have:

$$\text{Static Force or Torque Margin} = \left[\frac{\frac{u_1}{u_j} F_1 + \frac{u_2}{u_j} F_2 + \dots + \frac{u_m}{u_j} F_m}{\frac{u_1}{u_j} L_1 + \frac{u_2}{u_j} L_2 + \dots + \frac{u_n}{u_j} L_n} - 1 \right] \cdot 100 \quad (19)$$

This expression can be converted to an incremental energy margin (or virtual work margin) by canceling out the reference displacement u_j , giving:

$$\text{Energy Margin} = \left[\frac{u_1 F_1 + u_2 F_2 + \dots + u_m F_m}{u_1 L_1 + u_2 L_2 + \dots + u_n L_n} - 1 \right] \cdot 100 \quad (20)$$

Or, restated:

$$\text{Energy Margin} = \left[\frac{\text{Drive Energy}}{\text{Resisting Energy}} - 1 \right] \cdot 100 \quad (21)$$

Each of the terms in the numerator of Equation 20 represents the incremental work done by each of the driving forces over each of their respective small displacements. The terms in the denominator represent the incremental work or energy dissipated by friction forces and the incremental potential energy gained by items such as the compressed fluid implied in the illustrations. (Sometimes the resisting energy can turn positive: for example, depending on the position of the crank and piston. Likewise, cable stiffness can assist rather than resist motion during a portion of the cycle. In some cases, the decision has to be made as to whether such terms belong in the numerator or denominator).

The formula for kinetic torque or force margin (Eqn. 20) can likewise be stated as a kinetic energy margin.

$$\text{Kinetic Energy Margin} = \left[\frac{\text{Drive Energy} - \text{Resisting Energy}}{\text{Required Kinetic Energy}} - 1 \right] \cdot 100 \quad (22)$$

One example of required kinetic energy would be the energy needed to ensure adequate separation velocity during vehicle staging. The drive energy would be the energy stored in the kickoff springs, and the resisting energy would be the energy required to extract the electrical interface connector pins from their sockets, or any other sources of frictional losses. In this case the displacements would be the full displacement required for complete separation.

If each of the terms in Equation 20 is divided by the time increment for these small displacements u_j , the expression represents the time average power margin over the increment.

$$\text{Power Margin} = \left[\frac{\text{Drive Power}}{\text{Resisting Power}} - 1 \right] \cdot 100 \quad (23)$$

The fact that Equation 20 can be altered to give Equation 19 by dividing numerator and denominator by any one of the small displacements u_j shows that the selection of reference point is arbitrary. The numerical result is the same regardless whether an energy margin, a power margin, a force margin, or a torque margin is calculated.

When restated as an energy margin, the force or torque margin is a measure of the kinetic energy acquired by the system as it accelerates from rest over a small displacement u_j at some arbitrary coordinate j . The kinetic energy increment over this small displacement is equal to the numerator of Equation 20 minus the denominator. (Equation 22 for kinetic energy margin shows this relationship explicitly for large displacements). Since the torque or force margins are numerically equal to the energy margins, this restatement of the torque or force margin as an energy margin is an argument for the validity of this method. Thus, the "net force" available for accelerating the system from rest using the equivalent force system, referenced to one coordinate location, is the same as for the original force system. The validity of this method is discussed further under the subject of virtual work.

Mechanical Efficiency

The efficiency of a mechanical transmission system is defined as the ratio of the output work divided by the input work. Mechanical efficiency is typically illustrated in textbooks by an example of a relatively inefficient device, such as a jackscrew or worm drive. This usage has similarities to the force and energy formulas as developed here, except that for mechanical efficiency the work output to the driven device is excluded from the resisting energy. Revising Equation 21 to include only the energy dissipated as friction:

$$\text{Energy Margin} = \left[\frac{\text{Drive Energy} - \text{Friction Energy}}{\text{Friction Energy}} \right] \cdot 100 \quad (24)$$

$$\text{Mechanical Efficiency} = \left[\frac{\text{Drive Energy} - \text{Friction Energy}}{\text{Drive Energy}} \right] \cdot 100 \quad (25)$$

Expressing Mechanical Efficiency and Energy Margin as ratios rather than as percentages, a simple relationship between the two can be formulated.

$$\text{Energy Margin} = \frac{1}{\frac{1}{\text{Mechanical Efficiency}} - 1} \quad (26)$$

For example, if the ratio of Drive Energy to Friction Energy is 4:1, the Mechanical Efficiency is 0.75 (75 percent) and the Energy Margin is 3.0 (300 percent).

Virtual Work and Virtual Displacements

In textbooks, the concepts of virtual displacements and virtual work are commonly developed for analysis of mechanical systems and structures in static equilibrium. A virtual displacement is defined as a fictitious or infinitesimal displacement – sometimes as a very small displacement. The mechanical system is considered to undergo virtual displacements, and the net virtual work that results from the forces acting through their respective virtual displacements is equal to zero.

The type of mechanical system being considered here typically has just been released from a launch restraint or is being energized by a current pulse to a stepper motor. The system is in a state of imminent motion with some finite initial acceleration, and an initial velocity equal to zero. To apply the method of virtual work, this system can be considered to be in a state of dynamic equilibrium, with the inertial forces due to the initial acceleration being in equilibrium with the applied forces and resisting forces (in accordance with D'Alembert's principle). The sum of the net virtual work done by the virtual displacements acting through the original force system and the virtual kinetic energy resulting from the virtual displacements acting through the respective inertial forces, is equal to zero.

From another viewpoint, during a test to measure force margin, the mechanism is sometimes restrained from motion by a load or torque gage, and the measured force or torque is gradually reduced by slowly withdrawing the gage. The measured force or torque at the point of imminent motion is used to calculate the margin. In this case, there is no acceleration until the point of release. Here, the mechanism and the test apparatus are in static equilibrium.

The technical approach using virtual displacements is essentially the same as for the preceding approach using small displacements. The terms “small displacements” and “energy” can be replaced by “virtual displacements” and “virtual work”. The arguments are similar and the conclusion is the same. The net virtual work done by the inertial forces and the sum of the drive forces and the resisting forces, after being referenced to a common point as equivalent or virtual forces, is zero; and the system remains in a state of equilibrium. Thus, the equivalent or virtual force system is equal in effect to the original force system, and the method described herein for calculating force and torques margins is theoretically valid.

If there is a conceptual advantage in describing this method of equivalent forces in terms of virtual work, it is that virtual displacements, being considered infinitesimal, do not involve any approximation due to small changes in mechanical configuration (if linkages are involved). Likewise, there is no need for a conceptual distinction between static friction and dynamic friction.

The virtual work approach was not employed explicitly in the example, partly because the mechanical device is in a state of imminent motion, and real displacements can be considered appropriate for the analysis. Moreover, the increased level of abstraction should not be necessary to the understanding and acceptance of these concepts.

Derivative Notation

If a functional relationship can be established for the displacements, this relationship can be differentiated and the displacement ratios can be calculated as derivatives of the displacements to the reference

displacement. Using the letter “v” to represent displacements that are not necessarily small or starting from zero, Equation 14 defining the influence coefficients can be represented in derivative notation.

$$k_{ij} = \frac{dv_i}{dv_j} \quad (27)$$

This approach would be particularly useful where the displacement ratios are not constant, and are describable by a mathematical function, such as for the crank linkage of the example.

Concluding Comments

The presentation of this energy-based method has proceeded from an illustrative example to more general forms of the formulas for force and torque margins. The object has been to adapt these commonly used formulas to complex mechanical systems having elements interconnected by gears, jackscrews, belts, and linkages. In extending the force and torque margin formulas to include energy and power margins, the relationship between force and torque margins and mechanical efficiency has been shown. It is believed that this method is intuitively recognizable to those in the academic field and others who do mechanical analysis. The method is believed to be theoretically correct and consistent with the method of virtual work. It is hoped that the comments regarding the validity of the method are convincing and that this presentation will be helpful to those faced with the types of analyses discussed.

The use of force margins offers somewhat more versatility than mechanical efficiency, because force margins can include resisting loads where mechanical work is done (i.e., motor driven pumps) or potential energy is gained (i.e., a hydraulic or mechanical jack). It is conceivable that a more general understanding could lead to extended usage of force and torque margin criteria in the mechanical engineering community, especially for other critical applications such as actuators for aircraft control surfaces.

References

1. “Moving Mechanical Assemblies for Space Vehicles, Design and Testing Requirements, General Specification for”, MIL-A-83577 (USAF), 15 June 1975.
2. “Moving Mechanical Assemblies for Space Vehicles, General Specification for”, DOD-A-83577 (USAF), 15 March 1978.
3. “Moving Mechanical Assemblies for Space Vehicles, General Specification for”, MIL-A-83577B (USAF), 01 Feb 1988.
4. “General Environmental Verification Specification (GEVS) for STS and ELV Payloads, Subsystems, and Components”, Rev. A, Goddard Space Flight Center, 29 August 2000.

Establishing Adequate Performance Margin for Space Flight Stepper Motor Mechanisms

David B. Marks*

Abstract

Adequate Stepper Motor performance margin is critical for mission success. Often, it is not clear from system specifications what the stepper motor performance requirements should be, because the concerns and methods for defining and applying a stepper motor may not be well understood. "Establishing Adequate Performance Margin for Space Flight Stepper Motor Mechanisms" presents practical guidelines for the correct specification and application of stepper motors used in space flight mechanisms and provides some basic lessons-learned from flight hardware experiences.

Introduction

System or mechanism specifications and the associated stepper motor specifications are typically different in terms of how the motor related characteristics are presented. It becomes important then for the stepper motor specifications to include a comprehensive definition of motor parameters to cover the system spec requirements but also those requirements derived and indirectly required to support the system motion control. In the system specifications, motor specifications, or within the motor supplier's sizing of the design, the performance margin over and above the actual motor or mechanism output should be determined for stepper motors.

Unlike brushless DC motors, stepper motors cannot be relied upon to produce output torque as a function of input current. Motor speed, torque loading, and system dynamics affect the stepper motor's ability to respond to input commands. Because stepper motors generally operate without feedback for commutation, velocity, or position (an advantage that simplifies the system and reduces cost), care must be taken to assure the stepper motor supplied can perform over the range of characteristics associated with the particular motion control system. Torque margin or voltage margin analyses must consider mechanism internal losses, external load and coupling variations, electrical tolerances, temperature change effects, viscous damping, and excitation pulse characteristics. The specification and sizing approach should evaluate minimum torque conditions, minimum stability conditions, system resonance, and minimum unpowered holding torque. Other considerations may apply, too, depending on the mechanical configuration, such as the maximum motor torque capability.

So, to compensate and account for inherent system variabilities and their influence on stepper motor-based mechanisms, adequate design margin must be built into the motor sizing. Established guidelines exist among users and manufacturers of stepper motors for quantifying margin requirements, but every application will hold unique concerns. Performance analysis using motion simulation tools is usually required to quantify the stepper mechanism performance over many varying conditions of operation. Heritage designs and their applications serve as a good reference and should be consulted along with analysis and simulation, but ultimately hardware testing will demonstrate the success of the stepper motor mechanism.

The motor specifications, analysis assumptions, and hardware testing should agree in methodology as closely as possible. Otherwise, the design and test approach will be flawed. It is possible to provide a well designed and tested stepper motor or stepper mechanism that does not meet the system requirements if the methodology used does not relate well to how the mechanism will actually be used. Or, specification requirements that are too severe can penalize the program with unnecessary weight, costs and delays. It

* Moog, Inc., Durham, NC

is important to have an understanding of stepper performance specification development, performance margin and methodology, stepper simulation and analysis, stepper hardware testing, and past lessons learned.

Lessons learned from stepper motor usage on space mechanisms can be categorized into four different areas that will be explained further. These Lessons Learned areas are: torque production assumptions, temperature effects, under-margin and over-margin, and electrical input effects on step stability. Critical motor application errors can be avoided if these areas of concern are consistently addressed.

Background

A two-axis stepper motor / harmonic drive rotary actuator typically applied in such applications as antenna pointing mechanisms is shown in Figure 1. Margin on stepper motor requirements is required, because unlike similar brushless dc motors, the stepper motor runs in an open loop mode without any feedback to regulate its commutation or rotation other than the motor input pulses.

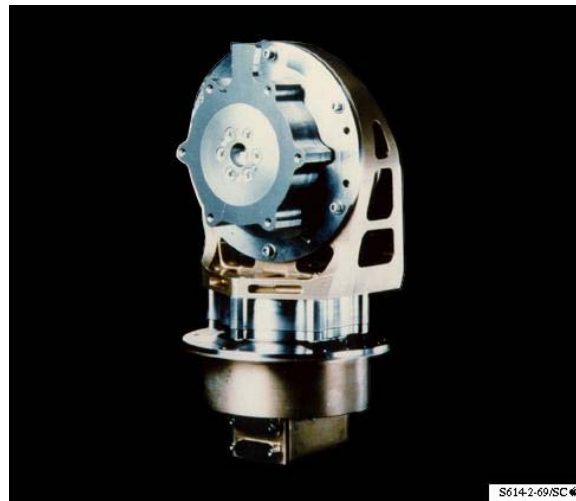


Figure 1. Stepper Motors with Harmonic Drives for a Two-Axis Antenna Pointing Mechanism

It is necessary in applying a stepper motor to carefully define ranges (minimums or maximums) on many parameters, such as the motor speed (pulse rate) to assure that the motor and load rotation remain synchronous over all conditions of voltage variation, temperature and internal frictional drag changes, load variations, etc. Synchronous operation is the precise electro-mechanical interaction required between the motor controller, stepper motor, and output load so that every discrete motor rotation (step) that is commanded results in the proper and precise incremental rotation of the load. This is accomplished without any position feedback devices for control (other than perhaps an end of travel sensor or potentiometer.) Electrical pulses are sequenced, counted, and supplied to the motor. Multiplying the known motor step angle by the pulse count determines the angular rotation of the motor output, if the system remains synchronous. The corresponding angle of the load rotation is related by any gear reduction that is present between the motor and the load.

Since the stepper motor does not operate in a closed, servo loop mode of operation (which results in a simpler, less expensive operating system), the effective torque production varies according to a number of factors, and so the traditional dc motor method of determining torque as presented in Equation 1.0 does NOT apply:

$$T_{\text{output}} = (K_t \times I) - T_{\text{loss}} \quad (1)$$

Where,

T_{output} is the net output torque of the motor

K_t is the motor torque sensitivity constant, torque output per amp input

I is the motor input current

T_{loss} is the sum of all internal motor, bearing, drag, etc. torques.

The stepper motor torque cannot be calculated simply based on K_t as with brushless motors, so margin to compensate for this must be imposed in the performance analysis. Margin factors for stepper motors are used to either increase the torque requirement (internal and external) or to reduce the available voltage. It is common to apply established margin factors to the internal and external load requirements to arrive at a set of speed and torque conditions that the proposed stepper design must meet (typically by analysis). If the performance analyses cannot show the design will comply, then it is deemed to have insufficient margin to assure satisfactory test and flight operation. The margin factors used are typically those established by the company designing the system or the motor manufacturer supplying the motor design and will vary somewhat.

The process of deriving motor requirements from system or mechanism performance requirements and of imposing sufficient margin for the particular mechanism application is essential to proper stepper motor sizing. A comprehensive stepper motor specification must include an approach that correlates the specifications, simulation and analysis, and hardware testing. The motor specification approach outlined in Table 1 is suitable for guiding this process. However, it will need to be tailored to the specific application and technical requirements. Table 1 is applications oriented, directed towards the systems or mechanism designer desiring to utilize a stepper for a space flight mechanism. Typically, the systems or mechanism engineer will require assistance in working through the detailed level of evaluation and simulation normally required for stepper motors in space applications.

Table 1. Guidelines for the Stepper Motor Specification Process

	<u>DEFINITIONS</u>	<u>LIMITATIONS</u>	<u>CORRELATION</u>
<p><i>(1.a) Translate System and Mechanism Specs into Stepper Motor Requirements</i></p> <p style="text-align: center;">↓</p>	<p><u>Key Derived Ratings:</u> Speed (Pulse Rates) Load Torques Inertial Loads Step Angle and Output Resolution (Trade-off Analyses)</p>	<p><u>Key System Limitations:</u> Unpowered Holding Maximum Output Torque Pulse Width Input Power Driver Circuitry Scheme Hard-stops</p>	<p><u>Margin Approach:</u> Heritage Review Torque Margin Voltage Margin Combination [Ref. Table 3]</p>
<p><i>(1.b) Evaluate and Iterate Motor to Meet Requirements</i></p> <p style="text-align: center;">↓</p>	<p><u>Key Motor Parameters:</u> K_t and DCR Ranges Detent Torque Range Pull-in and Out Torques Rate Capability Viscous Damping Rotor Inertia</p>	<p><u>Thermal Limitations:</u> Duty Time-On Ambient Range Winding Temp. Rise Cold Start Drag Torque Installation Mounting Thermal Mass</p>	<p><u>Analysis and Test:</u> Test to Spec with Margin only in Analysis...or Include Margin at Testing</p>
<p><i>(1.c) Simulate Dynamic Performance and Confirm with Hardware Testing</i></p>	<p><u>Dynamic Models:</u> Assess capability of motor to meet specs, margin, and duty</p>	<p><u>Worst Case Limitations:</u> Environmental Extremes Electrical Combinations Mechanical Combinations</p>	<p><u>Test Confirmation:</u></p> <ul style="list-style-type: none"> • Motor Only • Mechanism • System

Translating System and Mechanism Specs into Motor Requirements

Translating system and mechanism specs into specific motor requirements is highlighted in Table 1, section (1.a), and broken up into three parts: Definitions – Key Derived Ratings, Key System Limitations, and Correlation – Margin Approach. Failure to address any of these three areas during development of

the stepper motor specifications will result in performance difficulties or failures later on in the project. Following this process is (1.b), Evaluation and Iteration of the stepper motor to meet the requirements developed in (1.a). Developing the specifications in (1.a) will depend significantly on trade-offs associated with the selection of the mechanical reduction (planetary gears or harmonic drives typically.) Because stepper motors are fixed angle, speed sensitive, and torque limited, a careful trade between reduction ratios and motor performance is necessary.

It should be understood that stepper motors come in specific packages that tend to restrict the step angle size as a function of diameter. A large angle stepper will usually come in a small diameter package. Conversely, a small angle step motor usually comes in a larger diameter package. Table 2 indicates for reference step motor angles and corresponding motor diameters. Note that the step angle is also dependent on the number of motor phases. There is a style of industry stepper referred to as “Hybrid” that possesses a small step angle (1.8 degrees) in a comparatively smaller diameter and so is “out-of-family” with the typical diameter versus step angle size shown in Table 2. This difference makes the Hybrid 1.8 degree stepper popular for some applications.

Table 2. Motor Step Angle and Typical Diameter Relationships

Step Angle (Degrees)	Diameter Range (mm)	No. Winding Phases
90.0	27.1 – 63.5	2 / 4
45.0	27.1 – 44.6	2 / 4
15.0	27.1 – 63.5	2
3.75	50.8 – 140	3
2.0	117	2
1.8 *	38 – 86.4	2 / 4
1.5	99 – 117	3

*1.8 degree stepper shown is of special Hybrid configuration.

A stepper motor having a 2.0-degree step angle would need to be pulsed at a rate of 180 pulses per second (pps) to achieve one revolution in one second (2.0 deg x 180 pps = 360 degrees of rotation per second). By comparison, a 90-degree stepper motor could go through one revolution with only a 4 pps excitation rate (90 deg x 4 pps = 360 degrees of rotation per second.) So, the larger step angle motors can operate at slower rates but achieve greater speeds. But, actuator resolution is also affected by the step motor angle chosen, and the 2.0-degree stepper will have 45 times smaller angular resolution than the 90-degree stepper. Hence, clear trade-offs exist between actuator resolution, motor pulse rate, and motor torque. While there are exceptions, most space-rated stepper motors are specified to operate with a maximum rate between 200 and 1000 pulses per second, depending on the size and voltage input.

Because changes in gear reduction affect the motor operation rates, usually a trade exercise occurs to determine the optimum torque and speed maximums within the capability of the motor. Stepper motors are uniquely sensitive to speed and torque ranges and do not have a linear speed-torque curve. A single axis stepper motor harmonic drive unit like shown in Figure 2 is bounded by a maximum no-load speed range or pulse rate and a maximum powered holding torque (comparable with “stall torque.”) This is similar to a brushless dc motor, but due to the absence of commutation control, the performance curve between no-load speed and stall torque is non-linear, may have “drop-out regions”, and may even differ

for every application. The best first approach is to identify stepper motors and manufacturer's data that are comparable with the new application, either through knowledge of steppers that have been used before or through manufacturer's catalog data. Then, narrow the selection of motor models based on further trades and analyses.



Figure 2. Single Axis Stepper Harmonic Drive Unit

Load torque is essential information for developing initial stepper motor specifications, but it must be understood that selecting a stepper from catalog data based on load torque requirements will not yield satisfactory results. Typically, catalog data is provided for operation at room temperature and has little if any margin applied to assure that performance goals will be met in a space application. It becomes important, then, to also know the full range of the mechanism's loading over temperature and other extremes and the amount of margin that is deemed sufficient. From the stepper motor's perspective, the internal drag associated with its bearings under cold start-up conditions can be as significant as the external load reflected through the gear reduction. Hence, stepper motor specifications must attempt to address the range of external loads, internal loads, and the extent of torque margin required before a motor can be sized.

Another torque characteristic typically needed with stepper motor applications is called "unpowered holding torque." This property is the result of magnetic detent within the motor that causes it to hold its position when no power is applied. A certain amount of detent is necessary to assure that when step excitation has ceased the motor rotor position rests at the expected location. This may not be true if external dynamic effects are sufficient to overcome the unpowered holding torque. Unpowered holding torque is commonly used within space mechanisms to hold the mechanism position against rotation once power is removed from the motor.

If a minimum amount of unpowered holding torque is present within the motor design, then a minimum amount of mechanism holding can be expected. So, it is common for the mechanism and hence motor to have an unpowered holding torque specification. It should also be noted that too much motor detent torque can interfere with meeting dynamic torque requirements, so it may be necessary to have both a minimum and maximum holding torque spec (commonly defined through the motor's detent).

Unlike brushless dc servomotors, which have varying power inputs depending on the changing load requirements, stepper motors operate on a constant level of power input. This at first may seem surprising, but once it is realized that the stepper actuates based on series of electrical pulses, the power situation becomes better understood. The full level of power is applied at every motor step regardless of the loading situation. Since the power input is essentially at maximum for every step, an assessment of the duty cycle, average power input, and motor thermal capability becomes very important. A motor may be chosen that meets step resolution and the speed – torque requirements but be found to have

insufficient size and thermal capacity. The motor mounting characteristics should be included if possible in the specifications.

As a consequence of full power being applied at every step of a stepper motor during its operation, schemes have been developed to reduce the average applied power. A common stepper driver feature that accomplishes this is the practice of restricting the “on-time” of an electrical step pulse to only a fraction of its theoretical maximum duration. This practice of operating with a reduced or “partial pulse width” may reduce average motor power consumption and internal motor heating, but it can also affect motor stepping capability. If a partial pulse width is intended for operation, this needs to be indicated early on. Besides the possibility of operating with a partial pulse width, it is also common to have a current limit applied. Because the driver design can play a critical role in the operation of a stepper motor, it is important to have the intended drive electronics and its features defined.

Once the motor specifications have been derived from system level requirements, drive requirements, and trade-offs to arrive at optimum rates and torques, the issue of performance margin for the mechanism must also be addressed. Performance margin may be addressed as margin on torque, voltage, or losses. Performance margin for space mechanisms can be defined through use of several methods that are sometimes used together as summarized in Table 3. It should be noted that margin can be applied twice or more through the specification process, sometimes unintentionally, resulting in hardware that is oversized.

Generally, the hardware should be designed to meet several times the actual performance requirement (as determined by the margin), and then tested to meet the actual requirement over worst-case conditions. If hardware must be tested at several times the actual requirement, then the motor must be sized with additional factors that may unnecessarily increase motor weight and volume. Table 3 assumes that margin is only applied one time for purposes of meeting the specified requirements derived from the actual mechanism demands. While the Table 3 methods are commonly known, it is hoped that clarification and possibly standardization of their use will result.

Table 3 provides guidelines that the system or mechanism level designer can use to specify margin for space stepper motors, so that when the design is created and analyzed sufficient design margin will be present to assure actual torques and speeds are met over all the worst-case conditions at test. It is important that the specifications be clear as to whether the margin applies for design analysis purposes only or if factors shall be applied at test as well. Sometimes it is desired that the requirements for test be set beyond the actual needed values by some margin factor. If this course is chosen, the system or mechanism level engineer must realize that the stepper motor will be sized accordingly with some additional size and weight penalty.

Torque load and internal loss margin factors can vary, because applications are different. Stepper motor designers also vary in their conservatism. The actual factors to apply should rest in a mutual agreement between system, mechanism, and stepper motor design engineers for their specific project but based on successful heritage margin values. In general, it is not uncommon to see load and loss torques increased by factors of several times to assure steppers will function as desired (reference Table 3.a). The same is nearly true of taking voltage reductions, although these generally must be applied more thoughtfully, since voltage affects both speed and torque (reference Table 3.b)

Heritage data (reference Table 3.c) may provide a reference of acceptable margins from test history but may not be as clear regarding the actual design margin used if the hardware is from a very mature program. So, heritage data should be taken as reference if older or intended margins are unclear, and then combined with one of the other methods of margin. It is of great importance that the margin methodology agrees from specification to analysis to test.

Table 3. Specifying Margin in Stepper Motor Performance

Specifying Margin in Stepper Motor Performance	Specification	Analysis	Test
(3.a) Apply Factors to Loads and Losses during analysis to assure actual requirements are met in test	States specific load and loss torques with factors that should be applied during analysis but not in hardware test	Use torque values that include the margin factors and simulate to show compliance	Test at the required torque values under worst case conditions but with no factors applied
(3.b) Reduce Applied Voltage during analyses; but test with normal voltage	Specify a reduced applied voltage that reflects desired margin for analysis purposes only	Use reduced voltage for simulating operation and specific performance points	Test using the normal voltage to meet specified performance
(3.c) Use Heritage Mechanism Data to Qualify Similar New Designs	Reference the Heritage specifications	Reference the Heritage analyses and make minor modifications as needed	Test similarly to the heritage mechanism

The application of margin factors to load and loss torques may take on another form besides that shown in Table 3, the torque margin being derived from an equation relating measured to required values. For example, a measured maximum output torque value under worst case conditions would be divided by an expected torque loss value (sometimes measured also) to arrive at a margin factor above internal losses. Additional torque loading may be added to represent an output load or may be factored into the margin equation.

This approach is not uncommon but tends to compound the margin within a stepper motor application. The reason for this is that when margin factors within a specification must be demonstrated at test by a calculation based on measured torques, the analysis component of the process must contain “additional padding” so that margin over the tested amounts is present. A stepper’s response is not linear or predictable like that of a brushless design. In order for a stepper to produce, for example, three times more torque output than the requirement, the sizing of the motor must go some factor beyond that in order to actually test out a margin factor of three. Hence, the motor design might need to incorporate a factor of five over expected torques, for example, in order to test out a factor of three times the torque requirement. So, the specification of torques and application of margin must be thought through very well and correlated with the analysis and test approach to achieve a reasonable outcome.

Evaluation, Simulation, and Testing of the Stepper Motor

Preliminary evaluation of the stepper motor performance comes through a review of its catalog or historic use data. This involves looking at the available torque production capability, and realizing that the rated value of torque will need to be de-rated in accordance with the margin factors chosen. Speed maximums should also be reviewed with a close look at the motor step angle and number of motor phases. The peak and continuous output data (if available) must always be judged relative to the conditions associated with the rating. Typically, space environments offer the least favorable conditions from a thermal standpoint. Tolerances on the motor winding constants, magnetic detent, voltage, current, temperature extremes, etc.

must be considered to begin developing a complete analysis of the performance. Additionally, mechanical characteristics such as coupling stiffness, bearing drag losses, motor and load inertias, etc. must also become a part of the performance simulations.

While most of these parameters are readily available from the system description, motor catalog specifications, and historical references, it is essential that the performance analyses include these over the full range of operating conditions. While it is beyond the scope of this paper to address how to accomplish a stepper motor and mechanism performance analysis, the preparation for doing such is well known. So, it is worthwhile to at least recognize the basic performance analysis parameters as part of establishing adequate performance margin for steppers:

- Motor step angle
- Motor number of phases and winding type
- Motor torque sensitivity, K_t , with tolerances
- Motor winding resistance with tolerances and effects of thermal rise
- Motor inductance with tolerances
- Motor mounting, heat dissipation, and thermal rise model
- Motor rotor inertia
- Number of motor poles
- Minimum and maximum motor detent torque
- Supply voltage and tolerances
- Supply current maximum and any pulse width restrictions
- Environmental temperature range
- Temperature range effects on bearing drag torques
- Load drag torque, load inertia, and coupling stiffness
- Operating profile and duty cycle
- Gear reduction characteristics.

Failure to consider the worst-case extremes of these parameters will result in improper performance assessment and operating anomalies. It should be well understood but is worth mentioning that in stepper mechanisms the performance analyses may detect areas of concern not related to meeting the margin goals but related to dynamic stability at certain speeds, commonly resonances. Hence, it is impossible to develop a thorough stepper motor mechanism performance analysis based solely on static estimates associated with margin. In fact, a well-established method for simulating the stepper mechanism motion over a broad range of operation conditions is essential. Commercially available and custom software are used for accomplishing the motor and system level performance simulations.

Performance simulation is best done using methodologies that have been successful in the past in correlating with test results. Sometimes it is difficult to replicate the stepper mechanism in its precise flight configuration, because of model and / or test set-up limitations. So, it is important first of all to realize what the modeling and test deficiencies are and secondly to make sure that the performance modeling and lab testing are intended to correlate well. Correlation must be present between performance modeling and lab tests. Often it is easier for the performance simulation to replicate the flight configuration than it is for the test set-up. This can occur when the flight configuration involves large masts or solar panels. If the performance modeling accurately simulates the flight configuration but not the test lab configuration, then anomalies in test can occur that reflect test set-up deficiencies rather than potential flight problems.

Hardware testing should consist of tests at every level of the system, from the stepper motor components to the mechanism assembly. Of primary importance is identifying the specific tests and limits that will best represent the actual flight conditions and then assuring that the design, simulations, and testing follow consistently. Testing at the motor component level looks at the parameters that determine torque, speed, power, angular movement, and positional stability. Testing at the mechanism level looks at torque output and margin, rate and resolution, and step stability. Testing for both the motor and mechanism should incorporate environmental factors, especially temperature extremes. It is very desirable to use flight-like

drive electronics for testing. Table 4 summarizes the types of testing generally performed on stepper motors and mechanisms and how these should follow from specification and analysis strategies.

Table 4. Basic Stepper / Mechanism Testing for Correlation with Specifications and Analyses

<u>Specification Parameter</u>	<u>Analysis Correlation</u>	<u>Motor Component Test</u>	<u>Mechanism Test</u>
Electrical Characterization	Estimate motor K_t , R_{ph} , and L_{ph}	Verify electrical parameters	(Usually only minimal electrical verification)
Output Resolution	Define Step Angle	Step Accuracy Test if applicable	Output Resolution
Unpowered Holding Torque	Estimate Minimum Detent and Bearing Drag	Motor – measure detent Bearings – measure drag over temperature	Measure unpowered holding torque over temperature
Powered Holding Torque	Motor gross output torque less internal losses must provide margin over loads; simulate with margin on losses and loads	Measure net output torque and internal losses; adjust analyses and simulation models for any loss variations	Measure powered output over temperature to confirm PHT spec is met (no margin applied)
Specific Torque and Rate Operation (using driver pulse width, current limit, etc.)	Optimum gear reduction with motor rate and torque, simulate over worst cases with flight driver limits	Dyno test motor and include margin on losses over worst case thermal concerns; use flight-like driver	Test output rate and torque at worse case w/ flight driver. Can test above rate and torque spec for reference.
Dynamic Performance (New stepper motor characterization should go beyond mechanism requirements)	Predict & analyze pull-in and pull-out torque performance and if electronic rate ramp is needed for operation	Especially for new designs, perform pull-in and pull-out torque characterization; evaluate rate ramp	Verify mechanism performance over dynamic ranges required and all worst case conditions

The margin approach used in Table 4 is the same as used in Table 3, which does not compound the margin factors. However, if the margin must be demonstrated during test beyond that actually needed to meet the specification, then the additional margin must be built into the analyses and motor testing as well. Some test anomalies are the result of not following the same margin strategy through from spec to test.

Lessons Learned in Establishing Adequate Performance Margin

Proper sizing with thorough analysis and test will usually address most stepper motor applications concerns. However, there are some problem scenarios that should be identified in a lessons learned format. These are largely from historical lessons and should be considered relevant when establishing

performance margin in a stepper mechanism. Lessons learned from stepper motor usage on space mechanisms can be categorized into four different areas:

- Torque Production Assumptions
- Temperature Effects
- Over / Under Margin Use
- Electrical Driver Features / Differences.

Incorrect Torque Production Assumptions

Incorrect torque production assumptions can be made during the motor selection and sizing phase due to the casual usage of the motor K_t . In a stepper motor, the K_t is a reference figure used in helping to determine the winding scaling and in comparing motor capabilities, along with the motor constant, K_m . But, if the K_t is multiplied by the current to obtain a “torque estimate” without recognizing the open-loop operation characteristics of the stepper and without any margin considerations, then the motor sizing will be very lacking in torque capability. This concept is at the heart of establishing adequate performance margin, because K_t and K_b by themselves cannot be used to predict what the speed-torque output will be.

Unanticipated Temperature Effects

Unanticipated temperature effects can have a great impact. The first concern is attempting to size a motor working only with the ambient temperature resistance. The hot ambient temperature can be used to easily calculate the change in winding resistance from nominal to hot conditions. But of equal or greater importance, is the potential for thermal rise due to internal motor heating. This is much more difficult to address than the effects of a hot ambient temperature. The mounting conditions and thermal transfer from the motor into its flight mounting may not be well defined; this in combination with an uncertain duty cycle can create uncertainties in the winding temperature. Elevated winding temperatures, which may be within the rating of the motor materials, can exceed that expected in the performance model. And, so the expected performance can suffer.

Inadequate or Inappropriate Uses of Margin

Inadequate or inappropriate uses of margin either by the torque or voltage method is sure to cause performance deficiencies. Because stepper motors are different in design and their applications also vary considerably, there is some understanding that torque margin factors may vary within a reasonable range. As these factors are applied over a history of programs, a basis for establishing the necessary ranges of factor values is developed. To the extent that performance simulation tools increase in accuracy of prediction, the factors may be reduced a bit. Fundamentally, the stepper motor's output is very dependent upon the dynamics of the system. And, so to evaluate a stepper motor independently of the system in which it will be used is not acceptable. Hence, the need is present to incorporate torque margin factors from a well-known range to help assure that performance goals will be met.

It should also be understood that the inclusion of such margin factors does not guarantee that performance will be satisfactory under every condition, because other influential conditions may exist such as system resonances. In fact, some conditions of the worst-case system analysis are not correctly simulated if the torque margin is applied to the loads and losses. These simulations that evaluate the motor and system stability are better served if the margin factors are omitted and losses are reduced closer to the minimum values. Closely related to this type of concern is speed dependent damping associated with the motor magnetic properties and the electronic drive circuitry.

In a broader sense, to cover the full perspective of performance margin, it is necessary to evaluate not just the torque requirements and associated margin factors but also the dynamic stability of the motor in its system. While this is certainly understood by system and mechanism designers, for the sake of presenting a complete perspective of stepper motor performance it is mentioned. In addition to the conditions of operation where factors are applied and those conditions where they are not, other unique conditions should also be considered. For example, if there is the possibility of the mechanism encountering hard-stops, then the requirements outlined in harmonic drive catalogs for ratcheting torque must be observed. Restrictions may be required to prevent the over-production of motor torque, that is, the maximum motor torque possible should not reach or exceed a percentage of the maximum harmonic

drive ratcheting torque rating. Otherwise, damage to the harmonic drive could result. This additional aspect and others like it associated with unique system design concerns must be addressed as well as the obvious performance margin concerns.

The Electronic Driver

The electronic driver for the stepper motor can have as significant an effect on performance as the system dynamics. Excluding the obvious factors of available voltage and current, other driver parameters if overlooked can impair the resulting system performance. Probably the most significant driver parameter to be concerned about is the use of a partial pulse width. As already explained, this is implemented to help reduce the average power consumption of the motor. But, if the partial pulse width feature is overlooked in the motor design analysis, then the performance can suffer at lower speed ranges where it takes effect. Specifications must be clear about this feature, and performance simulations must take its use into account. A similar and more obvious feature is the current limit.

In some systems, a stepper may be required to start at a rate that exceeds its capability. So, an electronic rate ramp can be part of the drive electronics to start the motor at a workable speed and quickly advance to the higher rate. This type scheme is typically not proposed in a driver but is the result of the motor and system performance analyses, which may show that such a feature is required. If the performance analyses fail to uncover this concern, then it will surely be uncovered during testing.

A more common problem that occurs is the result of using commercial drive electronics for motor components testing that usually differs in design from the space flight drive electronics. This can introduce minor performance differences or major ones, depending on the electronics. In many cases the flight drive electronics are not available for use with the motor components, but a reasonable compromise is to build a commercial grade drive box based on the flight electronics schematic.

Summary and Conclusions

Adequate stepper motor performance margin is critical for mission success. System or mechanism specifications and the associated stepper motor specifications are typically different in terms of how the motor related characteristics are presented. Unlike brushless DC motors, stepper motors cannot be relied upon to produce output torque as a function of input current. Motor speed, torque loading, and system dynamics affect the stepper motor's ability to respond to input commands. To compensate and account for inherent motor and system variabilities and their influence on stepper motor-based mechanisms, adequate design margin must be built into the motor sizing. The motor specifications, analysis assumptions, and hardware testing should agree in methodology as closely as possible.

It is necessary in applying a stepper motor to carefully define ranges (minimums or maximums) on many parameters, such as the motor speed (pulse rate) to assure that the motor and load rotation remain synchronous over all conditions of voltage variation, temperature and internal frictional drag changes, load variations, etc. The process of deriving motor requirements from system or mechanism performance requirements and of imposing sufficient margin for the particular mechanism application is essential to proper stepper motor sizing. A comprehensive stepper motor specification must include an approach that correlates the specifications, simulation and analysis, and hardware testing. Table 1 is applications oriented, directed towards the systems or mechanism designer desiring to utilize a stepper for a space flight mechanism, and provides guidelines on specifying and correlating stepper motor requirements for motor specification, analyses, and testing.

Preliminary evaluation of the stepper motor performance comes through a review of its catalog or historic use data. While most of the relevant parameters are readily available from the system description, motor catalog specifications, and historical references, it is essential that the performance analyses include these over the full range of operating conditions. Failure to consider the worst-case extremes of these parameters will result in improper performance assessment and operating anomalies. Performance simulation is best done using methodologies that have been successful in the past in correlating with test results. Correlation must also be present between performance modeling and lab tests. Testing at the motor component level looks at the parameters that determine torque, speed, power, angular movement,

and positional stability. Testing at the mechanism level looks at torque output and margin, rate and resolution, and step stability.

Inadequate or inappropriate uses of margin either by the torque or voltage method is sure to cause performance deficiencies. It should also be understood that the inclusion of such margin factors does not guarantee that performance will be satisfactory under every condition, because other influential conditions may exist. In a broader sense, to cover the full perspective of performance margin, it is necessary to evaluate not just the torque requirements and associated margin factors but also the dynamic stability of the motor in its system. Table 3 provides guidelines that the system or mechanism level designer can use to specify margin for space stepper motors, so that when the design is created and analyzed sufficient design margin will be present to help assure actual torques and speeds are met over all the worst case conditions at test. It is important that the specifications be clear as to whether the margin applies for design analysis purposes only or if factors shall be applied at test as well.

Stepper motors have been an important motor type for use in space applications offering advantages over brushless and brushed motors in many applications. It remains relevant that those who design stepper motor based mechanisms and are involved in developing specifications for stepper motors understand their application concerns. This is truer with steppers than brushless and brushed motors, because steppers tend to change their individual performance characteristics from one system to another. Establishing adequate performance margin is therefore a critical process and should be carefully explored as new applications emerge for stepper motors in space flight.

HST Solar Array 3 Latches

Mike Garrah*

Abstract

The Hubble Space Telescope Servicing Mission 3B, completed successfully in March of 2002, included installation of two new Solar Array (designated SA3) Assemblies. The SA3s are of a completely new design that minimizes on-orbit jitter, and maximizes power generation. The SA3 Latches, developed by Swales Aerospace under contract with NASA Goddard Space Flight Center, were used to carry the SA3s into orbit in the Space Transportation System 109 Cargo Bay. These latches were engineered to meet a wide array of requirements covering almost the entire spectrum of mechanism design. During the course of this presentation, the details of the overall latch system design, as well as the design of each individual latch will be presented. An overview of the latch environmental test program will be presented with emphasis on solution of problems encountered during that process. Because this hardware has been successfully designed, tested, and flown, there is a vast array of practical information available that will be of definite value to mechanisms engineers. A summary of "lesson learned" during the development process will be provided at the end of this presentation.

Introduction

The design of large Extra-vehicular Activity (EVA) released structures such as the SA3 Assemblies, carried into space by the Space Transportation System, is predicated on addressing a wide range of unique requirements. These include mission safety, EVA timelines, human factors, tool capabilities, and weight and volume constraints. To support the replacement of the arrays, the hardware had to be first carried to orbit using a system of unique latches that could accommodate the launch environment as well as on-orbit thermal distortions. Upon reaching orbit, the latches had to allow for tool assisted astronaut actuation for release of the arrays. The design, fabrication, qualification, and successful mission operation of these latches, known as the SA3/RAC Latches is the subject of this presentation.

Overall System Description

The SA3 Latch system consists of two sets of five discreet latches (for a total of 10), mounted on opposite sides of a vertical structure known as the Center Support Structure (CSS), which is in turn mounted to a pallet in the shuttle bay. Each set of five latches structurally supports one SA3 during launch and landing (if required). Four of the latches (designated Latch 1 through Latch 4) support the rectangular shaped SA3 at each of its four corners. The last latch (designated Latch 5) supports a deployable mast on the top of the SA3. Figure 1 illustrates the SA3/RAC Latch locations with the stowed SA3 and mast.

Latch 1, shown in the upper right corner of Figure 1, consists of an active half mounted to the SA3 structure, and a passive half mounted to the CSS. The SA3 mounted side incorporates an internal 7/16" (11-mm) hex drive ACME screw that picks up a floating ball nut inside of the conical passive half mounted to the CSS. A semi-spherical fitting on the end of the active Latch 1 housing mates with an interior conical surface on the passive (CSS) side which aids in alignment and provides 3 degrees of constraint. Latch 2, shown in the lower right corner of Figure 1, is a vise-type latch with an integral 90° bevel gear set driven through a rotary input shaft. A 7/16" (11-mm) hex drive located on the Latch 1 housing, coupled to a drive extension rod, transmits torque to the input shaft. This latch incorporates a "V" guide and clamps down on a semi-cylindrical swivel fitting on the SA3, providing 2 degrees of constraint. Latch 3, shown in the upper left corner of Figure 1, is a vise-type latch with a directly driven semi-spherical pad that clamps down on an attachment fitting at the upper left corner of the SA3. The front (clamping) portion of the latch is hinged

* Swales Aerospace, Beltsville, MD

and can be manually rotated out of the way after latch release to aid in removal of the SA3. This latch provides 1 degree of constraint. Latch 4, shown in the lower left corner of Figure 1, is a vise-type latch that has an internal mechanism similar to that of Latch 2. A 7/16" (11-mm) hex drive located on the Latch 3 housing, coupled to a drive extension rod, transmits torque to the input shaft. Semi-spherical pads on this latch clamp down on attachment fittings on the corner of the SA3 to provide 1 degree of constraint. Latch 5, shown at the top of Figure 1, consists of a CSS mounted tower with a locking bolt and clevis, which pick an attachment fitting on the stowed solar array mast. The unique degrees of constraint provided by each latch allow the overall system to accommodate misalignments and mechanical and thermal distortions.

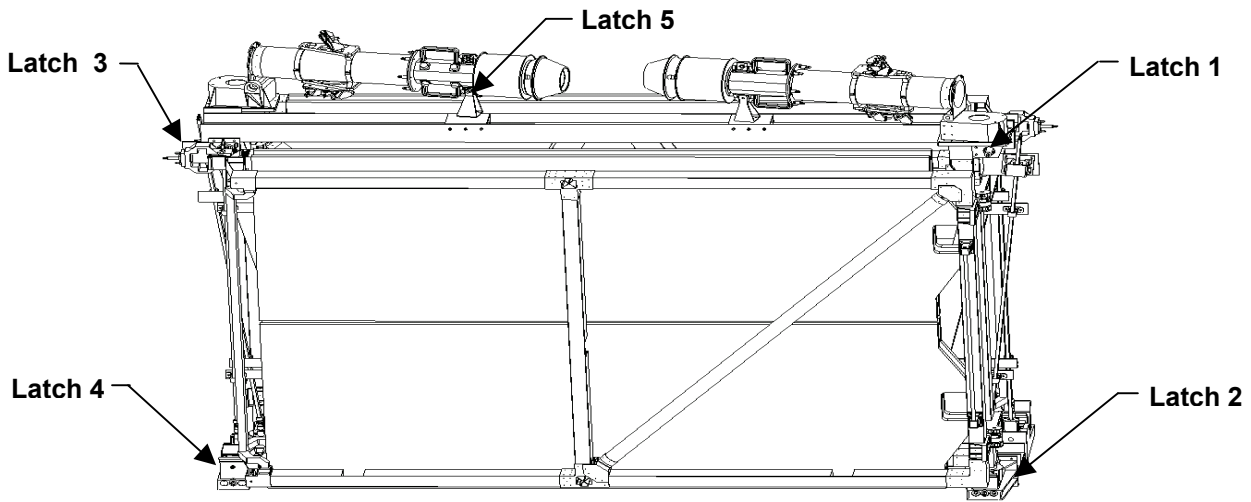


Figure 1. Latch Mounting Locations with SA3

The pallet and Center Support Structure are an integral assembly provided by Orbital Sciences Corporation and is designated the Rigid Array Carrier (RAC). Figure 2 shows an end view of the RAC and SA3s in the launch configuration prior to shipment to Kennedy Space Center. The gold colored structure in the center of the photo is the CSS, and the SA3s are mounted to the left and right sides and are silver colored with gold handrails on the edges. The SA3 masts are not shown in this photo because they were shipped separately to Kennedy Space Center and installed prior to launch.

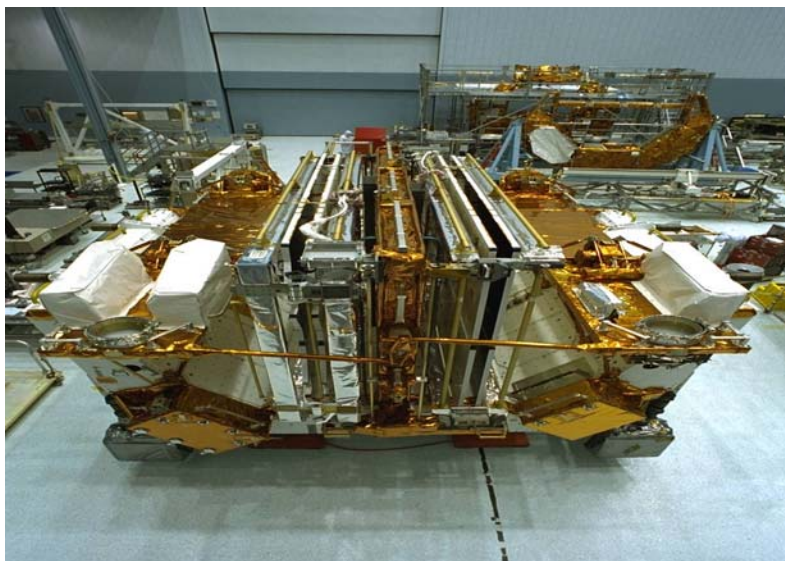


Figure 2. Launch Configuration of the SA3

Overall System Requirements

- High load carrying capability during launch (maximum of 20Gs supporting a 318-kg (700-lb) Solar Array Assembly).
- Very high preload capability.
- Ability to accommodate large misalignments due to on-orbit thermal gradients.
- Accessibility for Extravehicular Activity – All latches are astronaut actuated.
- Compatible with existing EVA power tools.
- Operational torque less than 34 N-m (25 ft-lb) for on-orbit disengagement and engagement (power tool limits).
- Low turn count for on-orbit disengagement and engagement (minimized crew workload).
- High repeatability in torque and turn count.
- Allow for relatively blind re-installation of the SA3 if unable to install onto HST (SA3 would be returned to earth).
- Independent EVA override.
- Independent launch lock at each latch drive.

Latch Design Details

Photos of the actual flight latches 1 through 5 in the launch configuration are shown in Figures 3 through 7, respectively. Basic design features of the SA3/RAC latches are detailed below:

Drive Mechanism

- All latches are rotationally driven through 7/16" (11-mm) EVA tool compatible hex nuts.
 - Latch 1 – Spring loaded directly driven ACME screw with alignment guide rides on opposing deep groove ball bearings.
 - Latches 2 and 4 – Input shaft drives 2:1 integral 90° bevel gear set which outputs to ACME screw and linear stage.
 - Latch 3 – Directly driven ACME screw drives clamping pad.
 - Latch 5 - EVA-removable bolt with alignment guide on end.
- All latch drives incorporate independent positive locking features for launch.
- Latches 1, 2, and 4 drive trains incorporate matched deep groove ball bearing pairs for maximum thrust capacity and minimum torque.

Nominal Latch Preload

- Latch 1 = 1588 kg (3500 lb); Latch 2 = 1361 kg (3000 lb); Latch 3 = 272 kg (600 lb);
- Latch 4 = 318 kg (700 lb); Latch 5 = 272 kg (600 lb).
- Belleville washers incorporated into load path to allow preload compliance and accurate setting

Torque and Turns Required to Disengage Latch

- Latch 1: T < 31 N-m (23 ft-lb) (20 turns); Latch 2: T < 20 N-m (15 ft-lb) (12 turns);
- Latch 3: T < 20 N-m (15 ft-lb) (8 turns) Latch 4: T < 20 N-m (15 ft-lb) (12 turns);
- Latch 5: T < 20 N-m (15 ft-lb) (8 turns)

Dimensions and Weight

- Latch 1: Dimensions: 298mm (11.75")L X 146mm (5.75")W X 89mm (3.5")H Mass = 6.3 kg
- Latch 2: Dimensions: 381mm (15")L X 254mm (10")W X 197mm (7.75")H Mass = 17 kg
- Latch 3: Dimensions: 432mm (17")L X 152mm (6")W X 135mm (5.3")H Mass = 6.3 kg
- Latch 4: Dimensions: 635mm (25")L X 152mm (6")W X 203mm (8")H Mass = 23 kg
- Latch 5: Dimensions: 102mm (4")L X 102mm (4")W X 191mm (7.5")H Mass = 1.4 kg

Materials for Major Components

- ACME Screw: CRES 17-4PH
- Barden 107H Ball Bearings: CRES 440C
- Latch Housing: Al 7075-T73



Figure 3. Latch 1 (Array Stowed)

Latch 1 consists of an active rectangular shaped housing mounted to the SA3 structure with internal 7/16" (11-mm) hex driven ACME screw. A spherical fitting of the end of this housing mates to a passive cone on the CSS that contains an internal swivel nut.



Figure 4. Latch 2 (Array Stowed)

Latch 2 incorporates a moving linear stage with a spring pad that clamps down on a semi-cylindrical fitting on the lower right corner of the Solar Array structure. The fitting is constrained by a "V" guide on the latch housing.



Figure 5. Latch 3 (Array Stowed)

Latch 3 consists of a swing arm with integral directly driven spring pad that clamps on a fitting at the upper left corner of the Solar Array.

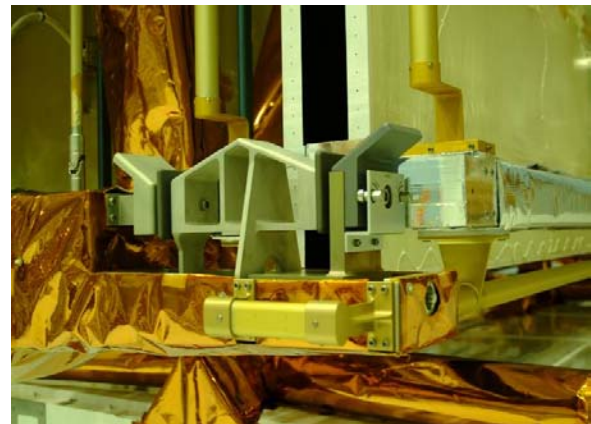


Figure 6. Latch 4 (Array Stowed)

The basic mechanism of Latch 4 is similar to that of Latch 2. The vise action of the latch causes semi-spherical spring pads to clamp down on two separate fittings at the lower left corner of the Solar Array. A floating spacer provides separation between the two Solar Array fittings.

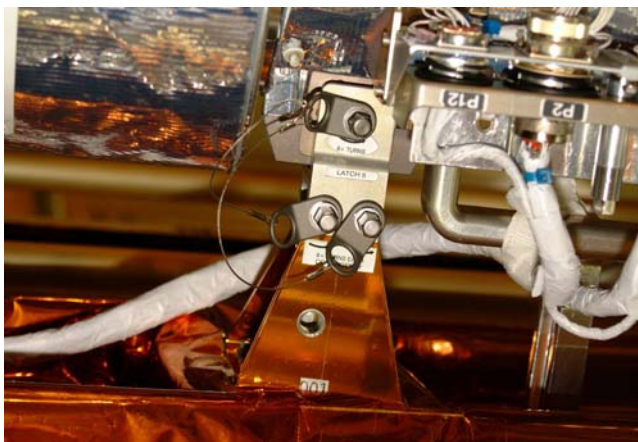


Figure 7. Latch 5 (Mast Stowed)

Latch 5 consists of a tower mounted to the top of the CSS with a clevis and captive bolt which pick up a fitting on the Solar Array Mast. The mast fitting contains a floating spherical bearing which accommodates thermal and mechanical misalignments.

Environmental Test Program

Engineering Units

Prior to build of the flight units, Engineering Test Units (ETUs) of all latches were built to qualify the design for space-flight use. Strength tests, qualification level acoustics tests, and thermal vacuum tests were successfully performed on all latches.

Flight Units

Random Vibration Test

An acceptance level random vibration test was performed on each of the flight latches. Test fixtures were designed to realistically simulate the launch configuration. During this testing, several design flaws in Latch 3 were uncovered.

- 1.) Excessive wear and galling occurred between the semi-spherical spring pad on the latch, and the fitting on the Solar Array. Both parts were fabricated from Aluminum Alloy 7075 coated with a Teflon impregnated hardcoat. Changing the material of the latch spring pad to uncoated phosphor bronze solved this problem.
- 2.) Wobbling of the drive screw and spring pad during lateral vibration caused the screw to “walk out” of the launch lock jaws and unscrew. This problem was solved by tightening up clearances to eliminate wobble, and redesigning the lock jaws to provide a more positive hold on the drive screw.

Acoustic Test

An acoustic test at the payload level was performed, and the latches operated nominally.

Thermal Vacuum Test

Each flight latch was subjected to 8 thermal cycles in a vacuum at the worst-case predicted mission thermal environment plus margin (-40°C to +60°C). The latches were operated after soak at each temperature extreme, and during transitions. Torque versus turns was measured during functional tests using a digital torque transducer. Typical data for Latch 2 is shown in Figure 8.

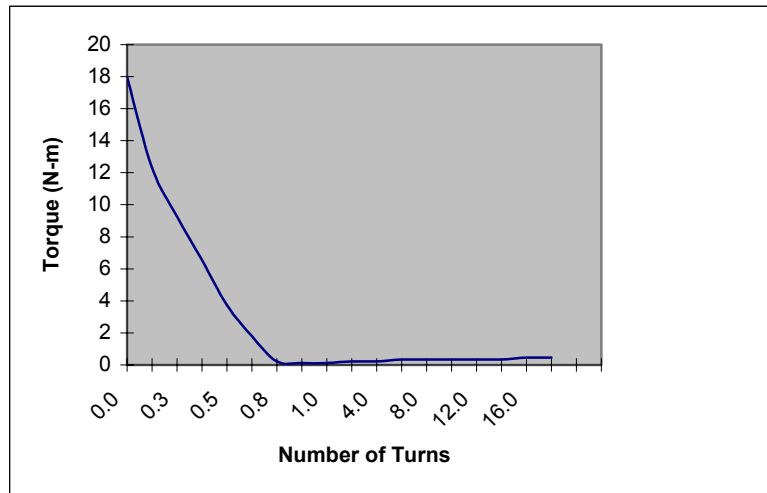


Figure 8. Typical Thermal Vacuum Torque vs Turn Data

During testing of Latch 3, a design deficiency was uncovered. Excessive wear and galling occurred between the launch lock jaws and the cam on which the jaws slide. This problem was solved by specifying a much smoother surface finish on the cam, and treating it with a dry lubricant coating (Dicronite). This problem was present on flight unit, and not on the ETU due to the fact that the jaw spring force was increased after the problems encountered during vibration testing.

Lessons Learned Summary

Throughout the development of the SA3/RAC Latches, many lessons were learned. Random vibration and thermal vacuum tests on the flight units uncovered several design deficiencies that were not uncovered during ETU testing.

- 1.) Perform as thorough a test program as possible on the Engineering Test Units prior to building an testing flight hardware
- 2.) Random Vibration test may uncover design and workmanship flaws undetected by an acoustics test.
- 3.) Hard coatings in high contact stress areas can be problematic. Softer non-coated materials should mate with hard-coated surfaces. Softer part should be made replaceable in the event that excessive wear occurs.
- 4.) If possible, a combination of design approaches should be utilized to minimize friction and wear on highly stressed sliding parts. These include:
 - Proper material selection
 - Smooth surface finish
 - Surface coatings (Tufram, Tiodize, Dicronite, etc.)
 - Additional Lubrication (Braycote 601, 602)
- 5.) Mechanisms should avoid slop and excessive play wherever possible in order to eliminate unforeseen motion during vibration.

Conclusions

The SA3/RAC Latch development and space flight qualification has been fully completed culminating in the successful launch and completion of the Servicing Mission 3B mission. The SA3/RAC Latches operated flawlessly during the mission, and were instrumental in the transport and installation of the Solar Array 3 Assemblies.

Data obtained from thermal vacuum, strength, vibration, and stiffness tests performed during the development process as well as design improvements along the way were instrumental in the success of the flight hardware. The environmental test program uncovered design flaws prior to launch that were corrected as described in previous sections. This is definite proof that a robust test plan is essential in the development of any mechanism designed for harsh environments, whether for space-flight use or merely for use on the ground. Torque versus turn data measured at various temperatures during thermal vacuum testing provided essential data for on-orbit verification of proper latch operation. This data was also used for programming the HST power tool which can be set to shut-off at a predetermined torque or turn count.

Lessons Learned on Cryogenic Rocket Engine's Gimbal Bearing Lubrication Selection

Christian Neugebauer* and Manfred Falkner*

Abstract

The bearings for a gimbal of a cryogenic upper stage rocket engine are highly loaded, exposed to corrosive environment and have to cope with a wide temperature range down to cryogenic temperatures. "Cronidur 30" steel was chosen for the bearing material. To satisfy the demand of low friction moment under these conditions a tribological concept should be found. This paper describes the selection process for the tribological concept suitable for this specific application that resulted in the selection of sputtered lead as lubricant for the gimbal bearings.

Introduction

Austrian Aerospace has the privilege to develop the gimbal for the next generation upper stage engine of the ARIANE 5 Launcher family, the VINCI engine. The challenges for bearings of a gimbal for a cryogenic upper stage rocket engine are:

- high loads due to the transmission of the thrust of the engine,
- high reliability requirements for both environments: atmospheric conditions and space vacuum,
- wide temperature ranges down to cryogenic temperatures,
- considerable number of only small oscillatory cycles,
- low friction and wear requirements.

Previous gimbals use common bearing materials similar to the bearing materials used in today's satellite mechanisms such as SAE 52100 or AISI 440C steel. FAG (FAG Kugelfischer AG, Germany) recently developed a novel bearing steel "Cronidur 30" which combines the advantage of high load capability with the advantage of high corrosion resistance, better than AISI 440C. Moreover "Cronidur 30" demonstrates excellent mechanical properties at cryogenic temperatures [1]. For this reason we selected "Cronidur 30" as the material for the gimbal bearings.

We expect "Cronidur 30" to increasingly become the substitute for today's commonly used bearing steels for space mechanisms. Currently little information is available and little experience exists concerning lubrication of "Cronidur 30" under space environment and specifically the behaviour of solid lubricant coated bearings made of Cronidur 30.

Keeping in mind the needs of the rocket engine gimbal bearing, Austrian Aerospace had the task to investigate possible lubricants; to make a trade between those candidates by aid of development tests; to select a suitable lubricant; and to qualify the chosen tribological system for the use on the ARIANE 5 launcher.

This paper details the development work performed to date (December 2003).

Description of the Mechanism

The main functions of the gimbal are to fix the engine in its defined position, to transfer the thrust and all inertial forces from the engine to the stage and to allow the gimbal operation.

The gimbal consists mainly of an engine-side bracket, the cardan cross and the stage-side bracket, connected by two pairs of bearings.

* Austrian Aerospace GmbH, Vienna, Austria

Needle roller types were selected due to the high load capability and the low friction moment under the specified environmental conditions, combined with a small envelope.

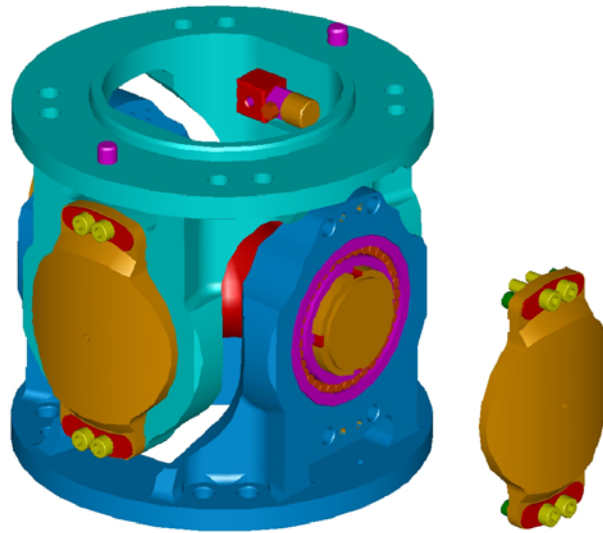


Figure 1. Gimbal design

The bearings are kept as small as possible due to the stringent mass and envelope restrictions. This leads to high Hertzian contact pressures between the needle rollers and the bearing rings. The Hertzian pressure will be more than 4000 MPa.

Demands on the Tribological System

The main demand on the tribological system formed by the bearing's inner and outer rings, needle rollers and the lubricant is to attain a low coefficient of friction during the whole lifetime of the bearings and after exposition to environmental attacks. This low coefficient of friction shall be attained despite the high Hertzian pressure and for operation in air as well as in vacuum.

The tribological system shall be compliant to the following requirements:

- compatibility to corrosive media, LOx and LH₂, and the operating temperature range that includes cryogenic temperatures.
- material compatibility to the bearing material Cronidur 30.
- no impact on the bearing precision
- the application process shall be suitable for the needle roller geometry selected.

Selection of the Lubricant Candidates

The decision either to operate without a lubricant or to use a lubricant was driven by the risk of cold welding under vacuum environment using a full "Cronidur 30" design comprised of rollers as well as races made of "Cronidur 30" without a lubricant. To avoid this risk the use of a ceramic material for the rollers was discussed. However utilizing ceramic needle rollers is not feasible for the gimbal bearings as bending stresses in the needle rollers would possibly cause destruction of ceramic needle rollers.

Fluid lubricants are not usable for the gimbal bearing lubrication at cryogenic temperatures and heating of the bearings is not possible. The operating temperature range goes down far below -75°C, which is known to be the lowest temperature limit for fluid lubricants. For these reasons a dry lubricant was selected.

Dry lubrication by sputtered silver was first discussed due to the vast heritage of the use of silver as lubricant in space mechanisms on conventional bearing steels. However a systematic approach was taken.

For a pre-selection, 27 dry lubricants were assessed in terms of friction coefficient, wear rate in air and vacuum, applicability for high precision bearings, heritage, temperature range, corrosion and electro-galvanic aspects and development risk for the application process.

Without going into more details concerning this pre-selection, the remaining promising candidates of this pre-selection were:

- Sputtered MoS₂ (Molybdenum Disulphide)
- Sputtered Ag (Silver)
- Sputtered Pb (Lead)
- Air-blasted WS₂ (Tungsten Disulphide).

Trial depositions with these candidates were performed on representative rollers of “Cronidur 30”.

Performance Testing of the Pre-Selected Lubricant Candidates

No information could be found in the literature regarding the behavior of these candidates together with “Cronidur 30” under corrosive environment. Therefore environmental tests were carried out as a first step. To investigate the behavior of the coatings applied on the “Cronidur 30” base material under corrosive environment, a salt spray test was performed as an accelerated test simulating environmental conditions that may occur during storage, integration, transport and test of the gimbal itself and of the gimbal integrated on the engine.

A transparent test rig was manufactured that held the sample rollers on both ends. The samples were exposed to a salt fog for two cycles comprising of 24 h with and 24 h without salt fog (pH=6.85±0.35) each at 35°C±1°C.

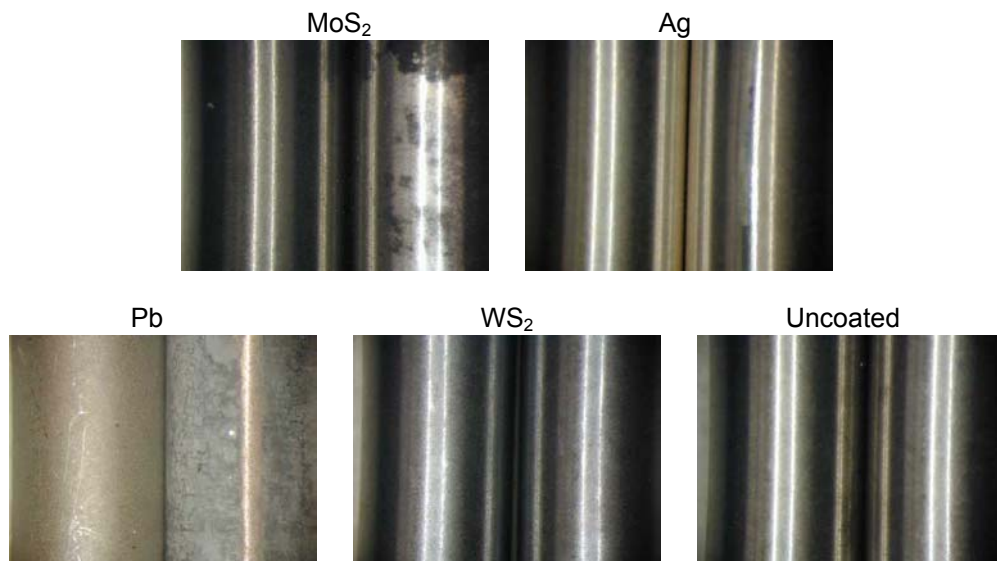


Figure 2. Salt Fog Test Results

In Figure 2, the results of the environmental tests are shown. The pictures show magnifications of two roller surfaces of each candidate of un-tested rollers (left roller surface in each picture) and tested rollers after exposure to the environmental test (right roller surface in each picture):

A visual examination showed the following results:

- | | |
|---|--|
| - MoS ₂ on "Cronidur 30" (upper row left): | Massive removal of the lubrication layer. |
| - Ag on "Cronidur 30" (upper row right): | Undistorted Ag covered surfaces kept unimpaired. |
| - Pb on "Cronidur 30" (lower row left): | Formation of a lead salt layer. |
| - WS ₂ on "Cronidur 30" (lower row middle): | No visible degradations. |
| - Uncoated witness sample of "Cronidur 30" (lower row right): | No visible degradations. |

For this reason, the MoS₂ coating was not an option for the gimbal lubrication.

To gather information about galvanic corrosion, the test was performed on samples with distorted coatings. The upper end of the rollers kept uncoated to simulate a distortion of the coating.



Figure 3. Salt Fog Test Results of Samples With Distorted Coatings

In Figure 3, the test specimens are shown after the performance of the test. Two samples of each kind are shown in the picture: 2x MoS₂, 2x Ag, 2x Pb, 2x WS₂, and 2x uncoated samples of "Cronidur 30" (from left to right).

Surprisingly the silver-coated samples showed indications of severe galvanic corrosion in combination with the "Cronidur 30".

XRF examinations were performed by ESTL to verify this result. One of the results was that the XRF of the red colored areas of the silver coated samples suggested a slightly higher concentration of iron. This result confirmed that galvanic corrosion has occurred. For this reason, the silver coating was not an option for the gimbal lubrication.

The XRF examination of the lead coated sample showed that still enough lead was present to provide lubrication. As lead salt itself is soft and will be cracked up and embedded between the remaining lead no negative impact on the lubrication effect is to be expected.

Besides the environmental loads on the tribological system, there are demands on the friction coefficient and the load capability to be satisfied. For both remaining candidates, WS₂ and lead literature describes sufficiently low friction coefficients for the intended operation profile as well for operation in air as in vacuum. Further investigations on the WS₂ showed that the coating is not appropriate at the high Hertzian pressures that occur in the gimbal bearings in the light of the bearing life time requirements.

Result and Outlook

The result of this investigation and the test campaign was that only the sputtered lead coating showed the potential to act as lubricant for the gimbal bearings. This selection is based on:

- The proven compatibility of the lead coating with the environmental loads, as concerns our specific application.
- The known and demonstrated excellent performance of a lead coating under high mechanical surface pressures and under oscillatory motion [2].
- The vast heritage of the standard sputtering lead coating process by ESTL (European Space Tribology Laboratory, UK).
- The lead's compatibility to oxygen. If oxidation should occur a lead-oxide layer is formed which encapsulates the underlying lead. This lead oxide itself has lubricating properties and acts as lubricant itself. Moreover the thickness of the oxide layer (about 20nm) is small compared to the coating thickness.

Currently the qualification of the coating (performed by ESTL) and manufacturing of the bearings for the first 4 gimbal models (performed by FAG) is under way and representative friction measurements are planned beginning of August 2004.

These friction measurements will include investigations on the impact of oxygen, life time behaviour of the coating, and overload testing of the bearings.

Conclusion

Based on investigations of a variety of lubrication alternatives showed that for the specific application on the gimbal requiring survival under high Hertzian contact stresses and high resistance to environmental impacts it was determined that lead lubrication performs best on the "Cronidur 30" substrate.

In contrast to the expectations that

- Silver coatings which is widely used on conventional bearing steels on space application would perform in an excellent manner, and that
- "Cronidur 30" material is fully resistant to corrosion

It turned out that

- Silver coating on a "Cronidur 30" substrate leads to severe galvanic corrosion problems
- Severe corrosion effects can occur under certain circumstances even though "Cronidur 30" steel has excellent corrosion resistance compared to other bearing steels.

References

1. Trojahn, W. et al. "Progress in Bearing Performance of Advanced Nitrogen Alloyed Stainless Steel, Cronidur 30." *Presented at the 5th International ASTM Symposium on Bearing Steels, New Orleans, Louisiana, USA - Nov. 19-21, 1996*
2. N.N. "Space Tribology Handbook, 3rd Edition." *AEA Technology plc - ESTL Cheshire, UK, 2002*

Remark

Ariane 5 is an ESA program, managed by CNES, prime contractor of VINCI is SNECMA.

The Integration of a Load Limiter to an Orbiter Over-Center Mechanism

Adam Gilmore* and Tim Rupp*

Abstract

This paper summarizes the design process used to relieve the predicted high loads on a Space Shuttle Orbiter mechanism prior to the STS-112 flight. The overloading of the mechanism was due to a dynamic response between the orbiter and payload that was specific to this payload's mass and attachment scheme. A solution was devised by adding a component that prevented overload of the mechanism. In addition, the introduction of the new component neither interfered with the normal operation nor required extra-vehicular activity from a crewmember. By utilizing rapid prototyping technology, engineers were able to verify clearances and feasibility while preparing to build the flight hardware. This design solution was successfully flown on STS-112 and STS-113.

Introduction

The Shuttle Remote Manipulator System (SRMS) (also known as the Shuttle Robotic Arm) is located and stowed on the port sill of the payload bay for orbiter launch and landing (Figure 1). The SRMS is used to deploy satellites into orbit or move and attach segments to the International Space Station. The SRMS is supported by four Manipulator Positioning Mechanisms (MPMs), which rotate the SRMS inboard to enable closure of the payload bay doors (stowed configuration) and outboard to allow clearance for the removal of payloads from the orbiter (deployed configuration).

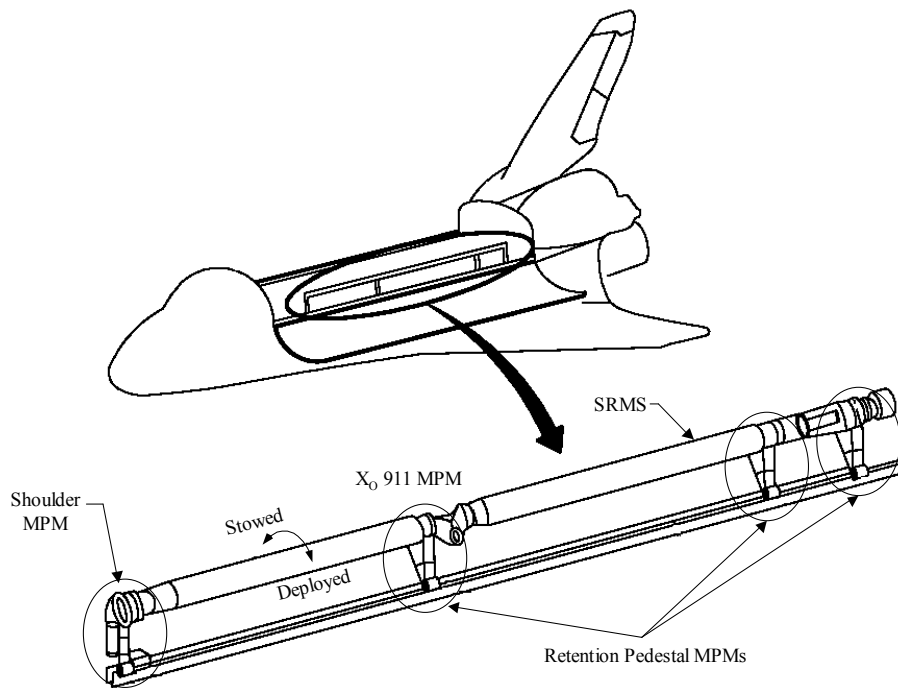


Figure 1. SRMS and X₀911 MPM Location

* NASA Johnson Space Center, Houston, TX

Problem Description

Prior to the launch of the S1 Truss (STS-112, October 2002), unusually high loads were predicted in the X₀911 MPM due to the S1 Truss mass and unique attachment scheme using a dual keel Orbiter interface. As a result of the Solid Rocket Booster ignition overpressure and dynamic response between the S1 Truss and the Orbiter, a low frequency structural mode was excited in the SRMS. This mode, in turn, was predicted to cause a deflection in the X₀911 MPM that would overload and fail an internal MPM splined shaft (Figure 2). Because the MPM is an over-center mechanism, launch loads drive the mechanism further over center, thus increasing the splined shaft loads.

While there were many technical challenges associated with this problem, schedule was also important. Implementing a solution that would ensure a safe flight was of the utmost importance; however, the Orbiter was already at the launch pad and the S1 Truss could not be installed until this problem was addressed.

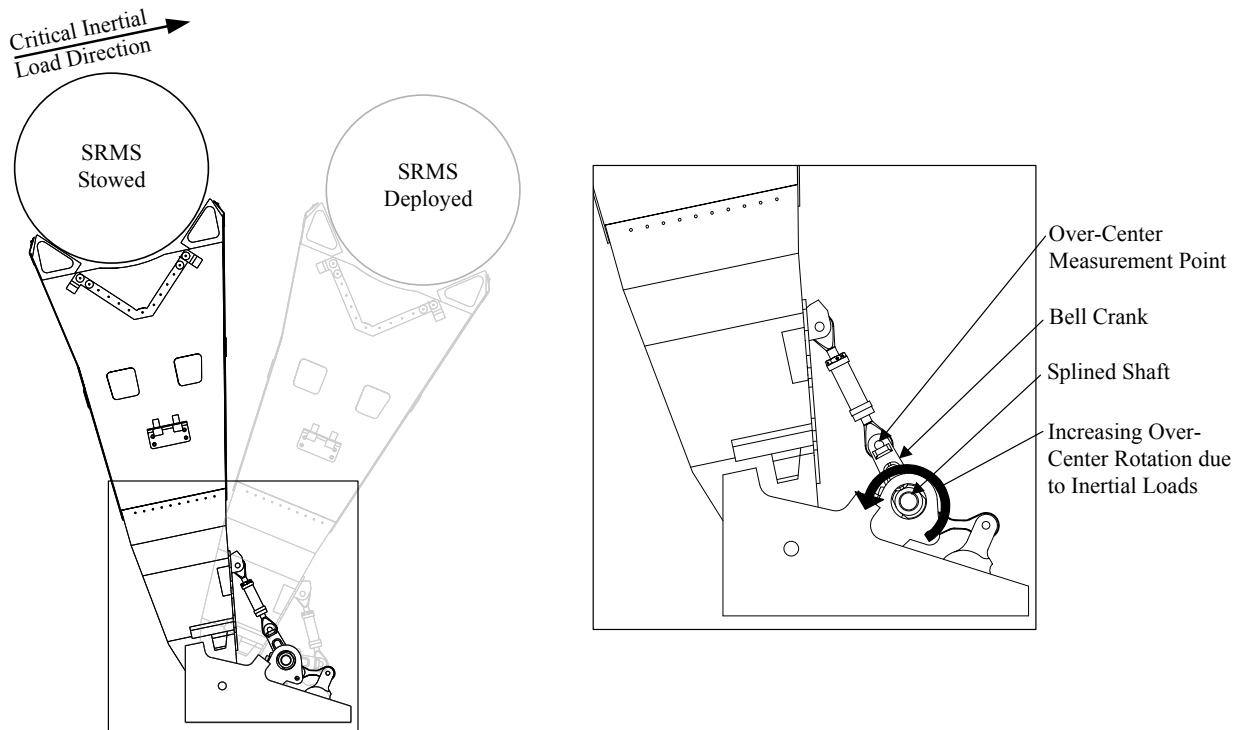


Figure 2. View Looking Aft with Load Applied to X₀911 MPM in Stowed Position

Solution Description

The solution involved devising a means of limiting the deflection in the MPM, thus preventing overload in the splined shaft. There were several constraints that had to be addressed in designing this solution: no permanent modifications were to be performed on existing orbiter hardware, interference with the function of the mechanism was prohibited, it had to be assembled on the launch pad, and the solution had to be designed and installed within a ten day schedule.

The design of a two-part assembly, named the Splined Shaft Load Limiter (SSLL), satisfied all the aforementioned requirements. The assembly, which sandwiched an existing MPM component, was located using existing MPM features and mechanically fastened together. The primary locating features on the MPM were lightening pockets on the Bell Crank (Figure 3). Matching protrusions were created on

the SSL to provide proper alignment. These protrusions also provided a shear reaction point on each half of the SSL. The features that actually limit MPM rotation, thus relieving splined shaft loads, were the lower legs that are shown below. The lower legs contact the MPM pedestal (Figure 4) when the loads in the splined shaft approach its operational limit. As the mechanism starts to structurally overload the splined shaft, the legs contact the MPM Pedestal creating an alternate load path.

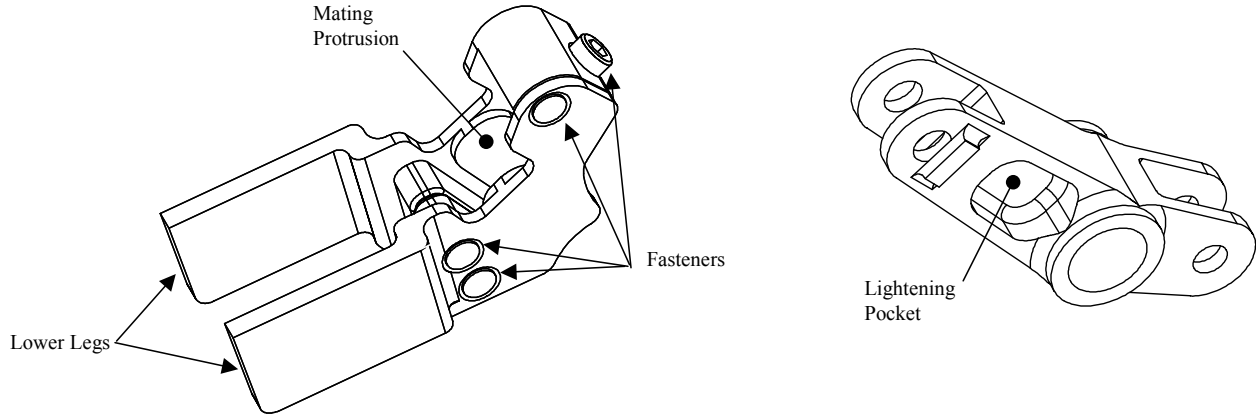


Figure 3. SSL (Left) and MPM Bell Crank (Right)

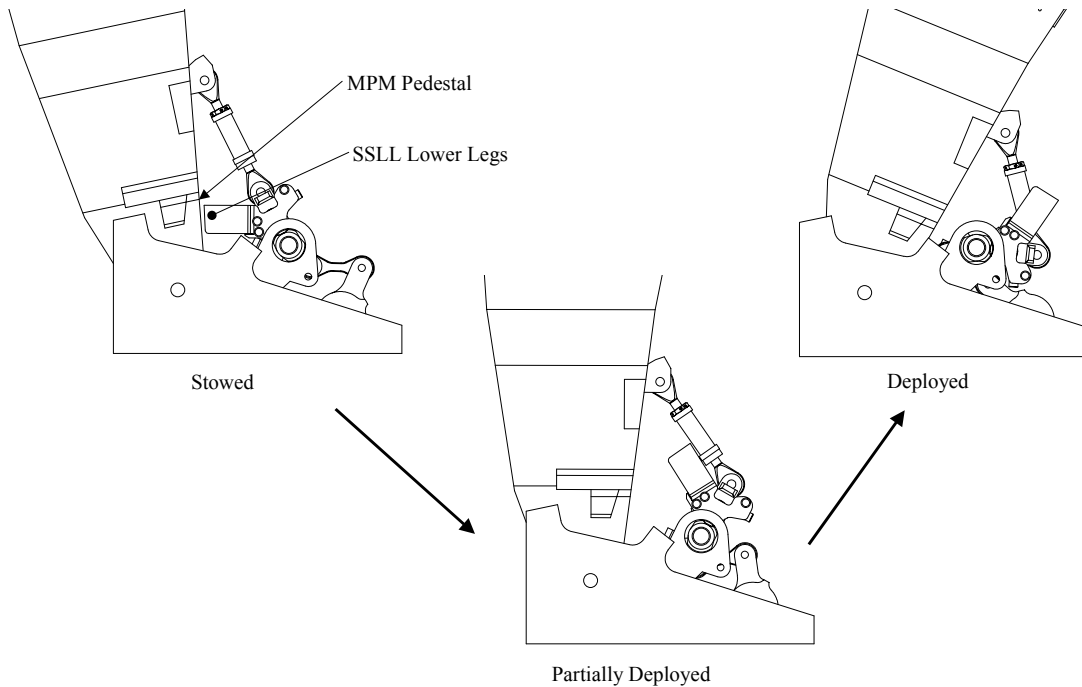


Figure 4. Sequential MPM Deployment referencing Figure 2 Detail View

During the design process, kinematic modeling and rapid prototyping were used to optimize the design and streamline the installation. To ensure that interferences were eliminated, a kinematic model was built to examine the MPM through its full range of motion. The results of the model are shown in Figure 4 with clearances verified in the stowed through deployed position. Rapid prototyping was used to create full

scale, high-fidelity plastic parts that were used in fit checks on other Orbiters, to verify the ease of installation, and to create installation procedures. The critical features on the prototypes were manufactured within 0.25 mm (0.010 in) of their theoretical values. The information obtained through the use of rapid prototypes provided valuable information that was incorporated into the final design of the SSSL. The SSSL was successfully flown on STS-112 and subsequently, on STS-113 due to payload similarities.

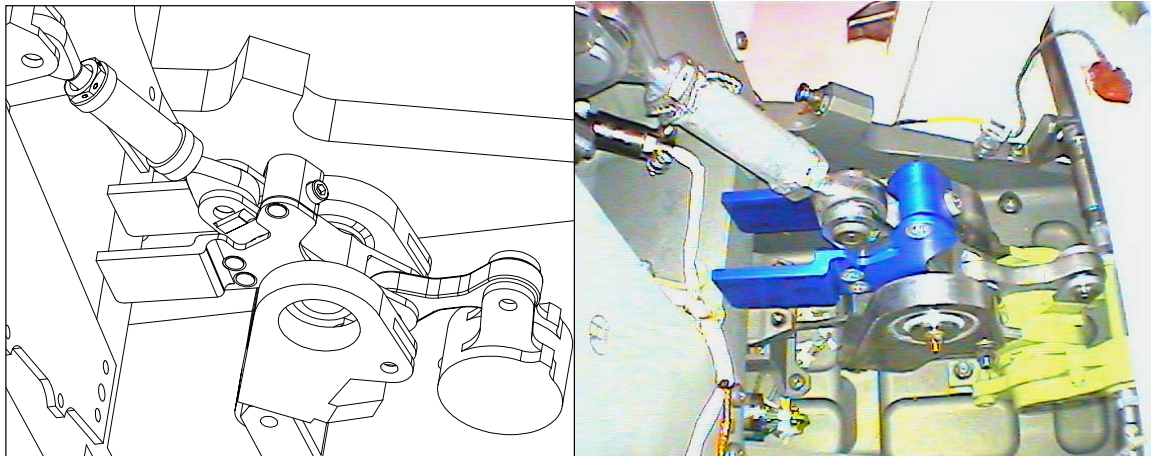


Figure 5. Isometric View of Model (left) and SSSL Installed for STS-112 (right)

Lessons Learned

Installation procedures for complex mechanisms are often difficult to determine in a timely manner with common solid modeling practices. In this case, rapid prototyping was used to create full-scale plastic parts that not only helped create installation procedures, but also verified assembly clearances. The MPM was operated through its full range of motion with a prototype of the SSSL installed; this allowed engineers to check for interferences while technicians rehearsed installation procedures.

For this design process, existing features on an MPM component were used to locate the new hardware. In designing the first version of the SSSL, engineers overlooked a subtle drawing revision on this particular feature. The use of rapid prototypes provided immediate feedback to correct the SSSL design with minimal cost and no schedule impact.

Conclusion

This design process provides a good model for maintaining a critical schedule and minimizing design risks. The use of a high fidelity kinematic model and a rapid prototyping process contributed to a design that increased the load carrying capability of the over-center mechanism with no impact to the launch schedule. At the time this paper was written, the SSSL had successfully flown on two separate missions (STS-112 and STS-113).

Minimizing Torque Disturbance of Stepper Motors

Jim Sprunck*

Abstract

As the resolution of space-borne instruments improves, the stability of the satellite platform becomes more critical. While the attitude control system is paramount in providing this stability it does have finite ability to reject external torques and forces imparted to the spacecraft. This has translated to demanding requirements for low disturbance mechanisms. Starsys has successfully employed microstepping techniques in moving mechanisms to reduce disturbance levels. This allows smooth motion to be achieved using stepper motors and avoids the need for high cost brushless D.C. servo systems. This paper discusses the key aspects of system, component and test design for microstepping systems.

Introduction

Historically, many spacecraft mechanisms have been designed using stepper motors. Stepper motors provide a simple means of controlling both position and rate without complex closed loop control. However, as platform stability has become more critical, the torque impulses resulting from incremental motion of a stepper motor can be unacceptable in some applications. This results in a need for an alternate control scheme for stepper motors that can limit torque reactions.

The solution is to employ commercial microstepping technology. Microstepping techniques have long been used in commercial applications where low cost motion control is required. Microstepping allows relatively coarse stepper motors to be operated with very fine step resolution. A secondary benefit in the commercial system is the smoothness of operation resulting from the reduced step size. It is this characteristic that has been exploited in spacecraft mechanisms to reduce torque disturbance.

When designing a system using microstepping it is important to note the differences between this approach and standard stepper motor system design. This technology has unique characteristics and inherent limitations that must be considered in the design process. The motivation for this paper is to summarize these characteristics and limitations as a reference for microstepping system design.

Theory of Operation

The basis for microstepping is based in the fundamental theory of stepper motor operation. A modern stepper motor employs both rotating and stationary magnetic fields.¹ The rotating field is generated by permanent magnets installed on a rotor assembly. The stationary field is generated by a wound stator assembly. The stator is wound in multiple phases with each winding phase corresponding to a specific electromechanical phase angle. By selectively exciting one or more stator phases, an electromagnetic field is generated at a specific angle. Unrestrained, the rotor rotates to align its field with that of the stator. Further rotation is produced by sequentially exciting the individual motor phases. In each case the rotor rotates to maintain alignment with the generated field so long as applied torques and commanded speeds are within the capability of the motor.

The typical excitation scheme used with a stepper motor advances the motor in incremental steps from one detent position to the next. Using microstepping it is possible to position the rotor to some finite

* Starsys Research Corporation, Boulder, CO

¹ The term modern is used here to differentiate both permanent magnet and hybrid motors from variable reluctance motors that generate no internal field. As variable reluctance motors are extremely size and weight inefficient, they are rarely and perhaps never used in space applications.

number of sub-increments between detent positions. This is achieved by simultaneously exciting two or more stator phases to generate an electromagnetic field at a desired angle. The angle of the generated field is controlled by the relative amplitudes of the excitation signals applied to each winding phase. The vector sum of the excitation signals dictate the effective angle of the resultant magnetic field.

The excitation applied to each winding is a quantized sinusoid. Each quantum level of the sinusoid corresponds to a unique excitation state for the motor. The size of a single microstep is determined by the number of excitation states per inherent step of the motor. In an ideal system, the step increments are uniform and the microstep size is equal to the motor step angle divided by the number of states per step.

System Design

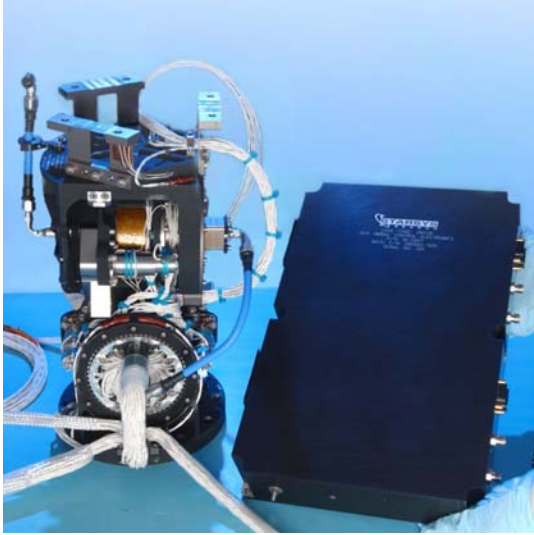


Figure 1. Low disturbance Deep Impact antenna pointing gimbal

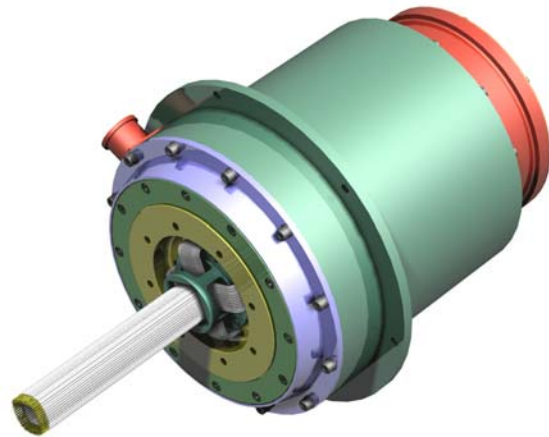


Figure 2. NPP solar array drive with ultra quiet slip ring assembly

The design of the microstepping system starts with accurate performance estimates to determine key requirements for motor, mechanism and drive electronics. The necessary performance estimates are made by constructing a high-fidelity computer simulation model. This model includes representations for the motor, motor driver and mechanical system. The motor driver generates quantized sinusoidal excitation signals, the motor produces torque in response to the excitation, and the structural model responds to the applied torque. The result from this simulation is a time domain estimate for torque disturbances resulting from the input motion profile.

In many applications the ultimate torque disturbance requirements are derived from rate and pointing errors imparted to the spacecraft. To determine these errors it is necessary to translate the disturbance torque back to the spacecraft through the transfer function of the attitude control system. As such, further processing of the simulation data is required to obtain frequency domain data. Generally, the time domain data obtained through simulation is converted to the frequency domain through a fast Fourier transform. The output frequency domain data is passed through the transfer function to determine the resultant pointing and rate errors.

Motor Design

The stepper motors used in microstepping applications can be of either permanent magnet or hybrid² design. However, in each case it is important to specify key motor parameters to improve the

² Hybrid motors use a single permanent magnet oriented axially to magnetize end caps with small teeth machined along the circumference. They are referred to as hybrids as they combine both permanent magnet and variable reluctance technology in the design.

performance of the microstepping system. The key characteristics of the motor that affect microstepping performance are the back EMF profile and detent torque.

The ideal back EMF profile for a microstepping system is sinusoidal with low harmonic distortion. Having a sinusoidal back EMF profile insures accurate incremental motion with quantized sinusoidal excitation. With permanent magnet motors the quality of sinusoidal profile is primarily controlled by the width of the individual magnet poles on the rotor. For hybrid stepper motors, the back EMF profile is controlled by the tooth geometry of both rotor and stator.

Minimizing detent torque is also critical for extreme low torque disturbance applications. Applied torques to stepper motors result in some finite deflection of the motor shaft resulting from the effective compliance of the energized motor. This is also true for motors used in microstepping systems. When the motor is subject to the sinusoidal detent torque during operation, the output is perturbed and velocity jitter results. These small variations in velocity and associated accelerations produce torque disturbance.

In low disturbance applications, the detent torque of the motor is minimized. This does reduce the unpowered holding torque of the mechanical system but this is the compromise required if disturbance torque is critical. The detent in the stepper motor is controlled through the stator geometry. Like a typical servo motor, the stator slots are skewed to minimize magnetic detent.

Motor Driver Design

The function of the motor driver in a microstepping system is to generate quantized sinusoidal excitation signals. The typical motor used in microstepping applications is a two phase motor requiring a bipolar two phase driver. Three phase motors can also be used in microstepping applications but the electronic control is slightly more complex. The basic architecture of a microstepping motor driver is illustrated in Figure 3.

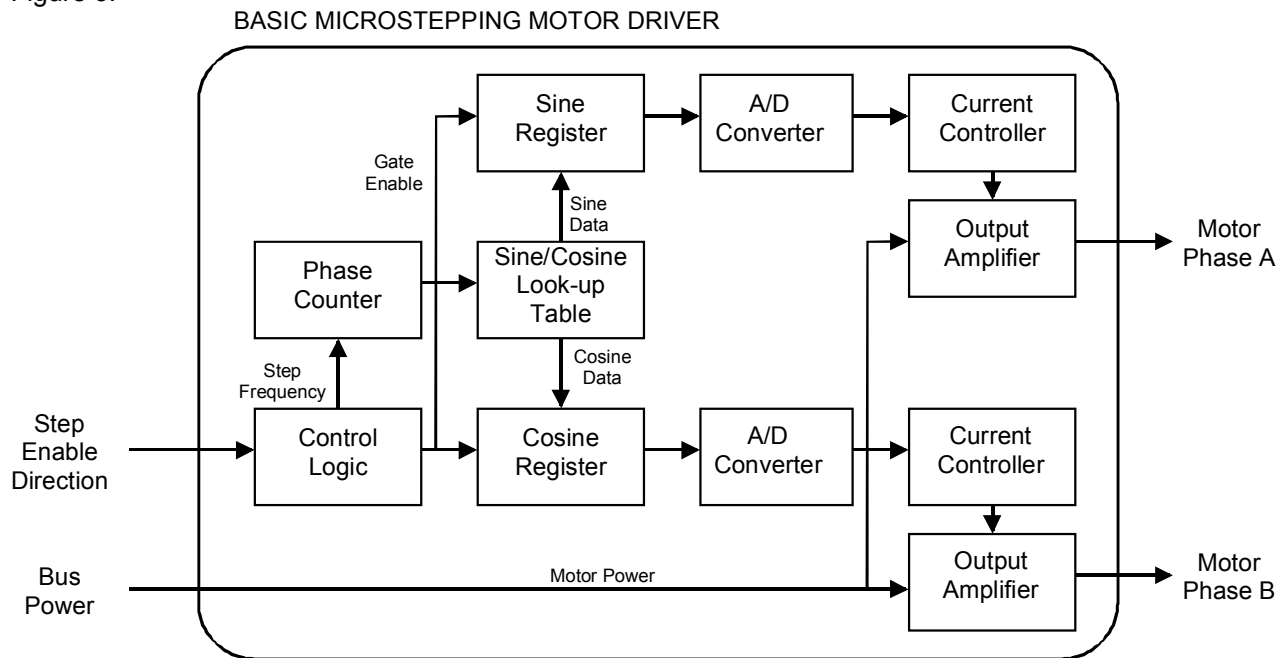


Figure 3. Block diagram of basic microstepping motor driver

As the focus of this paper is on the overall electromechanical system, the details of the electronic design are not discussed. However, the selection between voltage mode and current mode operation are relevant and are presented.

Like all stepper motors used in spacecraft applications, the selection between current mode and voltage mode control is critical. Voltage mode control is the simplest and requires the least electronics. However, when operating in voltage mode the motor performance is subject to significant variation resulting from bus voltage fluctuation and temperature sensitivity of the winding resistance. As motor torque is ultimately controlled by current, changes in voltage and resistance will directly affect motor current and output torque.

Current mode control is typically preferred in precision systems as the effect of external variables is reduced. This does come at the expense of more complex electronics. In standard stepper motor applications, simple current mode control can be implemented using peak current control. Using this scheme the motor current is allowed to ramp up to a preset threshold and then modulated³ to maintain the peak current level.

Unfortunately, peak current control does not lend itself well to high performance microstepping systems. This is an artifact of the relatively poor dynamic range offered by peak current control. Dynamic range is a measure the ability to maintain control accuracy over a broad range. Controlling peak current is complicated by the switching noise associated with the current feedback signal. At smaller signal levels the noise becomes more significant than the underlying feedback signal and it is impossible to extract the actual peak current level. This limits the achievable dynamic range. This is not desired in microstepping applications as the entire profile of the sinusoidal excitation signals should be accurately generated.

As such, average current control is preferred for microstepping applications. Using average current control, the transients in the current feedback signal are heavily attenuated with a multi-pole low pass filter. While the switching noise still corrupts the feedback signal, the effect is minimized as the desired signal level is increased. This is due to the fact that the entire motor current is being measured as opposed to just the peak.

Mechanism Design

The mechanism design for the low torque disturbance applications is also critical. As the microstepping system is inherently open loop, the mechanism must operate quietly and smoothly. The microstepping control scheme does not compensate for output motion error and cannot attenuate external sources of mechanical noise. The key aspects to mechanism design for these applications are stiffness, zero backlash, and smoothness.

Determining the appropriate mechanism stiffness is critical for proper system operation. The mechanism stiffness must be matched to the system inertia to control resonate frequencies. The resultant amplification from resonant modes can significantly increase resultant torque disturbances. In most systems designed to date, harmonic drive gearing has been used to achieve the desired stiffness. Attention also has to be paid to the structural elements within the mechanism to insure the desired system stiffness is not degraded by any component in the stiffness path.

The harmonic drive also provides zero backlash, another key mechanism design requirement for microstepping applications. Backlash effects system performance by creating a region of relatively low stiffness and damping. Any perturbations imparted to the system can result in oscillatory motion within the backlash region. Furthermore, this motion can produce torque impulses each time the backlash region is traversed.

Smoothness, often associated with servo mechanism design, is also important in microstepping applications. Smooth mechanism operation is characterized by low friction and relatively constant resisting torques. Mechanism smoothness can be the limiting variable when designing a microstepping system. Mechanical noise can excite structural modes that can allow minor noise levels to produce

³ In motor drivers, modulation refers to the pulse width modulation or the process of switching the excitation on and off at a high frequency to control the effective voltage applied to the motor.

significant vibration. Mechanical noise in these systems is minimized by controlling bearing cleanliness and preload. Close attention is also paid to harmonic drive interfaces. Proper run-in and cleaning are critical for smooth transmission operation.

System Operation

Operation of the microstepping system is different from operation of a standard stepper motor. Particular attention must be paid to construction of the output motion profile. The profile should be smooth and avoid unnecessary accelerations. This is primarily dependent on how speed change is commanded. As step frequency is typically controlled by discrete values, each speed change results in an instantaneous change in step frequency. The magnitude of this frequency change determines the magnitude of the resultant disturbance torque. Typically, the acceptable magnitude for any discrete frequency change is determined through system simulations and later verified by test.

Additionally, the system must be operated consistent with the inherent limitations of the microstepping system. The limitations that must be considered when operating the microstepping system are summarized below.

- During operation the motor must be continuously energized to maintain the sub-incremental position. If power is removed, the motor will settle to the nearest stable detent position
- As the unpowered holding torque of the system is reduced to minimize disturbance torques, precautions must be taken when operating in a 1-g environment. Typically this requires power to be maintained so long as the mechanism is maintained outside of a gravity neutral position.
- As the motor will settle to an inherent detent position when power is removed, the motor must be commanded in increments of the inherent step angle of the motor. This allows power to be removed without disturbing motor position.
- As the above constraints require the motor to be energized for longer periods relative to a standard stepper system, power consumption and heat dissipation are elevated in a microstepping system. This can limit the achievable operational duty cycle.

Test Design

The disturbance levels achievable with a microstepping system are extremely low, on the order of 10 - 100 micro-g's. Measuring torques and forces at these levels is a challenge. The key requirements for the test fixture design are sensor sensitivity and stiffness. Sensor sensitivity must be sufficient to measure torques in the 0.1 in-oz range across a typical frequency range of 0.1 Hz to 500 Hz. Also the fixture stiffness must be sufficient to achieve a natural frequency outside the frequency bands of interest.

To satisfy these design requirements an instrumented hexapod is employed. Each strut of the hexapod contains a quartz force sensor. The dynamic range of the force sensors is 1 to 300 Hz. While the sensor range does not meet the overall measurement goals, it has been previously demonstrated that the data is sufficient to characterize system performance. The data collected from the hexapod struts does require post processing to translate the measured strut forces back to torques and forces along six degrees of freedom in an orthogonal coordinate system. A Matlab script is used to perform this operation as well as the required FFT to generate the frequency domain data required for compliance verification.

During testing, the system is operated on a vibration isolation table in an acoustically quiet room. At these measurement levels both seismic and acoustic noise are significant. The measured noise threshold for this system was 10 micro-g's. Given these constraints, it is not possible to verify disturbance levels in either thermal or vacuum conditions. The data collected under ambient conditions is used to generally confirm overall system operation.

Test Results

The highest fidelity testing performed to date was on the Deep Impact antenna pointing gimbal. In this test, the disturbance torques from the mechanism were measured while the gimbal was performing the

basic motion profile required for the mission. During this test, time domain data was collected at various points while the mechanism was moving at different speeds.

In general, the measured disturbance torques did correlate to analytical predictions however there were some notable exceptions. Some significant disturbance was observed at the first resonant frequency of the system. The analytical model did not predict this well but this may be attributed to the relatively low order model used for the structure. The suspicion was that parasitic mechanical noise was exciting the structural resonance, however, this remains unconfirmed. Several tests were performed in an attempt to avoid exciting the structure but some residual disturbance remained. While this disturbance was outside the specification at that particular frequency, further analysis at the spacecraft level determined that the resultant pointing and rate errors were within established budgets.

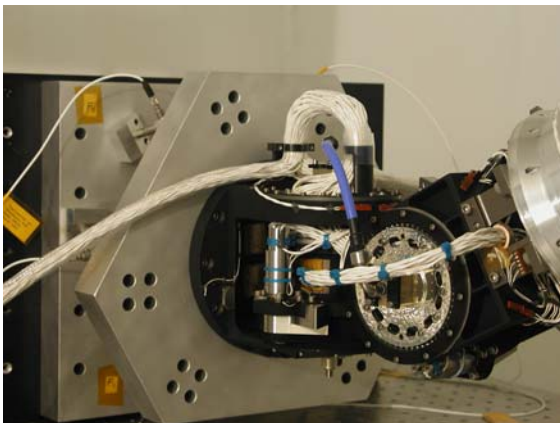


Figure 5. Deep Impact antenna gimbal installed in instrumented hexapod.

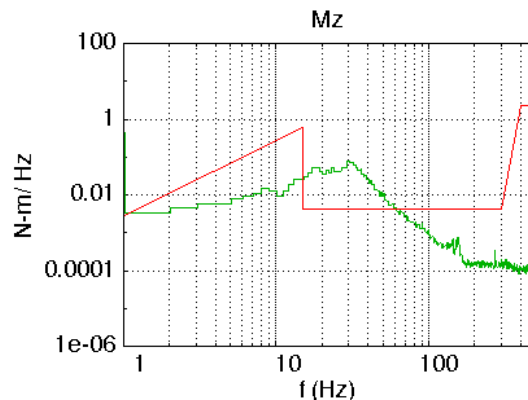


Figure 4. Typical disturbance torque results from Deep Impact tests.

Conclusions

From this development experience it has been demonstrated that microstepping systems are a viable option for low torque disturbance applications. It has also been learned that numerous aspects of electromechanical design must be considered for proper system operation. Specifically, the lessons learned in the work to date are summarized below.

- Accurate system modeling is critical for determining design requirements for the motor, motor driver and mechanism.
- Low harmonic distortion of the motor back EMF is important for obtaining uniform micro-step increments.
- Minimizing motor detent is required to achieve low disturbance levels.
- Well controlled performance is best achieved using average current control for the motor excitation.
- Mechanism should be designed for high stiffness, zero backlash and smooth operation.
- Motion profile needs to be constructed in a manner to limit maximum instantaneous changes in step frequency.
- Operation of the microstepping system needs to accommodate the inherent limitations of the technology.
- Test fixture should be sufficiently stiff to preclude amplification of structural modes.
- Parasitic mechanical noise can be significant when extremely low disturbance torques and forces are required.

SARA[®]21 - A New Rotary Actuator for Space Applications

Olivier Secheresse^{*}, Laurent Cadiergues^{**} and Julien Rabin⁺

Abstract

SNECMA MOTEURS and CNES have recently qualified a new rotary actuator called SARA[®]21, intended for fine orientation of space mechanisms. This SARA[®]21 is a very small, light and compact actuator designed around a new super-flat CSD 20-160 harmonic drive. Its optimized and robust design allows for great performance such as sustaining high loads and rotating into position with an extreme precision of 0.00625°. All characteristics, from lifetime functional behavior to strength against mission environments like launch vibrations, were demonstrated with margins during the 2003 qualification test program. The investigation described in this paper confirmed the good behavior of the SARA[®]21 components.

Introduction

For many years, SNECMA MOTEURS has developed Solar Array Drive Mechanisms for spacecraft, and more than 40 satellites and space vehicles are now equipped with SNECMA SADM products. This past and present experience has borne fruit to a new product called SARA[®]21. In association with CNES who co-funded the program, SNECMA MOTEURS has designed, developed and qualified a highly efficient rotary actuator for space mechanisms.

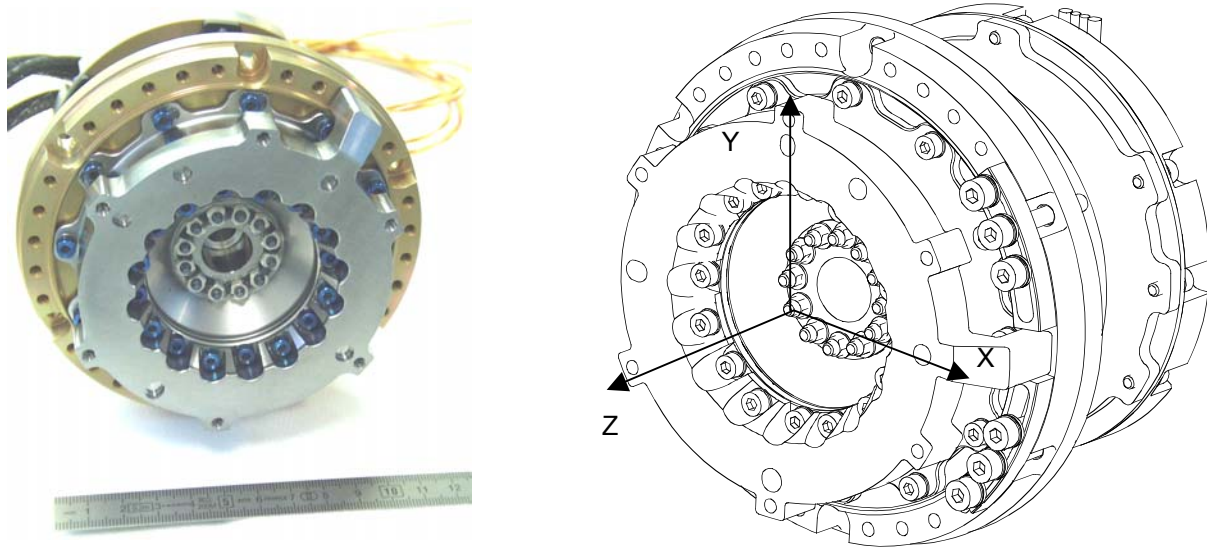


Figure 1. SARA[®]21 rotary actuator

It can be used for one or multiple-axis rotating mechanisms, such as for antenna accurate orientation, solar array deployment, or other specific applications. Its design has been highly optimized to minimize mass and increase compactness, mainly with the use of the new CSD 20-160 super flat Harmonic Drive component.

^{*} SNECMA Motors, D.M.S. – D.P.E.S., Villaroche Nord, France

^{**} CNES, Toulouse, France

⁺ ACSIENCE, Paris, France

Its performance has been thoroughly checked during a extensive qualification tests during 2003 that covered mostly functional, environmental and lifetime tests. The investigation performed has allowed control of the state of the new harmonic drive. Four flight models have already been delivered to our first customer ALCATEL SPACE for a scheduled launch date in 2004.

The SARA[®]21 function, design, performances and qualification test results are discussed more in detail hereafter.

Design Description

SARA[®]21 rotary actuator is intended for space mechanisms orientation as well as providing the associated positioning signal with extreme precision to the spacecraft on-board electronics. The SARA[®]21 main functions are:

- sustaining the mechanism: the actuator is able to withstand high loads and can absorb important environments throughout all lifetime phases, and in particular throughout orbit transfer phases
- rotating the mechanism: the actuator can rotate either in forward or reverse directions, and motion is not limited to a restricted angular zone. Rotation is also regular and highly precise, each step being equal to 0.00625°. Finally, it can operate over a great speed range.
- measuring the mechanism position: measurement is ensured by potentiometers that detect each motor step.

While fulfilling those required functions of the rotary actuator, providing low weight and compactness has been one of the major guidelines for designing the SARA[®]21. On the basis of its experience on SEPTA mechanisms, SNECMA MOTEURS has therefore chosen the CSD 20-160 Harmonic Drive as one of the key components of the rotary actuator. This element manufactured by Harmonic Drive[®] is composed of:

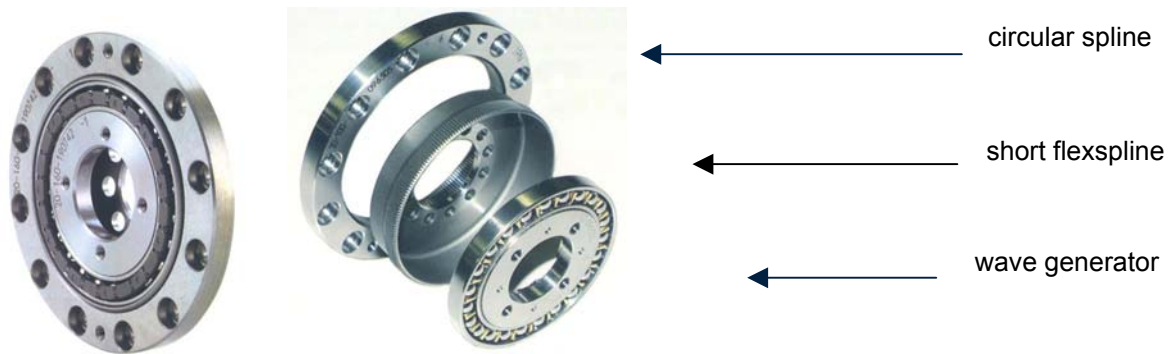


Figure 2. SARA[®]21 CSD 20-160 Super Flat Harmonic Drive

- a wave generator: a thin-raced ball bearing fitted out an elliptic plug serving as a high efficiency torque converter
- a circular spline: a solid steel ring with internal teeth
- a short flexspline: a flexible cylinder with external teeth and a flanged mounting ring

The complete element is a super-flat (type-20) harmonic drive gear box allowing a 160-reduction ratio. Its very small dimensions and high performances have allowed SNECMA MOTEURS to develop an optimized design for the SARA[®]21 in its entirety.

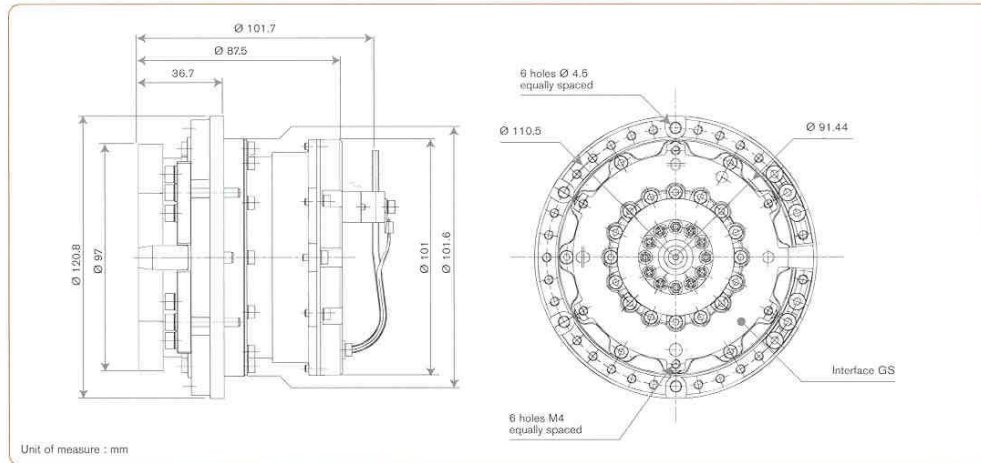


Figure 3. SARA[®] 21 mechanical interface

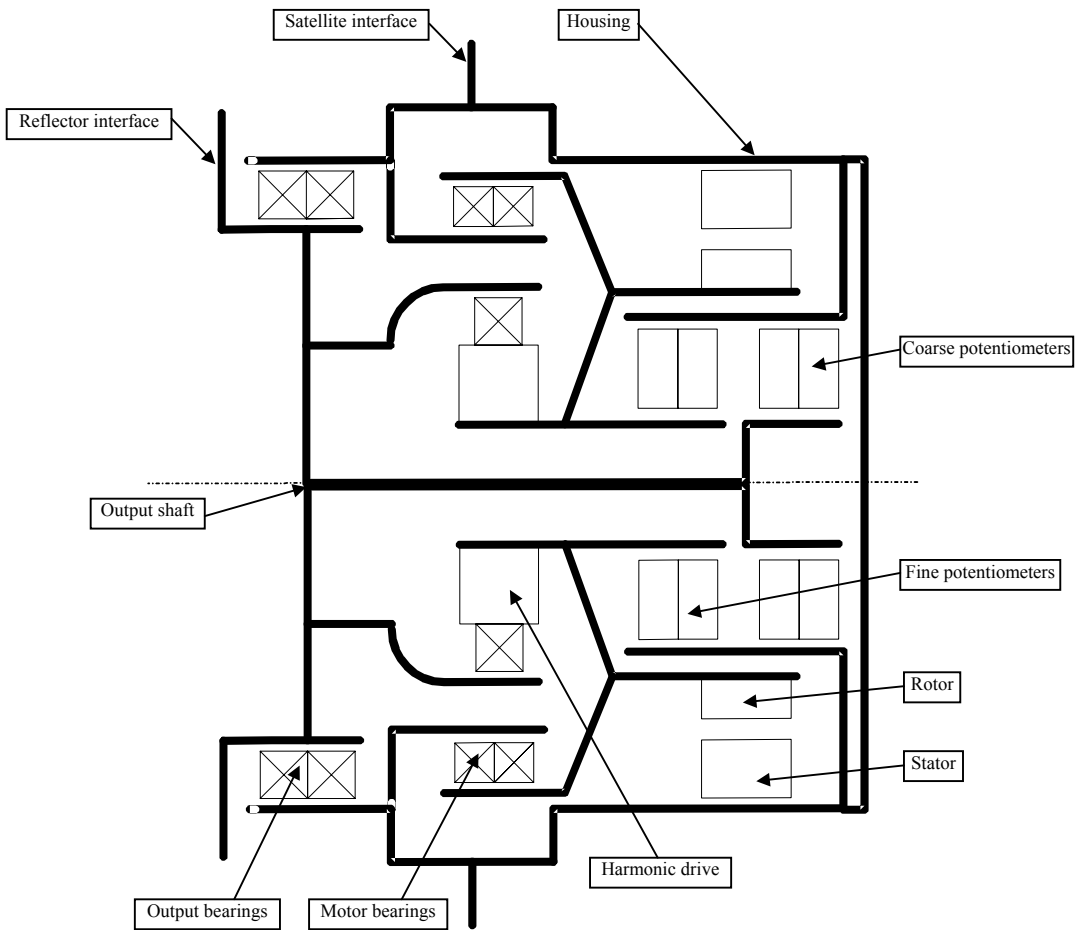


Figure 4. SARA[®] 21 kinematic scheme

The other key components of the rotary actuator are:

- a two-phase permanent-magnet stepper motor with redundant stator windings that provides 360 steps of 1° per turn under 76 Ω. It is commanded simply by step-to-step mode, voltage-regulated (± 26 V) or current-regulated modes.
- duplex bearings that are lubricated and rigidly preloaded in order to give the SARA a great tolerance both to thermal gradients and vibration loads
- two fine and two coarse potentiometers (main and redundant) that provides a instantaneous measurement of the output flange angular position. The fine potentiometers are able to detect each motor steps, while the coarse potentiometers give non-ambiguous indication of which revolution the associated fine is on. Both fine and coarse have a full course of 357° (3° dead zone only).
- a housing that is composed of an aluminum alloy satellite interface, a titanium part that is glued the stator motor, an aluminum flange that the wires go through
- a titanium reflector interface

All are reliable components and some have even proven their efficiency on previous SEPTA® SNECMA MOTEURS mechanisms with very close configurations, such as the stepper motor (in its 285 Ω form), super duplex bearings and potentiometers.

Performance

The most important performance requirements for which the SARA®21 has been designed are:

Table 1. SARA®21 Performance

SPECIFICATION	UNIT	BASIS	DATA
Motor step angle	°	standard	1
Harmonic drive ratio	-	standard	160
Output step angle	°	standard	0.00625
Steps / revolution	-	standard	57600
Output shaft speed	step/s	maximal	200
	°/s	maximal	1.25
Axial stiffness	10 ⁶ N/m	maximal	300
Radial stiffness	10 ⁶ N/m	maximal	150
Bending angular stiffness	m.N/rad	maximal	50000
Torsion stiffness	m.N/rad	min / max	13000 / 25000
Axial load capability	N	maximal	10000
Radial load capability	N	maximal	8000
Flexion load capability	m.N	maximal	200
Power consumption (under 26 V)	W	nominal	10
Inertia capability	Kg.m ²	maximal	200
Output torque	m.N	nominal	45
Holding torque	m.N	nominal	70
Detente torque	m.N	nominal	8
Non operating temperature	°C	min / max	-100 / + 100
Turn-on temperature	°C	min / max	-65 / + 95
Operating temperature	°C	min / max	-50 / + 85
Total mass	kg	nominal	1.8

Qualification Campaign

The SARA[®]21 has recently achieved an extensive qualification campaign during which the performances detailed above were verified and associated margins established with regards to our first customer ALCATEL SPACE operational requirements and specified environment conditions.

Following is a brief description of the most important tests the SARA[®]21 Qualification Model (QM) went through.

Functional tests

- Power consumption control
- Electrical controls: potentiometers or motor winding resistance and insulation
- Accuracy and output step size control + hysteresis / repeatability and linearity control
- Torque capability control
- Stiffness control (axial / radial / bending / torsion measurements) + combined loading tests

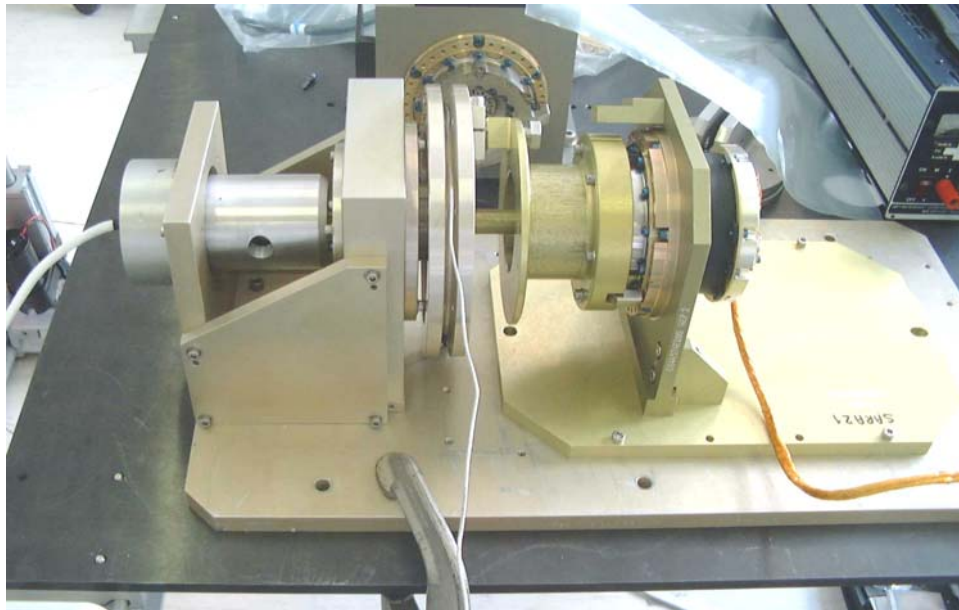


Figure 5. SARA[®] 21 functional test set-up

Environmental tests

- Vibration tests: sine and random vibrations were performed along all three axes for 6 minutes, as well as torsion load vibrations along X-axis (Figures 6 and 7). The QM survived the vibrations with all frequencies superior to 385 Hz when vibrated with a 3-kg yoke mass.

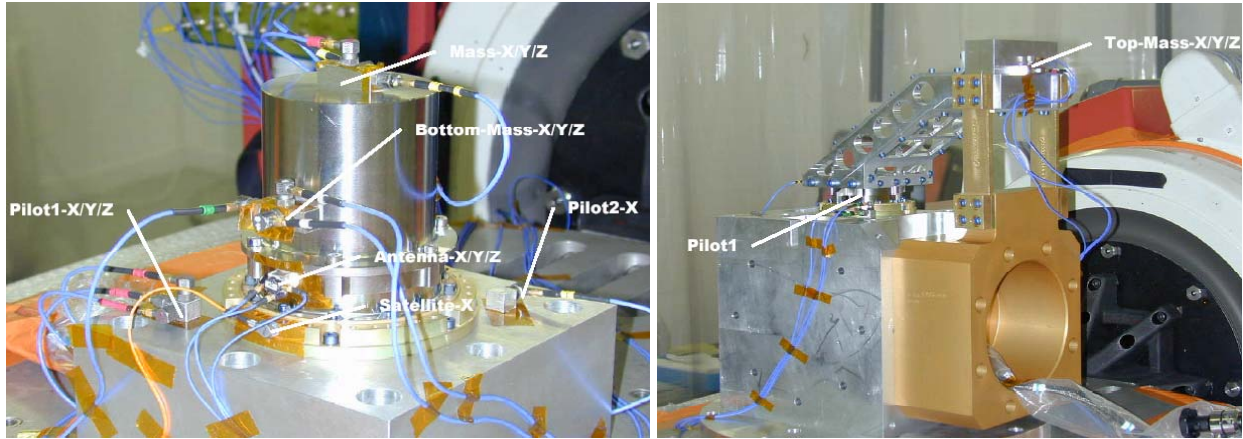


Figure 6. SARA[®] 21 vibration test set-ups (centered mass for sine and random + deported mass for torsion load)

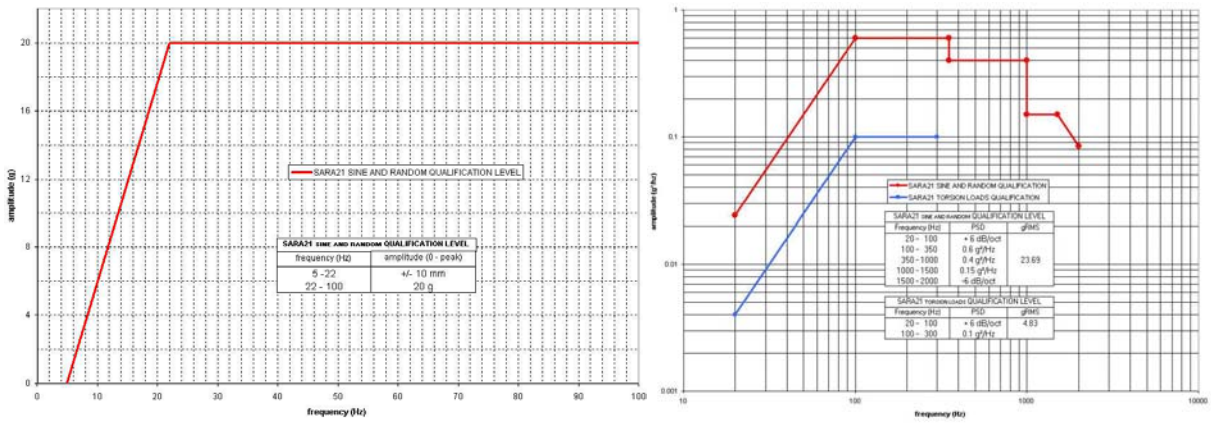


Figure 7. SARA[®] 21 sine and random vibrations levels

- Shock test: Pyrotechnic shocks were simulated along all three axes at the levels shown in Figure 8. The QM survived those shocks without failure; performances were nominal after the tests.

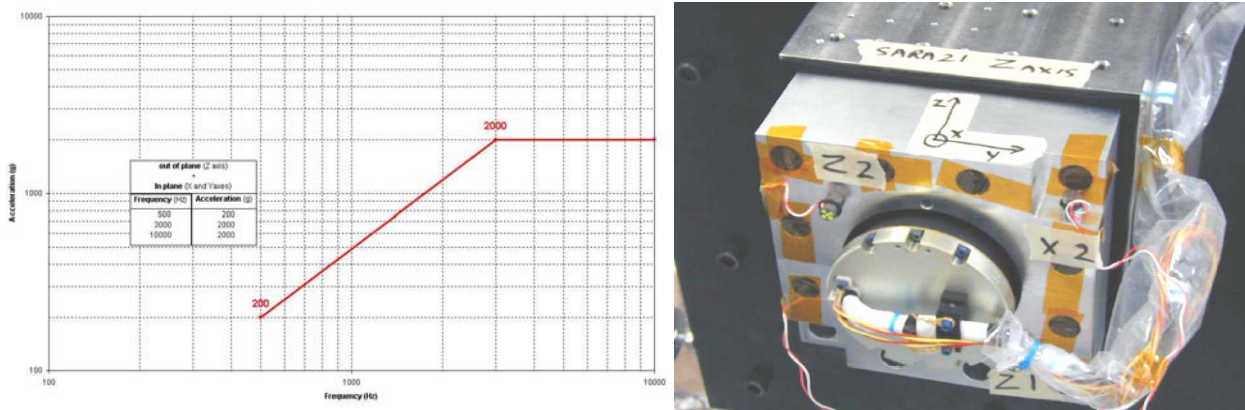


Figure 8. SARA[®] 21 shock level and test set-up

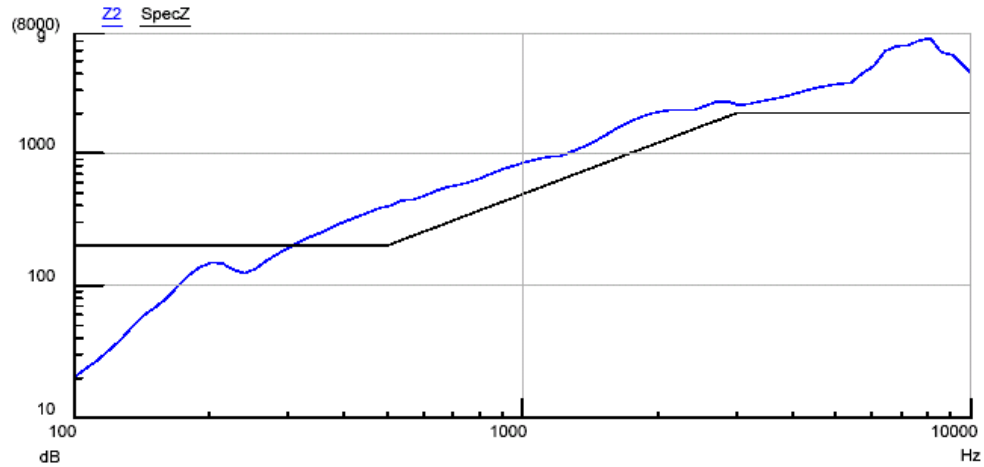


Figure 9. SARA® 21 shock response spectrum along Z-axis

Thermal tests: Thermal tests were performed in ambient and vacuum conditions at the temperature levels given in Table 1. The QM survived those thermal cycles nominally. Temperature did not over pass 100°C for the housing and interfaces, nor 120°C for the winding. Regular functional tests such as power consumption controls, motorization margins and motor capability tests, were performed without detection of any degradation.



Figure 10. SARA® 21 thermal vacuum life test set-up

Lifetime test

Lifetime test were performed in various thermal and vacuum conditions:

- ambient conditions cycles : 75 complete revolutions
75 cycles on 4°
1500 cycles on 0.2°
- vacuum conditions cycles : 20 complete revolutions
750 cycles on 4° (250 at 85°C, 250 at -50°C, 250 at 20°C)
975 cycles on 18° (325 at 85°C, 325 at -50°C, 325 at 20°C)
75000 cycles on 0.2° (25000 at 85°C, 25000 at -50°C, 25000 at 20°C)
- additional vacuum cycles : 50000 cycles on 0.2° at 20°C
20 cycles on 13.5° at 20°C

The second vacuum cycles were performed in addition to the scheduled qualification tests in order to gain more confidence within the SARA[®]21 by proving very comfortable lifetime margins.

Investigation

After completing the tests, an investigation was initiated to analyze the condition of the various components of the SARA[®]21 QM after completing the qualification tests.

The mechanical parts show very good condition after the qualification tests with only very slight fretting traces apparent upon some parts because of qualification vibration levels.

The harmonic drive has been fully disassembled and inspected. The lubricant was still present in nominal quantity without any specific marks, evolutions or loss. The geometry of the different parts was nominal without traces of load damage or degradations.

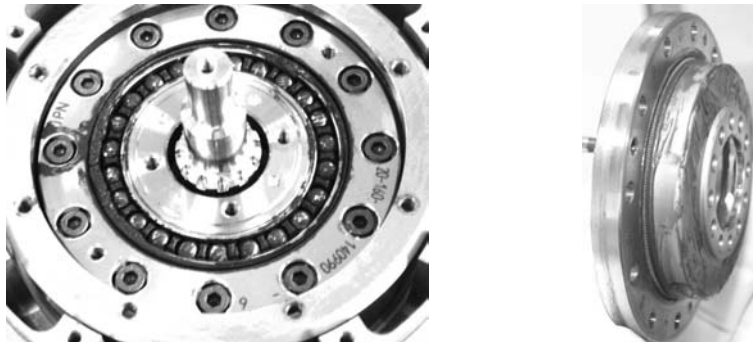


Figure 11. SARA[®]21 QM CSD 20-160 Harmonic Drive after qualification tests

This demonstrates the ability of the new CSD 20-160 Harmonic Drive to sustain very high loads with margin. Therefore, this component is very attractive for space mechanisms with a very precise position of the three harmonic drive parts (given by the bearings) and with a good lubricant.

The stepper motor was controlled and is fully operational with its nominal performance.

The potentiometers were checked too; only some slight marks were present on the tracks due to vibration loads for coarse potentiometers (local marks) and due to extended lifetime for fine potentiometers (circular marks). In each case, wear of the track / cursor was nominal without impact on signal.

Conclusion

The SARA[®]21 ability to sustain and position a reflector with extreme precision was demonstrated throughout a complete qualification test program during which all of a standard mission phases were taken into account to establish the environment conditions and levels of the tests.

The SARA[®]21 performance results were as expected and the investigation that followed on the qualification model has confirmed its small and compact design has been correctly sized.

Models are now ready to be integrated upon spacecrafts, and will soon be flight proven.

Rolamite Joints for Spacecraft Subsystem Vibration Isolation

Gregory A. Compton* and Matthew M. Botke*

Abstract

A one-degree of freedom joint with unique performance requirements has been designed and built for use in a passive isolation system for structurally-connected deployable spacecraft subsystems. Using a Rolamite approach, a nearly frictionless and zero spring rate hinged joint can be achieved that is capable of passing significant electrical power and data harnessing. Implementing a Rolamite joint in a system design with requirements typical of spaceflight must be accomplished in a very judicious fashion in order to maintain the expected performance benefits. The following describes the design progression, trades and lessons learned in developing and building this mechanism.

Introduction

Rolamite describes a class of single degree of freedom (DOF) hinges with kinematics similar to a gear pair, zero backlash, ideally zero spring rate and very low friction. Joints of this type are comprised of two flexible elements (tapes or cables) arranged in opposing serpentine fashion around a pair of cylinders in rolling contact. Figure 1 illustrates the elements of a Rolamite joint. The unstrained free state of each tape is straight. The tape routing enforces joint kinematics and maintains constant stored strain energy in the system. The need for a zero-spring-rate, low-friction hinge had been identified as the functional element of a passive vibration isolator for structurally connected spacecraft subsystems such as solar arrays and reflectors that have high mass properties relative to the host. The isolation system is illustrated in Figure 2. A chain of six near frictionless and zero-spring-rate joints is arranged to yield full relative mobility between the subsystem and host. By eliminating sources of energy storage and dissipation, the only transmitted forces are those due to the inertial forces (D'Alembert forces) of the isolation system itself. Therefore, induced jitter on and agility of the host is decoupled from the subsystem mass properties and becomes solely dependant on isolation system dynamics and operation.

Since the ideal isolation system is zero spring rate and nearly frictionless, system mass was identified as a significant performance driver early in the design. As typical spacecraft requirements were imposed on the system, achieving zero spring rate and minimizing friction became at least as important as mass properties. Implementing a Rolamite joint that is stiff in the remaining five degrees of freedom, able to be driven, locked for safe mode, and carry the required electrical harnessing while maintaining the desired performance presented many design challenges. A point design was optimized that included an assumed subsystem with mass properties and stiffness to be isolated from a typical large host bus. The first mode natural frequency of the subsystem to be isolated was used to bracket accelerations of the isolation system within an operating envelope. A system mass budget was imposed and D'Alembert forces calculated. All other contributors to transmitting loads to the host such as sources of energy storage (spring rate) and energy dissipation (friction) were limited to a fraction of the predicted D'Alembert forces.

A Rolamite joint engineering unit comprised of synchronizing tapes and harness simulators has been fabricated as a proof of concept and is currently under test. The design trades and lessons learned are presented in this discussion.

* ABLE Engineering, Goleta, CA

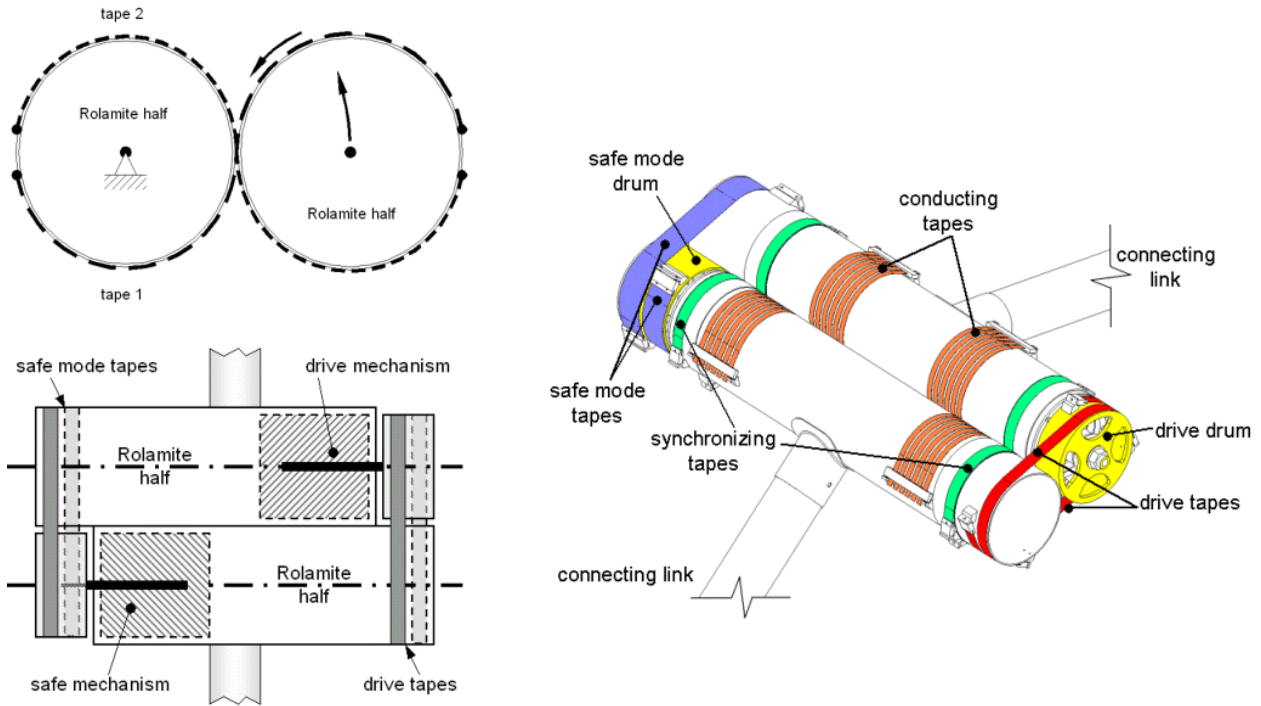


Figure 1: Rolamite Joint

Background

As the relative mass properties of mechanically connected subsystems increases, the vibration-induced jitter also increases (degrading pointing accuracy), while host agility (slew rate) decreases [1]. The need for an isolation system was identified during the design of a spacecraft with aggressive pointing and agility as well as high solar-generated power requirements. The initial power requirement of the solar array was 100 kW. The predicted mass properties of the array and performance requirements of the host were the impetus behind development of the isolation system.

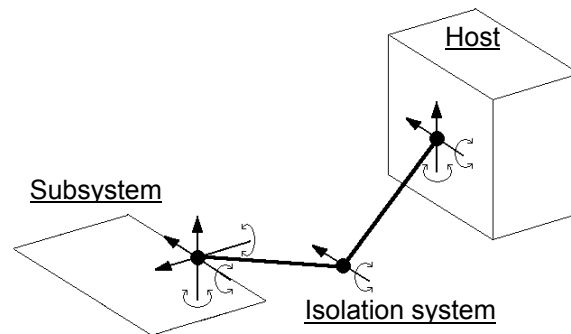


Figure 2. Isolation System Hinge Arrangement

In order to minimize the complexity of the isolation system and burden on the host, a passive system was desired. Active systems require significant engineering effort and necessarily expensive and complex components including fast control algorithms, sensors and motors. The novel approach developed in [1] has been predicted to meet isolation requirements for the point design and has potentially wide applicability for any subsystem with high mass properties relative to the host.

Several mechanisms were considered for the hinges in the system including twist capsules and slippings. In all other cases considered, either friction or spring rate were found to be difficult to mitigate early in the design process. Ideal Rolamite joints were found to meet the requirements of the system while minimizing complexity. Significant electrical power and data harnessing could be passed across the joint while maintaining the desired minimal spring rate and friction performance by routing electrical conductors in like fashion to the synchronizing tapes. Also, the incorporation of additional functionality appeared to be straightforward given the available volume within and at either end of the Rolamite cylinders.

Design

The current point design is an isolation system for a 25-kW solar array. Mass properties of the subsystem to be isolated have been assumed for a thin-film solar array with an average areal mass density of 0.25 kg/m^2 . Natural frequency estimates for the array were based on previous work as referenced in [1] for a 100-kW array and scaled accordingly. Performance requirements for the isolation system were imposed based on typical spaceflight requirements wherever applicable. Assumed requirements were imposed or derived if in the course of design, no requirements had yet been established. Assumed requirements were in many cases imposed in order to bracket the achievable performance of the isolation system in to establish the scalability of the isolation system.

Isolation system requirements relevant to joint performance include;

1. Pass power harnessing required for a 25-kW solar array operating at 300 V.
2. Pass data harnessing as typically required for a solar array.
3. Impart no more than T/n parasitic torque into the isolation system where T is the equivalent worst-case inertial force of the system transmitted to the host and n is the number of joints in the system.
4. Position the solar array and isolation system to a commanded location and orientation. Each joint must be motorized and able to be driven.
5. Transmit forces resulting from gravity gradient and solar radiation pressure to the host (to be reacted by the host attitude control system) while still isolating subsystem vibration.
6. Self-rigidize (lock) for safe mode operation. Safe mode locking must occur within 30 seconds and subsequently require no power to remain in either safe mode or normal operational mode. Safe mode loads resulting from a 0.003-g acceleration in any orientation must be reacted through the isolation system.
7. Package compactly for launch and deploy once in orbit.

Three distinct modes of operation become apparent; passive isolation, drive and safe mode. In order to accomplish all required functionality while still maintaining desired performance, additional mechanism had to be packaged within the Rolamite. Specifically, a method to drive the joint as well as a locking mechanism was required.

The design of the Rolamite progressed by investigating each functional mode required of the isolation system and subsequent joint requirements. The majority of the operational life of the isolation system is expected to be in passive isolation and therefore was investigated first. Also, adding drive and safe mode functionality was determined to be a straightforward design progression.

Passive Isolation Mode

Passive isolation mode must exhibit zero spring rate and near zero friction in the intended degree of freedom and be stiff in the remaining five degrees of freedom. Maximum parasitic torque is on the order of $1\text{E}^{-5} \text{ Nm}$. Maximum spring rate is on the order of $5\text{E}^{-6} \text{ Nm/rad}$. A Rolamite with two cylinders and two opposing serpentine tapes requires an external force to balance the resultant couple produced by the displaced lines of action of each tape (the tapes can not be routed in the same plane or pass through the same point). In order to achieve a balanced system, at least three tapes are required; two tapes straddling a center tape routed in opposite serpentine fashion. Since electrical harnessing would require significant cylinder length, two sets of synchronizing tape pairs were located at either end of the joint to enforce synchronization. The length of the Rolamite could then be scaled to accommodate harness requirements between the synchronizing tapes.

The synchronizing tapes enforce joint kinematics and result in one degree of freedom as well as one relatively low stiffness direction. As the synchronizing tapes pass from one cylinder to the next through the line of rolling contact between the cylinders, the mechanical advantage of the tapes decreases to zero to react a force through the centers of the Rolamite cylinders and acting away from the line of rolling contact (a tensile force). This low stiffness direction is addressed via the locking and safe mode mechanisms discussed later. Synchronizing tapes on the engineering unit have been fabricated using Elgiloy, a highly-processed cold rolled nickel steel with very high tensile modulus.

Since the isolation system must be repeatedly cycled, fatigue must also be considered in many aspects of the design. Electrical harnessing must be passed across the joint in similar fashion as the synchronizing tapes. In order to maintain zero spring rate and near zero friction, the electrical harnessing must remain elastic to the greatest extent possible throughout a range of strain rates and temperatures. Further, each electrical conductor must be fully insulated to prevent arcing to adjacent circuits or grounding to the structure. A composite modulus of elasticity sufficient to preclude fatigue failure and minimize viscoelastic losses became a significant design challenge. The current engineering joint hardware under test is comprised of six Kapton-laminated flex circuits using acrylic adhesive. Creep and viscoelastic loss of the acrylic at upper temperature extremes has been identified as a concern and demonstrated in the hardware. Low temperature embrittlement of cycled polymers is also a concern, but can be mitigated via active or passive thermal management. Thermal functional testing is underway on the engineering hardware to establish a data point on performance of the harnessing. Conductor material must have an infinite fatigue life while transmitting electrical power at low loss. Harness tensioning is only intended to ensure that the harness dynamics are tightly coupled to the joint and do not induce additional vibration modes of the isolation system. Harness tensioning and stiffness are therefore much lower than the synchronizing tapes and do not react external loads across the joint. Heritage conductor material such as copper is not suitable for repeated cycling even at very low loads. A Beryllium copper alloy was found that adequately met infinite fatigue life and low resistivity requirements. Additional insulating techniques are currently under investigation to minimize creep and viscoelastic loss. In order to minimize functional changes due to thermal expansion at temperature extremes, synchronizing tapes as well as harness flex circuit tapes are terminated on the Rolamite cylinders via low spring rate decoupling springs.

Drive Mode

The drive mechanism is capable of transmitting torques between the host and subsystem to react small disturbance forces as well as those required for subsystem repositioning. Solar radiation pressure and gravity gradient are sources of disturbance forces considered here and are two orders of magnitude lower than that required for subsystem repositioning. A passive dual drive mechanism has been designed that requires only one actuator.

A drive drum is located on one end of one Rolamite cylinder with tapes routed in belt drive fashion to the other Rolamite half (see Figure 1). A stepper motor is coupled to the drive drum through a very low spring rate spiral spring. The stepper motor winds the spring to achieve the desired torque, and the spring allows the joint to oscillate in vibration isolation mode without significant changes in torque thereby reacting small, nearly constant disturbance forces. A local control loop is designed to null commanded torque and measured torque at an update rate multiple times slower than the lowest natural frequency of the subsystem (for averaging). This aspect of the vibration isolation system differs from active control in that the update rate bandwidth does not scale closely with subsystem frequency and must only accommodate for relative drift between the subsystem and host.

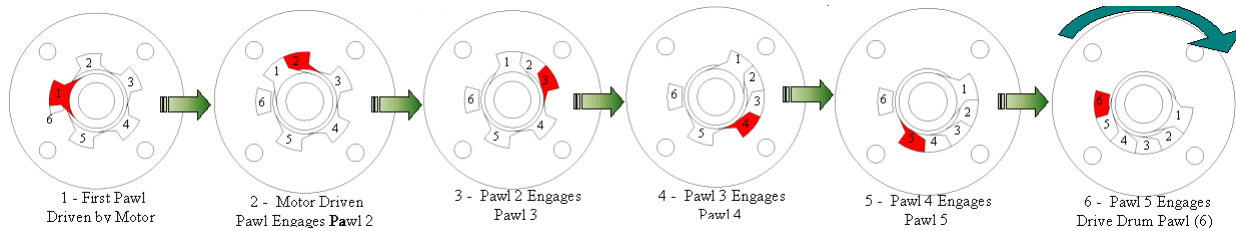


Figure 3. Two Turn Engagement Mechanism Dual Drive Mechanism

In order to engage the high torque mode of the drive mechanism, the motor becomes directly coupled (in the driven direction) to the drive drum after ± 2 revolutions from the spring free state. A passive mechanism, similar to a car odometer consists of several independent pawls mounted on a common shaft between the motor and drive drum. Each pawl enables almost one full revolution before engaging the next adjacent pawl. Two revolutions from the free state is sufficient to eliminate buckling stability concerns of the spiral spring, which is typically limited to ± 3 revolutions. After two revolutions in either direction, the motor pawl has rotated each independent pawl and engages the drive drum pawl in the direction of revolution thereby providing a direct load path. Dithering (reversing) torques are applied at a rate multiple times lower than the angular speed capability of the motor.

Safe Mode

In the event of the host spacecraft entering safe mode, each Rolamite hinge must have the ability to lock and withstand very significant moment loads, estimated to be 27 Nm for a 25-kW solar array. In order to achieve this, a mechanism was required which was capable of reacting these loads as well as remaining in either the locked or unlocked state without external power. A conventional friction brake was considered, but packaging and mass requirements eliminated this possibility. The final configuration consists of dual cam driven pawls, which engage a large internal spline with a tapered tooth profile to prevent binding. The cam profile has been designed such that any radial loads while in the locked position will be reacted through the center of rotation of the cam, reducing the possibility of torque on the spline counter rotating the cam and unintentionally disengaging the mechanism. The cam is actuated with a bi-stable rotary solenoid coupled through a torsion spring to allow full motion of the solenoid in case the pawl teeth do not initially line up with a spline. An external detent spring holds the solenoid output shaft at either extreme to meet the power-off requirement. Figure 4 illustrates the safe mode mechanism concept.

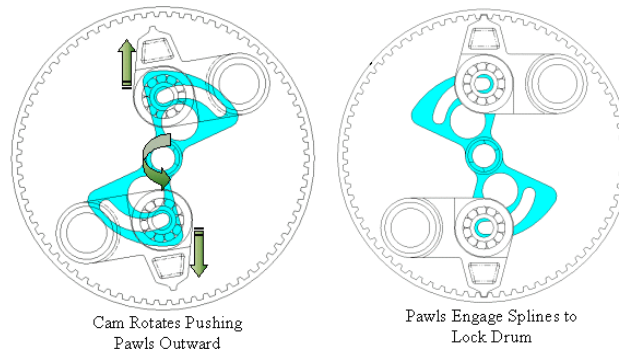


Figure 4. Safe Mode Mechanism Concept

Conclusions and Lessons Learned

The Rolamite approach has proven to be a sound fundamental mechanism for this application and preliminary hardware testing has validated this as well. Scalability and available volume for additional mechanism packaging are just as important as fundamental mechanical operation when considering an approach for a developmental application. Several related lessons have been learned so far; components normally regarded as sources of low friction can prove to be otherwise and normally acceptable manufacturing techniques and tolerance can also prove to significantly influence system performance

depending on the application. This is especially evident when designing a mechanism intended to function in distinctly different modes. Passive isolation mode requires many orders of magnitude lower parasitic torque performance than is required to be supplied in the driven or safe modes. In order to achieve required mechanism strength and stiffness while still maintaining desired performance, component selection, arrangement and manufacturing must be evaluated given the more stringent requirements.

Significant redesign and repackaging of the drive and safe mode mechanisms occurred during the course of this development effort. The first design iteration was comprised of drive and safe mode drums mounted to the Rolamite cylinders via large diameter rolling element bearings. However, the large-diameter bearings combined with the drive and safe mode tape preload resulted in an analytical model with unacceptably large friction. A more acceptable solution was found that reduced the friction to acceptable levels. The drums are currently mounted on smaller diameter shafts with higher precision bearings. One desirable/non-critical safe mode system requirement was relaxed in order to reduce required tape preload and therefore reduce bearing friction even further. The required packaging location changed for both the drive and safe mode mechanisms from each end of the Rolamite cylinder to within the cylinder itself. The repackaging was generally straightforward, but underscores the need to provide significant volume for mechanisms at the conceptual level when developing a new system.

Rolling element bearings in spaceflight mechanisms of this size are traditionally considered to contribute negligibly to overall system friction. Quantifying the total available friction budget from all components early in the design process helps to establish a valid design path and reduce the chance of necessary redesign.

Initial testing of the engineering unit has shown a preferred angular position and therefore exhibits significant spring rate. An investigation revealed that the Elgiloy tapes were slightly curved in the free state. The manufacturing process and packaging of the material is such that the tapes are cold-rolled to the desired thickness and then spooled for shipment. The rolling process imparts high surface residual stresses that lead to yielding of the material during spooling. Two opposing equally curved tapes ideally still maintain a constant strain energy state on the Rolamite. However, tapes with differences in curvature were found on the unit upon closer inspection causing the unit to seek a lowest energy state. Further yielding of the material may have been the source of the curvature difference. An alternate tape material such as 17-7 PH SS has been identified as a potentially better material choice for this application and will likely be incorporated on the next hardware build.

Small strain state differences in a tape driven system are typically not considered to significantly influence performance. In this case, a balanced strain state is critical to system functionality and therefore must be characterized early in the design process in order to bracket acceptable material choices and geometry tolerance. Flex circuit tapes of multiple conductors laminated in Kapton are often utilized across kinematic joints in order to reduce parasitic torque. Similarly constructed tapes with Beryllium-copper conductors have been designed for the Rolamite in order to pass the required power and data harnessing. Preliminary testing of the engineering unit with such tapes has indicated that even at very low strain, significant creep occurs. Visco-elastic loss testing will be performed to further quantify flex circuit performance. Alternate flex circuit designs are currently under investigation such as fiberglass lamination and direct liquid polymer coating.

In both of the above cases, requirements for each new application should be considered when designing with normally common or heritage components since past acceptable performance may not be the current case.

As is typical of spaceflight hardware development, many trades and compromises have occurred during the course of this effort in order to incorporate operational functionality. Both the drive and safe mode mechanisms were designed in order to compile the first performance estimate. Since the Rolamite joint must operate in several diverse modes, even greater scrutiny was found to be required of each component and assembly.

The lessons learned from the engineering unit have been incorporated into the current design of the Rolamite joint. A comprehensive testing program has begun at the component level and will culminate in the characterization of a fully articulated two-dimensional isolation system on an airbearing floor. Amplitude and frequency sweeps will be conducted on the 2-D isolation system in the operational envelope with resultant transmitted force at the simulated host recorded. The data will then be correlated to the analytical model. Joint performance will be evaluated both from the system as well as from component level testing.

References

1. T. Murphey, M. Botke, R. Blankenship, N. Hague, "An Articulated Motion and Vibration Isolator for Spacecraft", AIAA-2003-1829, May 2003

Free Space Optical Communications System Pointer

Mark E. Rosheim* and Gerald F. Sauter*

Abstract

Free Space Optical (FSO) communications pointing problems will be described and a solution presented. Conventional systems used in sea, land, and space are illustrated. Our integrated approach investigates three major problems areas: kinematics, structure, and dexterity. Their interrelationship will be discussed.

Introduction

FSO/RF communication systems offer the potential of much higher bandwidth, unencumbered by FCC or ITU restrictions. FSO/RF communication is also covert with low probability of intercept, jam-resistant, resistant to EMI and co-site interference, low power, low weight, small size, and low cost. FSO/RF communications systems acting as advanced, next-generation Airborne Communications Nodes also offer the potential for significant logistics savings. In Desert Storm, the deployment of Army Signal Units required 40 C-5 sorties and 24 ships. By being largely self-deployable, a UAV-based Airborne Communications Node could reduce the number of airlift sorties required for communication support by half or more.

Office of the Secretary of Defense reports that *"The key trend for future communications systems is increasing data rates brought on by migration towards higher RF frequencies and the emerging dominance of optical over RF systems. Laser-based systems will offer data rates two to three orders of magnitude greater than those of the best future systems. The advantages of optical communication were demonstrated in 1996 when a ground-based laser communication system (lasercom) provided data rates of 1.1 terabits/sec at over 80 nm [nautical mile] range. Airborne and space borne Tbps lasercom systems will certainly be possible by 2025. Although lasercom will shortly surpass RF in terms of data rate, RF will continue to dominate at the lower altitudes for some time into the future because of its better all weather capability."*

The Pointer Problem

A key component of any practical, covert laser communication system regardless of space, sea, mobile or man-portable system will be the advanced, light weight, low cost antenna pointing and tracking mechanism (Figure 1). The optical community is only beginning to look at this element of the overall problem of FSO. Such a system requires a mechanism that is (1) easily manufacturable and therefore inexpensive; and that has (2) high slew rate; (3) high accuracy; and (4) wide, singularity-free range of acquisition. Ross-Hime Designs, Inc. (RHD) believes that it has developed a new, innovative mechanism that can meet these demanding requirements. RHD proposes that a Free Space Communication System Sensor Pointer be based on the Omni-Wrist III. The Omni-Wrist III is a revolutionary, patented, low-cost, lightweight, compact, rugged, high-dexterity pointing device for space, land, and sea-based communication applications [2-5]. It is a major advancement over conventional azimuth/elevation mounts because it offers 180 degrees of unimpeded (singularity-free), hemispherical movement; low manufacturing costs; and a streamlined design integrating pivots into the body of the device. These features combine to produce a reliable, high-performance pointing device capable of greater precision than existing designs.

Ross-Hime Designs has won a NAVY SBIR Phase I for "Low Cost Submarine UAV Communication System and Data Link." According to Mark Rosheim "The key aspect of our approach will be to reduce

* Ross-Hime Designs, Inc., Minneapolis, MN

the lifecycle cost of an airborne line-of-sight TCDL data-link and increase the range of the data link to be limited only by the UAV altitude, up to a distance of 322 km (200 mi)." A bi-product of this contract is the new plastic Omni-Wrist III shown here. Benefits expected to arise from the SBIR include: high capacity multimedia data exchange, jam-resistant communication, small transmit/receive aperture, low power and weight and resistance to EMI and co-site interference.

The test and evaluation Omni-Wrist III unit (Figure 2) addresses technology gaps in existing approaches to sensor pointing. Typical precision solutions have involved the use of either a distributed axis system or a gimbal. Both of these types of conventional azimuth/elevation mounts suffer from slowed response times and/or limited range of motion, or from singularities (voids in the work envelope). The first type of design has a sensor mounted on a fork for elevation (pitch) that in turn is mounted on a rotating base for azimuth (yaw). Such a design requires the positioning of two independent systems, which increases response time by introducing unnecessary path optimization calculations into every pointing operation.

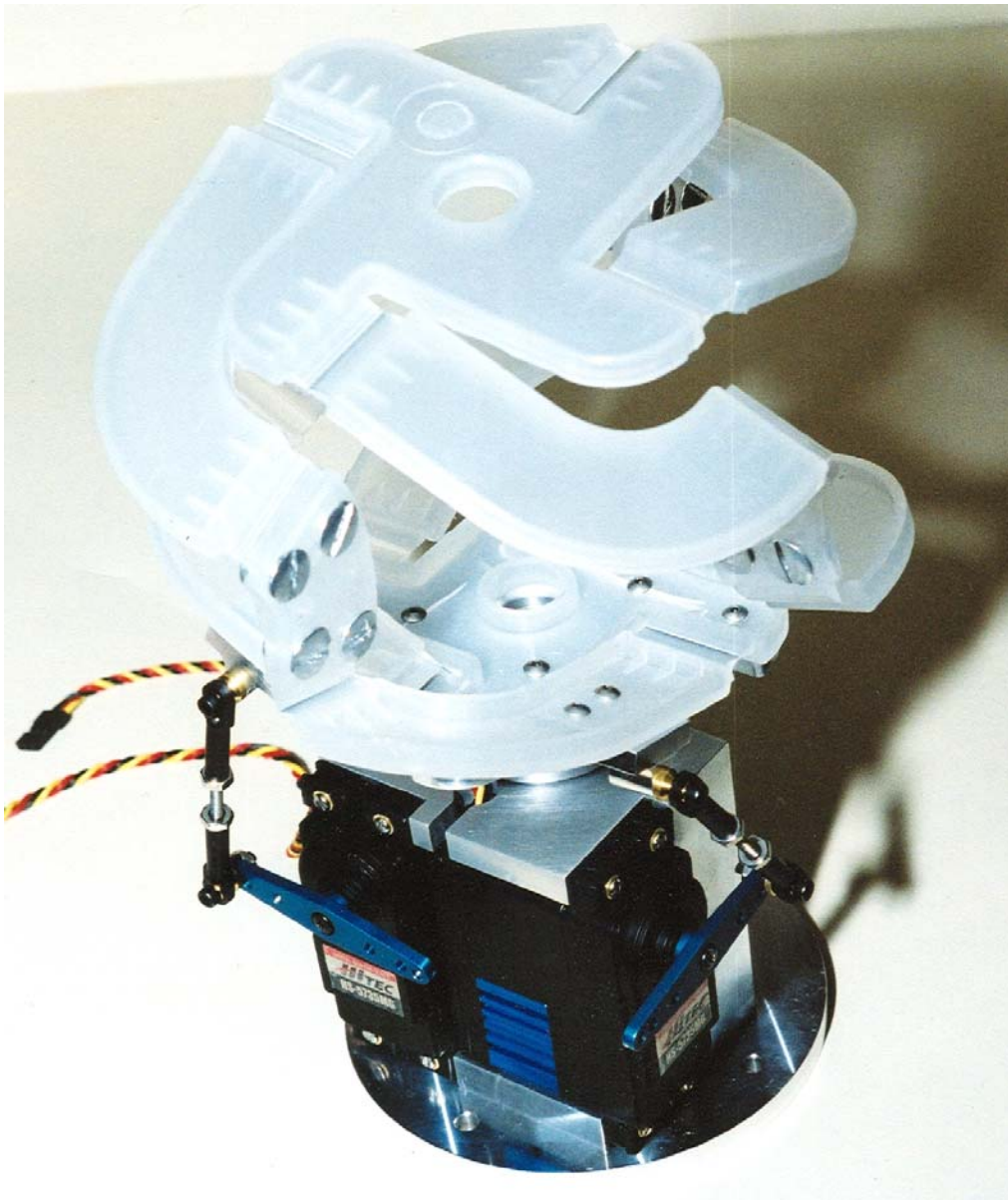


Figure 1. Advanced UAV Antenna Pointing System

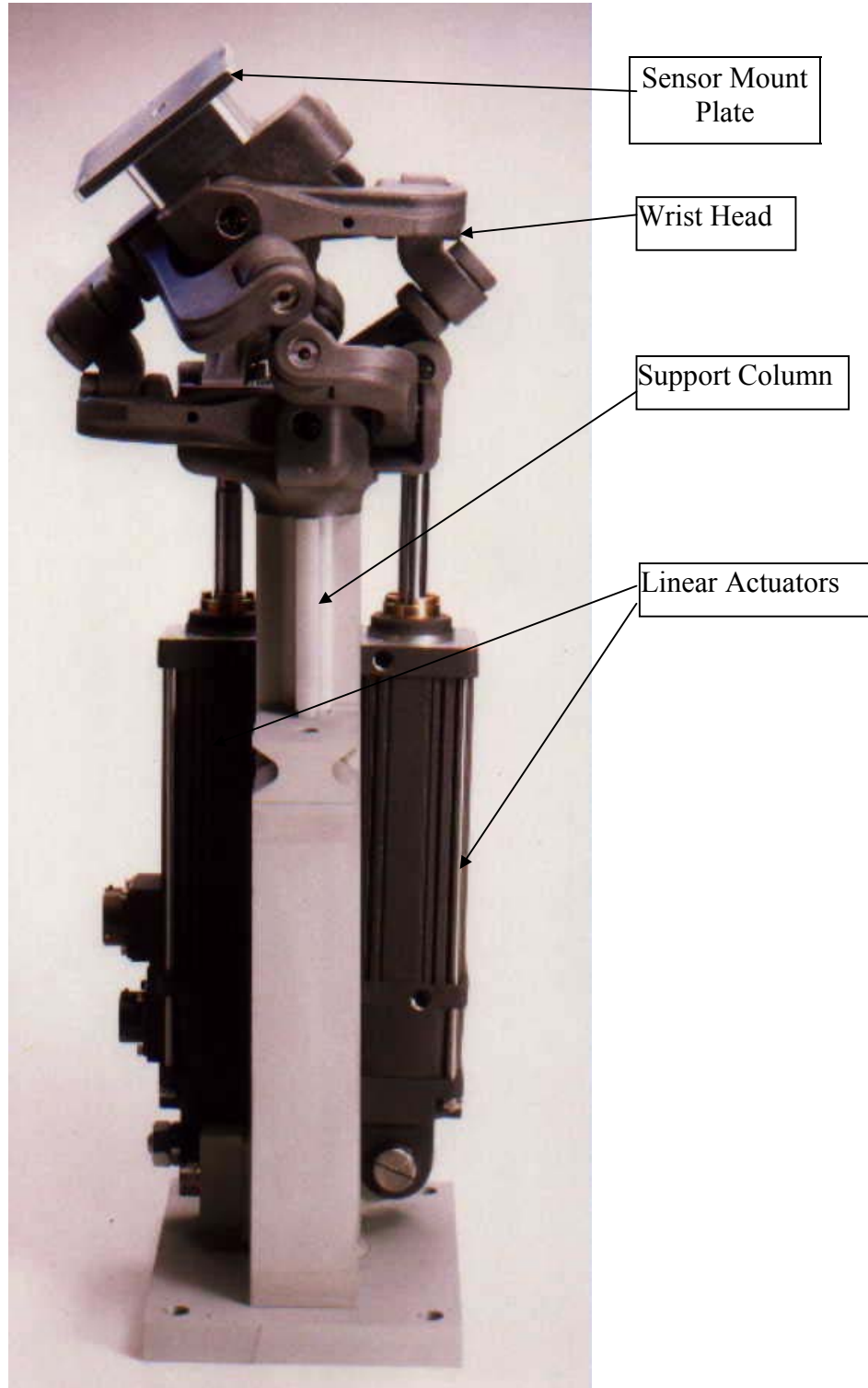


Figure 2. Omni-Wrist III Pointer

Presently two forms of precision antenna pointing systems dominate the ground-based and space-based markets (Figure 3). Schaeffer Magnetic, Inc., Chatsworth, California “Biaxial Drive” represents the most common design, also know as an azimuth and elevation or yaw-pitch type drive [6]. Schaeffer’s system is

composed of two harmonic drives powered by DC motors with redundant winding and electronics. Wiring for electronics, motors and antenna is integrated within the structure. The simple mechanical design is very stiff and rugged. Although compact and precise, within limits, this design has a singularity (it jams) when the antenna is pointed straight up. Yaw becomes roll and the resultant singularity degrades precision and complicates control. This is particularly evident when tracking high speed objects or in the case of ship pointing systems where the ship is pitching and yawing due to rough seas. Another popular packaging variation is manufactured by Wescam, Inc, Toronto, Canada this spherical sensor platform appears to be based directly on the ball turret from World War II bomber aircraft (Figure 4).

The second common antenna pointing system is represented by the “APS” manufactured by the Honeywell Space Systems Group, Phoenix, Arizona [1]. Two perpendicularly mounted actuators produce ± 110 degrees each. Singularity is mitigated when the antenna is pointing straight up because of the perpendicular orientation of the two actuators. However, singularity or gimbal lock occurs when the pointing system attempts to move in circumduction (a combination of pitch and yaw motion) at the extremes of its range of motion. Example: when the pointer is tracking along the horizon the upper actuators must toggle over each other in a saddle shaped profile making precision pointing impossible. The Honeywell design lacks stiffness because the orientation of the joints creates longer lever arms that could cause deflection under high inertia loading. As in the Schaeffer system two harmonic drives with redundant motor windings and electronic power the system. Complex flexible cables (a major design problem) are found in both designs.

KVH Industries has received a license for its sales of certain of its stabilized satellite communications antenna products that include robotic wrist actuator technology under U.S. Patent No’s. 4,723,460, 4,729,253 and 4,686,866 originated by Mark E. Rosheim.

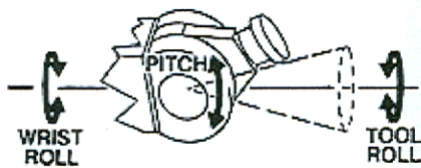


Figure 3. Schaeffer Kinematics

From the above one may conclude that aside from improvements to motor speed reducers, i.e., Harmonic Drive devices, the fundamental kinematics and structures for sensor pointers has not been advanced since W.W.II. They are still predominantly simple azimuth/elevation devices or variations on the simple gimbal. Singularity-ridden, they are unable to maintain a lock within the full hemisphere which is required for horizon-to-horizon tracking.

To answer the growing need for improved singularity-free pointers that complement the growing sophistication in optics and control, Ross-Hime Designs, Inc. sensor pointer was developed under Phase I and Phase II SBIR contracts for the Ballistic Missile Defense Organization. By way of contrast it uses a

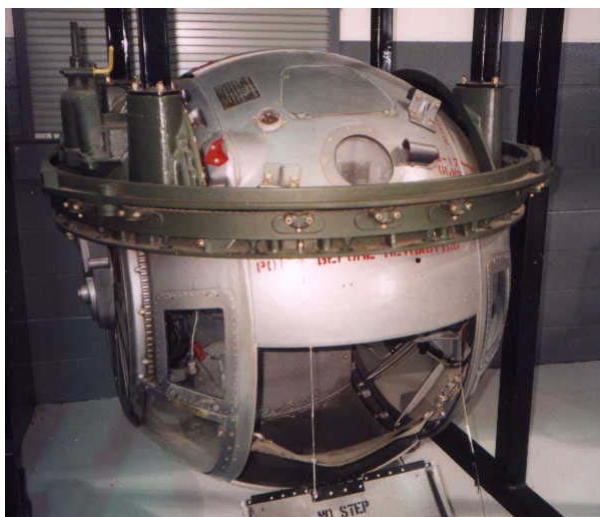


Figure 4. W.W.II Ball Turret

range of motion problem is solved by adding a second joint. Simplicity is maintained by phasing the two

joints together mechanically rather than powering each gimbal independently. What is often unappreciated by designers and engineers is the radical transformation that a gimbal must go through to achieve a perpendicular orientation of the output in any direction from the mechanism centerline. While it is common to make pointers with stock actuators and components they invariably have singularities. This is a result of either their kinematics, structure or both.

**Table 1. Preliminary Free-Space Communications
Sensor Pointer Performance Goals**

Load capacity	4.5 kg (10 lb)
Output Speed	60 deg sec
Unit weight	9.1 kg (20 lb)
Accuracy	0.06 deg > 3.6 arc minutes >216 arc seconds
Range of motion	180 degrees Hemisphere (2π steradians)
Dexterity	Singularity-Free
Construction	17-4 Stainless Steel, Engineering Plastic
Physical Envelope	Cylinder, 20.3 cm (8") Diameter X 45.7 cm (18") high

Test Results

This section presents a summary of the test results for the Omni-Wrist III Sensor Mount. A detailed report was included in a paper presented at the SPIE Conference in Seattle, July 2002 [2]. Two test methods were used to determine the pointing accuracy. A Coordinated Measuring Machine (CMM) was initially used and a second test method utilized an attached laser pointer to determine the repeatability of the pointing accuracy. In this last test, the Omni-Wrist III Sensor Mount was exercised through various deflections.

CMM Test Results

The CMM was capable of high precision measurements of any point on the Omni-Wrist III Sensor Mount. The tip of the Sensor Mount was used for these measurements. As the Sensor Mount was exercised the position of the tip was precisely determined. These positions were then compared with expected values and the various errors were calculated. The Sensor Mount was placed within the CMM and exercised at two azimuth settings, (0 and 45 degrees). At each of these positions the declination angle was changed from 0 to 81 degrees in several steps. All told there were 58 separate positions. The pointing error was less than 0.05 degree (180 arc seconds).

Laser Pointer Test Results

Figure 5 shows the Omni-Wrist III Sensor Mount attached to its mount that was anchored to the wall. A laser pointer was attached to the Sensor Mount at the center hub. The central hub also incorporated the means to attach various weights. We used regular bar bell weights for the testing. Weights of 2.1 and 2.8 (4.6 and 6.1 lb) were the primary values used.

The Omni-Wrist III Sensor Mount was exercised through many different sequences. Two home positions, (Dec = 0, Az = 0) and (Dec = 89, Az = 180) were used. The test sequences consisted of large angle deflections, small and medium angle deflections, and multiple angle movements. A weight of 2.1 kg (4.6 lb). was attached to the Sensor Mount for most of the tests. For all the tests only one of the tests produced an average repeatability error greater than the goal of 216 seconds of arc. In general the reproducibility error was less at the home position (0, 0) than at (89, 180). At (0, 0) the actuators are retracted and the Sensor Mount movements were more certain than when the actuator positions were at their extremes. Speed tests indicated that an angular deflection greater than 160 degrees/second could be accomplished - much faster than the goal of 60 degrees/second.

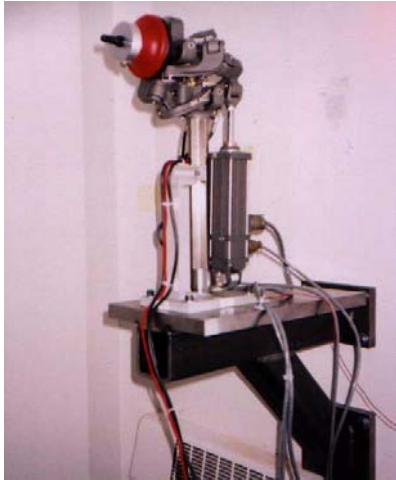


Figure 5. Omni-Wrist III Test Setup

Table II shows the positions used in the tests. Figures 6 and 7 plot the test results. Each value represents the average of at least three repetitions. Figure 8 is a plot of the resultant $[\text{SQRT}(x^2 + y^2)]$ pointing error. The median pointing error was 60.84 arc seconds.

Table II

Home Position Dec = 89; Az = 180

Test #	DEC	AZ
1	0	0
2	45	90
3	45	270
4	45	0
5	75	180
6	75	45
7	80	170
8	89	90
9	89	270
10	45	45
11	80	0
12	89	135
13	89	225
14	15	315
15	30	315
16	89	45
17	35	315
18	40	315
19	50	315
20	60	315
21	70	315
22	80	315

Home Position: Dec = 0; Az = 0

Test #	DEC	AZ
1	89	0
2	89	45
3	89	90
4	89	135
5	89	180
6	89	225
7	89	270
8	89	315
9	45	0
10	45	90
11	45	45
12	45	135
13	45	180
14	45	225
15	45	270
16	45	315
16	45	315

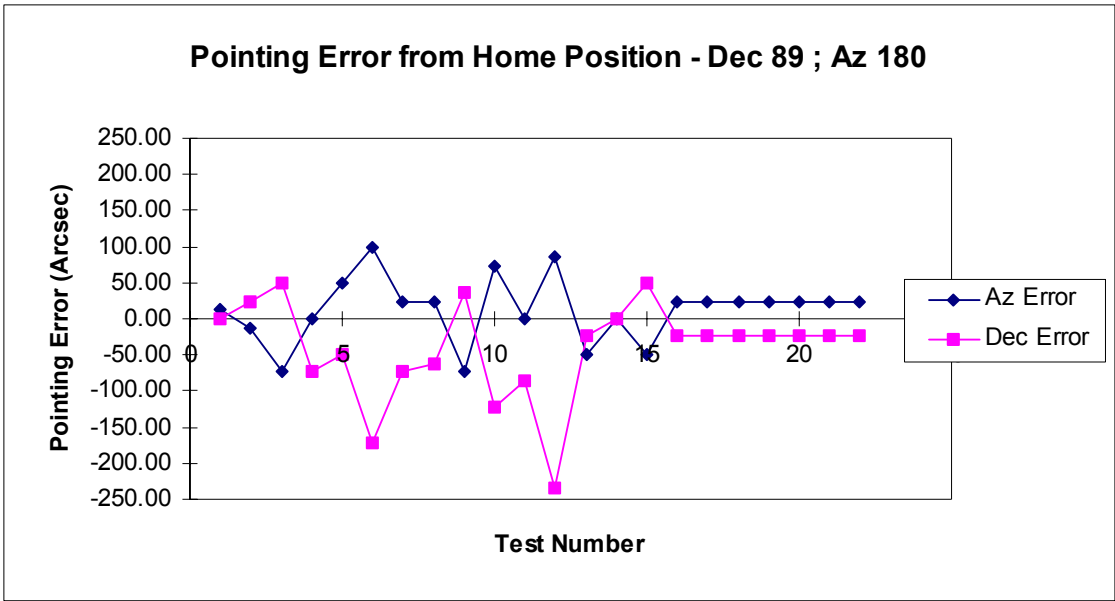


Figure 6. Azimuth and Declination Pointing Errors for the Omni-Wrist Sensor Mount

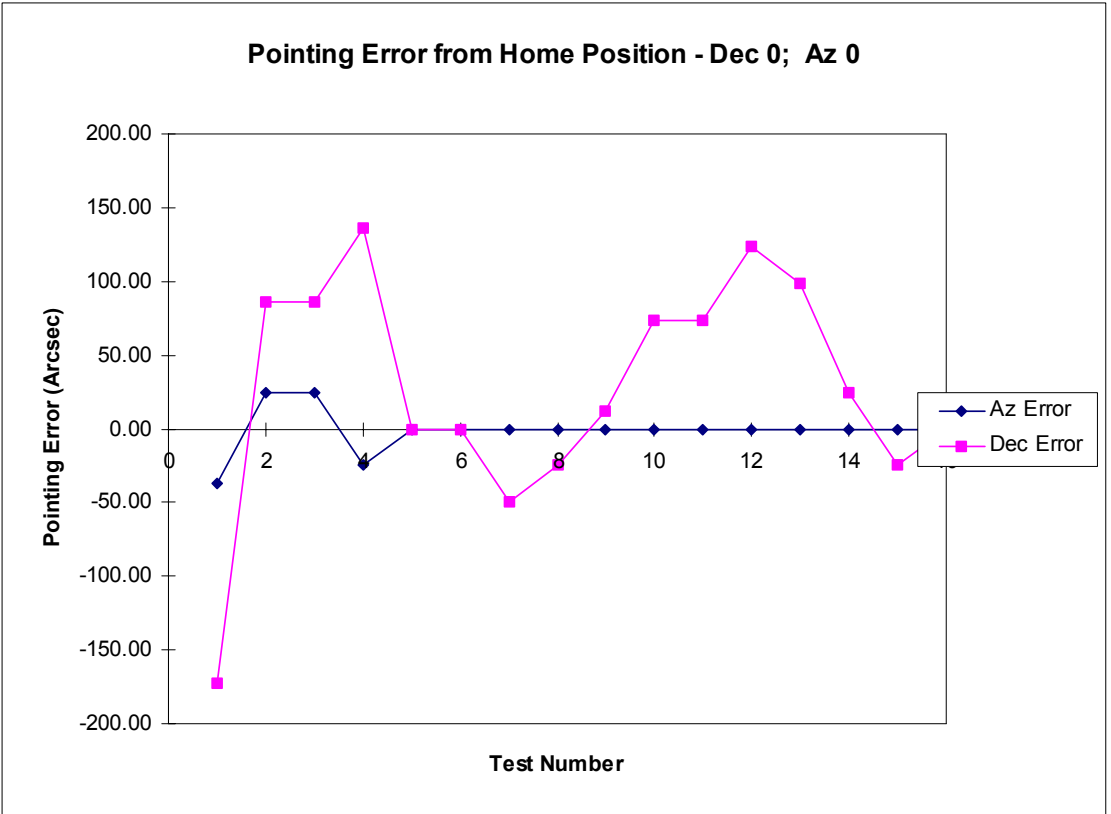


Figure 7. Azimuth and Declination Pointing Errors for the Omni-Wrist Sensor Mount

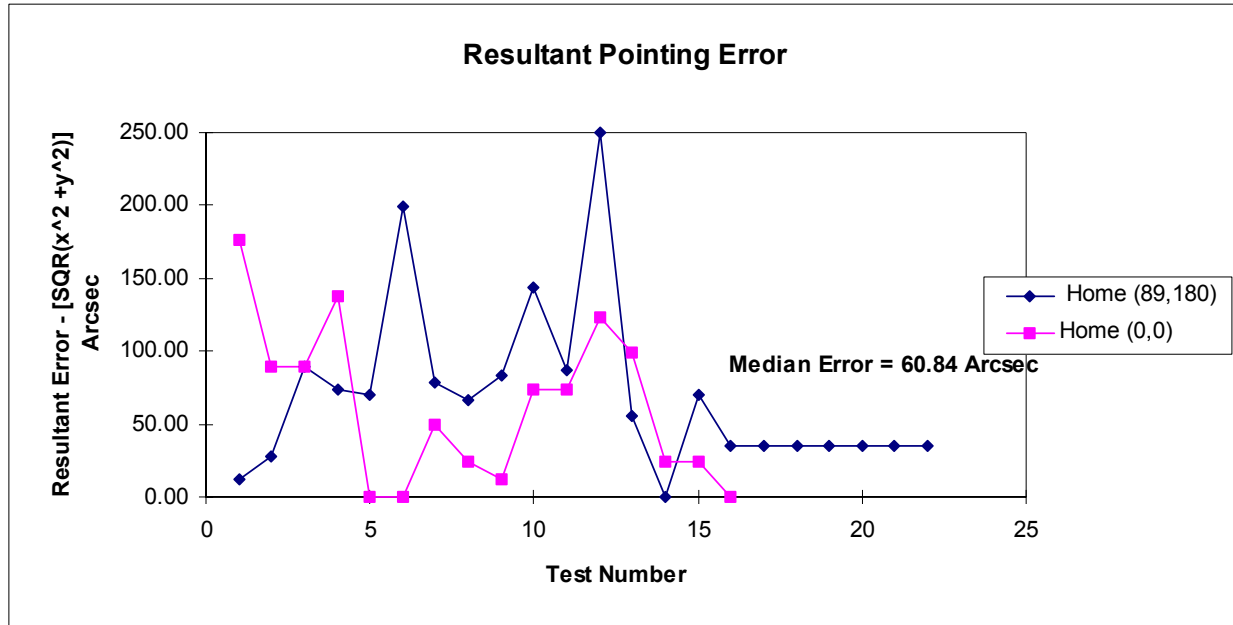


Figure 8. Resultant Pointing Error for Omni-Wrist Sensor Mount

Conclusions

A background on the pointer problem was presented with a discussion of desired capabilities. These capabilities include (1) full hemispherical range that is singularity free, (2) ease of control through single computation, (3) high slew rate, and (4) low cost. Historical sensor mount designs that persist to this day were related. The Omni-Wrist III Sensor Mount was presented as a candidate with advanced horizon-to-horizon tracking capability. The value of singularity-free motion was presented with test results.

References

1. Honeywell, 1996. M597B/CLR. "Rotary Actuator Characteristics." Specifications sheet on Honeywell's space qualified rotary actuator.
2. Rosheim, M., Sauter, G. 2002. "New High-Angulation Omni-Directional Sensor Mount." SPIE Conference Proceedings. Seattle, Washington, 8-11 July 2002, 482163.
3. Rosheim, M. 2000. U.S. Patent 6,105,455. "Robotic Manipulator." Filed Sept. 14, 1999; issued Aug. 22, 2000.
4. Rosheim, M. 1999. U.S. Patent 5,979,264. "Robotic Manipulator." Filed Oct. 16, 1997; issued Nov. 9, 1999.
5. Rosheim, M. 1999a. U.S. Patent 5,893,296. "Multiple Rotatable Links Robotic Manipulator." Filed Mar. 13, 1997 and issued Apr. 13, 1999.
6. Schaeffer, E. 1991. "Application of Harmonic Drive in Space." Presented at the International Harmonic Drive Symposium. Matsumoto, Japan. May 23, 1991.

Space Applications of MEMS: Initial Vacuum Test Results from the SwRI[®] Vacuum Microprobe Facility

P. W. Valek^{*}, D. J. McComas^{*}, G. P. Miller^{*}, J. N. Mitchell^{**}, S. E. Pope^{*}

Abstract

We have designed and built the first fully functional vacuum microprobe test facility specifically intended to optimize the development of Micro Electro-Mechanical Systems (MEMS) devices for space applications. This facility includes an ion-pumped, ultra-clean vacuum system outfitted with four three-axis precision microprobe stages. The testing is monitored with a long focal length microscope through a thin sapphire window. Testing of several initial MEMS designs shows extremely promising results for using such devices in space applications. In particular, we show that significantly reduced voltages are adequate to resonantly drive some MEMS devices in vacuum owing to significantly reduced damping and the consequent much higher Qs of the systems (~1000x) in the absence of air. We also show the results of a many cycle (>10¹⁰) test of a comb-driven, force-distance multiplied sliding aperture door and demonstrate that potential show-stopper issues such as stiction and vacuum welding can be overcome in MEMS devices properly designed for the vacuum environment.

Introduction

MEMS are an emerging technology, which promises to revolutionize many sensor and control systems applications. MEMS use micro fabrication technologies developed over the past several decades to build micro scale mechanical structures. Such structures can have many advantages over their macro scale counterparts including small mass and size, low power requirements, tight dimensional control, repeatability, potential for low cost with large production volumes, and very high reliability.

Because of the extremely high cost of launching instrumentation into orbit, the rigors of the launch and space environments, and the need for extremely high reliability devices, many of the advantages of MEMS technology are also well suited to space sensor and systems needs. Ultimately, space applications of MEMS could span the full range from science instrumentation to spacecraft engineering subsystems. Over the past several years, a number of groups have started to consider the use of MEMS for a variety of aerospace applications (e.g., see Table 1.2 in¹). The majority of these applications have been in the aeronautics end of aerospace research. Among the concepts targeting space applications, most, such as magnetometers and gravity gradient monitors (nano-g accelerometers), can work in sealed and potentially shielded packaging that mitigates the concerns of open exposure to space.²

Space applications of MEMS have several unique issues. First, the launch environment produces very serious vibration and acoustic loads. Once in space, safe operation over thermal ranges of ~70°C are typically required and, depending on the orbit, lifetime radiation doses of >100 kRad along with deep dielectric charging and surface charging from the local plasma are not uncommon. Potentially more serious are the concerns for open packaged MEMS devices – those that have direct access to the vacuum of space. Such MEMS face the potentially fatal issues of stiction and vacuum welding between moving parts. Because the gas molecules in general, and low level humidity in air in particular, are thought to act as lubrication between moving parts, careful design and long duration, many cycle testing of MEMS held continuously in vacuum is essential.

^{*} Space Science and Engineering Division, Southwest Research Institute, San Antonio, TX

^{**} Applied Physics Division, Southwest Research Institute, San Antonio, TX

The vacuum environment is also considered an impediment for devices that require gas-dynamic damping because the higher Q (frequency of resonance/bandwidth of resonance) makes electronic feedback more difficult.³ However, we believe that the reduced damping and higher Q in vacuum can be used to advantage in reducing required actuator voltages and thus power and power supply complexity. Because mass and power are tightly constrained in space applications, higher Qs and lower driving voltages could become a significant advantage for many such applications. Additionally, some applications such as RF filters and precision resonant frequency measurement are improved by higher Q devices.

MEMS for Space Applications

MEMS have begun to revolutionize sensor and control systems technology in the new millennium. Miniaturization of such functions is allowing the silicon revolution of the past several decades to extend and grow past the simple information handling of modern computing and into all aspects of our technology-driven lives. This is because the inputs (sensors) and outputs (controllers) are the bottlenecks that limit many everyday technology applications, particularly applications where dense nets of information or control are needed.

Since future satellite missions will be limited to small, low mass, low power consumption, and low cost instrumentation, instrumentation based around MEMS based technology are extremely attractive. MEMS devices are produced using the same techniques that have been developed by the semi-conductor industry to produce Integrated Circuits. Once the initial development of the fabrication process is completed, mass production of duplicate devices becomes very simple and inexpensive.

MEMS devices are intrinsically small and light. Typical minimum dimensions that are easily produced on MEMS devices today are approximately 1 μm . Despite their diminutive size, MEMS devices are surprisingly strong. The primary material used in the process, polysilicon, has an ultimate strength in tension that is nearly 4 times that of steel, but has about a third of the density. Tanner et al (2000) tested MEMS devices survivability to vibration loads. They tested their devices with a white noise spectrum with a frequency range from 20 to 2000 Hz with a power spectral density of 0.8 g/Hz, 40g RMS. At these high levels, they had 90% of tested devices pass and still function properly.

MEMS Vacuum Test Facility

We have designed and developed a vacuum microprobe test facility at the Southwest Research Institute (SwRI) specifically to enable the development, testing, and long term, in-vacuum, evaluation of MEMS devices for space applications⁴. To the best of our knowledge, the SwRI facility is unique in that it provides the full functionality of a flexible, well instrumented microprobe station within a high vacuum environment. The SwRI vacuum test facility, shown in Figure 1, has been developed to allow flexible and complete testing of MEMS devices while keeping them continuously within a high vacuum environment.

The centerpiece of this facility is our micro-manipulated vacuum microprobe station. Fitted to four of the ports are probes attached via movable bellows to x-y-z micrometer micro positioning stages. Stage motion is 5 μm per full turn in the lateral directions and 12 μm per turn in the vertical direction providing position control of the microprobes to $\ll 1 \mu\text{m}$. This fine manipulator control allows us to manually actuate the micromechanical devices if needed in addition to the basic function of providing input voltages to the various pads.

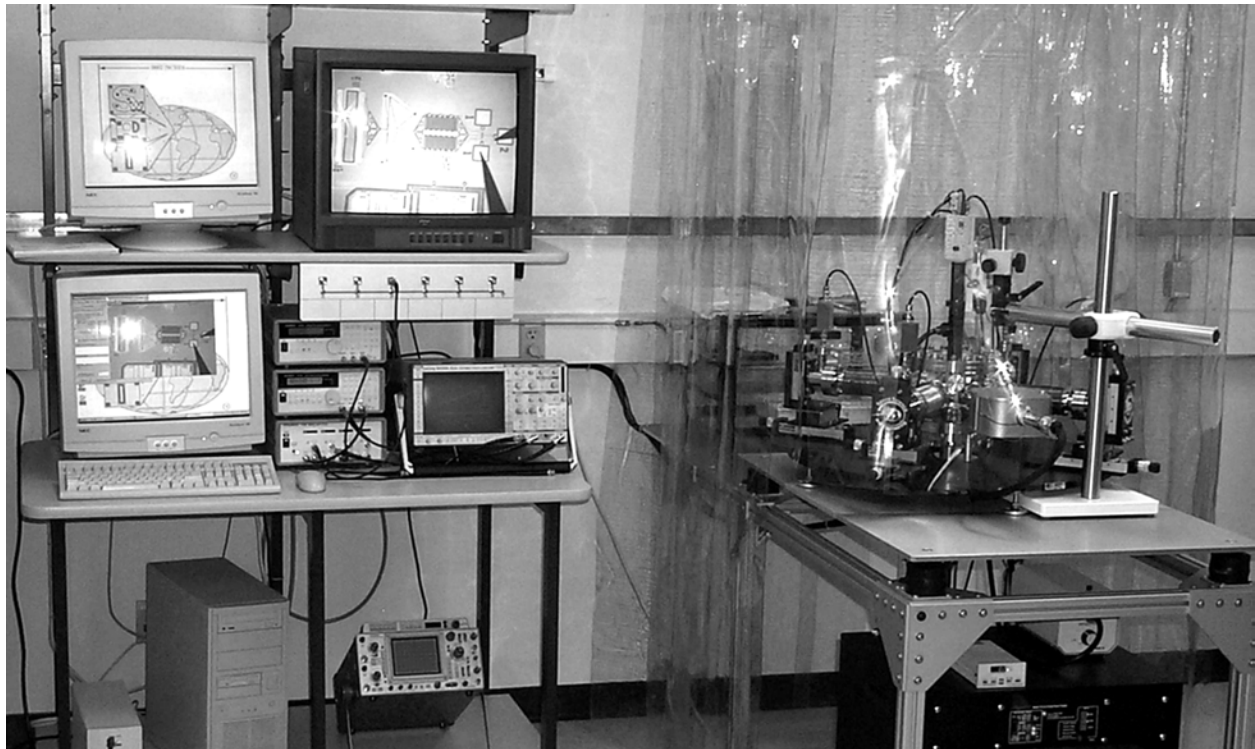


Figure 1. The SwRI MEMS development and test facility. The vacuum microprobe station, mounted on pneumatic dampers, and nitrogen-purged storage cabinet are inside the down flow clean tent while the control computer, ARBs, ARB signal amplifiers, and high resolution direct-feed monitor are on the adjacent workbench.

The station is contained within a HEPA-filtered, down flow environment, along with a nitrogen-purged cabinet where we store MEMS devices not presently in use. In this way, the MEMS chips can be removed from their transport containers and inserted into the vacuum microprobe station entirely within a clean environment. Continuous real-time imaging of the test devices is accomplished through a very thin (1.6 mm) single crystal sapphire window. Because of the large distance through the window and down to the test surface, we have developed an imaging system that incorporates one of two very long focal length primary objectives, followed by a CCD camera and image capture system. This provides coarse images that are $\sim 1280 \times 960 \mu\text{m}$, with $\sim 2 \mu\text{m}$ resolution and $\sim 320 \times 240 \mu\text{m}$, with $\sim 0.5 \mu\text{m}$ resolution, for coarse and fine imaging, respectively. A more thorough description of the facility is given in ⁴.

Initial Vacuum Testing and Results

These tests were set up to answer two fundamental questions about MEMS operation in vacuum. First, we sought to determine how important air damping is for the motion of MEMS devices. Second, we were very concerned that the air molecules in general, and the water vapor in the air, in particular were providing critical lubrication. Thus, it was important to determine if MEMS would work in vacuum at all. If they do function in vacuum, then it is critical to determine how their operational characteristics vary from those observed at atmospheric pressure and whether their functional lifetimes are adequate for typical applications.

We tested six separate size/type combinations of mechanical oscillators that are part of a materials test package developed at SwRI and fabricated using the Chronos MUMPS process.⁶ These oscillators consist of a simply supported beam with a mass at the distal end. The edge of the mass supports comb-drive fingers for actuation. Figure 3 shows a photo of one of our medium-sized oscillator devices. When operated at resonance, the end mass oscillates with a large displacement. The devices were operated in

the vacuum test chamber at various pressure levels using room air. At each pressure level, measurements were performed to determine the resonant frequency, the Q-factor, and the drive voltage required to achieve an end mass displacement of $\pm 8 \mu\text{m}$ as measured by the blur envelope on the scale fabricated at the tip of the beam.

All six oscillator geometries were operated over the pressure range from 1 atmosphere to $< 1.33 \text{ Pa}$ (0.01 Torr). Results of this testing are summarized in Figure 4 (from ⁴). For these tests, the system was started at atmospheric pressure and pumped down further between each set of measurements. The bottom panel of Figure 4 shows that the resonant frequency remains unchanged with pressure, as expected. In contrast, the required operating voltage decreases substantially at lower pressures from near 70 V at atmospheric pressure to less than 5 V at around 5 Pa (0.04 Torr). The Q-factor exhibits some interesting characteristics with pressure. As expected, the Q levels off at low pressures, however, this does not occur until $\sim 13 \text{ Pa}$ (0.1 Torr). Assuming that gas-dynamic damping would be the main damping force, we expected that almost all of the variation with pressure would occur above $\sim 130 \text{ Pa}$ (10 Torr), where almost 99% of the air has already been removed. Another surprise was the inflection in Q-factor at $\sim 130 \text{ Pa}$ (10 Torr), suggesting that some change in the physical mechanism of the damping process occurs around this pressure.

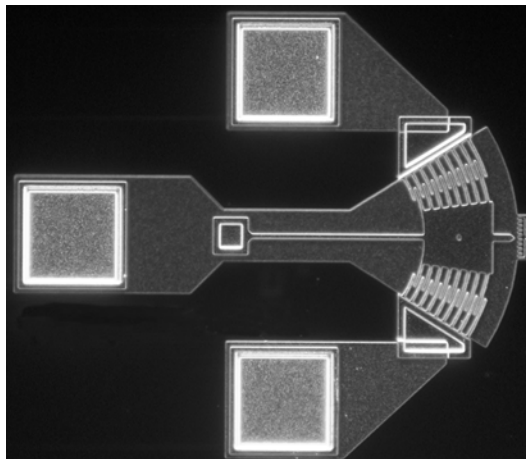


Figure 3. Photograph of a medium-sized type oscillator device.

Based on the results found in Figure 4, we decided to rerun this test with one device (P2S1) in order to determine if it mattered whether the MEMS were being further pumped down or let up in pressure (vented) between the measurements. Our thinking was that there might be some surface friction, owing to residual gas layers between the MEMS parts, in addition to the gas-dynamic damping. If so, we expected to see some hysteresis in the Q-factor as a function of partial pressure, with higher Q-values expected during times when the pressure was being let up compared to when it was being pumped down to a particular pressure level. Thus, we made our measurements in an increasing pressure regime after holding the MEMS parts under much lower pressure for an extended period. The increasing and decreasing pressure points coincided very well, showing no hysteresis.

Other interesting phenomena were observed on all devices tested at pressures below 13 Pa (0.1 Torr). The frequency response of a given device became asymmetrical, with the oscillation amplitude falling off much faster on the high frequency side of the resonance peak. Furthermore, very low damping leads to a slow ramp-up and ramp-down of the displacement amplitude when the drive signal is applied and removed. A device takes nearly a second to stabilize at maximum amplitude when turned on. Additionally, if the device was overdriven such that “pull-in” to the fixed comb fingers occurred, the device continued to resonate, merely bouncing off the fixed fingers. The low drive amplitude was not sufficient to short and hold the moving mass (as seen when overdriving normally at atmospheric pressure) until the drive voltage amplitude was increased to ~ 15 volts. This feature could be important for space applications of MEMS as it is harder to get the devices to lock up at the lower driving voltages, making them more robust.

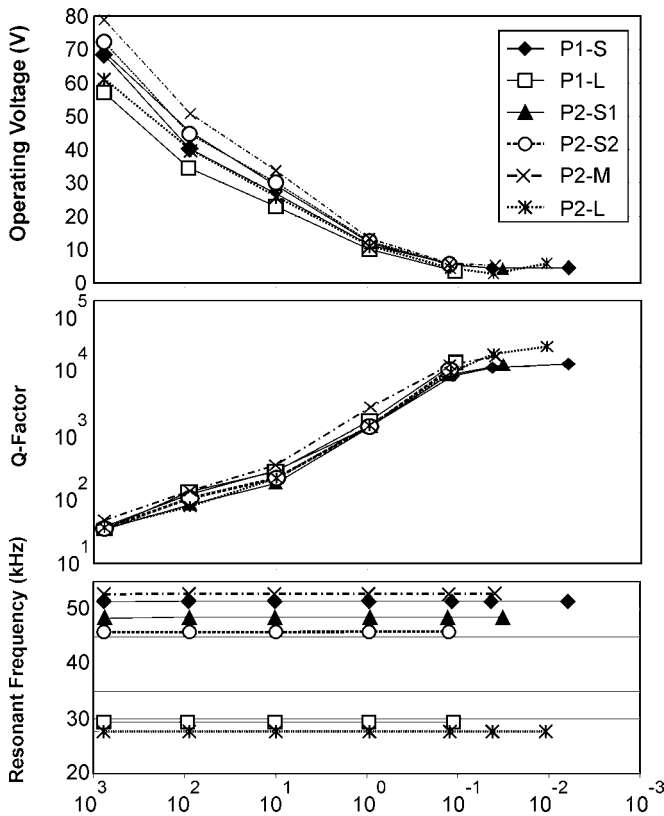


Figure 4. Required operating voltage, device Q-factor, and resonant frequency plotted versus partial pressure of air in the microprobe station. All six oscillator geometries show the same basic response, with full vacuum-type motions not being experienced until the pressure is below ~13 Pa (0.1 Torr).

entire mechanism. Throughout this time, the blur image was periodically monitored, and no obvious change in the motion was observed. At the end of the test, slow (1-10 Hz) cycling of the door was performed; this motion did not indicate any change compared to the pre-test motion.

Discussion

We have constructed the first vacuum microprobe test facility intended specifically for the development of MEMS devices for in-space applications. This extremely flexible and highly integrated facility allows us to optimize the development of MEMS for the rigors of the space environment. Further, initial in-vacuum testing has shown extremely promising results, indicating that MEMS will likely be suitable for numerous applications in various space sensors and control systems.

In addition to indicating that MEMS are suitable for space applications, these results suggest that many MEMS devices used in sealed packages for terrestrial applications might benefit from vacuum packaging instead. Vacuum packaging will significantly enhance the Q of various oscillators, improving their performance for applications such as RF filters and precision resonant frequency devices. Comparison of performance in air and that in vacuum indicates that the Q of the device was ~1000 times greater in vacuum. While some improvement in the motion was expected, this very large difference was not anticipated. In addition, the results shown in this study indicate that the damping process observed at various partial pressures does not appear to be due to simple gas-dynamic damping alone. Rather, a more complicated and interesting set of physical mechanisms appears to be at work.

In order to assess the survivability of MEMS devices over numerous cycles in vacuum, we set up a test of the large sliding door device. The device comprises a fringing field driven comb drive coupled to a force-distance multiplier,⁷ and then to 40x446 μm sliding door. This device was built using the Sandia National Laboratory SUMMIT process [http://mems.sandia.gov/scripts/index.asp] and made use of several standard parts from their design catalog.

We ran the door over a range of motion of ~20 μm using a simple sinusoidal driver. While this waveform is not optimized for the mechanical structure, frequencies up to 10 kHz were possible without abnormal motions. Because we ran the structure outside of its resonance, the peak driving voltage was relatively high (~100V). The test took place over several weeks of continuous vacuum exposure with several short intervals of oscillation during our set up process. We also exposed this device to over-voltage conditions on several occasions and had to mechanically return the structure to its nominal position using one of the microprobes. Thus, this process constituted a severe over-test of the structure compared to the sort of handling that would be done on space flight parts.

Once the driving voltages and frequency had been worked out manually, we began the long duration testing under the computer control. A total of >287 hours total running time was collected at 10 kHz, producing >10¹⁰ cycles on the

Thus, we have demonstrated that MEMS devices can function for many ($>10^{10}$) cycles in vacuum and that their motion is actually improved, requiring less voltage, in some applications. We have designed, built, and tested the first fully functional vacuum microprobe test facility specifically intended to optimize the development of MEMS devices for space applications and have embarked on the adventure of developing and ultimately flying MEMS-based scientific instruments and spacecraft systems on future space missions.

Acknowledgements

We gratefully acknowledge contributions to developing our MEMS devices and vacuum test facility by Troy Diaz, Ray Goldstein, Heather Hanson, Yvette Tyler, and Martin Wüest. The MUMPs fabricated resonators were provided courtesy of Dr. Steven Hudak. This work was funded by a Presidential Internal Research and Development Grant from the Southwest Research Institute.

References

- ¹M. Mehregany and S. Roy, Introduction to MEMS in *Microengineering Aerospace Systems*, edited by H. Helvajian (The Aerospace Press and American Institute of Aeronautics and Astronautics, 1999), pp. 1-28.
- ²J. Lyke and G. Forman, Space electronics packaging research and engineering in *Microengineering Aerospace Systems*, edited by H. Helvajian (The Aerospace Press and American Institute of Aeronautics and Astronautics, 1999), pp. 259-346.
- ³H. Helvajian and S.W. Janson, Microengineering space systems in *Microengineering Aerospace Systems*, edited by H. Helvajian (The Aerospace Press and American Institute of Aeronautics and Astronautics, 1999), pp. 29-72.
- ⁴McComas, D.J., G.P. Miller, J.N. Mitchell, S.E. Pope, P.W. Valek, Space applications of MEMS: The SwRI[®] vacuum microprobe facility and initial vacuum test results, *Rev. Sci. Instruments.*, 74(8), 3874-3878, 2003
- ⁴S.L. Miller, et al., Friction in surface micromachined microengines in *Proceedings, SPIE Smart Electronics and MEMS*, Vol. 12722, 1996, pp.197-204.
- ⁵D. Koester, R. Mahadevan, B. Hardy, and K. Markus, *MUMPs[™] Design Handbook: Revision 6.0*, (Cronos, Research Triangle Park, 2001). Latest version at <http://www.memsrus.com/mumps.pdf>
- ⁶S. Kota, et al., Synthesizing high-performance compliant stroke amplification systems for MEMS, *The Thirteenth Annual International Conference on Micro Electro Mechanical Systems*, IEEE, 2000), pp. 164-169.

The Challenges of Designing the Rocker-Bogie Suspension for the Mars Exploration Rover

Brian D. Harrington* and Chris Voorhees*

Abstract

Over the past decade, the rocker-bogie suspension design has become a proven mobility application known for its superior vehicle stability and obstacle-climbing capability [1,2]. Following several technology and research rover implementations, the system was successfully flown as part of Mars Pathfinder's Sojourner rover [3]. When the Mars Exploration Rover (MER) Project was first proposed, the use of a rocker-bogie suspension was the obvious choice due to its extensive heritage. The challenge posed by MER was to design a lightweight rocker-bogie suspension that would permit the mobility to stow within the limited space available and deploy into a configuration that the rover could then safely use to egress from the lander and explore the Martian surface. This paper will describe how the MER rocker-bogie suspension subsystem was able to meet these conflicting design requirements while highlighting the variety of deployment and latch mechanisms employed in the design.

Introduction

The primary role of the MER suspension subsystem is to provide the rover with a mobility system that has the kinematic range to permit the rover to safely traverse 20 cm obstacles and allow the wheel assemblies to rotate for rover "arc-turn" and "turn-in-place" maneuvers. In addition to these general traversability requirements, there were several requirements unique to the particular issues of the MER vehicle. Specifically, the suspension was required to 1.) Stow in an extremely small space and deploy the mobility into a stance that would provide the rover with 45 degree stability and 2.) Absorb a large percentage of the impact loads the rover would experience during lander egress and surface traverse.

The rocker-bogie suspension is a mechanism that, along with a differential, enables a six-wheeled vehicle to passively keep all six wheels in contact with a surface even when driving on severely uneven terrain (see Figure 1). There are two key advantages to this feature. The first advantage is that the wheels' pressure on the ground will be equilibrated. This is extremely important in soft terrain where excessive ground pressure can result in the vehicle sinking into the driving surface. The second advantage is that while climbing over hard, uneven terrain, all six wheels will nominally remain in contact with the surface and under load, helping to propel the vehicle over the terrain. MER takes advantage of this configuration by integrating each wheel with a drive actuator, maximizing the vehicle's motive force capability.

Another key feature of the suspension that has not been emphasized in previous technology and flight applications is the ability to absorb significant driving loads. In the past, rocker-bogie suspensions have been used on rovers where the loads generated during driving have been relatively low. Therefore, the suspension served primarily as a "rigid" kinematic link between the rover body and the wheels. However, the MER rover has the challenge of egressing from a lander poised on airbags and surface features, a maneuver that could require the vehicle to drop from a significant height above the surface. Instruments that had been stowed during the landing phase of the mission will be deployed during driving and were not designed to withstand large loads in their science-gathering configuration. A compelling design requirement was to therefore create a "soft" suspension to limit the accelerations experienced by the payload during driving. However, one of the more challenging design issues to address was how soft to make the suspension. A suspension that was too soft will result in large deflections where the rover body or its science appendages may contact Martian surface features in an uncontrolled manner. Therefore,

* Jet Propulsion Laboratory, California Institute of Technology, Pasadena, CA

the suspension had to be designed to give the rover a ride somewhere between a luxury vehicle and a truck. The suspension system stiffness target was one that would produce a translational impact load no greater than 6 G's and not let the rover body deflect below a 20 cm ground height. The resulting suspension structural members were fabricated from tapered, welded, titanium box beams tuned to meet these requirements. The design of these elements also provides exceptional bending and torsional capability while minimizing the volume and mass impact to the spacecraft.

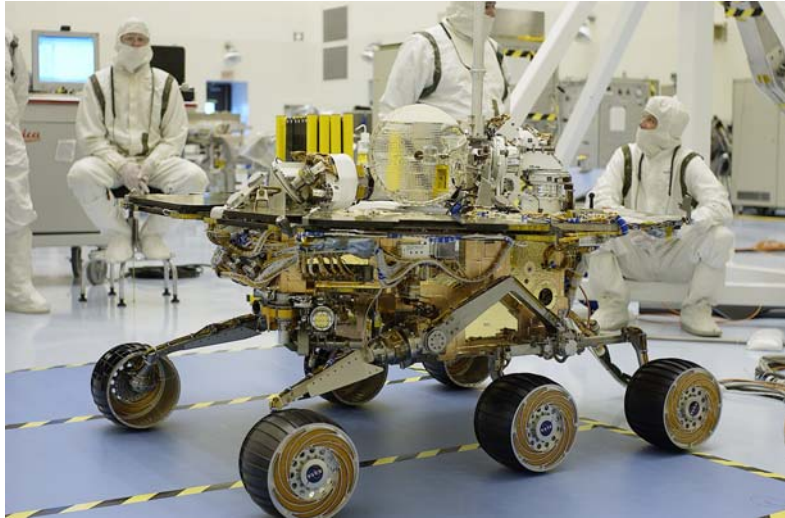


Figure 1. Mars Exploration Rover with a Deployed Suspension

The last and most difficult design requirement was to create a suspension that would stow within the tetrahedral lander, unfold and latch into a deployed configuration, and provide the rover with the ground clearance and stability necessary to navigate the Martian surface. This task required significant coordination with other rover and lander subsystems in order to produce a deployment sequence free of static or dynamic interferences (see Figure 2 & 3).



Figure 2. Stowed MER Rocker-Bogie Suspension on Assembly Fixture

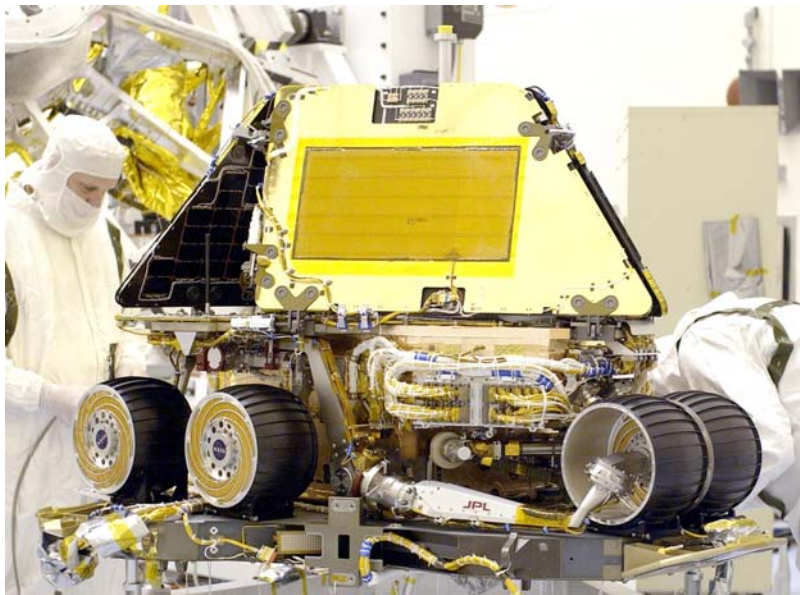


Figure 3. Stowed MER Rover on Lander Basepetal

Folding and Unfolding the MER Mobility

Determination of how the rocker-bogie suspension could be “broken” to enable it to stow within the allotted space was the first challenge faced in the design of the sub-system. As the name would suggest, the two primary components of this type of suspension are the rocker and bogie (see Figure 4). These two structural elements are connected via a free rotating pivot dubbed the Bogie Pivot. The right and left sets of rocker-bogie assemblies are connected to each other via the vehicle’s differential, a passive, motion-reversal joint that constrains the two sides of the mobility system to equal and opposite motion. Three unique break points were selected: the Rocker-Bridge Joint, a mid-span rocker folding joint; the Rocker Deployment Actuator (RDA) Joint, a motor driven deployment joint on the forward rocker arm, and a telescoping prismatic joint on the bogie member. Thus, a total of six joints must be reliably locked and latched into place during deployment to provide the rover with a safe and stable platform for driving.

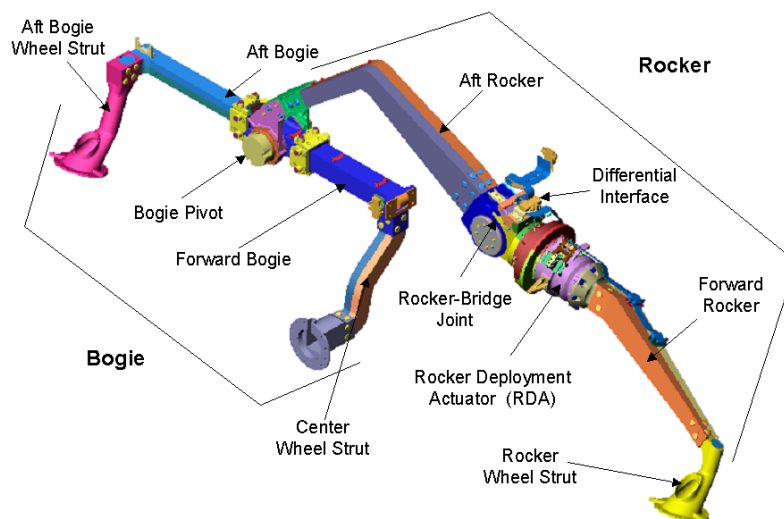
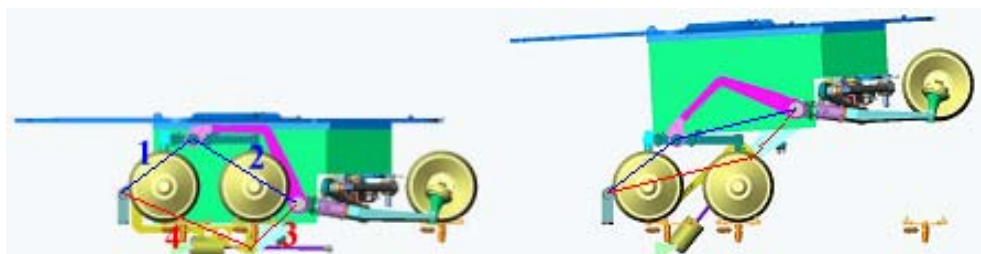


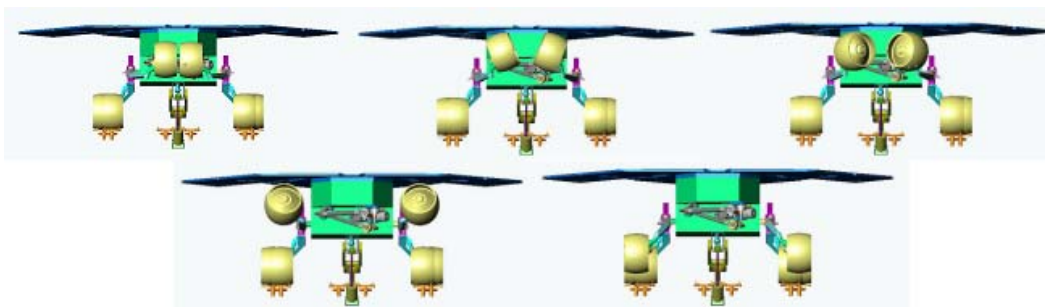
Figure 4. MER Suspension Nomenclature (Deployed Configuration)

Deployment of the rover takes place during the Standup and Deployment phase of the landed mission, after critical systems like the solar array and imaging mast have been deployed and the vehicle's health has been confirmed. The first step in deploying the mobility is to rotate and lock the Rocker-Bridge Joint into place. The MER mechanical design team had determined early on that a lander-based Rover Lift Mechanism, or RLM, would be needed to lift the rover from its stowed position. A rover-based RLM would have resulted in significant rover scar mass, as there would likely be a need for two actuators, one on each side of the rover, rather than one centralized device. As designed, the RLM utilizes portions of the suspension subsystem to create a four bar linkage that guides the rover body up into its ground clearing stance. By using the Bogie/Basepetal (Labeled 1 in Step 1) and the Aft Rocker (Labeled 2) as two links in a four bar linkage, the RLM needs only to provide the two remaining links and the extension force to raise the rover into its standing position [4].



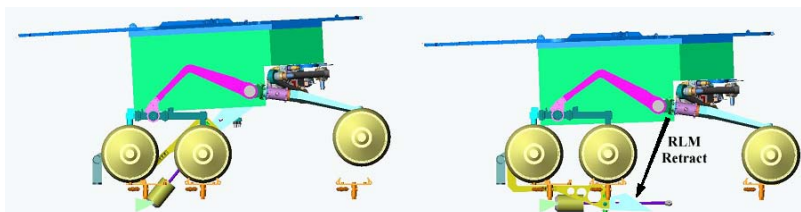
Step 1: Rover Lift

Once the body of the rover is lifted to its peak height, just beyond its nominal driving height, the second phase of rover stand-up begins. At the completion of Step 1, the forward rocker arm and the attached rocker wheel are still in their "up-side-down" stowed orientation. By activating the RDA on each rocker arm, the forward portion of the rockers is rotated 180 degrees into its full stance position. A mid-deploy-sequence steering motion was added to avoid interference of the wheels with the solar arrays. Once the RDA deployment is complete, the steering actuators are rotated to their forward driving orientation (see Step 2).



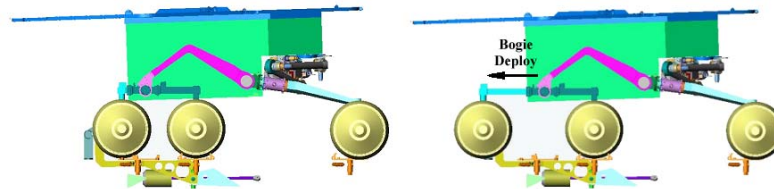
Step 2: Rocker Deployment (includes Steering Actuator rotation to clear Solar Arrays)

The third step in the stand-up sequence is the retraction of the RLM. Once the RDAs are deployed and latched into place, the rover is capable of supporting itself in its upright configuration. At this point in the deployment process, the rover is supporting itself on all six wheels (see Step 3).



Step 3: Rover Lift Mechanism Retraction

The fourth and final step in rover stand-up is the deployment of the suspension bogie member. A partnership was established with the wheel assembly subsystems to use the aft bogie wheels to pull the telescoping bogies out and latch them into their deployed position (see Step 4). By utilizing the wheel drives, the bogies can be deployed without the need to add two additional single use actuators. The only changes to the rover/lander system to enable this capability were a small redesign to the aft bogie wheel restraint and the addition of a cleated platform to ensure the aft wheel had the required traction to pull the aft bogie out of the forward bogie.



Step 4: Bogie Deploy

Material Selection

Titanium was used exclusively for the structural components of the suspension. This material was selected for several reasons. The high strength-to-weight ratio made it attractive for a mission where volume and mass was at a premium. In addition, the rover was mounted to a graphite/epoxy composite lander basepetal. Titanium's low CTE matched the lander's better than other potential suspension materials. Finally, the ability to weld titanium allowed the suspension structural components to be optimized for strength and flexibility. Eight of the ten suspension tube members were welded. The desire to increase the Ti-6AL-4V from the annealed to a solution treated and aged (STA) state was resisted. While the STA process would increase the strength of the titanium from 900 MPa (130 ksi) to 1100 MPa (160 ksi), the weld seams would remain in the annealed condition, creating an obvious and unacceptable weak link that could only be mitigated if the STA process was performed after welded. The possibility that the weld members would distort significantly during the STA process due to their thin walled construction was deemed too risky to accept. Therefore, all the suspension tube members were kept in their annealed condition.

Structural Member Fabrication

The desire to create a suspension that efficiently absorbs energy leads to structural members that are thin walled box beams. A box beam design is a mass efficient geometry for components subjected to both bending and torsional loads. The beams are also tapered wherever possible to increase mass savings. Based on these desired design features, the fabrication method selected to create the members was electron beam welding. The use of welding in the space industry is usually reserved only for propulsion tanks and tubing due to fears of poor workmanship and difficulty of inspection. Propulsion subsystems can be pressure tested to verify weld integrity. Spacecraft structure, on the other hand, does not typically lend itself to such proof loading methods. Because of these potential complexities, other alternative avenues of manufacturing were investigated, the most promising of which was investment casting. However, the small number of parts made this option prohibitively expensive per piece, so welding was ultimately chosen as the fabrication method.

The basic construction of each weldment is the joining of two C-channels. A less expensive option of welding a plate on an open box places the weld seam in the corner of the box beam was initially investigated. This location is undesirable due to the fact that the corner of the beam is the location of maximum stress in torsional load cases (see Figure 5), and therefore necessitates the more complicated C-channel approach. The typical wall thickness of 1 mm increases to 1.5 mm along the weld seam for extra strength. This design process also enables additional features to be machined into the welded members. The aft bogie member has a recess machined into it for the bogie latch pawl to reside. The "knees" in the aft rocker and center wheel struts are thickened up to accommodate the localized increase in stress.

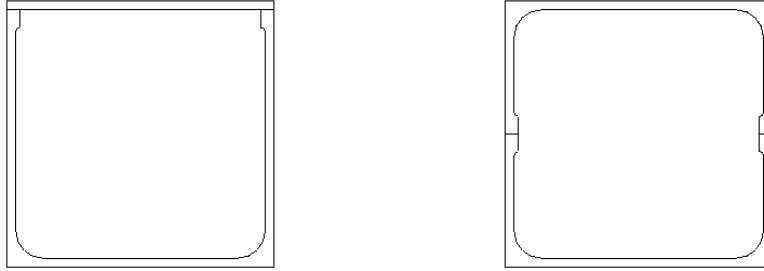


Figure 5. Open Box/Plate & C-Channel Options

After the selection of the fabrication process, a set of torsion tests were performed on 30 mm by 30 mm articles that were representative of the base of the forward rocker weldment. The torsional load in that location was 421 N-m (3725 in-lb). The test results indicated that the failures began near the corner of the weldment rather than the weld seam. Test results also demonstrated the box beam's tendency to yield rather than break at loads far in excess of its design capacity. This type of failure meant a driving impact case greater than the design load would result in "graceful degradation", allowing the surface mission to continue instead of causing a catastrophic system failure.

Detailed Description of Suspension Mechanisms

Rocker Bridge Joint and Latch Design

The rocker-bridge joint is essentially a yoke and clevis design. Each single-use joint pivots on two (2) 52 mm diameter Torlon 7130 thrust/radial bushings. Braycote 601EF grease is applied to the bushings as an added measure of friction reduction. Once deployed, the rocker-bridge joint needs to withstand a maximum 714 N-m (6325 in-lb) bending load generated when the center wheel falls into a 20-cm hole. The joint also simultaneously sees a 506 N-m (4475 in-lb) torsion load created by the 12 cm lateral offset between the rocker-bridge joint and the mobility wheels (see Figure 6).

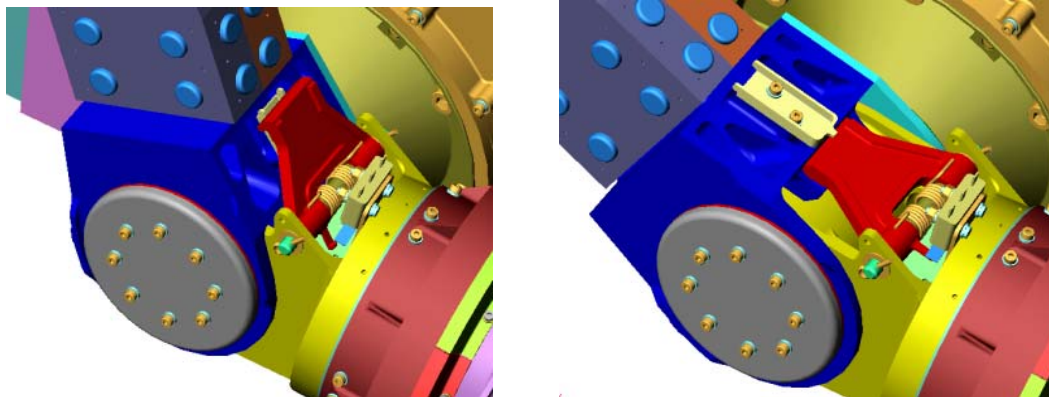


Figure 6. Rocker-Bridge Joint in Stowed & Deployed States

The rocker-bridge latch consists of a pawl that falls into place once the aft rocker has rotated 39 degrees from its stowed position. A small appendage on the forward side of the pawl was included in the pawl design to engage the microswitch lever arm to indicate the joint has successfully been locked. An intermediate step was also added to the latch design in order to isolate the latch from RLM stall loads. The intermediate latch position allowed the latch pawl to travel past its final position, causing the RLM to stall against its own internal hard stop rather than against the latch, which avoids unnecessary latch and suspension loading. Instead, once the RLM has stalled at the top of lift, it then lowers the rover and the latch pawl falls into its final latched position (see Figure 7).

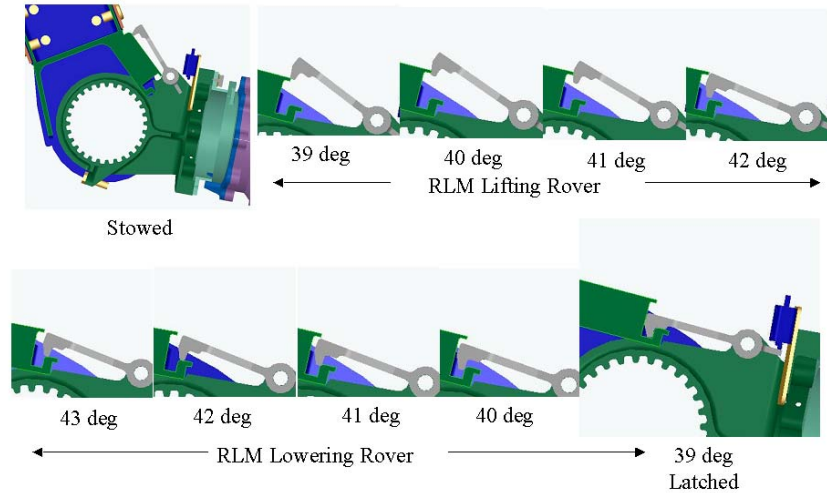


Figure 7. Rocker-Bridge Latch Pawl Action during the RLM Lift and Lower

Rocker Deployment Actuator and Latch Design

The triangular shape of the lander basepetal was a strong motivator to stow the front wheels directly in front of the rover. Following this motivation, a joint called the rocker deployment actuator (RDA) was added to the suspension to permit the front wheels to be stowed directly in front of the rover. During deployment, the RDA deploys the front wheels into a position that maintains the necessary rover pitch and roll stability. Once deployed, the RDA is required to withstand 390 N-m (3450 in-lb) bending and 421 N-m (3725 in-lb) torsional loads. The RDA is a 100-mm long, 80-mm diameter cylindrical body. A Maxon REO20 DC brushed motor with integral 5 stage planetary gearhead is employed to create the RDA's 20 N-m (175 in-lb) torque capability. The maximum predicted flight deployment load is 2.8 N-m (25 in-lb), giving the actuator considerable margin over its required task. Two pairs of 57.2-mm (2.25 in) diameter MPB angular contact bearings are utilized as the RDA's rolling elements (see Figure 8). The latch design chosen was based on a latch used on the Magellan spacecraft to latch the spacecraft's solar panels in place. The RDA latch can best be described as a variation on the common door latch. The two primary components of a door latch are the spring-loaded pawl in the door and a fixed strikeplate attached to the doorframe. The RDA latch inverts the dynamic and static roles in this latch design by fixing a pawl on the stator housing and allowing the rotor mounted strikeplate to pivot. In an effort to minimize the latch load, the diameter of the RDA was made as large as possible, the primary restrictions being the RDA's proximity to the lander side and base petals, rover body, and science hardware.

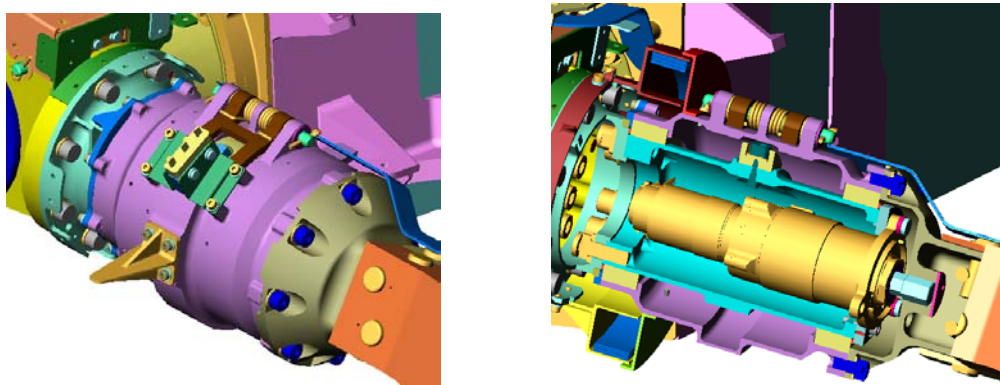


Figure 8. Rocker Deployment Actuator

Bogie Deployment and Latch Design

The original design of the MER suspension was one with a bogie of fixed length. As the MER rover design began to mature, its center of gravity began to rise. The flight system held a firm requirement that the rover would be stable to at least 45 degrees in vehicle pitch and roll. The increase in rover c.g. meant that the driving position of the aft bogie wheel needed to move backwards in order to meet the 45 degree stability requirement. Due to the volume constraints placed on the mobility in the stowed configuration, the bogie design needed to be modified to deploy, allowing an increase of the bogie length by an additional 17 cm.

The decision on how to deploy the bogie was reached relatively quickly. The aft bogie wheel drive actuator was the logical mechanism to pull the bogie into its final configuration. The aft bogie wheel drive, as designed for performing its primary rover traverse function, is able to supply up to 333 N (75 lbf) of deployment force. The addition of this capability brought with it both mass and complexity impacts to the design of the rover and the lander. On the rover, the bogie was split into two distinct structural elements, each having to house a portion of the mechanical components necessary to allow the bogie to deploy and latch into its final position. On the lander, a small, cogged platform was added to each of the aft wheel restraints, designed specifically to engage the wheel cleats and guarantee maximum traction during deployment.

The mechanism by which the aft bogie member moved within the forward bogie was originally slated to be skids to reduce system mass. The final design, however, was a system of roller assemblies supported by spring elements. The basis of this decision was the desire to decrease the friction in the design and increase the bogie's ability to tolerate thermal distortion. In addition, it was felt that rolling elements would be more tolerant to debris that could be ingested into the moving components during deployment. Whereas a sliding motion could seize due to a small amount of debris, a rolling system would be more forgiving, resulting in a robust overall design approach. The increase in bogie mass was considered acceptable in order to increase the deployment's reliability.

The design goal of the bogie roller assemblies was to suspend the aft bogie within the forward bogie. Four pairs of roller assemblies support the aft bogie and remove 5 of 6 degrees of freedom. By placing the two forward pairs as far away from the aft pair, roller loads are minimized and the roller size correspondingly reduced. This is particularly important in the bogie, which is located in an area of the rover where space was at a premium. The station distance between the pairs of roller assemblies is 10 cm (see Figure 9).

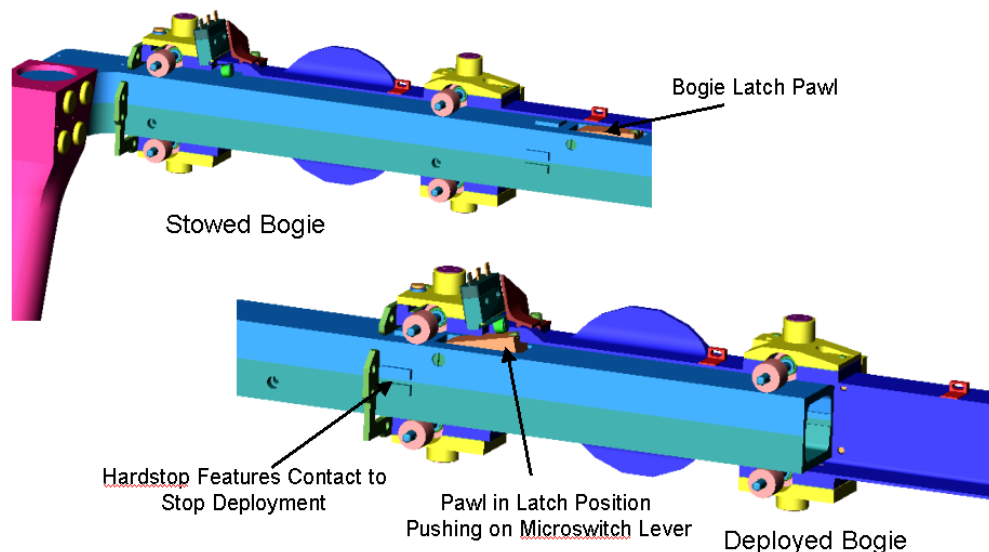


Figure 9. Bogie Deployment Diagram

A roller assembly consists of a roller pin with two needle bearings, one on each end of the pin. The rollers are positioned over the vertical portion of the aft bogie to allow load transfer through a stronger portion of the bogie cross-section. This roller placement also provides an efficient mechanical advantage for managing torsional loads applied to the aft bogie. Even with these considerations put into place, the wall thickness of the deployed aft bogie in the location where the roller rested had to be increased from 1 mm to 3 mm to withstand the roller point loads. The roller pin assemblies are nested between the aft bogie and a pair of belleville washers stacks. These stacks are needed to counteract any thermal or debris perturbations that could arise on the Martian surface during bogie deployment. A combination of washers in both parallel and series enabled the roller assembly to have a “soft” condition during the lightly loaded deployment phase and a “stiff” condition during the driving phase. The “soft” condition, engaged during deployment loading, was desired in order to reduce the drag in the roller needle bearings. Final analysis eventually required the addition of a stiffness phase to the roller design. Analysis of potential rover egress/driving “drop” cases indicated that the roller pins would fail in bending, despite being fabricated from MP35N high strength steel. Based on the results of this analysis, a decision was made to by-pass the belleville washer stacks during this large intermittent load and transmit it directly through the 440C steel roller sleeve and into the roller cover (see Figure 10).

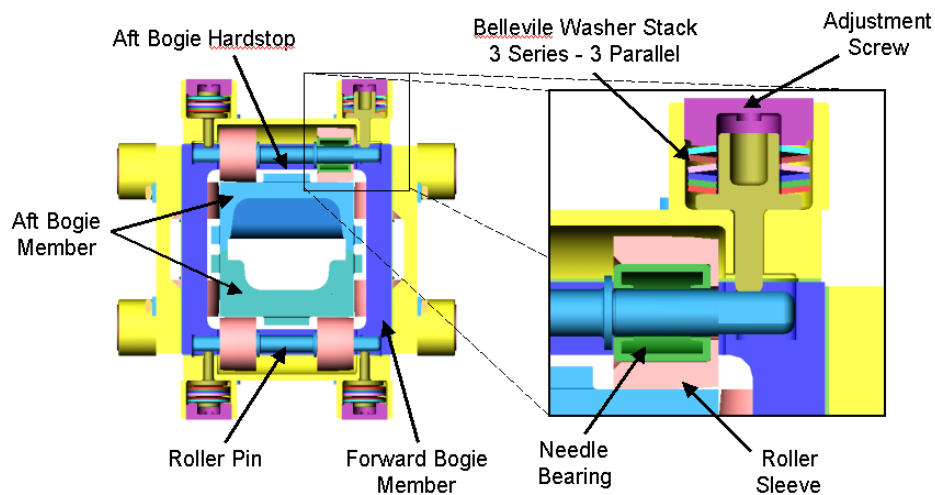


Figure 10. Cross-section of Bogie Roller Assemblies

The nominal applied load to the aft bogie wheel during bogie deployment is about 15% of the rover weight, or 97 N (22 lb) on Mars. This load increases as the rover is pitched up or sideways. A set of thermal tests were performed at room temperature and $-70\text{ }^{\circ}\text{C}$ to determine the assembly deployment margins. The tests showed a relatively small difference in the force required to deploy the bogie up to a 150% nominal applied load. Past this point the deployment force increases sharply. The worst-case deployment force of 224 N when a 222 N load was applied remained within acceptable limits of the wheel drive actuator’s 333 N capability (see Figure 11).

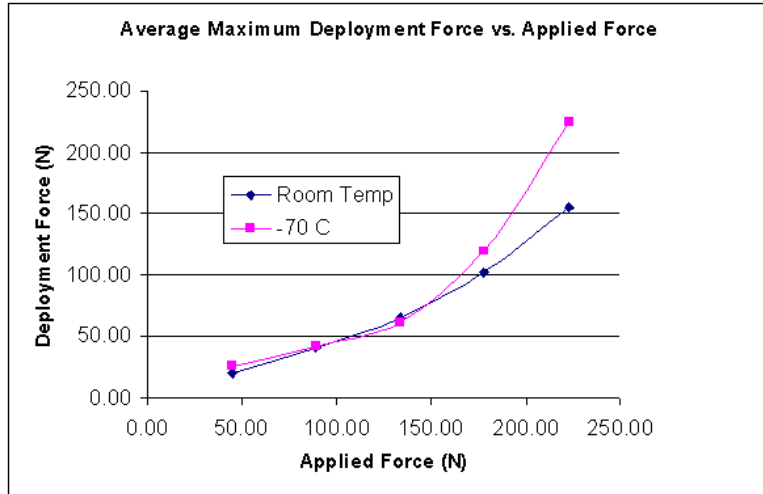


Figure 11. Results of Deploying Bogie at Cold Extreme

The bogie latch is a variation on the same basic latch design philosophy of the rocker-bridge latch: introduce an object that will not permit the further motion of the mechanism in any direction. Near the end of bogie deployment, an aft bogie-mounted latch pawl rotates upward into an opening in the forward bogie. A 12 degree deployment pawl angle was utilized to transfer the pawl load into the forward bogie with the addition of little mass.

Problems and Resolutions

Bogie Latch Pawl Design

During several of the most extreme rover mechanical validation and verification stand-up tests, the bogie pawl failed to fully rotate into its latched position. The failure was determined to be the result of the aft bogie rotating relative to the forward bogie along the deployment axis. The intentionally low stiffness designed into the bogie for reduced deployment loads was allowing the aft bogie to rotate up to 6 degrees under earth gravity, enough rotation to cause the latch pawl to hit the edge of the latch opening in the forward bogie, keeping it from fully latching.

A new bogie latch pawl was designed that had tapered edges that eliminated the previous interference. Fortunately, the original bogie pawl had sufficient margin to tolerate a reduction in cross-section (Figure 12).

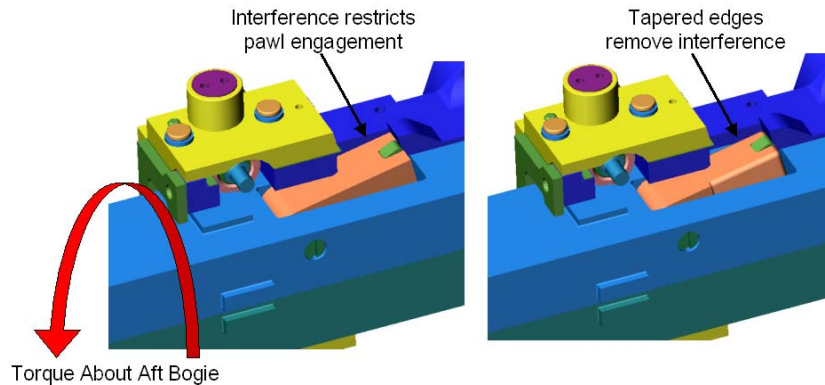


Figure 12. Original and Final Bogie Latch Pawl Design

Lesson Learned: Test the hardware under extreme conditions as soon as possible in the development phase. Testing will expose oversights in designs such as in this case where the non-linear stiffness of the mechanism was underestimated and resulted in a latch functional failure.

Implementation of Microswitches

The three primary components of the microswitch assemblies are the microswitch bracket, the microswitch, and the microswitch extension actuator (Figure 13). Each of the three unique latches utilize Honeywell 9HM30-REL-PGM microswitches to indicate if their respective latch had successfully engaged. The placement of the microswitches was such that the lever arm of the microswitch would be triggered by the latch pawl pushing on the arm. Due to limited space and the fear that the microswitch lever arm might be overextended, microswitch actuators Honeywell JS-151 and JS-152 were used to extend the range of the microswitches.

The features by which each microswitch was attached to its respective joint were intentional designed with large clearance holes. The thought behind this highly adjustable interface was to ensure that the microswitch could easily be positioned to register if a successful latch action had been achieved. However, this type of interface meant there was significant variability between the rovers in microswitch actuation. In addition, the interface left the microswitch susceptible to small changes in position due to dynamic loading or thermal gradients.

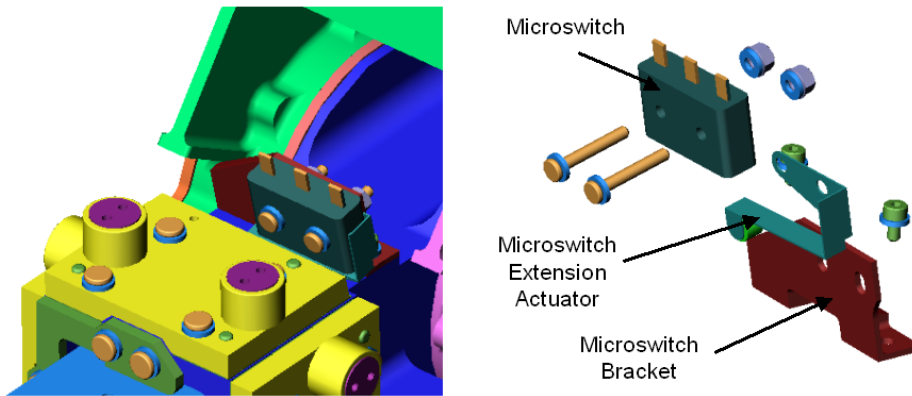


Figure 13. Bogie Microswitch Assembly

Testing of the rover standup phase yielded inconsistent results from the deployment microswitches. As a result, a detailed adjustment protocol was established for each of the microswitch assemblies that yielded consistent results. A new latch verification sequence was developed as an added measure to increase the understanding of the mobility latch states for use during rover standup and deployment. A post-latching command was added to each of the deployment sequences that drove the joint in the stow direction. The resulting stall of this motion was clear indication that a joint had successfully latched.

Lesson Learned: The use of microswitches to verify a latched condition should not be entered into lightly. The proper implementation of microswitches requires a consistent method by which the microswitch is positioned with respect to the relevant components. An alternate method such as driving the joint in the opposite direction and monitoring current can produce telemetry that is less dependent on the fine adjustments associated with microswitches.

Deployment Process, Mechanization, and Testing for the Mars Exploration Rovers

Ted Iskenderian*

Abstract

NASA's Mars Exploration Rover (MER) robotic prospectors were produced in an environment of unusually challenging schedule, volume, and mass restrictions. The technical challenges pushed the system's design towards extensive integration of function, which resulted in complex system engineering issues. One example of the system's integrated complexity can be found in the deployment process for the rover. Part of this process, rover "standup", is outlined in this paper. Particular attention is given to the Rover Lift Mechanism's (RLM) role and its design. Analysis methods are presented and compared to test results. It is shown that because prudent design principles were followed, a robust mechanism was created that minimized the duration of integration and test, and enabled recovery without perturbing related systems when reasonably foreseeable problems did occur. Examples of avoidable, unnecessary difficulty are also presented.

Introduction

The highly integrated, collaboratively engineered mechanisms of the 2003 Mars Exploration Rover represent a significant achievement for the team that produced this spacecraft in record time. Two of these spacecraft were created as successors to the acclaimed Mars Pathfinder "Sojourner" rover that landed on Mars on July 4, 1997. The identical rovers landed on Mars on January 3rd and 24th, 2004.

Relative to most spacecraft, each Rover and the landing system that accompanies it feature a uniquely high bulk density. The roughly rectangular prism of the rover fits snugly within the stowed tetrahedron configuration of the lander. A complex deployment process results from this dense packaging. A total of 24 devices and mission-critical deployments must correctly function just to prepare the MER for driving off its base petal landing platform. The design of several of these mechanical systems depended on successfully implementing the concept for standup to which the rover was committed at an early date. Figure 1 shows an overall view of the MER before standup.

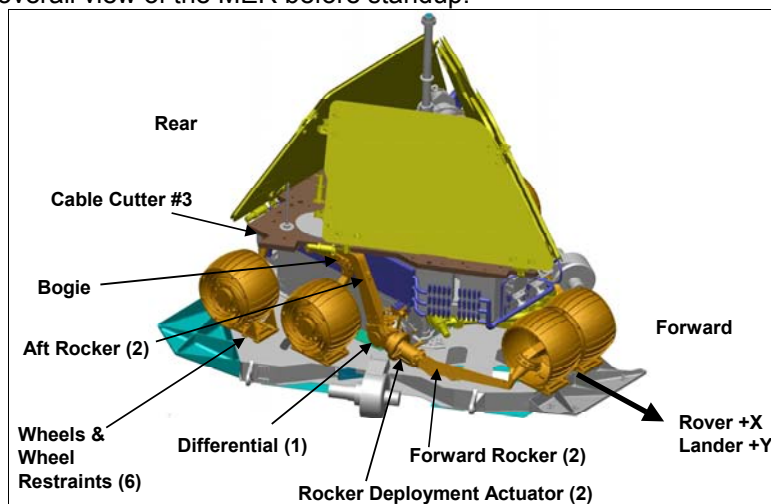


Figure 1. The stowed MER in its pre-standup configuration

* Jet Propulsion Laboratory, Pasadena, CA

The Martian environment also poses a severe challenge to mechanism designers. The design survival temperatures (which include margin) for the RLM's environment spanned from -120 to +35°C, and the qualification operating temperatures were between -60 to +35°C. The rover deployment system discussed herein must be able to survive these extremes over the 20 "sols" (Martian days) over which standup may occur immediately after landing. Some motors on the rover must survive many cycles from -105 to +8 °C over the mission's design lifetime, 90 sols. Additionally, beyond the anticipated high temperature during the mission, was the added necessity to reduce biologically active contamination to levels beneath those set by Planetary Protection engineers. Most mechanisms engineers on the MER met this requirement by baking their devices to +110°C for 50 hours prior to final integration with the spacecraft. Mechanisms had to survive not only routine launch vibration, but also the impact load up to approximately 49 g that would be experienced upon landing with the distinctive airbag cushioning system developed at JPL. As will be discussed, gales of dust particles were anticipated upon landing and during intermittent dust storms after landing.

Figure 2 shows the essentials of the standup sequence comprising the last of the mission-critical deployments and approximately when they occur. Figure 4 shows the rest of the sequence with a series of snapshots from the computer model. The functional requirements on the RLM throughout this process were as follows:

1. Lift the rover and suspension system far enough to allow the front wheels to clear the base petal (the plate to which the Rover was stowed) when they fully deployed. We designed to an arbitrary value, 75 mm, which proved to be adequate in all our tests. The time allocated to this function was 15 minutes.
2. Cause the rocker-bridge latch pivot, the juncture between forward and aft suspension, to rotate through a minimum angle of 42 degrees. (This angle was estimated to be about 39.5 degrees at the beginning of the project. It was identified as one of the poorly understood requirements, as it depended on the development of the rocker-bridge latch). The corresponding linear stroke requirement grew to about 244 mm (including 21 mm margin).

At this point, the front rockers and wheels rotate through their own deployment range of approximately 180°. This is accomplished through a series of motions shared between the wheel-steering actuators and the rocker deployment actuators. This sequence is detailed in the paper entitled "*The challenges of designing the rocker-bogie suspension for the Mars Exploration Rover*".

3. Upon reversing, allow the loose pivot joint in requirement (2) to latch up at a fixed angle. Continue lowering the rover without interruption, while accommodating the fundamentally different kinematic relationships of the system.

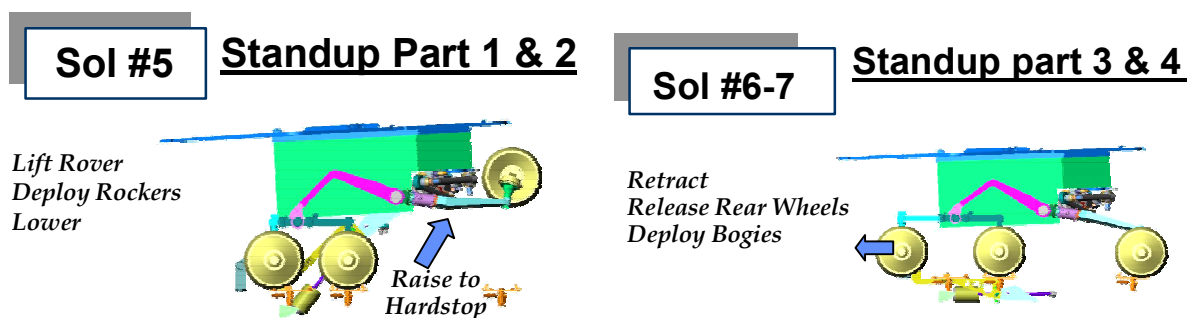


Figure 2. Sequence of Rover standup events

RLM Functional Requirement & Standup Sequence

The nomenclature of the RLM and its relationship to the rover is shown in Figure 3. This simplified computer model shows the rover's configuration just before the standup sequence is initiated.

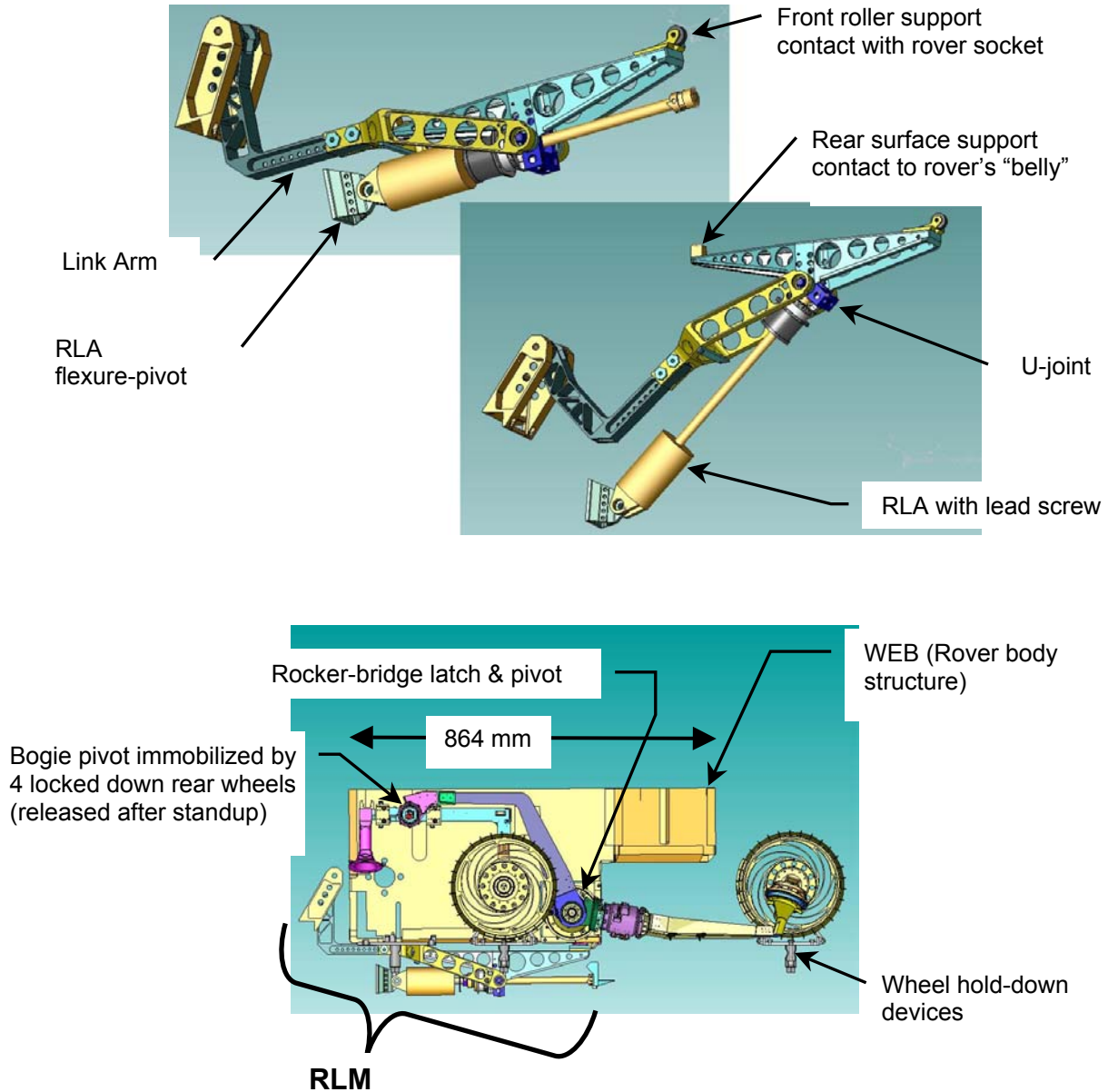


Figure 3

(Above) the RLM and its nomenclature, shown in stowed and deployed configurations. (Below) The rover before pyrotechnic separation devices release, showing the RLM nested within the thickness of the base petal. For clarity, only two of six wheels are shown.

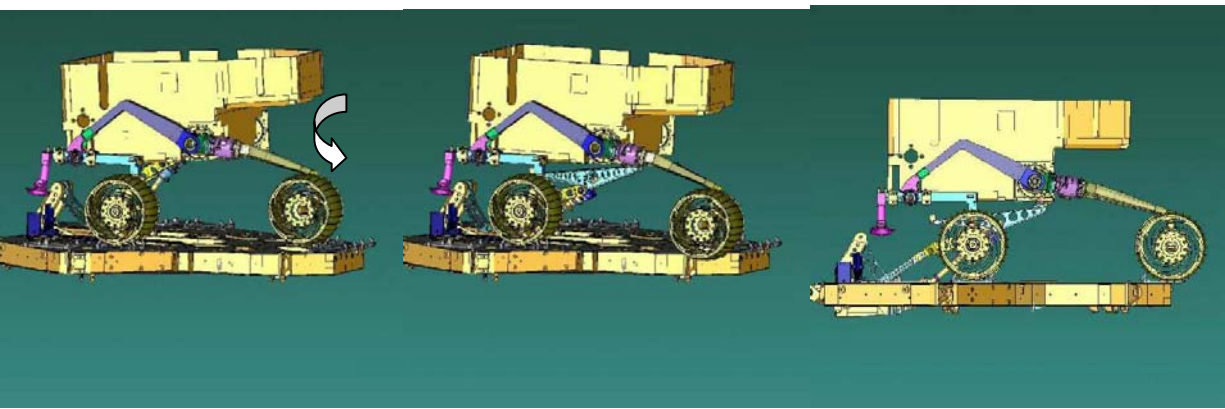
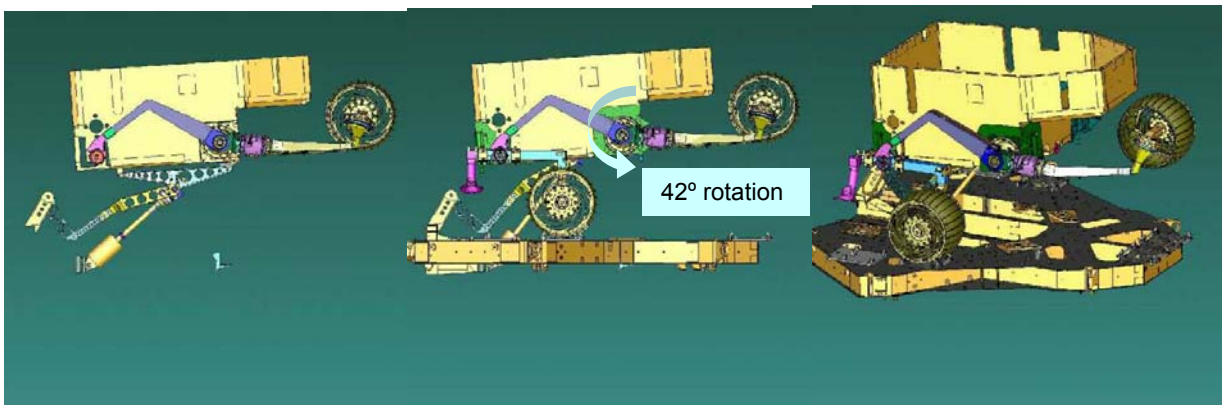


Figure 4
Sequence of deployments during standup

It was also desirable to accomplish the conversion between kinematic configurations in requirements 2 and 3 without resorting to pyrotechnic devices, as we anticipated testing the engineering unit many times while in a compressed schedule. Safety precautions and other issues peculiar to pyrotechnic devices posed a formidable threat to performing many tests in rapid succession.

The aggressive mass budget and restricted volume for this mission caused the engineering team to adopt an integrated, four-bar linkage approach to the stand up deployment scheme. The existing rover body structure (Warm Electronics Box, or WEB), lander, and the suspension system were utilized to create three of the four links and two of the four pivots, reducing the number & volume of the parts and active devices added to lift the rover.

The RLM functioned in two modes:

- First, it provided the motive force for lifting the rover in addition to functioning as the final link necessary for the four-bar system. That is, it controlled two degrees of freedom (vertical motion and rotation in pitch) when lifting in concert with the suspension system's linkage. In this lifting phase, the RLM supports the rover at two points: a shaped, Torlon pad that contacts the flat rover "belly", and a Torlon roller that is inserted into a specially shaped socket.
- Second, latches in the suspension system engaged in two steps as the deployment reached its apex and the RLM was reversed, thus altering the kinematics of the four-bar linkage by making the bridge joint between the front and rear rockers rigid. This second mode of operation then required the RLM to control only one degree of freedom, vertical motion. The disengagement of rotational (pitch) control is accomplished through passive means, by allowing the rear rover support to simply fall away while the front rover support roller rotates in its socket to permit the now-rigid rover and rocker system to rotate about a pivot on the rear bogie.

Actuator Selection

A trade study early in the design process identified a linear actuator as the preferred means of motivating the lifting process. The chief alternative, torque-actuated joints, was found to require very high torque and correspondingly high moments applied to beams and plate-type structural members. This resulted in an unacceptable mass and volume for a rotary actuator, along with the inefficient use of structural shapes. Only small angular joint excursion was required.

The actuator assembly was subcontracted. A leadscrew type of actuator was assumed (but not specified) in requests for proposal. When pure linear motion is desired from a leadscrew actuator, it is generally preferred that its torque be reacted internally to simplify the design of neighboring components. This would require extra mass, volume, and engineering effort however, so the mechanism's linkage was designed to react the leadscrew's torque. We ultimately selected a linear actuator from Ducommun-American Electronics (AEI); they offered an existing, qualified motor-gearhead with the addition of a leadscrew output module. Ducommun's actuator made use of their electronically commutated (brushless) motor design. JPL had already used another Ducommun motor of very nearly the same design in previous spacecraft, and it matched our drive electronics with its less-common center-tap winding configuration.

The leadscrew and thrust bearing stage represented a new design. The leadscrew, a two-start type with modified acme thread form, was custom made by Nook Industries. The completed Rover Lift Actuator (RLA) was qualification tested at the vendor on a linear-bearing dynamometer that was fitted with cables and weights to permit application of loads up to 4,087 N (920 lbf). The dynamometer was placed in a thermal chamber that allowed testing over the range of -60°C (with the aid of cold LN₂) up to +35°C.

Significant Design Features

When Ducommun proposed a leadscrew-based linear actuator, we required that it be provided with a dry, self-lubricating polymer nut. The reason was that the RLM was likely to be exposed to powerful jets of dust upon MER's landing and multiple bounces on the Martian surface. But with a stroke of about 244 mm (9.61 in) in a crowded space, we could find no viable design for a protective boot around the lead screw. We assumed that a conventional metal nut with wet lubrication would attract dangerous quantities of Martian dust to stick to the exposed leadscrew and seriously diminish the RLM's lifting capacity or jam it altogether. Instead of a flexible boot, dense brush wipers were added to sweep the screw ahead of and

behind the nut. We selected a nut made of Torlon® resin 4203 for its high strength and frictional properties, which we had characterized and found to be adequate in limited testing for other MER devices.

The RLM was required to have integrated hard stops to prevent the application of high force to the suspension system's elements when they meet their end of travel. The uncertainty in required stroke length was recognized early in the design process, so these stops were designed into the RLA's lead screw and made adjustable. The stop "dogs" were custom machined into adjustable steel nuts on each RLA and timed to engage with an appropriate overlap with corresponding dogs on the Torlon nut. Nook Industries machined their thread form into the nuts so that they could be adjusted by screwing back and forth on the leadscrew. One half-dog setscrew on each nut secured its final position and reacted the torque on each stop through shear force.

An early development test was designed to gain confidence in the leadscrew's ability to tolerate dirt. We purchased the closest commercially available item we could find that resembled our flight design: a single-start, rolled-thread acme screw with Polyethylene (PET) nut. We applied loads up to 1,156 N (260 lbf), which represented the highest load anticipated in Mars's gravity. Results were encouraging: torque required increased from 10% to 30%, with smaller increases noted at the highest load.

Most of the early part modeling and analysis was done in SolidWorks® and associated analysis software. However, due to limitations in SolidWorks at that time, the whole spacecraft database was maintained on Computervision® CADD5. When the engineer was satisfied with the general layout of the assembly, it was transferred by STEP or Parasolid file to the system to be integrated with the spacecraft. This translation presented an opportunity for error, and we did discover a significant error in the 4-bar pivot locations when the rover attitude at specific points along the lift trajectory did not match between the CADD5 model and the SolidWorks model. The discrepancy was discovered and remedied by a thorough comparison of the CAD models. We had made early plans to create an Interface Drawing to control swept volumes and critical interfaces, but the complexity of the design problem and the limited time available forced us to simply rely on the CADD5 database as the Interface control tool.

Lesson 1

Complex mechanisms comprising many parts with multiple motion trajectories are much easier to manage in CAD systems that show solid form in real time, that allow quick assignment of motion constraints, and allow real time movement of the system.

Lesson 2

Errors due to poor communication crept into the location of the pivots in the 4-bar link system. The errors resulted in frustration and wasted time when the two models gave incompatible trajectories for the WEB. This experience not only affirms the common wisdom that communication among team members is important, but especially points out that using two independent databases for design work requires careful planning to safeguard consistency of data. Much better still, use only one database.

Loads Analysis

The loads in the RLM were estimated with CAE software, and the effect of joint friction was estimated. Figure 5 shows the forces acting on the interface between the WEB and the RLM during the upward lift process. Two tools were used to evaluate forces: Dynamic Designer®, software that is integrated with SolidWorks, and ADAMS®. Several variable parameters were evaluated: rover/lander attitude with respect to gravity, different joint locations, and link lengths. The effect of increased friction at any one of the system's many pivoting joints could be studied this way as a means of quantifying functional margins. CAE simulation provided insight and understanding of system behavior, helping to design the system standup test plan. An example of analysis output for the linear actuator's force output is shown in Figure 6. Gary Ortiz of JPL performed the ADAMS modeling and documented the system's forces and kinematic behavior.

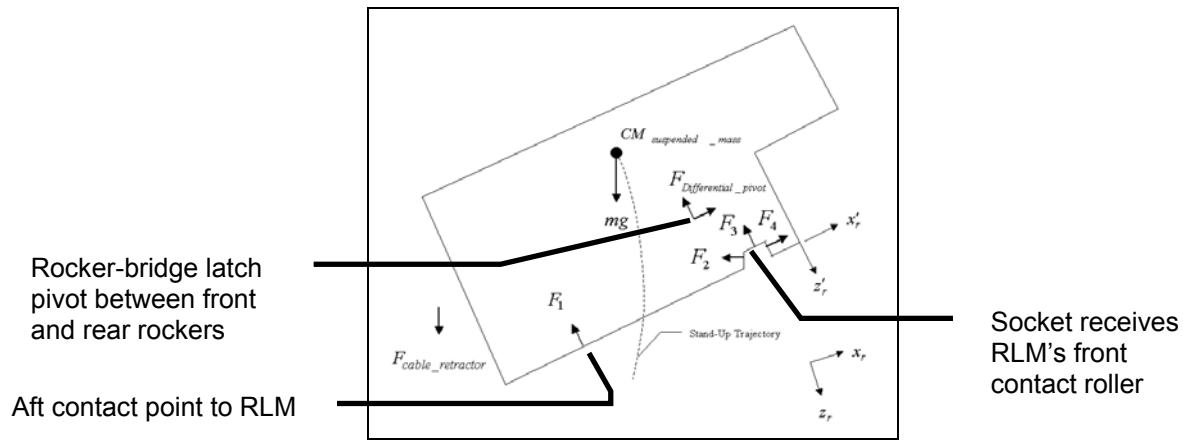


Figure 5

Free body diagram of the rover and its interfaces to the suspension system and RLM

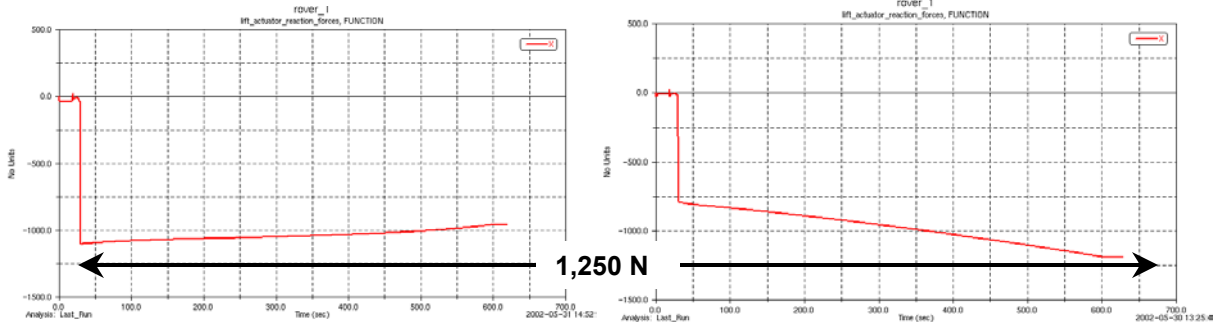


Figure 6

RLA force requirement vs. time for a nominal, flat lander attitude (left) and 20° pitch (right)

One gratifying indication from our analysis was that the maximum force required from the RLA would not be significantly different as a function of rover/lander tilt attitude; although the slope of the force curve would change, no one load case was clearly more difficult than another. We calculated forces at the actuator and joints over the whole envelope of possible deployment attitudes (MER is required to be deployable at any attitude up to 20° from horizontal).

Testing, Failure & Recovery

Our testing schedule demanded that parts must be fabricated before achieving complete confidence in the design. But CAE provided essential advance warning of problems when continuing analysis predicted that the rover's stability was threatened at certain tilt angles within the specification envelope. The RLM depends on a balance of forces due to gravity to hold it in firm contact with the rover, and it was feared that there was insufficient margin to prevent the front contact roller from pulling out of its socket at lander tilt attitudes greater than 20°. Anticipating that this joint would need refinement as a result of testing, the critical interface shape was designed as an easily machined and replaced titanium-alloy insert. The two plots in Figure 7 contrast the estimated contact force on the RLM's roller between the unstable configuration on the left with the remedied configuration on the right, that was designed long before the first test could be executed. This instability was confirmed in a (carefully controlled!) test. The replacement part was ready to be installed immediately, and the test program continued with little delay. Figure 8 illustrates the socket and replaceable insert.

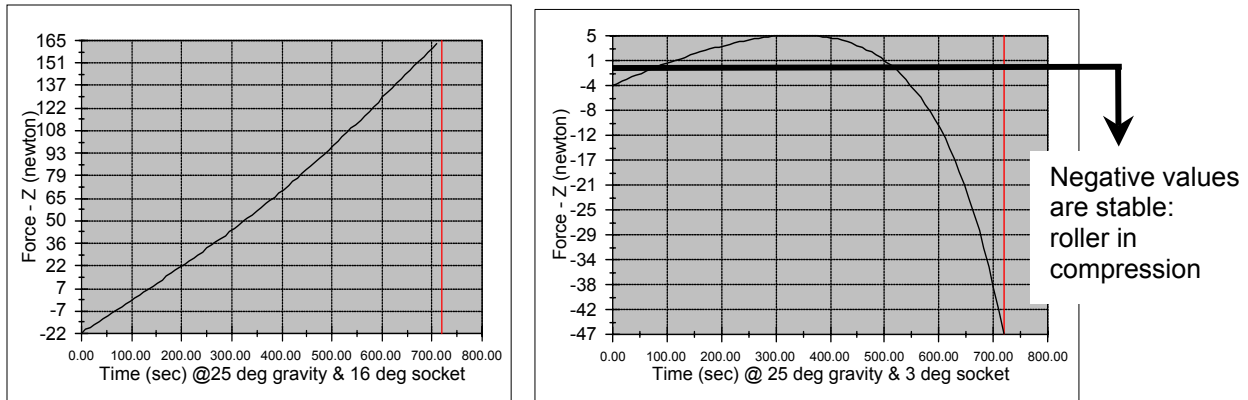


Figure 7

Contact force on the RLA's front contact roller vs. deployment time. Note the pronounced, monotonic transition through zero for the unstable joint configuration on the left. This indicates that the roller has lost compressive contact with its socket



Figure 8

Front roller to socket interface and the replaceable socket insert

Lesson 3

A modeling effort that continues concurrently with hardware assembly and test can prove beneficial, especially if uncertainties can be foreseen and modular components are utilized which can be easily modified or replaced as new information is made available.

Late in the test program, it was found that the real system strained so much in Earth gravity loads that the maximum travel of the RLA had to be extended by approximately 12 mm to cause adequate rotation at the rocker-bridge latch to approximately 42°. When modeling with ADAMS we had attempted to quantify the extra deployment made necessary by compliance and backlash, but the real system was too complex for an accurate estimate. The RLA's lead screw was designed to be long enough to provide adequate margin to allow this extension, although it was necessary to abandon the hardstop's adjustability feature and design a new hardstop with smaller volume to accomplish the stroke increase.

At about this same time, we noted another problem: a crack had opened up at the root of the hardstop that was machined into the Torlon nut. This occurred due to an oversight in the stress analysis; no stress concentrations had been considered in that location. The remedies for the cracked nut and to provide increased range of travel were accomplished in the same redesign; there was room at both extended and retracted positions to mount new steel parts (adding about 0.1 kg) that shunted the stop loads around the nut altogether. The broken Torlon nut is shown in Figure 9. Figure 10 illustrates the original extended stop design and the final version that used all the available screw length. The final design of the nut housing and retraction stop is shown in Figure 11.

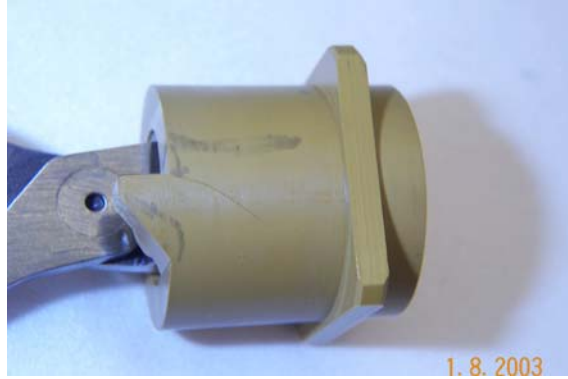


Figure 9

Torlon 4203 nut showing crack propagating from root of hardstop



Figure 10

Original extension stop design (left) vs. the redesigned version with longer stroke



Figure 11

Final nut housing and retraction stop design

Lesson 4

This reaffirms the previous lesson: modularity in design proved to be beneficial. Small, key components could be quickly unbolted and inexpensive replacement designs incorporated in a short time, rather than having to modify an expensive, complex machining with integral features. Try to foresee the need for extended capability and design for it.

Lesson 5

When significant uncertainties exist in the development of a design, try to provide room and features that permit different approaches to accomplishing the same task. There was adequate room at both ends of travel to modify the hardstops so that the original approach was discarded and new hardware fabricated at a late date.

The RLA was specified to work reliably at loads up to 3,685 N (830 lb_f). This would allow testing of the complete rover/ suspension system in Earth gravity without the assistance of off-loading devices. We considered this an important requirement, as it would support the difficult logistics of rapidly testing deployment in the many permutations of attitude and environment. It was also desirable to avoid off-loading devices to prevent possible damage to the delicate rover appendages. However, dynamometer tests on the actuator made it plain that it would not reliably exert the force required to test the lift process in Earth gravity. Instead, we found that, even at room temperature it would frequently stall at loads as low as 2,313 N (520 lb_f). Its capability was, of course, worse at -60°C, the lowest test temperature.

The force at which the RLA stalled was inconsistent from one test to another. In fact, one unit successfully (albeit slowly) lifted a rover in cold thermal-vacuum test, only to fail another test at ambient temperature in a supposedly identical RLM. We also noted that stall generally occurred at a motor speed of 26.0 rad/s (248 rpm) $\pm 5\%$ instead of nearly zero speed as we expected. Following the logic indicated in Figure 12, it was shown to high confidence that the poor and erratic performance was due to variable friction of the Torlon nut on the lead screw. The motor/gearhead put out consistent torque that indicated reasonable gearhead efficiency.

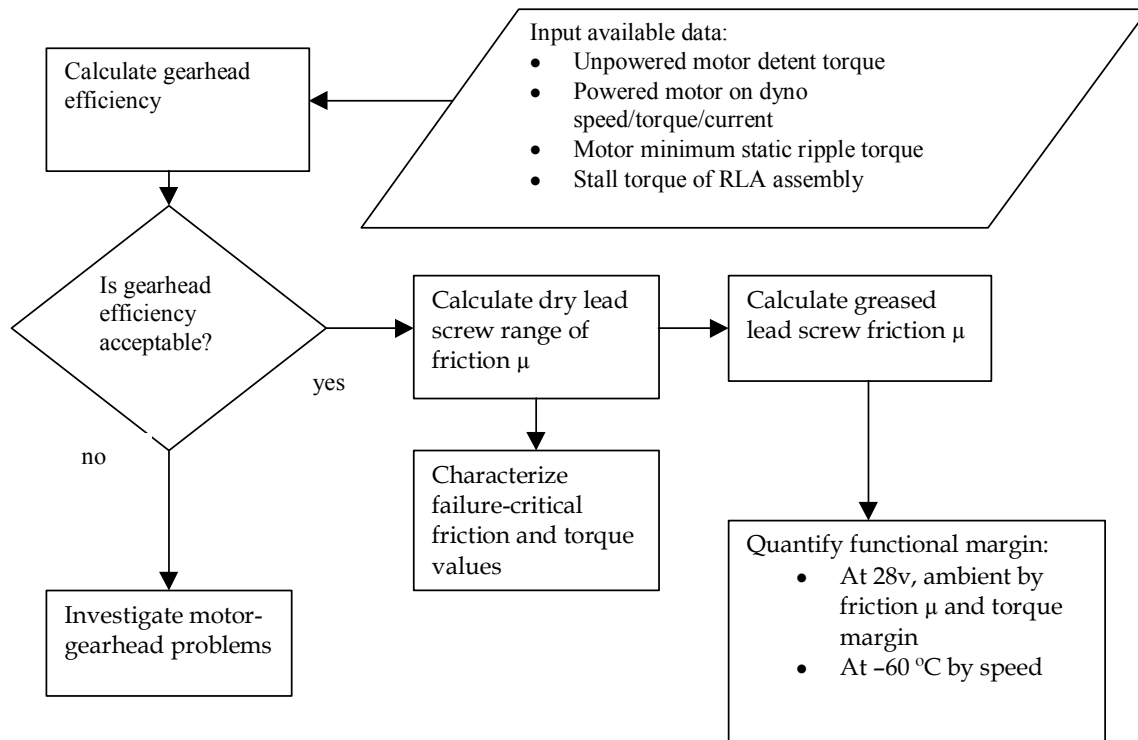


Figure 12
Diagnostic logic for RLA performance

We investigated several remedies. The first solution we attempted was to dry film lubricate the lead screw with a thin film of sputtered-on MoS₂. This process made the friction problem worse! Next, we removed the lubricant film and polished the screw with lapping compound. The Torlon nuts had a noticeably poor finish on their threads, so we tried polishing those too. Polishing improved the RLA's performance briefly, but the gains would not persist through all qualification tests; upon subsequent running-in, the level and variability of friction at the nut increased again.

With performance too poor for Earth gravity operation and schedule almost exhausted, we finally experimented with grease lubrication on the screw. Immediately after a failure to lift the rover in ambient conditions, we injected Braycote® 600 grease into the cavity just in front of the nut. As hoped, the rover deployed on the next try without the slightest trouble. Persuaded to favor grease lubrication by this dramatic improvement, now we had to prove that a blast of dirt would not jam the exposed leadscrew! The brush wipers, mentioned earlier, were made of electrically conductive brass-fibers to facilitate grounding across the interface between the steel lead screw to the u-joint that housed the Torlon plastic nut. They were intended to remove all but a fine layer of dust that might cling to the screw, but now we needed to show that a heavy load of mixed dirt would not pose significant risk to RLM operation. To make matters worse, we noted that some brush fibers came loose in some tests (Figure 13). It then became necessary to show that these fibers themselves could not jam the mechanism.

To prove that the RLM could tolerate stray brush fibers, we repeated a set of RLA dynamometer tests with a greased lead screw. Several brush seals were chopped up to prepare large amounts of brass fibers, and these fibers were applied aggressively to the lead screw before the RLA was activated. To our relief, no amount of effort to intentionally jam fibers of any length into the nut/screw interface succeeded in making a significant (>5%) increase in current required to lift any load up to the maximum test load. Photos of the lead screw and the Torlon nut covered with brush fibers are shown in Figure 14.



Figure 13

Photo showing brass brush fibers that were pulled out of their brush wiper assembly

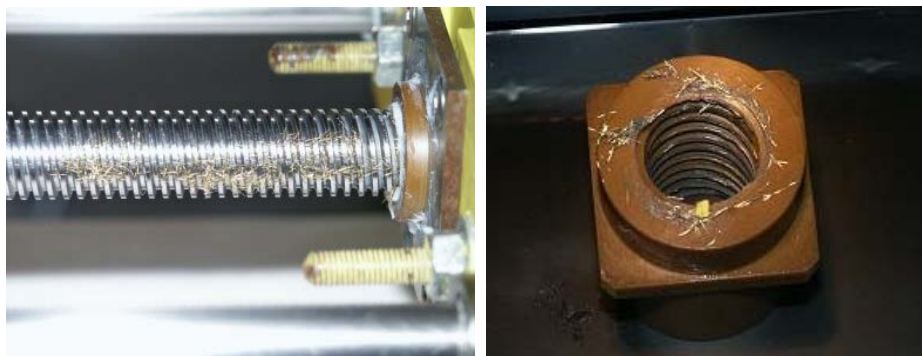


Figure 14

Left, the greased lead screw in the dynamometer covered with brush fibers. Right, the Torlon nut after the test. Performance was unaffected despite the trapped fibers

Finally, many system-level tests were performed over the whole standup sequence. The engineering model of the rover/ suspension/RLM package was tested for the RLM's ability to tolerate a heavy load of dirt. We formulated a mix of quartz particles of various sizes and basalt dirt and applied it to the full length of the RLM's lead screw in its pre-lift configuration. This material application was intended to simulate a worst case caking of dirt onto the leadscrew resulting from airbag impact and rolling. When the RLM achieved maximum lift, a coating of fine "Mars Dust Simulant" was applied to the lead screw in order to simulate the effect of airborne particles that might stick to the lead screw when it's exposed in the extended position. This measure addresses a contingency plan that anticipates the ground team is working on a standup or system anomaly for multiple sols.

Table 1 summarizes the material mixture that was applied prior to lift. Figure 15 shows a picture of this mixture and the appearance of the lead screw with this contaminant before lifting. The lead screw had residual Braycote 600 grease on it from a prior test. The material was forced onto and in between the threads of the screw from all sides through the entire length of the screw. Thus, both the total quantity applied and the level of penetration of the material into the thread depths was felt to be conservative relative to what could be naturally achieved during impact and rolling on Mars.

Table 1
Hard, sharp dirt contamination mixture applied to the RLA's leadscrew

Element	Volume Fraction
Nominal 420-1000 micron crushed quartz	1/3
MIL-E 5007 crushed quartz	1/3
ISIL (basalt) sand, $\leq 5\text{mm}$ particles	1/6
Athena "Mars Dust Simulant"	1/6

Figure 16 shows that a significant amount of material is gathered in the extension brush wipers of the RLM and that a small amount does escape past the brushes to the Torlon nut. In addition to the material entrained by the brushes, a significant fraction of the material is brushed off the lead screw and falls to the ground during operation.

No significant performance degradation was seen as a result of dirt testing, as measured by motor current necessary to raise the rover. Table 2 summarizes current and speed test data from system tests and the safety margins that correspond to those results.



Figure 15
The mixture of quartz and sand applied to the RLA's leadscrew for the dirt tolerance test



Figure 16

Views of the extension brush wiper after the dirt test and the Torlon nut with an accumulation of dirt

Table 2

Final MER 1 and MER 2 RLM/RLA margins as measured in system tests.

Test	Test Temp °C	Test Voltage	Measured stall current [mA]	Predicted stall Velocity, mm/s	Measured current [mA]	Measured Velocity, mm/s	Demonstrated Margin, Earth Weight		Predicted Margin, Mars Weight	
							current draw	velocity	current draw	velocity
MER 1 STT	-55	32.7	785	0.2	350	0.52	2.2	2.6	3.7	3.5
MER 2 STT2	-57	28.5	810	0.2	350	0.44	2.3	2.2	4.3	3.4

The performance margins noted here are robust, even in Earth gravity where wide margin is not required. It can be seen that the key to obtaining consistent performance was to control friction at the nut/screw interface of the RLA, and grease was the appropriate means to achieve this control. This affirms a motto—to quote Doug Packard, an esteemed, veteran engineer at JPL: “Grease is Good”!

Lesson 6

We responded to early indications that the self-lubricating Torlon® nut presented high and erratic friction with measures such as polishing and dry film lubrication. Unfortunately, the best solution we found could have been implemented much sooner if we had not been dogmatic about not flying a greased, “dust magnet” leadscrew. As it turned out, the greased screw was highly tolerant of large quantities of dirt, especially with its brush wiper-shields. If resources permit, it is wise to prepare and test a range of design solutions when significant uncertainties exist in all candidate solutions.

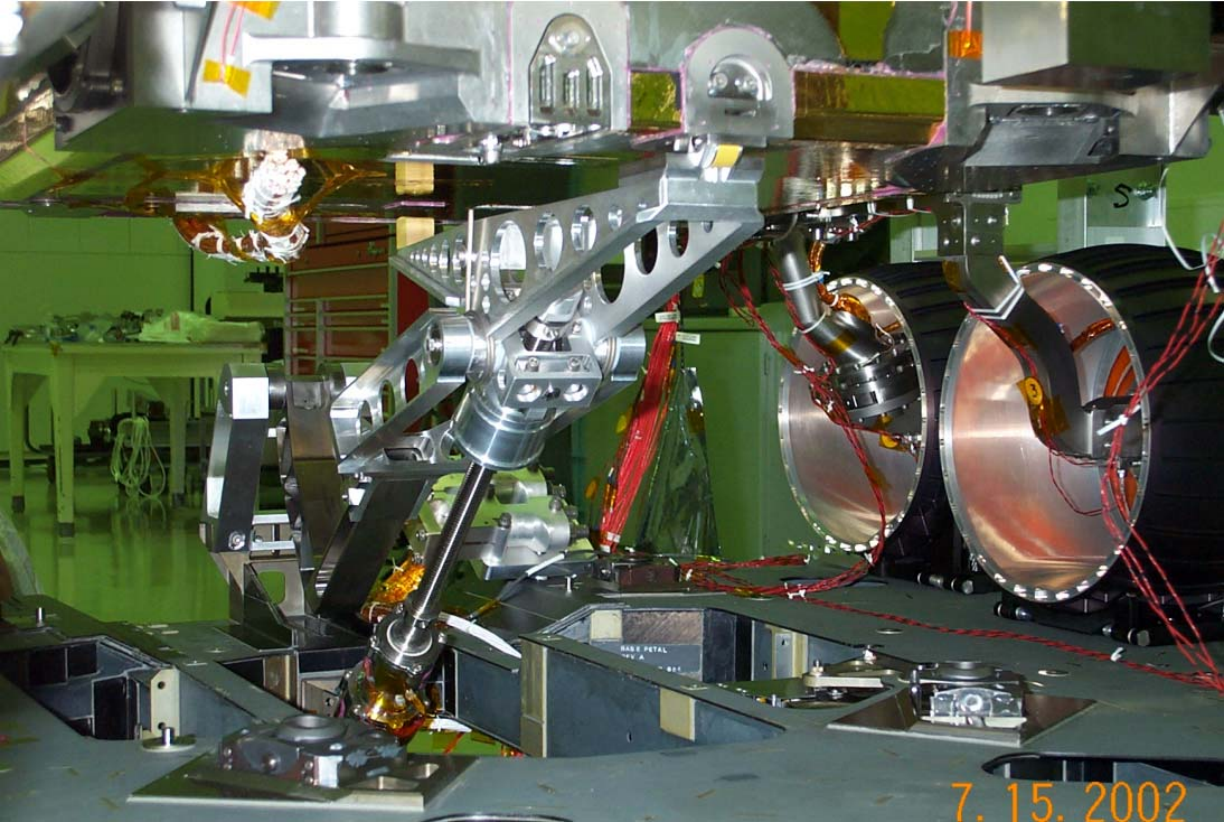


Figure 17
A view of the complete RLM underneath the rover

This research was carried out at the Jet Propulsion Laboratory, California Institute of Technology, under contract with the National Aeronautics and Space Administration.

Development of Mars Exploration Rover Lander Petal Actuators

Boz Sharif* and Ed Joscelyn*

Abstract

The twin robotic missions “Spirit” and “Opportunity” were launched in the summer of 2003 as part of the MER (Mars Exploration Rover) project for a rendezvous with Mars in early 2004. These identical twin rovers were designed to prospect the surface of Mars for evidence of past geological activity related to presence of liquid water. The mission was modeled after the successful “Pathfinder” mission that delivered the “Sojourner” rover to the surface of Mars in 1997. The new rovers are much larger and heavier than the “Sojourner” and are equipped with a large array of scientific instruments as well as communication gear for direct transmission of data back to Earth. The landing vehicles have also grown in size to accommodate the new rover configuration. After the Lander makes its hard landing protected by a cocoon of air bags, it is the job of any one of the 3 Lander Petal Actuators (LPA's) to right the spacecraft, if necessary, and open the remaining petals to allow deployment of the rover onto the surface of the red planet.

This paper describes the challenges in developing, building and testing the new LPA's in support of the MER project.

Summary

One of the challenges to Aeroflex was to design the Lander Petal Actuator to develop 3,300 N-m of torque within the required mass budget of 6.5 kilograms. The earlier “Pathfinder” LPA's were based on the use of a size 40, 160:1 reduction ratio, Harmonic Drive gear set as the output section of the actuator. The actuator was limited to an output torque of 1580 N-m as a result of the “Ratchet” limit of the Harmonic Drive gear set. These components were mass optimized to yield a total mass of 5.7 kg for the “Pathfinder” LPA. If a similar approach was taken for the MER actuators, the required size 65 Harmonic gear set would weigh 20.9 kg. Clearly, a new approach was required.

Each petal needs to rotate 110 degrees in 20 minutes or less giving a minimum speed requirement of 0.0153 RPM. The allowable power was a maximum of 50 watts per actuator. When the actuators were delivered to the program, the final power with brake was only 10 watts per actuator. This was accomplished through the use of planetary gear reduction systems that yield much greater efficiency at all operating temperatures (approximately 83% per stage at the cold operating temperature). The usual penalty for this approach is size for a given reduction ratio and stiffness.

Another challenge was the testing of such a large system over the required environmental temperatures (-60 to +55°C) as well as dynamic testing of the brakes at a cold temperature of -120°C. No off-the-shelf equipment was available for this task. A test apparatus was developed from scratch to perform the required testing while safeguarding the mission-critical hardware. This test fixture will be described later.

The MER LPA requirements were established based on the mass, size and the performance of the LPA units on the previous Pathfinder mission. These earlier units, developed by JPL, were approximately 150 mm in diameter, had a mass of 5.7 kg and were capable of a sustained output torque of 1350 N-m and a peak torque of 1580 N-m as a result of the “Ratchet” limit of the gear reduction unit employed. This mission successfully landed and deployed the Sojourner rover onto the surface of Mars in 1997. The MER mission strives to leverage the successful heritage of the Pathfinder mission to the extent possible. However, as it is usually the case when utilizing a heritage design for a new mission, some minor “tweaks” are necessary. In the case of the MER LPA's, the minor tweak was an increase in the output

* Aeroflex Motion Control Products, Hauppauge, NY

torque from 1350 N-m to 3300 N-m. This requirement was to be accomplished without a significant attendant increase in mass or size. The high torque requirement was a result of the increase in the mass of the rover and lander package from 330 kg for the Pathfinder mission to 441 kg for the MER program. The finalized requirements for the MER LPA's were as follows:

Output Torque:	3300 N-m
Speed:	0.0153 RPM Minimum
Mass:	6.5 kg maximum
Size:	App'x. 150-mm dia. X 250-mm long
Operating Temperature:	-60 to +55°C
Survival Temperature:	-120°C
Power Consumption:	50 watts Maximum
Un-powered Brake Holding Torque:	> 2280 N-m

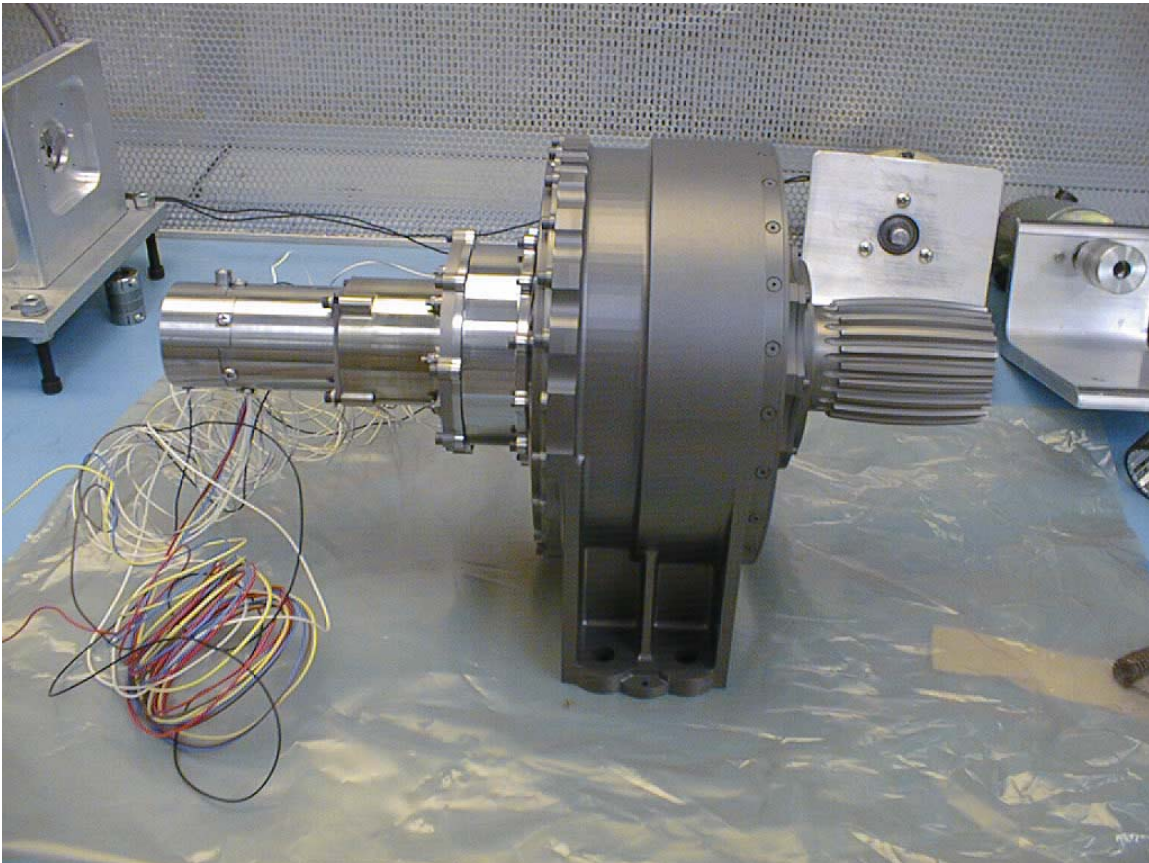


Figure 1. LPA First Article

Actuator Design

As mentioned, the use of a Harmonic Gear drive was not deemed practical due to the excessive mass penalty. Aeroflex had previously designed, tested and delivered to JPL a low mass actuator, capable of delivering approximately 2 N-m of torque at a total mass of 42 g, for use in the Muses program. Many of the design details as well as the overall philosophy of that actuator design were brought to bear on the LPA task.

This approach resulted in a design that consisted of an electronically commutated BLDC motor driving a 7-stage gear reduction system. The motor shaft was fitted with a brake to provide the required un-

powered holding torque. The gear reduction was divided into 3 separate housings so that each stage may be mass optimized as much as possible. Gear geometry was selected based on transmitted torque and running speed to allow an optimum balance between the number of teeth under load, the number of planets sharing the load and the overall mass of the unit. Gear teeth were of a size 64 DP at the motor input side to an 8 DP size at the output.

The actuator has an overall reduction ratio of approximately 320000:1 and is capable of delivering well in excess of the required 3300 N-m of torque. However final torque output is limited to 3300 N-m by utilization of a current limit to safeguard the actuator as well as the hardware downstream in the torque path.

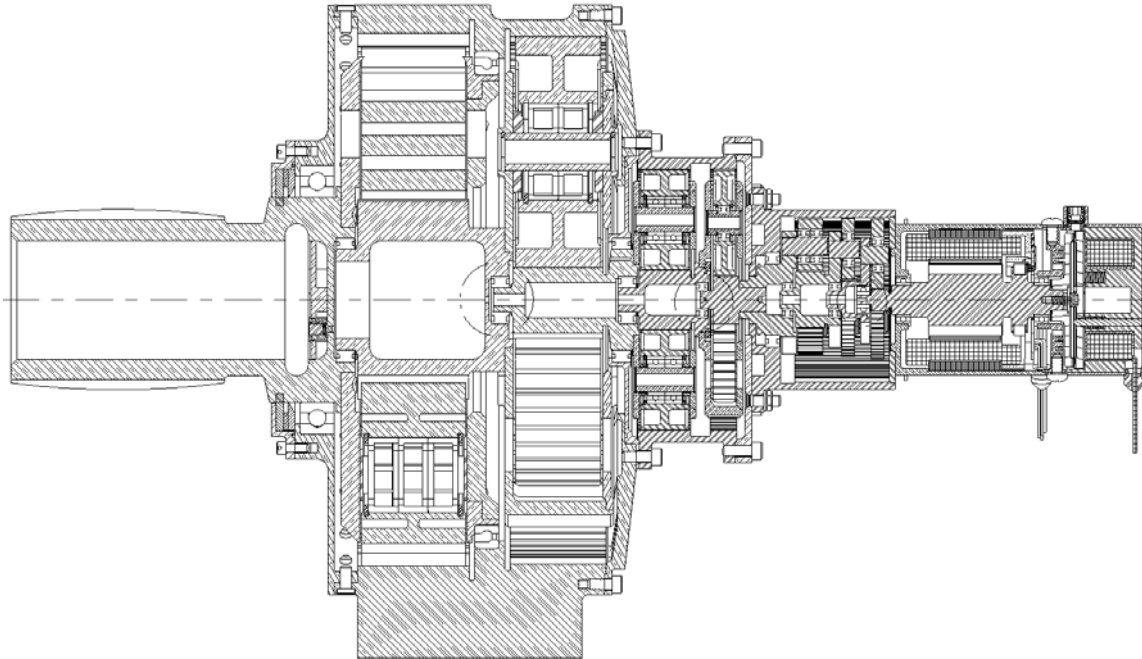


Figure 2. Actuator Sectional View

Gear Design

All of the gearing utilized in the LPA was designed and optimized using conventional CAD and FEA software. In each instance, maximum utilization of volume and mass was paramount to ensure compliance with the requirements. Each component was analyzed to allow maximum safe reduction in mass without compromising the required design margins. Particular attention was required for selection of bearings, bearing mounting and bearing pre-load selection.

As a result of the large overall reduction ratio, gear teeth at the input side were required to withstand considerably more load cycles than the output stage gearing. This would require that the input side gears be designed to have fairly moderate contact and bending stresses whereas the output section gears were primarily affected by the bending load (fatigue) stresses.

As the design progressed, it became apparent that the size of the input side gears would ultimately be governed by the available sizes of the rolling elements. The required dimensions for these bearings resulted in tooth bending loads and contact stresses that would easily meet the design loads. The effect of these size accommodations were a net increase of 70 g in the mass of the actuator.

On the other end of the actuator, a problem was encountered in fitting bearings to the output stage planets. These planets carried a load of 1450 kg at the peak output torque of 3300 N-m. The nearest size bearing(s) capable of the load were larger than the planets. The problem was resolved by selection of a roller bearing that in multiples of 3 would be able to carry the load with sufficient margin. These same roller bearings were also fitted to the second from last stage of planets with an attendant mass reduction of approximately 100 g compared to the ball bearings originally selected.

SLA Modeling as a Sanity Check

Due to the extremely tight schedule and the long lead times for fabrication of the gear components and the space rated bearings, the possibility of a pre-engineering-release prototype was out of the question. However, an SLA (Stereo Lithographic Apparatus) model was a possibility. The fabrication of the model, from extraction of the electronic files for the SLA process, until receipt of the components took approximately 2 weeks. The parts were cleaned, some minor machining was performed and a full prototype LPA was assembled using actual steel bearings and shafts. A prototype, functional motor was fitted and hence a top to bottom design verification was accomplished. This unit was actually operated on the bench. It was estimated that the plastic unit, based on the strength of the SLA materials, was capable of producing approximately 150 N-m of torque.

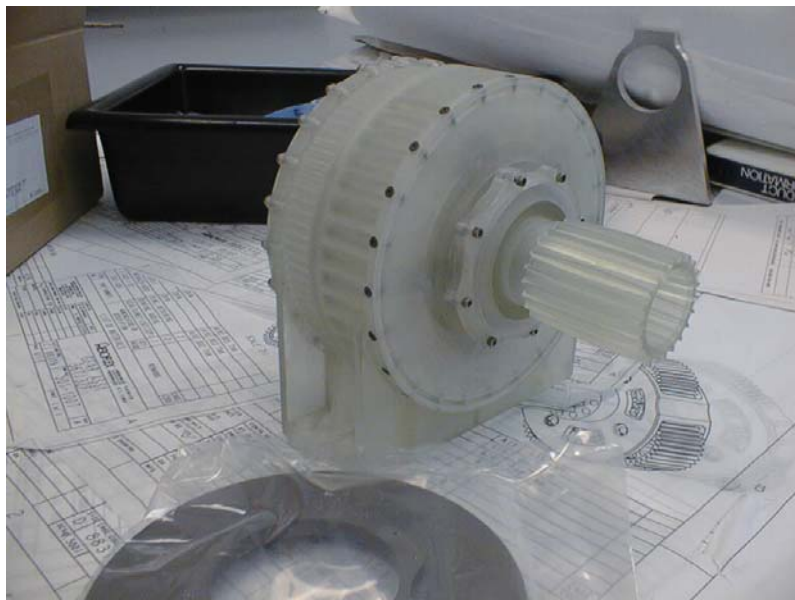


Figure 3. SLA Model of LPA

A Scary Moment

After successful integration of the actuator first article, full load testing began. Being the first time this large a load had been attempted using the relatively new Aeroflex technique, apprehension was in the air. Needless to say, design margins need to be carefully honed when the goal is as light a weight as possible.

The actuator achieved the rated torque of 3400 N-m again and again. At sometime that evening in the early morning hours, a great deal of elation was in the air and some personnel had even gone home when a loud bang was heard from the test apparatus. Of course, the couplings had snapped or perhaps even the torque transducer had failed. Fear that it was the actuator was pushed from our thinking.

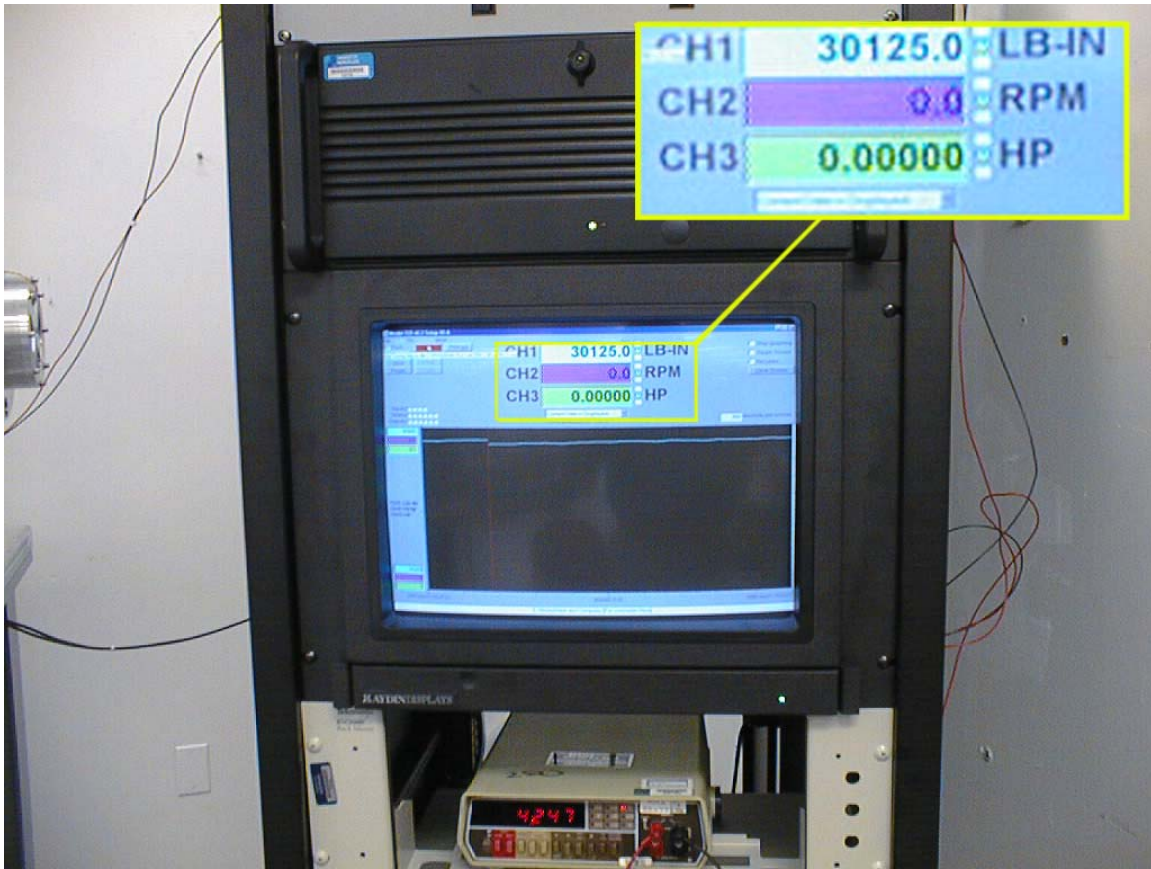


Figure 4. Moment Of Truth, Actuator Output at 3390 N-m

Indeed, after careful inspections, it was determined that a structural failure had occurred in the actuator output shaft. The output carrier to which the output pinion was affixed had snapped about the base of the pinion. Understandable since this is the region of most stress.

Further investigation revealed that the failure had occurred at a point where the wall thickness of the hollow output splined shaft was only 2.3 mm (0.090 in). The original design maintained a constant section thickness of 5 mm (0.200 in) throughout this shaft section. The section had been thinned due to the addition of a counter-bore to house the pilot bearing from the planetary stage behind the final output stage section. The size of the counter-bore was changed at the last minute when the original pilot bearing, which measured 12.7 mm (0.5 in) smaller in diameter, became untenable due to excessive lead time.

After calculations and FEA modeling had re-confirmed that the original design would have sufficient margin, the race against the clock was on to resolve the failure mode in time to deliver the flight hardware.

An additional complicating factor was that the failure had occurred in a region of the shaft immediately adjacent to an EB (Electron Beam) welded area. The condition of the welded region was carefully investigated to determine if any annealing of the material had occurred and had contributed to the failure. A careful microscopic and metallurgic examination of the failed part was performed at JPL to rule out this possibility.



Figure 5. Failed Shaft section

A Path Forward

The challenge to resolve the problem quickly and safely was compounded by the fact that virtually all the affected parts were at the end of their long (typical 16 to 20 week) fabrication cycles. There were a minimum of 5 vendors in the fabrication chain of the shaft. After a few sleepless nights, a solution was devised and proposed for implementation; rather than replace the failed part with a revised part with the intended section thickness (which would dictate the elimination of the pilot bearing or the substitution of the original unavailable bearing through the use of an off-the-shelf bearing), the part would be augmented with a series of pins inserted into the load zone to relieve the thin section of any load bearing. This solution was carefully examined by hand calculations and FEA modeling and a single part was fabricated and installed on the original EM test unit. After a few tense hours on the dynamometer, the solution was deemed a success. Additional pins were procured and installed on the remainder of the parts to support the delivery schedule. The net impact on project schedule was approximately 3 weeks.

Motor Design

The motor is a conventional 6-pole, 18-slot Brushless DC design with a center tap which is driven unipolarly. The drive electronics (LPAE's) were developed and manufactured by JPL. Because the actuator is capable of torques greater than 3300 N-m, current limiting in the LPAE controllers was necessary to prevent damage to downline mechanisms and was set using the first actuator.

The motors have a K_t of approximately 35 mN-m/amp with a winding resistance of approximately 5 ohms. The motors were capable of delivering approximately 12 mN-m (1.75 in-oz) of torque at the current limit. Motor speed varied from approximately 5000 to 7000 RPM depending upon supply voltage.

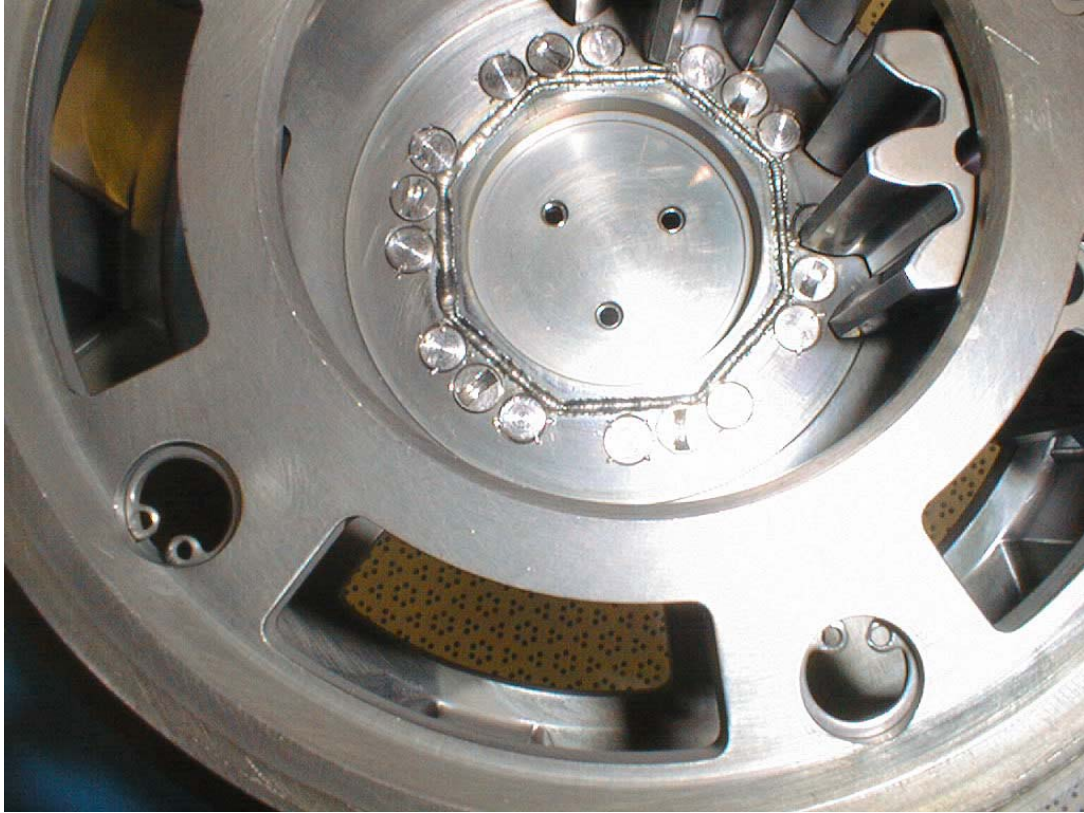


Figure 6. Pinned Shaft section

The motors were commutated using 3 latching ceramic Hall devices placed with a 120-degree electrical separation. Because the Hall devices contain electronic components, extreme caution concerning ESD and voltage excitation conditions had to be observed at all times. When not connected to the drive electronics, all commutation leads were twisted together. The motor used a separate magnetic target to excite the Hall devices. This allowed a 180-degree sensor pole arc target to be used to ensure CW and CCW performance was symmetric to within a small percentage of one another.

Each motor/brake assembly required passing a separate test procedure before integration with the gear assembly.

Brake Design

The brake is a conventional electromagnetic type used in other space mechanism motors developed by Aeroflex. The brake has 6 springs which forces two discs together. The discs have lapped chromium oxide surfaces which produces the friction. One disc is fixed to and rotates with the motor's rotor. The other disc is allowed to move axially and is rotationally restrained with 3 polished pins. The engaging motion is too short and the pin clearance too large to allow the pins to cock and hang up. To disengage the brake, an electromagnet is energized and attracts the disc that is restrained from rotation by the 3 pins. This action separates the two discs allowing the disc affixed to the rotor to rotate freely.

Only a few watts of power is necessary to release the brake. A non-magnetic spacer was inserted between the electromagnet and the movable brake disc to prevent residual magnetism from holding the brake dis-engaged once power is removed. The brake friction torque also exceeds the motor's capability of rotating the system (approximately 35 mN-m), i.e. if the motor was energized with the brake engaged, the motor would not turn.

There was a condition where a brake did not release in one of the 12 units manufactured. This interesting development and the resolution of the condition are described in detail in another paper presented by JPL.

Test Apparatus

Due to the extremely high torques produced by the LPA, it was necessary to design a special test bench. This test bench holds the LPA within an environmental test chamber while allowing torque transmission to the torque transducer and torque generating elements mounted in-line with one another outside the chamber. The LPA unit under test (UUT) was mounted on a custom fabricated cold plate held on the end of four 5-cm (2.0-in) diameter rods which passed through the walls of a modified thermal chamber and were anchored to a 4.4-cm (1.75-in) thick aluminum plate which comprised the base plate of the test fixture. This configuration isolated the chamber from all of reaction forces and allowed the torsional loads of operating the LPA to be resisted by the robust construction of the test bench.

The goal of the testing program was to measure the torque and speed of the LPA at different applied voltages (24 to 32.8 volts) as well as different applied torques (0, 680, 1355, 2033, 2260 Nm) up to 3300 Nm under various thermal conditions (-60 to + 60°C). Some special brake testing was to be performed at -120°C.

Because the LPA moves at such a slow rate of about 0.018 RPM (on average), conventional brakes would not work. Problems such as “stiction” for example could cause erratic torques leading to test anomalies. In the final configuration, in order to maintain smooth, precise control over the resisting torque, the LPA was allowed to drive a large step up gear system with an overall ratio of 1:17400 with a Himmelstein torque transducer mounted between the LPA and the load. The input to this gear system was a small control motor. With the small control motor stalled, the LPA could wind up the system to the maximum torque required. Running the small control motor in the same direction as the LPA would allow any torque loading required. Running the control motor to match the speed of the LPA would produce a no load condition to the LPA.

During testing a number of parameters, such as torque, velocity, motor voltage, brake voltage as well as a number of thermo-couples placed at various points on the LPA and the test chamber were continuously logged and recorded. The actuator was required to rotate 1 complete revolution in both CW and CCW directions under each of the specified environmental conditions at various voltages and loads. As an example, at a load of 2260 N-m with a 32.8 volt supply, the LPA required 55 minutes to complete a revolution in one direction.

To achieve the -120°C temperature in a “standard” chamber which is only capable of a -75°C lower temperature, a controlled flow of Liquid Nitrogen (LN₂) was introduced into a cold plate incorporated into the mounting base for the LPA. This was augmented, under closed loop control, by direct injection of LN₂ into the chamber itself. This method is not recommended by the chamber manufacturer as it freezes the refrigerant and trips limit relays. It takes several hours for the chamber to recover and operate normally.

The low temperature testing was to ensure that the brake would hold during the Mars night and not allow the petal to slip and upset the rover. The test actually included electrically releasing the brake with a torque applied to the LPA output shaft simulating the rover load and then re-engaging the brake when electrically deactivated.

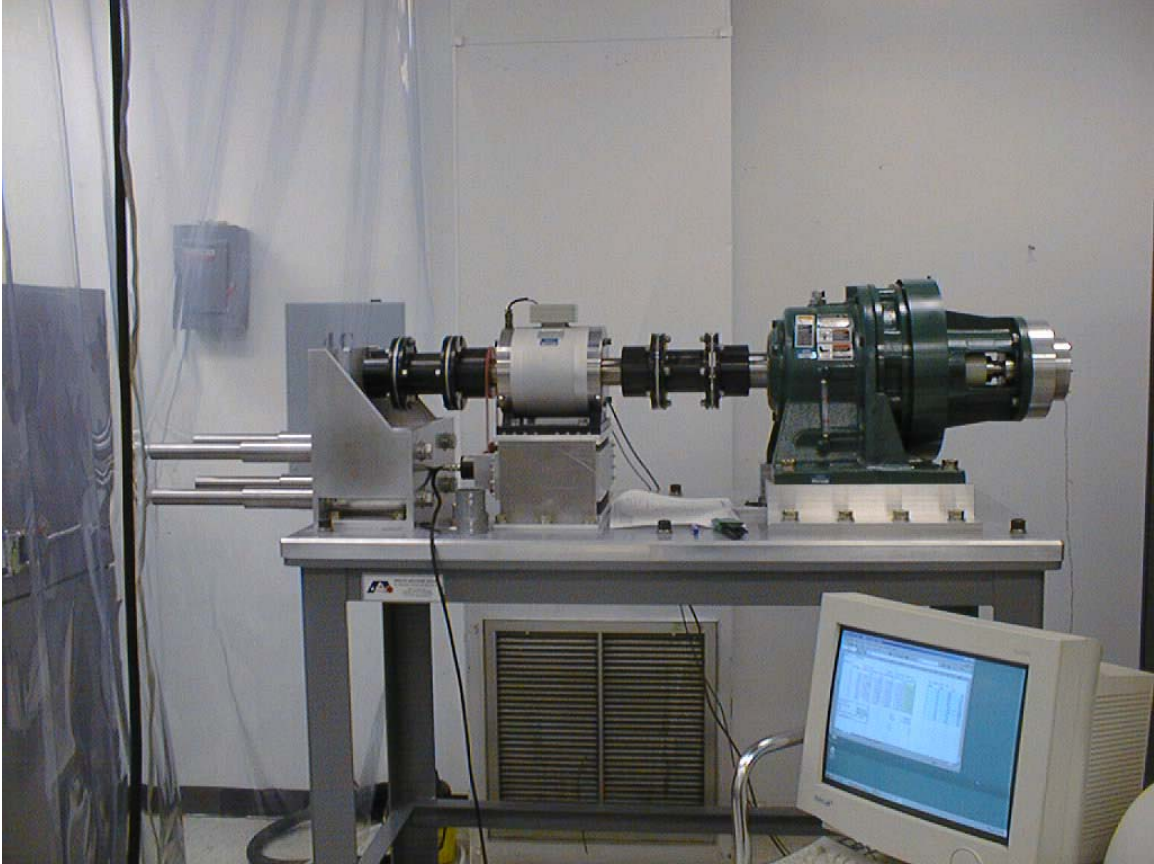


Figure 7. Dynamometer Portion of Test Apparatus

A total of 12 LPA's were assembled, tested and delivered to the MER project.

The results of the testing were a validation of the many design assumptions employed in the construction of the LPA's. In particular, the performance of the actuators over the required temperature range without the use of heaters or blankets was indicative of excellent gear efficiency and lubrication performance.

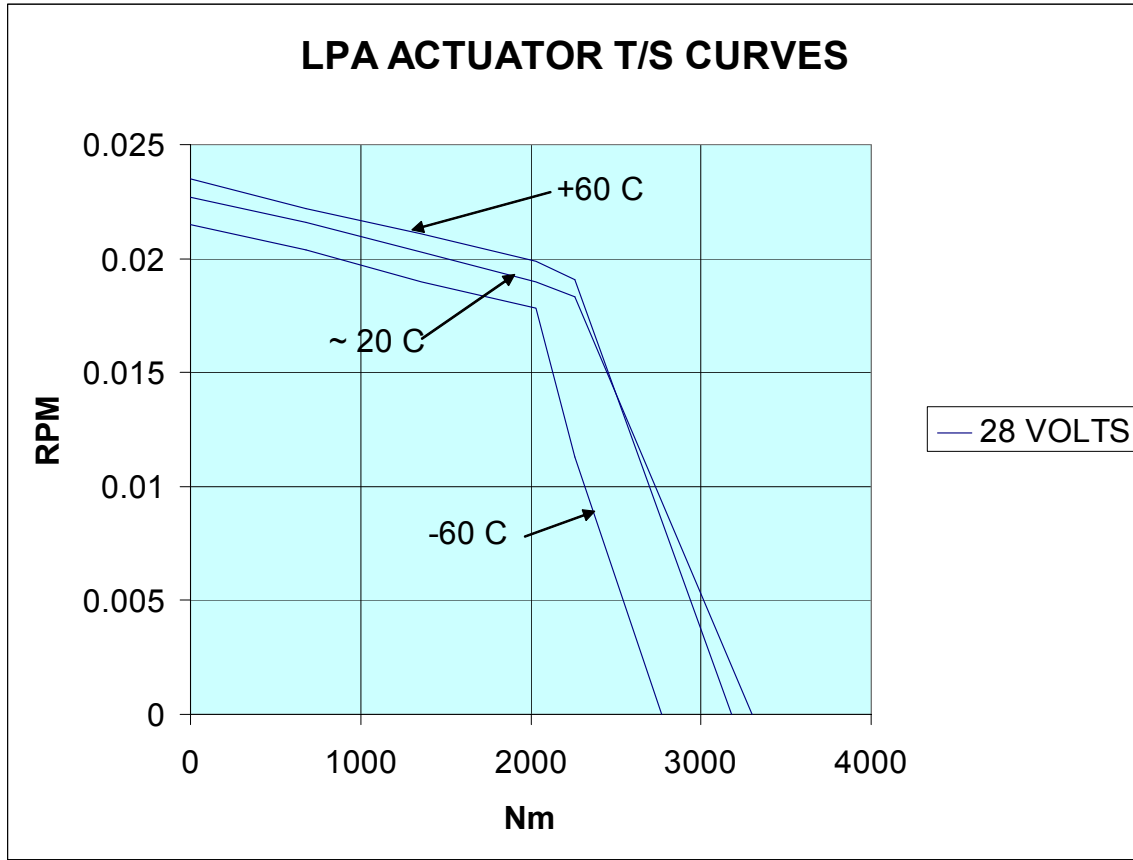


Figure 8. Actuator Torque/Speed Curve vs. Temperature

Lessons Learned

The LPA's were designed, built, tested and delivered under an extremely tight schedule. The key to the success of the project was extensive and early testing. SLA modeling was a great resource in determining design viability at an early stage.

An early and comprehensive overview of the design may help illustrate the relevant long poles of the effort at an earlier stage.

The use of planetary gear reduction for high torque applications is a viable approach so long as stiffness requirements can be satisfied with the values attainable with these systems. Careful selection of materials, gear size and lubrication is necessary to balance surface pitting (contact stresses), gear fatigue life (bending stresses) requirements vs. size and stiffness.

Brake Failure from Residual Magnetism in the Mars Exploration Rover Lander Petal Actuator

Louise Jandura*

Abstract

In January 2004, two Mars Exploration Rover spacecraft arrived at Mars. Each safely delivered an identical rover to the Martian surface in a tetrahedral lander encased in airbags. Upon landing, the airbags deflated and three Lander Petal Actuators opened the three deployable Lander side petals enabling the rover to exit the Lander. Approximately nine weeks prior to the scheduled launch of the first spacecraft, one of these mission-critical Lander Petal Actuators exhibited a brake stuck-open failure during its final flight stow at Kennedy Space Center. Residual magnetism was the definitive conclusion from the failure investigation. Although residual magnetism was recognized as an issue in the design, the lack of an appropriately specified lower bound on brake drop-out voltage inhibited the discovery of this problem earlier in the program. In addition, the brakes had more unit-to-unit variation in drop-out voltage than expected, likely due to a larger than expected variation in the magnetic properties of the 15-5 PH stainless steel brake plates. Failure analysis and subsequent rework of two other Lander Petal Actuators with marginal brakes was completed in three weeks, causing no impact to the launch date.

Introduction

Two Mars Exploration Rover (MER) spacecraft were sent to Mars, each with a rover to explore the Martian surface with its suite of instruments. After entering the Martian atmosphere in an aeroshell, the rovers were delivered to the surface in a Lander covered in airbags. Once the landing system came to rest on the Martian surface and the airbags deflated, three Lander Petal Actuators (LPAs) opened the three deployable Lander side petals, enabling the rover to exit the Lander. Approximately nine weeks prior to the scheduled launch of the first spacecraft, one LPA exhibited a brake failure during its final flight stow at Kennedy Space Center. The failure analysis of this mission critical actuator and the subsequent rework of two other marginal flight LPAs were all done without causing the launch date to slip.

The MER spacecraft, carrying the rovers called Spirit and Opportunity, were launched on June 10, 2003 and July 7, 2003. These spacecraft successfully landed on Mars on January 3, 2004 and January 24, 2004 respectively. All six LPAs operated without any problems.

Figures 1 and 2 show the LPAs installed in the Lander in both the stowed and deployed configurations. The tetrahedral Lander shape with its three LPA-deployed side petals is inherited from the 1997 Mars Pathfinder (MPF) program [1]. With this arrangement, the Lander can right itself from any side petal onto its base petal by opening that side petal until the Lander center of gravity tips the entire system onto the base petal. The LPA torque requirements for MER were much higher due primarily to the larger mass of the landed system, making a re-flight of the MPF LPA design impossible. The same MPF volume constraints for the LPA were applied to MER so the Lander would fit inside the aeroshell. Maintaining the same volume and nearly the same mass as MPF while producing three times the output torque was a significant challenge for the MER LPA. Each LPA had to develop sufficient torque to lift, overturn and right the Lander should it come to rest on a side petal rather than the base petal. Both the first MER lander and the MPF lander stopped on the base petal. However, the second MER lander came to rest on a side petal, causing that side petal LPA to right the lander. In addition, each LPA had to be able to over-deploy its petal to assist in leveling the Lander for a safe rover egress should it come to rest on uneven terrain. Thus, the actuator's unpowered holding torque (or backdrive torque) had to exceed the reaction load from the weight of the Lander supported on a petal with that petal in the fully deployed position. Petal adjustments were made on each MER lander to aid the rover egress. During petal opening, LPA position

* Jet Propulsion Laboratory, California Institute of Technology, Pasadena, CA

knowledge is provided by an incremental encoder signal constructed in the LPA electronics from the motor commutation sensor signals. The LPA electronics are brushless motor drive electronics, physically

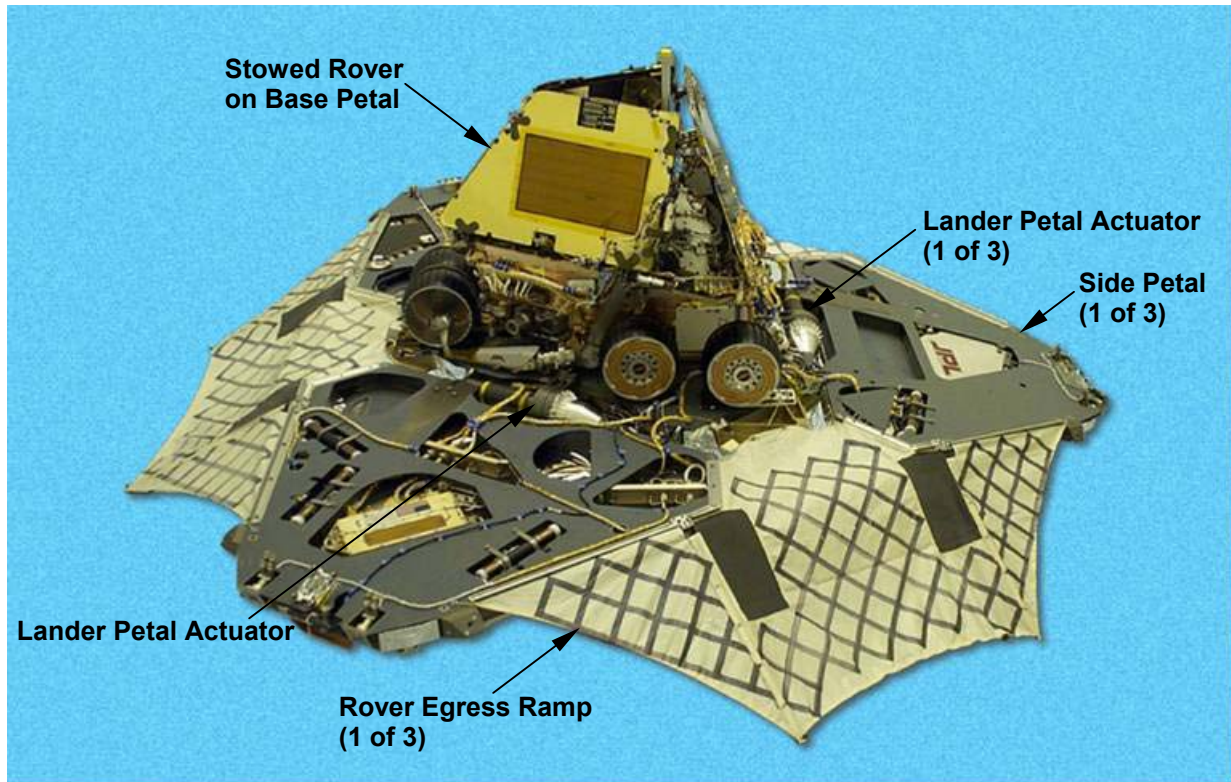
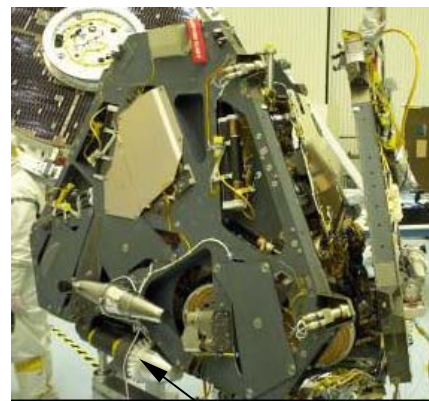


Figure 1. Lander Petal Actuators open each MER Lander side petal to the iron cross position, where all petals are coplanar. Petal motion past this condition is called over-deployed.



Lander Petal Actuator

Lander Petal Actuator

Figure 2. The MER Lander with two side petals stowed and the third side petal closing under the action of its Lander Petal Actuator

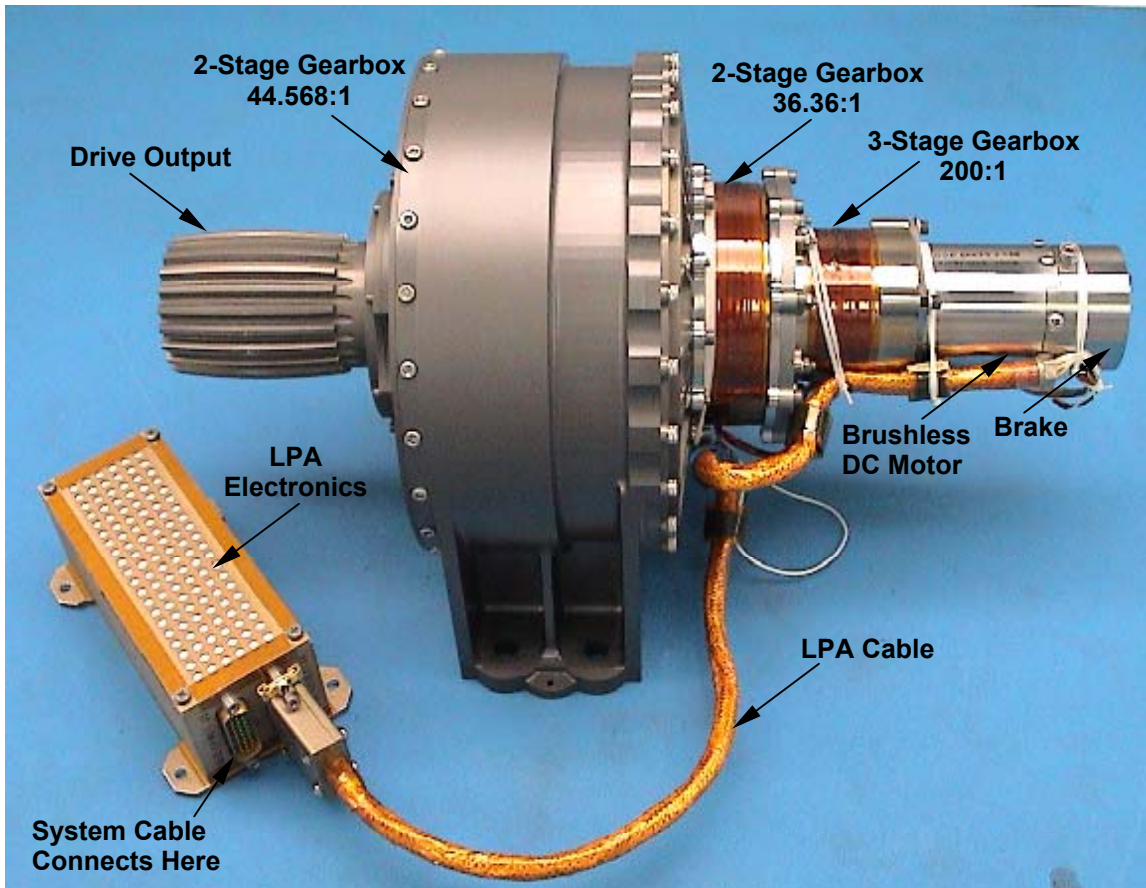


Figure 3. MER Lander Petal Actuator with its electronics

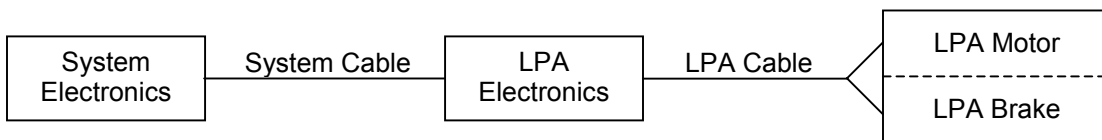


Figure 4. The LPA motor and brake are separately powered and commanded by the system electronics through the LPA electronics, a brushless motor drive electronics.

separate from the LPA and connected by a cable (Figure 3). Potentiometers at each of the petal hinge lines provide additional coarse petal position information, an absolute reference for rover egress.

Lander Petal Actuator

The MER Lander Petal Actuator (Figure 3) is a high torque actuator (3300 N•m output torque) produced by Aeroflex Laboratories, Inc., which consists of a brushless DC motor, a power-off brake, 7 stages of planetary gearing with an overall ratio of 324,099:1, and a crowned spline on the output shaft. The LPA required a brake to meet its backdrive torque requirements with power removed because of the high efficiency of the planetary gearing. The brake is mechanically engaged when non-powered to lock the motor rotor and ensure that the Lander petals cannot move due to external loads. The LPA motor and LPA brake are separately powered and commanded by the system electronics through the LPA electronics (Figure 4). During operation, power is first applied to the LPA brake to release it, followed by

power to the LPA motor to initiate petal motion. At the conclusion of motion, power is first removed from the LPA motor and then the LPA brake to avoid clamping the brake rotor at high speed. All LPAs were tested over temperature at the actuator level to restrain 3300 N•m externally applied to the output shaft. The brake design is a standard spring-applied, power-to-release configuration as shown in the motor/brake assembly cross-section (Figure 5). The brake rotor is attached to the motor rotor. With the brake unpowered, 6 compression springs push the friction plate against the brake rotor, preventing motor rotation. When the brake is energized to release the motor, the friction plate is guided on 3 pins and pulled against the springs by the solenoid. The total stroke of the friction plate is 0.13 mm. There is a 0.051 mm annular non-magnetic shim between the friction plate and the solenoid to break the magnetic flux path and prevent residual magnetism from permanently retaining the friction plate on the solenoid (the stuck-open position).

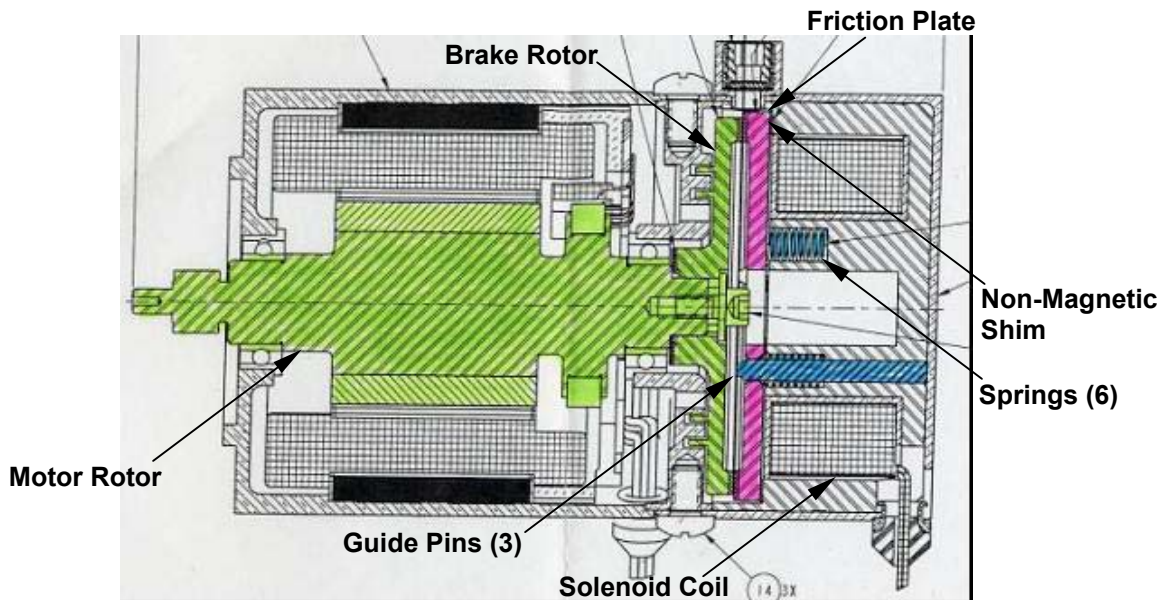


Figure 5. Cross-section of the Lander Petal Actuator motor/brake assembly

Failure and Failure Investigation

The LPA failure occurred about nine weeks before the scheduled launch of the first MER spacecraft. In preparation for closing the Lander for the last time, the spacecraft commanded the Lander petals through their range of motion using the LPAs so that cabling and other hardware near the hinge line could be observed for proper installation and clearance. Although the petals had been moved with the LPAs many times before, this was the first time that all the hardware including the flight airbags was installed during the motion. During a pause in the final flight stow sequence of the Lander petals using the LPAs, one petal drifted downward under gravity with the spacecraft unpowered. The weight of the assembled petal applied about 418 N•m of torque to the LPA output shaft or 13% of the tested backdrive resistance. A load of this magnitude clearly should not have caused the actuator to backdrive with the brake engaged. The failure was initially observed visually as an offset between the commanded position and the actual position. One petal seemed lower than it should be. A check of spacecraft telemetry from the hinge line potentiometers indicated that there was continued motion after completion of the commanded motion, on one petal only, although the current draw from the brake was as expected during the motion and went to zero upon completion of the motion. Once a problem was suspected, the continued motion was also visually observed. The anomaly was repeatable. In a separate check, the suspect petal moved when the LPA was commanded without energizing the brake, a further sign that the brake was not performing properly.

Even though all evidence pointed toward a problem with the LPA brake, a brake failure did not seem credible. Swift, decisive action was required to prevent a launch delay, however the closeness to launch made it even more critical to conclusively isolate the problem prior to removing the hardware from the spacecraft. Uncertainty in determining the cause of the problem would jeopardize the launch. The problem was conclusively isolated to the actuator using the following rationale. With the petal backdriving, the spacecraft was powered off and the connectors between the spacecraft, the LPA drive electronics, and the LPA were demated sequentially until the LPA was completely isolated from the rest of the system. The petal was still backdriving, which conclusively placed the failure in the actuator, eliminating the possibility that a stray current in the system or the drive electronics was keeping the brake powered and in the open position. The failed LPA (SN 007) was removed from the Lander and replaced by a flight spare and failure analysis began on the removed LPA. The failure investigation was conducted at Kennedy Space Center to eliminate the possibility that the failure would be lost during transportation of the LPA to either the Jet Propulsion Laboratory or Aeroflex Laboratories, Inc.

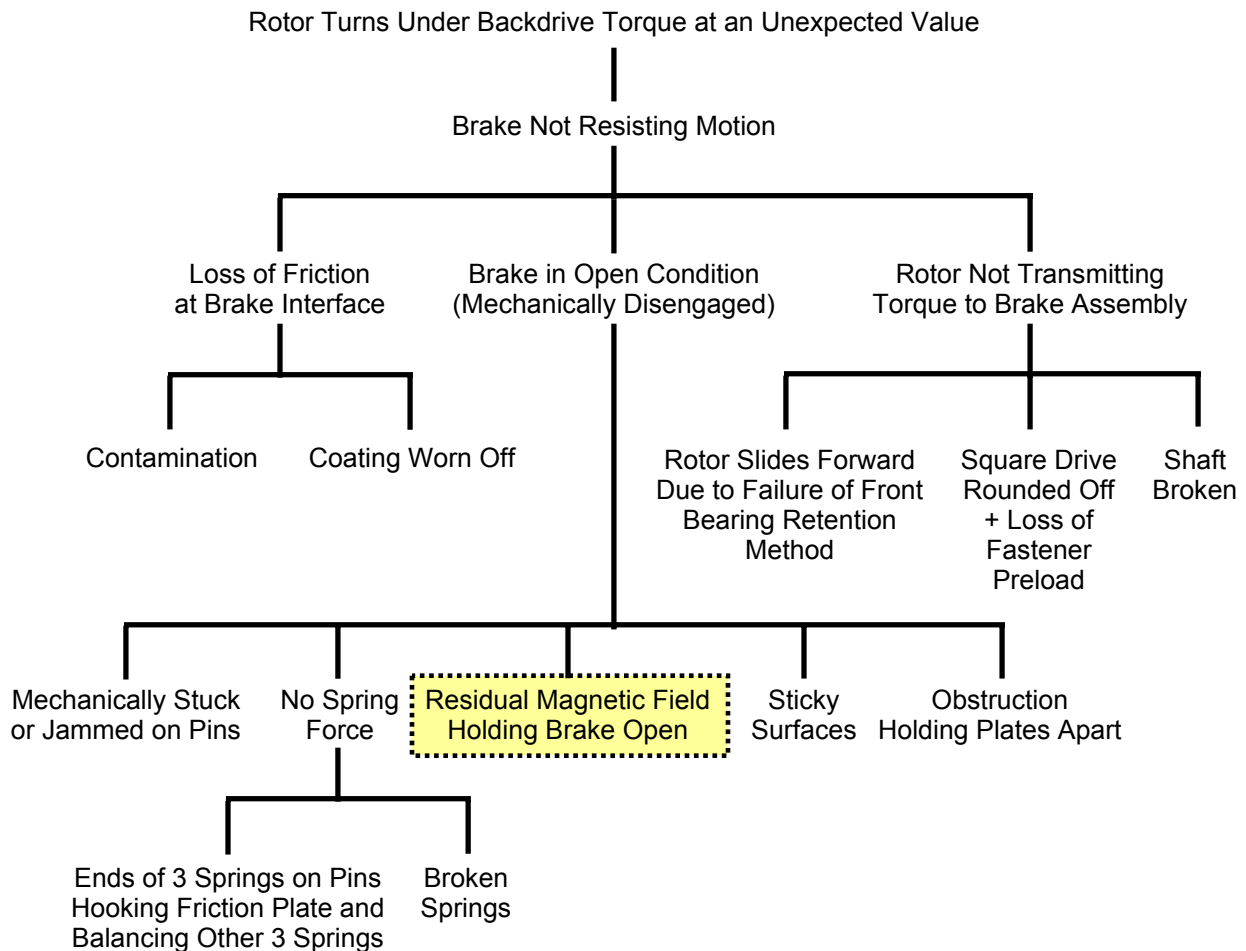


Figure 6. Fault tree for LPA brake failure with the actual failure highlighted in the dotted box

The evidence at this point only indicated that the brake was not resisting motion. Many different failure possibilities were considered which fell into the following general categories: “Brake in Open Condition”; “Loss of Friction at Brake Interface”; or “Rotor Not Transmitting Torque to Brake Assembly” (Figure 6). Many of the failures could only be observed through disassembly of the brake and some of these had the additional unfortunate characteristic that disassembly could cause the loss of the failure. After visual examination of the LPA indicated nothing unusual, the motor was operated with no power to the brake. Motor current indicated no-load operation, which meant the failure was still intact. Real time X-ray examination revealed the brake in a fully disengaged position even though no power was applied to the

brake. This observation eliminated two of the three branches of the fault tree, leaving only the failures listed under “Brake in Open Condition”. No tilting of the friction plate was apparent and nothing unusual was observed in the brake assembly. The only failure remaining that could be determined without disassembly was “Residual Magnetic Field Holding Brake Open”. While still under X-ray examination, a reverse polarity voltage was slowly applied to the brake starting at 0 volts, a demagnetizing action for the friction plate. At negative 0.3 volts, the friction plate moved to the engaged position against the motor rotor indicating the failure was caused by residual magnetism holding the friction plate against the solenoid even though a non-magnetic washer was in the assembly to prevent this particular failure. The motor stalled when operated again with the brake unpowered proving that the demagnetized brake was now fully mechanically engaged. Residual magnetism was the source of the failure in this LPA!

Assessment of Other LPAs

A survey of the acceptance test data for all LPA brake assemblies was performed as a consequence of the SN 007 LPA brake failure. Particular attention was given to the pull-in and drop-out voltages for the brake assemblies since these measurements are an indication of the electromechanical performance of the units. With no voltage applied to the brake, the friction plate is pressed against the brake rotor by the compression springs. Pull-in voltage is measured by slowly raising the brake voltage from zero volts until the friction plate is pulled in to the solenoid, mechanically disengaging from the brake rotor and permitting the motor to turn when the motor is powered with its drive electronics. Figure 7 illustrates the force balance for pull-in. Increasing the voltage across the brake coil causes the current in the solenoid to increase. As the current increases, the magnitude of the magnetic field increases thereby increasing the magnetic force, F_M , on the friction plate. The two forces that act in opposition to F_M are F_S , the total force from the 6 compression springs, and F_f , the friction force between the 3 guide pins and the friction plate. When the magnetic force exceeds the sum of the spring and friction forces, or

$$F_M > F_S + F_f \tag{1}$$

the friction plate moves away from the brake rotor and toward the solenoid, mechanically disengaging the brake. Once motion starts, the brake plate moves quickly open since F_M increases much faster than F_S as the air gap decreases. F_M is a squared function of air gap while F_S is a linear function.

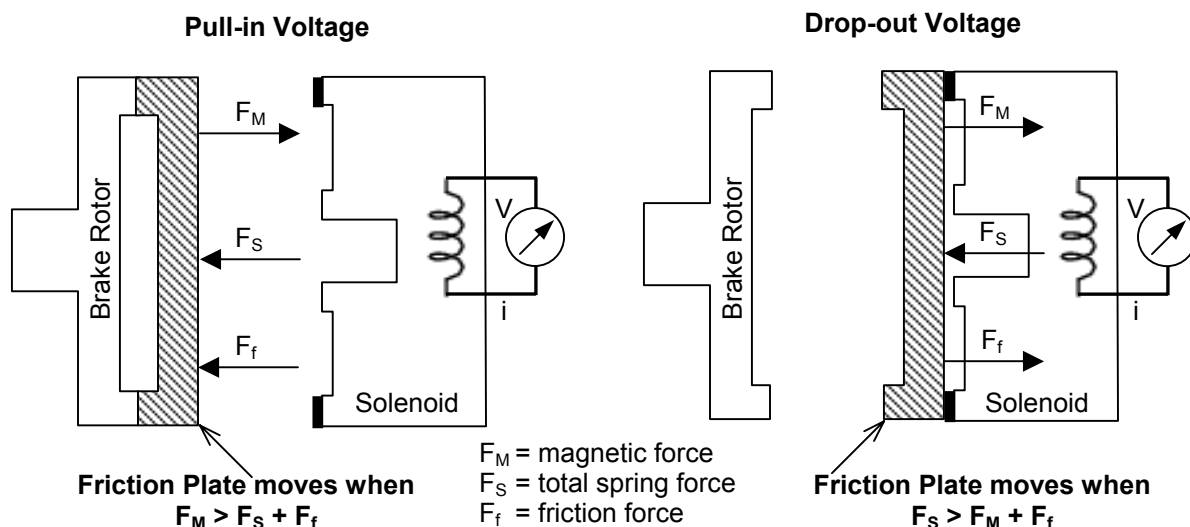


Figure 7. Force balance for brake pull-in and drop-out voltages

Drop-out voltage is then measured by slowly lowering the voltage until the friction plate releases from the solenoid, mechanically engaging the brake rotor again. Figure 7 illustrates the force balance for drop-out. Decreasing the voltage across the solenoid reduces its current and therefore the magnitude of the

magnetic field. As a result, F_M decreases. When the total spring force is sufficient to overcome both the magnetic force and the friction force, or

$$F_S > F_M + F_f \quad (2)$$

the friction plate moves away from the solenoid and reengages the brake rotor. Once motion begins, the friction plate moves quickly to the engaged position since F_M decreases much faster than F_S as the air gap increases. In the case of the failed brake, the condition in equation 2 was not met even though the solenoid voltage and therefore current was zero. F_M was non-zero due to residual magnetism.

The pull-in and drop-out motions of the brake are critical to the operation of the LPA and must be assessed for force margin like any other critical deployment. The desire was to have a force capability of at least twice the force needed to move the components over all conditions of environment and operating voltage. This equates to a minimum factor of safety (the ratio of force capability to force required) of 2.0. The flight brakes were measured to have a pull-in voltage <17 VDC, demonstrating operating margin from the minimum flight input voltage of 24 VDC. The magnetic force is 20 N at 17 VDC and 37.6 N at 24 VDC compared to a maximum total spring force of 10.45 N and an analytically determined maximum friction force of 0.013 N, surpassing the minimum desired force factor of safety for the pull-in deployment by a large amount. Drop-out voltage was measured to be <10 VDC, ensuring adequate separation between the pull-in and drop-out behavior. However no lower threshold on drop-out voltage was defined to ensure operating margin above zero input voltage. The lack of an appropriately specified lower bound for this parameter was an oversight that hindered the discovery of brakes with insufficient force margin for drop-out during acceptance testing. The minimum required force factor of safety for the drop-out deployment was not proven during acceptance testing. Since the failed LPA clearly did not have sufficient margin for drop-out, the other flight LPAs, which were already installed on the flight Landers, were evaluated. The pull-in and drop-out voltages of all LPA brakes were recorded during acceptance testing and measured again after the failure (Table 1). Although the failed unit had the lowest measured value of drop-out voltage, SN 003 and 008 also had very low values for drop-out voltage, raising suspicions that these two actuators might also have insufficient margin for drop-out. A proper specification of drop-out voltage defining sufficient force margin was needed to properly evaluate the flight LPAs and determine if rework was required. LPAs were switched between the two landers, placing the three flight LPAs with the highest values of drop-out voltage on the first lander being prepared for launch. This allowed preparations to continue on the most time-critical lander while the LPA assessment continued, maximizing the chance that the failure could be addressed without impacting either launch.

Table 1. LPA Pull-In and Drop-Out Voltage Measurements

SN (^a)Failed Unit	Acceptance Test Values (VDC)		As Remeasured (VDC)		Type of Unit
	Pull-In	Drop-Out	Pull-In	Drop-Out	
001	14.1	2.2	12.3	2.22	Qualification
002	Not avail.	Not avail.	12.9	3.25	Flight
003	14.3	1.9	13.6	0.79	Flight
004	12.0	5.0	15.9	3.79	Flight
005	15.5	1.0	Not meas.	Not meas.	Testbed
006	14.07	2.6	14.1	2.40	Flight
007(^a)	12.7	0.6	12.8	-0.3, 0.29	Flight
008	13.7	1.1	11.7	1.25	Flight
009	12.8	1.72	12.2	1.02	Testbed
010	15.1	0.85	Not meas.	Not meas.	Testbed
011	13.8	2.3	13.7	2.54	Flight Spare

There is no way to take a direct measurement of force in the brake assembly on the fully assembled LPA, therefore there is no way to directly verify the force margin for drop-out on each LPA. Since drop-out voltage is the only easily acquired measurement on the fully assembled LPA, what was needed was a relationship between drop-out voltage and force so that a minimum force factor of safety of 2.0 could be guaranteed. A series of tests was performed on a spare brake assembly to determine how drop-out

voltage varied with spring force. The nominal spring force was calculated from the spring constant and the geometry of the brake assembly. Starting with the friction plate pulled in against the solenoid, the voltage to the brake was lowered until the plate moved under the force of the springs. Reducing the number of springs in the brake assembly decreased the spring force pushing on the friction plate until the brake plate no longer dropped out at zero voltage (Table 2). At this condition, the residual magnetic force is greater than the spring force attempting to push the brake plate off the solenoid. An additional test was performed with no springs in the brake assembly. The voltage to the brake was reduced to zero and a measurement of the force required to separate the friction plate from the solenoid was recorded (Table 3). The same measurements were taken after adding a second non-magnetic 0.051 mm shim between the solenoid and the friction plate (Tables 2 and 3). Adding the second shim raised the drop-out voltage significantly (Figure 8) without changing the pull-in voltage substantially. These tests enabled a method to determine the force margin and illustrated a rework path that could increase that margin.

Table 2. Drop-out voltage vs. spring force as measured on a spare brake

# of Springs	0.051-mm shim		2x 0.051-mm shim	
	Nominal Force (N)	Voltage (V)	Nominal Force (N)	Voltage (V)
6	9.012	1.27	8.910	3.60
5	7.508	0.92	7.428	3.21
4	6.005	0.22	5.943	2.12
3	4.506	No release ^(b)	4.457	1.51
2			2.971	0.35
1			1.486	No release

^(b)No release at zero volts, released with -0.3 volts (reverse polarity voltage of 0.3 volts)

Table 3. Force required to separate the friction plate from the solenoid at zero volts as measured on a spare brake

# of Springs	0.051-mm shim		2x 0.051-mm shim	
	Nominal Force (N)	Voltage (V)	Nominal Force (N)	Voltage (V)
0	4.706	0	2.224	0

The required margin point for each shim condition was determined using the spring force test data and a tolerance analysis of spring force. A quadratic equation was fit to the test data in Figure 8 since force in the solenoid is a quadratic function of current and therefore voltage. Regression results in equations of the form:

$$F_M = aV^2 + bV + c \quad (3)$$

with a , b , and c all constants. Setting c equal to the minimum possible spring force of three springs minus the maximum possible friction force from the alignment pins shifted the curves. This ensures that when six springs are present, there is a minimum factor of safety of 2.0 on the force required to create drop-out at the zero voltage condition. The two shifted regression curves are plotted in Figure 9, one curve for a single, non-magnetic 0.051-mm shim and one for a double, non-magnetic shim or a 0.102 mm total shim thickness. The final margin point for each shim thickness was calculated from the regression curves as the drop-out voltage values corresponding to the maximum possible force from 6 springs plus an additional two times the friction force. An additional 0.1 VDC was added to account for measurement scatter resulting in required minimum drop-out voltage values of 2.05 VDC for the 0.051-mm shim thickness and 3.81 VDC for the 0.102-mm shim thickness. It should be noted that the drop-out voltage of 0.6 measured during acceptance testing of the failed LPA works out to a force factor of safety of 0.97. This was a unit that clearly should have failed.

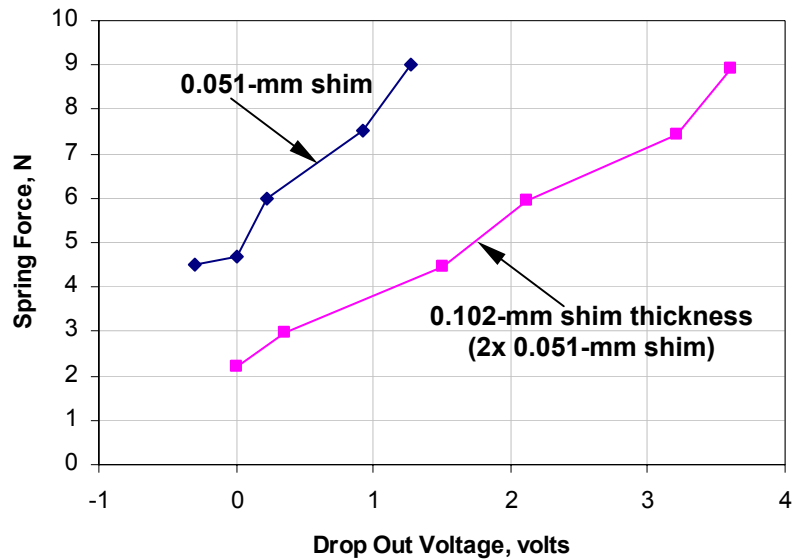


Figure 8. Test data from a spare brake assembly characterizes the variation of drop-out voltage with spring force for two different shim thicknesses.

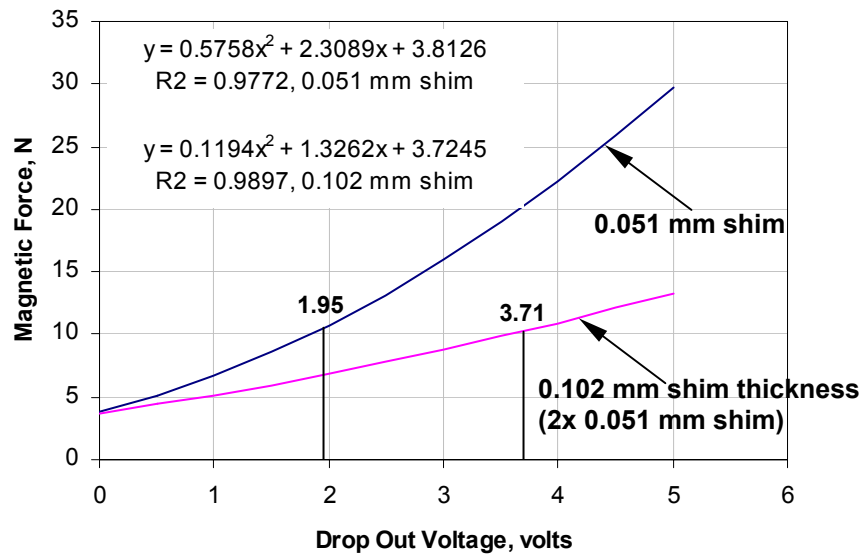


Figure 9. Regression curves from test data are appropriately shifted and used to determine the drop-out voltage required for a minimum 2.0 factor of safety.

Rework

Two flight units, SN 003 and 008, had drop-out voltages of 0.79 VDC and 1.25 VDC respectively, well short of the minimum drop-out voltage of 2.05 VDC required for one shim per the margin analysis. These two units were removed from the second flight lander and transported to Aeroflex Laboratories, Inc. for rework. Rework consisted of adding a second, non-magnetic 0.051-mm shim between the solenoid and the friction plate resulting in a total shim thickness of 0.102 mm. A shim was removed between the brake rotor and the motor rotor to maintain the same brake actuation stroke. The rework was relatively straightforward, however the schedule intensity of the activity was increased substantially due to the proximity of the second launch and the criticality of the LPAs to mission success. The brake housing was carefully removed from the motor housing (Figure 10) after heating the brake housing up at the bond line and removing three screws. Brake housing removal was performed with the brake leads powered so the friction plate was secure against the solenoid. This prevented the friction plate and the compression springs from falling out of the housing during disassembly. The two brake plates are visible in Figure 11a. The brake rotor was removed so that its shimming could be adjusted. The six compression springs are visible after power was removed from the brake assembly to enable removal of the friction plate from the brake housing (Figure 11b). This is the location where the second shim was added after the assembly was cleaned up and inspected. The brake was reassembled. After rework, SN 003 and 008 had drop-out values of 4.09 and 3.85 VDC respectively, which met the minimum requirement of 3.81 VDC for the 0.102 mm shim thickness. Table 4 indicates the performance of these two LPAs, before and after rework.

Dynamics testing was not performed on the reworked LPAs, however, the actuators were exposed to the protoflight temperature range of $-120\text{ }^{\circ}\text{C}$ to $+60\text{ }^{\circ}\text{C}$. Each actuator was operated at the voltage extremes of 24 and 32.8 VDC and over the entire output torque range at each acceptance temperature ($-60\text{ }^{\circ}\text{C}$, ambient, $+60\text{ }^{\circ}\text{C}$). There was no change in the torque/speed/current performance or backdrive torque capability from the original acceptance testing. A test to positively confirm brake drop-out after LPA operation in each direction, voltage, and temperature was added. This test consisted of operating the LPA motor with the brake unpowered and verifying that stall current was present. After successfully completing testing, the LPAs were returned to the spacecraft.

The entire process from the initial observation of the failure to the return of the LPAs to the spacecraft took only three weeks and caused no slip in the launch schedule.



Figure 10. The brake assembly is removed from the Lander Petal Actuator during rework to add an additional shim.



Figure 11a and 11b. Close-up views of the brake assembly during rework

Table 4. Drop-out performance for the reworked brakes

SN	Before Rework (with 0.051-mm shim)		After Rework (with 2x 0.051-mm shim)	
	Drop-Out (VDC)	Force Factor of Safety	Drop-Out (VDC)	Force Factor of Safety
003	0.79	1.08	4.09	2.12
008	1.25	1.38	3.85	2.02

Analysis Using Magnetic Circuit Equations

The results of the failure investigation, the force/drop-out voltage data from the spare brake assembly, and the corresponding margin analysis provided sufficient evidence and understanding to both conclusively attribute the brake failure to residual magnetism and to proceed confidently with the defined rework on two LPAs with marginally acceptable brake assemblies. Some analysis was performed to further explore the source of the unit-to-unit variation in drop-out voltage. The magnetic circuit model of the brake is shown in Figure 12, which leads to the following equation.

$$Ni = (\Phi R)_{CORE} + (\Phi R)_{SHIM} + (\Phi R)_{PLATE} + (\Phi R)_{GAP} \quad (4)$$

where Ni is the value of the magnetomotive force source of the brake coil, N is the number of turns in the coil, i is the current in the coil, Φ is the flux flowing in the magnetic circuit, and R is the reluctance of each component around the circuit. Reluctance of a material with length l along the flux path and cross-sectional area A is defined as

$$R = \frac{l}{\mu A} \quad (5)$$

where μ is the permeability of the material. Higher permeability materials, like the magnetic materials of the brake core and plate, have a lower reluctance and therefore flux flows more easily through them. Since flux is conserved around the magnetic circuit, equation 4 is rewritten as

$$Ni = \Phi(R_{CORE} + R_{SHIM} + R_{PLATE} + R_{GAP}) \quad (6)$$

The shim is nonmagnetic so its reluctance is that of free space (R_0) just like the air gap. The permeability of both the core and the plate is much higher than the permeability of free space (μ_0), therefore their reluctance is much less than the reluctance of free space resulting in a simplification of equation 6.

$$R_{SHIM} = R_{GAP} = R_0, \quad R_0 \gg R_{CORE}, \quad R_0 \gg R_{PLATE}$$

$$Ni = 2\Phi R_0 = \frac{2\Phi l_0}{\mu_0 A} \quad (7)$$

Making the common assumption that the flux density B is uniform over the cross-sectional area A exposed to the flux results in

$$\Phi = BA \quad (8)$$

The energy stored in the magnetic field in the gap is

$$U = \frac{B^2 l_0 A}{2\mu_0} \quad (9)$$

The magnetic force on the brake plate is equal to the rate of change of energy with the gap length.

$$F_M = \frac{dU}{dl_0} = \frac{B^2 A}{2\mu_0} \quad (10)$$

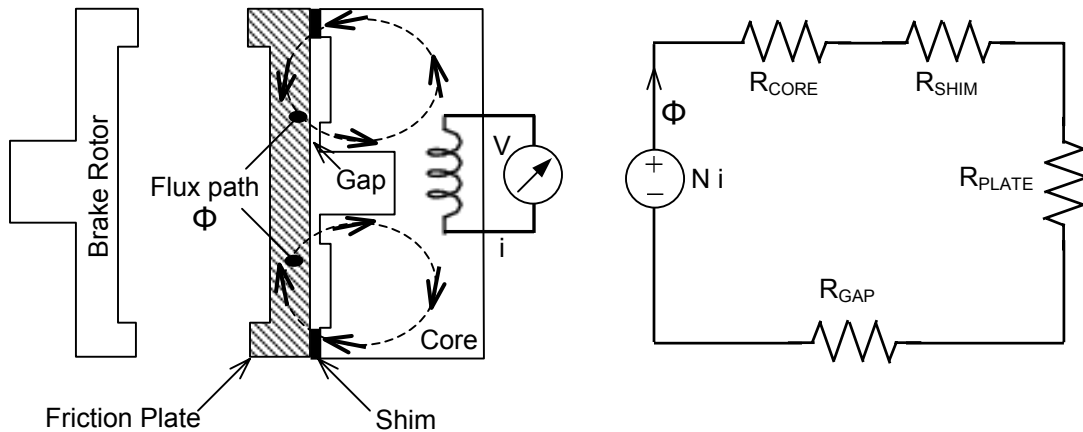


Figure 12. Magnetic circuit model

Substituting equation 8 into equation 7, and combining with equation 10 gives an expression relating the magnetic force on the brake plate to the shim thickness, l_0 .

$$F_M = \frac{N^2 i^2 \mu_0 A}{8l_0^2} \quad (11)$$

Since force on the friction plate is inversely proportional to the square of the plate's distance from the solenoid, the shim thickness has a large effect on the force balance in the brake assembly. This effect is larger when the friction plate is closer to the solenoid, which is why the addition of a second shim in the brake assembly has a significant effect on the drop-out voltage while having a minor effect on the pull-in voltage. This sensitivity allows the shim modification rework to be effective.

From Ohm's law, current in the solenoid varies with the applied voltage through a constant coil resistance. Using this relationship in equation 11 results in the observation that the drop-out voltage varies linearly with the shim thickness. The shim thickness in the LPAs can vary from 0.0459 mm to 0.0561 mm because of the part tolerances. The expected variation in drop-out voltage from shim thickness variation is a factor of $0.0561/0.0459 = 1.22$. This does not account for much of the variation in drop-out voltage seen over the range of LPAs, which is a factor of 6 to 10. At the drop-out position, the unit-to-unit force variation of the 6 springs is 7.65 N to 10.45 N due to the tolerances of the spring parameters and the geometry of the brake assembly. Since drop-out voltage is related to the square root of force, spring force variation could account for a factor of $(10.45/7.65)^{1/2} = 1.17$, also not sufficient to explain the observed variation.

Equation 6 as written contains the assumption that the only source of magnetomotive force in the solenoid is the brake coil. However the evidence of the residual magnetism in the failed brakes indicates differently. The flux flowing through the solenoid when the brake coil is energized causes the friction plate to magnetize. When power is removed, the friction plate continues to behave as a weak permanent magnet, making it an additional source of magnetomotive force in the solenoid. This behavior is caused by the large hysteresis loop in the B-H curve of the 15-5 PH stainless steel. The core material has a B-H curve with an extremely small hysteresis loop therefore it retains no field. When the additional source of magnetomotive force from the friction plate is added in series with the other elements in the magnet circuit model, equation 6 becomes

$$Ni + mmf_{PLATE} = \Phi(R_{CORE} + R_{SHIM} + R_{PLATE} + R_{GAP}) \quad (12)$$

Applying the same assumptions as before to equation 12 yields a new version of equation 7.

$$Ni + mmf_{PLATE} = 2\Phi R_0 = \frac{2\Phi l_0}{\mu_0 A} \quad (13)$$

Substituting equation 8 into equation 13, and combining with equation 10 gives a new expression relating the magnetic force on the friction plate to the shim thickness.

$$F_M = \frac{\mu_0 A}{8l_0^2} (mmf_{PLATE} + Ni)^2 \quad (14)$$

Table 5 shows the magnetomotive force of the friction plate in the spare brake, which was calculated using equation 14, the data in Table 3, and the geometry of the brake. Table 6 lists the magnetomotive force of the solenoid coil for the typical range of brake drop-out voltage, values which are of the same magnitude as the magnetomotive force of the friction plate. The effect of changes in the magnetomotive force of the friction plate on the drop-out voltage is derived from equation 14. Keeping all other parameters unchanged, decreasing mmf_{PLATE} causes an equivalent increase in Ni . The drop-out voltage increase corresponding to this increase in Ni is determined from $V = (Ni)(R_{COIL}/N)$, where R_{COIL} is the coil resistance. A decrease in mmf_{PLATE} of 13.4 causes an increase in drop-out voltage of 1.7 volts since $V = (Ni)(385/3040) = (Ni)(0.127)$. The exact range of variation of mmf_{PLATE} over all the LPAs is not known but varying this parameter clearly can have a significant effect on the LPA drop-out voltage. The rest of the magnetic circuit and the geometric parameters of the brake are well known, and their variations are insufficient to cause the observed range of drop-out voltage. Therefore, the conclusion is that the majority of the large unit-to-unit variation in drop-out voltage is due to unit-to-unit variation in the magnetic properties of the 15-5 PH stainless steel brake plates. This conclusion is consistent with the experiences of a JPL magnetics expert when dealing with this material.

Table 5. Magnetomotive force of the friction plate in the spare brake

	0.051-mm shim	2x 0.051-mm shim
mmf_{PLATE} (ampere-turns)	13.4	18.4

Table 6. Magnetomotive force of the solenoid coil versus voltage

Voltage (VDC)	1	2	3	4	5
Ni (ampere-turns)	7.9	15.8	23.7	31.6	39.5

Conclusions and Lessons Learned

Given the close tolerances of the parts in the brake assemblies, there was more unit-to-unit difference in drop-out voltage than expected. This was likely due to a larger than expected variation in the magnetic properties of the 15-5 PH stainless steel friction plates, which resulted in a significant differences in the amount of residual magnetism in the magnetic circuit from brake to brake. These variations must be carefully accounted for when using 15-5 PH stainless steel in a magnetic circuit.

Although residual magnetism was recognized as an issue in the design (hence the existence of the non-magnetic 0.051 mm shim), the lack of an appropriately specified lower bound on drop-out voltage prevented brakes with inadequate margin from being discovered and reworked earlier in the flight schedule. More specifically, drop-out should have been treated like any deployment, guaranteeing a minimum force factor of safety of 2.0 that was verified by test.

Acknowledgements

The work described in this paper was performed by the Jet Propulsion Laboratory, California Institute of Technology, under contract with the National Aeronautics and Space Administration.

The effort described in this paper encompassing the discovery of the failure, the failure investigation, the assessment of all LPAs, the rework of two LPAs, and the removal and reinstallation of LPAs on the flight landers, all in a three week period of time, required the combined talents of many people. In particular, the author gratefully acknowledges the contributions of Mike Johnson, Pablo Narvaez, and Don Sevilla of JPL, and Ed Joscelyn and Boz Sharif of Aeroflex Laboratories.

References

1. Gillis-Smith, Greg R. "Mars Pathfinder Lander Deployment Mechanisms." *Proceedings of the 30th Aerospace Mechanism Symposium*, (May 1996), pp. 255-271.
2. Hanselman, Duane. *Brushless Permanent-Magnet Motor Design*. New York: McGraw-Hill, Inc., 1994, pp. 13-59.
3. Wangsness, Roald K. *Electromagnetic Fields*. New York: John Wiley & Sons, 1979, pp. 320-333.
4. Slocum, Alexander H. *Precision Machine Design*. Englewood Cliffs: Prentice Hall, 1992, p. 663.

High Gain Antenna Gimbal for the 2003-2004 Mars Exploration Rover Program

Jeff Sokol*, Satish Krishnan** and Laoucet Ayari*

Abstract

The High Gain Antenna Assemblies built for the 2003-2004 Mars Exploration Rover (MER) missions provide the primary communication link for the Rovers once they arrive on Mars. The High Gain Antenna Gimbal (HGAG) portion of the assembly is a two-axis gimbal that provides the structural support, pointing, and tracking for the High Gain Antenna (HGA). The MER mission requirements provided some unique design challenges for the HGAG. This paper describes all the major subsystems of the HGAG that were developed to meet these challenges, and the requirements that drove their design.

Introduction

MER Overview

The 2003-2004 Mars Exploration Rover mission consists of two long-range rovers that carry a payload of science instruments. The goal of the mission is to determine the history of climate and water at sites on Mars where conditions may once have been favorable to life. Two landing sites were chosen (Gusev Crater and Meridiani Planum) because they offer evidence that liquid water was once present. The science instruments will be used to read the geologic record at each site and to determine how suitable the conditions may have been for supporting life. The two rovers were named “Spirit” and “Opportunity” and were launched in June and July of 2003 with a scheduled Mars landing in January of 2004. Each rover has a mass of approximately 180 kg and has a range up to 100 meters per Martian day (~24 hours and 39 minutes) [1].

Figure 1 shows the rover in its deployed configuration. The topic of this paper, the High Gain Antenna Gimbal, can be seen on the top deck of the rover along with the Low Gain Antenna and the Panoramic Camera Mast Assembly. The HGAG provides the pointing and tracking capability for the High Gain Antenna RF communication system.

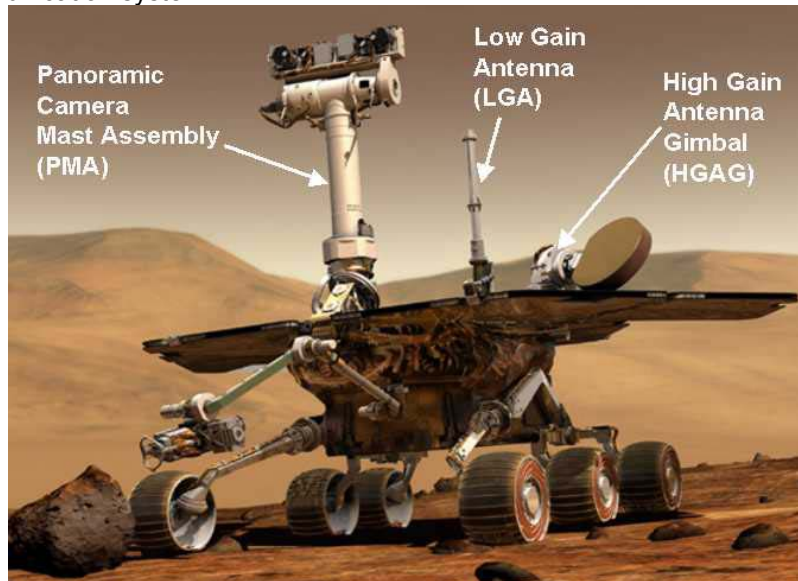


Figure 1. Mars Exploration Rover [1]

* Ball Aerospace & Technologies Corp., Boulder, CO

** Jet Propulsion Laboratory, Pasadena, CA

HGAG Program Discussion

The HGAG program was a cooperative effort between Jet Propulsion Laboratory (JPL) and Ball Aerospace & Technologies Corp. (BATC). The overall design architecture and initial drive train component sizing for the gimbal were established at JPL. The design was then turned over to BATC who was responsible for the final detail design, production, and test of the HGAG. A number of design components (motors, harmonic drives, potentiometers, RF rotary joints and flex cables) were specified early in the design process by JPL and they were delivered to BATC as customer supplied components for use in the HGAG design.

HGAG Design Overview and Driving Requirements

The gimbal consists of two drive mechanisms mounted at 90 degrees to one another. The High Gain Antenna is mounted at the end of the elevation drive and both the elevation drive and antenna are mounted in a cantilevered fashion on the azimuth drive. This configuration accommodates the confined packaging requirements for launch on the rover while providing the necessary field of view and rotation angles for the HGA. The position of each drive is monitored using motor encoder information. In addition, potentiometers are incorporated into each drive to provide gross position determination in the case of a power cycle condition during the mission. Figure 2 shows the HGAG with the HGA attached.

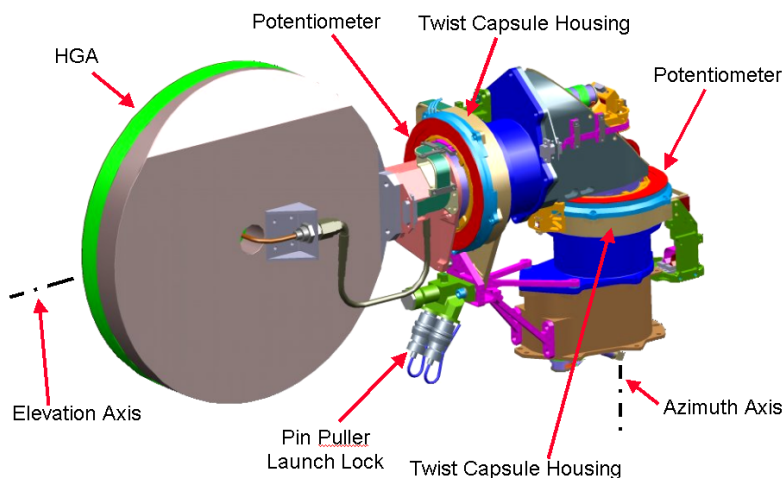


Figure 2. HGAG with HGA attached

The assembly requires a locking mechanism to prevent drive rotation under launch and landing loads. This was accomplished by incorporating a single pyrotechnic pin puller, with redundant NASA Standard Initiator (NSI) charges, to lock both the azimuth and elevation drives. Once on Mars, the pin puller is fired and the drives are freed to rotate away from their stowed position. During deployment, the azimuth drive moves through a spring-loaded gate mechanism that closes once the drive has passed. After it is through the gate, the azimuth drive can no longer return to the original stowed position, protecting against potential interference between the HGA and other rover components during elevation drive rotation.

Because of the somewhat large angles of rotation (280° azimuth and 234° elevation), and the need to pass power and signal electronics over both the azimuth and elevation drives, two twist capsules were developed to house the flex cables. In addition, the RF signal from the antenna also needs to pass through the elevation and azimuth drives while meeting a specified RF signal loss budget. Both the flex cable twist capsule and the rotating RF system will be described in this paper.

The Mars operating environment for the gimbal assembly provided specific challenges during design and test of the hardware. The dusty Martian environment requires special attention to mechanism contamination control, the thermal environment requires specific external surface treatments and heaters, and stringent planetary protection guidelines dictated high bake-out temperatures prior to launch that drove material and design choices. Drive testing was performed under expected operating temperatures, atmospheric pressures, and loads. Table 1 summarizes the significant driving requirements for the HGAG design.

Table 1. MER HGAG significant driving requirements

Requirement	Value	Unit
HGAG mass allocation (no HGA)	4.5	kg
Distance from HGA boresight to Azimuth Axis	0.33	m
Azimuth Drive Angular Rotation	280	deg
Elevation Drive Angular Rotation	234	deg
Minimum mechanical control and knowledge	0.5	deg
Drive operational step size	0.2	deg
Minimum drive rotation speed	0.78	RPM
Operating voltage range	22.5 to 34	V
Maximum MER incline with respect to gravity during operation	40	deg
Quasi-static design load (stowed)	45	g
Stowed first modal frequency (minimum)	50	Hz
Deployed first modal frequency (minimum)	14	Hz
Contamination control bake out temperature	110	C
Survival temperature range (non-bake out)	-120 to 60	C
Operating temperature range	-70 to 45	C
Motor revolution limit (testing / flight)	2.5E+06	revs
RF loss between HGA and Rover bulkhead	1.8	dB

Three HGAA assemblies, 2 flight and one Engineering Model (EM), were delivered to JPL during the third quarter of 2002 for integration into the rover assemblies. The flight assemblies were successfully integrated and launched aboard the two Mars Rover missions, "Spirit" and "Opportunity", during the summer of 2003 for arrival on Mars in January 2004. The engineering model was integrated on the EM Rover that is currently being used for mission control testing at Jet Propulsion Laboratory.

Design Discussion

Drive Train

The gear train and RF system were designed concurrently to accommodate packaging and performance requirements. While the expected maximum external torsion load on the azimuth drive (2.9 Nm starting and 2.1 Nm running) is larger than the elevation drive (1.3 Nm starting and 0.6 Nm running), both drives were designed to accommodate the higher azimuth drive loads. In order to simplify the design, analysis, manufacturing, and assembly of the gimbal, both drives use identical gear trains that consist of a gear motor, spur gear stage, and a harmonic drive that combine to produce a 5424.7:1 gear reduction. A cross section view of the system is depicted in Figure 3. Early design trades included a more modular design, with the RF coax routed external to the main gimbal structure. This approach simplified the gear train design (and should therefore be considered for future gimbal designs) but required additional envelope external to the gimbal. Because of the tight packaging requirements on the MER, the decision was made to route the coax cables internally.

By assuming worst-case performance for all drive train components in the mechanism analysis, the need to pre-screen components prior to assembly was eliminated. Overall, simple and robust design principles were used to minimize the gimbal's sensitivity to variability in the performance of each component.

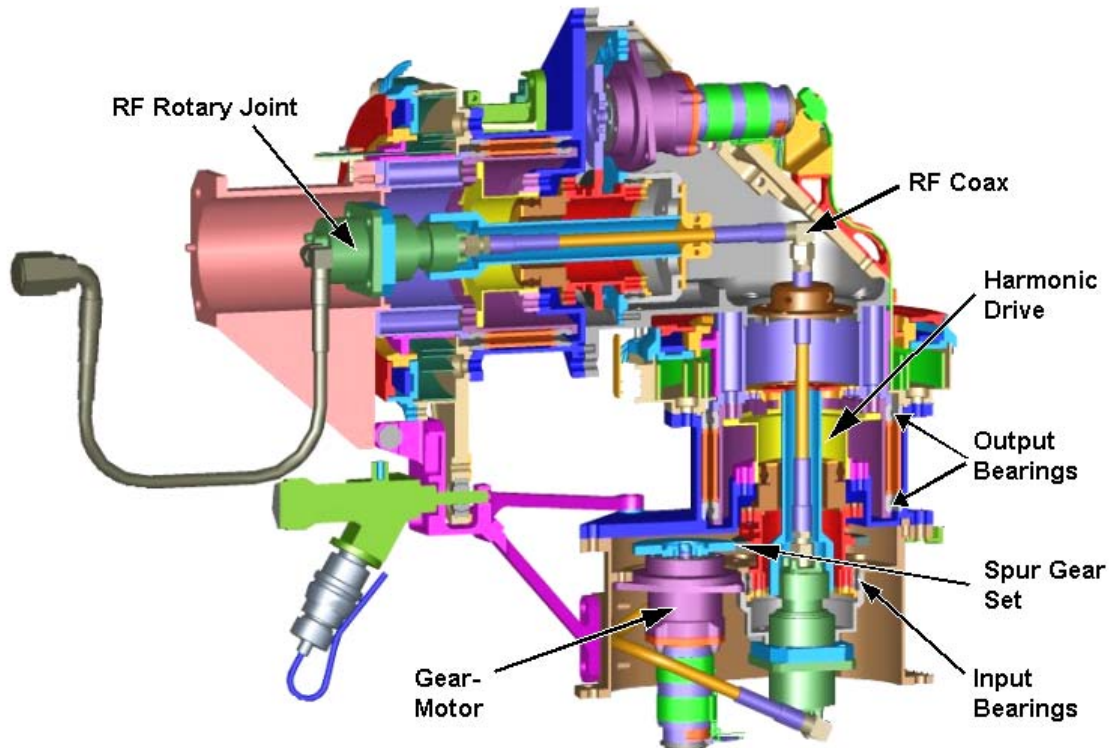


Figure 3. HGAG cross-section

Drive Bearings

The HGAG drives each contain two pairs of back-to-back mounted angular contact bearings. Both bearing pairs were manufactured by Timken Super Precision (MPB) and were lubricated at Ball Aerospace & Technologies Corp. The larger drive output bearings are required to carry the axial, radial, and moment loads generated during launch, landing, and MER maneuvering. The smaller drive input bearings are required to support the harmonic drive input loads as well as the radial and moment loads from the gear motor to harmonic drive spur gear stage. The bearings are made from 440C stainless steel (which helps to match the CTE of the surrounding titanium housings) and have phenolic retainers. Because of the operating environment on Mars as well as the mechanism life requirements, all the bearings are lubricated with Brayco Oil Company 815Z oil along with a 10% grease fill of Braycote 601. Although this lubrication allows the HGAG to survive the operating conditions and meet its life requirements, it does significantly increase the starting and running torque of the system at the cold operating temperatures. The increase in cold temperature starting and running torque made it critical that the minimum diameter bearings were chosen that could meet our structural load and packaging requirements. In both cases, the bearing pairs employ a “hard preload” assembly that utilizes precision shims to achieve the desired preload in the bearing set. After assembly, the bearing set preload and stiffness were verified by running torque and load tests.

Gear motor

In an effort to minimize the number of different drive components used on the overall MER system, the majority of mechanisms employ one of two brush DC motor sizes supplied by Maxon Corporation. The large gear reduction in the HGAG mechanism allows the gimbal to use the smaller Maxon REO20 motor (20-mm diameter), in lieu of the larger Maxon RE25 motor (25-mm diameter). By using the smaller motor, the HGAG design saves mass and reduces power consumption. Nearly all of the gear train calculations assumed the worst-case performance REO20 motor (except for mechanism

strength margin analysis where the maximum performance motor was used). The assumed motor had the lowest torque constant, the minimum speed constant, and the maximum armature resistance.

The gear motor assemblies were supplied by Starsys Corporation and used a three-stage, 81.37:1, planetary gearbox to minimize the effects of viscous losses caused by the bearings and harmonic drive on the motor. Once again, the gear motor analysis assumed worst case starting torque and no load running torque for the gear motor, as reported by Starsys.

Spur Gear Stage

Since the RF system is routed coaxial with the drive axis of rotation, a spur gear stage is used to offset the gear motor. The spur gear stage also provides a 1.33:1 gear reduction. Both the gear motor's pinion gear and the spur gear were made from 15-5 PH corrosion resistant steel. The spur stage was lubricated with MoS₂ filled Braycote 601 to meet the mechanism's life requirements.

Harmonic Drive Stage

The HGAG used a custom-built, hollow shaft harmonic drive made by HD Systems, Inc. The harmonic drive was based on HD Systems' standard model SHF 14-50 drive (with a 50:1 gear ratio) with changes made to accommodate the mounting requirements for the HGAG. This harmonic drive was chosen for the following reasons:

- Hollow design accommodated RF routing
- High gear reduction in a compact package
- Drive stiffness was high enough to meet accuracy requirements but low enough to prevent damaging hardware inside and outside the gear train when the mechanism rotates into its hard stops
- The drive was sufficiently accurate (low backlash, small hysteresis, and high repeatability)

For the harmonic drive, JPL initially explored using special aerospace grade materials recommended by HD Systems, Inc. that would be less susceptible to cold embrittlement. However, based on the limited flight history for the special grade materials and the limited development time for the MER program, JPL chose to use the standard commercial materials instead. Because of this decision, additional cold temperature / high load testing was required on the EM unit to validate the robustness of the harmonic drive.

Gear train Analyses

The principle analyses performed on the gear train were:

- Ensuring the motor would not overheat during worst-case loading and duty cycles. (As the motor runs, current flowing through the motor's armature warms the windings. Exceeding the maximum allowable winding temperature of 110°C would damage the motor).
- Ensuring the gimbal would meet its pointing accuracy requirements (backlash, hysteresis, wind-up)
- Assessing whether the mechanism would backdrive under MER mobility loads (induced by situations like driving over or off of large rocks).
- Ensuring that the mechanism would not damage itself or surrounding hardware if the mechanism drove into a hard stop at peak voltage.

Motor Overheat Analysis

Each drive was required to perform the following operations in rapid succession at both protoflight operating temperature extremes while at the minimum operating voltage:

1. Slew from hard stop to hard stop at 6 deg/sec
2. Stall for 2 seconds against the hard stop at the motor current limit
3. Slew back to the other stop at 6 deg/sec
4. Slew back 180 deg at 6 deg/sec
5. Rotate one 0.2 deg step (i.e. overcome starting torque)

This test was designed to ensure that the drive would be able to perform operational requirements, even after the Rover suffered a power reset condition. Thus, if the drive was at the end-of-travel hard stop, ground controllers could home the drive (1st slew plus 2 second stall), and then send the gimbal to the end-of-travel hard stop as if to resume communications (2nd

slew). If the earth's trajectory then forced the drive to "flop," the drive would slew 180 degrees in the opposite direction (3rd slew). Finally, overcoming the starting torque again and moving in 0.2 deg increments is required to resume the regular operation duty cycle.

Since the viscosity of the Braycote grease increases non-linearly with a reduction in temperature, meeting this requirement was a challenge. Development testing suggested that the no load running torque for the input bearings, harmonic drive, and output bearings increased significantly when the temperature drops from +25°C to -70°C (at 50 RPM at the input, the no load running torque increases 4 times with grease plate and 8 times with grease plate + 10% grease fill for these components.) Through measuring or estimating the starting and running torques internal and external to the drive, the required motor torque was determined.

After calculating the expected torque on the motor shaft as a function of environmental temperature, a thermodynamic model was used to estimate the peak motor rotor temperature during the operating conditions described above. To pass the test, two conditions must be met:

- The motor must not overheat
- The peak armature resistance must be low enough to allow rover system to deliver the current limit for that temperature at the minimum operating voltage (22.5V). Note: As motor's resistance increases, the peak current the system can deliver decreases, for a given voltage.

Given the results of the development testing, the following torque margins were predicted:

Table 2. Predicted Drive Torque Margins Under Maximum Load at Temperature

	Temperature		
	-70 C	-60 C	+25 C
Running Torque Margin	1.4	2.0	2.0
Starting Torque Margin	1.5	2.0	2.0

Since a 2.0 torque margin at the minimum protoflight operating temperature (-70°C) could not be predicted, the HGAG drives were all tested and verified at the minimum flight acceptance operating temperature (-60°C).

Pointing Accuracy Analysis

The maximum uncertainty in each drive's pointing angle was conservatively estimated by summing the following sources of error at each level of the gear train.

- Detent forcing the motor shaft into the subsequent detent well: 90 deg at motor shaft (or 0.017 deg at the drive's output)
- Backlash in the gearbox: 0.37 deg at gear motor output (or 0.006 deg at the drive's output)
- Backlash in the spur gear stage: 0.14 deg at spur gear output (or 0.003 deg at the drive's output)
- Hysteresis and repeatability error within the harmonic drive: 0.02 deg at the drive's output
- Gear train windup on Mars (Under starting torque condition): 0.07 deg for Azimuth drive and 0.06 deg for Elevation drive
- Expected tolerance stack of housing misalignments (including thermal distortions): 0.186 deg

The total HGAG maximum pointing uncertainty was then found by an RSS combination of each drive's error. The maximum estimated uncertainty in the HGAG's pointing angle was 0.43 deg, which met the 0.5 deg requirement.

Backdriving Analysis

When the Rover drives over uneven terrain, the induced g-loading may apply a torque on the azimuth and elevation drives. Since the elevation drive was nearly balanced, the induced loading would have to be very large to cause any concern. The azimuth drive, however, was more susceptible to back driving since its center of mass was offset from its rotation axis by

approximately 150 cm. In order to estimate whether the azimuth drive could withstand the maximum expected 6.6 g loading without back driving, the maximum expected drive train efficiencies were conservatively estimated:

- Harmonic drive back drive torque: 0 Nm
- Harmonic drive starting torque: 0 Nm
- Planetary and spur gear efficiency: 1.0
- Harmonic drive efficiency: 0.85
- Minimum detent holding torque: 2.7 mNm

Using these assumptions, the azimuth drive could only withstand a 2.2 g load before it would start to back drive. Because the drive could not meet the 6.6 g requirement without any movement it was important to understand how much movement would result from the event. A finite element analysis indicated that the 6.6 g loading resembled a 20Hz sine wave that would decay over 1 second. Under this condition, it was estimated that the maximum angular excursion for the drive would be 0.07 deg. This 0.07degree excursion was deemed acceptable by the MER system. In addition, it was determined that the minimum motor detent size required to stop motion would be 1.6 mNm which is well below the minimum detent holding torque of 2.7 mNm for the HGAG motors.

Drive Impact Analysis

To ensure that the drive would not damage itself when driving into a hard stop, the maximum torque that would develop as the hard stop halted motion was determined. This was found by estimating the total inertia of the moving parts, the maximum angular velocity, the torsional stiffness of the gear train, and the maximum contribution of the detent in adding to the detent torque. Since the reflected inertia of the gear train increases with the square of the gear ratio, the majority of the total inertia was the gear train's early stages. In fact, the inertia of components attached to the motor shaft was 10 times larger than the inertia of the entire mass attached to the drive's output. Fortunately, the harmonic drive's torsional compliance mitigated the peak torque developed and helped to ensure that no damage would occur when the drive impacts the hard stops.

RF System

Once the drives have correctly positioned the High Gain Antenna to send and receive communication signals, the HGAG must provide an RF system to transfer that information from the antenna to the Rover electronics. The HGA and coax routing within the gimbal comprise the RF system. The HGA used was almost identical to the HGA used for the Mars Pathfinder Lander, with structural modifications made to accommodate the cantilevered mounting on the HGAG. Given the 0.5 dB maximum loss requirement, it was important to minimize RF cable length and the number of RF fitting interfaces used, in order to limit transmission and insertion losses.

The RF signal must be carried across both the rotating elevation and azimuth drives of the gimbal. It was not desirable to accommodate the large rotation angles required in the drives through bending or flexing of the RF cables. To avoid this, the design employs two RF rotary joints to transmit the signal over the rotating interfaces. The rotary joints are positioned internal to the gimbal and are aligned with the axis of the azimuth and elevation drives. The hollow center design of the drive train allows the RF system to be located right on the center axis of each drive which simplifies the overall RF system. Routing the RF system predominantly internal to the HGAG also helps to protect the cables and rotary joints from damage as well as large temperature gradients. The rotary joints were supplied by Kevlan Corporation under contract from JPL. In order to limit the amount of torque required to rotate the RF joints, small heaters are placed near the bearings in the joints in order to maintain a minimum operating temperature. Between the two rotary joints, the RF signal is carried through semi-rigid coax cables supplied by W.M. Gore under contract from JPL.

The final RF design areas that needed to be addressed were how to provide the torque required to turn the rotary joints without carrying the torsion load through the semi-rigid RF cables, and how to protect the internal drive components from contamination entering through the RF system. In order to prevent the rotary joint torsion load from being carried by the cables, a "torque tube" is attached to each drive output. The torque tube reaches back down the center hole in each drive and engages two flats on the input to

the rotary joint. As the drive turns, the torque tube provides the force required to turn the rotary joint. Because of the clearance fit required between the torque tube and the rotary joint for assembly reasons, the RF cable is required to accommodate a small amount of rotation prior to the torque tube engaging. However, this small amount of torsion is within the capability of the semi-rigid coax cable. Figure 4 shows the torque tube arrangement.

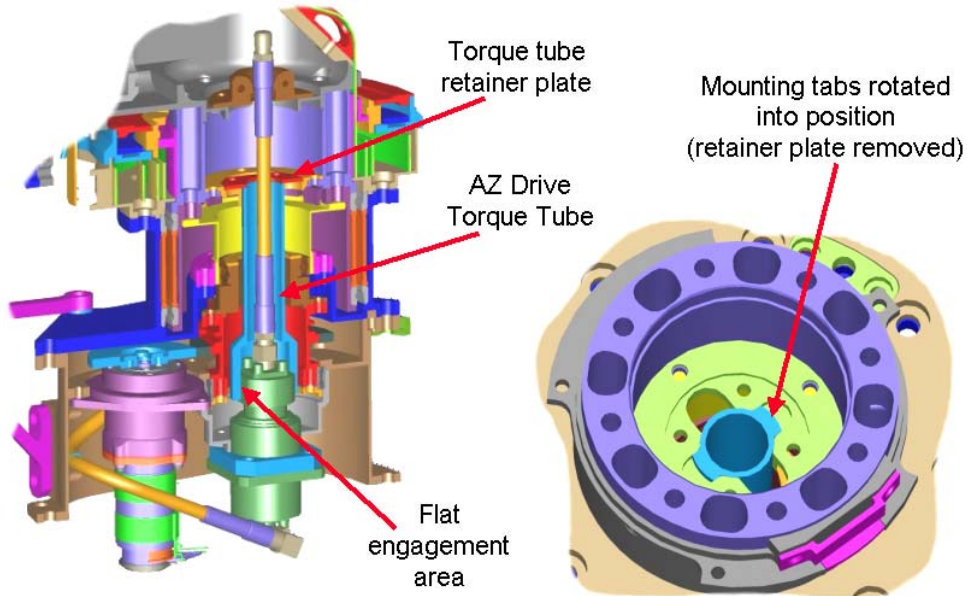


Figure 4. RF system torque tube

A seal system is used to prevent contamination from entering the drive train at the point where the RF system exits the drive. An O-ring is slipped over the RF cable prior to final assembly. During final assembly, the O-ring is located into the groove of a two-piece seal clamp that is mounted to the output of each drive. Figure 5 indicates the seal location and design.

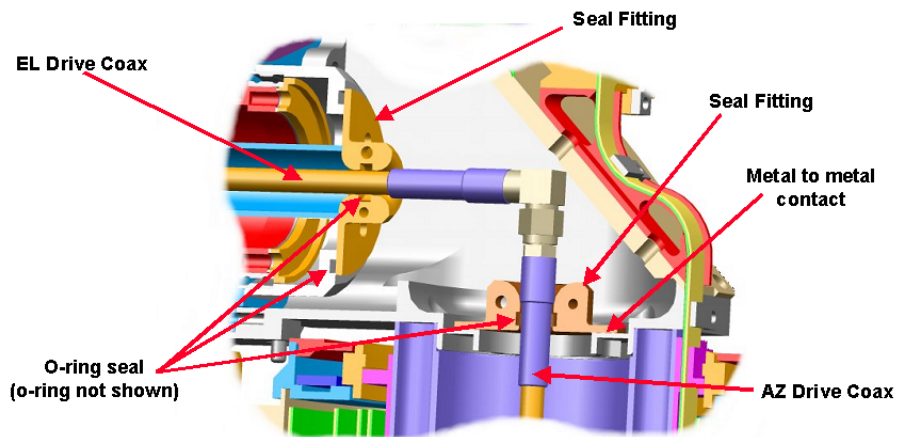


Figure 5. RF coax contamination seal

Flex Cable System

The gimbal design requires that electrical power and signals be passed across both the rotating azimuth and elevation drives. To accomplish this, flex cable twist capsules were used at the output of each drive. The flex cables are wound inside the capsules “clock spring” style, and wind and unwind as the drive rotates. Care was taken to size the flex cable lengths to prevent the system from binding up at either end

of travel as well as allow for shrinkage in the cable lengths due to decreases in temperature. The housing that forms the floor and outside diameter of the twist capsule is also used to clamp the outside race of the main angular contact bearing pair. Once the cables are installed, the radial potentiometer locates on the top of the outside walls of the capsule and forms the lid of the system. The azimuth drive incorporates two flex cables wound as a pair while the elevation drive uses a single flex cable. In order to prevent contamination from entering the system, a potting compound is used to seal the cable exit and entry points at final assembly. Outside of the twist capsules, the flex cables are routed external to the gimbal housings by a system of cable tracks and tie downs. Figure 6 shows the basic installation of the flex cables into the gimbal azimuth drive.

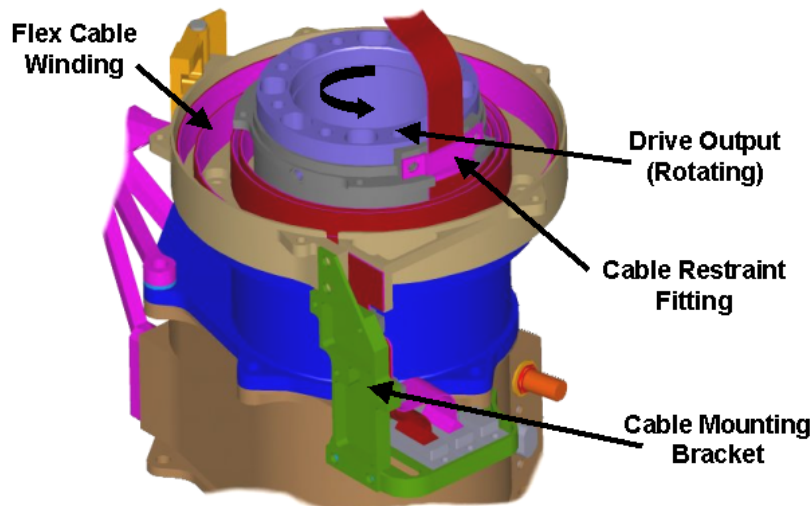


Figure 6. Flex cable twist capsule installation

Launch Lock System

The requirement for the first mode fundamental frequency of the gimbal during peak environmental loading as well as the need to prevent the drives from back driving during these loads necessitated the use of a locking system. The locking system on the HGAG uses a single pyrotechnic pin puller with redundant NSI charges and an adjustable contact pad to restrain both the azimuth and elevation drives. The pin puller and contact pad are cantilevered off the lower azimuth drive housing using a four-strut mount. The pin in the pyrotechnic device engages an integrally machined flange in the elevation drive twist capsule housing. The interface between the pyrotechnic pin and the housing flange is a spherical bearing that is mounted into the end of the flange. The spherical bearing helps to prevent over constraining the assembly. The bearing also accommodates any angular misalignment that exists between the four-strut mount and the housing flange that could result in increased pin pullout force or binding. Because the housing flange is attached to the static portion of the elevation drive, this system only effectively restrains the azimuth drive from rotating. A second locking feature is required to lock the elevation drive. The elevation drive locking system uses both the elevation drive internal hard stop and an external adjustable contact pad to prevent drive rotation in either direction. The contact pad is threaded into a hole in the same four-strut mount that supports the pyrotechnic pin puller. Once the elevation drive has been positioned for launch, the contact pad is adjusted until it contacts a pin feature on the HGA support arm (located on the rotating output stage of the elevation drive). After it is adjusted, it is locked in place using a pair of locking nuts.

The basic procedure for initially setting up the launch lock system is as follows: The azimuth drive is driven to its launch position using motor encoder feedback. At this point, the azimuth drive is not located against any of its internal hard stops because the pyrotechnic pin will restrain azimuth drive rotation in both directions once it is installed. The elevation drive is also driven to its launch position. For launch and landing, the elevation drive is located against one of its internal hard stops to prevent rotation in one direction. After both drives have been positioned, the four-strut mount and pyrotechnic pin puller assembly are positioned in the vertical plane such that the pin moves freely in and out of the spherical

bearing. The two horizontal mounting pads of the four-strut mount are then shimmed and fastened. The final step is to adjust the elevation drive contact pad until it just touches the feature on the HGA arm and then lock it in place using the two jam nuts. During subsequent re-stowing operations, the four-strut mount is not readjusted. The drives are simply driven back to their launch positions and the pyrotechnic pin puller is reinstalled. This mount provides the system with the additional structural stiffness required to achieve the 50 Hz first mode fundamental frequency requirement during launch and landing. Figure 7 shows the launch locking features on the HGAG.

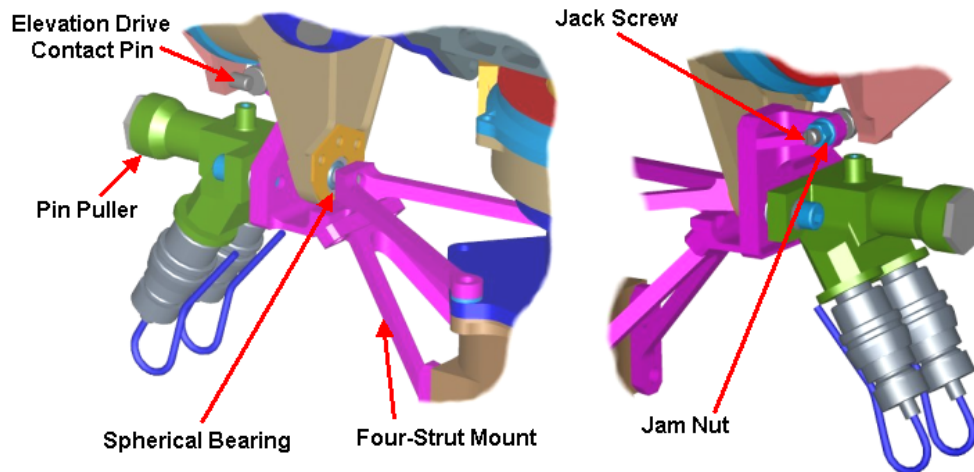


Figure 7. HGAG launch lock features

Pyrotechnic restraint devices are used in a number of mechanisms throughout the MER system and underwent a number of development tests throughout the life of the program. One significant design issue that was discovered during this testing is that the shock load induced by the pyrotechnics has the ability to damage the brush DC motors (as well as other sensitive components) that are being used on all the MER mechanisms. Locating the pyrotechnic device a sufficient distance away from any motor, or attempting to try and isolate the pyrotechnic mount from the rest of the system mitigates the risk. On the HGAG, there was concern that the pyrotechnic device was located too close to the azimuth drive motor and that the four-strut mount provided a direct path between the pyro-shock and the motor. Analysis results were inconclusive, so it was decided to verify the design through additional testing. Final design validation was performed on the Engineering Model (EM). The EM was fitted with a redundant pyrotechnic pin puller whose two charges were rated at 120% those of the flight design. Both charges were fired simultaneously and the motor survived the test. Additional pyrotechnic event tests were performed by JPL at the MER system integration level, including tests at the cold operating temperatures. In all cases, no performance effects were seen on the HGAG drive motors.

Internal Hard Stops and Azimuth Drive “Flipper” Hard Stop

Both the azimuth and elevation drives employ internal hard stops at the end of travel for each drive. These stops provide a consistent mechanical “home” for the drive electronics and prevent the mechanism from exceeding its dynamic envelope and damaging any of the other hardware on the MER. The hard stops consist of an integrally machined titanium boss on the rotating output housing of each drive and a stationary Nitronic 60 hard-stop that is pinned and fastened to the stationary portion of the drive. The Nitronic 60 piece is removable to allow for continuous drive rotation during subassembly testing, but the interface is designed to remain repeatable after consecutive installations. The stop materials were chosen to prevent galling in the system. Figure 8 shows the internal hard-stop features.

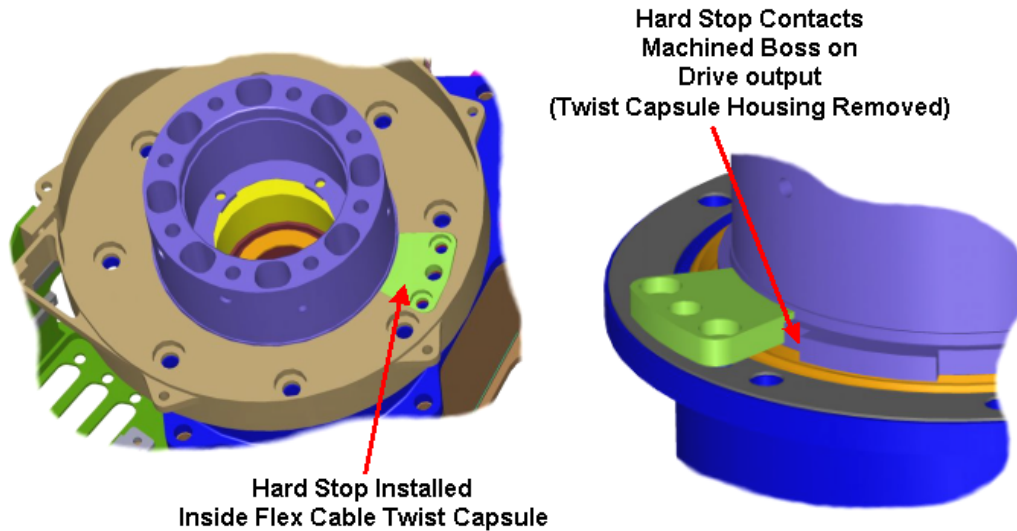


Figure 8. Drive internal hard stop features

In addition to the internal hard stops, the azimuth drive must also provide a secondary hard stop that is engaged after the first azimuth drive deployment. This secondary stop is necessary because the dynamic sweep envelope of the High Gain Antenna on the elevation drive can violate the envelope of the Low Gain Antenna if the azimuth drive is in its launch locked position. To avoid this, during its first sweep away from the launch position, a pin feature on the azimuth drive passes through a spring-loaded “flipper stop” that closes behind the drive once the pin feature has passed. The new “flipper” hard stop will only allow the azimuth drive to return within 15 degrees of the original launch lock position. At this spot, the elevation drive is free to rotate the HGA through its full dynamic envelope without endangering the Low Gain Antenna. The flipper stop employs two redundant torsion springs that are sized to independently provide enough closing force to keep the flipper secure against the housing during launch and landing. The materials of the pin feature and flipper as well as the shape of the sliding surfaces were chosen to minimize the torsion load required to pass through the spring-loaded gate. Drive level testing was performed to verify the starting / running torque required to pass through the gate as well as to verify the repeatability and strength of the stop under numerous hard stop contacts. Figure 9 shows the secondary azimuth drive “flipper” hard stop.

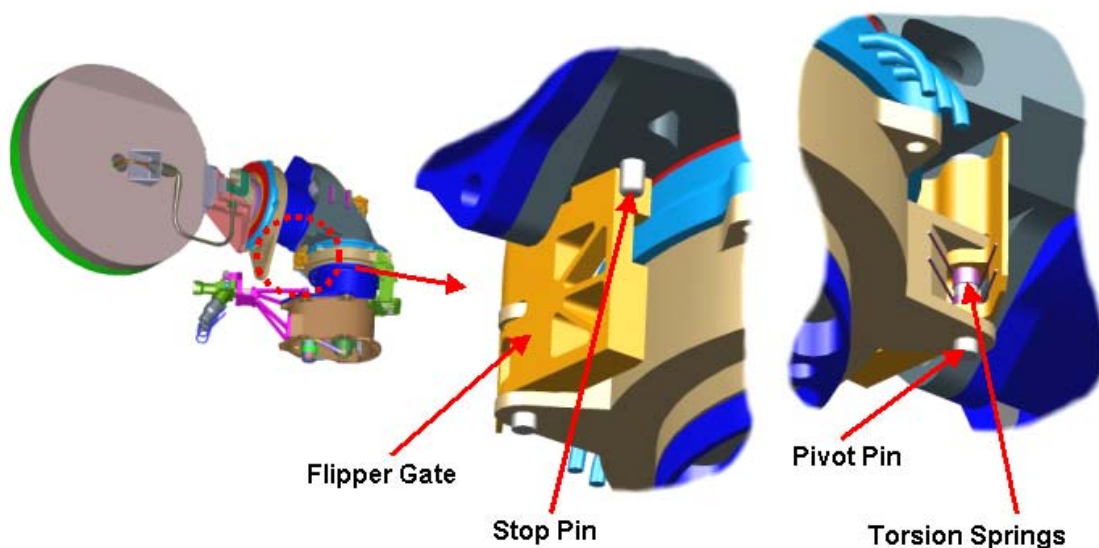


Figure 9. Azimuth drive “flipper” hard stop

Structural Analysis Overview

Two of the significant driving requirements for the HGAG system were the launch locked first fundamental frequency of 50 Hz and the deployed first fundamental frequency of 14 Hz. A detailed finite element model of the HGAG assembly was developed to predict the overall stiffness of the system and assist in finalizing the design. The model was statically and dynamically calibrated to provide accurate mass distribution.

Stiffness predictions for the elevation and azimuth bearing sets were determined using BEAR3D [2], a nonlinear program that allows the analysis of three-dimensional assemblies of linear elastic beams and bearings. The computer program is based on the stiffness method of structural analysis and the bearing technology presented in the New Departure Engineering Handbook of 1946 [3]. The New Departure developments were established for two-dimensional bearing analysis. The techniques were extended to full three-dimensional analysis with five degrees of freedom to represent each bearing. BEAR3D generates a bearing stiffness matrix that is easily incorporated into a MSC.NASTRAN structural system model of the mechanism. In addition to the bearing stiffness predictions, the minimum manufacturer published values were used for the harmonic drive spring rate.

Nonstructural lumped masses include the gear motors, the HGA, the pyrotechnic pin puller, and the potentiometers. All lumped masses were attached to the structure in such a way as to not stiffen, nor strengthen it. The pin puller mount was modeled as four titanium bars of square cross-section. The pin puller was solidly attached to the apex of this four-strut mount. The modal predictions and test results are shown in Table 3. The deployed first mode is largely dependant on the spring rate of the harmonic drive. Because the lowest published value for the spring rate was used in the FEA model, the prediction was lower than the actual test results achieved by the flight hardware.

Table 3. First mode frequencies of the HGAG with the HGA attached

	Launch Locked	Deployed
Requirement	50 Hz	14 Hz
Predicted	54 Hz	19.5 Hz
Actual	51 Hz	26 Hz

Analysis was also performed on the structural stresses in the assembly induced by launch, landing, and mobility loads as well as thermal gradients experienced while operating on Mars. For the launch and landing loads, the 45 g quasi-static load was applied to the model in each of the three primary orthogonal axis with the launch lock restraint engaged. For the mobility loads, the expected maximum g load was applied in each of the 3 axis with the launch lock restraint eliminated. In all cases, the structural elements of the gimbal showed acceptable positive margin.

The HGAG is exposed to the environmental temperature extremes during Martian operation. The thermal stress analysis for the structure was done using the same FEA model. Overall system temperature changes (-120°C to +110°C) induce no appreciable stress in the system because all the structural elements are either identical (titanium) or closely matched in CTE (440C steel bearings). However, thermal gradients in the gimbal system can develop from some components seeing direct sunlight while others remain in the shade. It was important to analyze whether or not these gradients could induce enough additional load in the pyrotechnic pin puller system to cause it to bind prior to being fired. The worst-case gradients come from the hot transient case. During this transient case, it was predicted that the assembly could develop a 17.9 MPa peak stress and a 9.8 N side load on the launch lock pin. This result was found to be well within the performance capabilities of the pyrotechnic device.

HGAG Test Discussion

The HGAG Mechanism test verification plan included individual drive testing and full assembly level testing under all operating conditions. Each individual drive was characterized for performance (including torque speed curves, current limits, pointing accuracy, and stiffness) prior to being integrated together to form a complete HGAG assembly. System level verification tests included structural, RF system loss, pointing accuracy, and dimensional compliance. Every attempt was made to simulate the Martian operating environment for design verification. Thermal vacuum chambers were used to achieve the low operating temperatures and low atmospheric pressures required. Many tests were run with the gimbal mounted on an incline or working against weight and pulley systems to simulate the possible operating orientations and drive loads aboard the rover. After each significant testing milestone, a standardized ambient functional test was performed on the entire system to monitor the health of the mechanisms and ensure that no performance degradation was seen. At the end of its testing protocol, the Engineering Model (EM) underwent a rigorous life test where each drive was cycled under the maximum expected load for the total required number of motor revolutions. In the end, the HGAG units were shown to meet or exceed all design requirements. Figure 10 shows one of the flight HGAA assemblies just prior to shipment to JPL for Rover integration. The thermocouple wire bundles that can be seen coming from different locations on the HGAG were used by JPL during system level testing and were removed or clipped by JPL prior to flight.

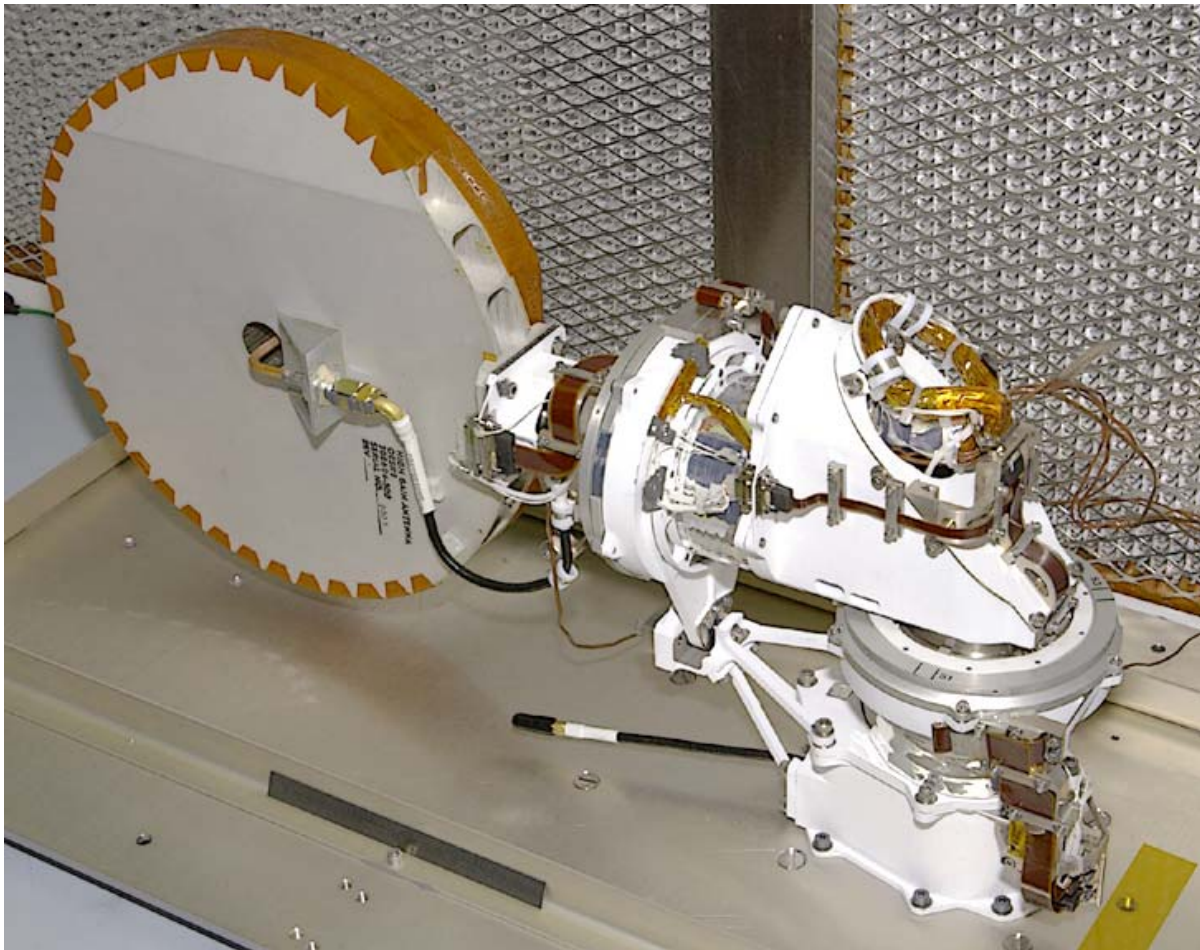


Figure 10. Flight HGAA shown just prior to shipment to JPL

Conclusion

The design, assembly, test, and delivery of the HGAG mechanisms were a cooperative effort between JPL and BATC. It is difficult to capture all of the lessons learned on a development program such as this, but it is safe to say that all personnel involved with the HGAG program received a valuable education in what it takes to deliver qualified flight hardware for a time sensitive planetary exploration mission. One design lesson that does stick out because of its risk to the HGAG program is the potential damaging effects of the shock load created by pyrotechnic launch lock devices like the pin puller. Care must be taken to properly isolate sensitive components (electronics, motors, etc.) whenever possible. In the case of the HGAG, the problem was discovered late and could not be shown to be acceptable analytically. This required additional verification testing, which in turn introduced additional risk, schedule, and cost late in the program. Fortunately, the design was proven to be robust through testing and any potential redesign was avoided. The HGAG successfully met the design and schedule challenges that it faced, and is on its way to play an important role in the communication system of the MER mission.

Acknowledgements

The authors would like to thank all the HGAG program technicians, machinists, designers, engineers and managers at BATC, and the entire MER team at JPL, for their commitment to developing these mechanisms.

This work was performed under a contract with Jet Propulsion Laboratory, California Institute of Technology, for the National Aeronautics and Space Administration. Reference herein to any specific commercial product, process or service by trade name, trademark, manufacturer, or otherwise does not constitute or imply its endorsement by the United States Government or the Jet Propulsion Laboratory.

References

1. "Mission Overview". Athena Mars Exploration Rovers website. Cornell University. Date of access October 24, 2003. <http://athena.cornell.edu>
2. R. N. Taylor, "BEAR3D Users Manual," Internal Report, Ball Aerospace & Technologies Corp., Boulder, Colorado, 1993.
3. A. B. Jones, New Departure Engineering Handbook, Analysis of Stresses and Deflections, New Departure, Division of General Motors Corp., (out of print) 1946.

A Low Mass Translation Mechanism for Planetary FTIR Spectrometry using an Ultrasonic Piezo Linear Motor

Matthew Heverly*, Sean Dougherty*, Geoffrey Toon**, Alejandro Soto**, Jean-Francois Blavier**

Abstract

One of the key components of a Fourier Transform Infrared Spectrometer (FTIR) is the linear translation stage used to vary the optical path length between the two arms of the interferometer. This translation mechanism must produce extremely constant velocity motion across its entire range of travel to allow the instrument to attain high signal-to-noise ratio and spectral resolving power. A new spectrometer is being developed at the Jet Propulsion Laboratory under NASA's Planetary Instrument Definition and Development Program (PIDDP). The goal of this project is to build upon existing spaceborne FTIR spectrometer technology to produce a new instrument prototype that has drastically superior spectral resolution and substantially lower mass, making it feasible for planetary exploration. In order to achieve these goals, Alliance Spacesystems, Inc. (ASI) has developed a linear translation mechanism using a novel ultrasonic piezo linear motor in conjunction with a fully kinematic, fault tolerant linear rail system. The piezo motor provides extremely smooth motion, is inherently redundant, and is capable of producing unlimited travel. The kinematic rail uses spherical Vespel® rollers and bushings, which eliminates the need for wet lubrication, while providing a fault tolerant platform for smooth linear motion that will not bind under misalignment or structural deformation. This system can produce velocities from 10 – 100 mm/s with less than 1% velocity error over the entire 100-mm length of travel for a total mechanism mass of less than 850 grams. This system has performed over half a million strokes under vacuum without excessive wear or degradation in performance. This paper covers the design, development, and testing of this linear translation mechanism as part of the Planetary Atmosphere Occultation Spectrometer (PAOS) instrument prototype development program.

Introduction and Background

The Planetary Atmosphere Occultation Spectrometer uses the solar occultation technique to search for trace gases in a planetary atmosphere. The instrument, a Fourier Transform Spectrometer (FTS), views the sun through a planet's atmosphere at sunrise and sunset. As the sunlight passes through the planet's limb, the gasses in the atmosphere selectively absorb certain wavelengths of light. The instrument measures the flux of the incident light at different wavelengths and is able to quantify the atmospheric composition as a function of altitude from the depths of the various absorption lines. Since the sun is a very bright radiation source, these occultation spectra can be of very high spectral resolution and signal-to-noise ratio, providing ultra-high sensitivity to trace gases in the planetary atmosphere under study.

At the heart of any FTS is a Michelson interferometer, which splits the incoming radiation and sends it down two arms with different path lengths. When the two beams recombine interference occurs. By varying the optical path length difference between the two arms of the interferometer, the incoming light is interferometrically modulated. The different wavelengths present in the radiation are modulated at different frequencies. So applying a Fourier transform to the interferogram produces a spectrum of light absorption levels vs. wavelength and reveals the composition of the observed atmosphere. The spectral resolution of an FTS is a function of the maximum optical path difference (OPD), and the quality of the spectra is critically dependant upon the uniformity of the moving cube corner's motion. An example spectrum for the atmosphere of Saturn's moon Titan is shown in Figure 1.

* Alliance Spacesystems, Inc., Pasadena, CA

** Jet Propulsion Laboratory, California Institute of Technology, Pasadena, CA

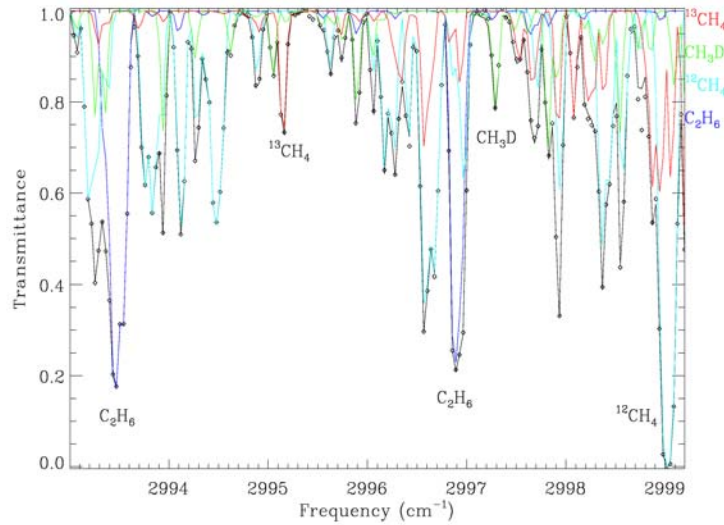


Figure 1. Simulated limb transmittance spectrum (0.05 cm^{-1} spectral resolution) at 300 km tangent altitude in the atmosphere of Titan, showing the absorption contributions of ethane and various isotopomers of methane. This 6 cm^{-1} interval represents less than 0.2% of the full PAOS bandpass

Most spaceborne, high-resolution Fourier transform spectrometers to date have been Earth-orbiting instruments constructed using traditional electromagnetic actuators in the form of direct drive voice coils or brushless DC motors with lead screws or belt drive systems to drive the translation stage (Persky, 1995). These mechanisms are either too massive or don't have the requisite spectral resolution for future exploration of planetary atmospheres. Figure 2 below shows a comparison of the PAOS instrument requirements with other Fourier Transform Spectrometers by plotting the overall instrument mass versus the number of spectral channels (simultaneous spectral bandwidth divided by spectral resolution) (Toon, 2001).

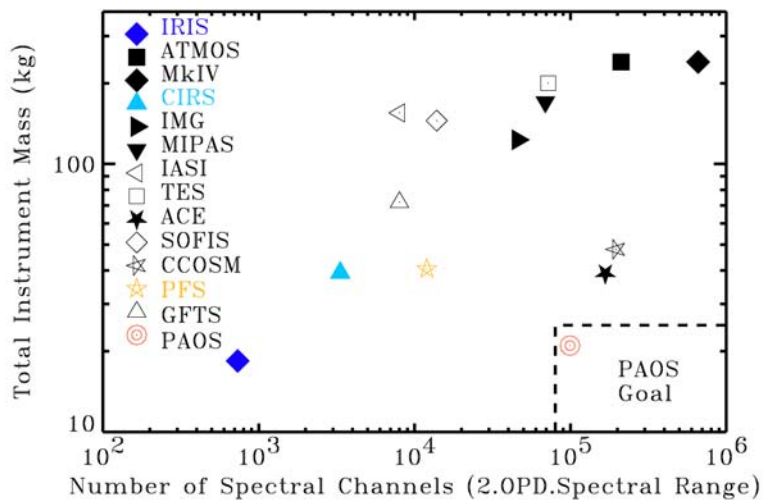


Figure 2. Comparison of PAOS mass and spectral resolving power with other FTS. Colored symbols represent planetary instruments. Filled symbols represent launched instruments.

Prototype Mechanism

The PAOS instrument will incorporate new technology in several different areas. It will use new laser diodes for the reference laser and new electronics for on-board data processing and compression. The subsystem with the lowest technology readiness level at the time of the PIDDP proposal, however, was the translation mechanism and thus it has been the focus of the PIDDP effort up to the time of this publication. The mechanism is required to move a 125-gram cube corner retro-reflector through a 100 mm stroke at a constant velocity of 30 mm/s with less than 1% error in velocity (± 0.15 mm/s rms) over a life of one million strokes. The goal of the development was to make a mechanism that could accomplish all these requirements while packaged as small as possible, consuming less than 5 watts of power on average and having a mass less than 4 kg. Because this is an interferometer, it is sensitive to motions as small as a few nanometers and can sense disturbances into the megahertz range.

In modern FTSs, the effects of velocity errors are removed, to first order, by means of a reference laser that traverses the same optical path as the infrared radiation of interest. The laser is used to trigger the sampling of the infrared interferograms, ensuring that they are at equal increments of optical delay. But due to the fact that the laser beam hits different parts of the optics from the IR beam, and the fact that the laser is at a different frequency, there still remain significant second-order effects that arise from velocity non-uniformities. Since these second and third order disturbances are very hard to model analytically, our development approach was to build several prototypes and test them as early as possible. Once tested, the performance of the mechanism could be characterized and the causes of velocity jitter could be better understood. Several different concepts including voice coils, lead screws, linkages, and belt drive systems were tested. Off the shelf mechanisms as well as quick, custom prototypes were built and evaluated. This helped to reduce the time involved in the development process while still providing valuable data about the root causes of velocity error. The lessons learned during each of these tests were then folded back into the next iteration of the design cycle to continually improve the mechanism performance and robustness.

The final prototype mechanism, shown in Figure 3, uses an ultrasonic piezo motor to move the sled that carries the moving hollow cube-corner retro-reflector (HCCRR). The sled is guided by a kinematic rail system that uses three spherical Vespel rollers along with the preload of the piezo motor to fully constrain the cube corner sled's motion. The sled is moved through the required 100 mm stroke and follows a trapezoidal motion profile spending 85% of its duty cycle at the target speed of 30 mm/s. The second cube corner, required for the interferometer, is held stationary and is attached to a common base plate. A top view of the mechanism is shown in Figures 4 and 5 with the moving sled at its left and right ends of travel positions respectively.

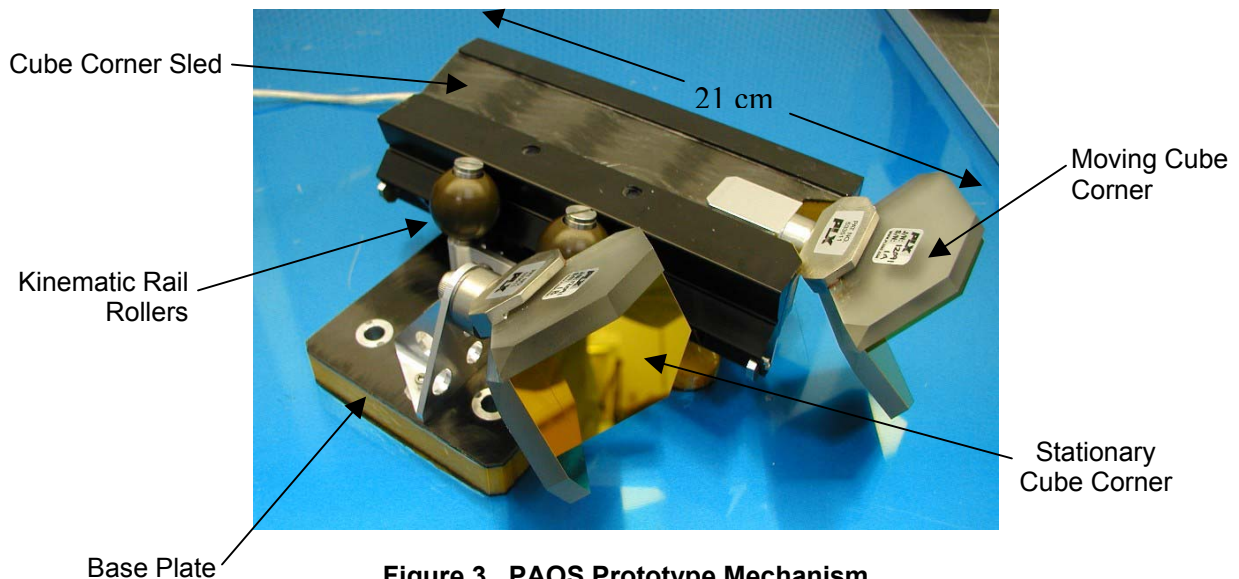


Figure 3. PAOS Prototype Mechanism



Figure 4. Left End of Travel

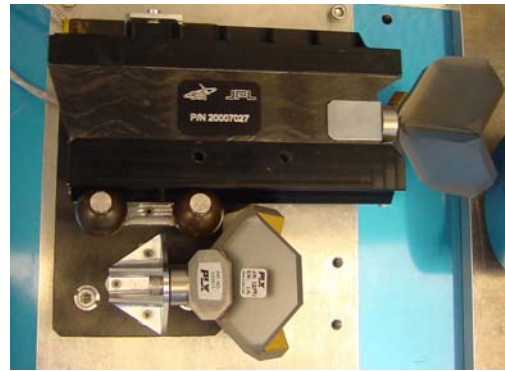


Figure 5. Right End of Travel

Linear Piezo Motor

Ultimately the design goals and the developmental nature of the project led to the decision to use new technology in the form of an ultrasonic linear piezo motor developed by Nanomotion Ltd, Figure 6. This motor allows for drastic mass savings over more traditional systems while, at the same time, producing very constant velocity motion. Piezoelectric materials allow mechanical strain to be directly coupled to electrical potential. The motor works by simultaneously exciting both a longitudinal (Figure 7) and transverse (Figure 8) bending mode in a piezo element using two sinusoidal voltage inputs. The result of these combined modes is an elliptical motion at the tip of the piezo element that drives a linear stage through a preloaded friction interface.



Figure 6. HR-4 (Four Element) Linear Piezo

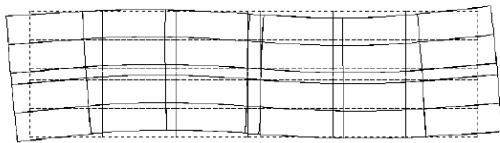


Figure 7. Longitudinal Extension Mode

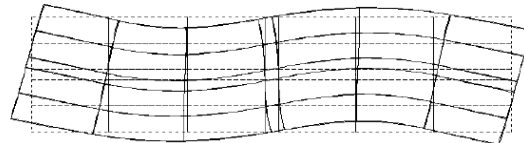


Figure 8. Transverse Bending Mode

The piezo elements have a hard ceramic alumina finger tip attached to the element body, which interacts with an alumina strip mounted to the mechanism's moving sled as shown in Figure 9. This provides an optimum coefficient of friction and significantly reduces wear. During extension and bending of the piezo element the sled is actively forced in the desired direction, while during contraction and bending in the other direction, the piezo either slides on, or separates slightly from the ceramic drive strip. This motion results in a net forward movement of the sled over one cycle of the piezo element. This elliptical motion takes place at a frequency of 40 kHz. Because of the speed of this oscillation, the mass of the moving object mechanically filters any jitter, resulting in extremely smooth linear motion. The magnitude of the displacement during any one cycle is proportional to the voltage applied across the piezo element. This voltage can be changed rapidly to control the velocity of the moving sled. Since the piezo element displacements are on the nanometer scale, these motors can also be used to achieve positional accuracies of less than 10 nanometers. A standard servo controller with any standard feedback device can close the control loop and servo the applied voltage in order to follow a desired trajectory profile.



Linear Optical
Encoder

Linear Piezo
Motor

Ceramic Drive
Strip

Figure 9. PAOS Mechanism Rear View

The piezo elements can be stacked side by side and operated in parallel to give a proportional increase in driving force. This also introduces redundancy such that if one element fails, it simply results in a decrease in available force rather than catastrophic failure (Uniformity of velocity in this configuration is yet to be quantified). The current prototype uses a vacuum-rated, four-fingered piezo motor with a mass of 73 grams. It is able to provide approximately 4 pounds of force in the driving direction. This allows ample margin for driving the mechanism in any orientation (including vertically against gravity), which allows for versatility in earth testing.

A factor in the decision of whether or not to use piezo motors for this development was their lack of flight heritage. It was decided that although these motors have never flown on a space flight mission, they possessed all the necessary qualities for a flight mechanism and offered such dramatic benefits that they could not be overlooked. Given the research and development nature of the PIDDP program, the piezo motors were incorporated into the design. Piezoelectric materials have been flown in the past on projects such as the Large Angle and Spectrometric Coronagraph (LASCO) telescope aboard the Solar and Heliospheric Observatory (SOHO) spacecraft, but have primarily been used as a stack of piezo wafers with an applied DC voltage to give highly accurate, but extremely small deflections, in the μm range (Burger, 1995). The ultrasonic piezo motor uses the same materials, but employs an AC voltage to excite the natural frequency of the piezoelectric element to create motion. These motors have been used for several years in vacuum environments for applications such as scanning electron microscopes and are available in vacuum-rated versions rated down to 10^{-10} torr. Nanomotion Ltd. has conducted thermal testing, proving a survivability temperature as low as -120 deg C and an operational range of -55 deg C to $+85$ deg C. A 4.6 million-cycle vacuum life test has also been run showing no degradation in motor performance over the life of the eighty-day test. Outgassing tests performed per ASTM E 595-93 standard have shown a total mass loss (TML) of 0.60% and less than 0.018% collected volatile condensable materials (CVCM) under vacuum conditions, which exceeds the recommended $\text{TML} < 1.0\%$ and $\text{CVCM} < 0.1\%$. ASI is currently working to fully qualify these motors for space flight applications. The development of this motor as an alternative to traditional motors looks very promising, as the most substantial issues have already been addressed in the construction of these motors for terrestrial vacuum applications.

Rail Design

Several rail systems were tested in the early stages of the program including recirculating linear ball bearings, crossed roller bearings, as well as flexure and linkage systems. With all systems that used recirculating balls, the impact of the ball bearings striking the guiding rod was evident in the velocity error (whose measurement is described later). The prototypes that used crossed roller bearings all performed well, but the crossed rollers have issues that make them less desirable for space mechanisms. Linear crossed roller bearings require a caging system to separate and equally space the cylindrical rollers. Over time the cage can migrate to one end of travel. This will lead to the cage striking one end of the rail system and gradually reducing the range of travel, which will eventually lead to a mechanism failure. This is not generally a concern in terrestrial applications because the cage can easily be reset by hand, but for

a flight mechanism, additional design elements must be introduced to mitigate this problem (Roberts, 1994). A crossed roller bearing is also inherently over-constrained and depends upon tight machining tolerances to prevent the system from binding. A slight misalignment or small change in preload (due to thermal expansion for example) can produce a drastic increase in the force required to move the sled, which could cause binding.

After investigating the pros and cons of various designs, a rail system was developed that uses the preload of the piezo motor in conjunction with three spherical rollers to create a fully kinematic rail system that guides the moving corner cube sled. Figure 10 shows a two-dimensional schematic of the rail configuration. A spherical roller (furthest right in the figure) is attached to the base structure. The sled has an integral V-groove that rides on the spherical roller, resulting in two contact points. A separate spherical roller (furthest left in the figure) is also attached to the base structure and creates another point contact on a flat surface on the moving sled. The piezo motor is preloaded against the moving sled producing a force that results in a moment around the V-groove roller that is reacted by the single roller, resulting in a fully kinematic design.

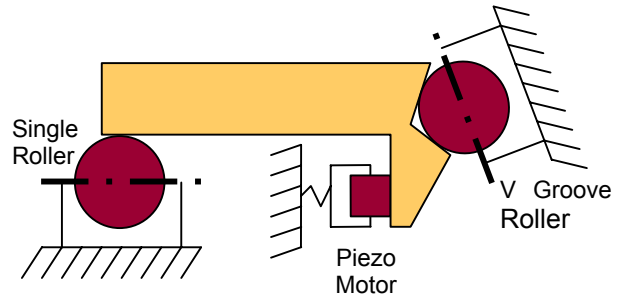


Figure 10. 2-D Kinematic Rail Schematic

The rail design can be expanded to three dimensions by adding a second V-groove roller (shown in Figure 11). If the single roller and piezo motor preload force act between the two v-groove rollers, the rail system becomes kinematic in three dimensions, leaving the translation of the sled as the only remaining degree of freedom. Since the rail system is kinematic, the force required to move the sled should not change if small misalignments are introduced due to thermal distortion of the structure. The design also helps to reduce the need for tight machining tolerances in order to align the system properly.

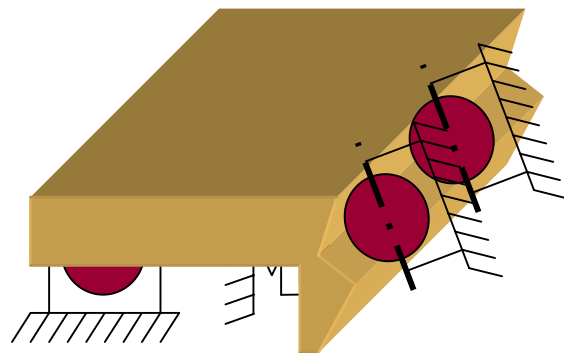


Figure 11. 3-D Kinematic Rail Schematic

All three of the spherical rollers are made from Vespel SP3. Initially, a pair of preloaded radial ball bearings was used inside each of the spherical rollers, yielding good velocity uniformity performance. Tests were then run without the ball bearings using only the Vespel rollers as bushings, sliding on steel pins coated with Diconite® dry film lubricant as shown in Figure 12. These tests yielded similar results to the tests using bearings, but without the requirement for wet lubrication. This is advantageous because the lubrication under vacuum conditions could outgas and contaminate the optical surfaces. With the rollers acting as bushings the force necessary to move the mechanism is proportional to the preload of the piezo motor and the coefficient of friction between the sliding Vespel/Diconite interface. Under normal ambient conditions the mechanism requires approximately 4 N of force to move the sled. Under vacuum conditions, the coefficient of friction for Vespel SP3 reduces by a factor of 10 due to the removal of moisture on the contacting surfaces. This further reduces the power required by the system and increases the motor's force margin over stall conditions.

The V-groove and flat track of the sled are hard anodized aluminum with a surface finish of 8, giving a hard, smooth surface for the rollers to contact. And even if the rollers were to bind on the steel pins, they are still able to slide on the anodized aluminum tracks. This makes the system single fault tolerant. Tests

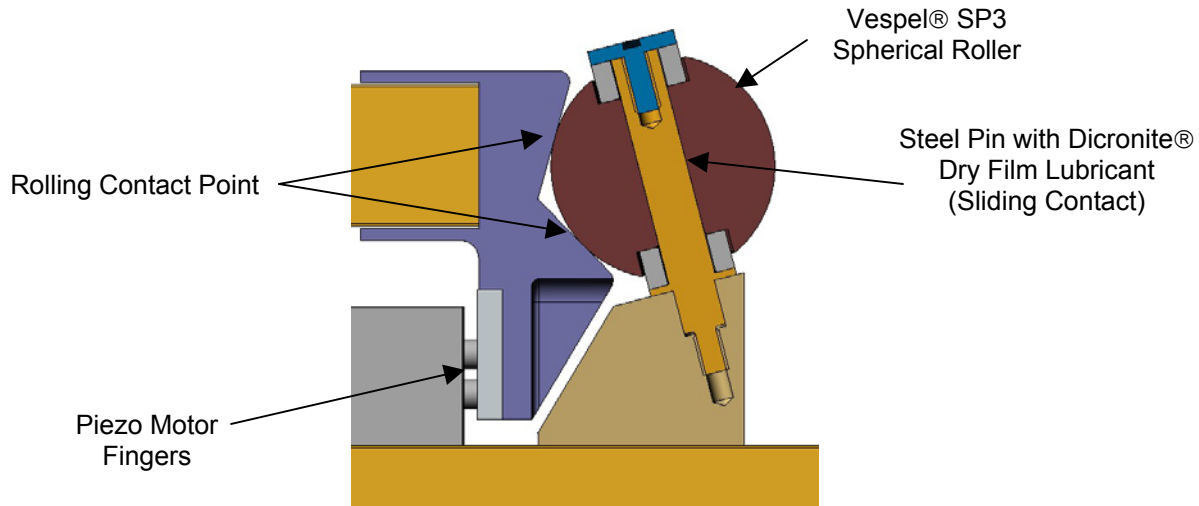


Figure 12. Spherical Roller Cross Section

were performed in this condition, resulting in only a slight increase in the required force and no compromise in velocity smoothness.

Design Details

Unpowered Holding Force

The piezo motor moves the output stage through an oscillation of the piezo fingers through a friction interface. When the motor is not powered, the piezo fingers are still preloaded against the moving sled. This static interface between the piezo fingers and the sled gives the benefit of unpowered holding force. Under ambient conditions the current prototype has a holding force of approximately 13 N, which is directly proportional to the preload of the fingers and the number of elements used in the motor. The mechanism can however, be readily backdriven by simply overcoming the frictional holding force without any damage to the motor or friction interface. This holding force is likely not enough to cage the mechanism for launch conditions, but will hold the mechanism during orbital maneuvers of the spacecraft after the launch lock mechanism has been released.

Mechanical Hardstops

Two mechanical hardstops are incorporated into the mechanism, one at either end of travel. These hardstops protect the mechanism and the optics from overtravel, but also allow for positional calibration of the mechanism at startup. Since the piezo fingers slip on the ceramic drive strip when the stall force of the motor is exceeded, there is no damage done to the mechanism when the moving sled encounters a hardstop. To calibrate the mechanism it is driven in one direction until a position error threshold is exceeded. The position tracking software is then re-zeroed to create a home position in the controller, which eliminates the need for an absolute feedback device.

Power Consumption

The four-element piezo motor itself consumes approximately 3.25 watts of power under normal operating conditions on Earth. Power consumption will be slightly reduced (although exactly how much has yet to be quantified) on orbit due to the decrease in the coefficient of friction of the Vespel rollers in vacuum and the corresponding reduction in the force necessary to move the cube corner sled. The drive electronics used in the prototype are not designed for efficiency as they are for industrial applications, and consume approximately 4 watts giving a total of 7.25 watts total power consumption for the mechanism. The piezo elements require a sinusoidal voltage of 120 volts for excitation. The control electronics currently run off of a 24 or 48 volt DC bus and a majority of the drive electronics' power consumption is used for voltage conversion.

Feedback and Control

The prototype currently uses a vacuum rated, Renishaw 0.1-micron linear encoder for positional feedback to control the velocity profile. A standard servo controller running a cascaded velocity/position control loop is used to control the motion profile. The interferometer's reference laser will eventually replace the encoder as the mechanism's feedback device. The zero crossings of the sinusoidal laser interference pattern can be counted in much the same way as a traditional encoder allowing a standard controller to be implemented. Using the laser as feedback should increase the robustness of the mechanism by decreasing the number of subsystems. It is also expected that this will increase the performance of the mechanisms due to the high resolution of the laser interferometer and the fact that the control system will feedback directly on the optical path difference, which is the variable of interest.

Testing

The prototype mechanism was tested using the double pass interferometer setup shown in Figure 13 to give true output velocity measurements. A 633-nm wavelength single-frequency He:Ne reference laser is sent through a beam splitter with one half of the beam going to the stationary cube corner and the other half of the beam going to the moving cube corner. The beams reflect off the cube corners onto the retro reflector where the beams then retrace their paths. The two beams then recombine at the beam splitter where their overlapping waves add and subtract, depending on their relative path difference, to produce an interference pattern. If the moving cube corner translates at a constant velocity, the interference pattern is a constant frequency sine wave. The waveform pattern in the detector is sampled at 1MHz and the data is analyzed using a custom analysis tool built by ASI.

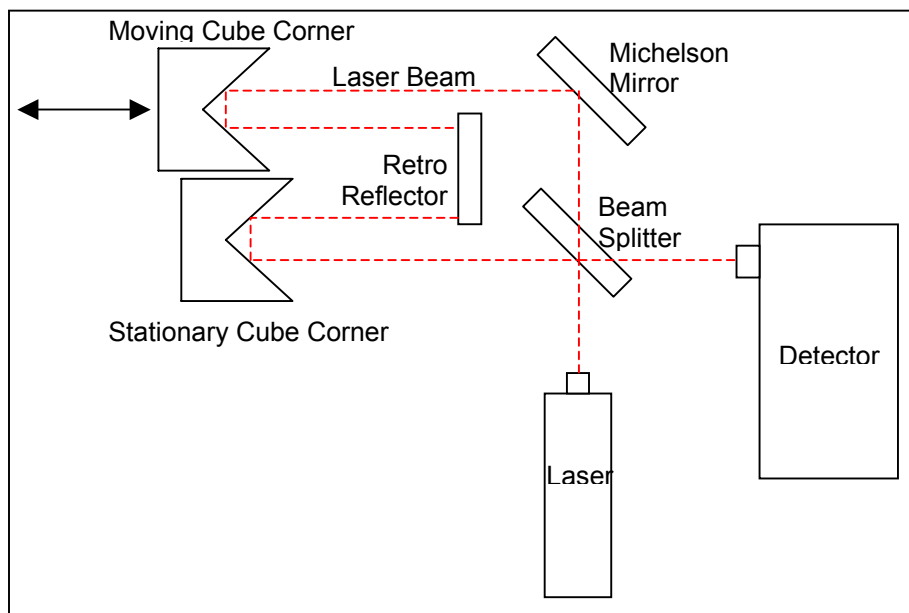


Figure 13. Laser Interferometer Test Setup

Figure 14 shows the original laser intensity depicted in the form of a sine wave. The Hilbert transform of this data is then taken to calculate the frequency of the data at every point. This frequency is directly proportional to the cube corner linear velocity. The calculated velocity is plotted in Figure 15. The Fourier transform can then be taken of the velocity data to identify the frequencies at which disturbances occur and their magnitude. This velocity error data is shown in Figure 16. Using this method, the true velocity error of the cube corner can be measured and the frequency of the disturbances can be quantified, which helps to identify and eliminate the sources of velocity error.

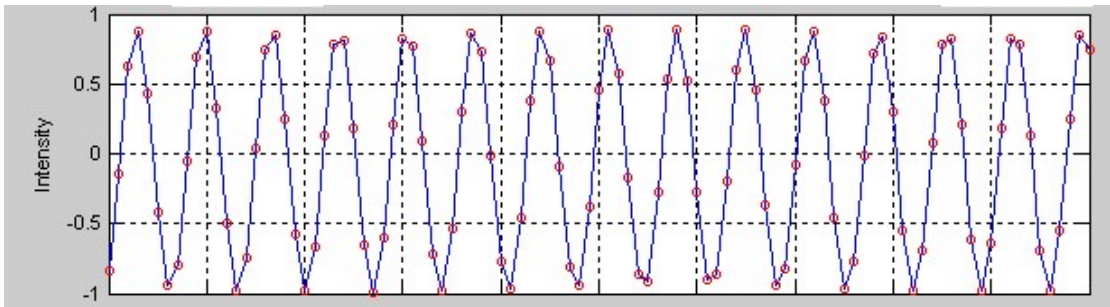


Figure 14. Original laser intensity data over 0.1 ms sample period (red circles are sample points)

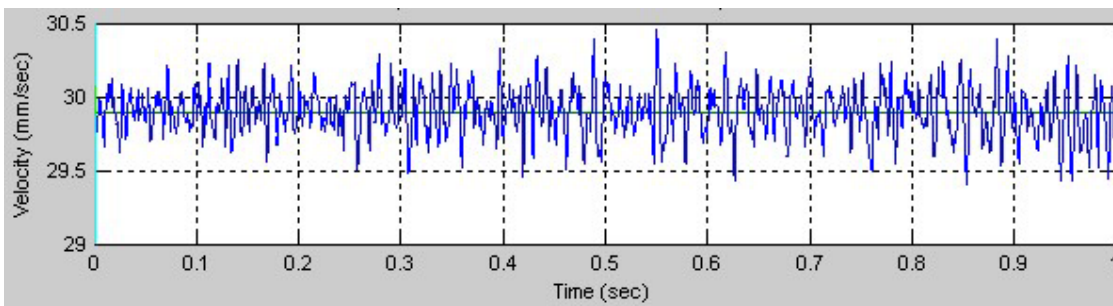


Figure 15. Calculated velocity (frequency) vs. time over 1 second sample period

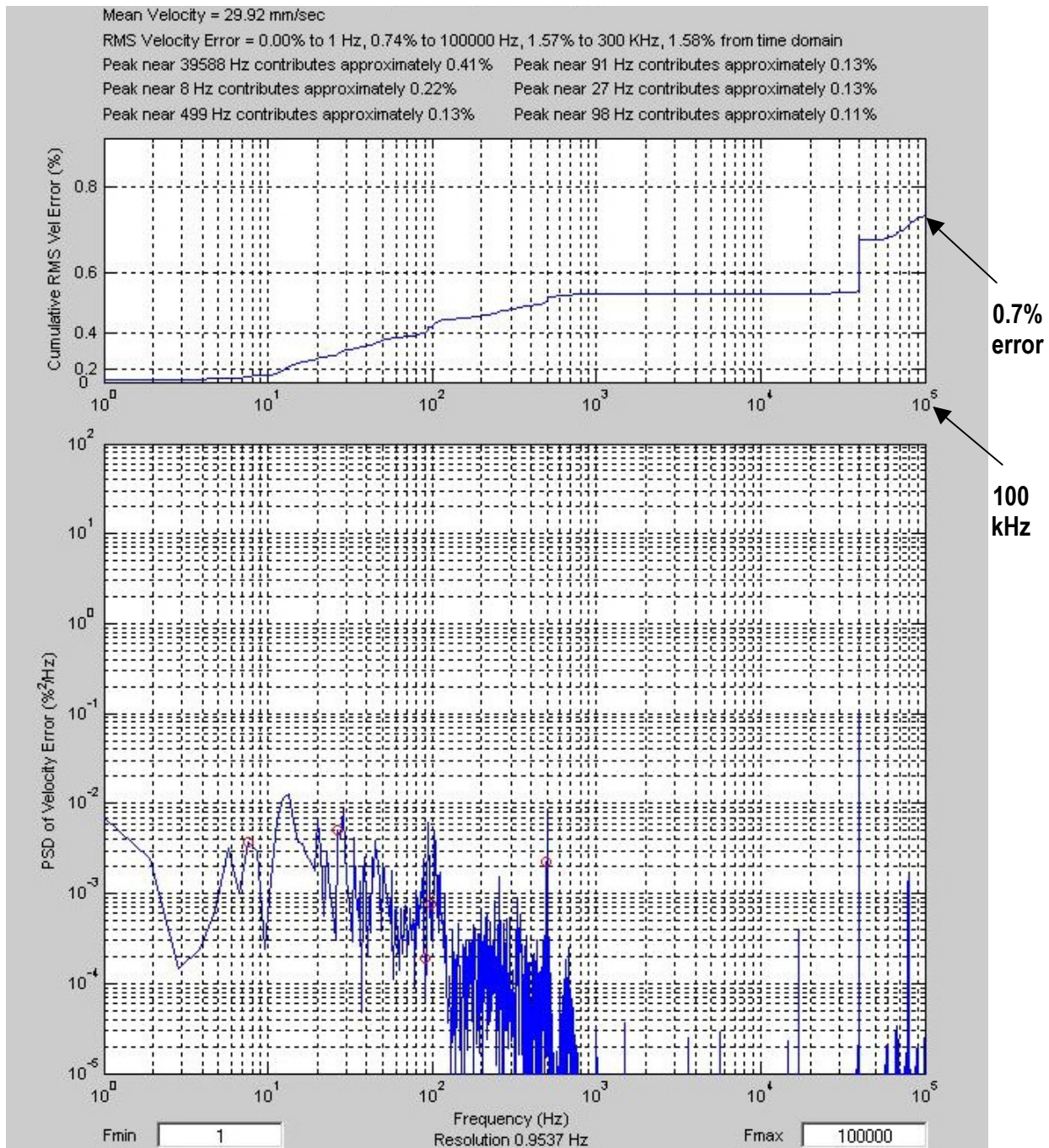


Figure 16. Velocity Error Data for the PAOS Mechanism

Over 500 runs have been conducted using the current prototype, characterizing its performance and robustness. The mechanism is consistently able to produce less than 0.7% cumulative velocity error at frequencies up to 100 kHz. It is anticipated that using the reference laser as feedback will further improve this error by rejecting low frequency disturbances that are within the servo range of the control system.

Future Work

At the time of this writing, a life test of the mechanism had been started. The test is an ambient condition life test in which the mechanism will run continuously for one month, resulting in 300,000 full cycles of the mechanism at the nominal speed of 30 mm/s. This test will characterize wear at the interface between the piezo motor fingers and the ceramic strip, in the Vespel rollers sliding against the steel pins, and the rolling contact between the Vespel rollers and the hard-anodized aluminum sled. The test will also characterize any change in the force required to move the mechanism, positional error along the velocity profile, and velocity error over the life test. A second life test will then be conducted for a two-week period in a vacuum chamber. This test will characterize the mechanism's performance as well as heat dissipation under vacuum conditions.

It is planned that the next design iteration will incorporate a locking device to protect the mechanism during launch vibrations. It will also incorporate all of the optics on a single structure and use the interferometer reference laser as the primary feedback device.

Work to qualify the piezo motor for space flight applications will continue. Further thermal-vacuum testing will be conducted to better characterize the properties of the motor under these conditions, as well as characterize the heat dissipation. Vibration testing will be conducted to better understand how the motors will react to launch load environments. The drive electronics will also be re-designed and qualified for space flight. Once these motors are qualified they can easily be incorporated into a new mechanism design without the need to re-qualify the motor at the piece part level. The motor is a stand-alone component that can be integrated into a system to quickly and cost effectively create a linear or rotary mechanism.

Lessons Learned

In order to reduce the mass as much as possible in the current design, the piezo motor was used to preload the kinematic rail system. While this eliminated the need for a fourth roller and reduced the overall system mass, it also reduced the stiffness of the system. Each of the piezo elements are preloaded against the ceramic strip with independent springs that are soft when compared to the rest of the system. This reduces the natural frequency of the system and, in turn, reduces the margin of stability in the control loop. In future designs an independent roller will be used to preload the rails, and the line of action of the preload force from the piezo fingers will act directly through the center of the dual spherical rollers. This will allow the mechanism to have an adjustable preload independent of the fixed preload in the piezo motor fingers.

The use of the piezo motor to preload the system also precluded testing of the rails and motor individually. The drag force of the rail system alone could not be directly measured due to the necessity of the piezo motor to complete the system and the associated friction holding force. While combining functionality of key components saves packaging space and mass, it makes individual component performance characterization difficult. The addition of independent preload rollers in the next design will slightly increase the mechanisms size but it will provide the ability to better characterize the performance of the rail system at the sub-assembly level and understand its contribution to the overall mechanism performance.

The ability to quickly build prototypes and conduct tests was invaluable for this type of development project. When dealing with such stringent requirements, new technology, and complex systems, there is no substitute for testing the actual hardware. During the course of the prototype development, more than ten mechanisms were built and tested using the interferometer setup. This gave a tremendous amount of insight into the causes of velocity error over a broad frequency range. Inevitably things that are not accounted for in the design will show up in testing, and the sooner the mechanism can be tested, the sooner design iterations can be incorporated into the next hardware design.

Having custom data reduction software to quickly quantify and visually characterize the results of performance testing saved a tremendous amount of time during the actual testing of the mechanisms.

Nearly 1,500 total runs on different mechanisms were conducted over a six month period of time. Having a software tool that collected, analyzed, and displayed data real time made it practical to change one variable at a time in order to clearly understand how that variable affected the mechanism. It also made it easy to collect a number of samples and verify that the results were consistent and not a product of a transient phenomenon.

Early testing revealed a sharp velocity disturbance at an input frequency of 40 kHz, which was quickly dismissed as electrical noise in the data acquisition due to the sinusoidal voltage used to excite the piezo elements. After further testing and unsuccessful attempts to eliminate the error with electrical shielding it was revealed that the disturbance is actually mechanical vibration and not simply electrical noise. This vibration can be filtered mechanically using springs in the cube corner mounts but careful consideration must be given to this input when dealing with mechanisms that are sensitive to disturbances over such a wide frequency range.

Conclusions

A new linear translation mechanism has been developed that will allow the PAOS instrument to offer improved performance and lower mass compared to existing spaceborne spectrometers. The low mass (< 1 kg) of this mechanism is a direct result of the enabling technology represented by the ultrasonic piezo motor. These motors provide a new alternative for linear space mechanisms and offer smooth, precise motion, inherent redundancy, low mass, and simplified integration. The kinematic Vespel rail system provides a solution that is fault tolerant and insensitive to structural misalignments due to thermal distortion or manufacturing tolerances. The design can easily be adapted to provide any stroke length over a wide range of velocities. Initial testing shows consistent velocity error of less than 0.7% in a mechanism that requires no wet lubrication and is small enough to hold in a single hand.

Acknowledgements

We acknowledge funding from the NASA Planetary Instrument Design and Definition Program. Part of this research was performed at the Jet Propulsion Laboratory under contract with NASA. We also acknowledge the extensive assistance provided by Nanomotion Ltd. in the evaluation and implementation of the piezo motors and drives.

References

Karasikov, Dr. Nir (2000). *A Novel Non-Magnetic Miniature Motor for Ultra High Vacuum Applications*, paper for Nanomotion Ltd.

Persky, M.J. *A Review of Spaceborne Infrared Fourier Transform Spectrometers for Remote Sensing*, presented at The American Institute of Physics, October 1995.

Roberts, E.W., et al. *Development of Long-Life, Low-Noise Linear Bearings for Atmospheric Interferometry*, paper presented at the 34th Aerospace Mechanisms Symposium on May 18-20, 1994.

Toon, Dr. G.C., et al (2001). *Planetary Atmosphere Occultation Spectrometer: A Miniature High Resolution Fourier Transform Infrared Spectrometer*, proposal for Jet Propulsion Laboratory.

Burger, F., Eder, J. *High Precision Pointing Device for the LASCO instrument on SOHO*, paper presented at the 6th European Space Mechanisms & Tribology Symposium on October 4-6, 1995.

Pancam Mast Assembly on Mars Rover

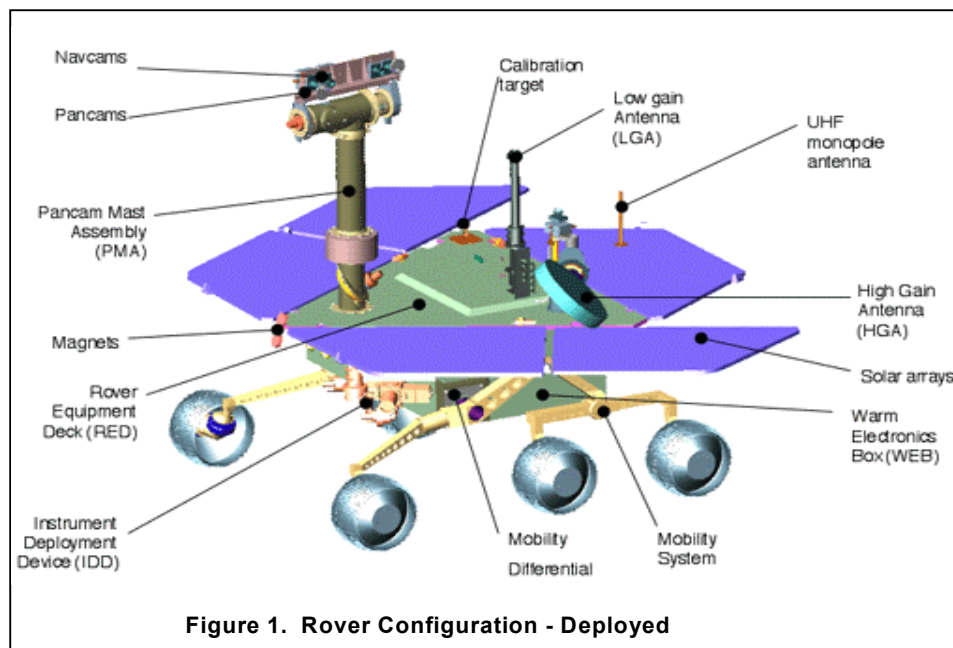
Robert M. Warden*, Mike Cross* and Doug Harvison*

Abstract

The Pancam Mast Assembly (PMA) for the 2003 Mars Rover is a deployable structure that provides an elevated platform for several cameras. The PMA consists of several mechanisms that enable it to raise the cameras as well as point the cameras in all directions. This paper describes the function of the various mechanisms as well as a description of the mechanisms and some test parameters.

Designing these mechanisms to operate on the surface of Mars presented several challenges. Typical spacecraft mechanisms must operate in zero-gravity and high vacuum. These mechanisms needed to be designed to operate in Martian gravity and atmosphere.

Testing conditions were a little easier because the mechanisms are not required to operate in a vacuum. All of the materials are vacuum compatible, but the mechanisms were tested in a dry nitrogen atmosphere at various cold temperatures.



Introduction

The Pancam Mast Assembly is one of the two main mechanical systems that mount on the top of the Rover Equipment Deck (RED); the other being the High Gain Antenna System (Figure 1). The mast lays flat against the RED from launch to landing and is held in place to the RED with a Launch Restraint Mechanism. After the Rover has landed and the Solar Arrays have deployed, the Launch Restraint is released. The Mast Deployment Drive then elevates the mast from horizontal to vertical to give the cameras better visibility. The Azimuth Drive rotates the upper part of the mast left and right while the Camera Bar Drive raises and lowers the cameras. The Mini Thermal Emissivity Spectrometer, or Mini-TES, is located beneath the RED and looks up through the center of the PMA like a periscope. An

* Ball Aerospace & Technologies Corp., Boulder, CO

adjustable mirror at the top of the mast allows the Mini-TES to look up and down independently of the other camera.

PMA Mechanism Overview (Figure 2)

- Launch Restraint holds the mast to the RED and releases on command. Allows for Rover flexibility and thermal expansion.
- Mast Deployment Drive moves mast from the horizontal position to the vertical position. Latches into place when deployed. Contains seals for light and dust.
- Azimuth Drive provides 360 degrees of rotation. Rotates Pancams, Navcams, and Mini-TES mirrors in azimuth.
- Camera-bar Elevation Drive rotates Pancams and Navcams up and down. Hard stop at one end of travel is used to provide pointing reference position.
- Mini-TES Elevation Drive rotates the Mini-TES mirror up and down independently of the camera bar. Also rotates the mirror to point at the internal calibration target. Calibration position closes the aperture to provide dust and stray light protection during calibration. Hard stops provide pointing reference position.

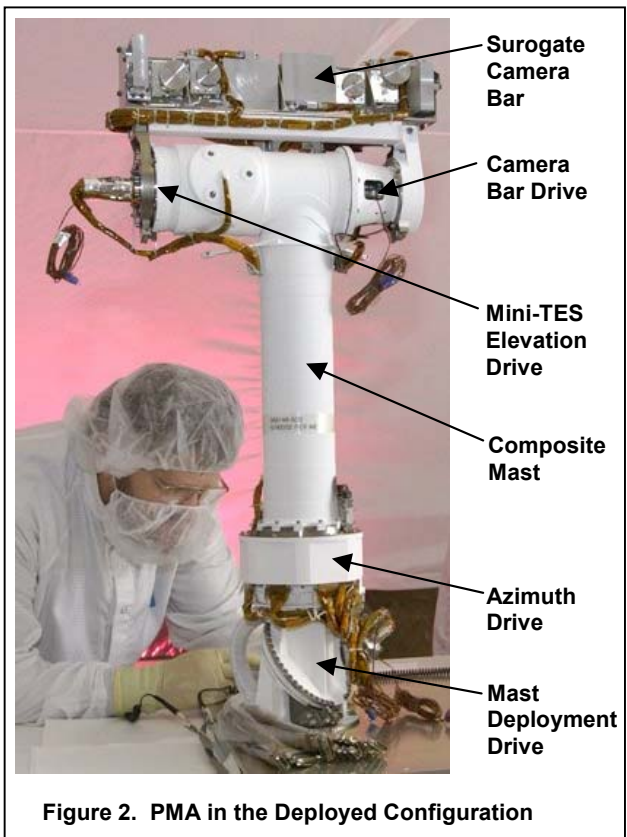


Figure 2. PMA in the Deployed Configuration

Stowed Configuration

In the stowed configuration, the PMA lays against the equipment deck under the parachute canister as shown in Figure 3. The deck is covered with solar cells except for specific areas reserved for attachments. The Mast Deployment Drive supports the mast at the base but the “head” of the mast needed additional support to withstand the launch and landing loads. The launch restraint mechanism secures the mast-head in two places and when combined with the MDD, results in a three point mount. In

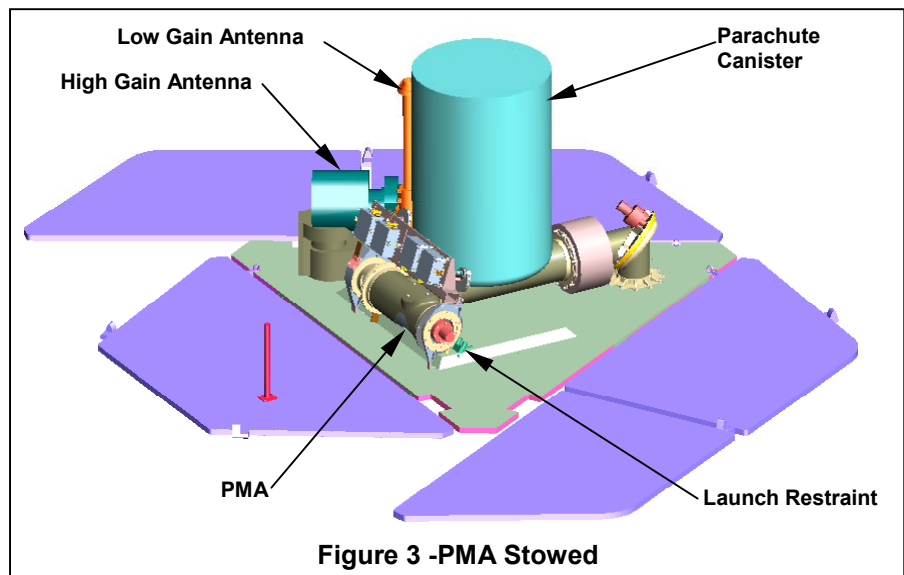


Figure 3 -PMA Stowed

addition, the solar panels fold up against the parachute canister to form a pyramid. Three-dimensional CAD modeling was essential for packaging the PMA in the required envelope. Note that the camera bar assembly is tilted toward the center to avoid contact with the solar panel. This volume is also shared with the High Gain Antenna and Low Gain Antenna. Clearance was required to prevent damage to the fragile solar cells mounted on the inside of the deployable panels during launch and landing.

Launch Restraint Mechanism

The first mechanism to operate is the Launch Restraint System. The PMA must be held down to the Rover deck during launch, flight and landing. After the Rover lands and the solar panels are opened, the launch restraint must release to allow the PMA to deploy. In addition, the mechanism that raises and lower the cameras must also be constrained to prevent damage. The customer directed that redundant, pyrotechnically actuated pin-pullers would be used to engage (or disengage) the launch restraints.

The biggest challenge for launch restraint mechanism was to provide a launch lock that would not over constrain the system or be too complicated. There is significant differential movement due to the difference in thermal expansion between the mast and the Rover deck. Also, the Rover deck is somewhat flexible. The restraint system must allow movement along the axis of the mast yet provide restraint in the other two axes. Another constraint is that the top of the rover is a honeycomb panel assembly covered almost entirely with solar cells. Only a few small areas were allocated to support the PMA in the stowed position.

Basic Requirements:

- Hold PMA to deck
- Constrain PMA rotation to protect MDD gear train
- Constrain Camera Bar rotation to protect Camera Bar Drive gear train
- Use maximum of 3 pin-pullers (only 2 implemented)
- Accommodate thermal distortion of deck
- Allow PMA conical deployment

Mast Restraint

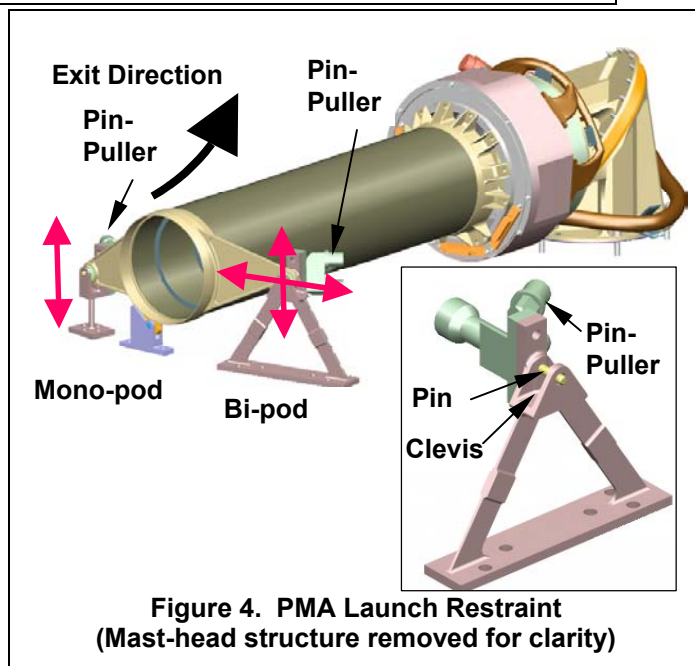
The primary launch restraint function is to secure the mast-head to the Rover deck. This is accomplished by attaching a bracket at the top of the mast that features two "ears" protruding to the side (Figure 4). These ears contain self-aligning journals in the form of spherical bearings. Each spherical bearings fits into a precision clevis or yoke, which are then pinned into place using the above mentioned pin-pullers.

The launch restraint system is designed so that the stowed PMA is not over constrained. This is accomplished by making one of the clevis supports in the form of a bi-pod to take lateral and vertical loads. The other clevis support is a simple mono-pod that only takes vertical loads. In this way, the mast-head is prevented from rotating but allowed to expand as needed. The pin-pullers are located at the top of the clevis supports. When deployment is required, a signal is given to actuate the pin-pullers. The securing pins are thereby pulled out of the spherical bearings and the mast is free to deploy.

Mast Launch Restraint summary:

- The bi-pod mount constrains in vertical and horizontal only
- The mono-pod constrains in vertical axis only
- Together they constrain rotation about the mast axis
- Spherical bearing used for self aligning journal
- Dissimilar metals used for sliding surfaces

Camera Bar Restraint



The second function of the launch restraint is to constrain the camera bar. The camera bar assembly is discussed in more detail later in the paper. For this section, however, it is important to note that the camera bar imparts a significant load to the drive motor during launch and landing. The packaging is very tight as shown in Figure 5. Any appreciable movement of the camera bar while the solar panels are folded up would damage the solar cells.

The customer requested that the quantity of pin-pullers be minimized to help reduce complexity and mass so one of the design goals was to avoid the use of any pin-pullers with the camera bar restraint. The design goal, therefore, was to combine the function of securing the mast to the deck with the function of securing the camera bar drive.

The camera bar features two small protrusions or "tabs"; one on each end as shown in Figure 6. These tabs rotate with the camera bar. The mast-head also features two tabs, but these are fixed to the mast-head. In the stowed position, the rotating tabs on the camera bar contact the fixed tabs on the mast-head. A floating clevis captures each tab pair, thereby preventing the camera bar from rotating with respect to the camera head. Each clevis is mounted on a compliant support so that the tab pairs can move with respect to the Rover deck but are still captured with respect to each other. As the mast deploys, the tab pairs are no longer captured allowing movement of the Camera Bar Drive. Note that after the mast starts to deploy, the camera bar no longer needs to be secured. This design uses the action of lifting the mast off of the Rover desk to release the camera bar.

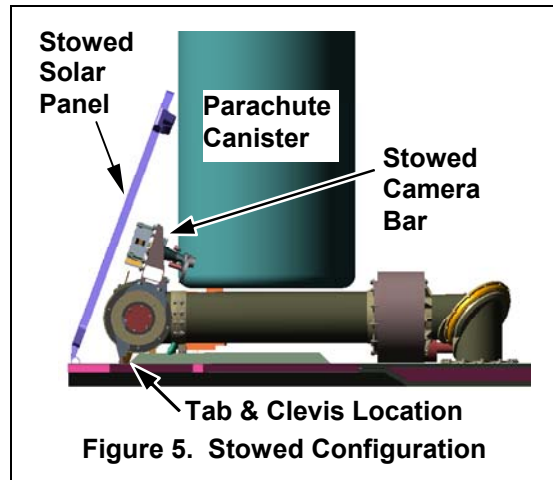


Figure 5. Stowed Configuration

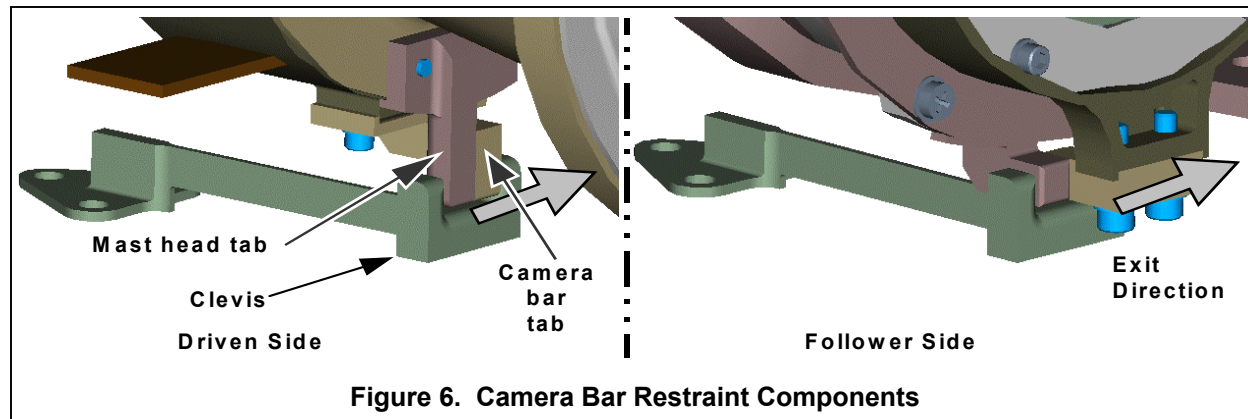


Figure 6. Camera Bar Restraint Components

The clevis surfaces have a slight spherical profile to allow relative rotation and have a slight amount of clearance to avoid binding. As the mast deploys, the tabs pull out of the clevises, which are attached to the deck. The tabs are then free to separate and the camera bar drive then controls the rotation of the camera bar. The materials are carefully chosen and the surfaces are coated to limit the possibility of galling and binding. Mockups of this system were built early in the design to verify the performance. Vibration testing of the final hardware resulted in scuffing of the coated surfaces but no failure of the coatings or galling of the surfaces.

Camera Bar Restraint summary:

- Constrains Camera Bar only in rotation relative to mast-head
- Only engaged in stowed configuration
- Flexible support eliminates over-constrained condition
- Imparts slight friction during deployment

Mast Deployment Drive (MDD)

The second mechanism to operate is the Mast Deployment Drive (MDD). This mechanism drives the mast from horizontal to vertical. The mast is stowed against the Rover Equipment Deck in the horizontal position from launch to landing. On command, the MDD moves the mast into the vertical position where it is latched in place. The MDD also handles the large bundle of wires that are required to operate the cameras and other mechanisms.

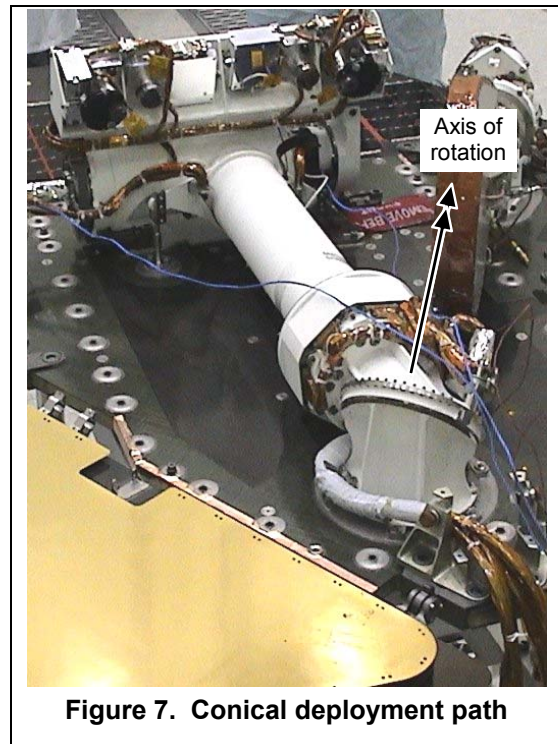
Requirement Summary: <ul style="list-style-type: none">• Drive mast from horizontal to vertical• Provide optical path when deployed• High stiffness• Control & support electrical cabling• “Reasonable” deployment time• Keep dust out	Interfaces: <ul style="list-style-type: none">• Base bolts to RED• 5 Electrical cables & connectors to RED• Top bolts to Azimuth Drive• 4 Electrical cables & to Az Drive• 1 Electrical cable to motors
--	--

Early in the program, a need was established for a stiffer deployment mechanism for the PMA. The first part of the design effort was to step back and look at how large, thin-walled, tubular structures can be bent. Elastic structures such as a garden hose are inherently flexible but need a secondary structure for stiffness. A bellows structure is very stiff in torsion but flexible in all other directions so it would also need a secondary support structure. The desire was to keep the design simple and to combine the structural function with the optical requirements.

The solution was found on top of a water heater. The flue pipe that carries away the hot gasses is made up of several angled couplings that enable the pipe to be bent as needed while maintaining structural integrity and internal clearance. This was the approach taken for the new deployment drive.

Unlike the flue pipe, however, the MDD uses only a single angled coupling in the form of a bearing mounted at an angle. The mast travels from horizontal to vertical in a conical path (Figure 7). The inclined bearing design is a simple and effective way to rotate the mast and keep the Martian dust out while maintaining structural integrity. Although the two main housings are fairly complicated, the overall design is quite simple and robust. There are very few parts and the mechanism is easy to assemble and test.

The single large diameter, small cross section bearing is an X-type that is internally preloaded. The large diameter of the bearing results in good strength and stiffness while the internal preload eliminates the need for a second bearing. This type of bearing does have limited life, but in this application the required operational cycles were well within the life of the bearing.



This conical deployment path also proved to have an advantage in allowing the mast-head to easily exit the launch restraint. The mast-head leaves the deck at about a 40-degree angle so that the vertical vector is about the same as the horizontal vector. The angle of the inclined bearing was made as large as possible to maximize the vertical vector.

MDD Components

Figure 8 show the five main structural components in the Mast Deployment Drive. The Inner Housing is bolted to the Rover Equipment Deck and remains fixed. The inner ring of the bearing is clamped to the Inner Housing with the Inner Clamp. The outer ring of the bearing is clamped to the outer housing with the outer clamp. The Outer Housing and Clamp are thus free to rotate on the bearing. The inside of the fixed inner clamp features a large diameter internal tooth ring gear. The gear-motor is attached to the Outer

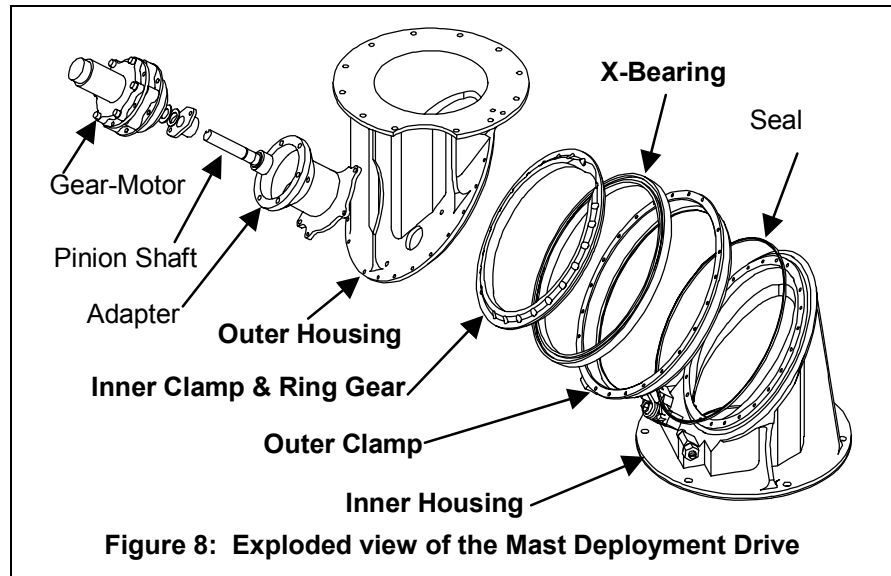
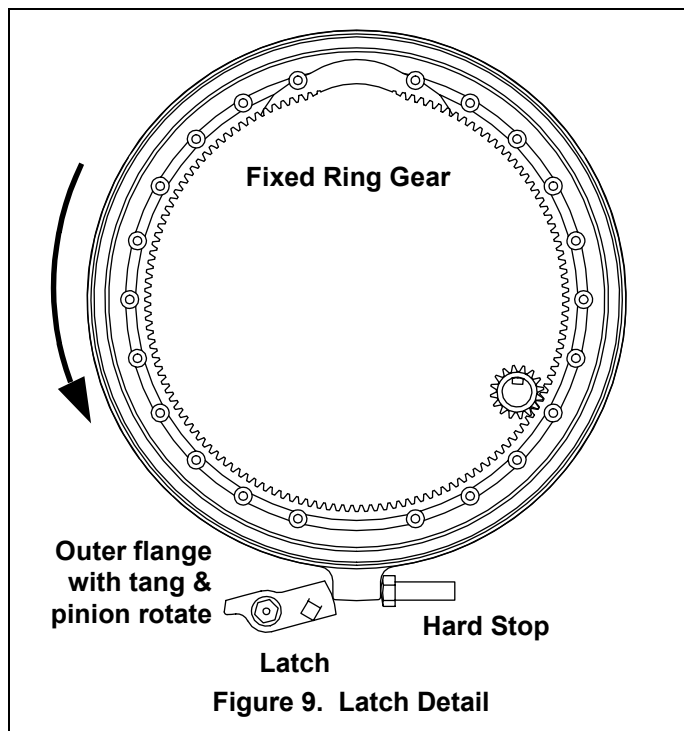


Figure 8: Exploded view of the Mast Deployment Drive

Housing by means of an adapter. The Pinion Shaft coming off the Gear-motor engages the ring gear to drive the outer housing. Note that the gear-motor rotates with the outer housing. This was done so that the gear-motors for the MDD and the Azimuth Drive (see next section) could share the same wire path. The Outer Clamp features a protrusion that engages a hard stop at full deployment.

Design Trade

One of the first design trades to be made with this mechanism was whether or not to have a separate latch to hold the mast in place in the deployed position. The detent in the motor through the gear train was enough to hold the mast in place under most conditions. The benefit of not having a latch is that the mast can be remotely deployed and retracted as often as needed. The benefit of having a latch is that the gear-motor is not in the load path so the gear teeth and bearings do not need to be as strong. The disadvantage of having a latch is that once the latch falls into place, it must be manually unlatched in order to stow the mast. The mass for the stronger bearings and gears was about the same as for the latch components. It was finally decided that the ability to remotely stow the mast was not as important as the guarantee that the mast would not creep out of alignment so the latch was added to the mechanism.



The hard stop was made adjustable in order to adjust the final deployed position of the mast. Materials were chosen so as not to have similar metals in contact with each other. The outer flange and tang are made of hardened Titanium. The latch and hard stop are made of hardened Nitronic 60. Published data shows that Titanium against Nitronic has very good resistance to galling.

MDD Test Description

The fundamental requirement for the Mast Deployment Drive is to move the mast from the horizontal position to vertical on Mars. A safety factor of two was imposed upon this requirement to assure adequate margin over uncertainties. In addition, it was desired to be able to deploy the mast on Earth for testing without counter-balances or other support structure. And if deployment on Earth was to be feasible, a factor of 20% was determined to be needed.

Designing a variable mass to simulate these different conditions on the Pancam Mast Assembly for testing was considered for a while but found to be very difficult to implement. Because the MDD primarily reacts torque, and torque is simply force times distance, it was decided to keep the force the same and change the distance.

The design of the variable load test fixture is shown in Figure 10. The main structure consists of a thin-walled Aluminum tube with flanges at each end. The threaded rod that runs the full length of the fixture is supported at each end by Vespel bushings. The sliding mass has a threaded feature in the middle to engage the rod and a slot on the outside to prevent it from rotating. Rotation of the rod causes the weight to translate, thus changing the torque on the MDD. The load test fixture was calibrated using a torque wrench to verify the torque at the various weight positions.

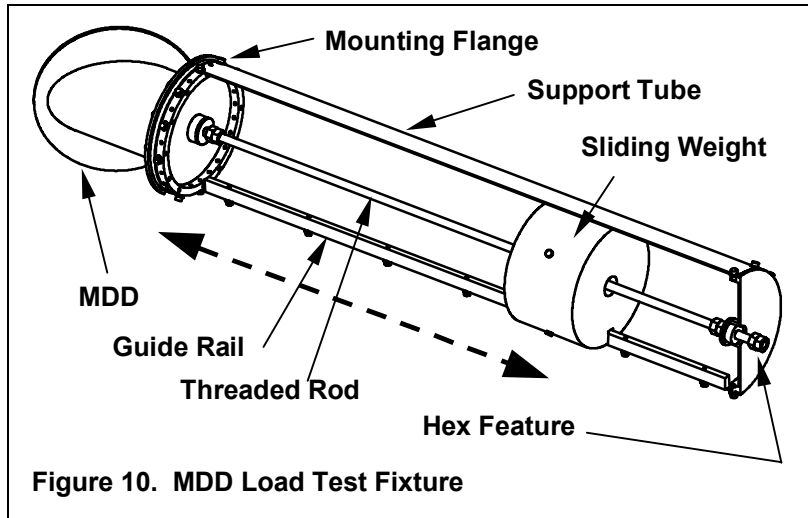


Figure 10. MDD Load Test Fixture

For the thermal functional test, the MDD was first bolted to a surrogate Rover deck. The load test fixture was then bolted to the MDD. The MDD was then deployed and stowed several times to obtain ambient deployment data. The assembly was then placed inside a large thermal chamber. A socket wrench was inserted through a small opening opposite the drive nut to rotate the shaft as needed. The weight and torque change due to the rod rotation is shown in the following table:

Gravity Condition	Weight of Mast (Deployed section)	Torque on MDD 0.46 M (18.1 in.)	Turns
1 X Mars	33 N (7.4 lb)	15 N-m (134 in-lb)	0
2 X Mars	66 N (14.8 lb)	30 N-m (268 in-lb)	163
1 X Earth	87 N (19.6 lb)	40 N-m (355 in-lb)	271
1.2 X Earth	104 N (23.5 lb)	48 N-m (426 in-lb)	357

Mast Deployment Summary

- Cable is well managed, not subject to extreme bending
- Big central hole for light path
- Meets Envelope and Interface Requirements
- Time to Deploy at -70 C is 2.5 Minutes
- Hard Stops can be adjusted to .012 mm.
- Position against stop repeatable to 0.0025 mm
- Tested under 1 X Mars, 2 X Mars, 1 X Earth, 1.2 X Earth
- Tested at warm, ambient and cold conditions
- Works well with launch restraint mechanisms

Azimuth Drive

The third mechanism is the Azimuth Drive, which rotates the upper part of the PMA. This drive allows the Rover to look left and right. The optical path for the Mini-TES instrument must pass down the middle of the drive. The principle requirements are as follows:

Property	Requirement
Angular range	+/- 180 degree
Angular accuracy	+/- 1 mrad.
Angular speed	0.5 revolutions per minute
Optical clearance	100 mm bore
Electrical interface	Upper flange: 4 x 37 pin connectors Lower flange: 4 x 37 pin connectors
Cable management	+/- 180 degree
Mechanical Interface	Upper flange to Mast Lower flange to MDD

The Azimuth drive was originally designed by American Technology Consortium (ATC) for the APEX program. ATC was then acquired by Starsys Research Corp. who redesigned the drive to reduce the outer diameter and add a fourth cable path.

The Azimuth drive is mounted to the top of the MDD to form the Lower Drive Assembly (Figure 11). By mounting these two drives at the base of the PMA, a significant portion of the mass is located near the RED. This has the effect of lowering the overall mass center of the assembly.

These two drives also take advantage of commonality in the areas of rotating shaft seals, large diameter bearings, lubrication, motor shielding and motor electrical connections. Internal and external surface coatings are also the same.

Note that the two motors are located in the same proximity. For both the MDD and the Azimuth drive, there was a choice to mount the motor on the fixed part of the mechanism or the moving part. By mounting the motor on the moving part of the MDD and the fixed part of the Azimuth Drive, the two motors could be mounted adjacent to each other. This, in turn, facilitated the routing for the motor electrical cables.

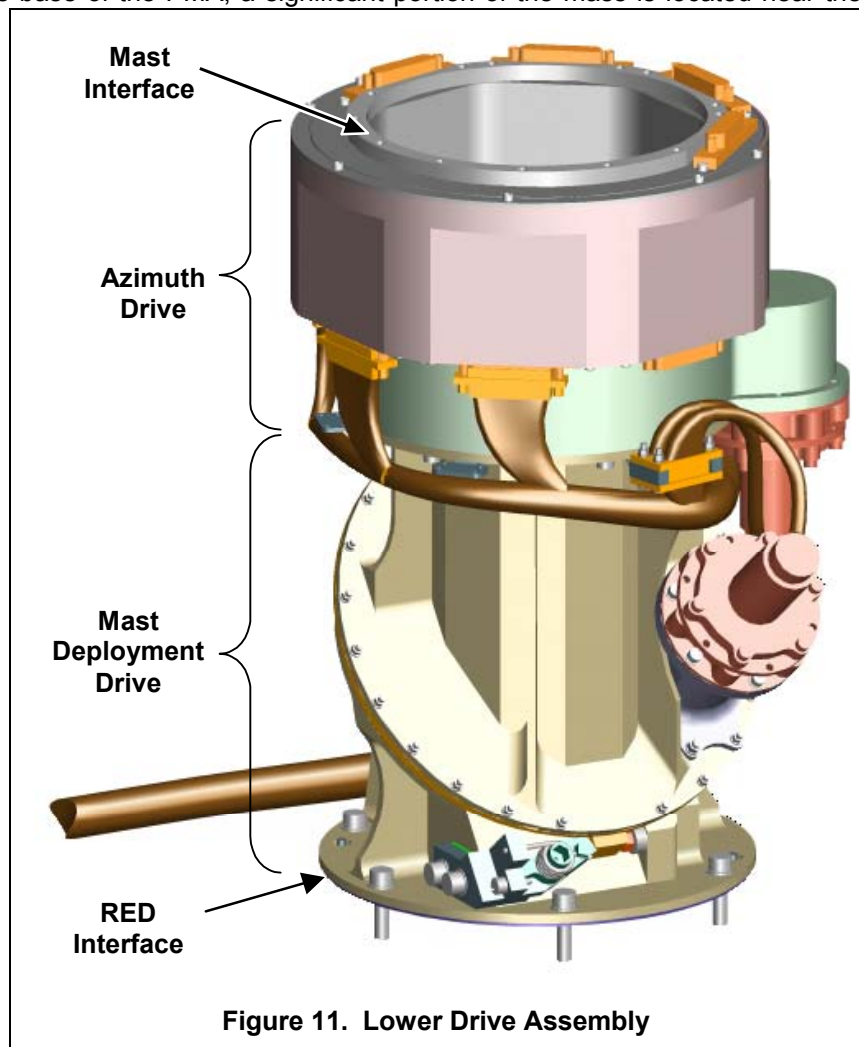


Figure 11. Lower Drive Assembly

Camera Bar Drive

The fourth mechanism is the Camera Bar Drive (Figures 12 & 13). A pair of panoramic wide-angle cameras and a pair of navigational small angle cameras are mounted on a common bar at the top of the mast. The camera bar drive rotates the camera bar allowing the cameras to look up and down.

Basic Requirements:

- Provide support of the Pancam and Navcam cameras
- Move the cameras about the elevation axis at 2 degrees/sec with a pointing error of 0.1 degrees
- Carry power and signals across the rotating joint
- Accommodate relative thermal distortions between mast and camera bar
- Allow separate integration and alignment of cameras as a sub assembly

The four cameras are mounted to a rigid angle bracket that maintains precise alignment between each camera. The assembly of cameras and angle bracket was integrated and qualified separately from the mechanism and the two were integrated during final integration of the rover. The camera bar mechanism consists of a rigid titanium box section tube that is supported at each end.

One end of the tube is supported by a large diameter thin section ball bearing and the other end is mounted to a bracket that is supported by the output shaft of a gear-motor. This gear-motor bracket serves as the housing for spiral wound flex cable assembly that carries power and signal across the rotating joint. The bracket design also incorporates a diaphragm that provides additional compliance within the assembly.

The motor is a custom DC brush motor with a custom hybrid planetary-harmonic gear-head with 8118:1 gear ratio. A magnetic detent mechanism is integrated between the motor and gear-head to resist back driving that may be caused by the cantilevered mass of the cameras and the jostling that occurs as the rover moves. The magnetic detent consists of a very small multi poled magnetic rotor inside a magnetic stator housing. To initiate significant rotation the magnetic detent must be overcome, but then it provides additional torque as you get over the "hump". This repeats every few degrees as the shaft is rotated. The detent increases the starting torque required of the motor but does not affect the operating torque margin since this torque ripple averages out.

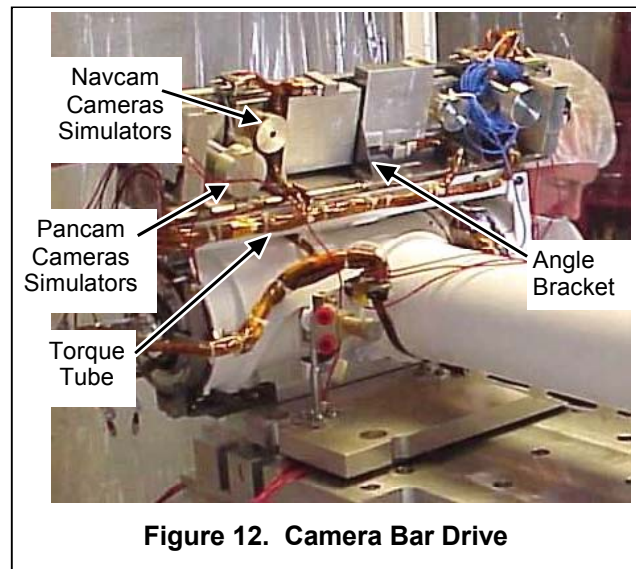


Figure 12. Camera Bar Drive

The gear-motor assembly includes a relative position encoder. Before each use, the mechanism must be rotated against the hard stop to zero the encoder. The gear train, structures, and hard stops must be capable of tolerating full motor stall torque many times. The same hard stops that are used for the launch lock are also used for this application.

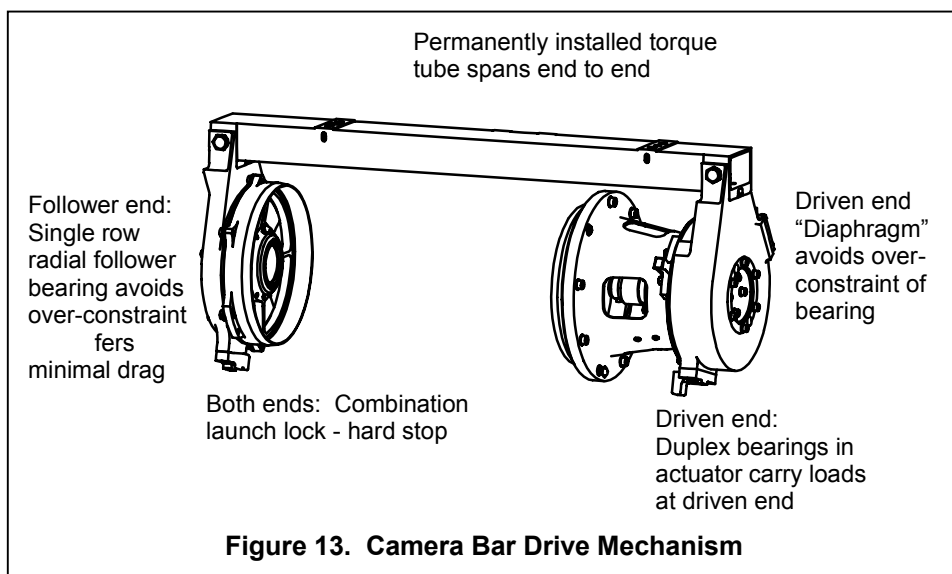
The thin section bearing that supports one end of the camera bar has very large internal clearance between balls and races. This slop in the bearing is required to accommodate the different thermal expansions of the titanium camera bar and the graphite mast structure. Since the cameras only image when the rover is stationary and the camera bar is not moving, the loose bearing does not lead to blurry images. Concern over damage to the bearing from rattling was alleviated by analysis that showed that motion of less than .010" did not allow enough velocity to cause damage.

Twist of the camera bar assembly due to gravity sag or due to follower bearing drag was a concern. The sag due to gravity was easily calculated and mitigated, but the drag of the bearing was unknown and subject to many variables. Contamination by Mars dust blown into the bearing after deployment or kicked

up during landing could significantly increase the drag. Due to the configuration of the mechanism, if the follower bearing were to drag and twist the bar, additional torsion would be imparted to the bearing potentially causing even more drag and a lockup situation could be created.

To exclude debris from the follower bearing, a careful seal design was implemented. Initially labyrinth-type convolutions were envisioned to exclude debris and impart the minimum amount of drag to the motor. Following the critical design review this design was modified to focus more on debris exclusion and less on motor drag. The seals are risky because of the -70°C operating temperatures and the large amount of play in

the bearing. A plastic seal with enough contact pressure to seal the bearing in one position may provide too much contact force when very cold and in a different relative position of inner to outer races. The solution was to use a thin metal shield with a relatively long cantilever. The stiffness of the metal changes much less with temperature and the long cantilever provided adequate deflection. On the inner side of the bearing a more convoluted labyrinth seal was selected which added no additional drag.



Mini-TES Drive

The fifth mechanism is the Mini-TES Mirror Rotation Drive. The Mini-TES is an Infrared spectrometer that is located below the Rover deck. The PMA serves as a periscope to enable the Mini-TES to look around from a higher vantage point. The Mini-TES mechanism rotates a mirror so that the instrument can look up and down and provides an enclosed calibration target. The Azimuth drive described earlier provides the left/right motion.

Basic Requirements:

- Support the mirror and provide an elevation axis of rotation
- Move the mirror at 5.7 degrees/sec with a pointing error of 1 mrad
- Provide an enclosed calibration target of known temperature
- Incorporate a rotating baffle that will exclude light and limit debris when closed

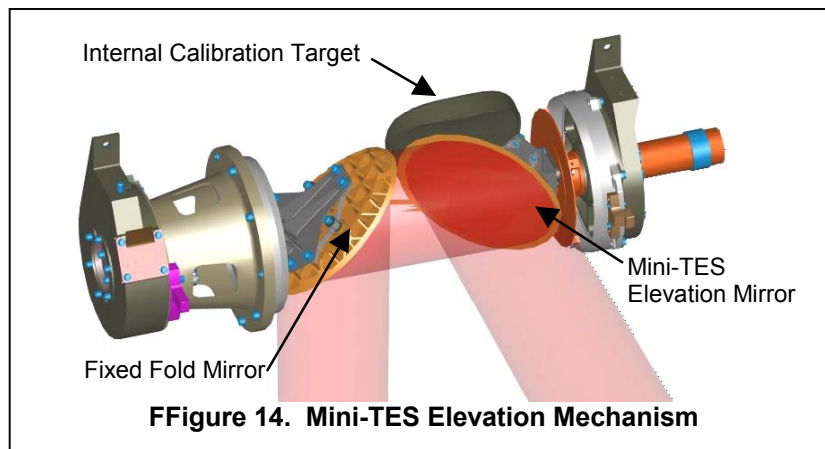
There are two 45 degree angled mirrors inside the head of the PMA. One mirror is fixed and the Mini-TES rotation drive controls the other. Light enters the PMA through an opening in the top "T" section, reflects off the moveable mirror and travels to the fixed mirror and then travels down the mast to the instrument as shown in Figure 14. A custom DC motor with custom hybrid planetary – harmonic gear-head is located in the top of the PMA and drives the first angled mirror about the horizontal or elevation axis. This elevation axis together with the mast azimuth drive provides the capability to point the Mini-TES field of view.

To limit the complexity and weight of the system the mirror is mounted directly on the gear-motor with no additional support. The mirror is cantilevered off the motor shaft and does not include a launch lock element or brake mechanism. There was concern that the launch vibration environment might cause the cantilevered mirror to rotate even though it is rotationally balanced. Deflection of the cantilevered mass under load effectively unbalances the system. In a rich vibration environment this configuration could

rotate. The issue was addressed by implementing dynamic braking in which the motor windings are shorted so that the motor acts as a brake. Dynamic braking is turned off during operation.

The bearings on the output shaft of the gear-motor were sized to support the mirror and support structure weight so that no additional support was required.

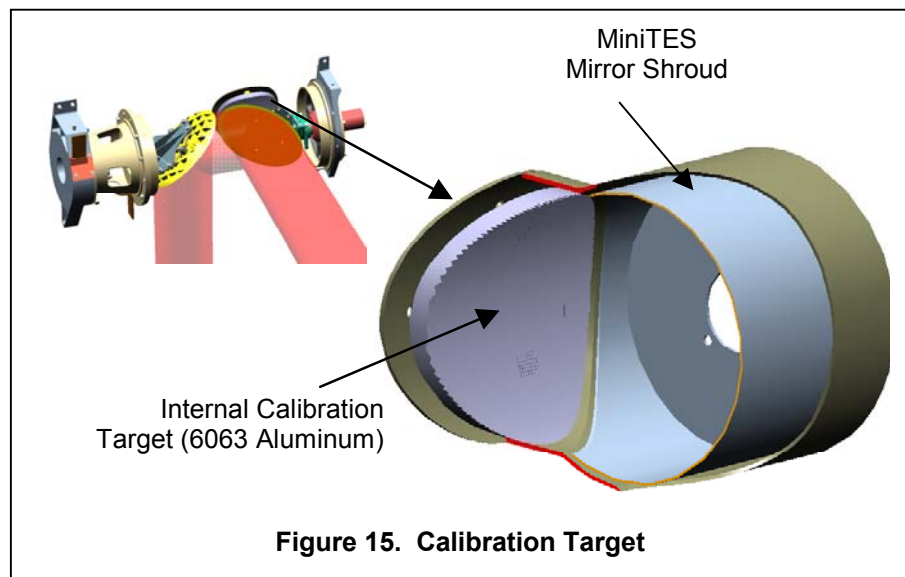
System level testing of pointing to meet the 1 mrad (0.057 degree) requirement was carried out at a number of specific pointing angles. The largest pointing error in tests prior to vibration was 0.035 degree, and after vibration of 0.046 degree.



Subsequent testing revealed a potential additional line of sight error of 0.03 degree when the mast assembly was subjected to lateral loads, however this error was found to be a single time error in the azimuth bearing immediately after the load was applied. Once the azimuth bearing was run through at least 90 degrees of motion, the alignment returned to its previous state.

and periodically during the mission, the instrument is required to observe a calibration target of known temperature and emissivity mounted in front of all mirrors. To accomplish this, the elevation mirror was capable of rotating completely around to point at the inside of the back of the mast where the calibration target was mounted in a recessed pocket. This target was constructed to have a high emissivity surface by machining small grooves across its surface and then applying high emissivity black paint. The

temperature of the calibration target was measured with redundant sensors potted in a blind hole in the back of the target. When the elevation mirror is rotated completely around to view the target, the Mirror Shroud effectively seals the front opening to exclude ambient light. The shroud, shown in Figure 15, is a thin graphite structure mounted so that it rotates with the mirror. It prevents stray light from entering the periscope and allows the instrument to be closed up somewhat when not in use to limit



contamination. The contamination concern is significant in the Martian environment. Martian dust is very fine and is easily carried up to the mirror level by the Martian wind. The air bags that surround the rover during landing are separate and do not form a sealed envelope around the rover. During landing, dust that is kicked up by the impact and subsequent 5 minutes of bouncing and rolling across the surface can easily pass between the air bags and affect the rover.

Tribology

There are four areas of tribology for the PMA mechanisms: bearings, gears, hard-stops, pin-pullers. The mechanisms must all operate under the same conditions and therefore have similar operational requirements. The most significant requirement is the lower operating temperature of -70°C. In addition, the mechanisms must function throughout ground testing under various temperatures, survive the hard vacuum during the trip to Mars and then function in the dusty Martian atmosphere. The mechanisms are mostly slow moving and the mission life is fairly short.

Several lubricants were considered for use on the PMA mechanisms. Silicone lubricants eventually break down and become abrasive. Silicone contamination on optical components is considered a major risk. Perfluoropolyether (PFPE) lubricants such as Brayco 815Z oil and Braycote 601 grease also polymerize, but generally outperform silicone lubricants. The lower operating temperature limit is -80°C. Dry film lubricants such as those based on Molybdenum Disulfide (MoS₂) or thin metal films can operate well at temperatures near 0 Kelvin. However, this type of lubricant has a lower load capability than wet lubricants. It is also a less robust lubricant because its life is compromised by humidity. Hybrid bearings such as those with Silicon Nitride balls in metal races can sometimes operate with little or no lubricant if the contact stress is very low. This was not feasible for the PMA mechanisms because the contact stress was too large due to the mass of the payloads and the Martian gravity.

PFPE lubrication was selected for use on all ball bearings and gears in the PMA mechanisms. Molybdenum Disulfide was added to the PFPE lubricant for sliding components such as the gears and the 4-Point contact bearing discussed in the Mast Deployment Drive section. Dry film lube in the form of Molybdenum Disulfide was used for the launch lock mechanism in which the pin-pullers have sliding pins within spherical bearing bores. No lubrication was used on the hard stops. Material combinations with anti-galling properties were carefully selected for both the pin-puller interface and the hard stops.

Testing

Testing was critical on the program. Even with the tight schedule, an extensive test program was established. The philosophy behind the test program was that since the design phase was short, testing was even more important. Working jointly with JPL, a comprehensive test program was put into place starting with testing of the gear-motor actuator at the subcontractor (Figure 16). The actuators for each mechanism were exposed to qualification levels for vibration and speed torque curves were generated over the operating temperature range. After delivery, the actuators were integrated into their respective mechanisms. Safe to mate testing was performed to ensure the mechanisms were wired correctly. Thermal tests were then performed to characterize the mechanisms as an assembly.

Three Pancam Mast Assemblies were built and tested. The first unit was the Engineering Development Unit (EDU) followed by the two flight units. All three were fabricated to the same specifications. One of the units was designated the EDU and additional testing including life cycle testing was performed on it. The EDU could be refurbished to flight standards, if needed.

Figure 16. Program test flow

Actuator Testing

- Integrate Actuator
- Safe-to-mate verification
- Actuator Run-in
- Vibration testing
- Drive characterization (speed/torque at temp)

Mechanism Testing

- Integrate Actuator to mechanism (Establish current limits)
- Safe-to-mate verification
- Drive run-in
- Drive characterization at temperature
- Pointing accuracy at temperature

System Testing

- System integration
- Continuity & isolation check
- Optical alignment
- Ambient functional test
- Vibration tests
- Pin-puller test
- Functional test
- Load testing
- Thermal testing
- Ambient functional

In order to facilitate the compressed test schedule, four separate test racks were built for the program. This allowed multiple mechanisms to be under test at one time. The test systems were configured to allow the use with any on the PMA mechanisms. These test systems had integrated commercial motor controllers, power supplies and a PC loaded with a specialized LabView program. The LabView program allowed many parameters to be controlled and also record all the mechanism/test parameters. Specialized thermal chambers were built that operated on liquid nitrogen to eliminate scheduling issues with the company's thermal chambers. Electronic controllers were used to maintain the specified temperatures. The mechanisms were loaded using weights and pulleys as shown in Figure 17. This allowed incremental loading of the mechanism to characterize the performance.

Once the mechanism level testing was completed and the PMA was integrated, the assembly was optically aligned and ambient functional tests performed. The PMA was then exposed to system required vibration levels. Testing of the pyro pin-pullers were also performed while on the shaker table. This facilitated instrumentation of the unit with small accelerometers to measure the shock levels.

In the stowed configuration, the PMA was subjected to 3-axis sine sweeps, random vibration and a quasi-static sine pulse. In addition, All, the units were subjected to a pyro-shock test from the pin-pullers. In the deployed configuration, the PMA was subjected to 2-axis sin sweeps and a quasi-static sine pulse.

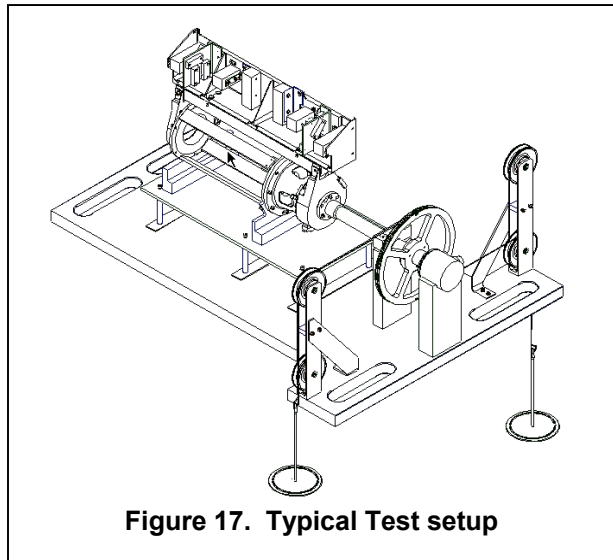


Figure 17. Typical Test setup

Next, the PMA was mounted on a thermal fixture and installed in a thermal vacuum chamber. A 10^{-5} torr vacuum was pulled on the chamber and a 3-hour bake-out at 110°C was performed to remove any moisture in the hardware. The chamber was back-filled with dry nitrogen to a pressure of 10 torr before proceeding with the remainder of the thermal tests. This pressure of nitrogen is thermally equivalent to the CO_2 atmosphere on Mars. The thermal testing profile exposed the hardware to the non-operational temperature limits before deploying the mast at the low operational temperature extreme.

Functional testing was performed at several different temperature plateaus as the temperature was cycled between the operating limits. At the end of the thermal tests, a 50-hour planetary protection bake-out was performed. Motor revolutions were recorded anytime the mechanisms were operated.

One of the challenges in the test program was the reduction of the test data. In most cases, the data was collected at a 10-Hz rate with tests lasting 10 to 20 hours for mechanism level testing, so the amount of data collected was substantial. Many different MATLAB scripts were developed to automate the data reduction. These scripts enabled engineers to quickly and accurately locate critical parameters within the large data files as well as to facilitate statistical analyses.

Lessons Learned

Communication and cooperation is critical between the contractor and the customer. Many unexpected issues were encountered over the duration of the program, which required both sides to understand the issues and impacts to the hardware. Both Ball and JPL have a deep commitment to get the job done right, so issues were resolved relatively quickly in order to keep the program on schedule.

Requirements creep in a program is costly, both in dollars and schedule. Many small changes add up to a large impact.

Define all interfaces early. Undefined requirements always need to be specified at some time and this can lead to changes late in the program.

Proven technologies sometimes aren't! Technology from a prior program cannot be assumed to transfer directly over to another program. The PMA program was initially envisioned as a rebuild of the Athena program hardware with some changes to meet the new requirements. By the end of the program, virtually every drawing was changed.

Testing is sometimes as complicated as the design and assembly. Good definition of the test requirements are important to delivering a qualified product in a timely manner. The PMA test program increased in scope over the length of the program to include unforeseen tasks. The finished assembly performed very well and was characterized to the level that JPL required.

Conclusion

The three qualified Pancam Mast Assemblies were delivered to JPL in September and October 2002. JPL then integrated the PMA on the rover and performed extensive environmental testing before delivery to Cape Canaveral in Florida. The Rovers were integrated on a Delta rocket and launched on June 16th, 2003 and June 30th, 2003. The rovers are scheduled to land on Mars in January 2004.

Recognition

The authors would like to thank all the many technicians, machinists, designers, engineers and managers at Ball for their commitment to developing these state of the art mechanisms. Also all the great folks at Starsys for the gear-motor actuators and Azimuth drive. And especially the entire Rover Team at JPL.

This work was performed under a contract with Jet Propulsion Laboratory, California Institute of Technology, for the National Aeronautics and Space Administration. Reference herein to any specific commercial product, process or service by trade name, trademark, manufacturer, or otherwise does not constitute or imply its endorsement by the United States Government or the Jet Propulsion Laboratory.

References

1. Athena Mars Exploration Rover home page, Cornell University site
<http://athena.cornell.edu/>
2. Mars Exploration Rover Mission home page, Jet Propulsion Laboratory site
<http://Marsrovers.jpl.nasa.gov/home/index.html>
3. Mars Exploration Rovers, Ball Aerospace site
<http://www.ball.com/aerospace/mer.html>

Rock Abrasion Tool

Thomas M. Myrick*, Kiel Davis* and Jack Wilson*

Abstract

The Rock Abrasion Tool (RAT) is designed to expose the interior of Martian rocks for identification and analysis. The RAT, contained within a cylinder 128-mm long and 85-mm in diameter, has a mass of 687 grams. Using three small DC brushed motors, the RAT grinds a 5-mm deep, 45-mm diameter hole into a targeted rock. During grinding, the grinding wheel, shaped as a paddle with a synthetic diamond-impregnated resin, engages a target rock when the Z-axis is extended. Unrealized during testing, under Mars conditions the grinding wheel wear rate decreases five fold when compared to operation under Earth conditions. In total, four Rock Abrasion Tools were manufactured, two flight units, and two engineering test units. After delivering the flight units, the motor current measured by the RAT's electronic interface did not provide a true reading. Follow-on testing permitted correlating the erroneous data with proper data. The flight units were installed on two separate spacecrafts for delivery to Mars in 2004.

Introduction

The Rock Abrasion Tool (RAT) is a critical subsystem of the Athena science payload. Designed to mimic the effect of a geologist's hammer, the RAT is used to expose a rock's interior for identification and analysis. Martian rocks cannot be thoroughly examined from the outside because of dust and oxidation. Consequently, from a surface view, most Martian rocks appear visually similar.

To effectively grind rocks on Mars, several key characteristics are required, primarily a desirable cutting material, enough power and force reaction while working, and knowledge of the target material. The first two requirements, cutting material and power and force can be researched and tested; however, information pertaining to the Martian rock composition was illusive prior to the successful use of the RAT. During the design phase, the behavior of Martian rocks with regards to cutting or grinding was not known and had to be estimated leading to complications in deriving our force and torque margins. Throughout the iterative RAT design process various discoveries provided critical knowledge on the development of drilling and grinding units for use on non-Earth planetary bodies. Particularly, important findings were made with regards to the grinding wheel development, the diamond abrasive material.

RAT Overview

The RAT is designed to grind a 5-mm deep and 45-mm diameter hole into rocks so that science instruments can view the rock's interior. The grinding depth is selectable within the range of the RAT's Z-axis and the topography of the rock surface. The typical command depth is 5 mm. A small rotating brush (Figure 3, label 7) can be used to clean a rock's surface without grinding. Through this method, a rock can be studied with a suite of instruments before and after the surface has been swept clean or grinded.

The RAT (Figure 3), 128-mm long, is contained within a circle 85-mm in diameter, and has a mass of 685 g. It is made primarily from a low density, high modulus alloy of aluminum and beryllium called Albemet, which has a coefficient of thermal expansion similar to steel. Other structural materials include aluminum (7075 and 6061), steel (Vascomax C-250, 4140, 302, 303, 440C, A286, Nitronic 60) and titanium (6AL4V), Vespel, Nickel and 18-karat yellow gold. All of the bearings and gears are lubricated with a grease plate application of Braycote 600 EF micronic and are sealed with Teflon V seals to prevent dust from entering the mechanism. The RAT, using three small DC brushed motors with magnetic encoders, consumes between 8 and 11 watts for a typical three-hour grinding session.

* Honeybee Robotics, New York, NY

The RAT is a stand-alone device in that it does not require any input or movement of the rover's IDD (Instrument Deployment Device) or "arm" once placed onto a rock's surface. The IDD must preload the RAT against the rock within a range of 10 to 100 N. It is desirable for the preload to be at least 50 N for stability. The device's three motors each serve a distinct function and operate in different modes. The RAT grinds a hole in the rock by rotating the grinding wheel (Figure 3, label 2) at approximately 3000 RPM whose center is offset from the center of the RAT by 11.11 mm. The grinding wheel is 23.37 mm in diameter, 6.35-mm wide, and looks like a "paddle wheel" but is referred to as a grinding "wheel". Mounted only along the outer region is a diamond-impregnated resin. The grinding wheel also revolves about the center of the RAT at a very slow speed of 0 - 1 RPM under closed loop control. The combination of high-speed rotate and revolve creates a circular grinding area 45 mm in diameter. The lower half of the RAT housing the grinding wheel is subsequently advanced into the rock in small incremental steps of 0.05 mm per revolution until the desired grinding depth is achieved.

Motors

The grind motor rotates the two shafts at the bottom of the unit where the grinding wheel and the rotate brush, used to remove cuttings from the excavated hole, are attached. These shafts are equally displaced from the center of the housing and centerline of the RAT by 11.11 mm and are therefore separated from each other by a distance of 22.22 mm. This motor operates at a set voltage parameter, typically 27 V, which will rotate the grinding wheel and rotate brush at approximately 3000 RPM. Simultaneously the current provided to the motor is monitored and used as feedback for the grind motor as well as the revolve motor. During mid-day activities, it is typically expected that the bus voltage will be between 28 and 34 V.

The revolve motor causes the revolve housing that supports the two rotate shafts to rotate about a common center point so that the grinding wheel and rotate brush sweep through a full circle 45 mm in diameter. Using a single 45-mm diameter wheel that rotates about the center of the RAT would not be suitable because the velocity of the grinding material at the center of the wheel would effectively be zero, preventing grinding at the center, and therefore halting any advancement of the wheel into the rock. Additionally, with a single wheel approach, removing cuttings would be problematic.

The speed at which the revolve housing rotates is inversely proportional to the grind motor current draw. For example, if a set point of 400 mA of current is commanded for the grind motor, the revolve housing will rotate at its maximum velocity when there is no load on the grind motor as in the case when the grinding wheel is not touching the rock. The maximum velocity of the revolve housing is also a set point that is selectable for each grinding task. Speed constants exist for the revolve motor applied to the grinding algorithm equations. As the current draw from the grind motor increases, the revolve motor slows down to prevent over aggressive cutting into the rock that can lead to stability problems. When the grind motor draws the same amount of current as defined by the current set point, the revolve motor will stop advancing the grinding wheel across the rock until the grind current draw drops when rock material is worn away.

The Z-axis moves the lower section of the RAT in a linear fashion. Extending the axis engages the grinding wheel with the target rock to grind to a user selectable depth. A very high resolution of motion from the Z-axis permits a very small amount of material to be removed with each full revolution of the grinding wheel about the center of the RAT. Attached to a planetary gear head is the motor with an 18.777:1 reduction. A set of spur gears further reduces the rotational output. A 5 mm x 0.5 mm lead screw, coupled to the output of the driven spur gear, provides linear motion.

The Z-axis has a magnetic detent brake built within the upper section of the motor next to the encoder. During launch, landing, or rover traverses the detent brake will prevent the Z-axis from migrating. The detent brake contains four small magnets (Figure 3, label 5) attached to the motor housing that surrounds a steel cross-shaped plate fixed to the motor's rotor. The attraction between the ends of the cross and the magnets acts like a rotation brake that has preferred alignment every 90 degrees. Governed by the gap between the ends of the cross and the magnets, the strength of the brake is designed to hold the shaft

from rotating under worst case loading conditions. However, when motion is desired, the brake is small enough to be overcome by the motor.

Using a predetermined amount of current, the Z-axis position is known through a "Home" routine that drives the lead screw up against a linear jamming hard stop. Afterwards, the lead screw is backed away from the home position by 0.25 mm resulting in the true home position from where all operations start. This hard stop method of positioning the Z-axis was chosen over a switch because of the undesired added real estate and wire count needed for a switch to be used.

Brushes

After grinding, the abraded surface must be free of debris for the microscopic imager, and other instruments on the IDD to accurately view the rock's grain structure and geological properties. For this purpose two fine stainless steel wire brushes are mounted on the RAT, the rotate brush mentioned earlier and a revolve brush fixed to the side of the revolve housing. These two brushes work together in removing dust and cuttings from the hole. The rotate brush removes cuttings from the hole as they are generated and deposits the cuttings atop the perimeter of the excavation site. As the depth of the hole increases, the rotate brush can no longer deposit material atop the increasingly high perimeter of cuttings. This is where the revolve brush aids in the cleaning operation. With every revolution of the revolve housing about the center of the RAT, the revolve brush pushes the building perimeter of material away from the edge of the hole so that the rotate brush can eject the cuttings onto a relatively debris free perimeter. This dual brush action keeps the hole clean and free of material that would otherwise interfere with the quality of data collected by the other instruments. Alternatively, the dual brush action can be used to clean the surface of a rock without grinding. Through this approach any of the science instruments can view a rock's surface dust free.

Butterfly Unit

The lower section of the RAT is made up of a butterfly mount and two butterfly wings that act as a preloading structure between the IDD and the rock. The butterfly assembly is required because the IDD is not stiff enough to suspend the RAT above a rock in a free-floating state and provide reaction forces to counter the grinding process. When the RAT is placed onto a feature of interest, whether it is a rock, duricrust, or blocky soil, the IDD preloads the knurled balls (Figure 3, label 4) of the butterfly wings (Figure 1, label 2) onto the rock. As the RAT engages a surface feature, two switches (Figure 1, label 5) that reside within the butterfly assembly will close when a preload of 5 N is reached. After the switches close, the arm will move further into the rock to establish the commanded preload for grinding. Should the preload drop below 5 N at any point during the grinding operation, possibly as a result of rover or rock movement due to settling, one or both of the switches will open and the software will command the Z-axis to back away from the rock and then re-engage the rock. Should repeated switch openings continue, the result is that the penetration rate will either stop or slow to the point where a revolve timeout flag will appear that will abort the grinding algorithm. This event will be sent to Mission Control along with all other RAT grinding data.

The design of the butterfly elements that engage and become preloaded against a rock was a formidable task. It is necessary to actually preload the ground structure of the RAT against the rock, effectively closing the loop, which will dramatically increase the overall stiffness of the IDD for force reaction. The need to reside the ground structure outside of the grinding area accounts for the design of the butterfly wings. The RAT engages the rock at the bottom surface of each knurled ball mounted to the butterfly wings. These balls have this hemispherical design to allow the wings to freely slide over the rock topography during the approach vector without getting caught on a ledge or vesicle until the preload is established. The pair of butterfly wings is free to rotate +/-16 degrees about the pivot point on the butterfly mount. Additionally, each butterfly wing can move relative to each other by about one degree (for contact switch motion) and have compression springs mounted between the two butterfly wings to provide a spring loaded bias of 5 N applied at the knurled ball area on the wings. In this way, when the butterfly wings are loaded against a rock surface, they will rotate relative to each other by about one degree until the gold switches are closed which also act as hard stops. The wings can accommodate engaging a rock

surface that is not normal to the approach vector because they are free to rotate ± 16 degrees in the pitch axis. This allows the wings to properly seat themselves against a rock surface so that equal force is applied to each of the wings' knurled balls. The knurled balls can accommodate approach vector errors of ± 15 degrees in a yaw axis as well because they protrude downward from the frame of each wing. If the rock surface plane is at an angle equal to or greater than ± 16 degrees in either the pitch or yaw directions, hard stops will prevent the butterfly wings from pivoting further, preventing the switches from closing. Typically, the IDD will present the RAT normal to the local surface plane of the rock at an angle that is within 5 to 10 degrees.

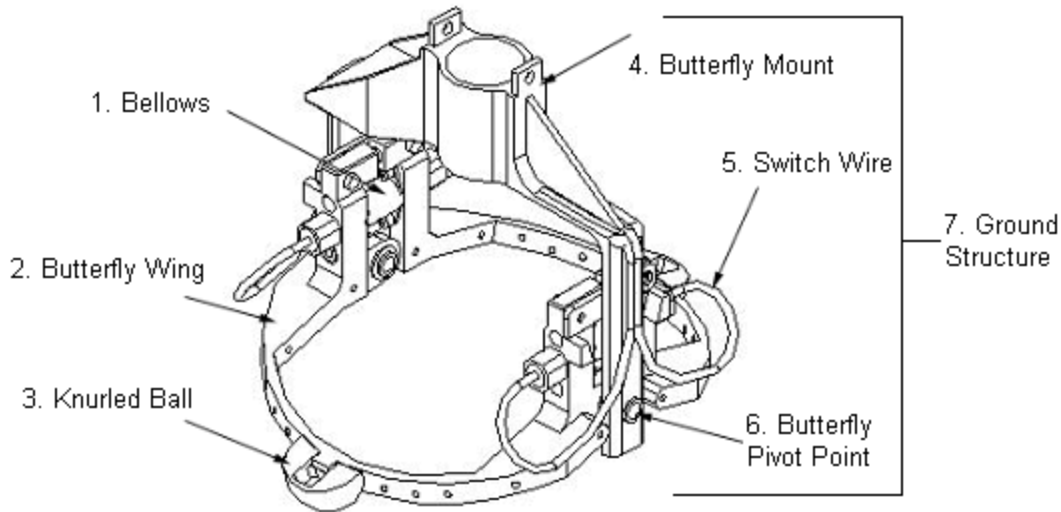


Figure 1. Rock Abrasion Tool -- Butterfly Isometric View

The switches were of particular concern due to the imposed requirements. They need to be small enough to fit within the very limited space allotted, they cannot have any hysteresis or dead band characteristics and they have to be dust proof. Additionally, the switches have to act as hard stops capable of withstanding loads as high as 125 N acting at the knurled balls which becomes about 222 N at the gold contacts. All of these requirements lead to designing and manufacturing custom made switches as commercial flight micro-switches could only satisfy the dust proof requirement. The contact material was made from 18-karat full hard yellow gold, which is also strong enough to withstand the relatively high compression loads. The gold contacts are insulated from the structure of the RAT via Vespel bushings. The backside of each switch half is back filled with epoxy at the point where each wire protrudes. This offers strain relief for the wire in addition to added bond strength for the gold and vespel bushing. The exposed gold contact heads are enveloped and sealed using a nickel bellows with custom end plates that are secured to each side of the wings. The breather vent had to be installed to allow trapped air to escape because assembly of the gold contacts (Figure 2, label 1) took place in Earth atmosphere. The vent was made using a stainless steel setscrew that was counter bored and filled with a 316 SS powder that was heated and compressed. This became a 2-micron filter, allowing gasses to exchange and equalize the pressure on both sides of the bellows yet prevent dust from contaminating the gold contacts. Had the breather vent not been installed, the spring constant of the butterfly switch system would have been greater than the 5 N calibration threshold.

Mounted within the bottom of the revolve housing are four small magnets (Figure 3, label 5) with varying degrees of strength. These magnets, provided by scientists from the University of Copenhagen, Denmark, will be used to characterize the magnetic properties of the cuttings produced by the grinding operations. For more information, see [Madsen et al., 2003]. The RAT magnets are designed to capture magnetic particles originating from the grinding of Martian surface rocks. A high-resolution stereo camera called Pancam, developed at Cornell University, will image the magnetic particles captured by these magnets. A major science goal for the Magnetic Properties Experiment (MPE) on the rovers is to identify the mineral(s) responsible for the magnetism of Martian rocks, soil and dust. In addition an effort will be

made to obtain information on the crystallite size of the magnetically ordered Fe (III) compound(s) in the dust.

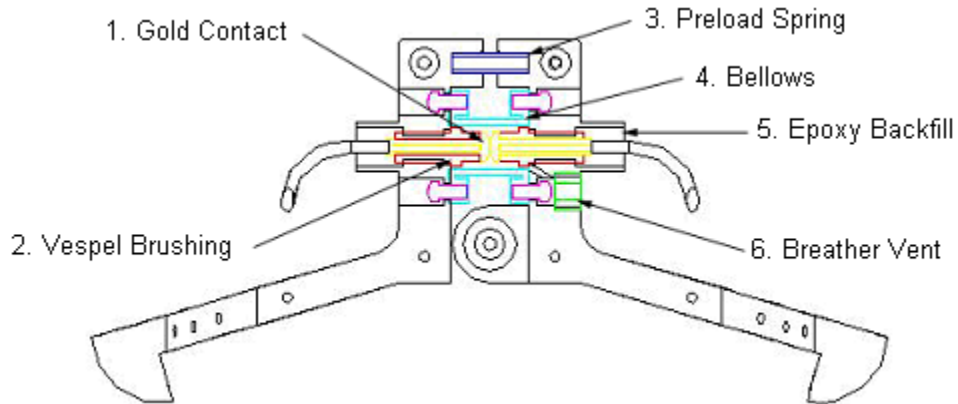


Figure 2. Rock Abrasion Tool -- Butterfly Switch Section View

The surface produced by the grinding operation will serve the science interests well. Typically, the surfaced is quite smooth and in some cases it is as smooth as a granite counter top. This clean, smooth surface should enable the microscopic imager to view grain structures and other features of the rock.

Science Return

In addition to grinding a clean, smooth surface, the RAT can also provide information characterizing the rock's physical properties. By analyzing the data set returned to Earth, the RAT generated data will be compared to information from an extensive collection of rock grinding data generated at Honeybee Robotics and stored in Honeybee's rock library. Other methods of manipulating the data will be used to determine the rock's physical properties. If the amount of material removed is known, the amount of required energy per unit volume of material can be determined. This ratio can then be compared to data within Honeybee's library to determine which type of rock tested on Earth most closely represents the excavated Mars rock, thus providing the rock's physical strength properties.

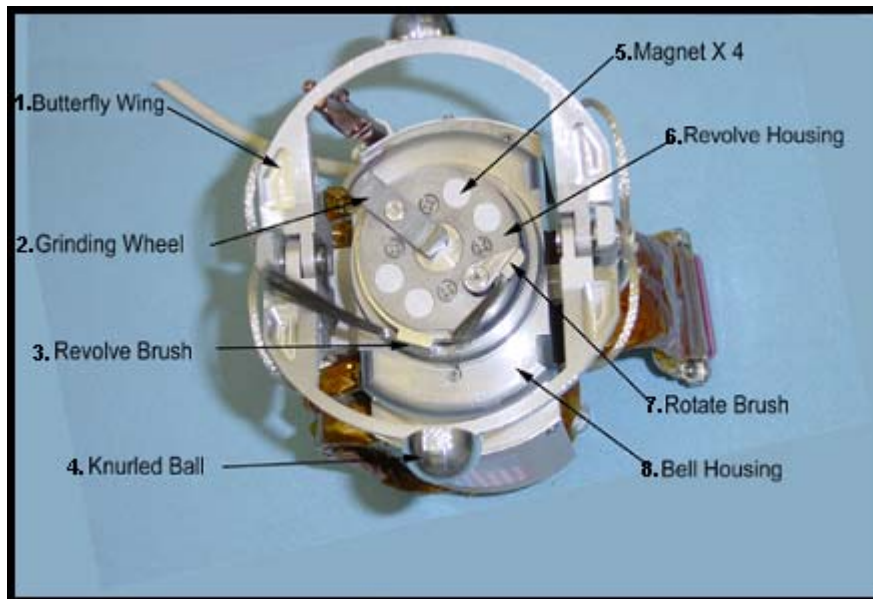


Figure 3. Rock Abrasion Tool -- Bottom View

Cutting Abrasive

A great deal of research, design and testing was conducted as part of the grinding wheel development process. We began our investigation of grinding wheel materials with an emphasis on diamond products. These are the hardest materials available, will operate at relatively high surface speeds and are subjected to low forces where tougher materials are not needed. We experimented primarily with synthetic diamonds, limiting our investigation of natural diamonds. The relatively minor additional hardness of natural diamonds does not outweigh the more predictable and repeatable properties of their synthetic counterparts. We tested large single crystal diamonds faceted to form a rake and relief angle needed for cutting and multiple large and small diamond crystals bonded in a single layer to a steel substrate. In all, we tested at least 50 different material and geometric combinations. Upon investigation we learned that the tips of the diamond grains developed flat spots that prevented further grinding within our bounded force limits. This discovery came as a surprise to us, as the force per grain is quite low and diamonds are much harder than the basalt that we were using as our test standard. These small flats created too much surface area for the low loading of the tool on the rock to have any cutting effect. A diamond abrasive with the ability to self sharpen was needed. In this approach, when the diamond grains wear, they fall out and expose fresh, sharp grains. Resin diamond wheels are designed especially for this purpose. Early testing of resin diamond wheels led to very poor results because whole wheels were used that presented a large surface area to the rock. A second approach, attempted later on, was designed to use resin diamond wheels also with very little down force. In this approach, the wheels were cut along two cords forming two small pads of resin along the perimeter of the "wheel" to engage the rock. Resultantly, the contact area with the rock was reduced, causing a higher force per grain. Ultimately, we settled on a grain size of 100-120 mesh (0.1-mm diameter) and a concentration of 112 (which has a volume of 28 percent diamond). The diamonds were coated with 56 weight percent Nickel that enhances the bond characteristics of the diamond to the resin. The resin is a phenolic with silicon carbide and cryolite fillers. This seemed to be the best formula for grinding within the given parameters. The sacrificial consumption of the grinding pad thickness was about 0.5-0.64 mm (20-25 mils) per grind event in hard rock in Earth atmosphere. This gave us a tool life of about five grindings in strong basalt. We then investigated the geometry of the actual resin diamond pads.

The size and shape of the grinding pads affected the level of success of each grinding experiment in how deep the bit was able to grind as well as how much time and energy was expended. Additionally, how much wear each grinding pad endured was important in the development of the pad design. If the pads were large in terms of surface area contact with the rock, it would see less wear than one of smaller contact area, yet the penetration rate would suffer. Furthermore, the shape of the pads was important in minimizing induced vibration and pad bond integrity with the substrate. The arc length of each pad must be inversely proportional to the width of the pad in order to maintain a given surface area. Through experimentation, we knew that the surface area of each pad must be on the order of 13 square millimeters or less. For vibration concerns, a large arc length would be better but this would make the width of the pads unacceptably thin in terms of bond integrity and manufacturability. Throughout the process of filling in an elaborate testing matrix, we settled on an arc length of 6.35 mm and a width of 1.5 mm. The usable thickness of the resin material is 2.6 mm. This thickness is governed by parameters set earlier in the design that involve among other things, the topography of the rock that can be dealt with and what clearance should be afforded in order to commence the grinding algorithm.

Force and Torque Margin Analysis

After completing the design of the RAT, we built four units. The first two are labeled Engineering Model 1 (EM1) and Engineering Model 2 (EM2). These units are exactly the same as the flight units but are used for testing here on Earth, EM1 at the Jet Propulsion Laboratory (JPL) and EM2 at Honeybee Robotics. We also built two flight units, Flight Model 1 (FM1) and Flight Model 2 (FM2). FM1 was installed on the Opportunity rover and FM2 was installed on the Spirit rover. FM1 and FM2 underwent Qualification Testing under a range of temperatures and loading conditions at Mars atmosphere. The Electrical Ground Support Equipment (EGSE) used for issuing the test commands and collecting the data products had an anomalous behavior that was not diagnosed until both flight units were delivered. The EGSE can be defined as the set of electronics and software that directly interfaces with the RAT actuators and sensors

and handles RAT control and data acquisition tasks. The problem with the EGSE was the motor current that it measured and stored was not the actual current consumed by the motors. In some cases, the EGSE showed more current than was actually consumed and in other cases, the EGSE showed less current than was consumed. It appeared that the Pulse Width Modulator (PWM) current output was not a linear relationship with respect to the commanded percentage issued to the PWM. As a result, the data collected could not be used to determine the amount of current needed for each motor given various loading and temperature conditions. Furthermore, torque margins could not be assessed based on the information at hand. Since the two flight units had already been delivered, we could not use them to perform a second round of tests with a proper measurement of the motor current. Consequently, we decided to dyno-test the EM2 unit using the same erroneous current collecting EGSE. This allowed us to compare the EM2 unit to the two flight units and make a determination as to whether the EM2 unit was “in family”, meaning the difference in behavior is insignificant, with regard to the two flight units. After completing the same no loads tests, using the erroneous EGSE equipment that were conducted on both flight units, and comparing the data, we concluded that all three units were indeed within “family”. With this understanding, we could then test the EM2 unit under Qualification Test conditions using a correct method of measuring each motor’s current and assess torque margins that we could apply to both flight units. The following is a detailed account of the methods we used in determining if the assembled units behaved the same and the technique of determining motor torque margins for each of the three motors within both flight units.

Dynamometer Tests

The purpose of the EM2 RAT actuator dynamometer testing was to characterize the speed-torque-temperature relationships of the RAT actuators including the drive trains, and to verify the ability of the actuator components to survive excursions to extreme temperatures. The additional purpose of dynamometer testing was (1) to determine the closed loop relationship between motor currents required for rock grinding and the actual forces and torques applied, (2) to verify that the performance of EM2, FM1 and FM2 RATs are “in family” and explain any disparities that exist, (3) to determine the torque margin on each actuator at key temperature set points, (4) to determine a set of FM1 and FM2 parameters that are safe for the RAT, but robust enough to successfully grind, and (5) to determine the maximum turn-on time for actuators that exhibit low margin at certain temperatures, using analytical and experimental methods.

Closed Loop Motor Current / Torque Relationship

All EM2 RAT motors have been dynamometer tested in order to characterize their current versus torque/force profiles at several different temperatures. Several grinding tests have also been performed with the EM2 RAT at 0°C. These grinding tests represent a worst-case scenario in terms of rock compressive strength and topology and the data was used to determine the worst-case torque and force requirements for all three RAT motors. The rock used for tests was a strong basalt, and the surface topology was flat (no peaks or valleys on the rock) in order to demonstrate the full capability of the RAT. Four grinding tests were performed on basalt, with the RAT at 0°C. These tests are numbered #197 - #200, and will be referred to as such.

Rotate (Grind) Motor Analysis

Using the erroneous EGSE data obtained from grinding tests #197 - #200, the amplifier current vs. time was plotted for the grind motor throughout the duration of the test. Occasional “spikes” were observed in the data where the amplifier current would jump much higher than the typical range of values. These spikes occurred over a very short time period and do not negatively affect the performance of the RAT. The peaks in the amplifier current data do not represent the worst-case grinding current because they only occur for very short amounts of time, and only a few times during a typical grind. Therefore, in order to determine the worst-case torque requirement, a statistical approach was taken for the data analysis.

Figure 4 shows a histogram of the grind motor amplifier current during grinding test #197. The vertical dotted lines show where 95 and 99 percent of the amplifier current fall and the resulting value. This approach was taken in order to help filter out some of the anomalous current spikes in the data, and to have a mathematical basis from which to define the current / torque relationship. The 99th percentile value of 415.16 mA was used from this test to determine the current / torque relationship for the grind motor.

In order to determine the actual grinding torque based on true motor current, a calibrated multimeter was placed in series with the grind motor during dynamometer testing. This data was then used to convert amplifier current to true motor current. Figure 5 shows the average motor current vs. average amplifier current obtained from dynamometer testing performed at 0°C (same temperature at which grinding was performed). The vertical line shows the 99th percentile grind motor amplifier current obtained from the grind motor histogram. The horizontal line shows the corresponding direct motor current of 459.65 mA. This is the worst-case scenario for motor current during grinding.

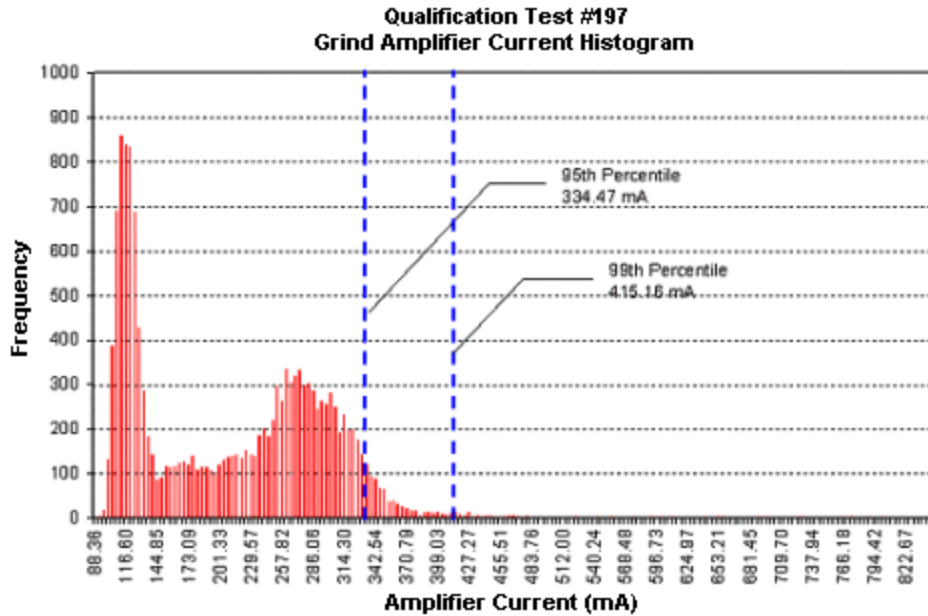


Figure 4. Grind Motor Histogram

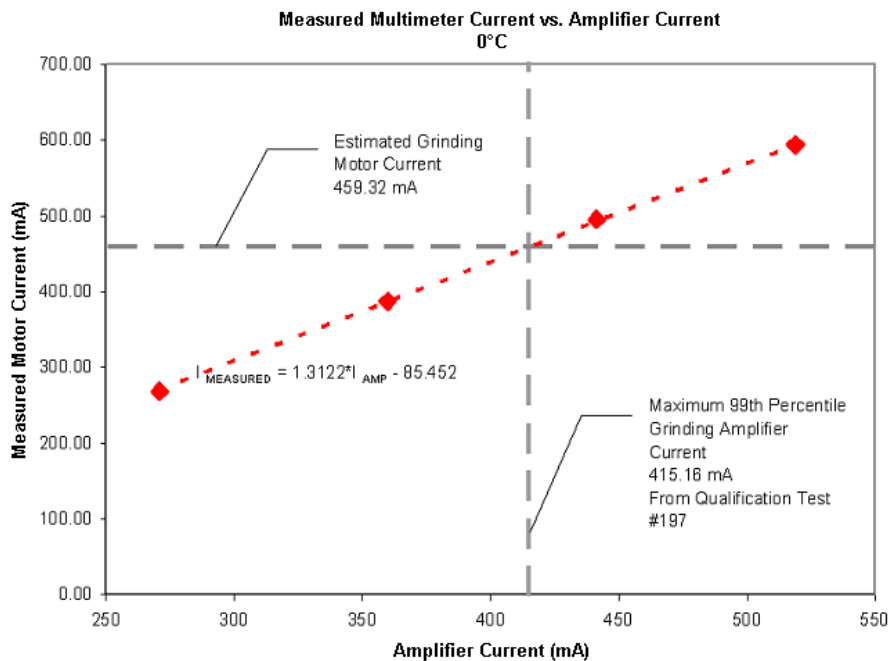


Figure 5. Motor Current vs. Amplifier Current

Figure 6 shows the motor current vs. torque for the grind motor at 0°C. This graph was obtained using averaged data from the grind motor dynamometer testing. The horizontal line represents the worst-case motor current during grinding, and the vertical line on the left represents the corresponding torque on the motor (25.13 mNm). This is the worst-case torque applied to the grind motor during a grinding operation. This value was used to define the torque requirement for the RAT margins.

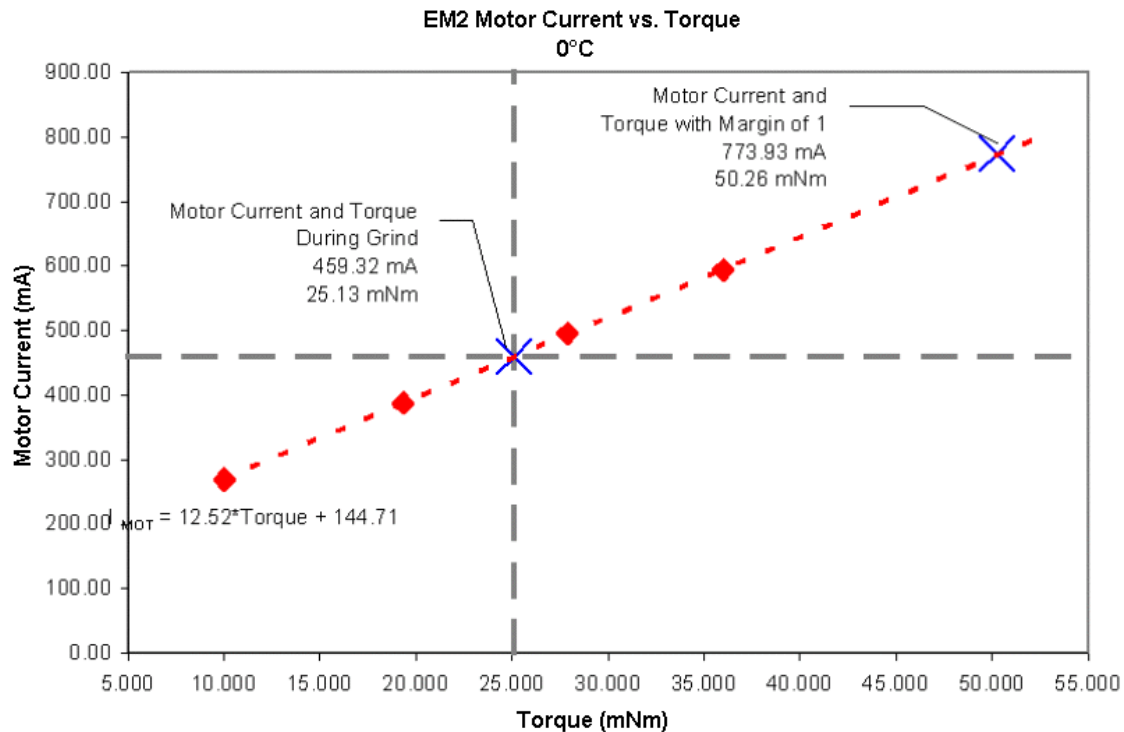


Figure 6. Motor Current vs. Torque at 0°C

Revolve Motor Analysis

The closed loop current / torque relationship was determined for the revolve motor similar to how the grind motor was analyzed. The worst-case amplifier current drawn by the revolve motor during a worst case grind was calculated to be 28.29 mA (99th percentile). From this value it is estimated that the revolve motor experiences a worst-case torque of 166.6 mNm during a worst-case grinding operation. The revolve motor is heavily geared down mechanically, and the majority of the grinding torque created is due to internal losses. This causes motor margin to be difficult to determine based solely on torque. In order to demonstrate that the action of grinding does not cause significant torque loads on the revolve motor, the amount of torque experienced by the motor with no load attached to it was calculated. To achieve this, the revolve motor was run de-coupled from the dynamometer, and the no-load current was measured. The amplifier current was then interpolated between 3 V and 6 V because the revolve motor typically runs at 4 V during a grinding operation. The heavy gearing of the revolve motor causes a torque of approximately 156.8 mNm, which is only about 10 mNm less than the torque seen during a worst-case grinding operation.

Z-Axis Motor Analysis

The closed loop current / torque relationship was determined for the Z-axis motor similar to how the revolve motor was analyzed since both motors are heavily geared down mechanically. The worst-case amplifier current drawn by the Z-axis motor during a worst-case grind was calculated to be 23.8 mA (99th percentile). From this value it is estimated that the Z-axis motor experiences a worst-case force of 5.907 N during a worst-case grinding operation. From no-load current values, it is estimated that the heavy gearing of the Z-axis motor causes a force of approximately 4.04 N, which is approximately 2 N less than the force seen during a worst-case grinding operation.

Table 1. Closed Loop EM2 Motor Current to Force/Torque Relationship Summary

Motor	Qualification Test #	99th Percentile Amplifier Current	99th Percentile Motor Current	99th Percentile Grinding Torque / Force
Rotate (Grind)	197	415.16 mA	459.32 mA	25.13 mNm
Revolve	199	28.29 mA	41.92 mA	166.6 mNm
Z-axis	197	23.8 mA	29.07 mA	5.907 N

EM2 RAT Thermal Margin Analysis

Grind Motor

The grind motor performance limits the RAT since it is the motor most likely to overheat. The heating of the grind motor is governed primarily by two variables, (1) the motor current and (2) the ambient temperature. Using the grinding torque found by closing the loop between grinding current and torque (25.13 mNm), the motor current can be found at all temperatures tested. This current, along with the corresponding ambient temperature, was entered into a RE25 motor thermal model in order to determine the time at which the motor will overheat. The temperature limits on the grind motor are +110°C for the rotor and +85°C for the case. At nominal operating torque (25.13 mNm), the motor will overheat in 28 minutes at +55°C. The motor does not overheat at the next lowest temperature tested, +35°C. For this reason, +35°C is specified as the maximum turn-on temperature (MTO). The thermal time limitation was found at a safety factor (SF) of 1.5 and 2.0 (margin of 0.5 and 1.0 respectively). This was done using motor current vs. torque data to find the motor current corresponding to a torque of 37.69 mNm (SF of 1.5) and 50.26 mNm (SF of 2.0). These values for motor current were then applied to the transient thermal model in order to arrive at a time limitation for the motor at margin.

Table 2. Grind Motor Thermal Margins

Temp. (°C)	Grind Current Margin of 0 (mA)	Grind Current Margin of 1 (mA)	Time to Overheat (min) for Margin of 0	Time to Overheat (min) for Margin of 0.5	Time to Overheat (min) for Margin of 1
+55	378.7	696.6	28	23.67	9.33
+35	396.3	710.77	Infinite	43.67	14.67
+23	400.83	704.27	Infinite	140.67	20
0	459.32	773.96	Infinite	Infinite	22
-20	471.37	779.3	Infinite	Infinite	31.67
-40	510.65	782.79	Infinite	Infinite	48
-55	539.5	844.45	Infinite	Infinite	41.67
-70	567.98	868.08	Infinite	Infinite	47.67

Revolve Motor

Due to the internal losses in the drive train of the revolve motor, the torque produced by a grinding operation is very small compared to the torque absorbed by the gear reduction. During a grind, the revolve motor has a much lower duty cycle than the grind motor, and for this reason there is no chance for the revolve motor to overheat. This necessitates a different way of determining the torque margin. There are two potential failure modes in the revolve motor's operation, (1) abnormally high internal losses in the drive train, and (2) unexpected areas of highly dense rock. Due to the relatively low contribution to overall torque of the grinding operation, the most probable failure point is within the drive train. Since the torque due to the drive train cannot be measured directly, the torque margin analysis will be based on a no external load motor current, rather than measured torque.

For each thermal test point (+55°C, +23°C, 0°C and -55°C), the motor was run in velocity mode to simulate the required speed that it needs to operate at during a grind (0.35 radians/sec). This was performed while de-coupled from the dynamometer. This no-load motor current was used as the basis for the torque margin since the revolve motor needs to draw at least this amount of current at a certain temperature in order to overcome internal losses in the gear train. To determine the torque margin, the

revolve motor was coupled with the dynamometer and again run in velocity mode at 0.35 radians/sec at each temperature set point. The dynamometer was used to apply a torque load on the motor until the motor current was as close to twice the no-load current as possible. For some temperature set points (0°C and +23°C) it was not possible to produce enough torque to double the no-load current due to the limitation of the dynamometer (maximum applied torque of 350 mNm).

To determine thermal margin, the peak motor current was calculated while running the revolve motor in voltage mode. This current was doubled and used in the RE020 motor thermal model to determine the transient heating of the motor at all temperature set points. It was found that the revolve motor does not overheat at any of the temperature set points or voltages.

Table 3. Revolve Motor Thermal Margin (RE20 Motor)

Temp (°C).	Maximum Motor Current (mA) at 3V, 150 mNm	2X Maximum Motor Current (mA) at 3V, 150 mNm	Overheat (min)	Maximum Motor Current (mA) at 6V, 150 mNm	2X Maximum Motor Current (mA) at 6V, 150 mNm	Overheat (min)
+55	34	68	Infinite	35.8	71.6	Infinite
+35	34.3	68.6	Infinite	36.9	73.8	Infinite
+23	36.1	72.2	Infinite	37.5	75	Infinite
0	35.8	71.6	Infinite	40.6	81.2	Infinite
-20	41.3	82.6	Infinite	53.1	106.2	Infinite
-40	67.7	135.4	Infinite	71	142	Infinite
-55	89.4	178.8	Infinite	74.6	149.2	Infinite
-70	142.1	284.2	Infinite	152.9	305.8	Infinite

Z-Axis Motor

As with the revolve motor, the force caused by a grinding operation is very small compared to the force absorbed by the gear reduction and friction due to internal losses in the drive train of the Z-axis motor. During a grind, the duty cycle of the Z-axis motor is an order of magnitude lower than that of the grind or revolve motors. For this reason, there is no chance for the Z-axis motor to overheat. The revolve and Z-axis motors share the same potential failure modes during operation. Again, due to the relatively low contribution to overall force of the grinding operation, the most probable failure point is in the drive train. The exact approach used to determine the revolve motor torque margin was also used for the Z-axis motor.

For each thermal test point (+55°C, +23°C, 0°C and -55°C), the motor was run in velocity mode to simulate the required speed that it needs to operate at during a grind (0.05 mm/sec). This was performed while de-coupled from the force controlled air cylinder. The motor was run for close to a full stroke of the output and the resulting motor current was averaged. To determine the torque margin, the Z-axis motor was coupled with the air cylinder and run in velocity mode at 0.05 mm/sec at each temperature set point. The air cylinder was then used to apply a load on the motor until the motor current was as close to twice the no-load current as possible. The maximum force that the load cell can measure accurately is slightly over 50 N (the load cell specification has 50 N as the maximum measurable load; however, it was observed through testing that this is not the absolute limit). For one temperature set point (-55°C) it was not possible to produce sufficient load to double the current because it would have well exceeded the limitation of the load cell.

To determine thermal margin, the peak motor current was calculated from dynamometer testing of the Z-axis motor in voltage mode. This current was doubled and used in the RE020 motor thermal model to determine the transient heating of the motor at all temperature set points. It was assumed that the motor was run constantly rather than intermittently. It was found that the Z-axis motor only overheats at and below -55°C when operating at a voltage of 8 V, with a load of 30 N or more on the motor, and at a safety factor of 2.0. This is well above the expected 4 V operating voltage, and far above the expected 6 N load on the motor during grinding.

Table 4. Z-Axis Motor Thermal Margin (RE20 Motor)

Temp (°C).	Maximum Motor Current (mA) at 4V, 30N	2X Maximum Motor Current (mA) at 4V, 30 N	Overheat (min)	Maximum Motor Current (mA) at 8V, 30N	2X Maximum Motor Current (mA) at 8V, 30 N	Overheat (min)
+55	46.6	93.2	Infinite	43	86	Infinite
+35	41.4	82.8	Infinite	39.1	78.2	Infinite
+23	40.2	80.4	Infinite	46.3	92.6	Infinite
0	46.1	92.2	Infinite	52.2	104.4	Infinite
-20	56.7	113.4	Infinite	73.7	147.4	Infinite
-40	100.9	201.8	Infinite	137.8	275.6	Infinite
-55	127.8	255.6	Infinite	172.7	345.4	24.33
-70	167.4	334.8	Infinite	285.1	570.2	2.75

“In Family” RAT Models

During the FM1 and FM2 dynamometer test, the methods for measuring motor current were inaccurate. The motor current data recorded during those tests was amplifier current. The true (direct) motor current was measured throughout the EM2 dynamometer tests and it is understood that the motor current is a nonlinear function of amplifier current and PWM duty cycle among other things. Sufficient data does not exist to allow the FM1 and FM2 erroneous motor currents to be transformed to actual motor currents. Therefore, in order to determine that the EM2 is “in family” with the FM1 and FM2, the amplified motor current had to be correlated to the direct motor current. The data shows that all of the actuators in the three units behave similarly at most temperature set points; however, there are a few disparities between the motors, which mostly occur at lower temperatures, -70°C in particular.

Most of the disparities can be attributed to (1) mechanical variations in the motor drive trains (the current obtained from the dynamometer tests include the current due to the internal losses in the drive train, and although all parts are made to same print, there are fitting differences and the lubricated parts can behave differently at cold temperatures), (2) set limits in the control software, and (3) an improper bake out during one test.

Disparities at -70°C:

- The FM1 revolve no-load current at 3 V is much lower than the FM2 and EM2. The FM1 revolve did not move at -70°C because the current reached its limit. When FM1 was tested, increasing current limits at colder temperatures was not considered due to lack of test experience. These limits were increased before FM2 and (subsequently) EM2 were tested.
- The EM2 revolve no-load current at 6V is much higher than the other two units. This is due to the revolve current reaching its upper limit and not moving.
- The Z-axis no-load motor current comparison at 8 V showed that the FM2 current is much higher than the FM1 current and the EM2 current is much higher than the FM2. For FM1 again, increasing the current limits at colder temperatures was not considered, therefore the FM1 Z-axis did not move at -70C because the current limit was reached. This current limit was increased for EM2 testing, but the unit was not properly baked out during the test, so the Z-axis did not move at -70°C because it reached its current limit. The effects of the improper bake out were also apparent at -55°C, where the EM2 Z-axis motor current was running high. However, it was determined that the EM2 Z-axis no-load current is close to that of FM2.

Overall, the differences between the three units at nominal operation temperatures are minor and it is concluded that all three units are “in family”, and so the results from the EM2 Margin Analysis based on the EM2 grinding and dynamometer test data can be applied to FM1 and FM2.

Lessons Learned

- 1) The delivery schedule of the grinding wheels for integration into the flight assembly was such that we did not have enough time to test the behavior of the diamond resin wheels in a simulated Mars environment prior to delivery. Obviously this is not the way we would have liked to proceed but we had no choice as the delivery deadline was fast approaching as we finished our last round of testing. Later, we were able to test the final wheel design under Mars environmental temperature and pressure. During these tests, we discovered that the wear rate of the diamond/resin decreased dramatically in a simulated Mars environment. Under Earth conditions, the wear rate was about 0.51-0.64 mm per basalt grind event. Under Mars environmental conditions, we saw wear rates of about 0.1-0.127 mm per basalt grind event. This is a five-fold decrease in the wear rate or a five-fold increase in tool life or about 25 basalt grind events. System level requirements imposed a tool life of three grindings with a margin of one (six grindings). In retrospect, if we knew that this wear effect was present, we would have decreased the concentration of diamond in the resin mix. This would have the effect of reducing the tool life through increased wear (something we could live with) and increased the grinding performance of the tool because with fewer stones in the matrix there would be more force per stone, thus increasing the grinding properties.

After learning of this diamond behavior under Mars conditions, a paper written by Hitchiner et al. (1983) from Oxford University provided complementary information. Hitchiner compares the effects of polishing diamond on an iron scaife in Earth atmosphere and at a vacuum of 0.1 Torr. His conclusions describe a five-fold decrease in the wear rate under vacuum. Therefore Mars acts more like a vacuum than Earth atmosphere with regards to diamond wear rates.

- 2) The Z-axis lead screw hard stop should have been designed so that it acted as a rotational hard stop. With small posts projecting upward on the lead screw and a small post projecting downward from the ground structure, this rotational hard stop could have been implemented. It would have given the instrument more repeatable positional information and it would not have depended as heavily on the temperature and thus current limit at which the system is activated.
- 3) The only Platinum Resistive Thermocouple (PRT) that was available to us was mounted on the Z-axis motor with the thought that it would more accurately provide the true morning temperature of the RAT as well as limit the number of wires that must flex while the RAT was in motion. However, in use, it seems that the PRT would be put to better use if it were mounted to the grind motor that has by far the highest duty cycle of all the motors. This would have allowed direct reading of the grind motor's temperature during operation as opposed to a thermal model looking for overheating, which is currently used.
- 4) During the assembly of the RAT engineering and flight models, the 37 pin micro D connectors were backfilled with an epoxy, model # PR-1590, made by PRC Desoto International. Throughout the process of verifying our mixing procedure, testing our Teflon mold, and applying this procedure to the engineering and flight models we learned that the compound was extremely sensitive to atmospheric humidity. If the humidity levels were greater than 30%, the compound formed bubbles that could not be eliminated even when immersed in a vacuum chamber, as part of our procedure designed as a precautionary step to prevent bubble formation. Regardless of the amount of applied vacuum, the bubbles continued to form in the presence of high humidity levels. Ultimately we kept our clean room at or below 30% humidity, yielding successful molds with no bubbles.

Conclusion

Using data obtained from grinding tests performed at 0°C and dynamometer tests performed at the same temperature, it is possible to close the loop between the amount of force and torque required by the RAT motors to grind a rock, and the corresponding current. However, the torque varies greatly with the type of rock that is being grinded. In order to determine the closed loop relationship, a worst-case rock was grinded (hard basalt with flat surface topology). It was found that the worst-case torque required by the

grind motor is 25.13 mNm, the worst-case torque required by the revolve motor is 166.6 mNm, and the worst-case force for the Z-axis motor is 5.907 N.

Using no-load revolve and Z-axis motor data, it was determined that the action of grinding a rock does not contribute greatly to the overall torque/force on the motors. Most of this torque/force is absorbed by friction in the drive trains of these two motors. The revolve motor gear train absorbs approximately 156.8 mNm, while the Z-axis gear train absorbs approximately 4.04 N.

Using motor dynamometer data and the torque required to grind a worst-case scenario rock, the thermal margin was determined for the grind motor, the motor most likely to overheat. It was found that with a temperature limit of 110°C on the rotor, and 85°C on the case, the RE25 motor does overheat at +55°C ambient temperature but does not overheat at an ambient temperature at 35°C after four full hours of grinding. The maximum turn on temperature (MTO) will therefore be specified as 35°C.

The thermal margin was also calculated for the revolve and Z-axis motors in the worst-case scenario that the motors operate continuously, rather than intermittently. It was found that the revolve motor does not overheat at any of the temperature set points with a safety factor of 2.0. It was also found that the Z-axis motor starts to overheat when run in voltage mode (at 8 V) at temperatures below -55°C, at a load of 30 N, and with a safety factor of 2.0. Since the Z-axis motor typically operates between 4 V and 6 V with a load of less than 6 N and a very low duty cycle, this was not seen as a concern.

The revolve and Z-axis motor margins were determined using the no-load current at several different temperature set points (+55°C, +23°C, 0°C, -55°C), since internal losses in the gear trains outweigh the forces and torques due to grinding. Torque and force loads were applied to the revolve and Z-axis motors until the motor current increased to close to double the no-load current. This shows that the motors can overcome the internal losses in the drive train.

Although the Rock Abrasion Tool was specifically developed for the Mars Exploration Rover Mission, the lessons learned during development provide crucial insight for future endeavors. Undoubtedly future missions targeting Mars and other celestial bodies will require drilling and grinding instruments. When specifying design criteria one must be more tolerant of the uncertainties of the unknown targets. System developers must realize the philosophy of designing mechanisms with force and torque margins for a truly unknown target environment should not be overlooked.

References

1. Hitchiner, M. P., Wilks, E. M., and Wilks, J. "The Polishing of Diamond and Diamond Composite Materials." *Wear*, (1984), pp. 103-119.
2. Gorevan, S. P., Myrick, T., David, K., Chau, J. J., Bartlett, P., Mukherjee, S., Anderson, R., Squyres, S. W., Arvidson, R. E., Madsen, M. B., Bertelsen, P., Goetz, W., Binau, C. S., and Richter, L. "Rock Abrasion Tool: Mars Exploration Rover Mission." *Journal of Geophysical Research*, 108(E12), 8068, doi:10.1029/2003JE002061, in press, 2003.

Review of International Space Station Mechanical System Anomalies

David S. McCann*

Abstract

The International Space Station (ISS) when completed will consist of over 32 different mechanical systems utilized in more than 150 applications providing functionality for assembly, rotation and deployment of major components, and maintenance. Currently, a majority of these systems have been launched and either functioned or checked out on orbit, and all have completed preflight testing and flight readiness processing. Within the ISS program the Structures and Mechanisms (S&M) System Problem Resolution Team (SPRT) is responsible for the resolution of problems associated with all ISS mechanical system during qualification, pre-flight checkout and on-orbit operations. This activity combined with the sheer number of complex mechanical systems on ISS has exposed the team to a great number of problems of interest to the Space Mechanism community.

The Problem Reporting and Corrective Action (PRACA) system is used to track, document, and approve the investigation and analysis, root cause determination, and corrective action and recurrence control for these problems. Formal SPRT's were formed in 2000. Since its inception the S&M SPRT has dipositioned over 350 ground and on-orbit problems. The PRACA database is used to store all problem records and can be used to generate reports on various metrics.



Figure 1. ISS on orbit

This paper will present the results of a thorough review of the mechanical system problems that have been addressed by the S&M SPRT. Metrics on the types and frequency of various problems will be presented. Problems with fastener installation and secondary locking features as well as tolerancing for thermal deformation and rigging are examples of the most common problems. The root causes will be categorized and the most prevalent causes will be discussed from a lessons learned perspective. Determination of root cause is often the most difficult part of a failure investigation and yields the most

* The Boeing Company, Houston, TX

Introduction

The PRACA system has been used since 1997 to track, document, and approve the investigation analysis, root cause determination, corrective action, and recurrence control for all hardware problems on ISS. The S&M SPRT manages the resolution of all structural and mechanical system problems. Since its inception the S&M SPRT has worked on over 350 problems ranging in severity from galled fasteners on the ground to failed deployment systems on-orbit. The PRACA database can be searched for key words or other field identifiers and is used for trending of system problems on the vehicle.

Problem Reportability Criteria

Most hardware non-conformances are not considered to be PRACA reportable. Hardware discrepancies that occur during the manufacturing process are usually dispositioned through a local Material Review Boards with standard repair procedures. A PRACA reportable problem is anomalous hardware performance that occurs during Qualification or Acceptance testing, or after delivery of the hardware from the contractor to NASA while the systems are being readied for launch, or occur during or after activation on-orbit. PRACA reportable problems that occur on the ground are investigated and worked until the hardware is either brought back to print or to a waiverable condition where it can be assured to meet all system requirements. On-orbit the problems are worked until the hardware can be repaired or an acceptable condition can be found so the hardware can continue to function and meet most of its performance requirements until a future time when a repair can be implemented.

PRACA Review

A detailed review of all S&M PRACA's was performed. The root cause of each PRACA was noted and categorized. It was found that most PRACA's could be grouped into one of 9 types. Figure 3 gives a percentage breakdown for these nine categories. As can be seen tolerancing errors and design errors account for almost 40% of the PRACA reportable problems that occurred in the structures and mechanical systems. Manufacturing type problems made up 15%. Fastener problems and environment/procedure problems accounted for 9% and 8% respectively. Test and STE related problems each accounted for 4% of the PRACA's. Panel Retention makes up 2% with the other miscellaneous problems making up 23%. While the miscellaneous category makes up a significant number of anomalies, there did not appear to be any recurring themes although each one represents a problem that had to be worked with the implementation of a corrective action and recurrence control.

PRACA Breakdown by Type

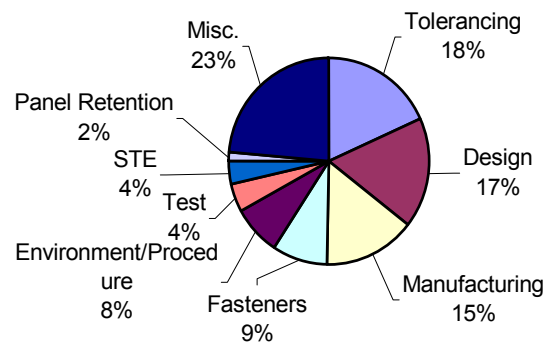


Figure 3. Problem Reporting Breakdown

Lessons learned from each of the major categories

For each of the major categories the root causes, corrective actions and recurrence controls were reviewed for lessons learned that could be useful in reducing the risk of similar failures on other space flight mechanism programs. An attempt was made to provide lessons learned that affected the highest number of PRACA's in each category.

Tolerancing

This category was used to capture failures attributed to insufficient design tolerancing for either thermal or mechanical deflections. For example, several moving mechanical assembly binding failures, which occurred during environmental testing, were caused by a lack of sufficient clearances. Root cause investigations determined that adequate tolerances had not been provided to account for the thermal expansion coefficient differences of the various components in the systems. Also, other hardware anomalies were found to be caused by poor mechanical tolerancing of moving components. In several cases, limit switch rigging tolerances did not account for the mechanical tolerances and run out of the interfacing mechanical components, resulting in the failure to achieve consistent and repeatable limit switch activation.

Most of the problems resulting from tolerancing errors could have best been prevented with good design reviews and more rigorous design analysis. It was found in a majority of these problems that the complexity of either the thermal or load environment was not considered in the original design. Whenever complex or even simple mechanical systems are being reviewed careful attention should be made to tolerances that could be affected by temperature or loads. In several problem reports, the root cause was not accounting for sufficient clearance in moving mechanical interfaces for the growth or contraction of components under the environment they were being designed to operate. In other cases, the orientation of the system in a gravity environment or unloaded condition affected the operation of the mechanism and resulted in anomalous performance. In several cases, failure to provide adequate margin for manufacturing tolerance build up resulted in failures of the units under test. A detailed design tolerance analysis accounting for manufacturing and worst case thermal and mechanical conditions can be used to mitigate the risk of having hardware failure in test or in operation.

Design

Failures attributed to design were characterized by problems in the detailed parts of the hardware. For example several cases of rotating components with out proper use of washers or bushing resulted in failure of the mechanism during testing. Also, interferences with fillets or other components, or having wiring routed too close to moving components resulted in test failures and the need to redesign hardware. Included in this category are failures attributed to insufficient strength of a fastener or other retention devices that should have been caught during design reviews or analysis. Failure to provide adequate design features to protect against galling, contamination, or to provide proper force or torque margins are also included in this category.

Although under initial review this category appeared to be a case of 20-20 hindsight, further review resulted in some interesting lessons learned. The most striking of these was that the failures were primarily caught during qualification or acceptance tests. The ISS program was forced by budgetary constraints to waive the requirements for many tests and thus relied on design reviews and analysis as substitutes. In review of the resulting hardware performance, many years later, it is clear that often times this is a risk that may result in unsuspected hardware failures. Many design errors or deficiencies can only be found in test, and whenever analysis or inspection is used in place of those tests, a higher degree of rigor is required to assure that design errors are caught. Another lesson that should be drawn from this category is that design reviews need to include a thorough peer review. In several cases simple design errors, that senior designers would have caught, were missed and only caught in subsequent testing. It is felt that many of these could have been prevented by having adequate review by senior designers and analyst. Detailed design checklists could be used to help systematically review new design for errors that had been found in previous designs. Design to minimum risk criteria when applied correctly can help identify areas in a design that need close review.

Manufacturing

Failures assigned to this category had root causes in the manufacturing process either from failure to detect a mis-manufactured part or the inability to manufacture to the tolerances called for on the drawings. Poor identification of mandatory inspection points (MIP's) on drawings was determined to be a root cause on several PRACA's. Also, reliance on very tight tolerancing to achieve system performance lead to parts or assemblies that could not be manufactured to print and ultimately had to be accepted with waivers.

The primary lesson learned from this category should be the integration of design and manufacturing engineers in the early development of a mechanical system. In several cases the original design placed unrealistic reliance on very tight manufacturing control to assure systems performance. When these requirements were unable to be met, redesigns and reanalysis were required to assure systems performance requirements could be met. In several cases operational limits had to be imposed to assure that the hardware could perform. Other cases involved the failure to detect mis-manufactured parts until later testing. The recurrence control for all of these problems was the addition of mandatory inspection points to the detailed design drawings. The addition of MIPs to any drawing should be reviewed to assure that dimensions that are critical to system performance are carefully checked during manufacture and not left for acceptance testing to catch. Unless identified as a MIP, most detailed part dimensions are not as rigorously checked by quality inspectors.

Fastener

This category includes all cases where fasteners failed because either galling or the loss of a secondary locking feature caused a failure of a mechanism. For example, to meet payload safety requirements all safety critical fasteners must have a verified secondary locking feature. This means that during installation the running torque of most interference type locking elements have to be verified. On numerous occasions the loss of these locking features resulted in significant rework. This does not include times when a standard repair was used to replace the locking element. In many cases modified or non-standard repairs were needed. This category also includes failures where cycling of multiple use fasteners resulted in galling. The root causes in these cases was attributed to a lack of or wear out of a lubricated threaded interface.

This category seems at first to be mostly simple problems, however because it resulted in almost 10% of the postproduction problems on ISS it is worthy of review for lessons to reduce the risk of recurrence on future development projects. The use of secondary locking features is common in spacecraft design and on most structural applications there are few problems because they are normally single use applications and failures can be handle with standard shop repairs. However, on many ISS applications, fasteners are required to be installed and removed numerous times in the preparation and use of the hardware. This resulted in many occurrences of failed locking features that cause significant delays and costly repairs. Many of these problems could have been avoided if the original designs had accounted for the need to replace locking features as part of the normal processing of the hardware. Some ISS designs utilized easily replaceable fastener locking features and avoided this type of problem. Another cause of a significant number of failures was the lack of proper lubrication of the fastener or insert. Careful attention should be made to assure that galling does not occur at the threaded interface between fastener and insert or nut, especially on designs that may require several installation/removal cycles. In several PRACA's the root cause was determined to be insufficient lubrication, or breakdown of existing lubrication over several fastener cycles. The corrective action in many of these cases was to either add a more durable lubrication or add lubrication to both the fastener and insert.

Environment/Process

This category was used to capture failures or hardware anomalies caused by the system being operated outside original design environments or operated in a manner not accounted for in the original design. Most of these failures or anomalies have happened on-orbit as a consequence of changes to the original design parameters and assumptions. Although this is not normally considered a design or hardware problem, this category represents an area where numerous hardware problems had to be worked and lessons learned can be drawn. These failures were a result of not assuring that original design assumptions were actually the environment or process that the hardware was to be operated in. Often it was found that early design assumption and operational baselines changed as the program matured. In

several cases the effect of the changes in either planning or updated environments was not properly assessed for its impact to already completed analysis and certification. This resulted in hardware being operated outside the design baseline. Corrective action included processes to assure that operational and environmental baselines used in design analysis and certification programs were carefully monitored, and that the cognizant design group reviewed any changes to operational plans or conditions. In several cases providing additional margin in the early design phase could have provided additional flexibility when changes were required later in the program

Test

These failures and anomalies were attributed to either test parameters not being met or test procedures not being followed. In either case the flight hardware was subjected to excessive loads or temperatures and had to be reworked or reanalyzed. In several instances a component had to undergo several repeat acceptance tests which was beyond the original qualification. Other problems resulted from an inability to perform the test as originally designed and specified. Several failures resulted from test procedures being poorly written and confusing to test operators.

The impact from this type of failure could have been reduced with more thorough reviews and verification of the tests that flight hardware was to be exposed to. In most certification programs the qualification environment is developed to certify the hardware for exposure to a given flight environment and either one or two acceptance test cycles. In several cases a flight unit for various reasons had to be reworked and then re-acceptance tested. When the original number of certified acceptance cycles was reached a great deal of extra analysis and sometimes limited retest was required to prevent over stressing the hardware. This could have been avoided if the original qualification had included more than one or two acceptance test environments. This should be considered especially on complex systems with a higher chance of needing repeated tests. On the ISS program many component level acceptance tests were eliminated and replaced with acceptance tests at the next higher system level. In cases like this a failure of any part of the system resulted in all components having to be exposed to another acceptance test cycle. Because these types of acceptance tests were so critical, procedural or operator errors had a much more costly impact, and thus should have had more rigorous reviews and verification. The institution of "Won't Fail Reviews" prior to new tests has proven to be a useful tool in reducing these types of failures. A "Won't Fail Review" provides an independent thorough review of a procedure by independent experts who focus on risk areas in a procedure.

Special Test Equipment (STE)

This category was used to capture all failures where the root cause was determined to have resulted from a failure of the STE, either hardware or software. These failures resulted in flight hardware needing to be reworked or retested. Several times lack of quality control or fault tolerance in the STE resulted in damaged flight hardware. Poor design of the STE also was a contributor to several anomalies.

A factor in several of these cases was a lack of detailed design review of the STE. Because STE hardware often times has direct effect on the flight hardware it must have the same level of design and functional review as the flight hardware. Where potential damage to flight hardware exists fault tolerance in the STE is as important as the fault tolerance in the flight system. This is also true in the manufacturing of the STE. In one case, poor quality control of the STE almost resulted in severe damage to very critical and irreplaceable flight hardware.

Panel Retention – Failure of quarter turn or other captive panel fasteners

This category was used to capture all anomalies with the internal and external ISS panels. Most of these failures were attributed to improper strength of a fastener or improper procedures used in the original assembly or use on orbit.

Again this category at first seems too simple for discussion, but because of the number of occurrences and on-orbit impact it warrants further investigation. Most of the panels both internal and external to the ISS are removable for access to maintainable hardware or for assembly tasks. Difficulty in the original assembly of the panels before flight was not correctly identified as having the potential to also be a source of failure on-orbit. These types of failures have required an excessive amount of crew time for

repair and rework. For future manned vehicle designs, care should be taken to provide very robust and easily replaceable fasteners for hardware like panels that will be frequently utilized by the crew.

Other Miscellaneous

Failure that could not be placed into one of the above categories, and the total number of similar events was less than 5. More categories were used in the initial review of the PRACA's like corrosion, configuration control, and unexplained anomalies, but none of them resulted in more than 4 occurrences and thus were grouped into the miscellaneous category.

PRACA's with Largest Program Impact

The original purpose of this review was to determine the types of problems that occurred most frequently in a large program like ISS. It became clear during this review that it would also be beneficial to discuss some of the failures that have had the largest impact or potential impact to mission objectives, cost or schedule.



Figure 4. Photo of BGA and 4-Bar Assembly

BGA Hinge Lock Failure and Excessive Deployment Force (PRACA 2389 & 2435)

This failure occurred during the deployment of the first solar arrays on the P6 element of ISS. During activation of the element a four bar mechanism is used to rotate the solar array mast canisters and blanket boxes from a launch position to an on-orbit position. Locking features at the base of four bars engage when full rotation is achieved. The deployment force on-orbit was significantly higher than expected and not all locks could be properly engaged. An exhaustive investigation revealed that insufficient control of the manufacturing tolerances allowed binding to occur in the mechanism which increased the required force to deploy and caused the hinge lock to malfunction. Also, a design feature that relied on friction to maintain alignment of critical parts failed when subjected to the binding loads. A redesign was undertaken to correct this on the remaining six solar array four bar mechanisms along with tighter control of the assembly process and functional checks to verify deployment forces.

Beta Gimbal Assembly (BGA) High Current (PRACA 2685)

The BGA is a direct drive mechanism located at the base of each of the ISS solar arrays and is used to rotate the array toward the sun. During early operation of the first two arrays on-orbit, higher than expected current spikes were noted. As time and cycles accumulated these current spikes eventually reach the maximum limit and a stall condition on the joint. These stalls have been recovered from and managed through a combination of operational procedures to limit the rotation required from the joint and planned rotation reversals. Although the root cause has not been absolutely determined an intensive investigation has narrowed the failure to the bearings and/or lubricant. It is believed that an anomaly in the lead based lubricant has cause some form of debris to be generate in the bearing causing erratic torque ripple that over time can lead to torque requirements beyond the motor capability. Rotation reversal has continued to be an effective means to regain rotation capability. A preplanned period of reversing rotations have reduced the frequency of the stalls and appears to date to be an effective means of controlling the anomalous performance. Without a definitive root cause it is hard to draw conclusive lessons from this experience, however it cannot be ignored that the bearing design was changed after development life testing had been completed, and that the original life testing did not include any of the environmental effects that the bearing would see on orbit. Cost and schedule were factors in the decision not re-performing the tests.

Solar Array Deployment Anomaly (PRACA 2397)

This failure also occurred during the deployment of the first solar arrays on the P6 element. As the arrays were being deployed, dynamic motion in the panels caused a failure of the blanket tension mechanism. This failure was attributed to small stiction forces between the solar array panels where silicon surfaces were in contact. Although the arrays were functionally tested on the ground, the effect of these forces was masked by ground support equipment and the effect of operating in a 1-G environment. Failure to recognize the effect that these small forces would have on the system resulted in a significant failure on-orbit. Only after the on-orbit failure occurred did detailed dynamic analysis demonstrate the effect. No preflight analysis of this type had been conducted. If this type of analysis had been conducted prior to flight, it would have identified a lack of force margin in the blanket tensioning system that was also a contributor to the on-orbit failure.

Hatch Handle Improperly Stowed (PRACA 3348)

The handle on the ISS common hatch is used to operate the latches on the hatch. After use, the handle is stowed in a position so that it does not interfere with the mechanism. The stowage procedure relies on crew training to assure that this is performed properly. As was the case on orbit, an improperly stowed hatch handle almost caused the loss of access to the airlock. A non-standard work around luckily allowed access to be regained and new procedures are in place to assure the condition does not happen again. In review of the failure it was determined that the design does not adequately protect against the miss stow of the handle. Adequate design features to prevent the miss operation of the hardware were not provided. Anytime that operator training is required to prevent what could be catastrophic consequences design solutions should be found to minimize the chance that they could occur. In this case guards are being added to the hatch to preclude improper hatch handle stowage.

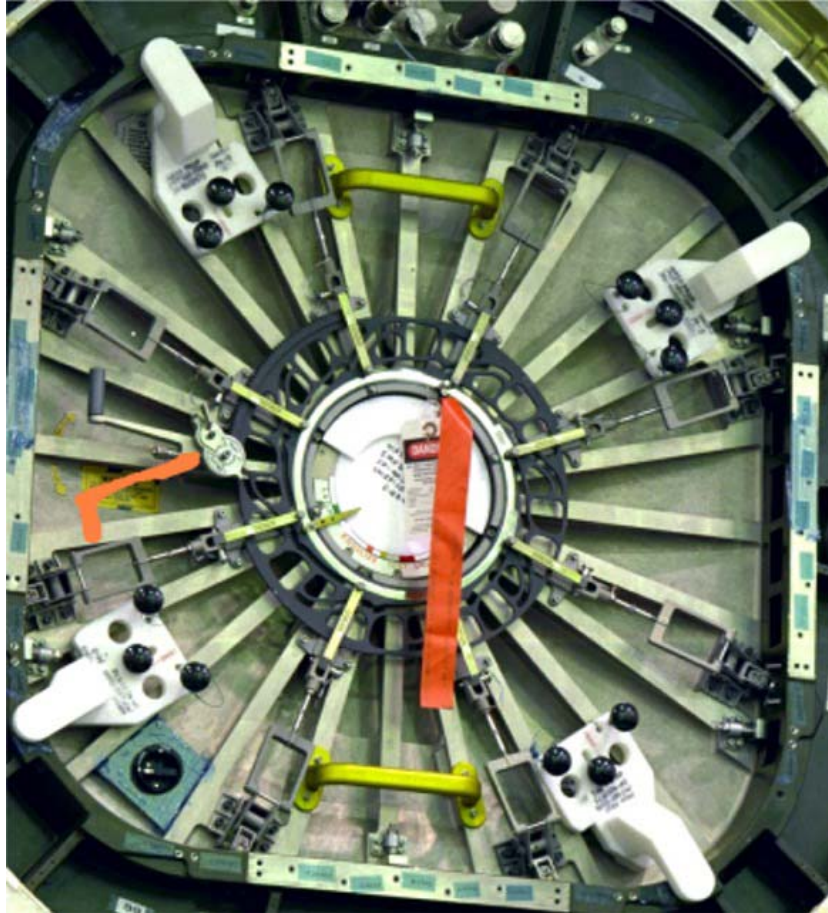


Figure 5. Photo of common hatch. Incorrect handle position in red.

Conclusion

Every failure should be looked at for lessons learned to prevent the same problem from recurring. This report attempts to look at the failures on ISS not on a case-by-case basis, but rather from a more global view of the identifying the most frequent types of failures and their root causes. A program as large as ISS affords the unique opportunity to do this because of the large number of mechanisms all being managed by one team. It was found that what appear to be the simplest of problems like tolerancing and fastener design are still the most common problems in the development and operation of spacecraft mechanisms. A large number of design problems were not identified until qualification and acceptance tests were performed, reinforcing the validity of these tests even in the face of cost and schedule pressures. Care must be given in design reviews of even the simplest mechanisms that adequate attention is paid to details especially when they can directly affect system performance. Mandatory inspection points should be called out to assure all critical dimensions are check and functional tests should always try to replicate the environmental conditions that the hardware must operate in. It is hoped that these results will be used to focus designers of future spacecraft mechanical system to be sensitive to the most common failures that have been experienced on ISS.

Space Station Berthing Mechanisms, Attaching Large Structures On-Orbit that were Never Mated on the Ground

Robert M. Foster*, John G. Cook*, Paul R. Smudde** and Mark A. Henry⁺

Abstract

A significant benefit resulting from the International Space Station (ISS) program has been the development of common mechanisms to attach the various modular components together in orbit. Several different mechanisms were developed to make assembly and growth of the ISS possible. This paper addresses the driving design requirements and verification activities associated with these mechanisms that ensure that all ISS modules, built in different parts of the world and not coming in contact prior to on-orbit assembly, would fit together without problems.

Introduction

Two basic types of berthing mechanisms are used on ISS. The first type, pressurized berthing mechanisms, require the establishment of a pressurized passageway for transfer of crew and equipment between inhabited volumes. Included in this type are the Boeing-designed Common Berthing Mechanism and a number of Russian-designed mechanisms that were used in their very successful MIR Space Station Program. The second type, unpressurized berthing mechanisms, is used to attach the various modules on the outside of the ISS. Included in this type are the Truss element assembly systems and their derivatives used to attach external payloads and other components to the ISS.

All major ISS elements are positioned using a robotic arm, either the Shuttle Remote Manipulator System (SRMS) or the Space Station Remote Manipulator System (SSRMS), resulting in similar initial mating conditions for all berthing mechanisms. However, the interface geometry and the resulting post-mate configurations are very different. Therefore, each of the berthing mechanisms is uniquely designed to meet the specific requirements and needs of the interfaces that they join.

This paper focuses on four berthing mechanisms used to assemble ISS components. They are as follows:

- Common Berthing Mechanism (CBM)
- Segment-to-Segment Attachment System (SSAS)
- Rocketdyne Truss Attachment System (RTAS)
- Common Attach System (CAS)

An exploded diagram of the International Space Station identifying the major assembly elements is shown in Figure 1. This figure shows which elements are already assembled in orbit and the additional elements, built by the United States and our International Partners, that are to be installed as the International Space Station is completed. Each of the mechanisms discussed in this paper has already been used at least once during assembly of the ISS.

* The Boeing Company, Houston, TX

** The Boeing Company, Huntington Beach, CA

+ The Boeing Company, Huntsville, AL

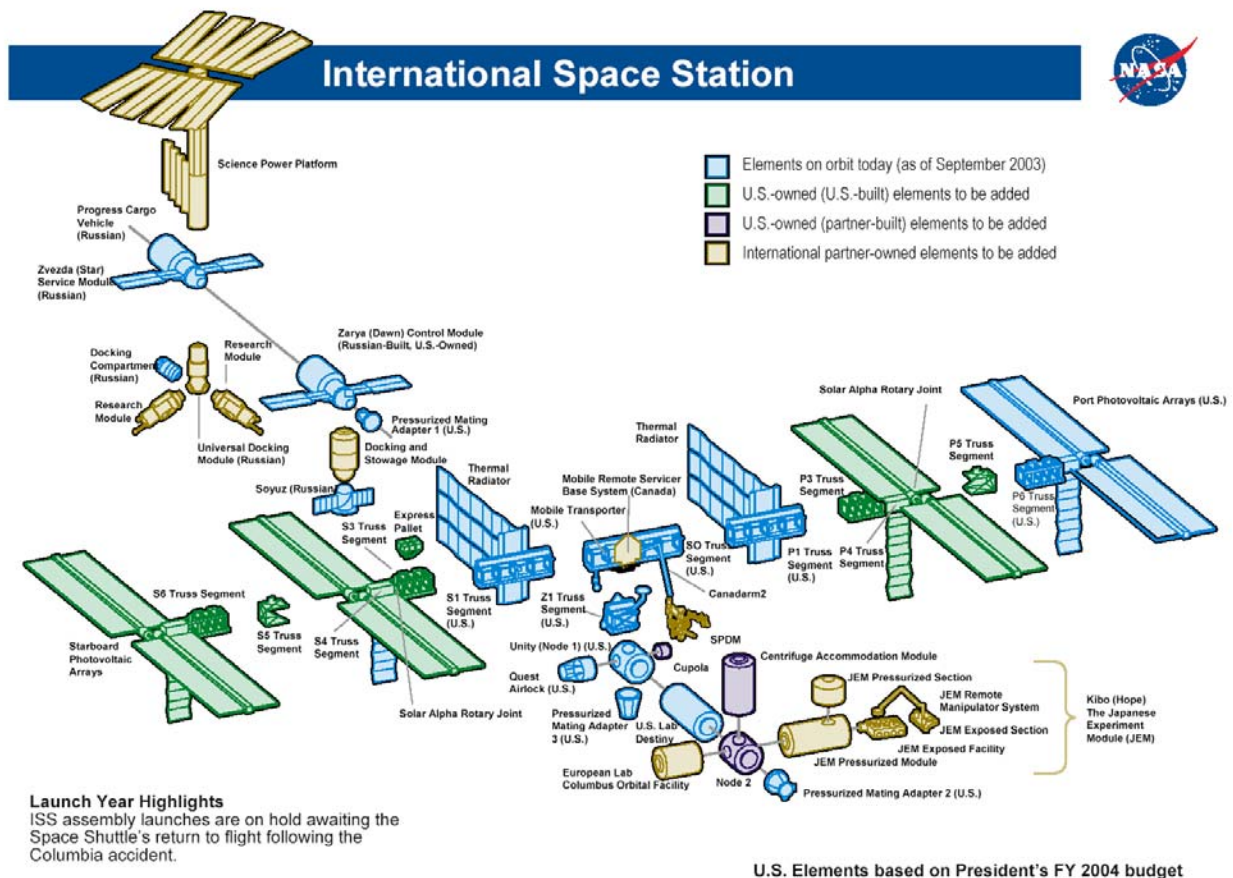


Figure 1. International Space Station Assembly¹

Generic Berthing Requirements

There are two distinct methods, berthing and docking, for attaching elements together in space. Both of these methods are used on ISS. Berthing is defined as assisted attachment using either the Orbiter (SRMS) or the Space Station Remote Manipulator Systems (SSRMS). Docking is unassisted attachment of an autonomous vehicle or element. Examples of docking are the Orbiter to ISS and Russian Soyuz or Progress vehicles to ISS. All of the ISS elements that are delivered in the Orbiter Payload Bay are berthed to the Space Station.

Many of the requirements that drove the berthing mechanism designs apply to all berthing mechanisms.² Each mechanism must accommodate uncertainties in Remote Manipulator System (RMS) control, dictating a relatively large capture envelope for the transition from RMS operation to berthing mechanism capture device operation. Final alignment, on the other hand, must be precisely controlled in order to orient the elements correctly, and the berthing mechanism design must be able to pull the elements into their final alignments, preload the interface, and then provide a structural attachment sufficient to react the interface loads. For the CBM, SSAS and CAS, the large capture envelope and remote operation of the mechanism requires feedback to indicate when the elements are in range of the capture mechanism, hence the incorporation of ready-to-latch indicators and telemetry. The RTAS has a similar capture envelope; however, the ready-to-latch indication is visual only due to the RTAS being manually operated.

¹ NASA Illustration: http://www.hq.nasa.gov/osf/ISS_Core_Program.pdf

² SSP 41000, "System Specification for the International Space Station", 01 Oct 2003

Each berthing mechanism design was also driven by unique requirements for that interface. The CBM³ must provide a pressure seal and a passageway for crew and equipment between modules. The SSAS⁴ is fully automated to minimize EVA operations for the inboard truss element berthing, while the RTAS is fully manually operated due to difficulty in getting power and data across the rotary joints between the inboard and outboard truss elements. The CAS, used for temporary installation of payloads and cargo carriers, has no requirement for a bolted structural attachment, but instead relies on the capture mechanism to carry structural loads.

Common Berthing Mechanism (CBM)

The CBM is the ISS-developed mechanism used to assemble the inhabited volume of the Space Station. All pressurized modules, with the exception of the Russian modules, use this mechanism design to provide a common attachment interface. The CBM (Figure 2) is a fully automated mechanical system that aligns, captures, and then bolts together the two elements. The CBM also provides the atmospheric seal features for establishing the pressurized passageway between the modules (shirt sleeve environment). The development of this mechanism was covered in a paper presented at the 26th Aerospace Mechanisms Symposium, "Space Station Freedom Common Berthing Mechanism", by Eric Illi of The Boeing Company⁵.

CBM Design Features and Operation

The CBM is a complex system of mechanisms that work together to accomplish berthing of pressurized ISS modules (Figure 3). A major design driver for this mechanism is the requirement to provide an unobstructed passageway through the CBM between the modules. This requirement precludes the use of a central capture mechanism to pull the interface together. This requirement drove all of the alignment, capture and preload mechanisms to the perimeter of the CBM system. At each berthed interface there is an Active CBM half and a Passive CBM half. The Active CBM half is located on the ISS side of the interface and encompasses all of the static and motor actuated mechanisms, telemetry and control system. The incoming element to be berthed contains the Passive CBM half, with all of the receiving mechanisms for the Active Half. The Passive CBM also contains the atmospheric seal that mates to the Active half seal surface. The CBM system is designed such that any Passive CBM half can berth to any Active CBM half.



Figure 2. CBM berthing of MPLM on Node 1 (on-orbit photo)

As the element being berthed approaches the ISS, The Active and Passive halves begin to interact. Coarse alignment guides begin to align and center the two halves as they are moved closer together by the Shuttle or Space Station Remote Manipulator System (SRMS/SSRMS). At about 11.4 cm (4.5 in) separation, Ready to Latch mechanisms are tripped, sending a signal to the RMS operator that the two halves are close enough for the CBM to take over the remaining berthing operations. Capture latches, with electro-mechanical actuators, on the Active half extend and pull the Passive half into the Active half. Coarse alignment guides continue the aligning until handoff to the fine alignment components. A set of

³ S683-29902 "Active Common Berthing Mechanism Prime Item Development Specification", 01 Oct 1998

⁴ SP-M-598D "Configuration Item Specification for the Segment to Segment Attachment System", 05 Dec 2001

⁵ Proceedings of the 26th Aerospace Mechanisms Symposium, May 13-15, 1992, page 281

fine aligning pins on the Active half engage sockets of the Passive half to begin the final alignment of the two halves. Standoff plunger assemblies (spring loaded shock absorbers) of the Passive half react against Strike Plates of the Active half to ensure relative motion of the halves is dampened and prevent uncontrolled seal contact and seal damage before capture is complete. Once capture and alignment is complete, the two halves are ready to be structurally preloaded together. This is accomplished by sixteen electro-mechanical actuator driven powered bolt assemblies, equally spaced around the perimeter of the Active half, extending and engaging floating nut assemblies on the Passive half. The powered bolts are loaded in a series of steps to evenly distribute the loads, ensuring proper seal contact and compression along with required preload for pressurization and on orbit loading of the berthed ISS modules. Shear and torsion loads are reacted by the fully engaged fine alignment pins and sockets. The electro-mechanical actuators on the powered bolts and capture latch assemblies are powered and controlled by individual motor controllers grouped into four sets of five controllers on removable controller panel assemblies. An RS-485 local bus network within the Active CBM interlinks the controller panel assemblies. The Active CBM is, in turn, linked to the ISS internal computer through a MIL-STD-1553 Bus network.

After berthing and pressurization is complete, the controller panel assemblies can be removed, thereby enlarging the available passageway between the ISS modules to the maximum allowed by the hatch envelope (an approximately 127 cm (50 inch) square opening).

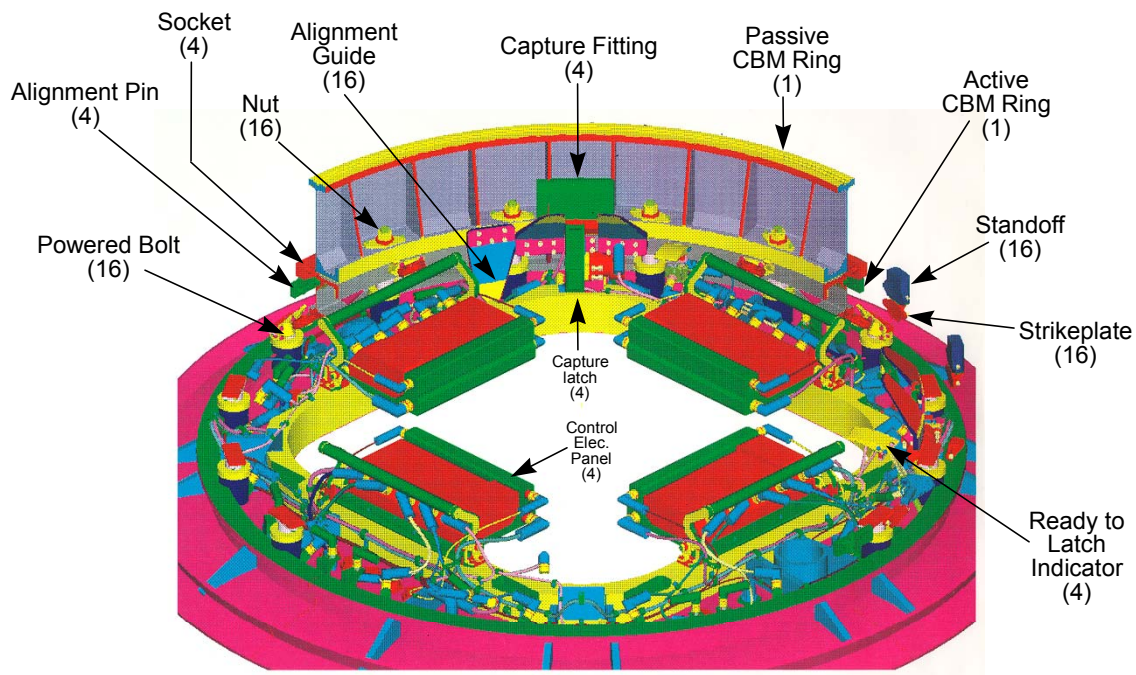


Figure 3. CBM major components

CBM Verification

The verification of the CBM system was accomplished using a combination of tolerance analysis, FEM and Thermal analysis, capture dynamics analysis and testing, component level testing, standalone system level testing and flight article testing.

Component Level Testing

Capture Latch, Powered Bolt and Floating Nut, Ready to Latch, Coarse Alignment Guides and Fine Alignment Pins and Sockets verification testing were performed at component levels. Alignment Guides and Pins/Sockets were subjected to static load testing only. Capture Latch testing established the component mechanism operation, reach ability and capture operation. Powered Bolt/Floating Nut testing established the component mechanism operation, reach and pre-loading capability. Ready to Latch testing established the component mechanism operation. Verification of operation for these three

mechanisms were also performed after random vibration testing and operation performed in a thermal vacuum with exposure to predicted hot and cold extremes.

System Level Testing

In order to ensure that the CBM design would work correctly for all of the different applications on ISS, including the different pressure and thermal environments it would see during berthing operations, three phases of system level testing were performed.

Phase 'A' testing developed the thermal profiles and sealing capabilities of the CBM in various configurations and conditions. A set of thermal balance tests were performed on full-scale CBM test articles at the Arnold Engineering Test Center Solar Simulation Test Chamber in Tullahoma, Tennessee. Thermal data obtained allowed validation of thermal models for establishing qualification testing thermal conditions. Full-Scale Seal Tests validated the sealing ability of the CBM at various deflected and thermal conditions.

Phase 'B' implemented six degree of freedom (Six-DOF) testing to validate the capture dynamic analysis and determine the capture envelope. Initial conditions were established which placed the Passive half in orientations (lateral offset, roll offset and pitch (wobble) offset) to the Active half in order to establish the capture envelope. Capture latch operations were performed to pull the Passive half to the Active half into the position for which bolting operations would begin. Initial testing was performed on the Marshall Space Flight Center (MSFC) Six-DOF table. A Six-DOF resistive load system was developed and placed into the 20-foot vacuum chamber at the MSFC facility. Follow on ambient and vacuum six-DOF testing was performed, establishing the initial condition parameters for the follow on Phase C testing.

Phase 'C' testing culminated in the CBM performing complete berthing operations at deflected conditions of the Active and Passive halves, thermally conditioned (hot active / cold passive, hot passive / cold active), at sets of initial conditions, based on Phase B testing, through complete capture and preloading events and performed at vacuum. This test set up was performed in the same 6-m (20-ft) vacuum chamber as the Phase B testing with the Six-DOF resistive load system. The test setup is shown in Figure 4. The separate pressure vessels in the vacuum chamber induced the pressure deflections to each CBM interface. Pressure deflections were based off of ISS pressurized module structural testing and validated FEM analysis. Leak rate testing was performed to ensure the sealed joint was leak tight. Complete de-berthing operations were performed to validate all the functional requirements.

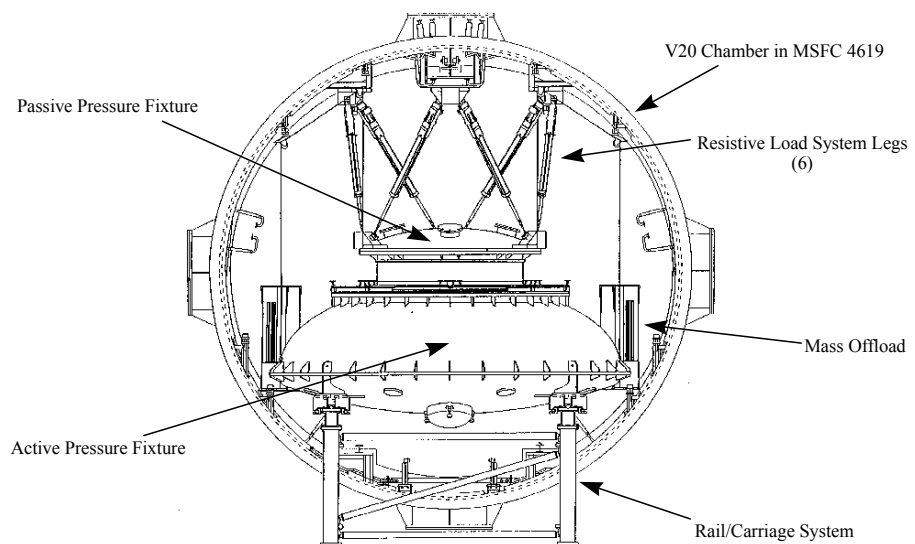


Figure 4. CBM Assembly Level Qualification Test Fixture

Flight Article Acceptance Testing

With all components installed and integrated in the flight configuration on the ISS pressurized module, a standalone acceptance test of the CBM is performed. The standalone test is performed at ambient conditions to assure the integrated CBM is satisfactorily configured prior to turnover for integrated testing

into the ISS pressurized module. The standalone test also allows parallel activities to occur on the ISS module without being constrained by the CBM and limiting access to the module hatchway.

On the Active CBM half, all mechanisms are exercised through their full motions, representing the on-orbit pre-berthing flight operations. Powered bolts are extended and retracted, capture latches opened and closed and ready to latch assemblies depressed and released. Power, command initialization and data feedback are performed and monitored through a separate support equipment control rack. Primary and redundant power strings are used with communications verified using both primary and redundant 1553 bus paths. Each Controller Panel Assembly is assigned as the Master controller through the power and data changes. A berthing simulator, representing a Passive CBM half (with interface seal) is mated to the Active CBM (Figure 5). The simulator is manually positioned to allow powered bolt engagement. Powered bolts are actuated using flight command steps and allowing load feedback to the support equipment control rack. Final load is approximately 25% of flight level pre-load, sufficient enough to allow seal compression and full contact at the interface. With the simulator mated, measurements are taken to ensure sufficient clearances between the coarse and fine aligning features of the CBM. Inspections are performed to assure clearances of the simulator Passive CBM components within the volume of the Active CBM half and surrounding module bulkhead features. A seal leak check is performed to ensure integrity of the Active CBM seal surface. De-berthing commands are performed to release the simulator for the Active CBM half. At this point, the Active CBM is connected to the pressurized module and becomes an integral unit of that module.

Integrated Active CBM and Pressurized module testing is performed using flight power and flight software for actuation and command of the Active CBM. Again, each mechanism is exercised through a set of motions for verification of control and data feedback. Each Controller Panel Assembly is assigned as Master for command and control functions. Conclusion of this testing verifies the Active CBM ready for flight.

On the Passive CBM half an Active CBM simulator is utilized. This is a more simplified test due to no powered mechanisms on the Passive half. The simulator is manually positioned, attached and loaded to a specified gap at the interface seal between the simulator and Passive CBM half. This gap represents the minimal compression on the interface seal for assuring leak testing of the seal. The same measurements between aligning features are performed and assurance of clearances within the Passive CBM volume made. A seal leak check is performed to assure integrity of both the Passive CBM seal surface and the installed interface seal. The Active CBM Simulator is removed and the Passive CBM is ready for flight. This set of testing is performed late in the Pressurized Module flow in preparation for flight due to the interface seal being exposed at completion of test and the location of the Passive CBM is generally the last hatchway accessed and closed for module processing.



Figure 5. CBM Berthing Simulator

The completion of standalone and integrated testing of the CBM on the Pressurized Module assures correct operation of the CBM and interchangeability of the CBM, to allow any Passive to berth and de-berth to any Active, is maintained. This set of verification and testing has resulted in the current successful twelve berthing and six de-berthing on orbit operations of ISS pressurized modules.

Segment-to-Segment Attachment System (SSAS)

The SSAS is an unpressurized mechanism used for structurally connecting the inboard truss elements (truss P1 to S0, S1 to S0, P3 to P1 and S3 to S1). The SSAS is a fully automated mechanical system that aligns, captures, and then bolts together two truss elements. The SSAS includes a centrally located capture latch assembly, three alignment guides and four discrete powered bolts to structurally attach each inboard truss element to the station as it is delivered by the orbiter.

SSAS Design Features and Operation

Since the SSAS is an unpressurized mechanism, it is not required to provide a pressure seal between elements, allowing a less complicated design solution than the CBM. A centrally located capture latch engages a capture bar and provides the force required to bring the interface into contact and ensure alignment for the bolting system (Figure 6). As with the CBM, the active elements of the SSAS, including the ready-to-latch sensors, capture latch assembly, and remotely actuated bolting system are on the active ISS side of the interface and interact with passive components on the element being berthed using the Station's robotic arm (Figure 7).

Using input from a digital imaging system and making visual observations of the interface, the SSRMS operator moves the element being attached into the berthing corridor. The SSRMS requires the berthing mechanism not induce constrained motion while the SSRMS operator is moving the payload (This was the main driver for designing the shape/size of the capture envelope and alignment guides). At about 7.6 cm (3 in) separation, ready-to-latch (RTL) mechanisms provide "positive" status feedback to the SSRMS operator. At RTL the interface is within sufficient alignment and reach for the Capture Latch to take over the remainder of the berth.

The Capture Latch is driven by either of two independent motor drive mechanisms for redundancy and has, additionally, a mechanical EVA-operated contingency override mechanism for the event of total electrical failure (both motors inoperable). As the latch claws close around the capture bar, they pull the elements into alignment and preload the interface. The latch preload provides the force to sufficiently seat the cup/cones, which align the powered bolts with their respective nuts. Once capture is complete, the four powered bolts are driven into the nuts. The bolts are engaged and tightened one at a time to provide the required bolt preload. The two Bolting System controllers and the two integrated motor controllers on the Latch Assembly are linked to the ISS internal computer network and control the bolts and capture latch respectively.

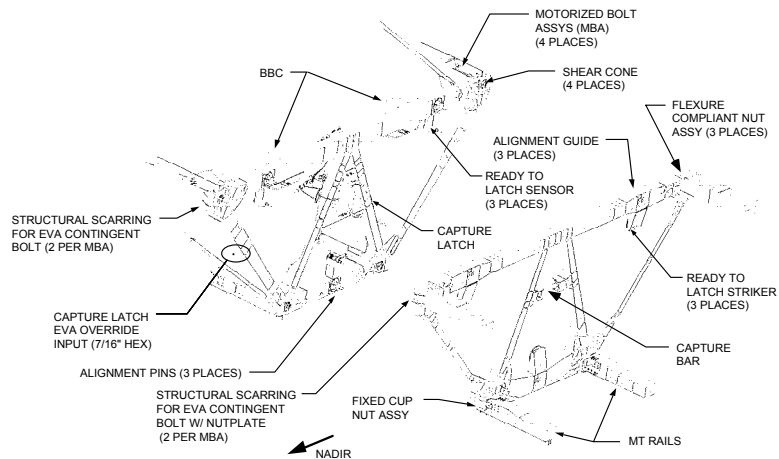


Figure 6. SSAS Components

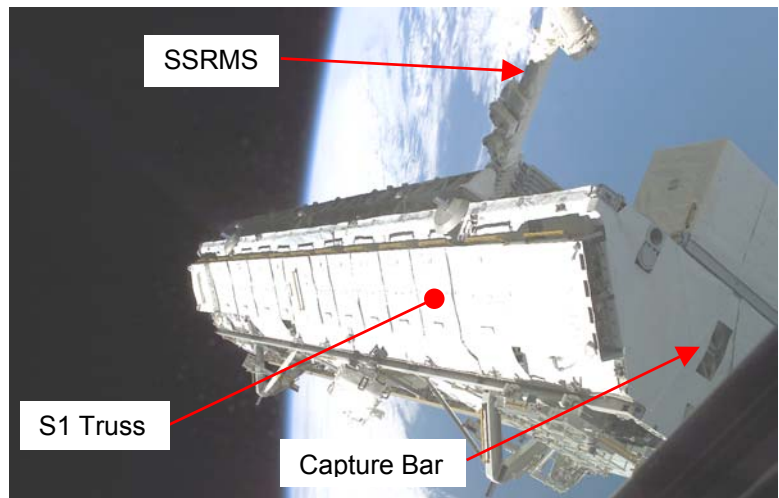


Figure 7. Truss Segment S1 being positioned for mate to S0 (on-orbit photo)

SSAS Verification

The verification of the SSAS was accomplished using tolerance analysis, FEM analysis, component testing, system level development testing, hardware fit checks and finally mission unique dynamic simulation analysis. Due to the size of each truss element (roughly 4.6 m (15 ft) in length and weigh 13.6 metric tons (30000 lb)) and the fact they have different structural and mass properties is combined with the fact the mating task is accomplished in a near zero gravity environment with one of the two truss elements being held by the SSRMS, performing a true representative system level test was deemed not practical. The cost effective approach was to perform individual component testing to validate the capability for the extreme misalignment conditions, perform limited system level development testing, perform hardware fit checks to verify installation and finally perform dynamic analysis for each of the four berthing events. Dynamic simulations, which include test proven contact dynamics characteristics of the berthing interface components, were used to verify system functionality, and prior to the system development test, used to determine the worst-case initial conditions for the test.

Capture Latch Assembly

The Capture Latch testing established the reach and preloading capability during and after exposure to the predicted environments. The assembly successfully underwent Random Vibration testing and was functioned in a thermal vacuum chamber at the hot and cold extremes. The latch testing verified the capability to capture and pull in the capture bar when anywhere within the capture envelope.

Bolting System

The Bolting system testing was performed in two phases. The first phase established the reach and preloading capability during and after exposure to the predicted environments. The assembly successfully underwent Random Vibration testing and was functioned in a thermal vacuum chamber at the hot and cold extremes. The bolt system testing verified the capability to engage the nut and preload when at the worst-case misalignment conditions. The second phase established the capability to drive together a cup and cone that are misaligned and mounted to structures of stiffness equivalent to the truss elements.

Simulation

FEM and multiple dynamic models were developed and validated using data from the S0, S1 (symmetric with P1) and P3 (symmetric with S3) truss static loads testing, the SSAS component testing, and the SSAS “system level” development testing. These validated models were refined to include the specific parameters and mating conditions for each of the four SSAS interfaces to be berthed on-orbit. The simulations were also used to verify berthing corridor, RTL performance and SSRMS interactions.

System Development Test

The key driver for the need of a development test was due to SSAS being an over-constrained system. Three of the four nut assemblies are housed inside an item defined as a “Flexure Assembly”. The flexure is a flexible structure that allows compliance in only one lateral direction. In the axial direction the flexure has an equivalent stiffness to the truss structure. The three flexure assemblies are positioned in the passive truss element such that the direction of compliance all point to the fixed cup (Figure 8).

The capture latch is required to generate preload sufficient to align the cone (bolt side) with the cup in the flexure assembly. The issue of most concern was the on-orbit structural-thermal deformations of the truss, which create the need for the flexure to move in the lateral plane perpendicular to the compliant direction. These structural-thermal

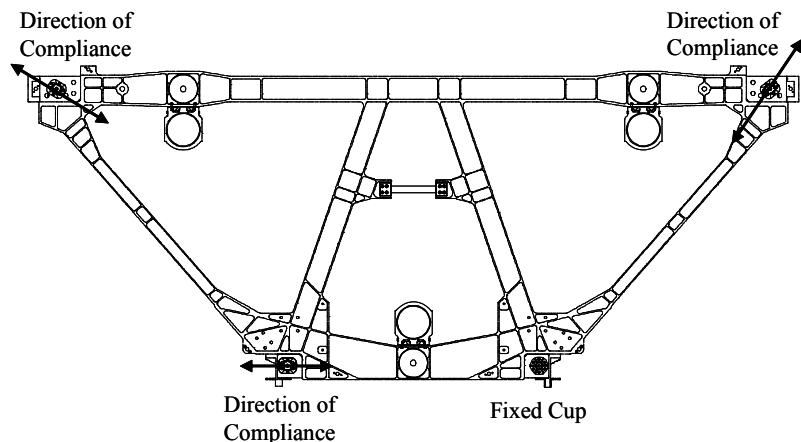


Figure 8. Flexure Compliance Illustration

models predicted deformations that translated into requiring the cup/cone interaction having to drive the truss structure back into shape. The latch preload alone was insufficient; however, the latch preload was sufficient in driving the cup/cones to a position where the remotely actuated bolt can acquire the nut.

The system testing demonstrated the bolting action was capable of deflecting the truss back into shape, seating the cup/cones and establishing the required bolt preload. The testing further demonstrated that for worst case conditions only a fraction (roughly 1/3) of the bolt preload was needed to fully seat the cup/cone.

The system test utilized the structural test article for the S1 truss outfitted with the SSAS passive interface and a structural simulator for the S0 truss was built and outfitted with the SSAS Active components. Thermal distortions were simulated by shims inserted into the joints of the S0 simulator. The S0 simulator was suspended and counterbalanced. The tests started with the S0 simulator positioned within the capture envelope. The tests concluded with all four bolts fully engaged and preloaded (Figure 9).

Acceptance Test

The acceptance testing consisted of component testing and verification of installation by three independent methods. The first installation verification was performed by the manufacturing team. The engineering drawings established the “as built” locations on the active interface as the “basic” dimensions, and the location of the mating passive interface was given a positional tolerance from these “basic” dimensions. The manufacturing team used laser tracker inspection techniques to measure the active interface and verify location on the mating passive interface. Engineering verification consisted of a hardware simulator “fit check” to check for potential interferences anywhere in the berthing interface combined with digital measurements taken using photogrammetry. The photogrammetry device uses two cameras to triangulate on a probe handle that has six light emitting diodes and calculates the location of the probe. Even though the laser tracker and photogrammetry devices are very different technologies, measurements taken by each yielded consistent data sets (on the order of 0.127 mm (0.005”)) of each other. These two independent devices alone verified the interface installation accuracy. For hardware installation accuracy the hardware fit check could have been eliminated. The SSAS has been successfully operated twice on orbit to assemble the truss elements.



Figure 9. SSAS System Test: Counterbalances are in foreground, large steel beams form part of the S0 simulator, aluminum structure in back is S1 Structural Test Article

Rocketdyne Truss Attachment System (RTAS)

The RTAS is a derivative of the SSAS, developed by Rocketdyne, used to assemble the outboard truss elements of the ISS. The RTAS is a manually driven mechanical system. The RTAS uses the same capture claw mechanism from the SSAS (except without motors, and is driven via the “contingency” manual override input), and unique, EVA crew operated, attachment bolts. Active and passive components of the RTAS are shown in Figures 10 and 11.

RTAS Design Features and Operation

The RTAS design was driven by the difficulty in getting power to the outboard truss elements on ISS during assembly. It was decided early-on to use EVA crewmembers to operate the RTAS mechanisms instead of providing computer controls and powered mechanisms. Ready-to-latch indication is provided by the EVA crew.

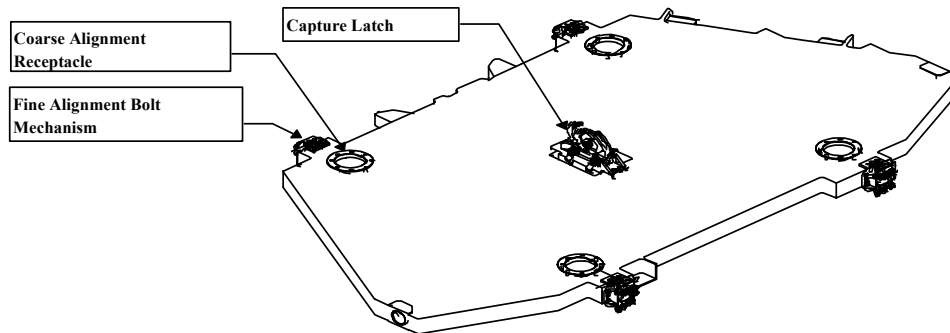


Figure 10. Active RTAS Components (Z1 Interface Plane)

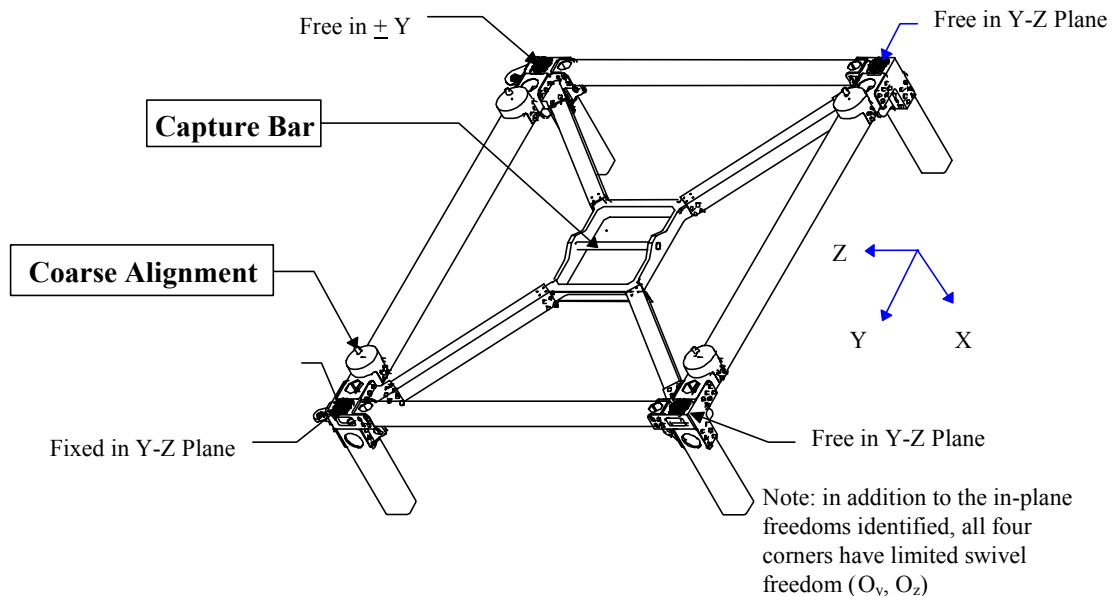


Figure 11. Passive RTAS Components (P6 Truss Interface Plane)

As the truss segment being berthed is brought into physical proximity, the visual Ready-to-Latch (RTL) indicator (a painted tip on the coarse alignment cones) disappears from view as the coarse alignment cones penetrate their receptacles. The capture procedure requires that three of four cones line up for "RTL criteria" to be met. This places the segment within the capture envelope of the RTAS. Crewmembers then use the electric EVA power tool to actuate the capture latch from the EVA worksite location. As the latch jaws close on the capture bar, the segments are pulled together. At a bulkhead-to-bulkhead distance of approximately 13 mm (1/2"), the fine alignment mechanism begins to engage

When the fine alignment mechanism fully seats in its receptacles, the capture bar is approximately 6 mm (1/4") from fully seated. Continuing to close, the capture latch deflects the capture bar an additional 6 mm (1/4"), which produces approximately 8.2 kN (1850 lb) of pre-load between the structures. At this point, the EVA crewmembers engage the primary structural attachment bolts to fasten the two segments to each other.

Bolts are tightened in sequence to ensure that they are engaging properly. Bolt pre-load is controlled with Pre-Load Indicating (PLI) washers located within the bolt mechanism. The EVA crewmembers will tighten each bolt, in series, a prescribed number of rotations before proceeding to full torque. After all bolts are fully tensioned, pre-load in the capture bar is released by EVA reverse actuation of the capture latch and the attachment process is complete.

Each corner fitting also incorporates two contingency attachment bolt/nut combinations to allow a structural connection to be made in the event the primary bolt cannot be engaged. A release mechanism, an EVA-operated PIP pin, allows disconnection should the primary EVA bolt become locked in the sleeved nut after assembly. RTAS design also includes capability to replace a nut (insert) in the RTAS fine alignment assembly. A threaded spacer serves to maintain the gap between the fine alignment housing and the corner fitting so that no bolt-bending loads are created. Shear is transferred through the shear cylinder on the main bolt.

RTAS Verification

The verification of the RTAS was accomplished in a similar manner to the SSAS verification, using tolerance analysis, FEM analysis, component testing, system level development testing, hardware fit checks and finally mission unique dynamic simulation analysis. Since the capture latch is common to both the SSAS and the RTAS, no additional component level verification beyond the capture latch verification performed for the SSAS was required. The fine alignment bolt assembly testing closely paralleled the two phase testing performed for the SSAS bolting system. Acceptance testing was performed at the component level and followed by assembly level verification of component locations using the same methods used for the SSAS. The RTAS was successfully operated on orbit to assemble the P6 Truss Element to the Z1 Truss Element.

Common Attach System (CAS)

The CAS is another derivative of the SSAS used to temporarily attach various payloads (experiment pallets, logistics pallets, etc) to the S3 and P3 truss. The CAS includes the capture latch mechanism, three alignment guides and an umbilical mechanism. The structural attachment is accomplished when the capture latch claws establishes a preload against the alignment guides.

CAS Design Features and Operation

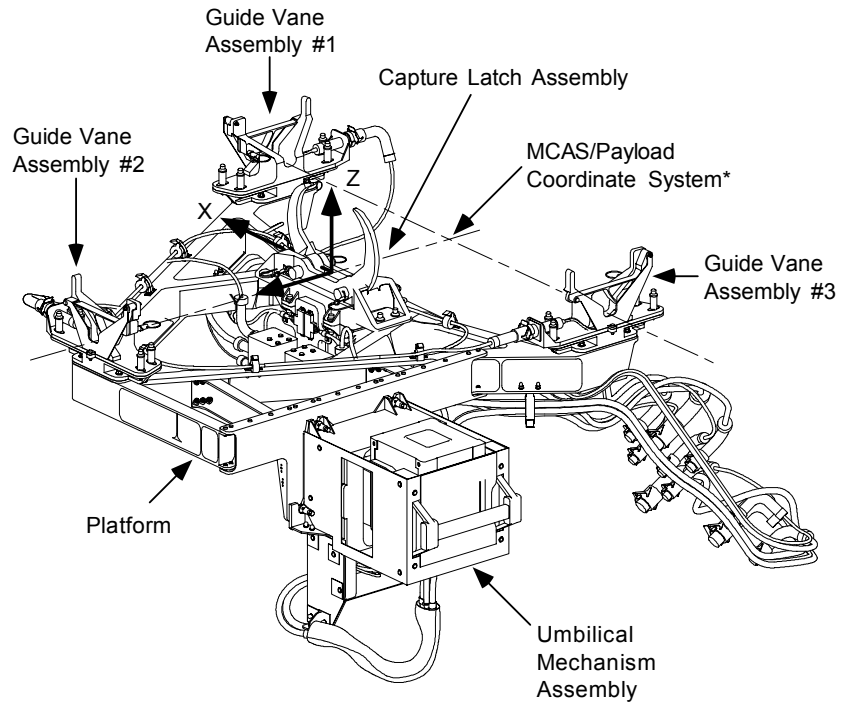
The CAS uses the same capture latch as SSAS; however, due to the alignment guides being part of the load path, they are of a different design (Figure 12). The berthing process is the same as SSAS except once the latch is closed the attachment is complete (no bolting system). The last operation is to engage a remotely operated umbilical mechanism (power and data). The umbilical mechanism is driven by either of two independent motor drive mechanisms (same motors as used in the capture latch) for redundancy and has, additionally, a mechanical EVA-operated contingency override mechanism for the event of total electrical failure.

CAS Verification

The CAS uses the same verification strategy as SSAS with one exception. Each active CAS must be compatible with all passive CAS. Unlike SSAS, the CAS design is not over-constrained and is therefore more compliant to variations between assemblies. Similar to SSAS the CAS verification entailed hardware fit checks and digital inspections. Due to there being only one passive simulator, all possible variations could not be verified. An analysis of the digital inspections in conjunction with the fit check data is used to verify the interface will indeed accommodate worst-case tolerances. A variation of the CAS was used successfully on orbit to stabilize and temporarily attach the S0 Truss to the U.S. Lab Module.

Final On-Orbit Assembly Verification

Assembly of the International Space Station, accomplished far from the manufacturing floor on-orbit, introduces some unique problems. Each stage of assembly, as hardware and increased capability is added to the vehicle, must result in a viable, life-supporting vehicle, with no loose ends or safety issues for the vehicle or the crew inhabiting it. Failure to berth a new element of the Station incurs immense costs as that element must then be returned to earth and re-launched or, possibly, discarded. Compounding the problem - time, distance and budget constraints in almost every case preclude trial assembly and fit on the ground prior to launch. In many cases, the new element was not even built when the element it is to be berthed to was launched.



* X-Y Plane located on GVA well bottom centerlines.
X-Z Plane located at CLA centerline.

Figure 12. Active CAS Platform

A process was developed to minimize the risk inherent in assembling the elements for the first time on-orbit. This process, titled "Assembly Analysis", uses a combination of CAD models, as-built measurements, and computer-based analysis tools to verify the berthing mechanism will fit properly, that pressure and thermally induced deflections and distortions can be accommodated, and that no hardware external to the berthing mechanism will cause interference problems. Use of this process has resulted in a number of hardware modifications prior to launch and a 100% success rate for on-orbit berthing operations.

Assembly Analysis uses kinematic CAD software to process multiple interference checks in an automated fashion. The CAD software moves the incoming element through a set of lateral and angular misalignments that bound the nominal approach corridor. During movement, at specific intervals, interference checks are conducted. The first interference for each path is identified, and the incoming element moves to the next start point. The interferences can then be plotted as a mesh (Figure 13). This mesh is a method to visualize the hardware constraint corridor. Use of this method makes it easy to visualize intrusions into the nominal approach corridor. By moving the incoming element through this regimen of interference checks, we can show that there are no interferences between the geometry.

As-built measurements are used to update the CAD models. This is accomplished by measuring the hardware in a common coordinate system. This is accomplished by using a digital photogrammetry system. This system allows for the precision measurement of the hardware relative to the CAD model of the hardware. The measurement data for each part is saved as a cloud of points. The CAD geometry for each part is then best fit to the respective cloud of points.

On-orbit effects are added by a similar process. Finite element models are created of the interface hardware and they are subjected to thermal and pressure loads to determine the deflections. These deflections are captured as a cloud of points and the CAD geometry is best fit to this cloud of points.

A critical aspect of this process is control of hardware and CAD model configuration. In order to obtain valid results, the CAD model must match the hardware. Configuration control is further complicated as the on-orbit hardware changes from the as-launched "Cargo Element" into an integrated ISS module through a series of on-orbit modifications and deployments. An example of the level of model fidelity is shown in Figure 14, where the hardware photo and CAD image are presented side-by-side.

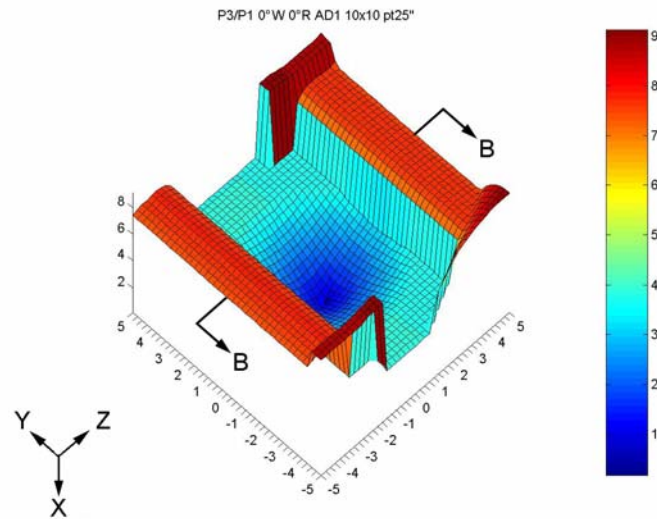


Figure 13. Assembly Analysis Map of Representative Berthing Corridor

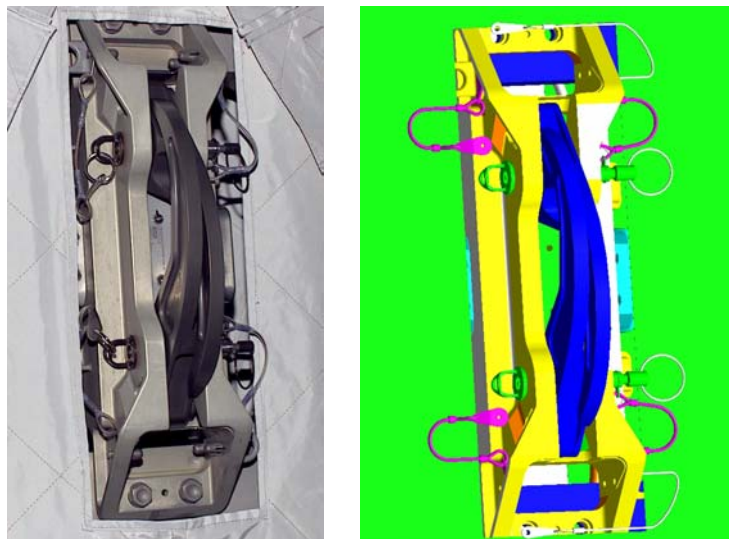


Figure 14. Photo of Common Capture Claw Compared with CAD Model

Lessons Learned

- 1) Qualification of mechanical systems should, as much as possible, establish the full capabilities of the system. Minimum testing that just meets the requirements, while initially less expensive, leaves no margin that can be exploited later to resolve unforeseen problems or operations changes.

As each of these mechanism designs matured, and our understanding of the overall integration task for ISS grew, additional requirements surfaced. A prime example of this is with the modified RTAS mechanism used to assemble the outboard truss elements. Initially the short spacer between the two solar array trusses was planned to be installed by the EVA crew and the mechanisms designed with that in mind. Only recently, operational concerns have led to a requirement to use the SSRMS to perform the initial installation of the short spacers (P5 and S5, See Figure 1). This change has resulted in a tremendous amount of analysis and testing to determine the compatibility

of this interface with the robotic arm and the possible redesign of parts of the mechanism. More thorough exploration of the mechanism capabilities during qualification would have reduced the amount of work needed later to adapt to this new requirement.

- 2) Configuration control of the entire process, including CAD models, drawings, manufacturing steps and operations planning is essential to successful integration of complex systems.

Without rigorous configuration control, integration of the numerous subsystems and components of a complex system like ISS becomes nearly impossible. It is impossible for each person working on the project to keep track of everything that is being done, to understand how changes to one subsystem affect others, and to coordinate their efforts without a controlled configuration, and a clearly defined process for updating that configuration. With rigorous configuration control, new processes (i.e., Assembly Analysis) have greatly reduced the risk inherent in first-time on-orbit assembly of ISS elements.

- 3) The analysis process must accommodate the need for configuration control with the need to minimize CAD model size and complexity.

Currently, the state of the art in computer aided design and modeling does not provide the processing capability or storage space for fully detailed models of the entire Space Station to be manipulated. Therefore, simplified models must be built in order to perform the needed analyses. Controlling the configuration of these simplified models, which of necessity do not match the configuration-controlled master becomes very difficult. The ISS-developed CAD modeling architecture, wherein high-fidelity models of individual details can be easily placed in their correct locations in an overall low-fidelity assembly, makes it possible to see the points of current interest in an assembly in great detail, without overloading processing capability or memory.

- 4) Much benefit can be realized by emphasizing communication between teams that are designing similar hardware and utilizing common hardware across designs.

A prime example of the benefits of this approach can be seen in the various mechanisms developed for berthing the unpressurized truss elements of ISS. Each variant, designed by different groups to differing requirements, builds upon the others, with a common capture latch used throughout. This commonality resulted in a reduction in required testing and analysis and in a reduction in crew training.

- 5) For complex interfaces such these on-orbit berthing mechanisms it is essential that the engineering design, manufacturing and CAD modeling teams work together through the entire process.

Common CAD models, first developed by the designers, were used by the manufacturing teams for planning, then updated using as-built measurements by the assembly analysis team to verify final fit and function.

Berthing mechanisms and the assembly processes developed for ISS are an essential component of any future manned operations in space. Rendezvous and docking between different vehicles and assembly of Space Stations and large vehicles in space will require common interfaces. Compatibility of new berthing mechanisms with existing ones will be a requirement that will drive to a minimum number of common berthing interfaces for all space vehicles. A set of viable interfaces has now been developed, tested and is in use. Certainly improvements will continue to be made, but they will follow the path developed by the International Space Station Program.

Mechanism Analysis and Verification Approach for ISS Truss Assembly

Wesley Bruner^{*}, Carlos Enriquez^{*} and Sreekumar Thampi^{*}

Abstract

Analysis and verification of an International Space Station (ISS) element berthing mechanism is a highly integrated problem, due to its dependency on other systems like robotic manipulators. Yet the mechanism is required to be verified stand-alone with the understanding of all the integrated variables. Failure to do so, can severely constrain the functionality of the mechanism to the point of operational failure during on-orbit operations. This paper explores some of these variables as they are accounted for and imbedded in the analysis and simulations that must be performed to declare the mechanism verified and ready to fly, particularly in the area of contact dynamic simulations. Consideration is specifically given to Modified Rocketdyne Attachment System (RTAS) mating mechanism coarse and fine alignment geometry, friction coefficient, mechanism behavior under load during capture operations, and the ability of the mechanism to achieve “soft” capture. These and other areas yield the variables that are described, quantified and analyzed in an effort to make sure the mechanism performs without anomalies during the truss assembly operations. This paper discusses these challenges in an effort to state lessons-learned that can lead to advancements in the arena of verification of on-orbit assembly mechanisms.

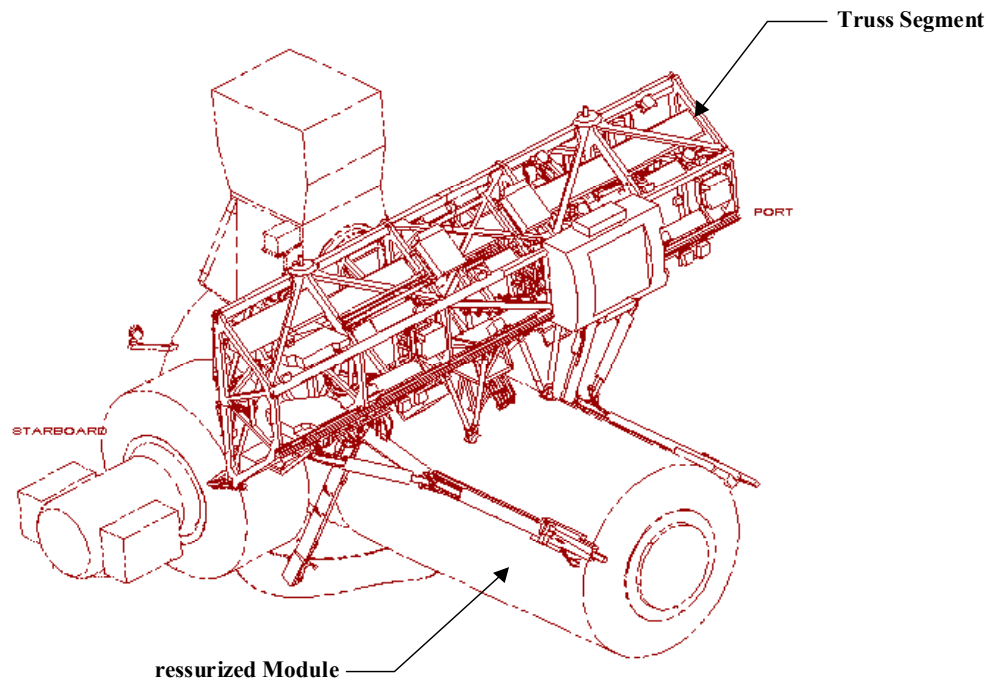
Introduction

The Boeing Company is the largest aerospace company in the world. Since the early 1900s, Boeing has been building commercial airplanes. It now builds nine commercial jet aircraft product lines that service airlines and countries throughout the world. The Boeing Company also builds military aircraft and other defense products. Boeing’s involvement in space dates back to the Apollo Program with achievements such as the responsibility for integrating the 363-foot-tall Moon-bound Saturn V rocket. On the final three trips, Apollo astronauts also explored the Moon with the Boeing Lunar Rover. Today, The Boeing Company builds commercial satellites and commercial launch vehicles. In addition, it is the nation’s largest NASA contractor¹.

In 1993, Boeing was chosen to lead the US industry team for the International Space Station. Since then, Boeing has undertaken the task to develop the processes to design, build, and integrate the largest space vehicle that has ever been assembled. Multiple pieces of the ISS are brought from Earth to be assembled in orbit. There will be a total of 43 assembly flights using hardware developed and manufactured in five different countries. After seven American assembly flights and four Russian flights, the ISS received a permanent crew on-board. Each assembly flight adds elements weighing approximately 15,875 kg (35,000 lb). Each of these elements brings critical components of every system that make the ISS self-sustaining until the next element is brought to be assembled.

To support the micro-gravity research and experiment goals of the ISS, it is composed of pressurized modules and trusses. Figure 1 shows representative modules and trusses of the ISS.

^{*} The Boeing Company, Houston, TX



The pressurized modules provide a habitable environment at Earth-normal atmospheric temperature and pressure. This environment allows research to be conducted in a shirtsleeve laboratory environment for the astronauts. The trusses are an open framework structure similar to a bridge truss. The trusses support the array of systems that are needed to make the ISS a viable orbital vehicle, such as the electrical power system; the thermal control system; the guidance, navigation, and control system; and the mobile servicing system.

The US-built elements of the ISS are assembled using berthing mechanisms, the types and uses of which are given in Table 1.

Table 1. Assembly Mechanism Types and Usage Summary

Assembly Mechanism	Qty	Type	First-time use	Final Attachment Mode
Common Berthing Mechanism	23	Pressurized	16	Automated
Truss Attachment System	6	Non-pressurized	4	Automated
Truss Attachment System	8	Non-pressurized	8	EVA Attached

The berthing mechanism used to attach pressurized modules together provides a pressurized path between the ISS habitable elements and maintains structural integrity between them. Another type of berthing mechanism is used to join the truss structures that are the backbone of the ISS. These truss attachment mechanisms provide structural attachment only, since truss segments are not pressurized. There are 48 first-time uses of berthing mechanisms. The Common Berthing Mechanism (CBM) is used to berth pressurized US elements and International Partners, except for the Russians. The Russians provide their own docking mechanisms that serve the same function as the US assembly mechanisms. The truss attachment systems are used only to join US-built truss elements¹¹.

Each berthing task is accomplished using a robotic manipulator system to maneuver the element from the US Space Shuttle cargo bay to the assembly location on the ISS. The element is positioned at the final pre-assembly location with an accuracy of ± 0.1 inches during berthing operations. The final phases of

assembly are performed automatically by the assembly berthing mechanism or with the help of astronauts performing manual tasks during Extra-Vehicular Activities (EVA).

The distance between the two mating elements at the final pre-assembly locations will be within 15 to 20 cm (6 to 8 in). At this point, all attachment mechanisms have similar specific functions that support the berthing operation. One of the functions is alignment and the other is forming secure, structural joints at the end of the mating phase. The mechanisms are composed of two halves: a passive half and an active half, each residing on opposite sides of the mating elements. All powered, moving parts that affect the berthing operation reside in the active half. These parts typically consist of gear-driven capture latches and bolts. The automated mechanisms are motorized and actuated by means of commands sent through remotely controlled computers. In the case of EVA-driven mechanisms, astronaut tools drive the capture latch and bolts⁷.

At the start of the berthing phase, each attachment mechanism provides the alignment function between two elements. Alignment guides or cup and cone arrangements that center the modules or trusses with respect to each other accomplish the alignment function. The alignment phase is performed in parallel with the capture phase. Mechanical attachment systems perform this operation by computer-controlled motors or EVA-driven latches. Capture is the most critical phase of operations. The final alignment or fit of the elements must be such that the active bolts can acquire the passive nuts to join the mating elements structurally.

During capture, the two elements being assembled interact through the berthing mechanisms and with the Space Station Remote Manipulator System. (SSRMS). The SSRMS positions the incoming truss within the prescribed positioning limits of the capture latch. Each mechanism has a capture system that may be composed of latches, or other devices that hold the two elements until bolts can be operated to final preload. The SSRMS provides a limited amount of push force due to the nature of its design. This force is also dependent on the configuration of its robotic joints. For one of the truss attachment mechanisms on Space Station, the MRTAS, the capture mechanism interaction forces must always stay below these limits in all conditions for capture to be successful. The interaction of this particular mechanism and the SSRMS during the alignment and capture phase is the subject of this paper.

Statement of the Problem

The criticality of fit and functionality of the mating ISS elements require assurance that the design verification methods used are accurate and that the mechanisms behave as analyzed and predicted. Mathematical models that quantify the forces of interaction between the active and passive mechanisms use techniques to correlate the predictions to component and system-level ground test data, on-orbit behavior with regard to friction, dynamic response and interaction with the robotic manipulator. These models are then incorporated into simulations that take into account the crew interaction with the manipulator and the environmental conditions during berthing³. Final predictions considering the integrated manipulator/mechanism the contact dynamic analyses yield quantified assurances that the mechanism can successfully achieve capture during berthing using the SSRMS.

Purpose of the Study

The purpose of this paper is to provide a brief summary of the initial contact dynamic analyses that account for the major variables that come into play to define the capture forces of the berthing mechanism for the P5 Truss, the Modified Rocketdyne Truss Attachment System (MRTAS). Due to the unique structural geometry in the area of the mating interface, the MRTAS is the one berthing mechanism on the ISS that does not have a long-reach capture mechanism. Therefore it must rely on the robotic manipulator to “push” the P5 Truss into the “soft dock” position a couple millimeters away from the final fully mated position. This of course requires precise guidance of this large truss segment into place by the SSRMS to avoid high resistive loads or “jamming” of the mechanism prior to achieving soft capture. In addition, the force that would have been provided by a long-reach mechanism to “seat” the interface, where it can be bolted, must also be provided by the SSRMS. Hence, it is necessary to accurately define the engagement and seating forces to assure berthing success.

Hardware Description

The P5 Truss is structurally attached to two other integrated trusses of the ISS on either side; the P3/P4 and the P6 truss segments. The purpose of the P5 truss is to separate the trusses that contain the solar power modules and arrays. These trusses produce power from large photovoltaic solar cells. The location of the P5 Truss on the port side of the ISS is shown in Figure 3.

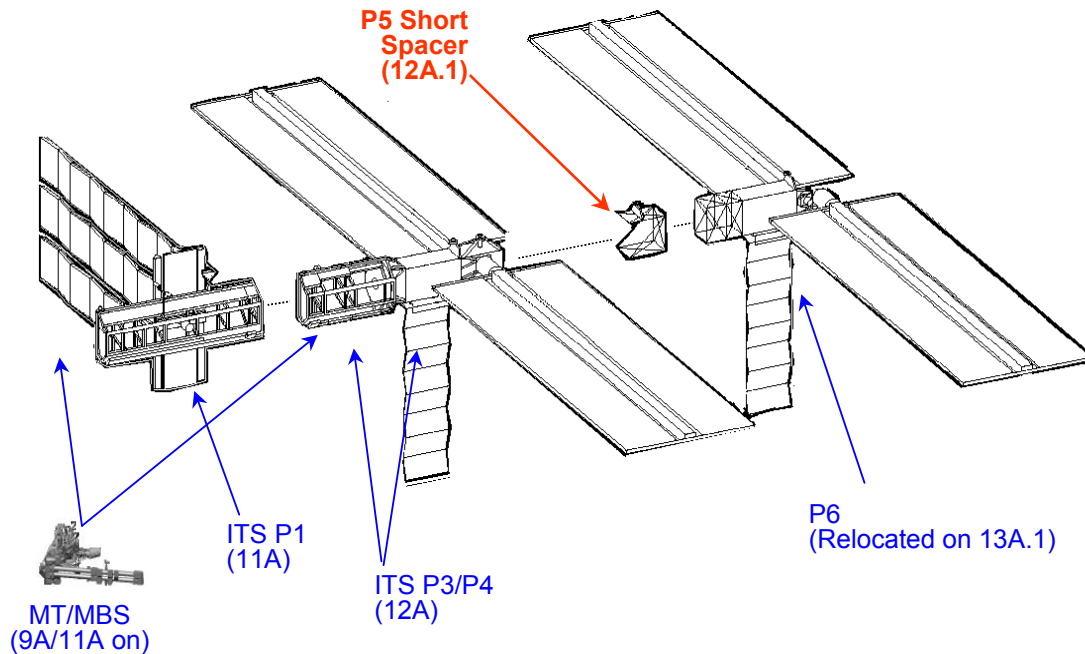


Figure 3. P5 Truss Location on the ISS

The P5 truss weighs approximately 1225 kg (2700 lb) and is composed of tubular aluminum members. These members are arranged so that one end is open and the other end provides a square planar arrangement. The truss can fit in a cubical space that measures approximately 4.6 m (15 ft) a side. The structure has a set of trunnions that interface with the Space Shuttle and serve the purpose of carrying the structural launch and emergency landing (if required) loads.

The P5 Truss has three interfaces of interest for this study. These structural and mechanical interfaces are shown in Figure 4. For clarity purposes, the figure does not show Multi Layer Insulation blankets that provide thermal protection⁵ for the truss during on-orbit operations.

On one end, the P5 truss interfaces with the P3/P4 truss segment through the MRTAS berthing mechanism, the focus of this study. On the other end, it interfaces with the P6 truss segment via another berthing mechanism, the Rocketdyne Truss Attachment System. Thirdly, the truss also has a Flight Releasable Grapple Fixture. Unlike other grapple fixtures on the ISS trusses, this grapple fixture is releasable, and as its name implies, it will be removed from the P5 truss after the berthing operation has been completed.

The grapple fixture allows the SSRMS to grasp or grapple the P5 truss to first remove it from the cargo bay, and then to translate it through space to the point of assembly with the ISS. Nominally, the SSRMS translates payloads in the berthing corridor at speeds between 0.3 to 0.9 cm/sec (0.01 to 0.03 ft/sec).

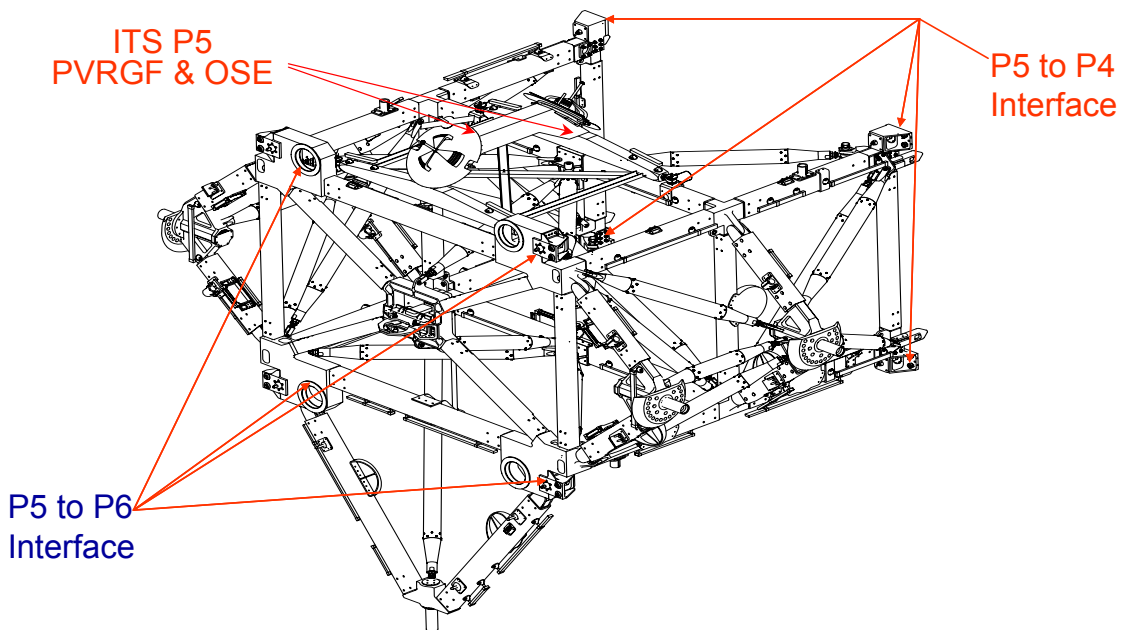


Figure 4. P5 Truss with Structural and Mechanical Interfaces

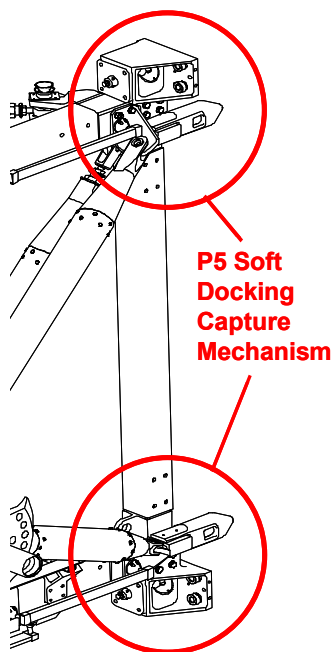


Figure 5. MRTAS Soft Dock Capture Mechanism

The MRTAS mechanism is composed of two subsystems. The capture or soft dock mechanism and the fine alignment bolts and nuts⁶. The capture mechanism uses a set of four slotted stingers called coarse cones that push aside a set of four spring-loaded pins that subsequently lock into the slots in the stingers. The coarse cones also serve the function of coarse alignment during the initial phase of capture. The coarse cones can be discerned in Figure 5.

Once all the coarse cones and all the spring-loaded pins have engaged, the P5 truss is considered to be “soft-docked” to the P3/P4 truss. During the berthing operation, the SSRMS positions the P5 in the trajectory for these stingers to acquire the circular housing on the P3/P4 side of the interface that houses the spring-loaded pins. As the stingers slide into the housing, and seek to push the spring-loaded pins, capture resistive forces arise. These forces are due to friction and due to the load in the pin springs.

During the capture phase, there is an embedded function. At the same time the coarse cones are attempting to engage the soft dock pins, a fine alignment function is taking place through the fine alignment mechanisms on the bolt side and the nut side. Details of this mechanism are shown in Figure 6. Since perfect alignment of these two interfaces cannot be guaranteed, due to SSRMS or operator errors, these features must serve to align the bolt and nuts on the trusses for them to be successfully

bolted together. For successful alignment to take place, a feature called shear cylinder, which surrounds the primary bolt, must acquire the floating primary nut. Once the shear cylinders are fully seated into the floating nut primary cavity, the trusses are now ready to bolt.

The MRTAS P3/P4 side of the truss also has four distinct corners. One corner is fixed; that is to say, the primary nut is not allowed any movement. The other three corners have “floating” primary nuts; where each is allowed to slide in a particular direction. Of these three corners, one corner has one degree of freedom in the direction of ISS X-axis. The other two corners have two degrees of freedom, in the X and Z-axes of ISS coordinate system. These degree-of-freedom allocations not only assure proper engagement of the fine alignment features during the capture and fine alignment process, but also assure the structure will carry the on-orbit loads appropriately following bolt up.

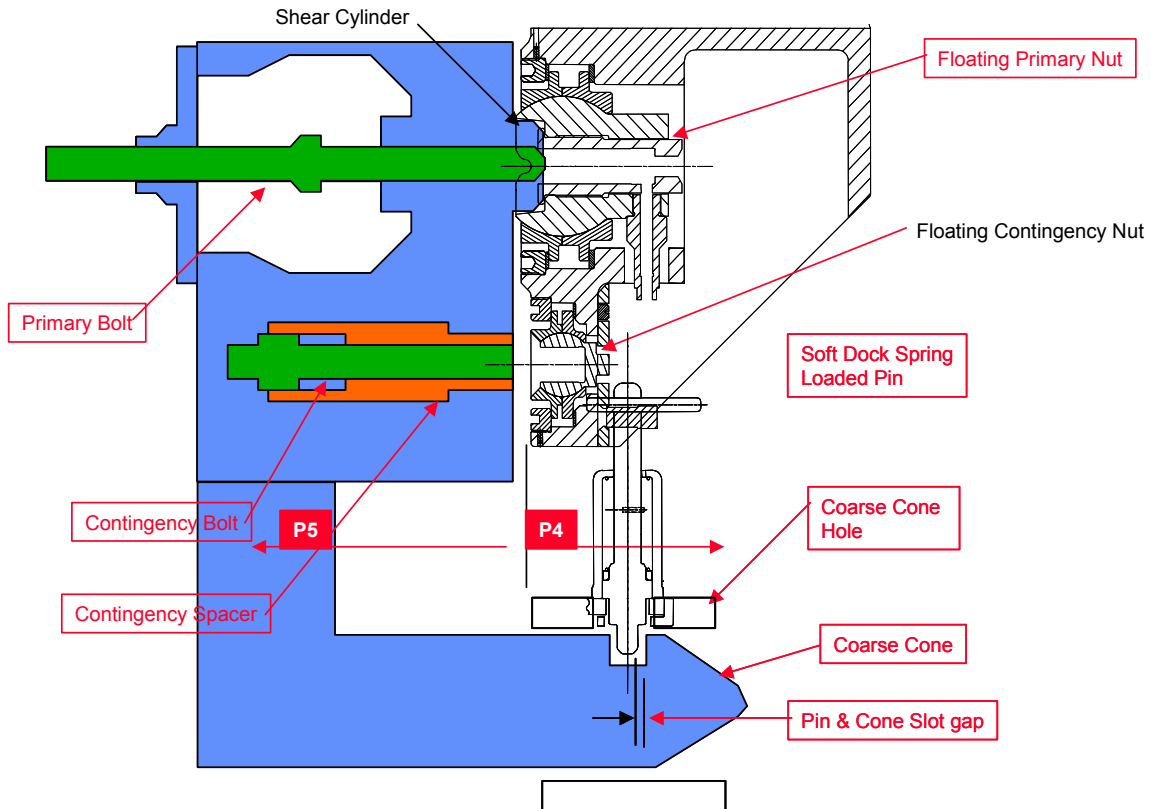


Figure 6. MRTAS Details of the Capture Mechanisms and Fine Alignment Sub-System

The fine alignment features also contribute to the overall allocation of the forces that must be accounted for. Several surfaces contribute to the capture and soft dock forces via friction. These must be accounted for accurately to compare the total sum to the SSRMS capability. Should this exceed the push force capability of the SSRMS, the mating could stall prior to capture complete. The contact dynamic simulation first, will consider the mechanism as-designed with tolerances. Later on, as field measurements are taken, these will allow considering the as-built condition of the trusses. In addition, as ISS on-orbit integrated thermal analysis is completed, thermal deflections also will be considered to represent the hardware interacting as close as possible to the on-orbit environment.

Methodology

The contact dynamic model of the MRTAS was built using MSC/ADAMS multi-body dynamics tool. The elements that come into contact during the berthing operation - capture pin to coarse alignment cone, coarse alignment cone to housing, and fine alignment nut to shear cylinder – are modeled in detail based on the final design drawings (Figure 7). While such detail is required for accurate results, complex

geometry can lead to long simulation times. The time required to retrieve contact intersection information from the geometric modeler is directly related to the complexity of the given geometry. Rather than importing the geometry from CAD models, they were built up from primitives such as cylinders, spheres, boxes and frustums. These shapes branch into much faster calculation algorithms in ADAMS.

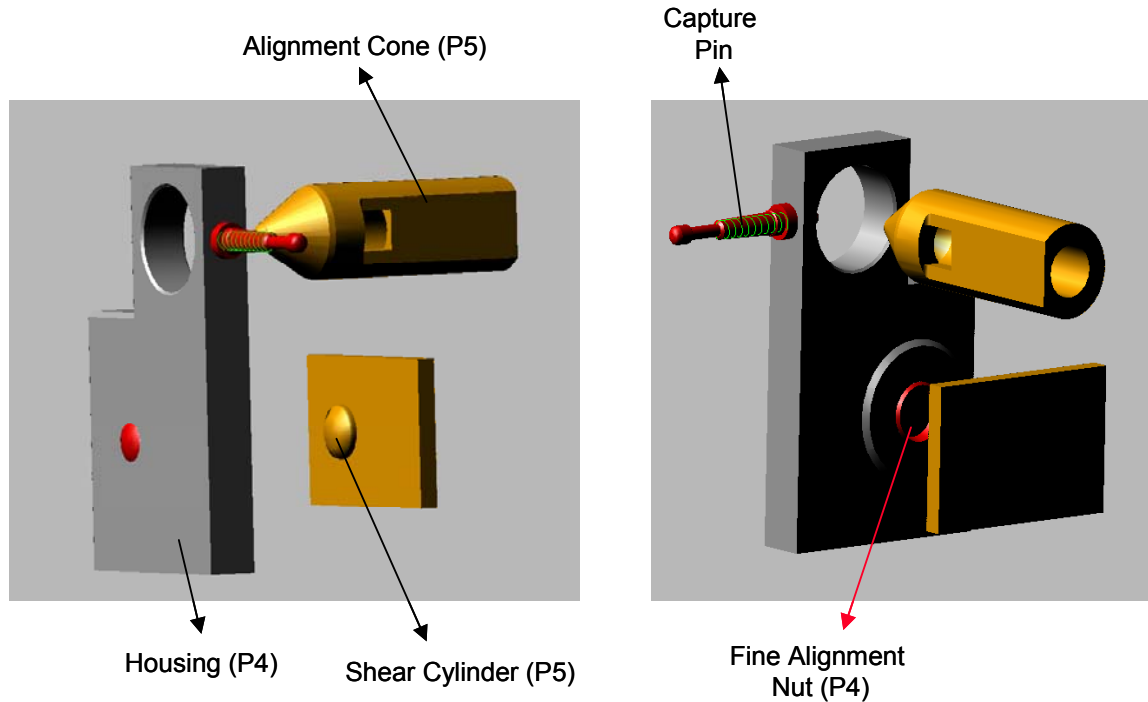


Figure 7. MRTAS Contact Features

The MRTAS model includes two tight dock and two easy dock corners (Figure 8) which are essentially identical except for one major difference; the easy dock coarse alignment cones are longer and extend farther out from the interface plane than the corresponding tight dock cones. During a “perfectly aligned” berthing event, the easy dock cones will pass through the corresponding coarse guide receptacles in the housing first, and engage the capture pins. The capture pins are spring mounted on the housing with a stiffness coefficient of 4.4 N/cm (2.5 lb/in) and pre-load of 0.75 kg (1.65 lb). The fine alignment nut is connected to the housing by a spherical joint and is free to swivel in all directions. Mechanical stops that restrict the rotation to ± 0.5 degree are modeled using the ADAMS bi-stop function. The shear cylinder that mates with the fine nut is fixed to the coarse alignment cone with the correct geometric offset. This modular construction allows easy modification of the model to account for “as-built” and thermal effects in future analyses.

The four corners of the MRTAS model are connected to the SSRMS grapple fixture location fixture by a NFORCE element representing the flexibility of the P5 truss. This element is formed from a 24 x 24 stiffness matrix that was generated from a test verified finite element model of the P5 truss². The mass of the truss is lumped at its center of gravity (CG) location. A bushing element was introduced at the grapple fixture location to represent the SSRMS flexibility. Stiffness values were obtained from an ADAMS model of the SSRMS² configured in the P5 truss ready-to-berth position.

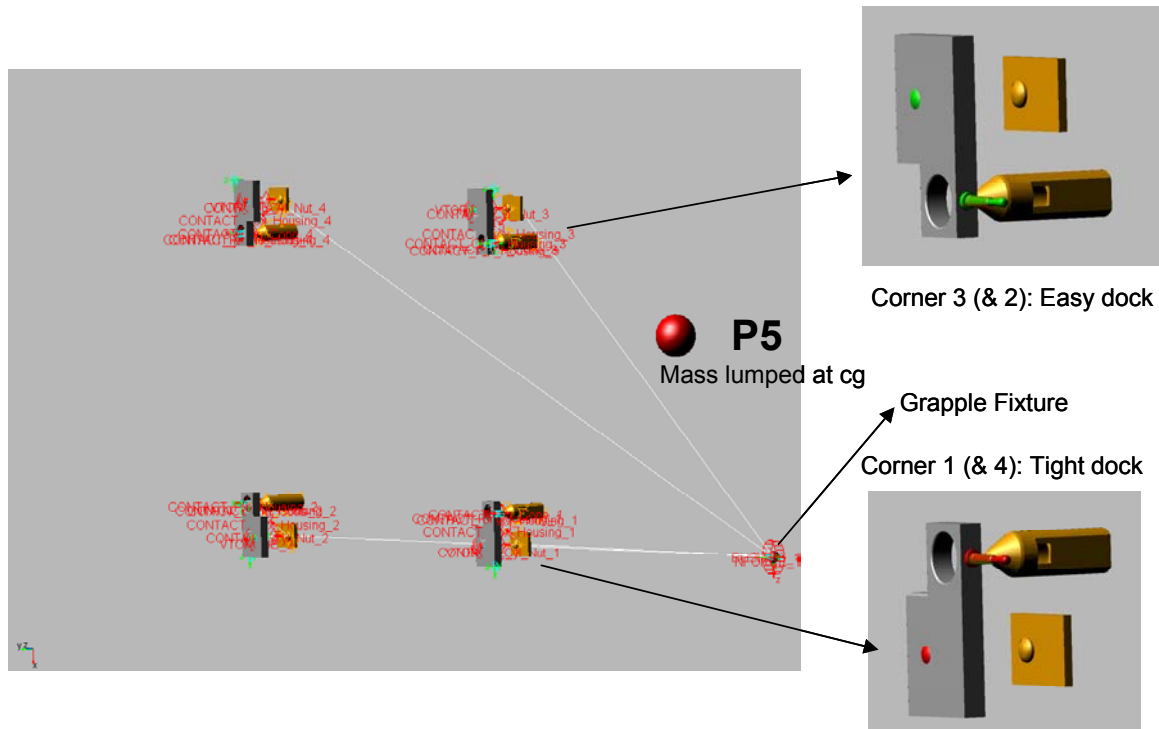


Figure 8. MRTAS Soft Docking features

For contact model geometry verification, the ADAMS MRTAS model geometry was output to another format readable by the Unigraphics CAD programs. The CAD analysis team imported the ADAMS geometry into Unigraphics and compared the geometry of the coarse and fine alignment features, as well as the soft-dock mechanisms, to the validated as-designed CAD model geometry for both the P4 and P5 truss elements. This comparison verified that the ADAMS model geometry was essentially identical to that of the CAD models, which were built from the final design drawings.

This provided confidence in the initial ADAMS study results, which primarily dealt with the forces required to achieve “soft-dock” condition when the P5 element is mated to P4. Again, current plans call for the P5 element to be mated robotically to P4 with the SSRMS which will push P5 into P4 until the four soft-dock mechanism pins on P4 engage corresponding slots on P5. The SSRMS has limited push force capability, depending on the arm geometry for a given operation, so analysis is required to verify the robot can successfully mate the element, even with less than the expected perfect alignment between the initial aligning features on either side of the interface.

Once the ADAMS model geometry was verified, we could proceed to berthing simulation correlation with the NASA engineering team. They had generated their own multi-body dynamic MRTAS simulation in the JSC-common simulation environment, TRICK. This model was planned to be used in the real-time robotic simulation training facility used by the astronauts for crew training. In that facility they incorporate these contact models of the Space Station elements to be berthed with the latest real-time simulations of the SSRMS, controlled by flight-like robotic control consoles, running the actual flight control software. In these simulations the crew can practice piloting the P5 into the soft-dock condition with P4 using the SSRMS, and can view the operation through graphics simulating the camera views they would have on-orbit. Therefore this planned correlation considering the critical MRTAS berthing contact geometry, interface stiffness, and sliding friction coefficients between the NASA simulation and the Boeing “truth” model in ADAMS was essential.

Results

Analysis Results

Four berthing cases are selected for ADAMS and TRICK simulation correlation to verify the adequacy of the TRICK simulation for real-time studies by NASA JSC engineers to later on be used in simulations with crew performing the berthing operation in command of the SSRMS. The cases presented are time histories of the P5 berthing operation in the ADAMS contact dynamic simulation realm and exercised the various coarse and fine alignment features leading to a successful soft dock configuration with all four soft dock pins engaged. A description of each case follows.

Case 1 Results

The P5 element is flown in with an initial velocity of 3 cm/sec (1.2 inch/sec) with no misalignments. For this simulation, the SSRMS spring is disabled and the truss is constrained to move in ISS y-direction (closing direction). Friction effects are not modeled. The effects of varying the contact force parameters of the contact model were studied using the following relationships:

$$F=K* \delta^{\text{exp}}$$
 from their baseline values

$$K= 1.0E5 \text{ lb/in}$$

$$\text{exp}=2.1$$

Figure 9 (Case1a) shows the forces in the spring-loaded capture pin as it engages the alignment cone. Initial contact occurs at the easy-dock corners (2&3). As the berthing operation proceeds and the capture pins are pushed up, the pin-cone z-contact force balances force in the capture-pin springs. After capture is completed and the pins have clicked in their respective slots, the spring forces return to the 7.3-N (1.65-lb) preload level.

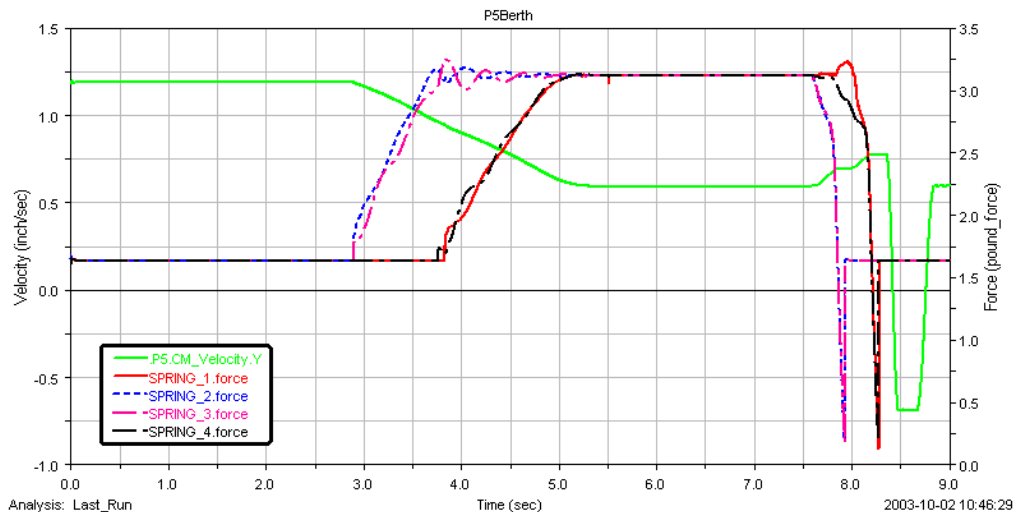


Figure 9. Berthing Case 1a: Forces In The Spring-Loaded Capture Pin

Figure 10 (case1b, 1c) shows the y-component of the pin-cone contact forces. Since there is no friction, the y-component of the pin-cone contact is zero as the pin rides along the cylindrical portion of the alignment cone. After capture pins click in, P5 rebounds as the shear cylinder hits the fine alignment nut, and additional impacts occur between pin and cone as it is trapped inside the slot.

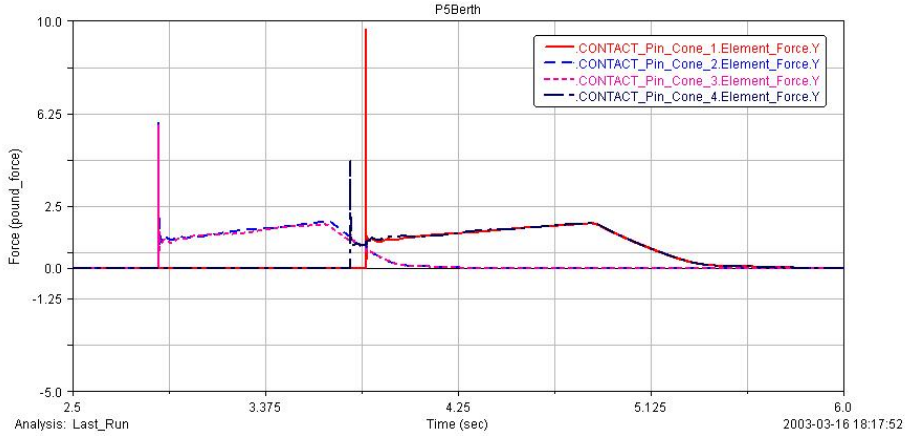


Figure 10. Berthing Case 1b,1c: Y-Component Of The Pin-Cone Contact Forces

Figure 11 shows the effect of changing the contact parameter exponent from 2.1 to 1.5. The result is to stiffen the spring and increase the peak load (green curve). This is the global view of the event. The circled portion of Figure 11 is shown on different scale in Figure 10.

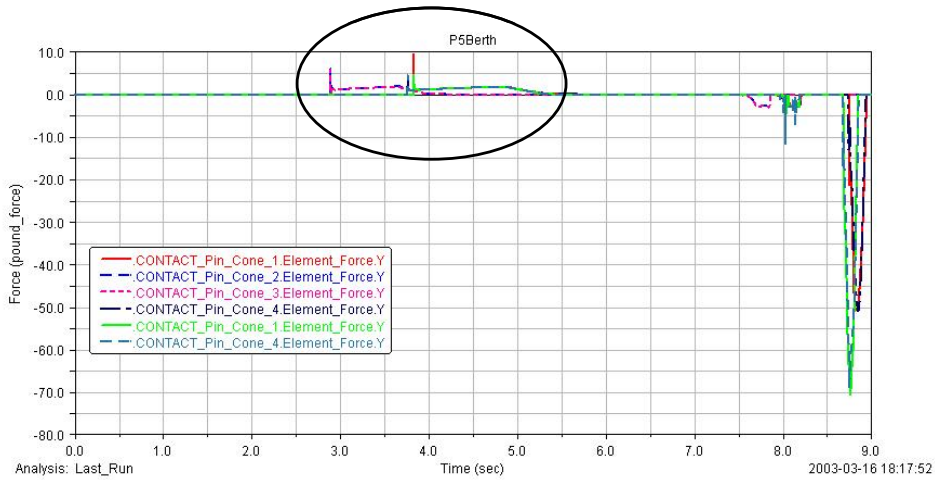


Figure 11. Berthing Case 1c: Y-Component Of The Pin-Cone Contact Forces

Figure 12 (case1d) shows the y-component of the fine alignment nut-shear cylinder contact. Impact at corners 1 and 2 are higher than 3 and 4 due to their proximity to the grapple fixture location.

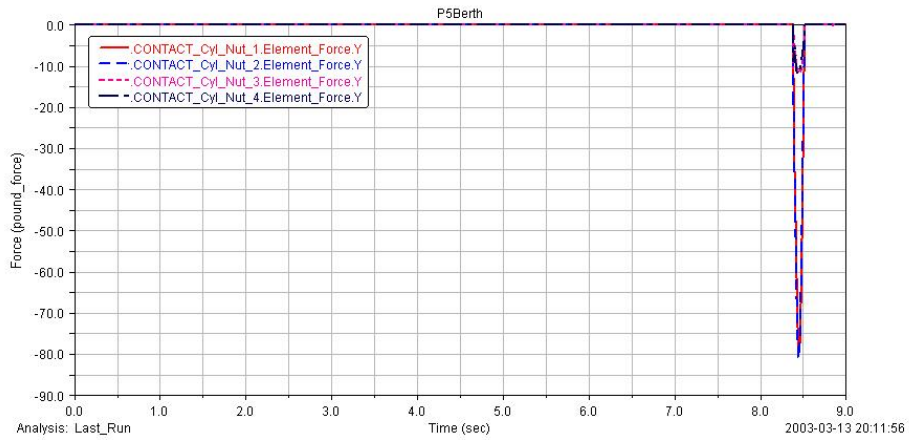


Figure 12. Berthing Case 1d: Y-Component Of The Fine Alignment Nut-Shear Cylinder Contact

Case 2 Results

Case 2 of the analysis performed is identical to Case 1 except that friction effects (coefficient of friction=0.1) are now included at all contacting surfaces and joints. The initial velocity had to be increased to 3.8 cm/sec (1.5 in/sec) to accomplish capture and Figure 13 (case 2a) shows the capture-pin spring forces.

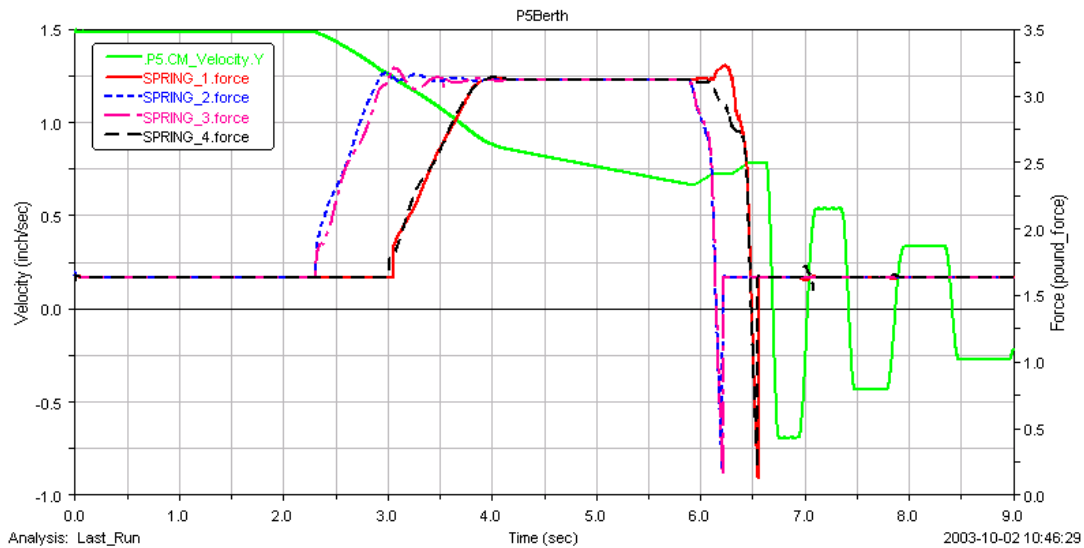


Figure 13. Berthing Case 2a: Capture Spring Forces

The effect of friction can be seen in Figure 14 (case 2b). The pin-cone contact force has a non-zero y-component as the pin rides along the cylindrical portion of the alignment cone.

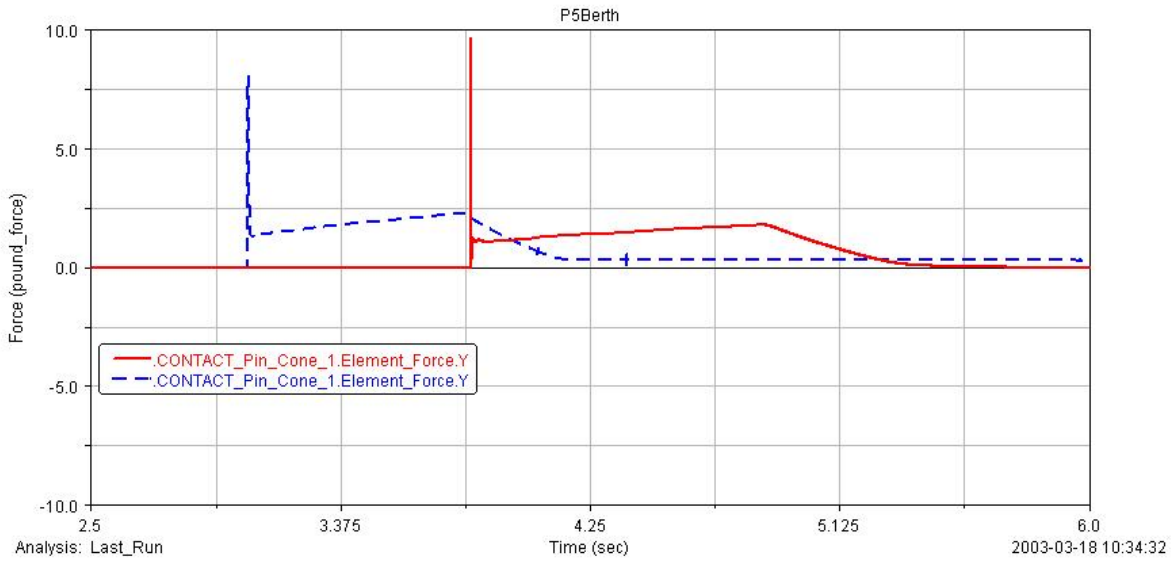


Figure 14. Berthing Case 2b: Capture Spring Forces with Friction Effects

Figure 15 shows that after the capture-pins have clicked in, multiple pin-cone impacts occur as the pin rattles in the slot. The impacts occur at the tight-dock corners 1 and 4 (Fig case 2c).

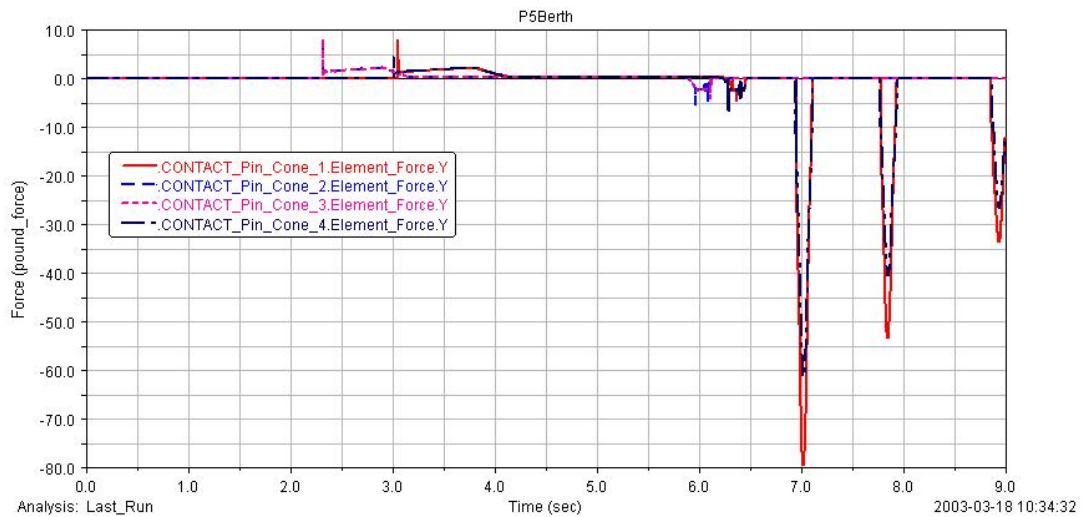


Figure 15. Berthing Case 2c: Impacts Inside Cone Alignment Feature

Figure 16 for the berthing Case 2d shows the y-component of the fine alignment nut-shear cylinder contact forces. Impact at corners 1 and 2 are higher than 3 and 4 due to their proximity to the grapple fixture location.

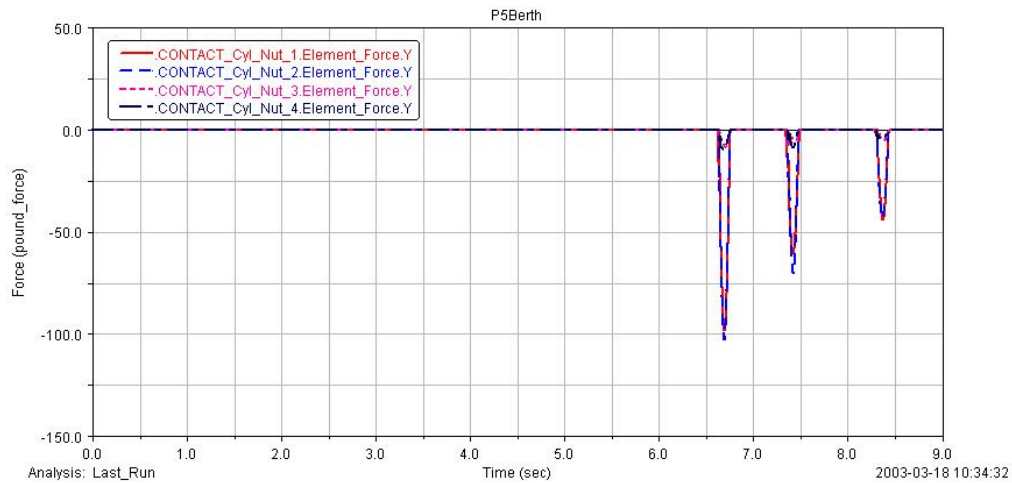


Figure 16. Y-Component Of The Fine Alignment Nut-Shear Cylinder Contact Forces

Case 3 Results

Case 3 includes the SSRMS attached at the grapple location on P5 as a spring to better represent the behavior of the berthing system. Friction effects are not included. The base of the SSRMS is constrained to move in ISS Y direction with a constant velocity of 3 cm/sec (1.2 in/sec). The sprung P5 is not constrained, so its velocity deviates from the enforced value at the SSRMS base during the capture operation. This is shown in Figure 17, case3a. The spring forces show the capture pins click in and then return to the preload value of 7.3 N (1.65 lb).

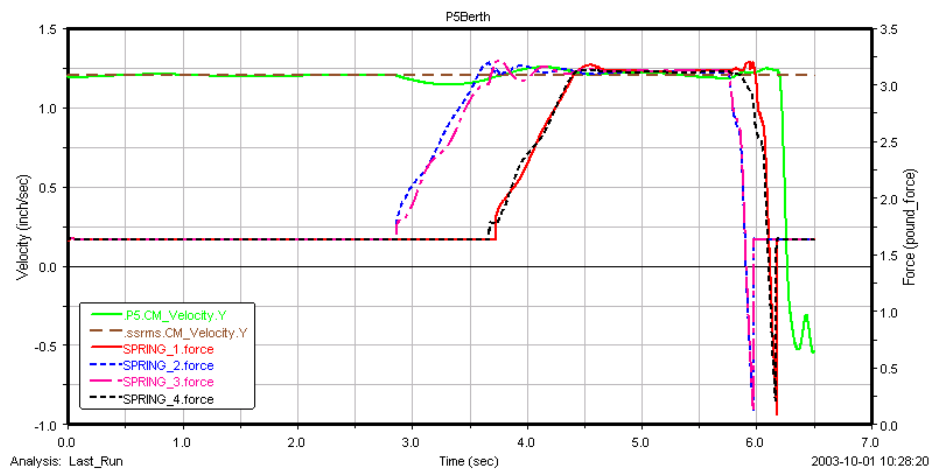


Figure 17. Berthing Case 3a: Soft Dock Spring Forces with SSRMS as a Spring

Figure 18, case 3b shows that the SSRMS spring forces (in x and z directions) and moments are balanced by the constraint forces in the base translation joint, where motion is enforced.

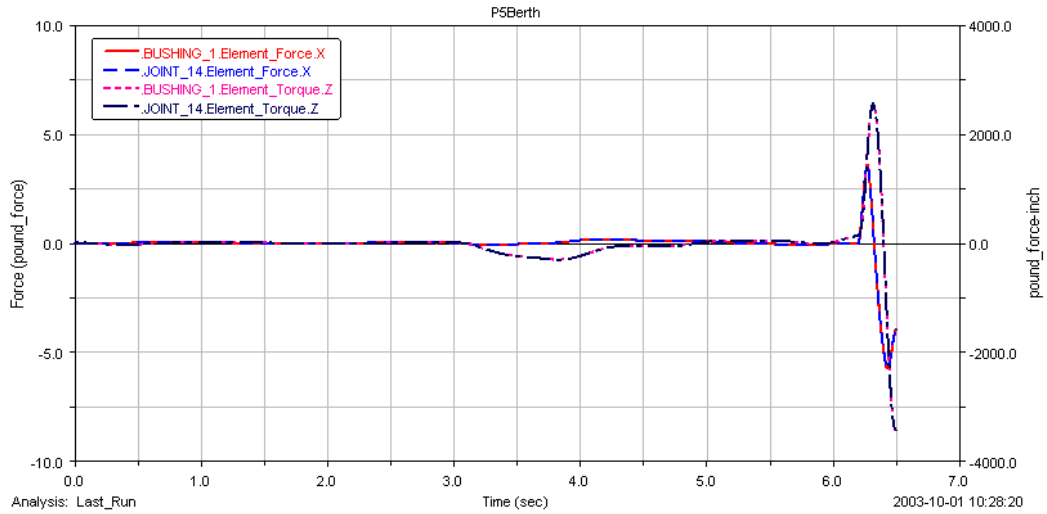


Figure 18. Berthing Case 3b: Soft Dock Spring Forces with SSRMS as a Spring

The SSRMS spring y-forces during the capture operation are shown in Figure 19, case3c. This is a measure of the push force required for berthing and its maximum of 23 N (5.2 lb) for this case is less than the SSRMS capability of approximately 151 N (34 lb).

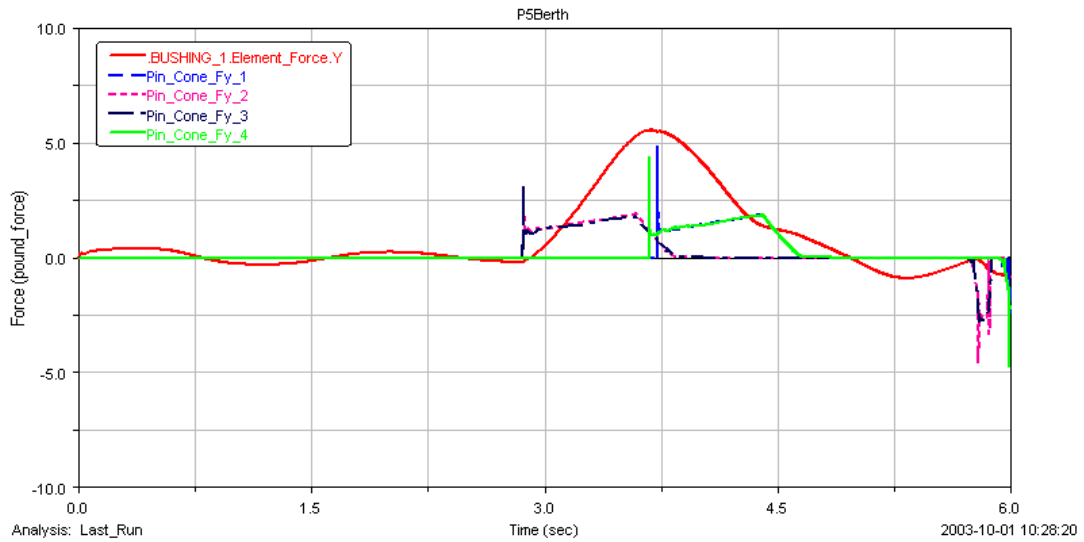


Figure 19. Berthing Case 3c: SSRMS Spring Y Forces During The Capture

The effect of adding friction is seen in Figure 20, case3d. The maximum SSRMS spring y force during capture has increased to 30.7 N (6.9 lb).

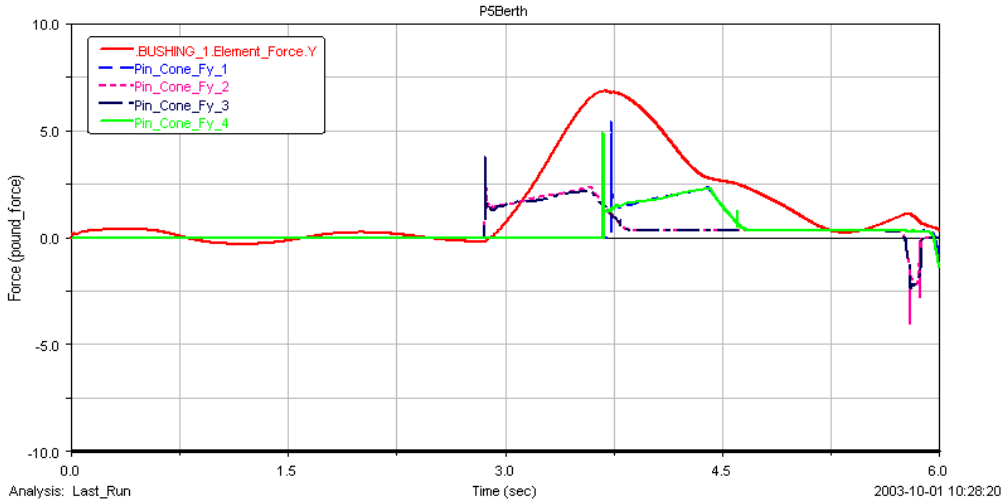


Figure 20. Berthing Case 3d: SSRMS Spring Y Force During Capture with Friction

Case 4 Results

This analysis case is similar to Case 3 except for a small misalignment in the initial berthing configuration. The P5 element is offset in +z direction by 6.3 mm (0.25 in). It is shown in Figure 21, case 4a, that this causes a relative shift in the initial contact time of the capture pins to coarse cone. Spring forces at corners 1 and 3 are smaller due to the offset. Once capture pins have clicked in, spring forces return to their preload value of 7.3 N (1.65 lb).

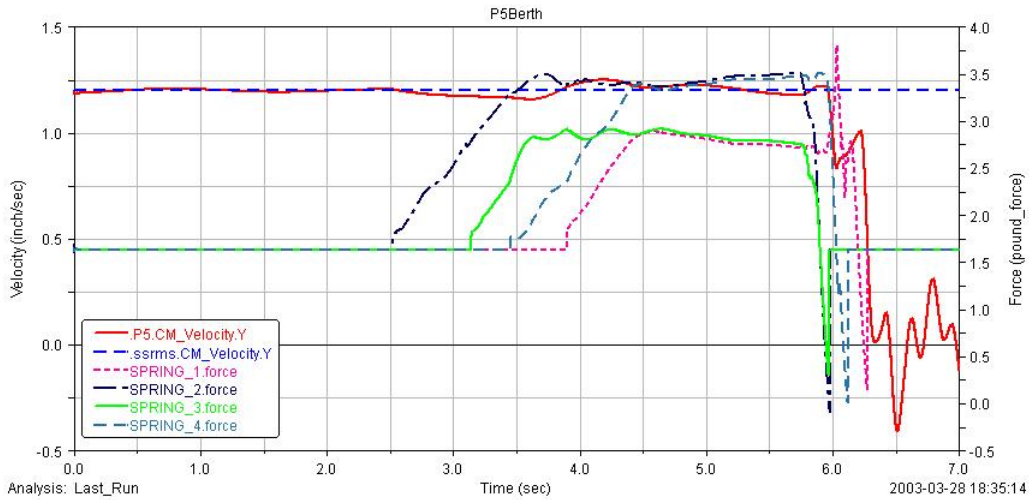


Figure 21. Berthing Case 4a: Contact Time Of The Capture Pins To Coarse Cone

Figure 22, case 4b, shows the SSRMS spring force Y force during capture operation. As in case 3, these forces increase when friction effects are included.

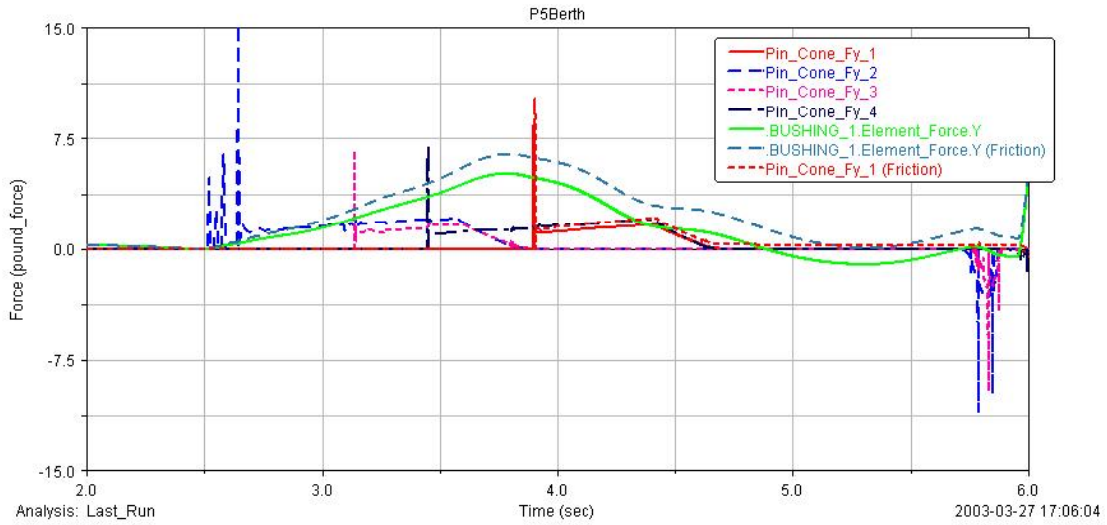


Figure 22. Berthing Case 4b: SSRMS spring force Y force during capture operation

Figure 23, case 4c, shows the shear cylinder to fine nut contact force. Corners 1 and 2 have higher peaks due to the proximity of grapple fixture. As the enforced motion continues to drive the SSRMS forward, the SSRMS spring forces are essentially reacted at corners 1 & 2.

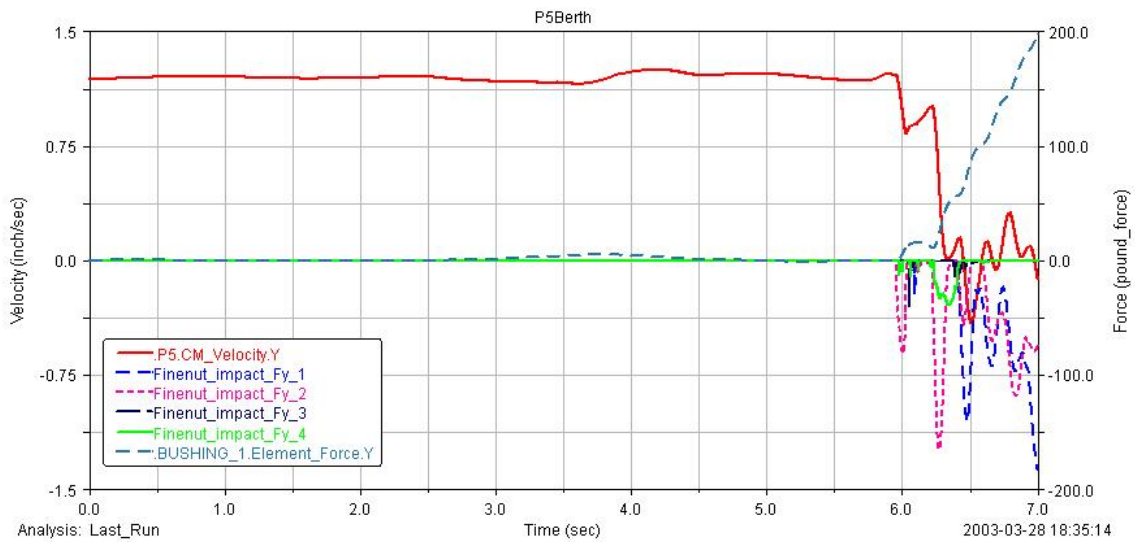


Figure 23. Berthing Case 4c: Shear Cylinder To Fine Nut Contact Force

Discussion Of Results

The analysis performed for the Cases 1 through 4 served the purpose to understand the sensitivities of the contact dynamic model to friction, SSRMS interaction and misalignments. The initial ADAMS simulation appears to indicate that the forces to “soft dock” do not exceed the SSRMS force capability. These results were also compared to the NASA simulation and they appear to be consistent for correlation purposes. This was one of the principal objectives of the analyses. It is also noted that the ADAMS simulation will be further modified and utilized to refine the set of analyses that will provide the final verification the MRTAS mechanism.

The modified ADAMS simulation will include all the contact surfaces that contribute to the total “soft dock” and seating force as well as the different degrees of freedom the MRTAS mechanism possesses at each of the corners. These steps are necessary to refine the knowledge that the alignment and soft-docking forces are within the SSRMS capability. More detailed contact surfaces may add to the total the current analysis has yielded. It is foreseen that the total force, once a detailed model has been constructed, will be higher.

The ADAMS simulation will also include a more detailed geometric model, since field measurements of the flight hardware will have been validated and available to be incorporated to the model. In addition, deflections due to the on-orbit thermal environment will also be incorporated. At each phase the results will be assessed and compared to the previous set of analyses, to achieve the goal of quantifying the total force to “soft dock” and seat the interface. These results will be also correlated, as previously stated with NASA’s models.

References

1. Boeing in Brief. [On-line]. Available: <http://www.boeing.com/companyoffices/aboutus/brief.html> (2000, April)
2. Bruner, Wesley "SSRMS ADAMS Simulation Models." *Boeing Technical Memorandum J332-2002-134*, (November 2002), pp. 1-2.
3. Department of the Air Force. *Space Environment for USAF Space Vehicles* (MIL-STD-1809 (USAF). Los Angeles, CA: Author (1991)
4. Housner, J. *Recent developments in deployment analysis simulation using multi-body computer code*. In J. Stroud, Computational Methods for structural mechanics and dynamics (p. 435). Hampton, VA: NASA (1985)
5. Jacobson, C., Price, M., & Rudd, R. *Space station on-orbit thermostructural analysis*. American Institute of Aeronautics and Astronautics Journal, AIAA-97-1040, 157-158, (1997).
6. Katell, G., & Asato, K. *Rocketdyne truss attachment system fine alignment bolt/nut misalignment qualification test report* (ETD-PQ4-C01189). Canoga Park, CA: The Boeing Company. (1999).
7. Lauer, M., & Gustavino, S. *Design of EVA-assembled utility connection systems for the international space station*. American Institute of Aeronautics and Astronautics, AIAA-98-1934, 1877. (1998).
8. Nagy, K. *Pre-integrated truss space station and method of assembly* [Abstract]. American Institute of Aeronautics and Astronautics. (1992, December).

Life of Scanner Bearings with Four Space Liquid Lubricants

Dean G. Bazinet*, Mark A. Espinosa*, Stuart H. Loewenthal*,
Lois Gschwender**, William R. Jones, Jr.+ and Roamer E. Predmore++

Abstract

The results of a life test program to evaluate bearing life with different space lubricants and cleaning solvents is presented. Thirty pairs of flight-like scanner bearings were tested over a period of seven years. Lubricants included two well known perfluorinated space oils (Brayco 815Z™ and Krytox 143AB™), a more recent synthetic hydrocarbon oil (Pennzane 2001™), and one yet to be in space service (silahydrocarbon oil). Bearings lubricated with Pennzane 2001 oil were found to have the longest lives. Life improvements up to 18X relative to perfluorinated oils and 3X relative to the silahydrocarbon oil were measured. No statistically significant life improvement was found with TiC-coated balls relative to standard plain steel balls for Penzanne 2001 bearings. Bearing life was generally longer when the bearings were cleaned with ozone-safe aqueous or hydrofluorocarbon (HFC) solvents as alternates to the discontinued CFC-113.

Introduction

Bearings for space applications have historically been cleaned with a chlorofluorocarbon CFC-113 (Freon) solvent until the early 1990's when the production of this ozone-depleting solvent was banned. The need arose to qualify alternate cleaners since bearing lubricant life was considered to be very sensitive to surface chemistry. A full-scale bearing life test program was initiated for NASA in April 1996 to evaluate three environmental-friendly cleaning solvents. The solvents included in this study were an aqueous-based cleaner (Brulin 815GD), a perfluorinated hydrocarbon (morpholine) solvent (3M PF-5052), and an HFC solvent (DuPont Vertrel XF). Intermediate test results previously reported [1, 2] showed bearing lives with these alternate cleaners were at least as long as those cleaned with the traditional CFC solvent. This was not consistent with earlier tests using a transient elasto-hydrodynamic apparatus in air, which indicated that bearing lifetimes might be compromised by some of the new cleaning techniques [3]. Later accelerated tests using a Spiral Orbit Tribometer in vacuum, however, yielded no detrimental effects on lubricant lifetime [4].

An equally important objective of the tests was to evaluate potential life improvements attended with improved space vacuum lubricants. Although extended mission lifetimes of many new space systems have driven the need to evaluate new flight lubricants, their acceptance is contingent on establishing an adequate life test database. The lubricants included in this study were traditional perfluorinated oils, which were compared with a relatively new multiply-alkylated cyclopentane oil (Pennzane 2001). At the time the intermediate test results were reported, the Pennzane 2001 bearing lives were much longer than those with the baseline perfluorinated oils and six of the eight Pennzane-lubricated bearings were still running. The present investigation reports the final life test results, with the addition of a new silahydrocarbon oil which has a good vapor pressure and good low temperature viscosity properties [5, 6]. The use of titanium carbide (TiC) coated balls as a means to increase bearing life over that of standard 440C stainless steel balls was also evaluated with Pennzane 2001.

Thirty pairs of flight-like scanner ball bearings were tested in a 10^{-6} Torr vacuum at ambient temperature in this current study. Periodic bearing health torque checks were performed, consisting of oscillations and

* Lockheed Martin Space Systems, Sunnyvale, CA

** Air Force Research Laboratory, Wright-Patterson AFB, Dayton, OH

+ SEST, Inc., Middleburg Heights, OH

++ Swales Aerospace, Beltsville, MD

continuous rotation patterns. Test acceleration factors included increasing the preload of each bearing pair by roughly a factor of three times from typical scanner bearings, reducing the amount of the lubricant to about one-third, and continuously cycling the bearings at a small stroke such that complete rewetting of the ball contact does not occur. At the time of this report, all but one pair of bearings had been tested to failure.

Test Description

Test Matrix

The original test series evaluated three different ODC-free bearing cleaning solvents against the CFC-113 (Freon) baseline. These consisted of an aqueous-based wash (Brulin 815GD), a perfluorinated hydrocarbon solvent (morpholine) from 3M (PF-5052), and a hydrofluorocarbon solvent from DuPont (Vertrel XF). A fourth solvent, heptane, was used in preparing the silahydrocarbon-lubricated bearings.

The baseline lubricant was Brayco 815Z™ oil, a perfluorinated polyalkylether (PFPE) linear fluid, currently distributed by Castrol Industrial North America. This oil has more flight history than any other class of space lubricant. The second test lubricant was a formulated multiply-alkylated cyclopentane (MAC) oil, generically referred to as Pennzane 2001™ and distributed by Nye Lubricants. This lubricant contained a triphenyl phosphate antiwear additive along with an antioxidant. The third test lubricant was a branched PFPE oil (Krytox 143AB™) manufactured by DuPont. The fourth and final test lubricant, a late addition to the test program, was a silahydrocarbon oil formulation. The molecular formula for this unimolecular silahydrocarbon base oil was $\text{CH}_3\text{Si}(\text{CH}_2\text{CH}_2\text{Si}(\text{C}_6\text{H}_{13})_3)_3$, with a molecular weight of 976 amu. This oil was synthesized and formulated by Nye Lubricants, with the same formulation as used in the Pennzane 2001. Originally developed by the Air Force for high temperature aircraft bearing applications, it has low vapor pressure and relatively low cold temperature viscosity making it a potentially good candidate for future space applications [5, 6]. Approximately one-third the normal amount of lubricant (60 to 80 mg of Brayco 815Z and 30 to 50 mg of the other test lubricants) was used in all test bearings, in order to provide for accelerated test results.

With the exception of the three pairs of silahydrocarbon-lubricated bearings, all of the solvent – lube combinations were tested in duplicate to provide greater confidence in the results. All test bearings were processed by the Miniature Precision Bearing (MPB) division of Timken, in order to represent end user application, again with the exception of those lubricated with silahydrocarbon oil. These latter test bearings were cleaned with heptane and lubricated at the Lockheed Martin facility with oil supplied by the Air Force Research Labs.

Test Bearings

The angular contact ball bearings used for test (Figure 1) were selected as representative of the type that would be used for a space scanner bearing application. The test bearings are 39.6-mm (1.56-in) bore by 50.8-mm (2.0-in) OD containing 34 balls of 3.2-mm (1/8-in) diameter. They were manufactured from AISI 440-C steel and hard preloaded back to back with 200 ± 22 N (45 ± 5 lb), resulting in a peak mean Hertz stress of 0.75 GPa (109 KSI). This preload provided additional test acceleration, in that it is approximately three times greater than that normally specified for this size bearing in a typical long-lived scanner application. The ball separators are alternating PTFE toroids. The races are finished to rms roughness of less than 0.08 microns (3 micro-inch). The test bearings had plain steel balls, except for a limited test series for two pairs of Pennzane-lubricated bearings where TiC-coated balls were tested. Further bearing specifications, including a highlight of differences between typical flight bearings and those used for life test are presented in Table 1.



Figure 1. Test bearing with toroid ball separators

Table 1. Angular Contact Ball Bearing Parameters

Parameter	Typical Flight Bearing	Life Test Bearing
Type	Angular Contact, Duplex, Tube Type	Same
AFBMA Precision	ABEC Grade 7 or Better	Same
Mount	Back-to-Back	Same
Bore x OD x Width	39.6875 x 50.8 x 6.35 mm (1.5625 x 2.000 x 0.250 inch)	Same
Preload	67 ± 9 N (15 ± 2 lb)	200 ± 13 N (45 ± 3 lb)
Max. Contact Stress	758 MPa (110 ksi)	1130 Mpa @ 200 N (164 ksi @ 45 lb)
Ball Number / Diameter / Grade	34 balls / 3.175 mm (0.125 inch) diameter / Grade 3	Same
Contact Angle	20 ± 3 deg	Same
Race Conformity	52 to 53%	Same
Lubricant	Grease	Oil
Angular Runout, pair	< 20 arcsec	Same
Radial Runout, pair	< 152 nm (60 microinch) (non-repeat < 100 (40))	Same
Lube Weight per Row	160 – 190 mg (≈15% fill)	30 – 50 mg¹
Race Material	AISI 440-C per AMS 5630 (ESR)	Same
Ball Material	AISI 440-C per AMS 5618 (CEVM)	Same
Ball Treatment	Passivated	Same & TiC Coating
Toroids	PTFE, alternating	Same
Running Torque Variation	± 20% max.	Same
Max. Weight per Pair	54 g (0.12 lb)	Same

¹60 to 80 mg for Brayco 815Z

Test Conditions

The bearing pairs were mounted into a cartridge and then hard preloaded, with the inner bearing races clamped on a geared shaft (Figure 2). The cartridges were then installed into one of Lockheed Martin's 45.7-cm (18-inch) diameter vacuum bell jar life test stations (Figure 3), which was then pumped down to 10^{-6} Torr range. A computer controlled motor located external to the bell jar drives a central bull gear, which in turn drives up to twelve test bearing pairs concurrently. The outer bearing cup is mounted in flexures, so that the bearing's torque can be measured via the test computer using a strain gaged torque reaction element.

The bearings were continuously cycled at a stroke of ± 12 degrees at a speed of 2.5 cycles per second. The stroke does not allow for complete rewetting of the contact, being slightly greater than the inner race ball track overlap but less than one complete ball rotation. Periodic functional tests were performed approximately every five million cycles, in order to ascertain bearing health. During these functional tests, the bearing oscillation was stopped and the bearings were immediately rotated three revolutions in each direction at a rate of 60 deg/s. The resulting torque signature was plotted for comparison with prior health check results.

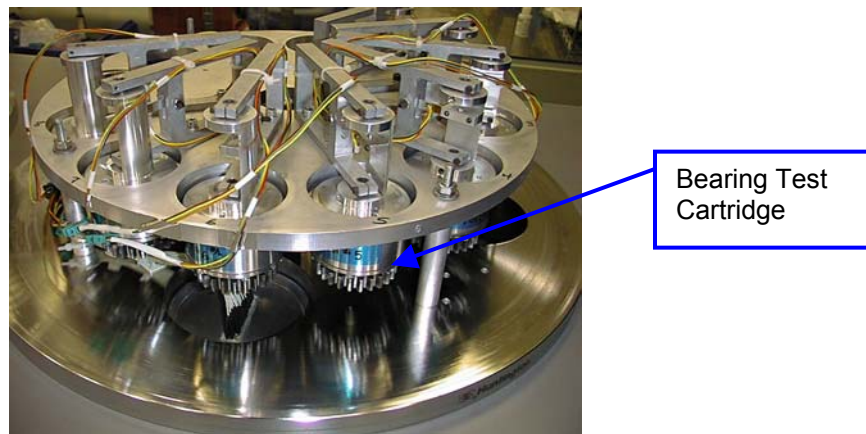


Figure 2. Bearing life test fixture with individual strain gaged bearing cartridges

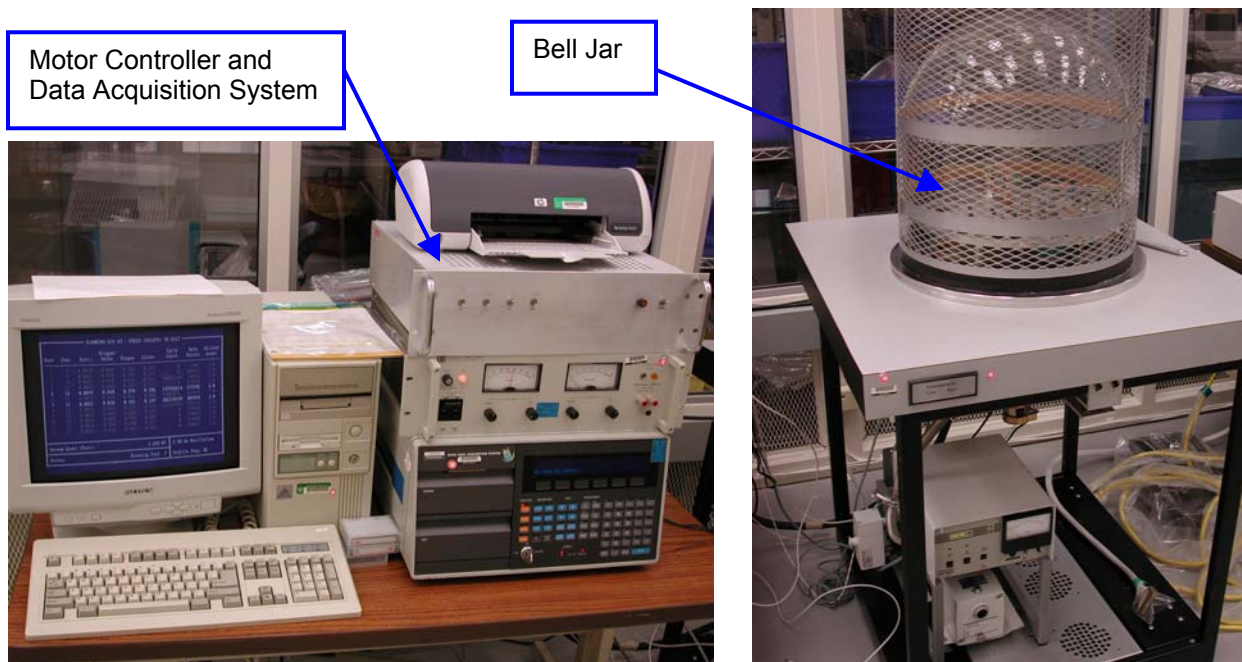


Figure 3. Bearing Life Test Setup

Results

The torque was observed to be extremely stable for typically more than 90% of the life for each pair of bearings. As an example, the torque trace of a Pennzane-lubricated bearing just after being installed into the fixture (Figure 4) is nearly identical to the trace measured after 453 million cycles (Figure 5). Note the transition from the constant test oscillation to the constant rotation pattern used only during health checks.

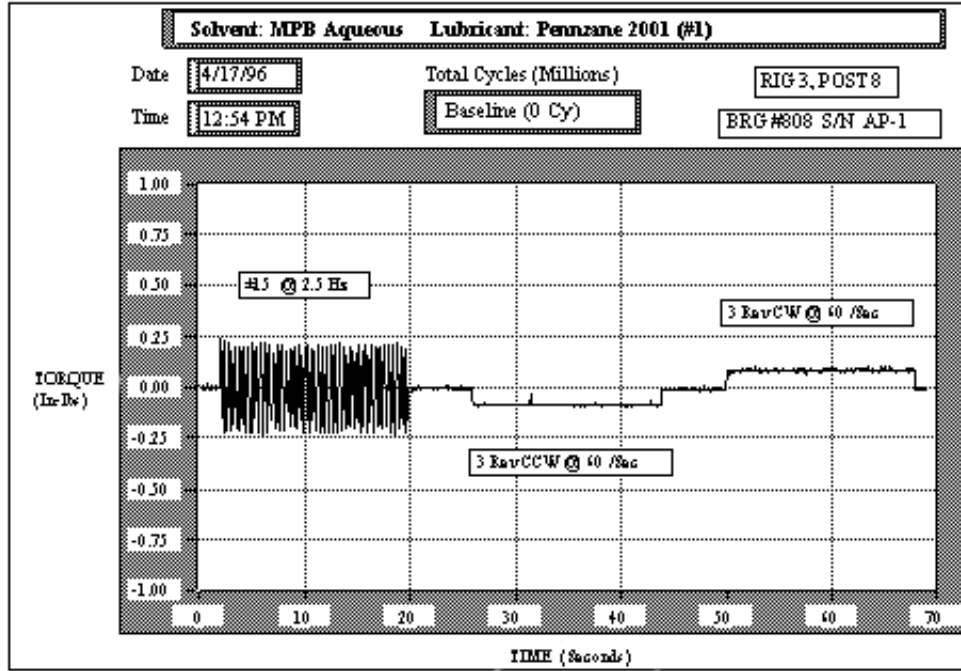


Figure 4. Pennzane 2001 Bearing Torque Trace at 0 cycles

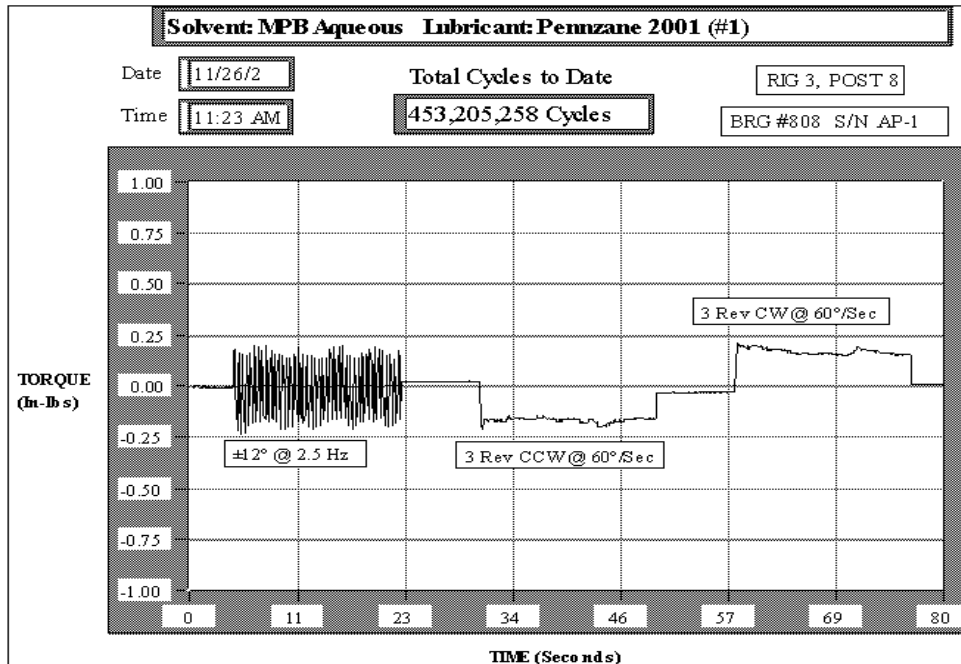


Figure 5. Pennzane 2001 Bearing Torque Trace at 453M cycles

There are two indicators of lubricant degradation observable in a bearing health check torque signature. The first, and more noticeable, is the development of torque bumps during the transition from oscillations to continuous rotation (Figure 6). This is an early indicator of lubricant breakdown for bearings operating in a gimbaling motion. Debris mounds form at the end of each stroke as the back and forth motion over one spot on the bearing race continuously stresses the lubricant without the ability to bring “fresh” oil into contact. The result is small amounts of lubricant being degraded into a sludge-like friction polymer (Figure 7). Eventually this leads to torque bumps, when the stroke is increased. Subsequent roll-overs cause the balls to break through this buildup, which helps smooth out the torque. Bearing failure is considered to occur when the torque reaches three to four times the starting steady state torque. The other indicator of bearing degradation is increased average torque and torque hash (high frequency noise) during the constant rotation portion of the torque test. This occurs in a later stage of lubricant degradation. Note the marked change in torque signature between Figures 5 and 6 in just 20 million cycles (5% life).

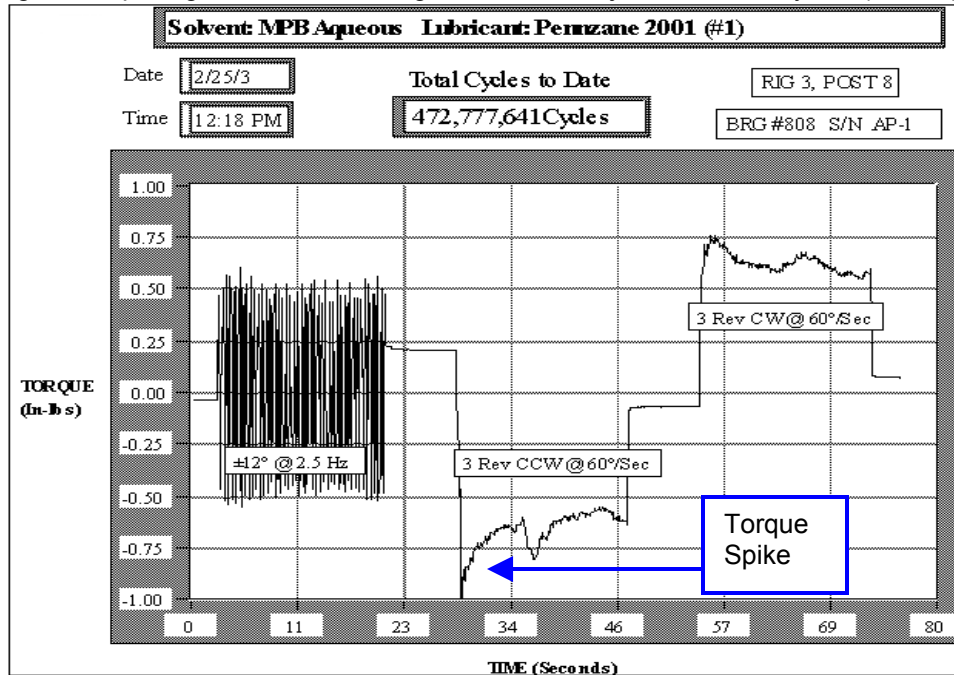


Figure 6. Pennzane bearing torque trace approaching failure. Note torque spike of > 1 in-lb from debris bump at transition to 3 revs of continuous rotation



Figure 7. Typical Bearing Lubricant, Post-Failure

Summary of Results

The cumulative test results are summarized in Table 2. These results show that bearings lubricated with Pennzane 2001 oil had the longest life. It is clearly superior to the other lubricants, independent of solvent cleaner. Average life was extended by a factor of approximately 9X when compared to those bearings lubricated with Brayco 815Z. The results also show that Krytox 143AB offered no life improvement relative to Brayco 815Z. The silahydrocarbon lubricant extended average life by 2.8X. A similar ranking of lubricants was obtained using a Vacuum Spiral Orbit Tribometer [7] where a silahydrocarbon relative lifetime was much greater than Brayco 815Z or Krytox 143AC lubricants but clearly not as good as Pennzane 2001.

The introduction of TiC-coated balls showed no statistical significant life improvement relative to the standard 440C stainless steel balls for the Pennzane-lubricated bearings (note that one of the TiC test bearings is still under test, currently at 386 million cycles). Similar results were found by Jansen et. al [8].

As shown in Figure 8, the three environmental-friendly cleaning solvents performed generally better than Freon 113. Heptane was used to re-clean the bearings prior to lubricating with the silahydrocarbon lubricant. It also showed performance as good or better than Freon 113. The variations in life are mainly due to the test lubricant.

Table 2. Summary of Results – Bearing Life, Million Cycles

Solvent	Lubricant				
	Brayco 815Z	Krytox 143AB	Pennzane 2001	Pennzane TiC Balls	Silahydrocarbon
Freon -113	10.1	9.0	265.5	-	-
Freon -113	12.6	40.0	118.5	-	-
Brulin 815GD	15.0	30.2	481.5	385.8 SR ²	-
Brulin 815GD	35.6	60.0	165.8	141.0	-
3M PF-5052	40.5	29.4	409.0	-	-
3M PF-5052	33.1	-	372.0	-	-
DuPont Vertrel XF	26.1	-	360.0	-	-
DuPont Vertrel XF	108.2	-	349.0	-	-
Heptane	-	-	-	-	131.0
Heptane	-	-	-	-	110.9
Heptane	-	-	-	-	62.8
Average Life	35.2	33.7	315.2	263.4	101.6
Ave. Life Factor	1.0	1.0	9.0	7.5	2.9
L10 Life	7.3	8.2	131.0	-	47.0
L10 Life Factor	1.0	1.1	17.9	-	6.4

²SR = Still Running

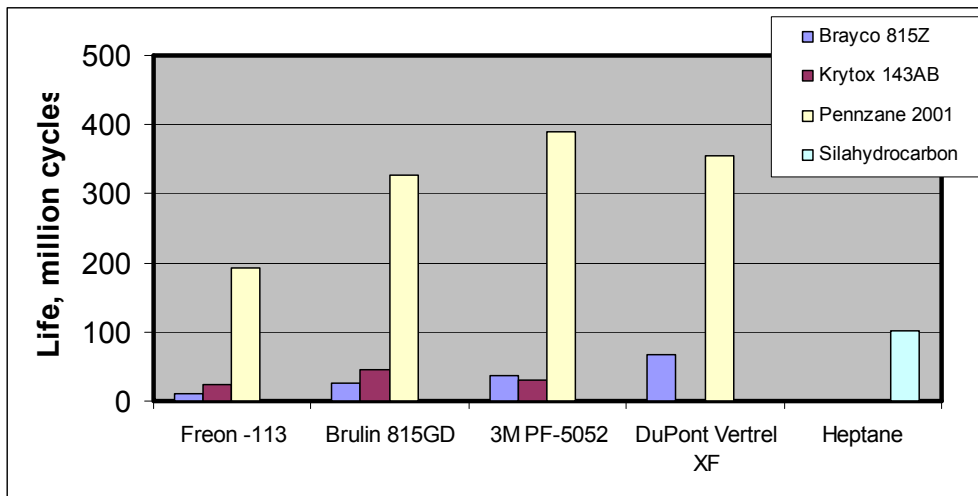


Figure 8. Effect of Cleaning Solvent on Average Bearing Life

Weibull analysis was performed on the test bearings to show the effects of reliability on measured life, Figure 9. The L10 lives (90% reliability) of the four test lubricants are shown in Figure 9. At the L10 level the life advantage of Pennzane 2001 relative to Brayco 815Z or Krytox 143AB is approximately 16 to 18 fold (see Table 2). The silahydrocarbon-lubricated bearings enjoyed about a 6X life advantage at 90% reliability.

Bearings lubricated with the four test oils exhibited similar failure distributions, i.e., Weibull slope. Life differences between Krytox 143AB and Brayco 815Z lubricated bearings are not statistically significant.

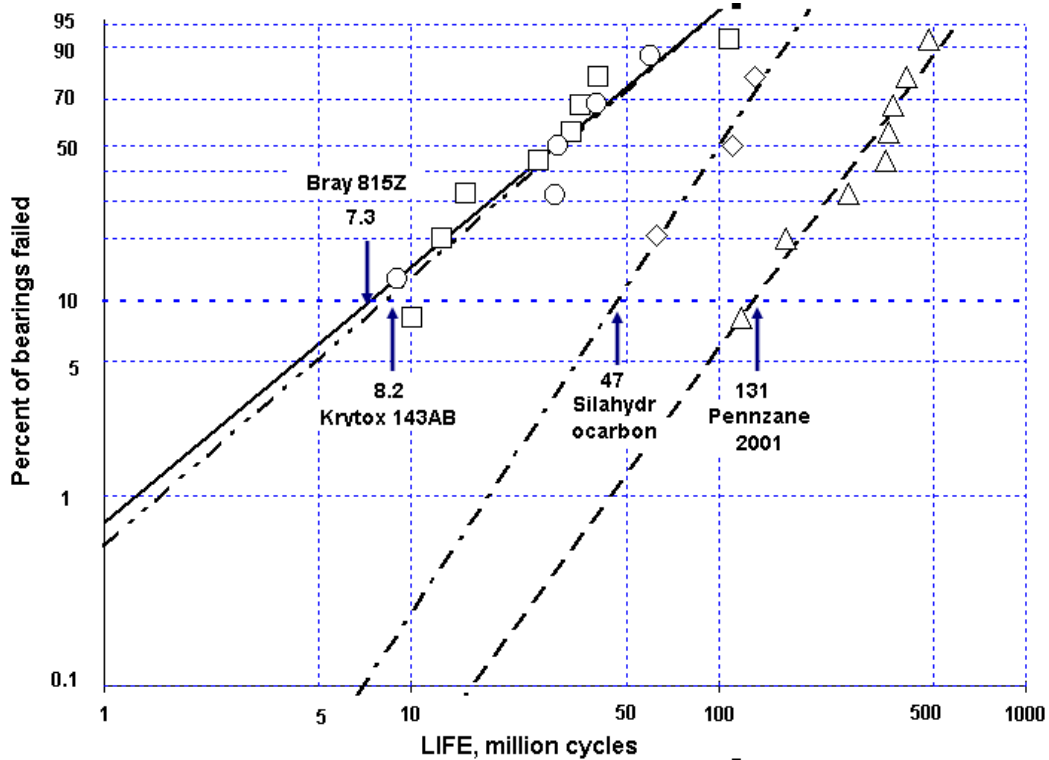


Figure 9. Weibull Analysis of Bearing Life

The life results presented above were affected by bearing test acceleration factors as noted. These factors include higher than normal preloads, less lubricant than normal, and nearly continuous dither over the same spot on the raceway. Flight bearing life under less severe conditions may actually be greater than that reported in this study.

Conclusions

The seven-year bearing life test program supports the following conclusions:

1. Pennzane 2001 lubricated bearings provided a 9X average life improvement relative to either the Brayco 815Z or Krytox 143AB lubricated bearings. The L10 life improvement was 16 to 18 times.
2. Krytox 143AB showed comparable life to the baseline Brayco 815Z lubricated bearings.
3. A silahydrocarbon lubricant produced an L10 bearing life that was about 6X greater than that with Brayco 815Z or Krytox 143AB.
4. TiC-coated balls did not offer a life advantage over 440C stainless steel balls for the Pennzane 2001 lubricated bearings.

References

1. Loewenthal, S.H., Jones, W.R. Jr., Grout, J., Predmore, R.E., and Thom, R., "Instrument Bearing Life With Non-CFC Cleaners", DOD Rolling Bearing Working Group & C.S. Draper Labs, *Proceedings of the International Rolling Element Bearing Symposium*, April, 1997.
2. Loewenthal, S.H., Jones, W.R. Jr., and Predmore, R.E., "Life of Pennzane and 815Z-Lubricated Instrument Bearings Cleaned With Non-CFC Solvents", *Proceedings of the 8th European Space Mechanisms and Tribology Symposium*, ESA SP-438, September, 1999.
3. Jones, W.R., Jr, Toddy, T.J., Predmore, R., Shogrin, B., and Herrera-Fierro, P., "The Effect of ODC-Free Cleaning Techniques on Bearing Lifetimes in the Parched Elastohydrodynamic Regime", NASA TM 107322, August, 1996.
4. Jansen, M.J., Jones, W.R., Jr., Wheeler, D.R., and Keller, D.J., "Evaluation of Non-Ozone-Depleting-Chemical Cleaning Methods for Space Mechanisms Using a Vacuum Spiral Orbit Rolling Contact Tribometer", NASA TM-2000-210050, May, 2000.
5. Gschwender, L.J., Snyder, C.E., Jr., Massey, M., and Peterangelo, S., "Improved Liquid/Grease Lubricants for Space Mechanisms", *Lubr. Eng.*, 12, 56, pp 25-31 (2000).
6. Jones, W.R. Jr., Jansen, M.J., Gschwender, L.J., Snyder, C.E. Jr., Sharma, S.K., Predmore, R.E., and Dube, M.J., "The Tribological Properties of Several Silahydrocarbons for Use in Space Mechanisms", *Proceedings of the Ninth European Space Mechanisms and Tribology Symposium*, SP-480, September, 2001.
7. Jansen, M.J., Jones, W.R. Jr., Predmore, R.E., and Loewenthal, S.H., "Relative Lifetimes of Several Space Liquid Lubricants Using a Vacuum Spiral Orbit Tribometer (SOT)", NASA TM 2001-210966, June, 2001.
8. Jansen, M.J., Jones, W.R. Jr., Pepper, S.V., Wheeler, D.R., Schröer, A., Flühmann, F., Loewenthal, S.H., Shogrin, B.A., "The Effect of TiC-Coated Balls and Stress on the Lubricant Lifetime of a Synthetic Hydrocarbon (Pennzane 2001A) Using a Vacuum Spiral Orbit Tribometer", NASA TM-2000-210525, October, 2000.

Hubble Space Telescope Fine Guidance Sensor Post-Flight Bearing Inspection

J. Pellicciotti*, S. Loewenthal**, W. Jones Jr.+ and M. Jumper**

Abstract

Aerospace mechanism engineering success stories often, if not always, consist of overcoming developmental, test and flight anomalies. Many times it is these anomalies that stimulate technology growth and more reliable future systems. However, one must learn from these to achieve an ultimately successful mission.

It is not often that a spacecraft engineer is able to inspect hardware that has flown in orbit for several years. However, in February 1997, the Fine Guidance Sensor-1 (FGS-1) was removed from the Hubble Space Telescope (HST) and returned to NASA Goddard Space Flight Center (GSFC) during the second Servicing Mission (SM2). At the time of removal, FGS-1 had nearly 7 years of service and the bearings in the Star Selector Servos (SSS) had accumulated approximately 25 million Coarse Track (CT) cycles. The main reason for its replacement was due to a bearing torque anomaly leading to stalling of the B Star Selector Servo (SSS-B) when reversing direction during a vehicle offset maneuver, referred to herein as a Reversal Bump (RB). The returned HST FGS SSS bearings were disassembled for post-service condition assessment to better understand the actual cause of the torque spikes, identify potential process/design improvements, and provide information for remedial on-orbit operation modifications.

The methods and technology utilized for this inspection are not unique to this system and can be adapted to most investigations at varying stages of the mechanism life from development, through testing, to post flight evaluation. The systematic methods used for the HST Fine Guidance Sensor (FGS) SSS and specific findings are the subjects presented in this paper. The lessons learned include the importance of cleanliness and handling for precision instrument bearings and the potential effects from contamination. The paper describes in detail, the analytical techniques used for the SSS and their importance in this investigation. Inspection analytical data and photographs are included throughout the paper.

Introduction & FGS Description

Hubble's three FGS's — its targeting cameras — provide feedback used to maneuver the telescope and perform celestial measurements. Two of the sensors point the telescope at an astronomical target and then hold that target in a scientific instrument's field of view. The third sensor is available to perform scientific observations. The sensors aim the telescope by locking onto "guide stars" and measure the position of the telescope relative to the object being viewed. Adjustments based on these constant, minute measurements keep Hubble pointed precisely in the right direction.

Each FGS enclosure houses a very precise optical interferometer. The pointing control system uses the Fine Guidance Sensors to point the telescope at a target with an accuracy of 0.01 arcsec. The sensors detect when the telescope drifts which gives Hubble the ability to remain pointed at that target with no more than 0.007 arcsec of deviation over long periods of time. This level of stability and precision is like being able to hold a laser beam focused on a dime 320 km (200 miles) away (about the distance from Washington, D.C. to New York) for 24 hours.

The Star Selector Servos "A" and "B" assemblies move independently of each other to affect the tilt of the wave front through the instrument. Each SSS is comprised of a brushless DC motor and 21-bit encoder

* NASA Goddard Space Flight Center, Greenbelt, MD

** Lockheed Martin Space Systems Company, Sunnyvale, CA

+ SEST Inc., Middleburg Heights, OH

** BEI Precision Systems & Space Division, Maumelle, AR

(M/E assembly), supported by a duplex pair set of thin section angular contact bearings (see Figures 1 & 4). The M/E duplex pair (DB) bearing is made up of an “A” bearing and “B” bearing. The inner, and outer spacers, races, and balls were manufactured with passivated, CEVM 440C Stainless Steel. The bearing conformity ratio is 52.5% (race radius / ball diameter). The races and 88 balls per bearing were treated with Tricresyl Phosphate (TCP) for 72 hours at 107°C (225°F) per federal specification (TT-T-656). Each bearing was lubricated with approximately 240 milligrams of Bray 815Z oil in November 1981 by Split Ballbearing. Both spacers were grease plated with Braycote 3L-38-RP, a teflon thickened grease using Brayco 815Z base oil. The bearing separators are Teflon toroids around alternate balls. Throughout this paper, references will be made to the two sets of bearings for each FGS Servo in the following manner:

FGS Servo	Motor/Encoder	Bearing Assy.	Bearing Pair
A	3009	007	0-107 A & B
B	3010	008	0-106 A & B

Previous engineering findings by Stu Loewenthal et al^[2] from ground-based life tests identified that a build-up of degraded lubricant from excessive CT cycling caused a “bump” for the ball to roll over prior to continuing to its required position (Figure 2). This bump caused a spike in the motor voltage as indicated by the Compensated Error (CE) signal, which is a direct indication of a high torque. This CT torque bump, occurring at nominal 9.8 degree ball defect spacing, has been observed to some extent on all FGS bearings, but primarily on A servos due to the method for sampling the CE signal. However, the principal reason for refurbishing FGS-1 was due to servo-B repeatedly stalling after direction reversal during vehicle offset slews (Figure 3). Unlike CT bumps, the exact cause of this “reversal” bump (RB) remained unknown although believed to be a distinctly different type of bearing anomaly, possibly related to internal or foreign debris. Only FGS -1B and -3B exhibited this problem, with FGS-3B in an early stage. However, FGS-3B is still in operation.

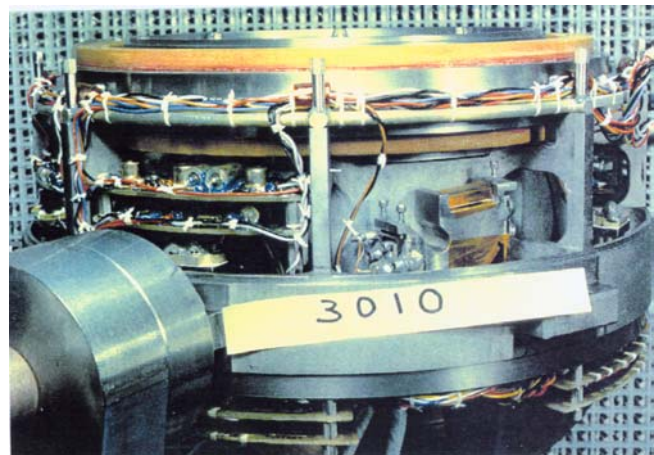
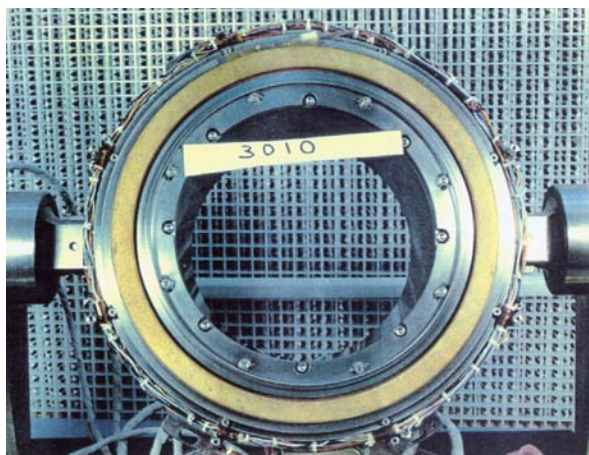


Figure 1. SSS Motor/Encoder assembly (Top). HST FGS-1 SSS-B after cover removal (Bottom) ^[3]

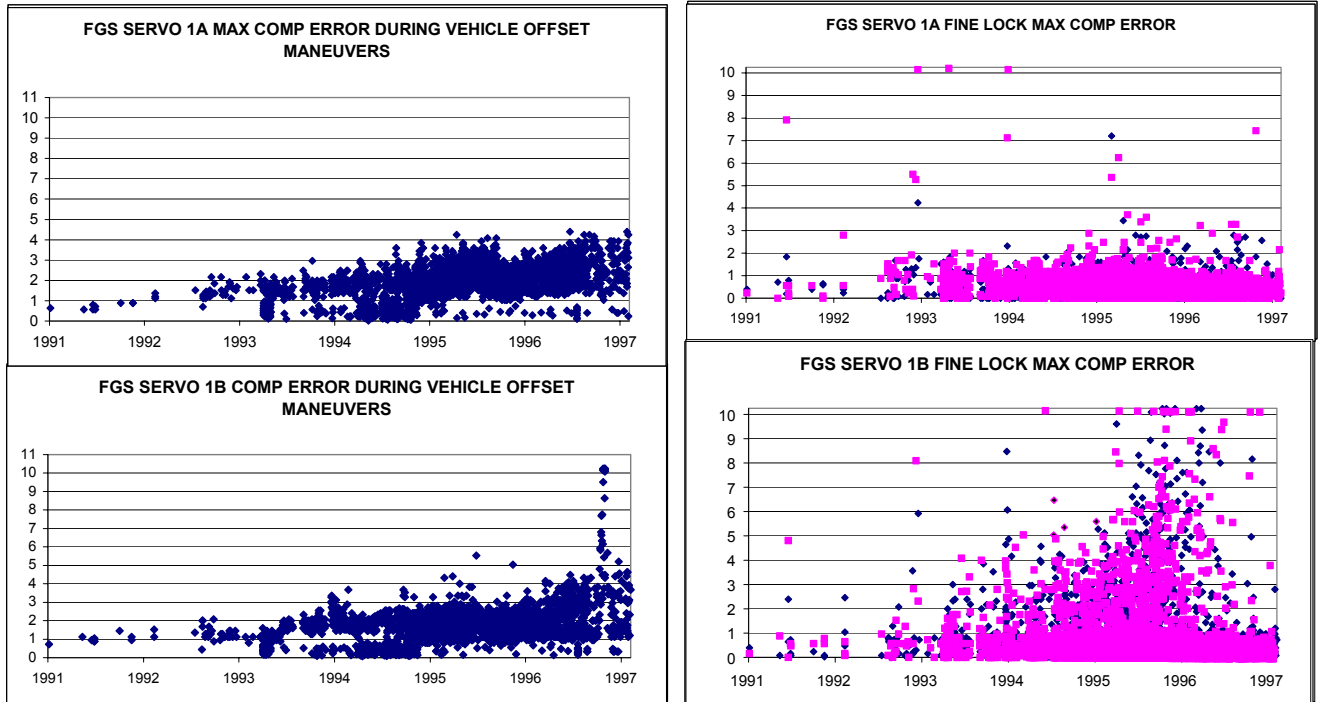


Figure 2. Max Compensated Error (CE) during vehicle offset maneuvers showing CT bumps (Left), and during Fine Lock showing Reversal Bumps (Right). Note: motor stall can occur above 10V Comp Error.

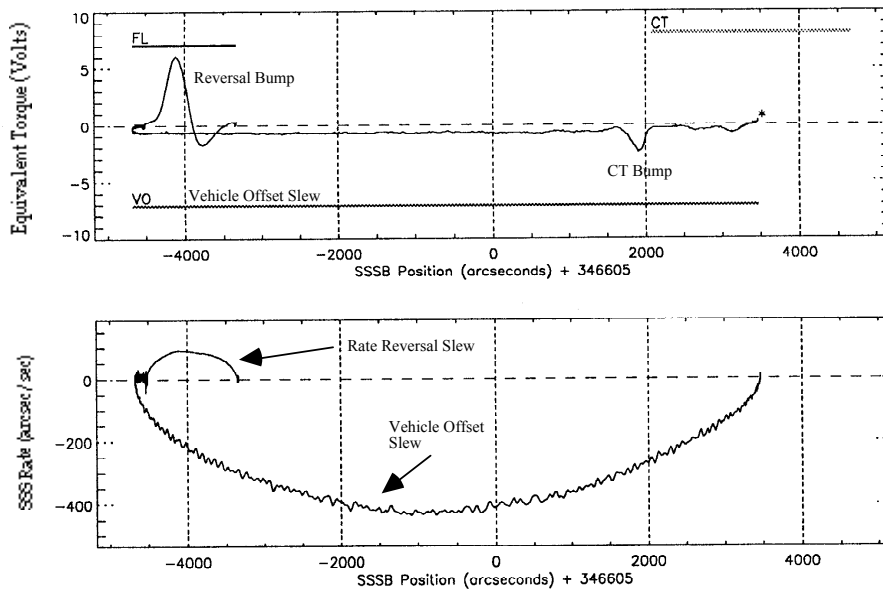


Figure 3. Example of FGS-1 SSS-B Reversal Bump. Initial direction of motion is right to left. Note CT bump at end of CT stroke (bar, upper panel). Direction reverses at a position of about -4,700 arcseconds and a 6.1-volt Reversal Bump forms. [2]



Figure 4. FGS-1 Motor/Encoder SSS-A bearing assy. Encoder optical disk shown (white particulate identified by white arrows) (Left). Clamp Ring removed and 0107B bearing exposed for inspection (Right).^[1]

Inspection Planning & Technology

The objective of the disassembly and inspection of the SSS assemblies were to verify the cause of the CT bump anomaly, but even more importantly, determine the cause of the reversal bump anomaly since it was felt that ground testing well characterized the CT anomaly but could never accurately explain the cause of the reversal bumps. After return of the FGS instrument from SM2 to the HST test facility at GSFC, several ground tests were performed at the instrument assembly level in an attempt to reproduce the on-orbit anomalies. The CT bumps encountered were similar to that on-orbit, although much smaller in magnitude. Reversal Bumps were much smaller than those observed on-orbit (4.4V maximum vs. 10V saturation). By the third day of testing, the Reversal Bumps disappeared and the CT bumps were less than 2V peak.

At the completion of instrument level testing, the M/E's were removed and sent to their manufacturer for additional testing and tear down to the bearing assembly level. Once the motors and encoder electronics were removed, the units were sent to the Material Analysis Laboratory at Lockheed Martin for detailed inspection. The inspection/operations flow is outlined in Figure 5.

The process of planning and creating the procedure for the inspection was critical to having a comprehensive flow that provided the best chance for resolving the anomaly causes. A good plan results in the most efficient use of time during the inspection and test process when support personnel are at the peak and critical equipment must be scheduled around other tasks.

The first step was to determine the most probable causes of the anomalies from the available data. This provides a focus on the task, but should not limit the ability to shift focus onto other areas of concern or potential causes. Conclusions should not be drawn here, but allow for a wide range of *probable* and *likely* reasons for the anomaly. All relevant drawings, test and flight data should be collected and reviewed in support of these hypotheses.

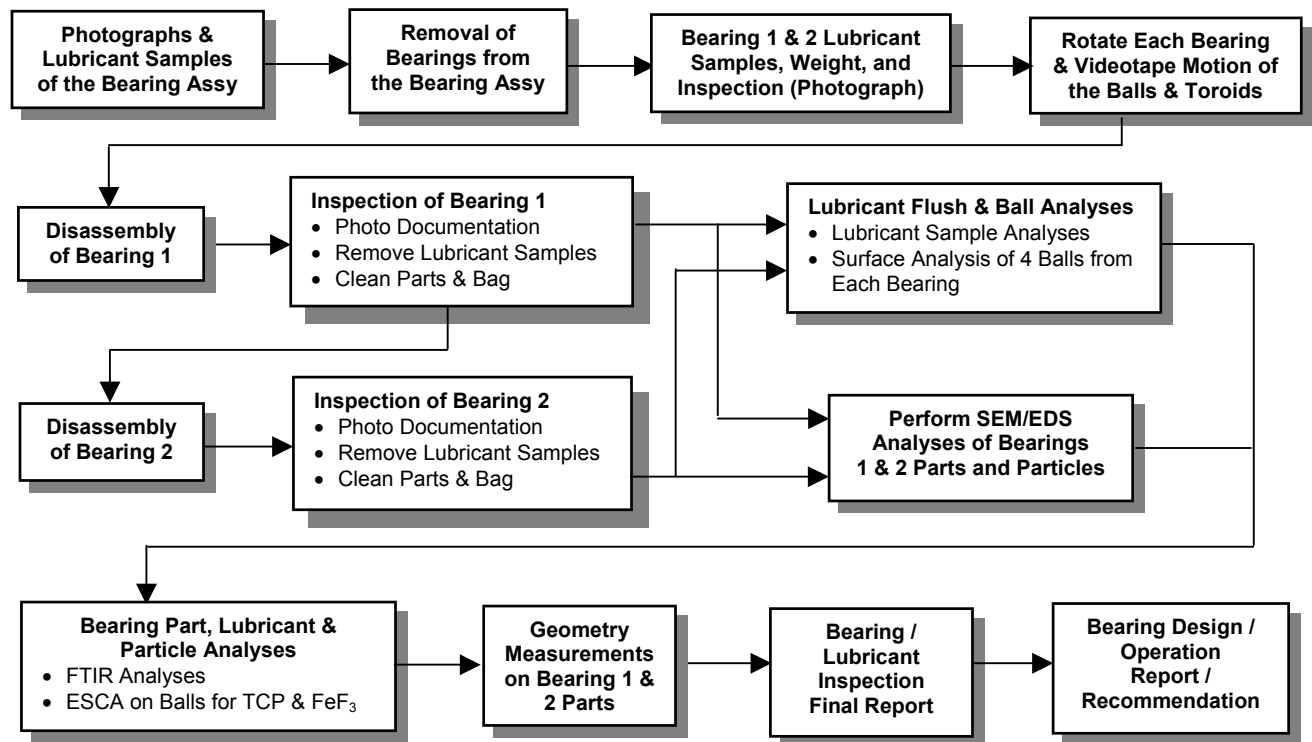


Figure 5. Bearing Inspection and Operation Flow

It is a rare occasion that the nominal acceptance or qualification tests will be sufficient for investigating a specific mechanism anomaly. Therefore, a test plan should be generated to gather more detail regarding the likely causes of the anomaly. Once the unit is torn down, it is probable that it could never be reassembled in a way that would reproduce the identical anomaly. Generally, mechanism torque information can be deduced from motor current amplitude and profile, motor voltage levels, torque transducer tests, and velocity tests. Position accuracy tests can provide an indication of mechanism wear, slop or hardware failure. Often, these tests may need to be run at operational environmental temperature and vacuum conditions to obtain accurate data. Other testing may be necessary based on the specific functions of a mechanism. The key is to be familiar enough with the mechanism and the analytical techniques available to completely evaluate the unit.

Once the test program is complete and the unit disassembly has begun, there are several methods available for investigation of the moving mechanical parts such as the bearings and lubricant in the case of the FGS SSS. It is important to take contamination and lubricant samples at various points throughout the tear down process since these may later provide an indication of anomaly sources. Samples can be taken by using a clean swab on the surface, performing a Freon or IPA (Isopropyl Alcohol) filtered rinse or simply removing a large particle using a clean tool such as dental pick or tweezers. Techniques for hardware surface and contaminant analysis used for the FGS Servos include FTIR, SEM/EDS, XPS (or ESCA), ICP/MS and OLM (defined below). Component weights should always be included in the process when lubricant quantities are in question. However, caution should be used in drawing conclusions from mass measurements since lubricant amounts can be extremely small and lubricant loss can be replaced by contaminants resulting in a false inference.

FTIR (Fourier Transform Infrared) Spectroscopy Analysis provides detailed molecular information on organic complexes and some inorganic groups, thereby aiding in material identification. The instrument

used was capable of examining areas as small as 10 μm , making it feasible to examine microscopic particles, fibers and small quantities of residues. FTIR is also useful for identifying lubricant degradation products.

SEM (Scanning Electron Microscope) equipped with an EDS (Energy Dispersive Spectroscopy) system is used to identify elemental composition of particles such as metallic debris found in bearings. It is also used to evaluate bearing race, ball and separator damage and potential causes at high magnification levels.

ESCA (Electron Spectroscopy for Chemical Analysis) provides compositional information from the top 5 nm of the surface region. Precise measurement of photoelectron binding energies provides the chemical state of surface atoms. Compositional information below the uppermost surface layers was obtained by ESCA in conjunction with argon ion sputtering.

ICP/MS (Inductively Coupled Plasma/Mass Spectrometry) typically detects 65 different elements at parts-per-million (ppm) levels. For the FGS M/E investigation, samples of the white residues from the clamp rings, submitted in plastic snap-cap tubes, were dissolved in 3 mL of 1% ultra-pure nitric acid. Control tubes were treated in the same manner along with the sample residues to check for background contamination. The nitric acid solutions were analyzed using the semi-quantitative feature of a Hewlett Packard Model 4500 ICP/MS (LIMS procedure ICPMS_SEMIQUANT). This method of analysis is generally accepted to be accurate to within ± 20 to 30% of the actual analyte values. The values obtained from this analysis were calculated to reflect the micro-grams of analyte per gram of sample as received ($\mu\text{g/g}$, or ppm).

OLM (Optical Light Microscopy) determines particle size distributions. These were done for the FGS Servos by manual inspection of filter samples of the debris collected from bearing flushes using a microscope equipped with a calibrated eyepiece reticule.

A determination of the logistical requirements for the anomaly investigation should be completed prior to commitment for execution of the plan. This includes facility requirements (floor space, cleanliness, handling of hazardous material (safety requirements)), wipes, swabs, required chemicals for cleaning or flushing debris, debris filters, glassware, packing materials, etc. Disassembly tools and Ground Support Equipment (GSE) necessary for the pre and post inspection tests, and tear down must be considered. In scheduling the task, individual support personnel should be identified by name and their availability confirmed. Finally, a realistic schedule should be generated that lists the major tasks to be performed with allowance for minor deviations resulting from in-process findings.

A final report deadline should also be identified and closely tracked. Since often the cause of an anomaly is not obvious, it is important to scour through all of the inspection data while it is fresh and there is an opportunity for more to be done. Creation of the final report provides a vehicle for systematically analyzing the data collectively to draw valid conclusions and report them to the interested parties.

Below is a general summary outline for the steps necessary in planning a mechanism anomaly investigation. Although some of the items discussed here were specific to the HST FGS M/E anomaly investigation, it can be used as a guideline in many other instances.

Inspection Planning Summary:

1. Determine the most probable cause for the anomaly.
 - a) Collect and review all relevant design drawings.
 - b) Collect and review all relevant test and flight data (if available).
2. Determine the desired testing program prior to tear down of the unit.
 - a) Thermal and/or vacuum environment required?
 - b) Motor current, voltage, torque transducer, velocity, position accuracy, operational vibration (accelerometer).
3. Surface, lubricant, and particle analysis techniques required to fully evaluate the unit to be inspected.

- a) These should include those required to verify the most probable findings in addition to other possible anomalies.
- b) Analytical Equipment includes: FTIR, SEM/EDS, ESCA or XPS, ICP/MS, OLM, and Gram Scales.
- c) Techniques to be used for taking samples.
 - 1) Surface swab samples.
 - 2) Manual extraction.
 - 3) Freon rinse and filter.
- 4. Determine the logistical requirements for the inspection.
 - a) Facility requirements (cleanliness, hazardous material, safety, etc.).
 - 1) Lab Coats, gloves, wipes, swabs, chemicals, debris filters, glassware, packing.
 - b) Tools and GSE needed for disassembly.
 - c) Available Personnel.
 - d) Schedule (provide sufficient time for changes to the plan based on findings).
- 5. Final Report

The outline above was not available for the HST FGS mechanism inspection; however, most of the steps listed were included in the initial planning process. The remaining detail, such as the actual analytical equipment used, was added during the inspection and documented in the final report.

FGS M/E Inspection & Findings

Prior to creating the FGS-1 M/E Inspection Plan, a general idea for the cause of the CT and RB anomalies was developed. It is difficult to predict what would be found during the detailed inspection and material analyses. However, industry tests in addition to the previously mentioned Life Tests^[2] provided a clue to what was expected. Therefore, the focus of this task became a lubricant and bearing degradation problem. It was anticipated that degraded lubricant would be found, however, the pertinent question was the cause of the degradation. Was it from a loading situation, contamination, operational scenario, workmanship, or some other phenomena?

Before the unit was disassembled, a battery of tests were conducted at the instrument level and the mechanism bench level^[3]. Table 1 provides a comparison between the performance of the M/E from its build Acceptance Tests in 1983 to its performance after removal from flight FGS-1 at the mechanism vendor's facility in 1998. It was concluded from this test data that there was a very slight degradation of positional accuracy in the motor encoders (probably due to degradation of the light output in the readstation LED's) but no other significant changes in performance was noted.

After all bench tests were completed, the M/E manufacturer disassembled the mechanism down to the bearing cartridge, which includes the housing, shaft, bearings and spacers. These are self-contained units, and it was not possible for contamination to enter this portion of the mechanism. The M/E's were then bagged, packed and shipped to the facility for final disassembly, detailed inspection and analyses.

After disassembly and inspection of the two M/E assemblies, the bearings were removed, visually inspected, photo-documented, and weighed. Some of the debris observed during the low magnification observations were lifted via probing and analyzed using a battery of analytical techniques, including FTIR, SEM, EDS, and ESCA (or XPS). Bearing motion testing was conducted to observe the behavior of the toroid ball separators under operation similar to on-orbit cycling. Subsequently the bearings were flushed to collect the remaining loose debris. Finally the bearings were disassembled, and the condition of bearing races, balls and toroids were evaluated visually under an optical microscope and with a SEM.

Both SSS-A and SSS-B bearings contained degraded lubricant residue, little to no free oil and were heavily contaminated with foreign fibers, metallic and non-metallic particles. None of the bearing components appeared to have experienced significant wear. With the exceptions that the lubricant in 0106 (SSS-B) bearings was slightly less degraded than the 0107 (SSS-A) bearings, and the 0107 bearings had less non-metallic particles (mostly skin), there was no other obvious differences between the relative condition of the bearings. The observed differences were insufficient to explain conclusively why the 0106 bearings in FGS-1B experienced reversal bumps and the A-servo did not. However, the

difference in location of the degraded lubricant on the toroid (faces of 0106 and bore / OD of 0107) with its observed motion during reversal provides a hypothesis of increased friction between the toroid and race land. The more degraded lubricant condition in the 0107 bearings is consistent with the observation that all of the A-side servos generally have more serious CT bump problems than the B-side servos. Figure 6 is photographs of the 0107 and 0106 bearings and lubricant degradation products.

Table 1. Star Selector Servo Subsystem Performance Test Data Comparison ^[3]

TEST PARAMETER	FINAL PERFORMANCE TEST 9 NOVEMBER 1983		INCOMING EVALUATION 6 MARCH 1988	
	ME 3009 & RU 4009	ME 3010 & RU 4010	ME 3009 & RU 4009	ME 3010 & RU 4010
Case Gnd to Circuit Gnd Isolation	> 10 Megohms	> 10 Megohms	> 10 Megohms	> 10 Megohms
Case Gnd to Case Gnd Pin Continuity	< 1 ohm	< 1 ohm	< 1 ohm	< 1 ohm
Running Torque (Comp. Error Signal):				
Amplitude	Unknown (1)	Unknown (1)	0.7 to 1.0 volts	0.8 to 1.2 volts
Spikes in Trace	None	None	None	None
Direction of Rotation				
Increasing Count	CCW	CCW	CCW	CCW
Decreasing Count	CW	CW	CW	CW
Sequence Test (SIGN Up)	No Errors	No Errors	No Errors	No Errors
Servo Bandwidth (Open & Closed Loop)	Acceptable	Acceptable	Acceptable	Acceptable
Power Dissipation				
M/E (Motor On)	5.07 watts	5.03 watts	5.16 watts	5.06 watts
R/U (Motor On)	4.04 watts	3.54 watts	3.59 watts	3.51 watts
Total System Power (Motor On)	25.79 watts		25.63 watts	
M/E (Motor Off)	3.59 watts	3.60 watts	3.60 watts	3.54 watts
R/U (Motor Off)	4.08 watts	3.63 watts	3.55 watts	3.48 watts
Total System Power (Motor Off)	22.34 watts		21.94 watts	
Position Accuracy (Max. Peak-to-Peak Error)	1.27 arc sec	2.10 arc sec	2.095 arc sec	3.034 arc sec

(1) 1983 Torque Traces were run without gridlines, so it is difficult to measure the exact amplitudes of the compensated error signal responses. Amplitudes are estimated to be between 0.5 and 1.0 volts for both motor encoders.

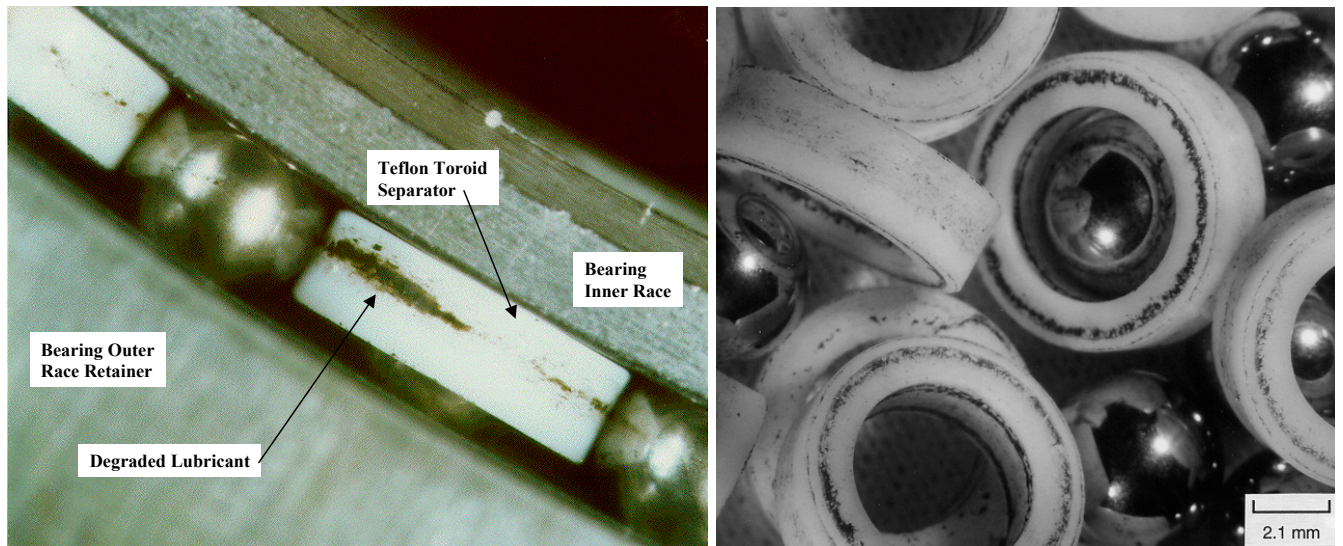
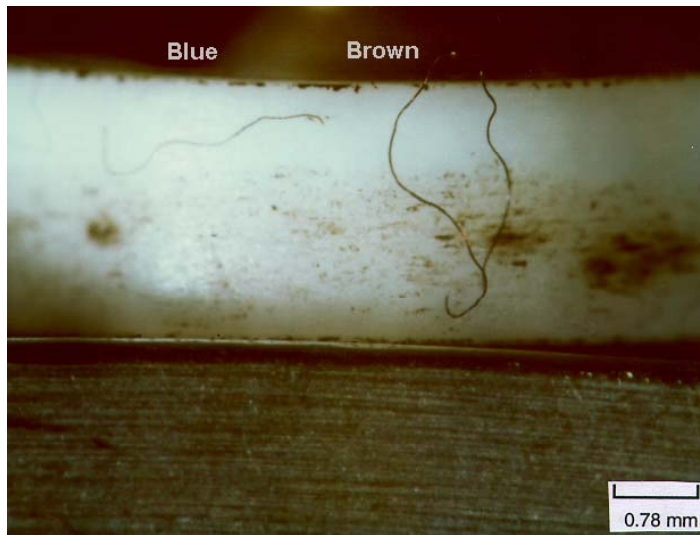


Figure 6. Bearing 0107B (SSS-A) mounted in bearing assembly housing (Left). Bearing 0106A (SSS-B), balls and toroids after bearing disassembly (Right). Note locations of degraded lubricant on the separator. ^[1]

There is no conclusive evidence that the foreign debris found in the FGS-1 bearings contributed to the problems observed on-orbit. It is surprising that torque spikes were not more prevalent during on-orbit service and during post-flight testing, considering the abundance of metallic and fibrous debris in both sets of bearings. It is unlikely that this debris was introduced during the inspection process, because strict attention was paid to contamination control during inspection. Also noteworthy are the observation of variety of contaminants with many types not even present in the inspection area, and less debris observed in the entry zone areas (such as the housing, clamp rings, etc.) as compared to that within the bearings. The presence of flattened fibers and metallic particles, and the extensive denting on the balls and races (potentially some of these inflicted by the debris) also indicate these are not artifacts introduced during disassembly. Although some of the aluminum particles could conceivably have been introduced from the aluminum motion tester, the flattened, plate-like appearance of the particles suggests that considerable torque would have been required. Furthermore, the energy required to roll over this debris would undoubtedly have caused hang-up of the motor. This suggests that the bulk of this damage likely occurred during early bearing run-ins prior to final instrument assembly. The following paragraphs describe the data achieved from each of the analytical techniques described in this paper.

Figure 7 shows the fibers from the 0106B bearing. Table 2 lists the fiber size distributions from each of the four bearings. Most obvious from the table is that the 0106B bearing flush has a greater number of fibers in each size-range class. Also, there were more fibers observed in the "B" bearings than in the "A" bearings. The entire filter surface was scanned at 50x magnification. As shown, a large number of fibers (>60 on each filter) were counted in the bearing-flush debris. To characterize, 8 to 9 fibers of different types were selected for infrared analysis. The infrared spectra show that the fibers from each of the bearings are predominately polyester and cellulosic based compounds. Several polyamide-based fibers (nylon 6 or 66 in some cases) and an acrylic fiber were also observed. Figure 8 shows the associated FTIR analysis for a particular fiber from this bearing.



M/E 3010, Bearing 0106B, Blue (left) and brown (right) fibers found on toroid prior to flushing. FTIR indicated blue to be cellulosic, and brown to be polyamide.

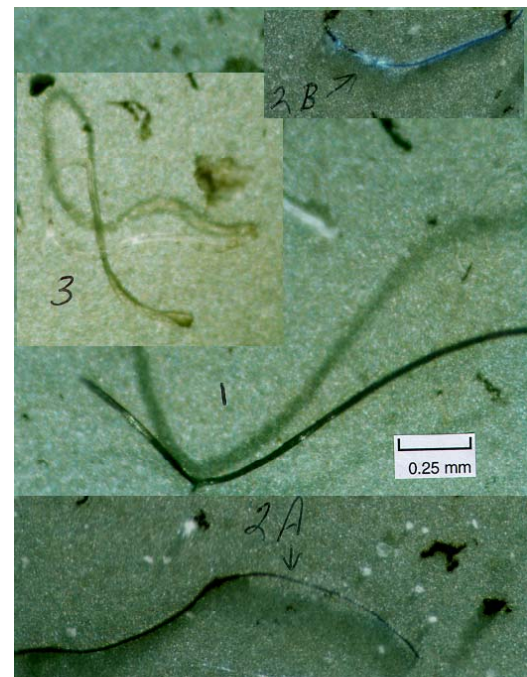
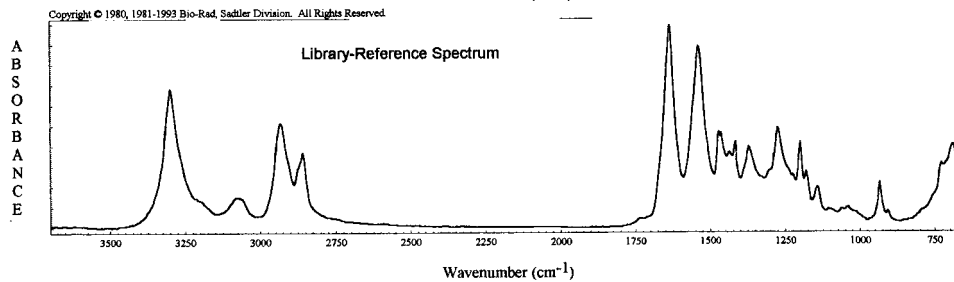
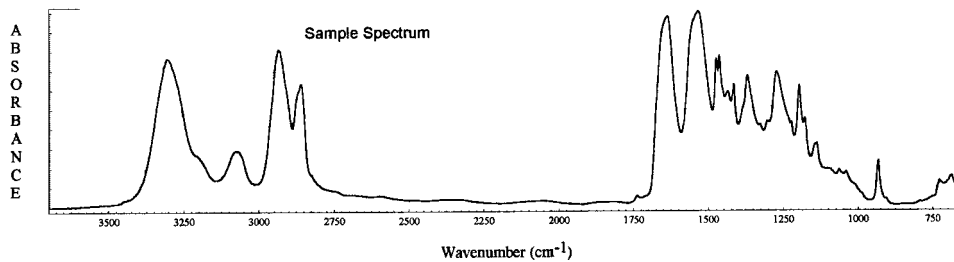


Figure 7. Bearing 0106B fibers removed from filter paper debris and analyzed by FTIR. [1]

Table 2. Fiber Size Distribution ^[1]

Size Range, microns	0106A Counts	0106B Counts	0107A Counts	0107B Counts
100-250	12	20	8	18
251-500	22	53	24	37
501-1000	23	47	20	34
>1000	10	28	13	11
Totals	67	148	65	100

AF1551S2.SPA



W1951 VYDYNE 66B HIGH MOLECULAR WEIGHT EXTRUSION GRADE NYLON 66

Figure 8. FTIR spectra of nylon library ref. (bottom) and fiber found in 0106B bearing (top). ^[1]

The bearing races, balls, and toroids were examined prior to additional cleaning using an Optical Light Microscope (OLM). The inner races and balls were also examined using Scanning Electron Microscopy (SEM). In both cases, too much residual lubricant was observed, that masked the wear or damage evaluation. Hence, the inner races and balls were further cleaned using Freon and a polyester swab and/or wiper to remove the residual lubricant. Due to the size limitation of the SEM chamber, only the inner races could be introduced into the SEM and examined; outer races were not examined.

Four balls per bearing were examined using SEM. The damage on the balls was similar to those observed on the races, except smaller, typically less than 20 micrometers. Multi-fragment dents and pits/pullouts were noted in at least one of the four balls from each bearing. The most prevalent damage in the ball track of the inner races, as observed using SEM, was indents. The indents typically ranged in size from 20-100 micrometers in diameter, a few were less than 20 micrometers. Some bearing inner races had indent patterns that were repeated on the same race which suggested that debris was able to cling to a ball or toroid as it rolled on the race. The Fringe, defined as plastically deformed metal at the edge of a pit or indent that resulted from excavated or plowed material, may be capable of causing repeated bumping during service, hence, the damage was categorized as with or without fringe. Figure 9 illustrates two examples of a damage fringe. One that has been rolled over during service operation and one that has not.

Flushed particles that appeared metallic were also analyzed by SEM / EDS to determine their origin. Figure 10 is an example of a 300 series stainless steel particle with a smooth surface. These surface characteristics indicate that the particle was most likely in the bearing raceway at some point and rolled over by the balls during operation. The origin of this particle is probably from the mechanism fasteners.

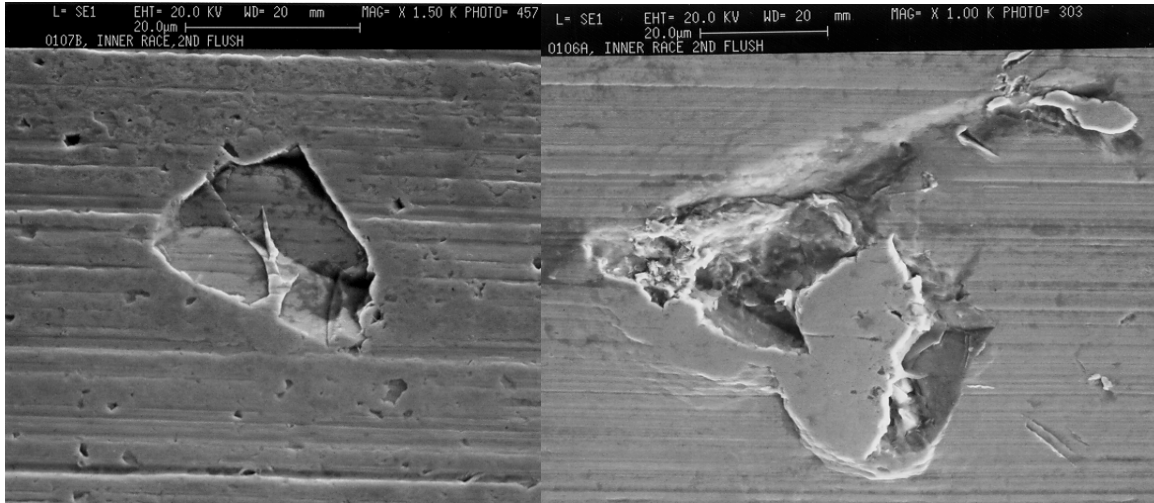
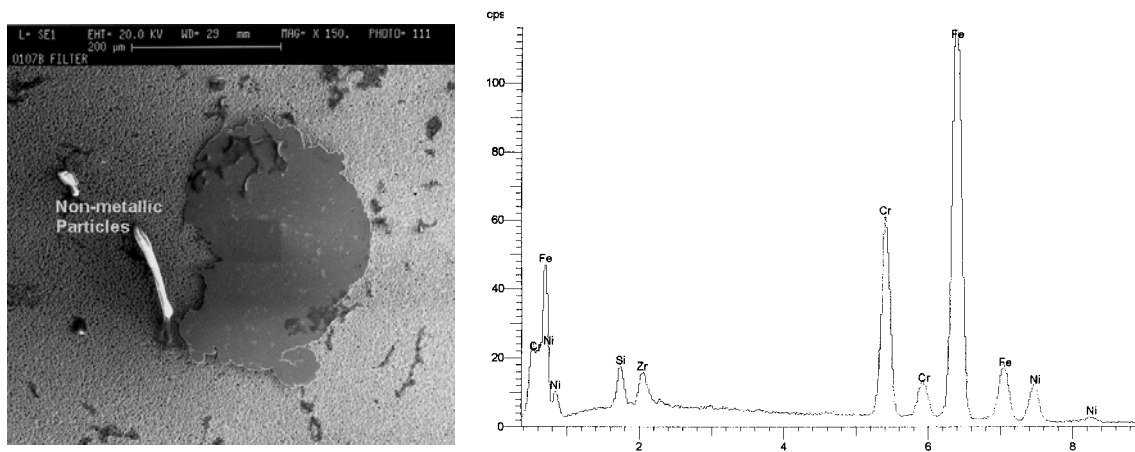


Figure 9. SEM photomicrograph of bearing 0107B indent without plastic deformation or without edge fringe (Left) and SEM photomicrograph of bearing 0106A with multi-fragment indent with plastic deformation or fringe (Right). [1]



Bearing 0107B, SEM micrograph (left) and corresponding EDS spectrum (right) of thick metallic particle, approximately 375 micrometers in length. EDS spectrum indicated Fe, Cr, Ni, and Zr, probably a 300-series stainless steel. Particle was thick enough to block filter paper Ag signal.

Figure 10. Bearing 0107B SEM of particle. [1]

ESCA (Electron Spectroscopy for Chemical Analysis) was used to examine the surface chemistry, and in particular to understand the presence of phosphorus reaction compounds (originating from TCP) and fluorine reaction compounds (from lube), if any. One ball per bearing was examined using ESCA. Table 3 summarizes the composition of the various ball surfaces after the initial Freon flush and after further flushing. The detection of ionic fluorine on the ball surfaces suggests lubricant breakdown and subsequent reaction with the metal(s) in the steel ball. The persistence of fluorine after flushes and

sonication suggests a potential strong bond of the lubricant with the steel. No phosphorous was seen on any of the ball surfaces, suggesting that it was either removed by surface wear during the bearing operation or the TCP treatment was inadequate. Race surfaces could not be examined for phosphorous due to limitation of physical size of the ESCA chamber.

Table 3. ESCA Results of Freon Flushed Bearing Balls ^[1]

<u>Specimen</u>	<u>Composition (Atom %)</u>						
	<u>F</u>	<u>O</u>	<u>C</u>	<u>Fe</u>	<u>Cr</u>	<u>N</u>	<u>Other</u>
#0106A, First flush	44	21	30	3.7	0.5	0.4	
#0106A, Second flush	21	27	42	6.9	1.6	1.0	
#0106B, First flush	44	20	32	3.0	0.5	0.4	
#0106B, Second flush	21	24	48	4.6	1.7	0.9	
#0107A, First flush	46	20	30	3.0	0.6	0.3	
#0107A, Second flush	17	30	42	6.8	3.2	1.0	
#0107B, First flush	48	20	28	3.3	0.6	0.3	
#0107B, Second flush	23	24	45	5.4	2.5	0.9	0.1 Cu, 0.1 Cl
#0107B, Sonicated in Freon	21	28	40	7.1	3.2	0.7	0.2 Cu, 0.3 Cl, 0.2 Na, 0.1 Mo
Braycote 815-Z	57	18	25				

A white-grainy material was observed on the shafts and clamp rings of both motor/encoders. The bearing clamp ring is machined beryllium S-200E, with no coating. The shaft material is also machined beryllium, but with an electroless Ni coating. After removing a small portion of the residue, the clamp rings were found to contain many small pits. Samples of the white residue were probed off both clamp rings, dissolved in 1% ultra pure nitric acid, and analyzed by ICP/MS (Inductively Coupled Plasma/Mass Spectrometry). High levels of beryllium were detected, however, due to the difficulty of isolating the white residues, only minute samples were tested thereby limiting the quantitative accuracy of the reported results.

During the investigation process, a report was found on a spare bearing set from the same lot as the flight units manufactured in the 1981 time frame. In 1987, this spare set was sent back to the manufacturer for refurbishment (well after assembly of the flight units). This refurbishment revealed contamination and debris particles in the bearing, rolled flat, of the same type found in the FGS-1 M/E's. The bearing races also showed evidence of brinelling. These spare bearings were subsequently cleaned, honed, and reassembled with new balls. The refurbished spare bearings functioned within specification requirements. It is thought that the metal partials described above were rolled flat probably during run-in at the bearing vendor prior to shipment. The contamination source may have been the solvents (unfiltered) used to clean the bearings prior to lubrication. It is surprising that all torque traces recorded during assembly of the flight mechanisms were in family and within requirements and that pre-disassembly torque traces showed essentially no evidence of the extensive debris in these bearings. Apparently, the debris was pushed out of the ball running track and content to stay in areas that didn't have much of an effect on torque.

Conclusions

The completed inspection as described herein resulted in several general findings for the FGS M/E bearings and some specific to each bearing. In general, no evidence of the anti-wear additive (TCP) was found on the bearing balls. The bearings appeared dry (some more than others) with degraded, "black tar

- like," lubricant with the degraded lubricant adhered to the races and toroids. There was a slight oil film noted around the balls when viewed under microscope at ~6x. Hundreds of skin particles and fibers were found in bearing flush filters. Many metallic particles were also found on the bearing flush filter and analyzed by SEM/EDS. Most particles were determined to be 300 - series stainless steel, galvanized steel, carbon steel, 6000 - series aluminum and brass. SEM results on the bearing races revealed damage (recorded only if in wear track) characteristics of indentations with fringes, indentations without fringes, multi-fragment dents with fringes, multi-fragment dents without fringes, repeated dent patterns, pits / pullouts and multi-fragment dents on the balls, and detection of ionic fluorine on ball surface that suggests lubricant breakdown. It was also observed during the bearing rotation test that the toroids tend to wobble from inner to outer race when the bearing reverses direction and at least one toroid in bearing 0-106A appeared to skip across the race land as the bearing rotated.

There is no conclusive evidence that the foreign particles alone contributed to the on-orbit anomalies. There were no torque spikes during initial build and test. The post flight torque traces were mostly clean, although not unexpected, the torque noise on the traces was about 30% larger, probably due to lack of lubricant, contamination, and damage to balls and raceways over life. The FGS life test bearings showed CT bumps without contamination - only degraded lubricant. The presence of numerous flat fibers and metal particles in the bearing and smooth torque traces show that the bearing run-in and functional testing flattened the particles and permitted smooth performance. All FGS bearings yielded smooth torque traces initially even though they most likely contain particles. Degraded lubricant was most significant contributor to an on-orbit Coarse Track torque increase. Degradation debris collected at the end of each stroke caused a bump for the ball to roll over. This was evident from the CT anomaly reproduced in life tests at Lockheed Martin Space Systems Company (LMSSC) in 1994^[2]. Operational changes in 1994 significantly reduced CT cycles.

Reversal Bumps were never reproduced during life testing at LMSSC in 1994 and ground tests on FGS-1 at the GSFC VEST facility, post SM2, were never able to reproduce the magnitude of RB's seen on orbit. After three days of tests, the existing RB's disappeared. There was inconclusive evidence from inspection to explain reversal bump phenomena; however a hypothesis is that a combination of degraded oil, dry bearing, particulate debris and blocking caused the Reversal Bumps. Reversal bump characteristics occurred at ~0.128 degrees (460 arcsec.) after reversal, suggesting a very steep torque slope. This indicates that a foreign particle may be caught between the ball and race upon reversing direction. As the ball rotates in one direction, the toroid edge acts as a wiper pushing a particle along the surface of the ball. When direction is reversed, this particle stays with the ball and gets wedged between the ball and raceway creating the RB. Also, an error or misalignment in the ring can cause the ball to spin and the contact angle to fluctuate as it travels around the bearing. The change in contact angle causes varying ball speeds that result in the balls applying load to each other (*Blocking*^[4]), leading to increased torque. As a result of this inspection exercise, several recommendations were made for the rebuild of the future FGS M/E's. These included bearing race conformity changes to reduce the ball spin, reducing the likelihood of blocking and similar oscillatory torque anomalies. Verification of adequate application of anti-wear additive coatings where a control sample from the treatment may be required to validate the adequacy of the process. Strict contamination control requirements for processing and handling of the bearings and bearing assemblies. Finally, addition of more lubricant to the bearings.

The methods and technology utilized for this inspection are not unique to this system and can be adapted to most investigations at varying stages of the mechanism life from development, through testing, to post flight evaluation. The systematic methods used for the HST FGS SSS and specific findings are the important subjects of this paper. The lessons learned from the hardware include the importance of cleanliness and handling for precision instrument bearings and the potential effects from contamination. The analytical techniques used for the SSS inspection and their importance in this investigation should be considered as a template for future anomaly studies.

Acknowledgement

The authors would like to acknowledge the invaluable contributions for the support and state-of-the-art methods used by the Lockheed Martin Materials and Failure Analysis Team and in particular Dr. A. Joshi who organized the lab work.

References

1. Joshi, A., Christensen, P., Jurta, R., Loewenthal, S., & Pellicciotti, J., *HST FGS-1 Star Selector Servo Bearing Inspection*, LMSSC/P505033, 4 September 1998.
2. Loewenthal, S., Esper, J., Pan, J., & Decker, J., *Space Telescope Fine Guidance Sensor Bearing Anomaly*, 30th Aerospace Mechanisms Symposium, NASA CP 3328, pp13-29, May 1996.
3. BEI Sensors & Systems Co., *Preliminary Evaluation Report for the As-Received Condition of Motor/Encoders S/N's 3009 & 3010 and Remote Units S/N's 4009 & 4010 Returned from the Hubble Space Telescope's Fine Guidance Sensor / Radial Bay Module S/N 2002*, 2 July 1998.
4. Todd, M.J., European Space Tribology Laboratory, UKAEA, Risely, England, *Investigation of Torque Anomaly in Oscillating PDM Bearings*, ESA (ESTL) 49, May 1981.

Effect of Test Atmosphere on Moving Mechanical Assembly Test Performance

D. J. Carré* and P. A. Bertrand*

Abstract

Satellites and many of the moving mechanical assemblies (MMAs) on board operate under the low-pressure conditions of the orbital environment. In order to assess the lifetime performance of these devices, it is desirable to test them under the same conditions they will experience during mission operation. However, many times contractors test MMAs in a nitrogen gas environment at ~1 atm pressure, assuming the test results will be comparable to those obtained in a vacuum test due to the inertness of the nitrogen gas. We were concerned that impurities in nitrogen gas, such as oxygen even at ≤ 1 -ppm levels, would lead to different chemistry and rates of reaction compared to vacuum conditions, where the oxygen levels are lower by at least a factor of 1000. In order to test this hypothesis, we performed a set of experiments using our in-house, thrust-bearing wear-test facility with hydrocarbon oils containing an aryl phosphate ester additive mixture. We used a load that resulted in a Hertzian stress of 1.52 GPa, at the high end of typical ball-bearing stresses. We used test time to failure to assess performance differences. The wear tests lasted at least a factor of 5 times longer in nitrogen gas than in vacuum. Since the temperatures of the vacuum and nitrogen tests were matched, this implies that there are chemistry differences occurring at the metal surfaces. We conclude from our test results that nitrogen gas at ~1 atm pressure is not a realistic substitute for vacuum conditions for life testing of MMAs that will operate under orbital low-pressure conditions.

Introduction

The external pressure in which interplanetary spacecraft and Earth satellites operate is typically $< 1 \times 10^{-4}$ Pa. Many of the moving mechanical assemblies (MMAs) are vented to the external environment so that the external and internal MMA pressures are equilibrated. It is desirable to perform life tests of these MMAs under the low-pressure conditions in which they will operate [1]. However, due to budget constraints, contractors often test the MMAs in a near-ambient pressure, nitrogen gas environment. The assumption is that the relatively inert nitrogen gas will give results that are comparable to those obtained in a low-pressure (vacuum) environment. We have held the belief that there are differences in chemistry between the two environments, as well as obvious thermal differences due to the presence or absence of convection. For example, in nitrogen gas with an oxygen content of ~1 ppm, a low impurity level, there is approximately a thousand times more oxygen than there is in a low-pressure test at a pressure of 1.3×10^{-4} Pa. This could lead to significant differences in the rates of surface reactions, which could adversely affect performance and invalidate the results of the nitrogen gas testing. In addition, the source of the nitrogen gas could play a pronounced role. Blow-off gas from a liquid-nitrogen storage tank typically contains more oxygen than 1 ppm. The presence or absence of water in the nitrogen gas could also play a role in surface reactions. To our knowledge, prior to our work, no systematic tests that compare liquid-lubricated MMA performance in vacuum and nitrogen gas have been reported. There have been reports in the literature of standard tests of specific lubricants that show differences in test life between vacuum and nitrogen gas [2] and between dry air and nitrogen gas environments [3]. Also, studies have been reported that show that solid-lubricated MMAs perform significantly better in nitrogen gas than in vacuum [4,5].

Hydrocarbon oils used to lubricate MMAs in spacecraft typically contain anti-wear additives to reduce the wear of the interacting metal surfaces. In previous work, we have shown that the extreme pressure additive, lead naphthenate, disappeared quickly from the lubricant in ball bearings under vacuum conditions. We determined that this was due to chemical reactions on the surface of the metal parts [6].

* The Aerospace Corporation, El Segundo, CA

We then conducted a series of experiments under vacuum and nitrogen gas conditions using hydrocarbon oils with lead naphthenate additive under several load conditions (loads resulting in Hertzian stresses of 0.36, 0.97, and 1.52 Gpa) and speeds [7]. Under the highest load conditions, the nitrogen gas tests lasted at least 10x longer without failure than the vacuum tests, which failed. Under the lower loads, there were significant differences in additive chemistry in nitrogen gas relative to vacuum [7]. We were interested in whether aryl phosphate esters would show similar behavior since they are commonly used as anti-wear additives in spacecraft applications. We undertook a series of wear-test experiments to determine whether the performance of hydrocarbon oil, formulated with aryl phosphate ester additives, is different in nitrogen and vacuum environments under the same load and speed conditions as our previous experiments with lead naphthenate additive.

Experimental

Lubricant

Nye 2001, a trialkylated cyclopentane synthetic hydrocarbon oil with 2% Syn-O-Ad 8478 phosphate ester additive, was used in the experiments reported here. The oil was purchased from Nye Lubricants, and is used in current spacecraft systems.

Testing

Wear testing was performed using our in-house, eccentric-bearing wear test facility, which has been previously described [8]. A thrust ball bearing in which one of the raceways can be replaced by a flat disk comprises the interacting component of the test fixture. The remaining raceway can be mounted slightly off the axis of rotation of the disk ("eccentric mode"), resulting in increased ball sliding on the disk surface and increasing the severity of the test conditions [8]. There was a ~17% sliding component in the ball motion for the tests reported herein. It is the sliding component that accelerates failure in these tests. Ball bearing temperature was measured using a thermocouple touching the bearing race.

The ball bearing raceways and balls, and the disks, were composed of 440C stainless steel. The thrust bearings have a raceway diameter of 2.29 cm and 12 balls of 0.476-cm diameter. The average raceway surface (R_A) was $\leq 0.25 \mu\text{m}$, and the R_A of the disks was $\sim 0.015 \mu\text{m}$. The balls were ABEC grade 5, with an R_A of $\sim 2 \mu\text{in}$ ($\sim 50 \text{ nm}$). The ball retainer was the steel ribbon retainer furnished with the thrust ball bearing. The loads on the retainer were low, so that the tests would not be impacted by reactions involving the retainer surfaces.

The metal components were cleaned using Brulin 815GD detergent (diluted with H_2O), rinsed in distilled H_2O , and rinsed in heptane before testing. The test speeds were chosen to fall within the speed range typical of MMAs, and the load was chosen to produce a Hertzian stress at the high end of the typical range in order to result in test failure in a reasonable test time.

External cooling was provided for the testing in vacuum to keep the ball-bearing temperature relatively low due to the lack of convective cooling. Cold water (20°C) was circulated through a heat sink in good thermal contact with the ball bearing housing. The temperature was measured using a thermocouple in contact with the outside of the raceway. The temperature was maintained at 24°C , similar to that of the nitrogen tests.

The tests were carried out in the eccentric mode with flat disk, either in vacuum (pressure less than $1.3 \times 10^{-4} \text{ Pa}$) or gettered nitrogen gas. The speed was 1800 rpm, the Hertzian stress was 1.52 Gpa, and the lubricant quantity was $10 \mu\text{L}$. The tribological regime was expected to be mixed or boundary [8]. The test was considered to fail when the nominal running torque increased by a factor of 1.7. Failures in this test facility are abrupt, so that the arbitrary choice of the torque increasing by the 1.7 factor does not significantly affect the test results. The tests were either run to failure, or run until a reasonable time period had elapsed without failure occurring. Six tests were run in vacuum and four under nitrogen gas conditions.

Results and Discussion

The results of the testing are given in Table 1 and illustrated in Figure 1. It is noteworthy that only one of the nitrogen gas tests failed (28.4×10^6 revs). The remaining three tests under nitrogen gas were stopped. We stopped one test at 17.32×10^6 revs prematurely, compared to the other tests. If we do not include this result, the average duration for the other three tests is $30.9 \pm 2.4 \times 10^6$ revs. Thus, we conclude that the nitrogen gas tests lasted at least a factor of 5 longer than the tests under vacuum conditions. This is similar to the results of our testing using lead naphthenate additive. Under essentially the same conditions, the lead naphthenate tests in nitrogen lasted at least a factor of 10 longer than the tests in vacuum [7]. In the case of lead naphthenate, we believe that the differences in wear life are related to the competition between oxygen and the additives for metal atom surface sites on the contacting metal parts. In nitrogen gas, the oxygen concentration is high enough that oxygen can compete with the additive for freshly exposed metal and passivate the surfaces. On the other hand, under vacuum, where the oxygen concentration is very low, the additive competes successfully for surface sites with which to react, its concentration in the oil is reduced at a higher rate than it is under nitrogen gas, and thicker Pb-containing films build up.

Table 1. Wear Test Results

Environment	Test Duration (revs x 10^6)	Ave. (revs x 10^6)	Failure (Y/N)
Nitrogen gas	28.4	27.5 \pm 7.1* (or 30.9 \pm 2.4**)	Y
	17.3		N
	33.2		N
	31.2		N
Vacuum	2.45	5.9 \pm 3.6	Y
	10.79		Y
	2.45		Y
	6.08		Y
	3.92		Y
	9.76		Y

*Including all tests.

**Excluding test that was stopped prematurely at 17.3×10^6 rev.

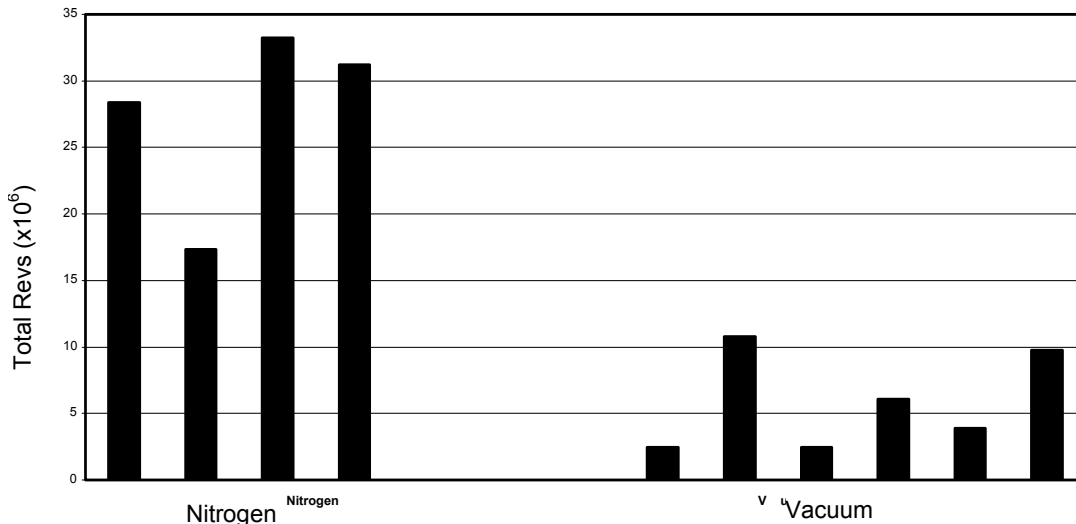


Figure 1. Wear Test Results

The mechanism of action of aryl phosphate ester additives is not completely understood. Aryl phosphate esters can react with oxidized iron and steel surfaces [9,10] at temperatures above 100°C , and pretreatment of bearing parts with phosphate additives at such temperatures, leaving phosphate-

containing films, is common. However, aryl phosphate esters can also react with iron metal [10,11], again leaving phosphate-containing films on the surface. The relative importance of these two reaction pathways in an operating bearing is unknown. If the reaction with iron metal is more important than reaction with oxide, there will be more reaction in vacuum than nitrogen gas since the additive will not have to compete with oxygen for metal sites. This would lead to relatively less additive in the oil, and more phosphate film on the surface than in nitrogen. If the reaction with metal oxides is more important, however, there will be more reaction in nitrogen gas than vacuum since the contaminant oxygen will prepare the exposed metal for reaction with the additive. This would lead to relatively less additive in the oil, and more phosphate film on the surface than in vacuum. The wear life itself cannot be used to distinguish between the two pathways since the test process is too complex for straightforward analysis. The tests are defined to fail at a particular increased level of torque. High torque could be due to adhesive wear due to metal on metal contact (i.e., ineffective additive function or exhaustion of additive in the oil), or to thick additive film buildup (over efficient additive function). The efficacy of the particular reaction product in extending life and the amount of additive present in the oil are also inextricably convoluted into the wear life. In future experiments, we intend to halt operation of bearings before failure, and analyze the oil and surfaces to discover the relative importance of the metal or oxide reaction pathways.

Conclusions

The results of this study indicate that the tribological performance of MMAs lubricated with aryl phosphate ester-formulated oils will be different in vacuum and nitrogen at atmospheric pressure. Apparently, reaction between the additive and the metal surfaces of ball bearing parts is retarded in nitrogen gas compared to vacuum conditions. Thus, a nitrogen environment is not a conservative choice for life testing, despite the potential cost savings of avoiding vacuum testing. In addition, the present study involved specific conditions of sliding:rolling ratio, contact stress, and lubricant formulation; other conditions could show differences with respect to relative nitrogen/vacuum behavior, so the life extension factor of at least 5 in nitrogen cannot be used predictively for other tests. It is even possible that some systems could have better performance occurring during testing in vacuum. These uncertainties indicate that on-orbit performance would be difficult to predict from the results of our study. Therefore, we conclude that it is prudent to test an MMA under vacuum conditions when that is the environment to which the MMA will be subjected in the application.

Acknowledgments

The authors thank S. A. Jackson for preparing the test articles and J. J. Kirsch for performing the tests. This work was supported by the U.S. Space and Missile Systems Center, Contract No. F04701-00-C-0009.

References

1. Robbins, E. J., *Proc. 1st European Space Tribology Symposium, ESA SP-111, Italy, April 9-11, 1975*, p. 101.
2. John, P. J., J. N. Cutler, and J. H. Sanders, *Tribol. Lett.*, 9 (2000) 167.
3. Cutler, J. N., J. H. Sanders, J. S. Zabinski, P. J. John, J. R. McCutchen, L. S. Kastern, and K. G. Tan, *Tribol. Lett.*, 8 (2000) 17.
4. Gardos, M. N., *Tribol. Lett.*, 1 (1995) 67.
5. Fleischauer, P. D., S. V. Didziulis, and J. R. Lince, *Proceedings of the International Tribology Conference 2* (2000) p. 1109.
6. Carré, D. J., P. A. Bertrand, and J. R. Lince, *Boundary and Mixed Lubrication: Science and Applications*, Tribology Series, 40, D. Dowson, ed. (Elsevier, Amsterdam, 2000) p.147.
7. D. J. Carré, P. A. Bertrand, and J. R. Lince, "Lead naphthenate tribochemistry under vacuum and gaseous nitrogen test conditions," *Tribol. Lett.* 16(1), (2004) 207–214.
8. Kalogeras, C. G., M. R. Hilton, D. J. Carré, S. V. Didziulis, and P. D. Fleischauer, *Proc. 27th Aerospace Mechanisms Symposium, 12-14 May 1993*, NASA Conference Publication 3205, p. 197.
9. P. A. Bertrand, "Reactions of tricresyl phosphate with bearing materials," *Tribol. Lett.* 3, 367-377 (1997).

10. D. R. Wheeler and O. D. Faut, "The Adsorption and Thermal Decomposition of Tricresylphosphate (TCP) on Iron and Gold," *Appl. Surf. Sci.* 18, 106-122 (1984).
11. E. S. Forbes, N. T. Upsdell, and J. Battersby, "Current Thoughts on the Mechanism of Action of Tricresyl Phosphate as a Load-Carrying Additive," *Inst. Mech. Engrs. Tribology Convention Papers*, C64172 (1973).

The X-38 V-201 Fin Fold Actuation Mechanism

Christian Lupo*, Brandan Robertson* and George Gafka*

Abstract

The X-38 Vehicle 201 (V-201) is a space flight prototype lifting body vehicle that was designed to launch to orbit in the Space Shuttle orbiter payload bay. Although the project was cancelled in May 2003, many of the systems were nearly complete. This paper will describe the fin folding actuation mechanism flight subsystems and development units as well as lessons learned in the design, assembly, development testing, and qualification testing. The two vertical tail fins must be stowed (folded inboard) to allow the orbiter payload bay doors to close. The fin folding actuation mechanism is a remotely or extravehicular activity (EVA) actuated single fault tolerant system consisting of seven subsystems capable of repeatedly deploying or stowing the fins.

Introduction

The X-38 Project consisted of multiple unmanned drop test vehicles of various scales and one full-scale unmanned space flight proto-flight Vehicle 201. The vehicle shape, derived from the X-24, is a lifting body that lands via a parafoil and skids. The project's purpose was to perform the development work for an operational International Space Station Crew Return Vehicle. In order to launch V-201 in the shuttle payload bay, the two vertical fins must be folded inboard to allow the payload bay doors to close.



Figure 1. V-201 (Fins Deployed) on Mobile Transport Fixture after Static Testing

Fin Fold Actuation Mechanism Overview

The fin folding actuation mechanism is a complex system consisting of seven subsystems housed in a structure that narrows to 13.97 cm (5.5 in.) at the highest load point, the mid hinge. The system must react greater than 11,300 N·m (100,000 in·lbf) at the fold line from aerodynamic loading and seal the fold line for re-entry from orbit. The mechanism is required to be a remotely actuated single fault tolerant system operated via laptop in the orbiter cabin. The mechanism is also required to include an interface for unplanned EVA actuation of the fin. Motors are used because hydraulic power is not available on V-201. The upper fin structure also served as the housing for the electromechanical actuators for the rudder.

* NASA Johnson Space Center, Houston, TX

This added additional challenges to the design due to the necessity to accommodate large power cables across the fold line and around the fin drivetrain. The rudder drivetrain will not be discussed in this paper. The fins are stowed (folded and locked) for launch and deployed (unfolded and locked) for free flight. The system is capable of being re-stowed for return in the shuttle and then re-deployed if required.

The fins are folded via two four-bar linkages that toggle over-center in both the stowed and deployed positions. In the deployed position, three additional latches are engaged to transmit load from the upper fin to the lower fin. All of these operations are actuated with a common drivetrain. Each fin drivetrain consists of a Power Drive Unit (PDU), an EVA interface, two commercial off-the-shelf (COTS) torque limiters, two secondary gearboxes, and various connecting shafts.

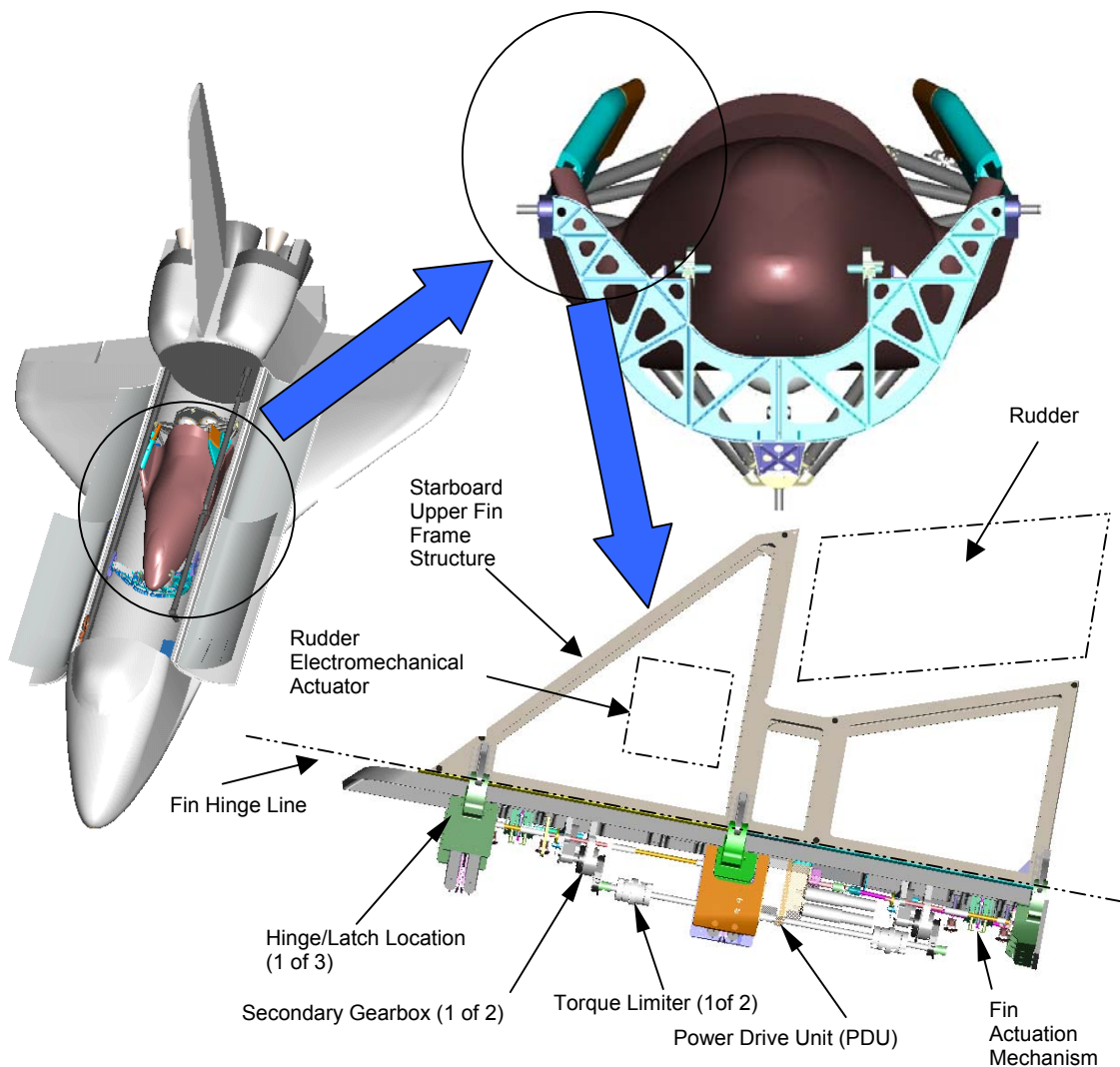


Figure 2. Overview of Fin Actuation

The PDU is the combination motor assembly/gearbox that provides torque to the fin folding and latching mechanisms. The PDU gearbox consists of planetary and translation gears that provide the mechanical logic to allow the fin to be actuated by a primary gearmotor, a secondary gearmotor, or an auxiliary manual/EVA input. A layout of the PDU is presented in Figure 7.

From the PDU, the torque is sent forward and aft with a torque tube to the torque limiters. The torque limiters are ball-detent slip clutches that are set to disengage when the torque in the torque tubes reaches a level that could potentially damage downstream components.

After the torque limiters, the torque is input into a secondary gearbox. The purpose of the secondary gearbox is threefold: 1) to shift the torque axis into the proper position for the mechanism shafts to pick up; 2) to further increase the torque provided to the fold mechanisms and latches; and 3) to split the single torque input from the torque tube into two separate and mutually exclusive torque outputs, one for the fold mechanism and one for the latches. Control of the relative motion of the two outputs is performed by a mechanism that is a separate subassembly contained within the secondary gearbox called the timing mechanism. From the secondary gearbox outputs, shafts deliver the



Figure 3. V-201 Port Fin Stowed

torques to the two fold linkages and the three latch linkages. The forward secondary gearbox delivers torque to the forward linkage, forward latch, and mid latch. The aft secondary gearbox delivers torque to the aft linkage and aft latch.

Cams on the shafts engage limit switch assembly pairs. There are five limit switch assembly pairs; one for each of the two fin actuation linkages and one for each of the three latches. Signals from these are used by the fin fold software in the V-201 computer to shut the motor(s) down and provide feedback to the crew on a laptop in the orbiter. For the stowed position, the motor is shut down when a signal from each of the two limit switch assembly pairs indicates both linkages are locked overcenter in the stowed position. For the deployed position, the motor is shut off when a signal from at least one switch of each of the five limit switch assembly pairs indicates both linkages and all three latches are fully engaged.

The linkages and latches lock the fin in the deployed position as well as compress the fin fold line environmental seals. The environmental seal is based on the shuttle landing gear door seal. An outboard thermal barrier consists of three layers of a alumina-boria-silica continuous filament braided tubular sleeving over a knitted Inconel X750 wire spring tube filled with silica mat or batting. The thermal barrier is capable of withstanding the high temperature of entry. However, it is porous. An internal Teflon coated, Dacron stiffened silicon rubber pressure seal prevents the pressure difference from the interior of the fin to the exterior of the fin from ingesting the plasma through the thermal barrier. This pressure seal cannot take the high temperature; therefore, the thermal barrier and pressure seal are both required for a complete environmental seal. The fin is covered with tiles on the outboard surface and leading edge. The inboard surface is covered with a blanket except for tile hinge fairings around the protruding hinge lugs.

A counterbalance mechanism was designed to be installed internal to the upper fin to make 1-G ground fin actuation more representative of on-orbit use. This mechanism is removed for flight. The mechanism will not be discussed in this paper.

Fin Actuation Mechanism Linkages

Fin Actuation Mechanism Linkage Description

The fins are folded via two four-bar linkages that toggle over-center in both the stowed (folded inboard) and deployed (locked in outboard for atmospheric flight) positions. The upper fin is driven by a crank on the lower fin that is attached to the upper fin via a turnbuckle coupler. The turnbuckle consists of a center sleeve with a right-hand thread on one end and a left-hand thread on the other. Two M81935/1 rod ends with spherical bearings are threaded into the sleeve. Hence, when the turnbuckle linkage is installed with the rod ends pinned they cannot rotate; rotating the sleeve will extend or shorten the turnbuckle. The

upper rod end is keyed to the sleeve with a NAS1193 locking device engaged in the castellated end of the sleeve and a jam nut locked with safety wire. The standard rod ends are cadmium plated, which is generally avoided in space vacuum environments. However, the JSC Materials and Processes Branch gave approval to fly these rod ends provided the exposed cadmium plated surfaces were painted with Super Koropon Epoxy Primer and the exposed cadmium plated threads were sealed with RTV-142.

The upper fin stow angle is set by two drag links, one forward and one aft of the four-bar linkage. The drag links are also turnbuckles. The crank and coupler linkage are housed in a sub-assy module to minimize assembly on the vehicle.

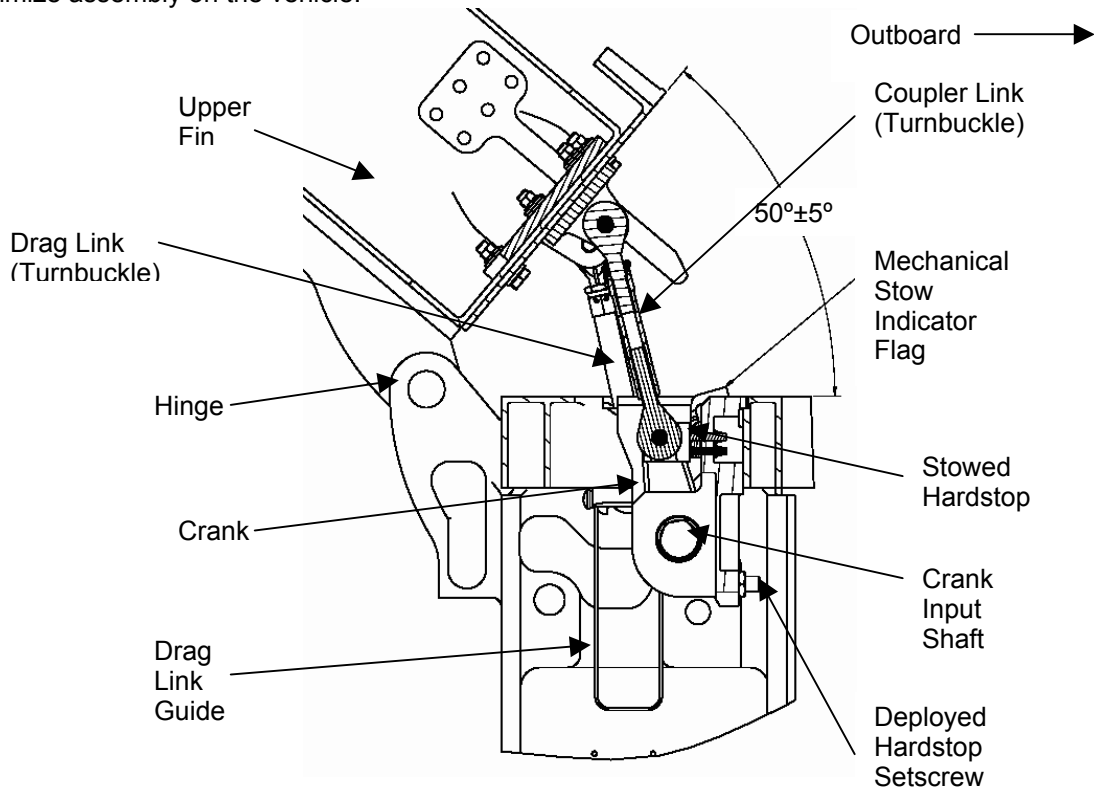


Figure 4. Fin Actuation Mechanism Linkage - Stowed

As the crank drives the fin to the stowed position (Figure 4), the coupler link must compress to rotate overcenter through the on-center position until the crank hits a hardstop. The link is over-center when the axis of the pin connecting the coupler and crank is rotated past an imaginary line drawn between the upper coupler pin axis and the Crank input shaft axis. A cam on the input shaft engages the limit switch assembly pivot arm which trips the limit switch. The hardstop is designed to stop the crank motion while the coupler link is still compressed. This compressed link preloads the coupler link in the overcenter position. Inertial and vibro-acoustic forces act on the fin during the shuttle launch. The direction of force may be outboard or inboard. Outboard acting forces only result in attempting to drive the linkage further overcenter. Inboard acting forces must overcome the compression preload in the coupler link and deform the drag links enough to get the linkage to an unstable on-center position. The compression preload can be increased by either lengthening the compression link or decreasing the fold angle by shortening the drag links. Reference SKK51356551 for rigging procedure.

As the crank drives the fin to the deployed position, the drag links retract into the lower fin along guides and the upper fin contacts hardstops on the lower fin. Due to space constraints, the deployed position is not shown; however, components described are visible in Figure 4. The crank continues to drive the coupler link over-center. Since the upper fin can no longer move, the crank must stretch the coupler link to rotate through the on-center position until the crank hits a hardstop in the crank assembly module. As the crank approaches the hardstop, a cam on the input shaft engages and trips the limit switch. The

hardstop is a setscrew that is set to stop the crank motion while the coupler link is still tensioned. A jam nut with lockwire retains the setscrew position. This coupler link preloaded in tension provides a clamping force to lock the fin in the overcenter position. Aerodynamic forces on the upper fin only results in attempting to drive the linkage further overcenter. The tension preload can be increased by shortening the coupler link or raising the hardstop on the lower fin. Reference SKK51356551 for rigging procedure.

If the test flight is aborted, V-201 will be returned in the shuttle with the fins locked in the stowed position. If the limit switches fail, the crank assembly module contains a mechanical indicator flag to provide positive indication that the fins are locked stowed (Figure 4). It was decided not to include a mechanical flag for the deployed position because the assumption was made that at least one of each of the limit switch pairs for each latch would be working or the test flight would be aborted. A mechanical indicator for the deployed position would have required penetrating the TPS and a complicated linkage.

Fin Actuation Mechanism Linkage Prototypes and Testing

The concept for this linkage is similar to the Shuttle's Remote Manipulator System Manipulator Positioning Mechanism (MPM) pedestal linkage. Despite this proven flight history, the concept was not accepted initially. In the stowed position for launch, the two over-center linkages are the only locking feature that restrains the fins from striking the shuttle door radiators. In order to further explain this concept, a working wooden mockup was made to demonstrate the kinematics of the crank/linkage/hinge four-bar mechanism. A full scale prototype of the fin actuation mechanism linkage was then designed and built. The prototype uses two rectangular box structures to represent the interface for a portion of the upper and lower fin structure. The box structures are hinged together and actuated by a single four-bar linkage. The linkage included an instrumented coupler link. The prototype demonstrated that the desired tension and compression preloads could be achieved with the linkage. It allowed for correlation between input torque and preload. This information was required in order to design the drivetrain. The prototype also had mockups of the TPS to provide clear visualization of the outboard tiles and thermal barriers, the inboard blankets, as well as location of the pressure seal. Later in the project, the loads changed such that additional preload was required for the stowed position. A new sleeve with an increased outer diameter was designed, instrumented, and assembled in the prototype to verify the desired preload/input torque combination could be achieved. Every linkage used in the prototype, qualification, and flight units was instrumented and calibrated and proof tested in tension and compression. The instrumentation consisted of strain gages wired into a full bridge designed to amplify the signal due to the strain.

Fin Actuation Mechanism Linkage Lessons Learned

Lessons learned from the early prototype influenced the final design. The prototype did not include a crank assembly module. However, due to the difficulty of assembling the hardstops, bushings, crank, and coupler unit on the prototype, all these items were combined into a single sub-assembly for the flight design. Further, it was noted that the hardstops for the crank in the stowed position were not adjusted on the prototype from the original nominal position. Therefore, these were replaced with a fixed dimension striker plate and pivoting head on the crank for the flight design. The prototype used fixed gussets with setscrews to set the stow angle. This resulted in large holes in the upper structure. The gussets were placed in bending which placed the lower fin rib web in bending. The setscrew had limited adjustment capability. These drawbacks led to the drag link concept using the same turnbuckle linkages. This concept minimized the hole size in the structure. The turnbuckle also had a much greater adjustment capability. The drag links could be instrumented just as the coupler link. This aided in the rigging of the mechanism to ensure each preload reaction was split between the drag links equally.

Although this drag link design was more robust than the gusset design, it did lead to other challenges for the flight design. Since the drag links retracted into the fin as it was deployed and extended as it was stowed, the links had to be guided. The drag link fitting occasionally jammed on the sheet metal track. This problem was still being resolved when the project was cancelled.

It was noted in the prototype that if the locking device tab was oriented incorrectly it would plastically deform during fin actuation due to interference with surrounding structure. This caution was incorporated into the rigging procedure for the flight mechanism.

The TPS mockups led to redesign of the lower tile hinge fairings so that they were mounted on carrier panels and could be removed to facilitate fin removal.

The coupler link calibration worked best when the strain gage bridge was placed at the center of the turnbuckle sleeve over the hollow section where neither the upper or lower rod end thread was engaged. This resulted in smooth linear plots with no jump between tension and compression. However, in the second prototype set, the strain gages were located near the bottom of the sleeve. This was done to improve the wire routing. However, this resulted in a jog between tension and compression. Further, it was noted that to perform stiffness calculations based on the linkage calibration, it was necessary to add displacement instrumentation between the two pin connections of the rod ends. Simply using the head displacement of the tension/compression machine did not provide accurate results. Reference "X-38 V-201 Fin Linkage Calibration Report" for the complete calibration report on all the linkages.

Fin Deployed Position Latch Mechanism

Latch Mechanism Description

The fins are latched in the deployed position via three latch mechanisms installed in the three hinge fittings: forward, mid, and aft. Many naval aircraft use two hinges with two hydraulically fired pins. The pins are long pins with a tapered nose. This long stroke allows the taper to self-align the lugs with the pin as it is fired. However, V-201 did not have hydraulic power as an option. In order to meet the single fault tolerance requirement, it was decided to drive all systems with a single PDU. See the PDU section for further description of single fault tolerance. This restriction limited the stroke and force that was available to drive a pin. Initial concepts all focused on using three pins. Because the fin environmental seal required significant force to compress, the pin concept was abandoned in favor of a latch that could compress the seal. This eliminated the pin and lug alignment issue.

It was decided to use three hinge/latch pairs instead of two for several reasons. The fin fold interface is approximately 2.13 m (7 ft.) long. The vehicle has three main frames that provide a load path all the way through the vehicle. Structurally, the main aerodynamic load from the rudder transferred down the mid spar of the upper fin frame. The cleanest load path was to have a hinge/latch pair at this mid location with a frame lined up with the spar. A single hinge/latch pair forward or aft would not be sufficient to react the remaining loads. Finally, three latches in conjunction with the two actuation linkages are necessary to compress the environmental seal and minimize gapping at the fold line under aerodynamic loading.

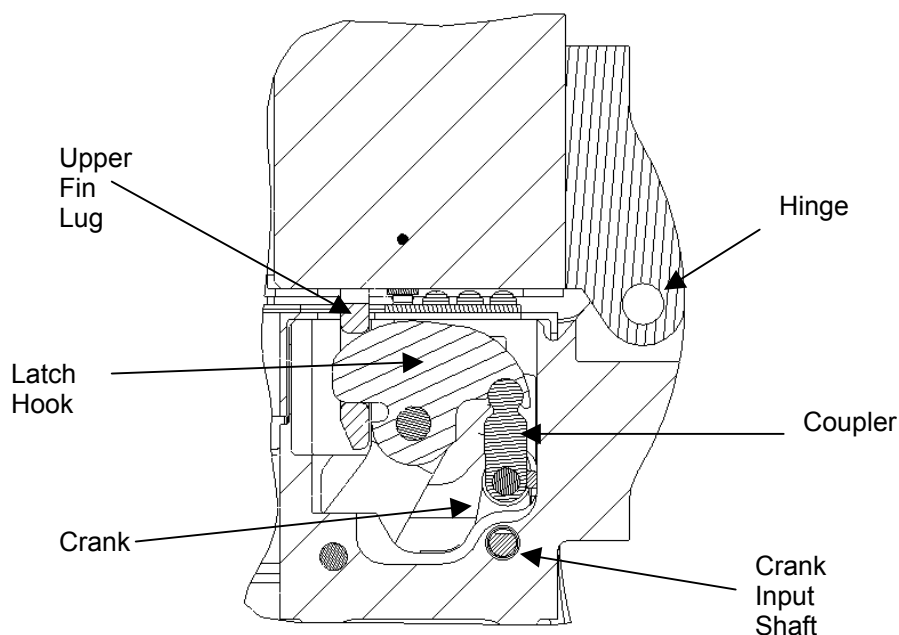


Figure 5. Fin Latch Mechanism

Each latch hook is driven by a four-bar linkage that toggles over-center to prevent the latch from disengaging. The linkage consists of a crank attached to hook via a coupler link. The entire latch mechanism is housed internal to an integrally machined hinge fitting. Due to limited available volume and access for assembly, the coupler-to-hook connection is a unique design that does not require an additional pin (Figure 5). The crank drives the hook to engage the lug attached to the upper fin, compress the seal until the upper fin engages a shimmed hardstop, and the coupler link is overcenter to lock the latch hook. As the crank approaches the hardstop, a cam on the input shaft trips the limit switch.

Latch Mechanism Testing

For all joints, the X-38 project required a positive margin of safety on the design load with a 1.5 factor of safety and a 1.15 fitting factor applied (or 172.5% of the design load). The mid hinge/latch analysis could not show positive margins with this fitting factor applied. The lead analyst agreed to waive the fitting factor if the joint was tested to destruction. The test assembly shown in Figure 6 was tested to destruction. It failed at the splice joint below the hinge line at a load equal to 171% of the design load. This closely matched the finite element predicted failure load and location. However, this margin must be reduced due to thermal considerations which results in an 8% decrease in strength for the aluminum hinge fitting. This reduces the margin of safety to 5% above the safety factor of 1.50. Reference "X38 V-201 Fin Mid Hinge/Latch Qualification Test Plan" and "X38 V-201 Fin Mid Hinge/Latch Qualification Test Report".

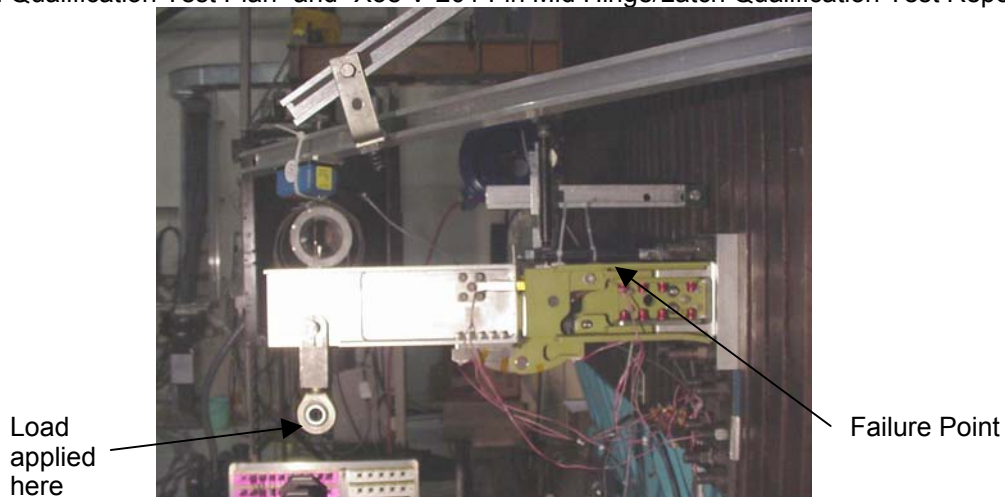


Figure 6. Fin Hinge/Latch Qualification Test Unit

Latch Mechanism Lessons Learned and Observations

- *Avoid shims.* Requires significant time to adjust small increments.
- *If you need shims, use laminated shims and manufacture extra shims.* Laminated shims allow small increment adjustment 0.05 to 0.08 mm (0.002 to 0.003 in.). However, it is easy to remove too many laminations when pulling the shims; therefore, it is important to have extra shims.
- *Negotiate interfaces carefully.* The failure point was a stress concentration that was originally away from the load path of the mechanism. However, as the mechanism evolved, the load path shifted closer to the stress concentration leading to a lower load capability.
- *Solid Film lubricants are often applied too thick.* It is a good idea to include a burnishing procedure in installation and/or rigging specifications. Often it is as simple of sliding the shaft into a mating bushing on the bench top to remove excess lubricant. This has been seen with Everlube and Tiolube.

Fin Actuation Mechanism Drivetrain

Power Drive Unit Description

The PDU gearbox consists of two planetary gear trains in series providing mechanical logic that allows multiple inputs. Translational gearing after the planetary gearing output is used to transfer the torque to the required output shaft axis of rotation. The first planetary train has one gearmotor attached to the sun gear and a second gearmotor attached to the ring gear allowing either gearmotor the ability to independently drive the first planetary train of the gearbox. The carriage output of the first planetary train

then drives the sun gear of the second planetary train and a manual EVA interface drives the ring gear of the second planetary train. This allows either gearmotor or the manual EVA interface to independently drive the overall gearbox. Each of the gearmotors has an electromechanical power-off brake (power to the gearmotor releases the brake) and the EVA Interface is locked when not in use. For overall fin actuation, the PDU provides full two-fault tolerance against motor failures. The CAD view in Figure 7 displays the geartrain.

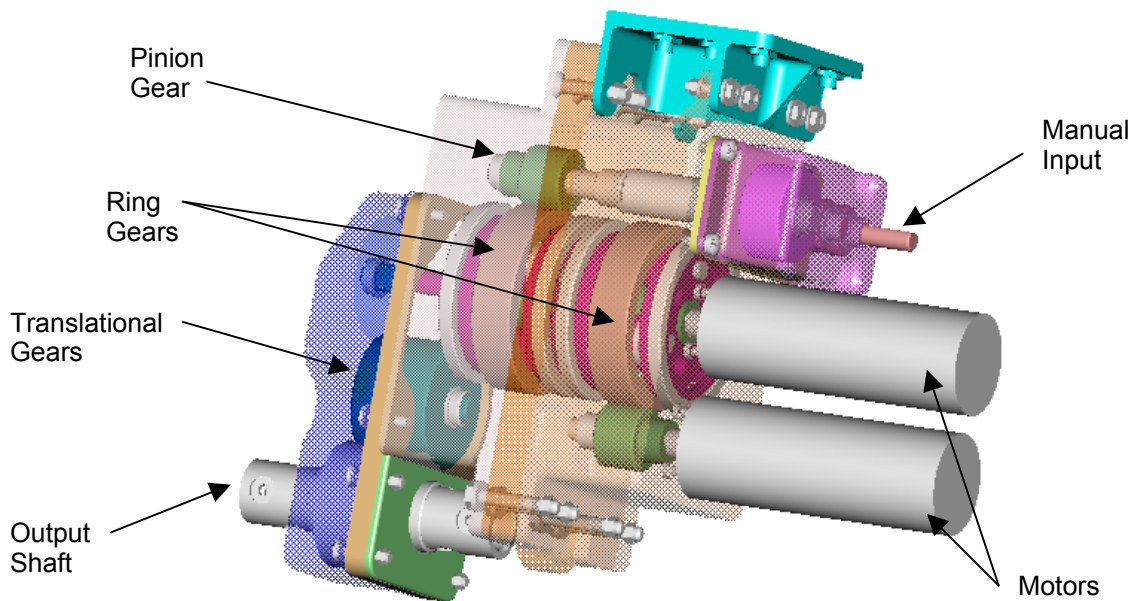


Figure 7. PDU

Each gearmotor assembly is equipped with a power-off brake that locks the motor shaft when not in use. This power-off brake is required due to planetary gear kinematics. Not locking the motor shaft of the un-powered motor would result in the powered motor backdriving the un-powered motor as opposed to supplying torque through the gearbox for fin actuation. The manual EVA interface is also locked while not in use for this same reason (see EVA Interface section). Originally, COTS DC brush motors were selected for use, but several problems were encountered. Problems included improper motor/brake assembly, unknown and unidentifiable materials usage, no secondary locking features for fasteners, non-vibration rated electrical interfaces, and inefficient volume usage. This eventually drove the team to specify custom flight-certified gearmotors for the final flight assembly. These flight motors were never purchased due to program cancellation. Each gear in the PDU is coated with a Diconite TiS₂ dry film lubricant, and due to the low rotational speeds their dual-supported shafts are housed in aluminum bronze bushings lubricated with Braycote 602EF, with the exception of the planetary carriages which were supported by thin-section ball bearings. Because high rotational accuracy of the PDU output shaft is not required, a small backlash was designed in and the center distance for all gearing was fixed without provision for adjustment.

PDU Testing

The PDU underwent many informal functional tests after assembly, during which time it was discovered that five of the six COTS motors had been sent from the vendor incorrectly assembled, causing them to seize after about a minute of running. Seizure was due to motor operation with a partially engaged brake that would heat and swell until torque/current cut-off. A work-around was implemented allowing the PDU, torque limiter, and secondary gearbox to undergo thermal-vacuum testing. The PDU worked as designed during and after all phases of testing. Later, a fin-level random-vibration test was conducted and the PDU passed this test with no problems as well.

PDU Observations

- Using Geometric Dimensioning and Tolerancing significantly enhances ease of assembly and reduces tolerance stackups.
- Work with gear manufacturers to establish pre-coating dimensions and tolerances to allow for removal of recast layer or tooling marks, case hardening, and/or dry film application.
- Work with materials and processes experts to select bushing, shaft materials and lubricants.

PDU Lessons Learned

- *Avoid using primer for corrosion protection on any of the mechanism housings.* The PDU housings use Super Koropon, which was found to flake and generate debris during assembly. Subsequent housing designs used a hard anodize finish.
- *Be sure to include alignment aids for features requiring high positional accuracy or that influence geartrain performance.* The original design assumed the bolt holes' positional accuracy for the housings were sufficient to provide alignment aids for the gear train. However, it was found that the hole sizes required to allow assembly of multiple fasteners allowed the housings to shift enough to significantly reduce gear train efficiency.
- *Design appropriate access for those design elements that may require removal.* Many components, including the gearmotors, could not be removed without disassembling most of the gearbox. This became very inconvenient when circumstances arose which required replacement of the motors.
- *Use caution when deciding to use COTS products.* In this application, fixing shortcomings and certifying COTS motors for flight was significantly more expensive than originally considered. However, COTS motors were useful for initial ground testing of the geartrain.
- *For lower level components in a drivetrain, be sure to understand assembly interdependencies at the next higher level.* Originally, the drivetrain torque tube passed through a bushing in the housing of the PDU. Upon assembly, it was determined that this bound the torque tube and the bushing was subsequently removed.

Torque Limiter Description

In order to protect components downstream of the PDU against overload caused by failures, jams, or hardstopping, torque limiters were inserted into the drivetrain between the PDU and the each secondary gearbox (See torque limiter in Figure 10). Sizing the downstream components to handle the contingency loads, given such large gear ratios, proved not to be feasible from packaging and mass standpoints.

Based on the lesson learned during PDU development, COTS candidates were carefully evaluated before determining if this was an acceptable way to proceed. Detailed discussions with vendors concerning materials, production methods, and feature modifications were held prior to the decision. In the end, a COTS vendor was selected, and a flight-like but undocumented set of torque-limiters was procured for testing. The product was COTS except for the use of Braycote 602EF in place of the standard lubricant.

The torque-limiter is an adjustable ball-detent slip clutch set to slip at 40.3 N·m (357 in·lbf) and which automatically re-engages after 360 degrees of rotation or reversing the rotation so that the synchronization of the two sets of mechanisms is not lost if one clutch slips and the other does not. The clutches are fixed to the torque tubes through a friction-clamp interface.

Torque Limiter Testing

Upon receipt, several torque tests were run on the torque limiters to verify the correct slip setting before using the torque limiters with the flight hardware. The torque limiters operated with no problems during and after exposure to all environments. For flight, a specification control drawing would need to be released documenting the modified COTS hardware.

Torque Limiter Lessons Learned

If you're careful, COTS can work well! Significant cost savings were achieved using COTS clutches which only cost a few hundred dollars total versus a custom design effort to develop a torque-limiter. Make sure that material vacuum compatibility, if required, is completely worked out prior to purchase.

Secondary Gearbox Description

The secondary gearbox serves as a mechanism for increasing torque, shifting the torque axis and splitting the torque output into two axes. The torque tube travels inputs to a gear train that shifts the torque to a planetary train similar to that used in the PDU. Because the locking and folding shafts must operate at mutually exclusive times a timing mechanism, described later in this paper, was designed to control the motion of the two outputs. The secondary gearbox is pictured in Figures 9 and 10.

Due to severe packaging limitations, most of the gearing in the secondary gearbox was herringbone helical gearing to allow maximum torque capability with the smallest possible face width. The gears were coated with Vitrolube, a ceramic solid film lubricant capable of withstanding the higher contact loads. The gear teeth were further coated with a light film of Braycote 602EF. These gears also were mounted in aluminum-bronze bushings with fixed center distances because there was simply no room for bearings that could withstand the magnitude of load required to react the tooth loading. The housings were hard-anodized with the bushing holes being masked and chemical conversion coated.

Secondary Gearbox Testing

Once fully assembled, the secondary gearbox underwent benchtop testing in order to measure the efficiency of the gearbox, necessary for torque margin determination and proper rigging of the mechanisms. The efficiency, as expected due to the necessity of using bushings under high loads, was poor. The gearbox also underwent thermal-vacuum testing with the torque limiter and PDU, and went through fin random vibration testing. In all cases, the secondary gearbox operated with no problems.

Secondary Gearbox Lessons Learned

- *Use hex-head fasteners whenever possible.* Originally many of the fasteners, of which there was a fairly large number for sealing purposes, used offset cruciform recess heads which can be very difficult to install to proper torque values and even more difficult to remove. Every fastener that could be swapped was replaced with a hex-head version and assembly became much easier.
- *If you can't use bearings, you'll pay the price in efficiency.*

Timing Mechanism Description

The original design concept for the timing mechanism was very simple and consisted of two discs similar to Geneva mechanisms mounted on the two output shafts (See Figure 8). A simple test article was developed to explore the concept. It became immediately apparent that though simple, the high torques involved (282.4 N•m (2500 in•lbf) in one shaft and 50.8 N•m (450 in•lbf) in the other) produced very high sliding friction forces on the discs which used all of the torque from the gearbox and allowed no motion.

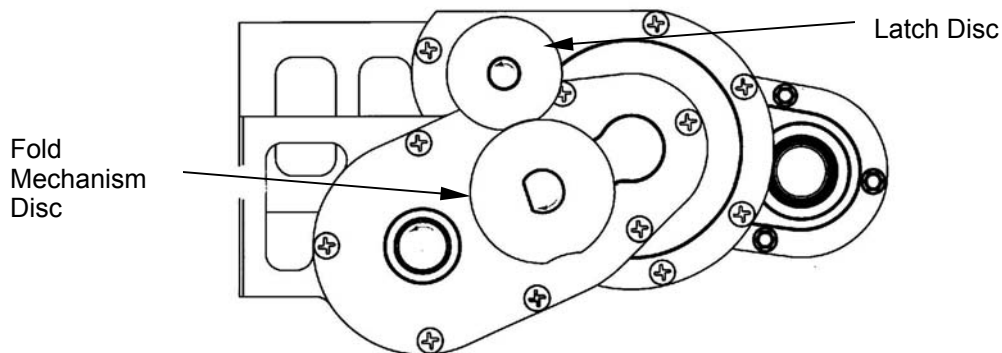


Figure 8. Geneva Mechanism Timing Discs

A second concept was developed to reduce the friction in the system. This was accomplished using a cam/roller/linkage concept that emphasized rolling friction rather than sliding friction. While the new design reduced the friction in the system, it also greatly increased the complexity and size of the mechanism. This larger design was moved from the output shafts to an open space between the gearbox housings (Fig. 9).

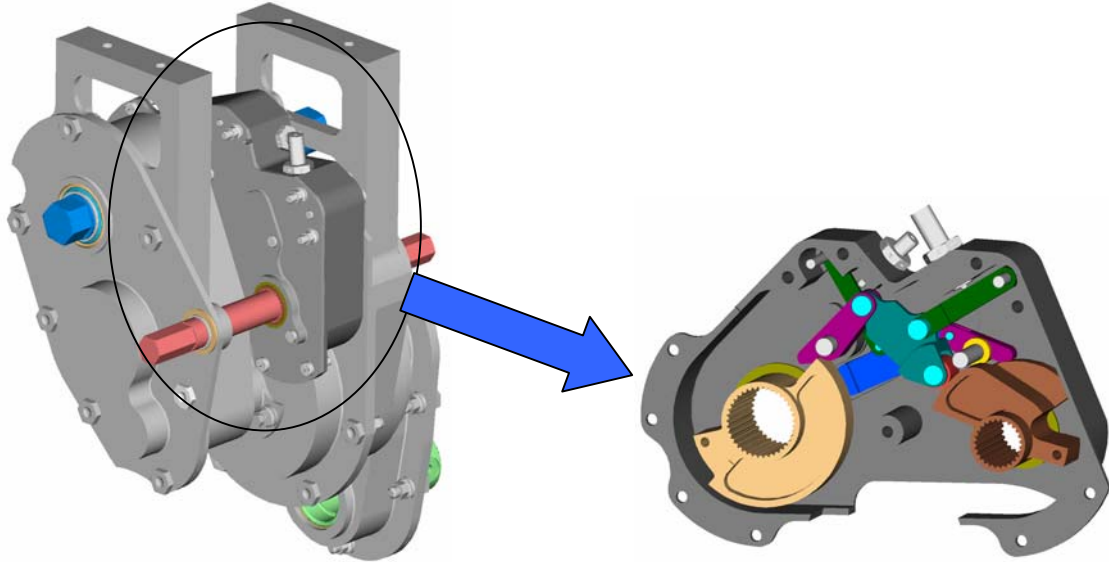


Figure 9. Cam/Roller/Linkage Timing Mechanism

The design was completed using solid models which were used for preliminary kinematic analysis. A detailed dynamic analysis was then performed. The strength analysis was performed with Mathcad based on the dynamic analysis results. An initial unit was then manufactured so that it could undergo operational proof testing. The proof test was planned to run to 100% of design limit load in the forward and reverse direction three times each, but during the initial cycle, the unit failed in the reverse direction. Upon opening the test unit, it was discovered that the pin upon which the roller rotated had sheared and the lug in which the pin rested experienced an ultimate bearing failure. In addition, other pins and holes in the linkage had yielded to various degrees.

Upon closer examination of the failure, it was found that the load applied to the linkage was not consistent with the magnitude or direction predicted in the dynamic analysis. An investigation of the dynamic model uncovered a small error in the application of the motion driver in the reverse direction that resulted in an incorrect load condition. Correction of the error produced new load vectors consistent in both magnitude and direction with that seen by the failed linkage.

The mechanism was modified in an attempt to correct the deficiencies in the original configuration by using a stronger material for the pins and links. Analysis indicated that this would result in very low, but positive margins in the pins so the test was repeated with the new pins. No failure occurred but subsequent inspection showed slight yielding in the pins was still occurring. The design was more broadly modified to increase the pin diameters slightly to increase their load capability. This was a design challenge given the tight confines but a solution was found.

The new design was then retested to the same loads. No failures were experienced and the mechanism operated as designed. A post-test inspection of the internal mechanism revealed no problems.

Timing Mechanism Lessons Learned

- *The simplest concept doesn't always work.* Mechanisms that work kinematically in the CAD system may not work when under the loads and friction of the real world.
- *Be careful with your analysis.* Be sure to review all assumptions
- *Always test!* Analysis may not be sufficient, and testing may be the fastest way to iterate a design.

Drivetrain Testing

The test unit shown in Figure 9 was thermal/vacuum tested. The sub-assemblies were later used in the fin engineering unit and have continued to operate reliably without incident. Reference "X-38 V-201 Fin Drivetrain Thermal/Vacuum Test Report" for description of thermal/vacuum testing.

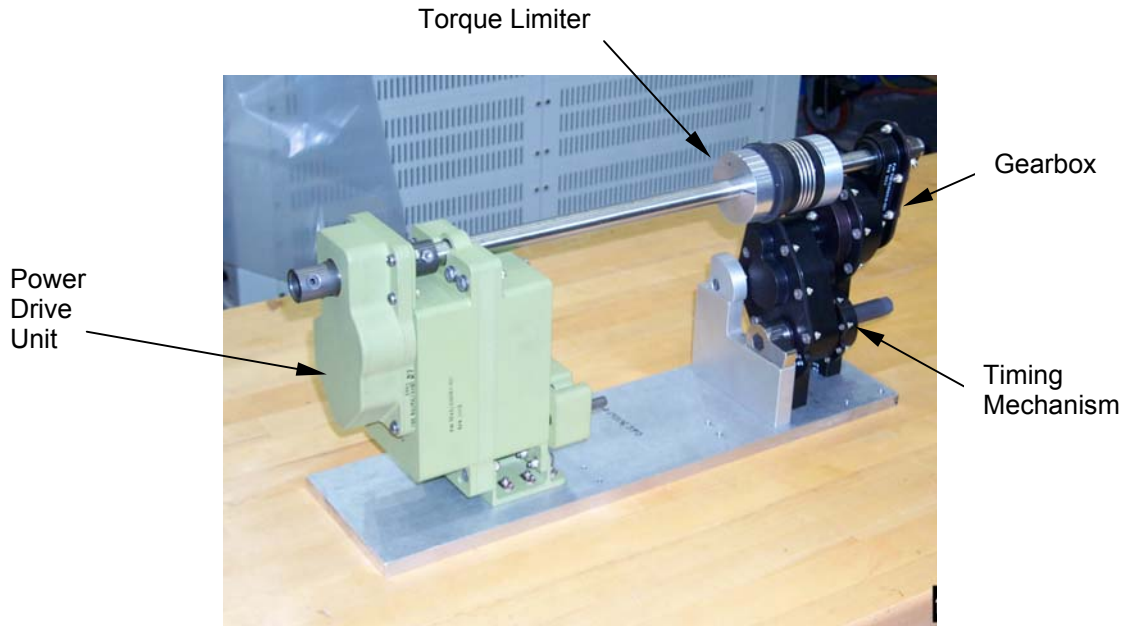


Figure 10. Drivetrain Test Unit

Limit Switch Pair Assembly

Limit Switch Pair Assembly Description

In order to indicate successful stow or deploy, five limit switch pair assemblies are used. First, the assembly positions the two limit switches side-by-side so that a single cam actuates both switches. The pair is required to meet the single fault tolerance requirement for remote actuation. Second, the assembly is designed to prevent damage to the switches. The pivot arm is spring loaded to engage the switches which are off-loaded as the cam engages it. In this way, over-travel of the cam could not damage the switches. See Figure 11.

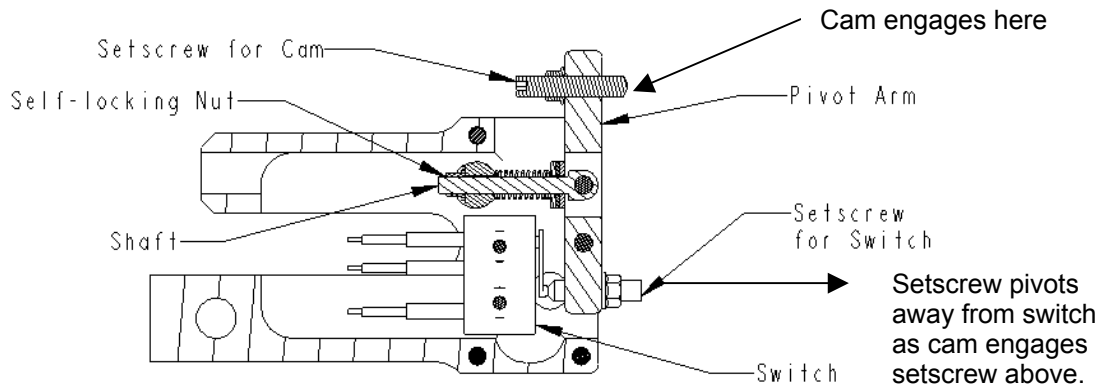


Figure 11. Limit Switch Pair Assembly

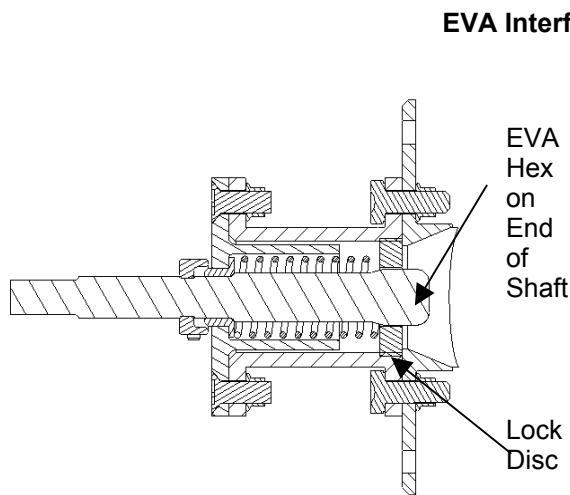
Limit Switch Pair Assembly Lessons Learned

Attempting to meet requirements for two locking features can result in other problems.

- The pivot arm has small # 6 setscrews (3.5 mm) made of 304 stainless which contact the limit switch arm in order to trip both limit switches simultaneously. The setscrews are locked in place using a self-locking insert with a self-locking jam nut. However, the 1.5 mm hex in the setscrew would occasionally strip while attempting to overcome running torque. Later versions of the assembly

replaced the setscrew with socket head cap screws which had a larger hex and could be driven through the running torque.

- The pivot arm sub-assembly spring is retained on shaft with a 2.8 mm (0.112 in.) threaded end. A self-locking nut is preloaded against the shoulder of the shaft in the current design. In the original design, the nut was not preloaded. The secondary locking feature to retain the nut was a cotter pin through the threaded portion of the shaft. During the design, the shaft with the 1.5 mm hole (0.062 in.) was viewed at enlarged scale. However, the CAD model did not include the minor diameter of the thread. The hole left so little material that the lower end of the shaft snapped when the nut was installed.



EVA Interface Description

The EVA Interface is a standard 11.1 mm (7/16 in.) EVA-compatible double-height hex head. The hex is locked from rotation with a disc that has a 12-point interface to the hex and a splined outer diameter. The disc is spring loaded in the locked position. The disc is disengaged by engaging a deep well socket for the Pistol Grip Tool (PGT).

EVA Interface Lessons Learned

It is critical to always fully follow procedures regardless of how familiar the operation has become. The procedure calls for actuating the interface using an extended deep well socket. During initial functional testing, the same socket

Figure 12. EVA Interface Assembly

was always checked out from X-38 tool control. However, during static testing the vehicle was moved to another location with a different set of tools. The static test required functional testing before and after the test. At some point during the testing, an extended socket was used. However, the socket was not deep well and only partially disengaged the locking disc. When the interface was rotated, the hex ground into the disc creating metallic chips. The interface assembly was disassembled and cleaned. A new disc was installed. A placard referencing the procedure was installed to prevent the event from occurring again.

Fin/Rudder System Level Testing

Fin/Rudder Static Testing

The fins were statically tested while installed on the vehicle in both the deployed and stowed positions. In the deployed position, the fins were tested to 100% of limit load. The Shuttle program requires proto-flight hardware be tested to 120% of limit load. However, the X-38 project decided to lower this requirement because 1) the mid hinge/latch pair only had 0.05 margin of safety, 2) the deployed fins only affected X-38 mission success, not shuttle safety, and 3) 100% of limit load provided sufficient data for model correlation. Reference "X-38 V-201 Integrated Structural Test Plan – Aerosurfaces Tests" and "X-38 V201 Fin Deployed Test Report".

Conversely, in the stowed position there was greater uncertainty in the load, but also larger margin over the design load. Therefore the fins were tested until the coupler links which are the lowest capability part in the system neared the rated load for the turnbuckle. The fins were tested up to 218% of design load for the stowed position. This provides additional test proven capability in the event that later analysis predicts higher-than-expected fin loads during launch. Reference "X 38 V 201 Integrated Static Structural Test Plan – Shuttle Launch & Landing Tests" and "X-38 V-201 Static Test Report – Shuttle Launch & Landing Tests".

Fin/Rudder Vibration Testing

The starboard fin/rudder was removed from the vehicle after static testing and installed on an engineering unit that had a representative lower fin structure housing the fin actuation mechanism. This unit was successfully vibration-tested in the X, Y, and Z axes. Reference "X-38 V-201 Fin Engineering Development Unit (EDU) Vibration Test Plan".

Functional Testing

The port and starboard fins have been actuated several dozen times. Before and after each static test and vibration test, the fin mechanism was actuated. The majority of the functional tests have been performed using the EVA interface either with a socket wrench or the PGT. The starboard fin was actuated multiple times using one of the COTS motors.

Conclusions

X-38 Status

The X-38 project was officially shut down in May 2003. NASA Headquarters decided that NASA needed to pursue a multi-use vehicle. The two B-52 drop test vehicles, V-131R and V-132, and the space flight prototype vehicle V-201 have been mothballed and are museum pieces at JSC. V-201 is approximately 80% complete.

Remaining work for Fin before Flight

Due to the cancellation of the X-38 project, the mechanism flight performance may never be known. However, the testing completed thus far indicates the mechanism would function in the thermal/vacuum environment after withstanding the vibro-acoustic launch loads and could also lock the fin deployed against the aerodynamic flight loads. Remaining testing would include a vehicle level acoustic test with the fins stowed and a vehicle level thermal/vacuum test where the fins would be functionally tested. The mechanism is currently in a ground test configuration with nonfunctioning motors installed. The fin can be actuated via the EVA interface. The 1-G counterbalance is also installed in the upper fin. The primary outstanding issue is the procurement of flight motors. A specification control drawing for the motors has been released. There are also several minor issues that have been documented in Discrepancy Reports that would have to be resolved in order to fly. The keys to success on this project included building prototypes early and performing sub-assembly level testing leading up to system level testing.

References

1. Robertson, Brandan "X-38 V-201 Fin Linkage Calibration Report" JSC-49740 – JSC Scientific and Technical Information Center
2. Lupo, Christian P. "Procedure, Fin Folding Drivetrain" SKK51356551 – NASA/JSC Engineering Drawing Control Center
3. Lupo, Christian P. "X38 V-201 Fin Mid Hinge/Latch Qualification Test Plan" JSC-28409 – JSC Scientific and Technical Information Center
4. Smith, James P. "X38 V-201 Fin Hinge/Latch Qualification Test Report" JSC-29294 – JSC Scientific and Technical Information Center
5. Robertson, Brandan "X-38 V-201 Fin Drivetrain Thermal/Vacuum Test Report" JSC 29911 – JSC Scientific and Technical Information Center
6. Edelstein, Karen S. "X 38 V 201 Integrated Static Structural Test Plan – Shuttle Launch & Landing Tests" JSC 29182 – JSC Scientific and Technical Information Center
7. Edelstein, Karen S. "X-38 V-201 Integrated Structural Test Plan – Aerosurfaces Tests" JSC 29184 – JSC Scientific and Technical Information Center
8. Lupo, Christian, "X-38 V201 Fin Deployed Test Report" (Draft available upon request)
9. Lupo, Christian, "X-38 V-201 Static Test Report – Shuttle Launch & Landing Tests" (Draft available upon request)
10. Edelstein, Karen S. "X-38 V-201 Fin Engineering Development Unit (EDU) Vibration Test Plan" (Available upon request).

The X-38 V-201 Flap Actuator Mechanism

Jeff Hagen*, Landon Moore**, Jay Estes**, and Chris Layer†

Abstract

The X-38 Crew Rescue Vehicle V-201 space flight test article was designed to achieve an aerodynamically controlled re-entry from orbit in part through the use of two body mounted flaps on the lower rear side. These flaps are actuated by an electromechanical system that is partially exposed to the re-entry environment. These actuators are of a novel configuration and are unique in their requirement to function while exposed to re-entry conditions. The authors are not aware of any other vehicle in which a major actuator system was required to function throughout the complete re-entry profile while parts of the actuator were directly exposed to the ambient environment.

Introduction

The X-38 Project consisted of multiple unmanned drop test vehicles of various scales and one full-scale unmanned space flight proto-flight Vehicle 201 (V-201). The vehicle shape, derived from the X-24, was a lifting body that lands via a parafoil and skids (Figure 1). The purpose of the project was to perform the development work for an operational International Space Station Crew Return Vehicle.

The configuration, shape, size, and function of the X-38 control surfaces (rudders and body flaps) were chosen to mimic that of the X-23 / X-24 as closely as possible. The X-23 re-entry bodies had fixed rudders and wedge shaped body flaps that replicated only the lower surface of the X-24 flaps while filling the otherwise void area between the top side of the flaps and the lower skin of the aft fuselage. The X-38 flaps more closely resemble the flaps of the X-24 low speed test vehicle, with a void area between the lower skin of the aft fuselage and the top surface of the relatively thin flap. Flight control required the capability to drive the flaps with up to 28,811 N-m (255,000 inch-pounds) of torque - including margins, and to rotate through an angle from zero to forty-five degrees from the lower side of the aft fuselage.



Figure 1. X-38 Family of Vehicles (V131R, V201, V132)

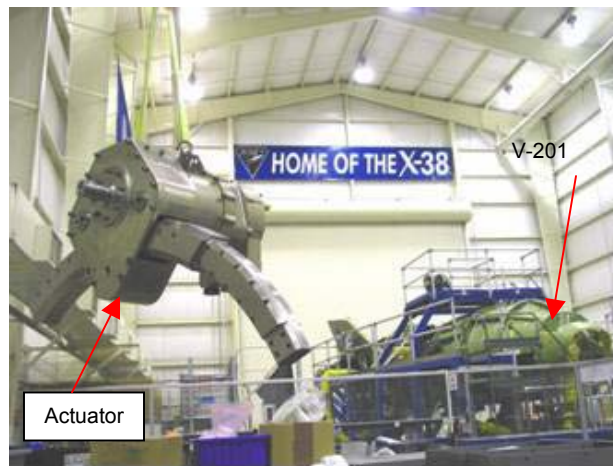


Figure 2. Actuator (foreground) and V201

* Lockheed Martin Space Operations, Houston, TX

** NASA Johnson Space Center, Houston, TX

† Moog, Inc, Motion Systems Division, East Aurora, NY

Due to the exposure of the relatively thin flaps of the X-38 configuration to the full re-entry environment, it was decided to fabricate them from a hot structure material. A conventional cold structure flap covered with thermal protection materials was deemed impractical for the volumetric constraints imposed on the flaps. Furthermore, as a result of the strength limitations of the selected hot structure materials, the X-24 driven geometry of the flaps, and the load environment experienced by the flaps, it was necessary to apply the actuating force to the flaps at a point as near as possible to the center of pressure, which coincided with a location near the center of the roughly square shaped flaps. This geometry dictated that the flap actuator be located in the aft fuselage in the region above the flap and that the linkage connecting to the flap would penetrate through the lower skin of the fuselage to connect to the topside of the flap, thus exposing the actuator linkage to the re-entry environment between the flap and lower skin.

The bulk of the X-38 airframe consists of a cold structure aluminum frame with composite skin panels covered by a thermal protection system (TPS). The flaps mounted on the lower side of the aft fuselage are directly exposed to the flow during re-entry and consequently experience peak surface temperatures that can reach as high as 1649°C (3000°F). The structural layout of the vehicle required that the entire flap fit within a thickness of approximately six inches, which would have been insufficient for a conventional cold structure flap of sufficient stiffness and covered with a TPS of the requisite thickness. Consequently, the flaps were constructed of a hot structure carbon silicon carbide (CSiC) ceramic matrix composite without a TPS. MAN Technologie of Germany supplied the flaps via a European Space Agency / TETRA (TEchnologies for future space TRANsportation systems) sponsored joint venture with NASA.

To accommodate the interface of the hot structure flaps to the cold structure airframe, MAN developed a high temperature journal bearing material based on CSiC, and designed a system of CSiC beams to support the flap at the hinge line bearings while accommodating the differential thermal expansion ratios of the hot and cold structures. The hot structure beams were surrounded by thermal barriers at the points where they penetrate the TPS of the cold structure. This prevented impingement of re-entry gases on the cold structure. In order to simplify the hinge line interface seals, the flap hinge line bearings and supports were located outside the airframe TPS such that the seals are entirely static and do not flex during rotation of the flaps.

Since the X-38 was an unpowered glider intended for long-term storage on orbit, it does not have an auxiliary power system or hydraulic system such as the Space Shuttle. All of the flight control surfaces are actuated with electromechanical actuators (EMA) that are driven by direct current from Nickel-Cadmium batteries. Prior development programs (EPAD et al) indicated then state of the art EMA technology could be successfully applied as a design solution for X-38. Further confidence was gained through X-38 drop testing (V132, V131R) performed at Dryden Flight Research Center using single string, linear output EMAs. At this point, it was evident that the available pulse-width modulated, brushless DC motor and motor drive technology was adequate to drive the type of power needed to control the V201. The technical concerns shifted to the optimum architecture that should be employed to facilitate human rating. The human rating requirements drove the system to be fully two-fault tolerant meaning that all flight control system requirements for load and rate be met even after two failures. The most fundamental architecture redundancy decision involved the choice between an active-standby system and an active-active system. It was clear that an active standby system would be simpler in terms of software and control, but would result in a more extreme control surface transient during a channel failure. The active-active system promised reduced failure transients at the expense of sophisticated control software that would marshal four highly responsive channels operating simultaneously while forced into lock step by being torque summed through a bull gear. Ultimately, the latter path (active-active) was chosen and successfully developed.

Design Evolution

The original actuator design consisted of a long linear ball screw with the top end anchored to a spherical bearing near the top of the aft fuselage structure and attached at the lower end to the high temperature spherical bearing near the center of the flap (Figure 3). Due to the kinematic layout, the linear actuator would have penetrated the skin at a dynamically changing location, complicating the thermal seal design.

It was assumed that the use of a spherical bearing at each end would prevent bending moments from being applied to the actuator. Aerodynamic analysis determined that skin friction drag parallel to the flap surface contributed only negligible loads to the flap system. The required flap driving moment translated into force of 44,482 N (10,000 pounds) at the chosen EMA attachment point if the maximum flap force were to be experienced.

The concept selection and the kinematic layout were frozen before the detailed design of the actuator or vehicle structure were fully understood due to the long lead time required for fabrication of the flaps. In particular, no satisfactory concept or technology was identified for the thermal seal where the actuator penetrated the fuselage skin. Accommodating such motion within the extremely limited volume and while exposed to the demanding environment led to design problems for the thermal seal that were never satisfactorily resolved for this configuration. Also, as design of the linear actuator matured, it became apparent that insufficient clearance existed between the lower part of the actuator and the fuselage lower longerons, which were already in production. Even after less than optimal modifications to the fuselage structure, there was no room left for growth in the actuator size or for accommodating an adequate thermal seal based on available technology.

A more detailed concept eventually emerged that consisted of a telescoping tube surrounding the actuator lower rod and mounted in a 'shoe' that could slide over a slot cut in the fuselage. However, even after extensive surveys of industry, no suitable technologies were found for implementing this sliding and telescoping thermal seal. The principle problem was finding materials capable of surviving the necessary temperature within the extremely limited space available and of accommodating the complex mechanical motions in the high temperature, corrosive environment.

During this time, technology development issues involving the high temperature CSiC bearings of the flap arose. Testing revealed that the bearings exhibited a far higher than anticipated coefficient of friction. This resulted in large bending moments being applied to the linear actuator for which it had not been designed. Reports from MAN Technologie indicated that the bearing coefficient of friction could exceed 0.7 or more. Additional testing later failed to show any meaningful relationship of the coefficient to load, speed, temperature, or other environmental and application factors. Efforts to reduce the friction by modifying the surface treatment or finish also failed to generate usable improvements. MAN Technologie informally reported promising indications of success with a new type of proprietary surface treatment, but the project schedule could not accommodate the necessary technology development effort.

The unexpectedly high friction of the bearing meant that rather than isolating the EMA from bending moments, the bearing could actually apply a large moment at the lower end of the linear actuator EMA. Due to the volumetric constraints on the actuator caused by the layout of the flaps and aft fuselage structure, the EMA configuration was forced to a slender design with a very high length to diameter aspect ratio that could not support bending loads well.

The newly imposed bending moment could only be accommodated with a substantial increase in the diameter of the lower link rod, thus driving up the overall size and weight of the EMA. It would also have been necessary to increase the power of the EMA to meet requirements under the additional load. However, because of the above volumetric constraints, there was inadequate room for the necessary expansion of the EMA and thermal seals. It thus became apparent that the EMA concept required a fundamental redesign. During this time the NASA EMA team began to devise alternative concepts in preparation for the anticipated necessity of changing the design.

Existing aft fuselage primary structure and flap design severely bounded alternative EMA layout concepts. All new design concepts also had to address the difficult thermal seal design problem. The development time line was also a driving issue, as the EMA redesign effort came about very late in the over-all project schedule. This precluded selection of designs or methods that appeared to require a substantial technology development effort.

The first concepts for a new EMA layout resembled the V-132 / V-131R atmospheric test vehicle flap actuators. They were based on a linear ball screw EMA in the aft fuselage, but mounted remotely from the flap, and drove the flap through a four-bar linkage. Only the final link rod would penetrate the fuselage skin and attach to the flap at the same location as the original design (Figure 4). Several variants were explored, trading EMA size, power, location, and minimizing rotation of the final link rod relative to the fuselage lower skin or the flap. Initially, it was hoped that isolating the EMA itself from the flap bearing would eliminate the problem of designing a linear ball screw to operate under a substantial bending load and that penetrating the lower skin with just a simple link rod would increase the space available for the thermal seal and reduce the insulation requirement for the lower rod.

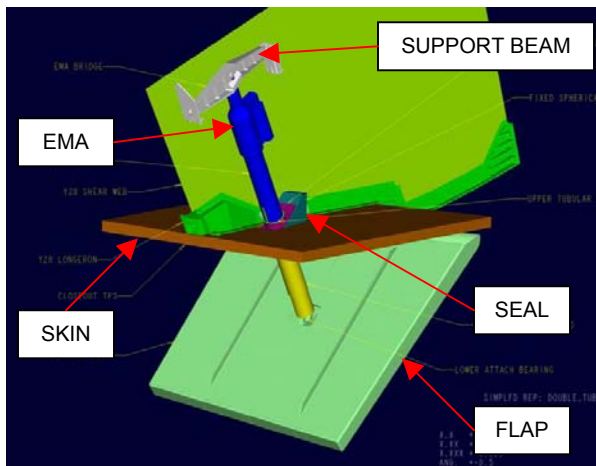


Figure 3. Original linear EMA concept.

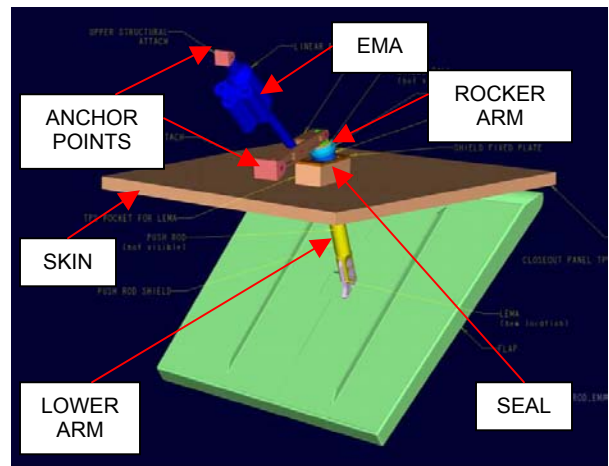


Figure 4. A conceptual 4-bar design

Unfortunately, the various factors did not trade very well. Reducing the amount of rotation required from the flap bearing increased the amount of movement relative to the skin and thus increased seal complexity. Reducing the amount of movement relative to the skin increased the amount of rotation at the bearing. Most of the configurations drove the final link rod to a more disadvantageous angle with the flap, which increased the loads on the flap bearing and the flap hinge bearings to potentially unacceptable levels. Another configuration minimized the rotation at the flap bearing and kept a better angle between the link and flap, but drove the EMA power requirements quite high and pushed it so far up and aft as to be of serious concern to the overall vehicle center of gravity. Additionally, this greatly complicated the thermal seal. Estimates ultimately indicated that all of the configurations would involve a significant weight growth, possibly even double the original design. Stabilizing the complex actuator and linkage train against out-of-plane loads would have introduced additional complexity and weight, which was not accounted for in the conceptual designs and which may not have been achievable. Finally, most of the layouts resulted in a link rod size suitable for the bending loads and relative motion that actually exacerbated the thermal seal design problem. Ultimately, the four-bar linkage concepts failed to address the basic problem of requiring large rotations between the actuator linkage and the flap through the high-friction CSiC bearing.

New Design

Eventually, it became apparent that barring a breakthrough in high-temperature bearing technology, the best chance for success required an actuator concept that eliminated the need for relative rotation between the final actuator link and the flap. Simplification of the relative motion between the actuator and the fuselage lower skin was necessary in order to develop a realistic thermal seal design using available technology. There also remained the requirement for any new actuator design to be compatible with the existing fuselage and flap structures.

Actuator Layout

The most obvious method of achieving the first two goals was to shift the center of rotation of the EMA from inside the fuselage to an axis coinciding with the axis of rotation of the flap, but without requiring any

additional penetration points in the fuselage skin. This was accomplished by changing the final actuator linkage rod to an arc shape analogous to a circumferential segment of a wheel with its center of rotation located on the hinge axis of the flap (Figure 5). The portion of the flap between the hinge bearing and the arc attachment forms one 'spoke' of the 'wheel' and the fuselage structure between the flap hinge mounts and the anchor points of the EMA forms a second 'spoke', which allows freedom of movement of the 'wheel segment' (arc) in the tangential direction.

Linkage

The actuator drive unit transmits power to the circular segment link through a pinion gear that drives a gear segment integrated into the periphery of the circular segment. The drive unit consists of three motors that simultaneously apply redundant power to the pinion gear through a cycloidal transmission. The drive unit holds the arc through a series of 'V' guide rollers that are integral to the drive unit. Two of the rollers are mounted on the same side of the arc as the pinion and to either side of the pinion, and the third roller is mounted directly opposite the pinion. The third roller is mounted on an eccentric cam that can be adjusted to provide the proper compression of the arc between the opposing rollers and thus minimize free-play without inducing too much friction. The pinion gear is mounted on an adjustable Belleville spring stack to maintain a constant radial force between the pinion and sector gear teeth (Figure 6). The only radial connection fixed relative to the circular segment consists of the flap itself. The drive unit is mounted to the fuselage through a bearing mounted trunion at each end of the axis through the pinion gear to form the other 'spoke of the wheel' and fully constrain the actuator location.

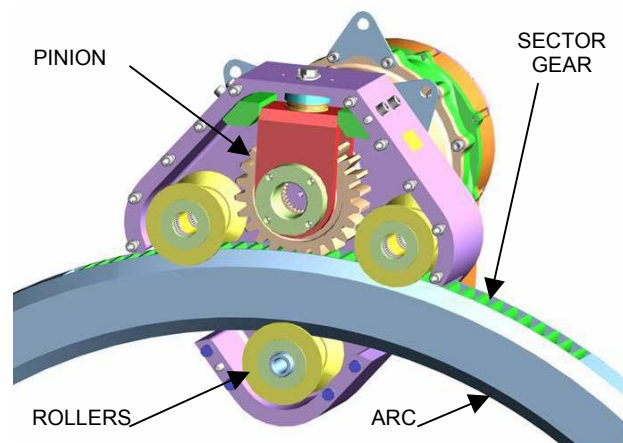


Figure 5. Flap Actuator Assembly Before Installation **Figure 6. Arc Pinon Gear Drive Assembly**

Since the drive unit is mounted completely inside the hull, and since the flap (including the hinges and actuator attach bearing) is mounted completely outside the hull, only the arc penetrates the hull. As the actuator arc moves in and out it remains fixed relative to the flap (since the flap acts as a radius of the circle that the arc moves through). The movement of the arc relative to the skin at the hull penetration is greatly simplified since the circular path of the actuator remains fixed relative to the hull. Since the portion of the actuator that passes through the hull has a constant cross section the seal has a static shape and remains fixed to the hull.

Deflection and Thermal Expansion Relief

Due to differences in the coefficients of thermal expansion of the ceramic flap and aluminum hull structure, the two radial connections to the actuator experience small relative changes through the re-entry profile. By mounting the actuator drive unit on an axis that is free to pivot slightly relative to the vehicle structure, the actuation system can still function even as the two radial fixations vary slightly with respect to each other. Such variations cause a slight displacement of the effective center of the actuator circular segment from the flap hinge line. As the flap rotates, the displacement of the centerlines causes a small rotation of the drive unit about its pivot axis in order to maintain the tangency of the drive unit guide rollers and the circular segment link. This rotation is permitted by allowing the circular segment to rotate

relative to the flap at the connection points by very small amounts, which are within the capability of the high temperature bearing. This also causes a small lateral motion of the arc's circular path relative to the skin at the hull penetration, which is accommodated by letting the seal mounting ring float a small amount parallel to the hull skin.

Redesign Constraints and Issues

Due to the pre-existing fuselage structure and flap geometry, major structural elements interfered with the most logical actuator locations, which caused the already large loads on the actuator to be substantially increased. Because of the canted angle of the flap hinge axis and the necessity of keeping the arc axis parallel to the hinge axis, the arc and its path of rotation were canted relative to the fuselage frames. With the actuator attachment point of the flap located under some of the fuselage primary load paths, it was not possible to locate the arc in an orientation that allowed its lower end to match up with the flap attach point. The flap team was able to make some minor modifications and re-orient the assembly of the support structure for the attach point bearing to move the attach point slightly outboard. An offset foot was then designed into the lower end of the arc to shift the attachment point of the actuator inboard sufficiently to connect with the flap. The offset resulted in large out of plane bending loads applied to the arc, which required the arc to be designed with a generous cross section.

This foot became the interface component between the metallic actuator arc and the CSiC flap bearing plates. The actual interface was accomplished with two large diameter, hollow core CSiC pins that connect the metal foot to the CSiC bearing plates that ride on the CSiC bearing of the flap attach point. One of the two holes on the foot side was slightly slotted towards the other hole to allow for the different thermal expansion rates and for manufacturing differences. Both CSiC pins were fitted snugly into the foot holes with individually cut to fit bushings made of PM1000 oxide dispersion stabilized high temperature alloy from Plansee Aktiengesellschaft of Austria. The bushings eliminated concerns of possible chemical incompatibility between the CSiC and Inconel at elevated temperatures. The bushings also provided an additional break in the conduction path and limited the size of the conduction contact patches, which proved important in reducing the amount of heat conducted into the foot by the hot flap. Thin sheets of woven 3M Corporation Nextel ceramic fabric were placed between the non-load bearing adjacent surfaces of the bearing plates and foot to provide additional thermal protection.

In order to carry the large loads while exposed to the very high temperature and highly oxidizing environment, the arc was fabricated from Inconel 718 super alloy and protected by a refractory metal shell. The offset foot was also fabricated from Inconel 718, but was protected by a semi-rigid fabric blanket composed of layers of woven Nextel ceramic fabric, ceramic batting, and Inconel foil.

The portion of the arc exposed below the thermal protection of the fuselage lower skin could reach surface temperatures well in excess of the capability of Inconel to support any meaningful load. Most of the heating resulted from radiation of heat conducted through the thickness of the flap and reflected off the lower fuselage thermal tiles. Also, the recirculating flow in the cavity between the flap and the lower fuselage skin was sufficient to potentially destroy the Inconel by oxidation. Accordingly, the exposed portion of the arc was protected by TPS. Originally it was planned to use the same blanket system that protected the foot, but testing revealed that under operational conditions it would not maintain sufficient strength to resist abrasion as it passed through the thermal seal. The ultimate concept was to wrap the lower arc with a thick layer of ceramic batting insulation that would be surrounded by a thin shell made of Hitemco R-512E silicide coated Oremet Wah Chang C-103 columbium alloy.

The lower part of the Inconel arc was necked down and the external cross section of the shell was identical to the cross section of the upper part of the arc so that the semi-rigid thermal seal would maintain contact with the arc as the flap rotated. The insulated region of the lower arc was bounded by the location of the lowermost drive unit v-guide bearing when the flap was fully retracted, which limited the flap to approximately half extension during the peak of re-entry heating. This met flight control requirements, with the exception of possible very brief extension of the flap to a sufficient angle to expose a very small region of the bare Inconel to thermal radiation. Analysis showed that with a sufficiently polished surface the Inconel could manage these limited exposures. Overall, the peak heat load would have generated a very large thermal gradient between the lower end of the actuator and the more

temperature critical elements of the drive unit at the upper end. This gradient was achieved primarily by constructing the arc and foot from ample amounts of Inconel, which acted as a very effective heat sink such that the brief heating period was insufficient to achieve anything close to temperature equilibrium.

The flap and actuator together comprised a system with indeterminate load paths, so the loads applied to each component were determined by applying the flight load to a finite element model of the complete system. Analysis of the actuator components ultimately required a very high fidelity finite element model of the complete arc and foot assembly and took considerable computation time. Applying the flap driving load tangent to, and through a curved beam rather than the original straight beam caused an increase in the total load. The increase resulted from the load vector being closer to parallel to the flap and thus 'loosing' the effectiveness of that portion of the load vector. (The actual EMA load vector was determined by the pressure angle of the pinion gear teeth on the 'arc' sector gear teeth.) The extra load applied in the direction parallel to the flap increased the radial loads felt by the flap hinge bearings, exacerbating the already serious friction problem of the CSiC bearings. Moving the drive unit location farther away from the flap caused the load vector to be more parallel to the flap and worsen the load conditions, but moving the drive unit closer to the flap reduced the length of the arc that could be insulated and thus reduced the amount of flap extension available during the peak re-entry heating. Locating the drive unit attach points far from elements of the fuselage structure applied loads that exceeded the capability of the structure, but locating the attach points close to the structure required clearance cut-outs that weakened the structure unacceptably. After an extensive period of iterative design and analysis, a compromise location for the drive unit was determined that kept the radial loads just within the limits of the flap hinge bearings, allowed just enough room for an insulated section of arc long enough to achieve the necessary flap travel, and kept the structural loads just within acceptable limits without causing any uncorrectable interferences with the existing structures. Fortunately the existing structure was able to accommodate a workable solution.

Although recirculating flow of hot gas between the flap and the lower fuselage skin caused oxidation problems for actuator components, the contribution of convection to the overall heating was fairly minor. Most of the heating in the actuator resulted from radiation from the hot structure flap and lower skin thermal tiles, and from conduction through the foot. With the large masses and thick sections of most of the parts, and the brief duration of maximum heating exposure, the total heat input to the parts was of more importance than particular surface or environment temperatures. The complex nature of the actuator design and its operating environment, along with the transient nature of the thermal state, required a separate high-fidelity finite element model for thermal analysis. Because many portions of the actuator reached temperatures that caused significant weakening of the materials, and because the thermal conduction between parts was largely dependent on the contact pressures between them, it was important to maintain an iterative loop between the thermal and stress analysis. Each of the finite element models required different simplifications, but both were derived directly from the detailed design models by direct computer model translation to achieve sufficient fidelity.

In order to minimize the extra load introduced into the flap (especially launch vibration loads) and to minimize the risk of jamming, the arc needed to be very stiff. Achieving sufficient stiffness was difficult in a curved, end-supported beam with a high length to cross section ratio (a good portion of which was substantially necked down) and which was subjected to a large tangential load. Additionally, the resulting high stresses had to be carried at temperatures that could exceed 538°C (1000°F) degrees in some locations. The result was an integrally machined beam composed of thick sections and dense internal webbing to minimize the length of unsupported spans, especially in the region where the guide rollers applied concentrated loads. (The rollers were slightly crowned to minimize friction caused by slipping as the tapered rollers contacted the angled surface with a radius that varied along their length, which reduced the size of the contact patches.) It was also necessary that the bearing surfaces of the completed arc maintain a precise and constant cross-section and have a very smooth surface to ensure proper passage through the rollers when under load. In order to maintain sufficient strength (roughly 80% of room temperature in the worst areas) and oxidation resistance at the elevated temperatures, Inconel 718 super alloy was chosen. Fabricating the large, complex, precision parts from very hard and difficult to machine material turned out to be quite time consuming and caused extensive, unanticipated delays.

A fully articulated, solid, parametric computer model of the flap and actuator system was constructed with all of the components modeled in complete geometrical detail (Figure 7). The complete model could be moved through the full range of flap rotation and deflections could be introduced that represented thermal expansion of the flap support beams and the main flap in both the longitudinal and vertical directions. By constraining the elements of the design model similarly to the actual hardware, it was possible to verify correct functioning of the design even with the main components in a deflected state before any hardware or mockups had been constructed. Essentially, the drive unit rotates about its mounting axis to maintain the tangency of the pinion gear and sector gear regardless of any shifts in the location of the flap hinge axis. Any such shifts cause the axis through the center of the arc path to no longer coincide with the flap hinge axis, which results in a small change in the normally perpendicular angle of the arc to flap connection. As the flap moves under this condition, the angle between the arc and flap will change minutely and within the limits of the bearing capability. Using the computer design model, it was possible to determine the actual amount of movement at the bearing with the system in a thermally deflected state and verify that the movement was acceptable. The computer model was also used to find and eliminate sources of interference and to verify adequate assembly access in the vehicle. Finally, the computer model proved critical for real-time determination of as-built component locations in the vehicle during the initial integration of the flaps and actuators. Without the articulated 3D model, it would have been very difficult to properly align the parts of the mechanism.

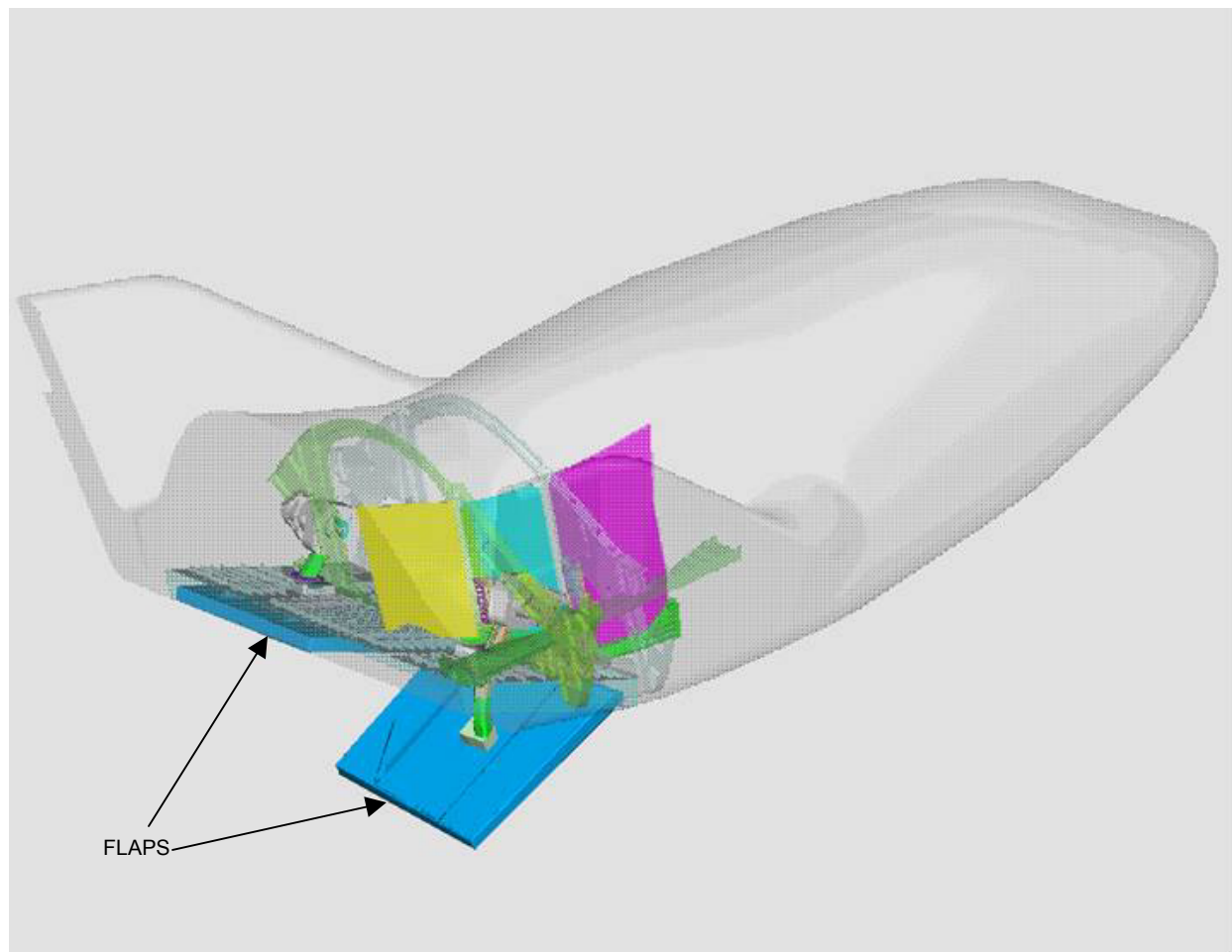


Figure 7. Vehicle Integration CAD Model

The gap formed between the arc and the skin at the location of the penetration through the fuselage required plugging with a thermal barrier or 'seal' to prevent the ingestion of hot gas into the aft fuselage (Figure 8). The seal was mounted to the fuselage skin and the arc slides through the seal as the flap rotates. It was comprised of two loops of conventional Nextel spring tube seals stacked one above the

other for redundancy, increased footprint, and decreased permeability. (The spring tube seals consist of a loose Inconel wire mesh shaped into a tube, wrapped with braided Nextel ceramic fabric, and filled with Saffil ceramic batting.) The tubes were stitched to the Inconel mounting plate with Inconel safety wire and were also captured between a lip in the fuselage skin thermal protection tiles and a lip in the top of the mounting plate. This design was chosen both for its ability to withstand the temperature and oxidation conditions, and because it provided a soft contact surface with the arc, which was critical to protecting the ceramic coating of the lower arc thermal protection shell from abrasion damage. However, it was also necessary for the sector gear teeth to pass through the seal for the flap to achieve full extension during testing and post re-entry flight. To prevent abrasion damage to the seal by the gear teeth, the portion of the seal contacted by the teeth was covered with an Inconel plate or 'shoe' that covered both tubes and prevented the spring tubes from protruding into the gear teeth. To prevent the 'shoe' from abrading the ceramic coating of the lower arc, the assembly of both spring tubes and the 'shoe' was wrapped with a layer of woven Nextel fabric, with the 'shoe' and over wrap held in place by the Inconel stitching. The seal mounting plate was fixed to a small, removable section of the fuselage skin to aid installation and was mounted with a flange captured between the skin section and a capture plate such that it could slide slightly in the plane of the skin to accommodate dislocations of the arc path caused by thermal expansion and aero loading of the system (Figure 9).

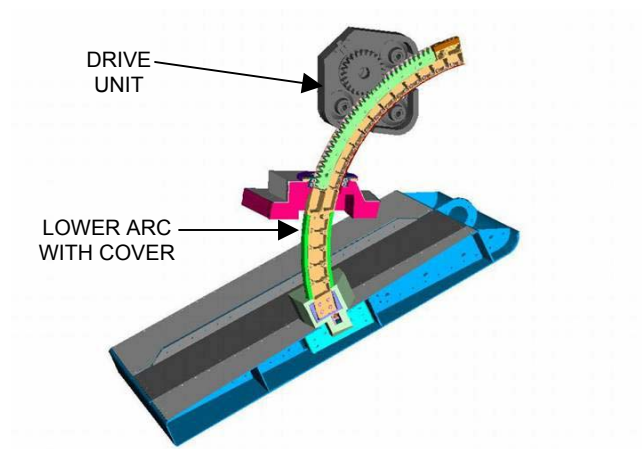


Figure 8. Section through Flap and Actuator System

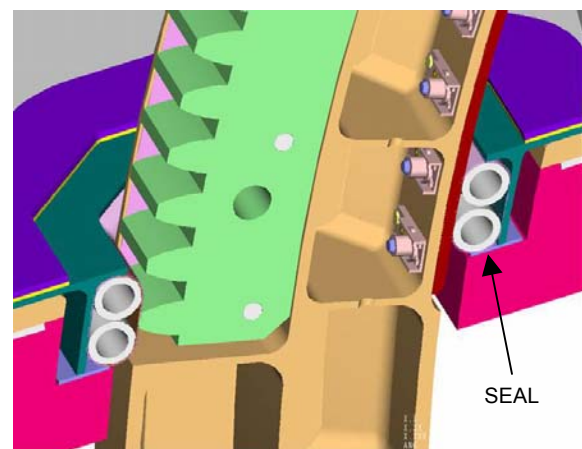


Figure 9. Close-up Section through Thermal Seal

Actuator Drive Unit

The CRV Body Flap Actuation control system (actuator & controllers) was designed, built and qualified by the Systems Group of Moog Inc (Figure 11). It was one of the first space-rated, dual-fault tolerant, electromechanical primary flight control actuation systems.

The actuator was designed to provide full torque and speed performance after any two electrical or controller channel failures. Drive train mechanical redundancy was not provided due to the weight impact and the effect of additional complexity on overall reliability. Instead, large margins of safety and failsafe designs were integrated into the individual components to overcome the reliability concerns.

As shown in the schematic (Figure 10) three redundant motors were torque summed around a common bull gear; which input into a cycloidal drive. The system was designed such that in the event of a motor channel failure the other channel(s) would drag along the failed motor. This eliminated the need for clutches and the problems associated with implementing such devices. The output of the cycloidal drive in turn was connected by a floating crowned spline shaft, which drove the sector pinion gear and subsequent sector gear arc of the flap. The overall actuator drive ratio was 2486.6:1.

Three brushless DC, rare earth, samarium cobalt magnet motors provided power. The rotors were banded with steel sleeves to prevent a rotor / stator jam due to possible failed magnet retention since peak operating speeds of 15300 rpm were possible. A cycloidal drive transmission was chosen because

of its low profile, high stiffness, low backlash, high efficiency and drive train robustness. The cycloidal drive has a large number of “lobe” teeth in contact, which minimizes the operating stresses and makes it ideal for high reliability applications. A crowned spline dog bone shaft bridged the output of the cycloidal transmission and pinion gear. This was required because the pinion gear was spring loaded into the sector gear and allowed to float vertically in order to eliminate backlash and absorb thermal variations within the gear mesh.

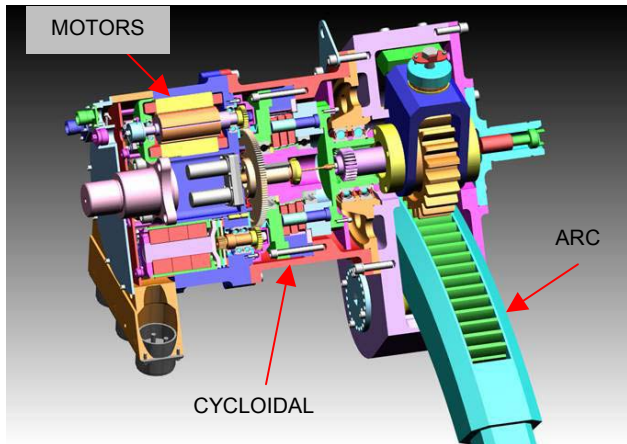


Figure 10. Cutaway View of the Flap EMA Assembly

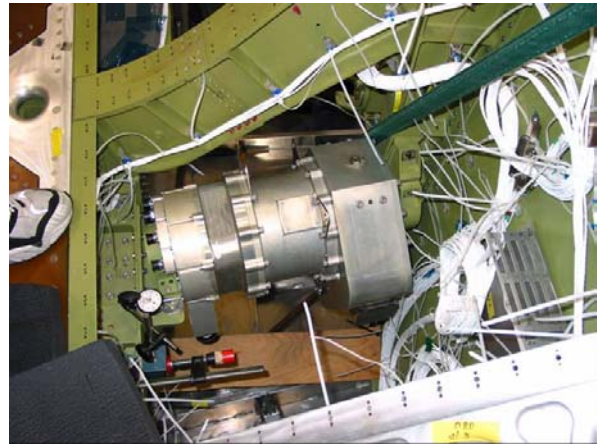


Figure 11. EMA installed.

The offset attachment of the foot to the flap created significant moment loading on the arc that raised concern over gear mesh alignment. To counteract this effect the sector gear was mounted inside an Inconel arc that was supported by three v-shaped conical rollers in a tripod arrangement inside the support box. An eccentric bearing cam pin in the bottom roller was then adjusted to minimize the radial play of the sector arc in relation to the three rollers. The pinion gear was also crowned to accommodate any additional misalignment problems.

The drive unit was mounted on trunions along the axis of the pinion gear. This mounting configuration allowed the actuator to rotate due to the thermal variations in the actuator and flap mounts.

The flap position was monitored by a geared, dual-tandem, brushless resolver (1 model channel / 3 position) that was connected to the pinion gear via a quill shaft arrangement. A triply redundant fail safe brake held the actuator in position during shuttle transport and provided the last defense of control by snubbing the energy and locking the flap in a fixed position in the event of an all out power failure. The brake engaged the same bull gear as the drive motors. The brake incorporated friction plates coated with plasma sprayed chromium oxide for stable operation in a vacuum environment. Dual mechanical limit switches attached to the output of the cycloidal drive protected the actuator when a single channel was active as well as providing an over travel limit.

Vehicle Integration and Testing

Integration of the actuation system with the flaps and completing the associated vehicle attachment proved to be a very challenging process. The process required integrating the flaps which are very large delicate, and expensive, to the vehicle. The axis of rotation of the flaps had to be positioned to extremely tight tolerances, and the rotation needed to be on an axis that was precisely parallel to the axis of the EMA rotating mount. The combination of tight tolerances, close clearances, extremely heavy EMAs (approximately 136 kg (300 pounds) each), and precision alignment provided unique challenges to the integration team.

The total weight of each flap was approximately 61 kg (135 pounds). For their size they are relatively lightweight, but due to the special processes involved in fabrication of them, special handling procedures

were required. Additionally, there are several coating processes that are performed on the ceramic that are sensitive to oils, and gloves are required for handling. Special drilling tools are required for drilling ceramic parts. Each body flap cost approximately 14 million dollars to design, fabricate, test, and qualify for space flight. Therefore, great precaution was taken to preclude damage to the flight units.

The scheme that ultimately proved successful for integration of the flaps and EMAs to the vehicle was a "top-down" installation. The EMAs are dropped into place from open access on the top of the fuselage. Precise positioning of the EMA axis was first performed to CAD specs. Using a laser system, a special tool was employed to measure and position the axis of the EMA rotating mount. The positioning of the EMA was based purely on CAD layout drawings. While the EMA mounts were adjustable, adjustments were very difficult with the unit in place due to the weight and close clearances with primary structure.

Once the EMAs were positioned as close as possible to CAD specifications, an adjusted flap hinge axis location (relative to the vehicle coordinate system) was derived based on the measured EMA axis. Next, physical positions on the flap (co-linear with the hinge-line) were determined using laser tracking. In order to do this, an empirical flap hinge axis was measured based on actual movements of the flap hinges. This empirical flap hinge axis was then positioned relative to the desired hinge-axis positioning on the vehicle.

In order to accommodate various manufacturing tolerances and tolerance build-up, the flap attachment to the vehicle was adjustable in six degrees of freedom at both hinges. Final alignment of the flaps was made through a trial and error combination of special flap positioning tooling and temporary clamping procedures (Figures 12 & 13). The resulting relative angle between the flap hinge-line and the EMA hinge-line was less than approximately 0.05 degree.



Figure 12. Flap Hinge (aft to left)



Figure 13. Flap Hinge Mounting (aft to right)

Once the alignment was finalized, manual test sweeps of the flap through full angular excursion were made to establish proper integrated function of the flap with the vehicle. With proper positioning established, the flaps were matched-drilled to the vehicle with under-sized holes (to allow potential future fine position adjustment), and fastened temporarily.

The final phase began by attaching the EMA arc to the flap at the foot. This process involved special tooling to protect the flap and aid in the positioning of the heavy moving parts of the EMA. Final mating of the arc to the foot and the flap was followed by manual movement of the entire integrated EMA, arc, foot and flap system while bolted to the vehicle. With successful full-range movement established via these manual sweeps, the temporary fasteners were secured in preparation for powered avionics tests.

Finally, with all parts precisely aligned, checked, and bolted together, the entire vehicle avionics system was powered up, flight software was loaded into onboard computers, and computer controlled movements were conducted. Onboard software provided test-movement sequences similar to those that would have been used in flight. The computer controlled movements included moving the flaps up and

down in prescribed sine-wave motions as well as simple step-commands. This testing verified a full functioning, multi-string on-board avionics flight control system with vehicle hardware.

The time from hardware delivery prior to first EMA install to conclusion of full-power avionics testing was approximately six weeks. TPS installation, final drilling of holes for fasteners, and final installation of the flaps were not accomplished before project termination.

Each surface actuation subsystem had four EMA controllers, each controlling three electric motors housed in the EMA subsystem unit. All four controllers are on-line at the same time, and each is talking to each of the three independent motors powering each flap EMA with motor synchronization codes in the controller preventing motors from fighting one another. So for the test with two flaps there were eight controllers and six motors up and running - all cooperating with one another.



Figure 14. Completed Installation (Starboard Flap Deployed)

The system is capable of having multiple failures of controller components and or motor components, and still functioning fully for flight. It is worth noting that this EMA design is unique in that no other redundancy system for control surfaces provides all motors up and running simultaneously. With other systems, other motors are present, but powered off until needed. With this design, everything there is being used, but if a component fails, the system continues to function and meet requirements with what is left running.

Status

The actuator mechanical units for the flight test vehicle have been fabricated and installed (Figure 14). Some functional testing was successfully completed with the unit installed in the vehicle before the project was terminated. A flight-design actuator qualification unit was successfully tested by the drive unit contractor, Moog, in a loaded test stand that simulated the full aerodynamic load. Initial component level testing of the seal showed promising success, but later testing indicated some seal abrasion problems that remain to be resolved.

The thermal seal system and actuator thermal protection system reached only component level prototype fabrication before the project was terminated. Detailed design of the thermal protection shell for the lower arc and of the seal mount to fuselage skin interface were not completed. The flight unit flaps were installed on the vehicle, but without using the flight design fasteners. The vehicle lower skin was temporarily removed for integration of the flaps and actuators, but was never reinstalled, which would require temporary removal of the flaps and actuators. The flight unit controllers were used for testing, but with temporary mounts and wire routings.

Conclusion

Despite the premature termination of the X-38 V-201 project, the flap actuator development team learned a number of valuable lessons.

Concerns regarding the feasibility of constructing and installing the arc with sufficient accuracy to permit smooth operation of the actuator beset the team from the beginning of the redesign, yet it ultimately functioned perfectly. However, with little experience to serve as a guide, all of the parts were designed and fabricated to the tightest possible tolerances and weeks of effort were spent to align the flaps and actuators as close to the theoretical locations as possible (including offsets for known errors). Also, many elements of the system were devised to reduce free play between the components as much as possible since it was unknown how much would be acceptable. Such extreme efforts added substantial expense and in the future it would be instructive to explore the tolerance for errors of this actuator configuration. In particular, the fabrication of the large Inconel parts became far more difficult than anticipated and only succeeded after multiple failed attempts, the details of which exceed the scope of this paper.

Altogether, creating the actuator system utilized at least five different computer aided design (CAD) systems. Three separate systems were used for the design: one each by the flap supplier, the drive unit supplier, and the vehicle integration team. The integration team alone also used two other systems, one for stress analysis and one for thermal analysis. Keeping all of the different models synchronized was a significant problem that was seriously compounded by the great difficulties of translating between the different parametric, solid model CAD systems. The difficulties of translating between human languages, different systems of measurement, and coordinating across worldwide distances were trivial compared to the problems and the vast amounts of lost time translating between the CAD systems. In retrospect, more effort should have been made to standardize on a single system as the practical state of the art in CAD translation leaves much to be desired.

Somewhat outside the scope of this discussion of the actuator, but worth noting, was the difficulty of installing and aligning the flap system. The hinge design had far too many degrees of freedom between all of the parts and required an inordinate amount of time to integrate on the vehicle. Future projects would do well to reduce the number of degrees of freedom during installation and design into the hardware tooling that allows for optimal mechanical positioning adjustment. Elements as delicate and expensive as hot control surfaces should not be left to hand-clamping systems for mechanical adjustments and installations.

Although incomplete, progress to date on the seal system has identified a dearth of suitable technology for flexible, high temperature and oxidation resistant materials that are sufficiently robust to form elements of a mechanical system intended to operate in the hypersonic environment. Several intriguing concepts

were identified, but their development would have exceeded the scope of the available time and resources of this project.

Insufficient understanding of the implications of the extreme operating environment on the actuator design and the absence of adequate detail of the actuator system early enough in the vehicle conceptual design process lead to an unworkable actuator design that was corrected only through a complete redesign of the system late in the project schedule. What would have been a very challenging design under any circumstances became all the more difficult due to the necessity of accommodating the advanced state of maturity in the rest of the vehicle design and operating under a compressed development schedule. In retrospect, the actuator conceptual design should have received higher priority during the overall vehicle layout and particularly in concert with the flap and aft fuselage configuration. As it turned out, only the adoption of an unusual, complex, and “challenging to implement” design and extraordinary effort by the team members along with a great deal of good fortune determined the difference between failure or success of the flap actuator system. Preventing the actuator redesign from becoming a pacing item for the project schedule with such a delayed start required the expenditure of substantially more resources than had been expected for this system.

It is easy to criticize the absence of emphasis on this system in the early project phases in hindsight, but the reality is that at the time, the team lacked the experience necessary to realize the challenges ahead in this system. During the early stages of the project, there was very little recent experience developing re-entry vehicles anywhere in the industry, let alone small re-entry vehicles with active control surfaces. Since the time of the project, the authors have been involved in and observed a number of other, similar projects in the early phases of development and many of them seem to also lack a sufficient early emphasis on understanding the issues of the control surface actuator systems. It must be understood that in a small re-entry vehicle with control surfaces mounted on thin airfoil sections, the actuators of those surfaces will be exposed to environmental conditions unlike anything found in lower speed aircraft and they can not be isolated from those conditions as effectively as would be possible in larger hypersonic vehicles. The actuator development risks simply cannot be estimated by analogy to similar sized airplanes or to the space shuttle, despite the natural tendency to do so.

Acknowledgements

The authors wish to acknowledge the team members that contributed to the system described in this paper: NASA Johnson Space Center (JSC) Engineering Directorate (System Integration, Actuator Mount and Linkage, Thermal Seals), Lockheed Martin Space Operations via NASA/JSC Science, Engineering, Analysis, & Test contract (System Integration, Actuator Mount and Linkage, Thermal Seals), Moog Inc., Motion Systems Division (Actuator Drive Unit), Oceaneering Thermal Systems, (Thermal Seal), MAN Technologie AG Space Technology Division (Body Flap).

References

1. Hagen, Jeffrey D. “Actuator Installation, V-201 Body Flap” SGK51355379 – NASA/JSC Engineering Drawing Control Center.
2. Eckert, A. & Steinacher, A. “X-38 Body Flap Assembly and Integration Procedure” TET-MAN-11-AIP-1013 – MAN Technologie.
3. Layer, C. “E.M. Actuator Assembly Model 176E111” C52002 – Moog Inc., Motion Systems Division.
4. Curry, Donald M. & Handrick, Karin E. “Dynamic and Static High Temperature Resistant Ceramic Seals for X38 Re-entry Vehicle” 53rd International Astronautical Congress – IAC-02-1.3.01.
5. Curry, Donald M. et al. “Further Investigations of Control Surface Seals for the X-38 Re-entry Vehicle” AIAA-2001-3628 – American Institute of Aeronautics and Astronautics.

REPORT DOCUMENTATION PAGE			Form Approved OMB No. 0704-0188	
Public reporting burden for this collection of information is estimated to average 1 hour per response, including the time for reviewing instructions, searching existing data sources, gathering and maintaining the data needed, and completing and reviewing the collection of information. Send comments regarding this burden estimate or any other aspect of this collection of information, including suggestions for reducing this burden, to Washington Headquarters Services, Directorate for Information Operations and Reports, 1215 Jefferson Davis Highway, Suite 1204, Arlington, VA 22202-4302, and to the Office of Management and Budget, Paperwork Reduction Project (0704-0188), Washington, DC 20503.				
1. AGENCY USE ONLY (Leave Blank)	2. REPORT DATE May 2004	3. REPORT TYPE AND DATES COVERED NASA Conference Paper		
4. TITLE AND SUBTITLE 37 th Aerospace Mechanisms Symposium			5. FUNDING NUMBERS	
6. AUTHOR(S) Edward A. Boesiger, Compiler				
7. PERFORMING ORGANIZATION NAME(S) AND ADDRESS(ES) Lyndon B. Johnson Space Center Houston, Texas 77058			8. PERFORMING ORGANIZATION REPORT NUMBERS S-930	
9. SPONSORING/MONITORING AGENCY NAME(S) AND ADDRESS(ES) National Aeronautics and Space Administration Washington, DC 20546-0001			10. SPONSORING/MONITORING AGENCY REPORT NUMBER CP-2004-212073	
11. SUPPLEMENTARY NOTES				
12a. DISTRIBUTION/AVAILABILITY STATEMENT Unclassified/Unlimited Available from the NASA Center for AeroSpace Information (CASI) 7121 Standard Hanover, MD 21076-1320 Subject Category 35			12b. DISTRIBUTION CODE	
13. ABSTRACT (Maximum 200 words) The Aerospace Mechanisms Symposium (AMS) provides a unique forum for those active in the design, production and use of aerospace mechanisms. A major focus is reporting problems and solutions associated with the development and flight certification of new mechanisms. Organized by the Mechanisms Education Association, NASA and Lockheed Martin Space Systems Company (LMSSC) share the responsibility for hosting the AMS. Now in its 37th symposium, the AMS continues to be well attended, attracting participants from both the U.S. and abroad. The 37th AMS, hosted by the Johnson Space Center (JSC) in Galveston, Texas, was held May 19, 20 and 21, 2004. During these three days, 34 papers were presented. Topics included deployment mechanisms, tribology, actuators, pointing and optical mechanisms, Space Station and Mars Rover mechanisms, release mechanisms, and test equipment. Hardware displays during the supplier exhibit gave attendees an opportunity to meet with developers of current and future mechanism components.				
14. SUBJECT TERMS mechanisms, deployment, tribology, actuators, optical, Rover,			15. NUMBER OF PAGES 405	16. PRICE CODE
17. SECURITY CLASSIFICATION OF REPORT Unclassified	18. SECURITY CLASSIFICATION OF THIS PAGE Unclassified	19. SECURITY CLASSIFICATION OF ABSTRACT Unclassified	20. LIMITATION OF ABSTRACT Unlimited	
